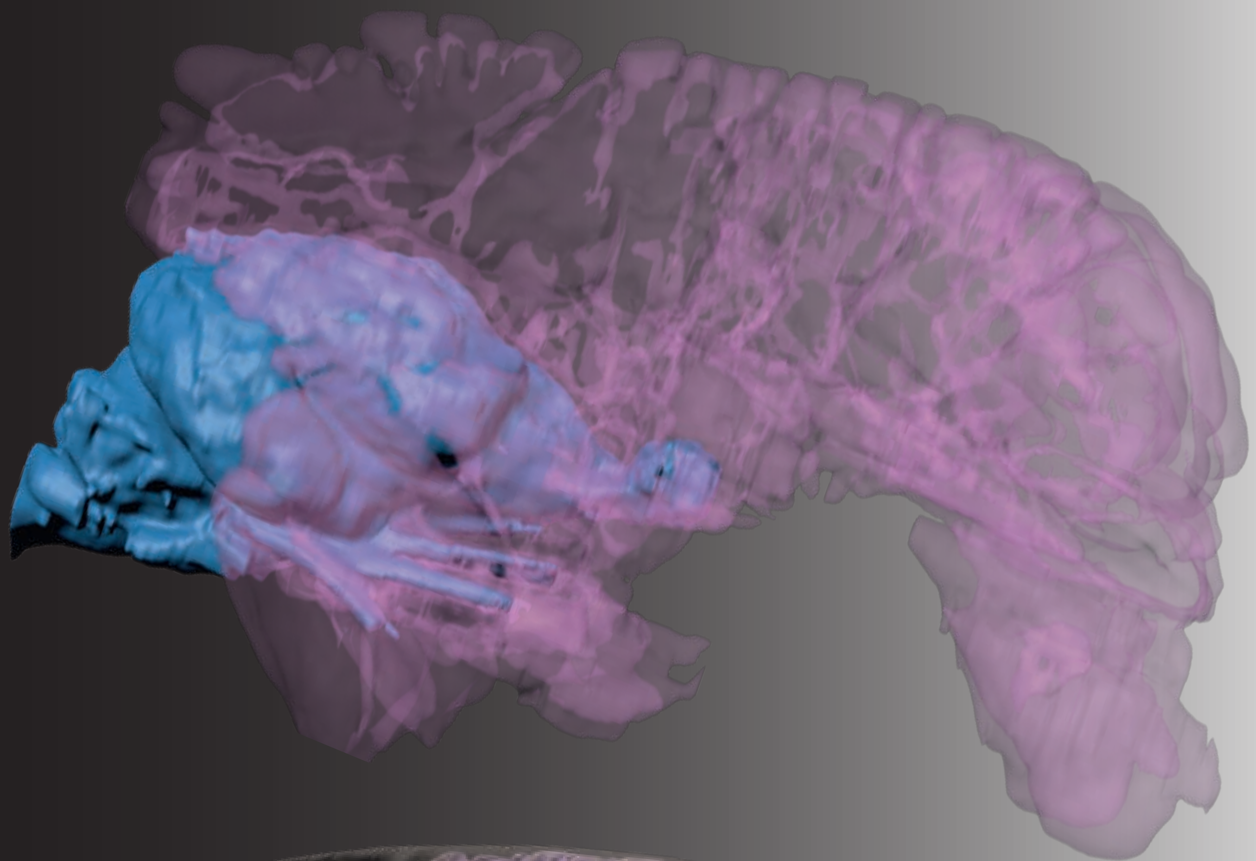

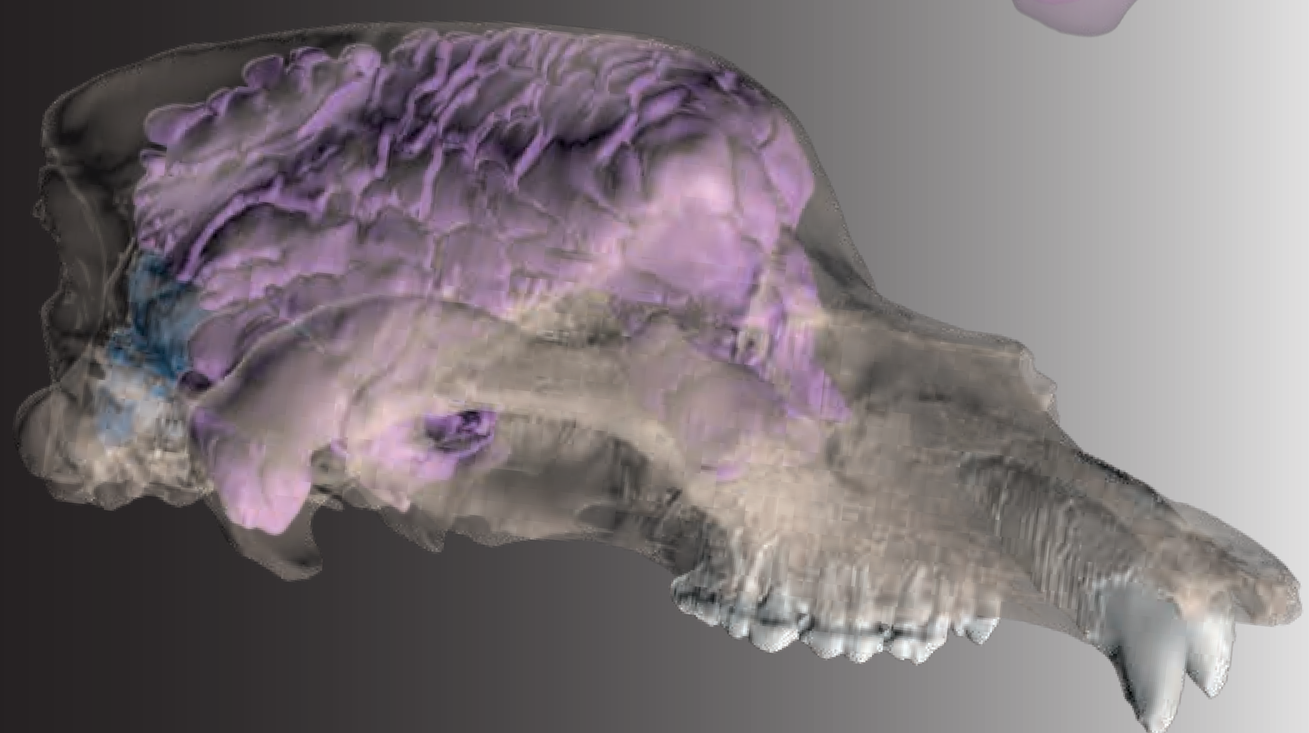

2020

New approaches in vertebrate ecomorphology and evolution: the palaeobiology of the cave bear and the short-faced bear as study cases

Alejandro Pérez Ramos

PhD THESIS

PhD THESIS

New approaches in vertebrate ecomorphology and evolution: the palaeobiology of the cave bear and the short-faced bear as study cases

by **Alejandro Pérez Ramos**

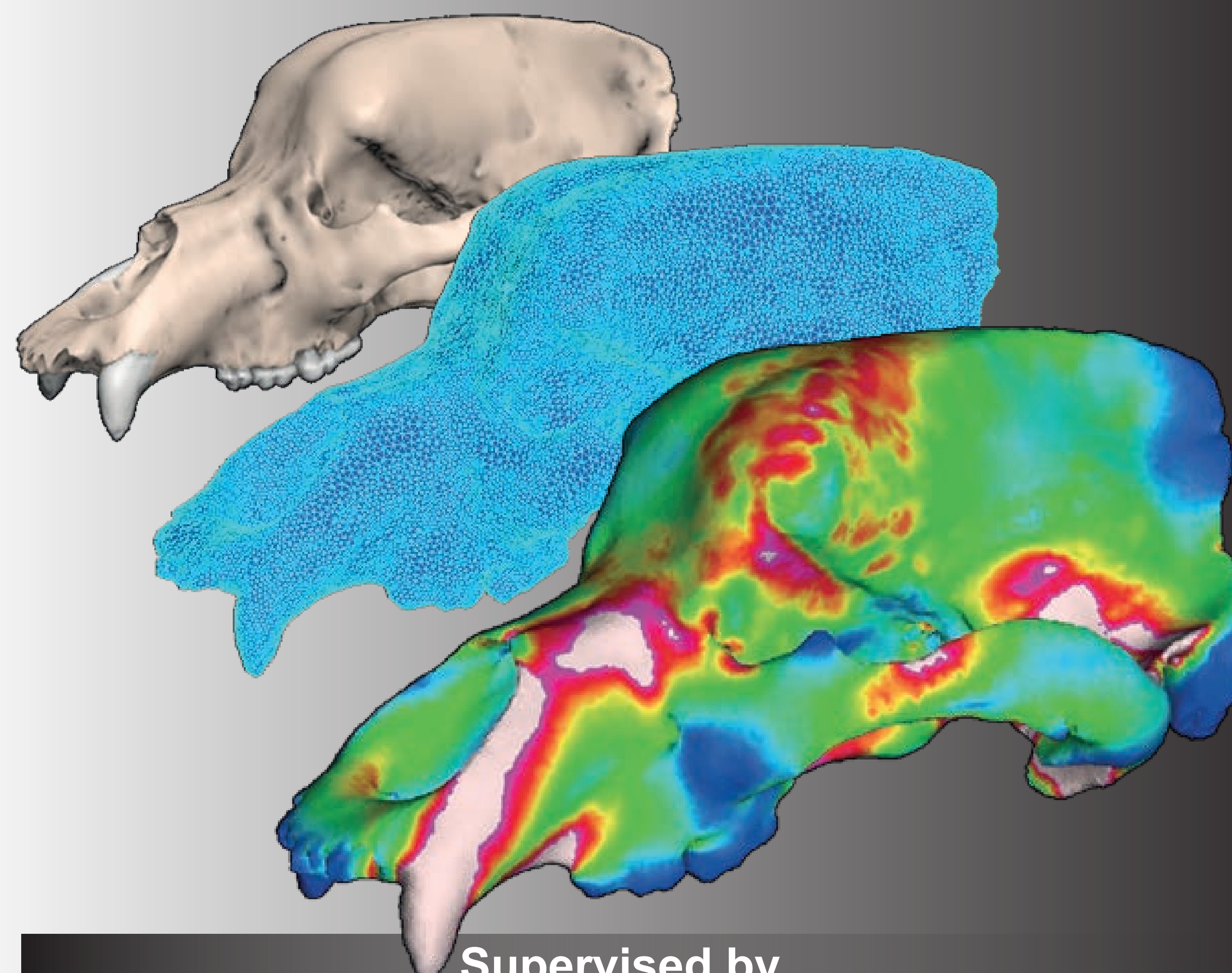

Supervised by
Dr. Francisco De Borja Figueirido Castillo

FACULTAD DE CIENCIAS
UNIVERSIDAD DE MÁLAGA

PhD Program: DIVERSIDAD BIOLÓGICA y MEDIO AMBIENTE

2020

UNIVERSIDAD
DE MÁLAGA

AUTOR: Alejandro Pérez Ramos

http://orcid.org/0000-0003-1417-4338

EDITA: Publicaciones y Divulgación Científica. Universidad de Málaga

PhD THESIS

New approaches in vertebrate ecomorphology and evolution: the palaeobiology of the cave bear and the short-faced bear as study cases

by Alejandro Pérez Ramos

Supervised by
Dr. Francisco De Borja Figueirido Castillo

FACULTAD DE CIENCIAS
UNIVERSIDAD DE MÁLAGA
PhD Program: DIVERSIDAD BIOLÓGICA y MEDIO AMBIENTE

2020

INFORME DE ACEPTACIÓN DE LA DEFENSA DE LA TESIS

Título de la tesis: New approaches in vertebrate ecomorphology and evolution: the palaeobiology of the cave bear and the short-faced bear as study cases.

Por el presente informe, **Dr. Francisco De Borja Figueirido Castillo** con **DNI 44796479T**, supervisor y tutor del investigador predoctoral **Alejandro Pérez Ramos** con **DNI 53219843M, CERTIFICA** que el desarrollo y la elaboración de tal tesis doctoral ha sido realizada de forma correcta a nivel de contenido, presentación y resultados. Tales resultados son avalados por dos publicaciones, una de estas publicaciones; "Dental caries in the fossil record: a window to the evolution of dietary plasticity in an extinct bear. Scientific reports 7:17813"; es esencial para su acceso a la lectura de Tesis. Por tanto, yo Dr. Borja Figueirido Castillo **AUTORIZO** la defensa y lectura de la misma.

Además en este presente informe se **DECLARA** que tanto por parte del supervisor/Tutor y el investigador predoctoral de **NO USAR** este artículo referido en otra tesis doctoral.

supervisor/Tutor
D. Francisco De Borja Figueirido Castillo

PhD candidate/ investigador predoc.
Alejandro Pérez Ramos

Dedicado a mis abuelos,

por darme el cariño y las fuerzas

para llegar hasta aquí.

Estéis donde estéis,

mis logros son vuestros logros!!.

Os quiere vuestro nieto.

Acknowledgments

After a long way of learning as a researcher during the progress of my PhD Thesis, personally, I feel very grateful and honored to be part of the Paleontology research group of the University of Malaga. I owe all this to my supervisor, Dr. Borja Figueirido for many reasons. First, to give me the opportunity to develop a PhD Thesis, and helped me to grow up as a researcher. Second, for his patience and understanding, which helped me to solve all the problems that arose during this period. Third, his ability to manage the research towards my main goals improved my as a researcher. Four, personally, he has helped me to known which are my strengths and my weaknesess. He has been there in my worst and best moments, helping me and advising me the steps to follow. For all of this, I am very gratefull to Dr. Borja Figueirido. THANK YOU!!

Along these years in the department of Ecology and Geology of the Faculty of Sciences, I have been able to meet professionally and personally, the team that makes up the Paleontology research group. Such researchers are Dr. Paul Palmqvist, Dr. Juan Antonio Pérez, Dr. Antonio Guerra, Dr. Alberto Martín, Dr. Francisco Jose Serrano, Dr. Patrocinio Espigares, Dr. Sergio Ros, Carlos Coca and the newly arrived graduate student Alejandro Granados.

I thank Dr. Paul Palmqvist for being always available to talk about many issues. I appreciate his great help and I appreciate the trust and friendship that has been generated between us. I also thank Dr. Juan Antonio Pérez for his great help and advice for developing mathematical analyses. Personally, he has a lot of charisma and sense of humour. He and Paul are the pillar of the group. I thank Dr. Antonio Guerra for being there from the beginning and advising me as a professional and 'personal father'. I appreciate very much his great tiramisu (very famous in the department). I thank Dr. Patrocinio Espigares and Dr. Sergio Ros for supporting and encouraging me to do my best in the PhD and for the good times we have been through. I thank Dr. Alberto Martín and Dr. Francisco Serrano for helping me from the beginning as if they were two brothers and for all those moments we have spent in the office talking about various topics. I thank my great friend, Dr. Carlos Coca. My friendship with him started at the University of Valencia many years ago, he is my confidant and the person who has helped me to disconnect from work. Thank you for all those moments of disconnection, visiting places in Málaga and the surrounding area and going to the cinema or talking about a thousand of topics. I also dedicate a big thank to who I consider my mentor and who in my hardest moments acted as a father, Dr. Miquel De Renzi, palaeobiologist at the Cavanilles Research Institute of Valencia. I started my professional career with him, within the line of EVO-DEVO, developing my skills in histology and evolutionary developmental biology. Within this line of research, I also thank Dr. Diego Rasskin for collaborating together and learning more about evolutionary theoretical biology. He is a great friend and person. In this field of study, I would also like to thank Dr. Ximo Carrasco, a specialist in bone medical histology and pathology, with whom I learned to use BoneJ software. He is the husband of a great friend from the University of Valencia, Dr. Ana Garcia, currently director of the Burjasot Campus Museum (Valencia), along with which I collaborated in her museum as a monitor and researcher. Another great friend, almost like a mother, Dr. Marga Belinchón, director of the Museum of Natural Sciences of Valencia. Thanks to her, along with Dr. Miquel de Renzi, and Dr. Diego Rasskin, I was able to start in bone evolutionary research. On the other hand, I thank Dr. Plinio Montoya, who gave me the opportunity to excavate a paleontological site (Venta del Moro) when I was a university student. Personally he is a great professional friend with whom I have had a great time. In this excavation, I met Dr. Juan Abella and Dr. Alberto Valenciano, thank you for trust in me when collaborating together and for the great professional relationship we have. During this time I have also meet Dr. Jorge Morales (Director of the Batallones site). I really appreciate the opportunity that he gave me to go to this site. At the same time, I also met Dr. Manuel Salesa, Dr. Gema Siliceo and the great illustrator Mr. Mauricio Anton. I appreciate everything I learned during my stay with them and their friendship. They also encouraged and supported me to reach the end of the PhD Thesis. I thank Dr. Paco Pastor for offering me material for my thesis and for collaborating with my supervisor. I also thank Dr. Joan Madurell, Dr. Aurora Grandal, Dr. Anneke Van Heteren and Dr. Blaire Van Valkenburgh for helping me to obtain cranial material for my PhD Thesis. Without their contribution, it would have been impossible to execute and finish my PhD Thesis. I appreciate Dr. Jack Tseng for all these years that has helped me to learn the knowledge in biomechanics necessary for the development of my Thesis in this area. I also thank Jack for your contribution and support in cranial tomography samples. On a professional level, it is a great opportunity to collaborate with him and start new research projects. On a personal level, he is very kind and close person, who has helped me during my training as a researcher in virtual Paleontology. I also thank other international researchers, such as Dr. Rabeder, thank you for the confidence you have had in my research, and for the help with the access to the cranial material of cave bears. For me it is a pleasure to collaborate together in the development of my thesis.

I also thank Dr. Daniel de Miguel, Dr. Marta Pina, Dr. Josep Fortuny, Dr. Jordi Mercé, Dr. David Alba and Dr. Angel Hernadez for supporting me during my stay at the ICP. Finally, I thank Mr. Sergio Llacer for being my right arm. Finally, I thank Dr. Pertusa Grau, who showed my interest in image analysis and enhanced my knowledge in this scientific area. He is a great friend with whom I always learn professionally and personally. Finally, Dr. Alejandro

Romero for being always prone to help me and advice me in the research on teeth evolution in mammals.

THANK YOU ALL FOR HELPING ME TO GET WHERE I AM AND TO BE WHO I AM!

Index

1. Introduction and Aims..1

1.1. Introduction..3

1.1.1. General overview...3

1.1.2. The palaeobiology of the cave bear (*Ursus spelaeus*) and the American short-faced bear (*Arctodus simus*)........................6

1.1.3. Brief introduction to Pleistocene palaeoclimatology...11

1.2. Aims...15

1.3. References...17

2. Material and Methods. 27

2.1. General overview...29

2.2. Image acquisition of 3D models 30

2.3. CT scans processing 33

2.3.1. Image stack calibration and CT segmentation 33

2.3.2. Image cleaning filters 37

2.3.3. Unifying parts of image stacks 39

2.3.4. Interpolation process..40

2.4 Virtual reconstruction of fossil skulls...44

2.4.1. *Ursus ingressus* skull (PIUW3000/5/105).........................44

2.4.2. *Ursus spelaeus spelaeus* skull (E-ZYX-1000) 46

2.4.3. *Ursus spelaeus eremus* skull (PIUW-SW 483).................48

2.4.4. *Ursus spelaeus ladinicus* skull (PIUW-CU 703)................49

2.5. Mesh post-processing and mesh topological deviation 51

2.6. References. 56

3. Results & Discussion. 59

3.1. A three-dimensional analysis of tooth-root morphology in living bears and implications for feeding behaviour in the extinct cave bear. 60

3.1.1. Abstract 61
3.1.2. Introduction 62
3.1.3. Materials and Methods 63
3.1.3.1. Materials. 63
3.1.3.2. CT pre-processing 64
3.1.3.3. Tooth-root area calculation 65
3.1.3.4. Dietary classification of living taxa....................................69
3.1.3.5. Statistical analysis 72
3.1.4. Results 73
3.1.4.1. Profiles of RA and the association with diet.............73
3.1.4.2. Multivariate analyses 78
3.1.5. Discussion 83
3.1.5.1. Patterns of RA profiles and feeding behaviour in living bears 83
3.1.5.2. Feeding ecology of cave bears as inferred from RA profiles of maxillary teeth 85
3.1.6. References 88
3.1.7. Supplementary Material 98

3.2. Evolution of dental complexity and feeding behaviour in extinct cave bears (*Ursus spelaeus* s.l.)..103
3.2.1. Abstract 105
3.2.2. Introduction 106
3.2.3. Dental Topography: a new tool for inferring feeding adaptation in mammal...108
3.2.4. Materials and Methods 109
3.2.4.1. Materials..109
3.2.4.2. Moulding dental casts 109
3.2.4.3. Three-dimensional processing 110
3.2.4.4. Quantifying complexity of tooth crown surfaces 111
3.2.4.5. Statistical Analyses 112
3.2.5. Results. 113
3.2.5.1. The influence of phylogeny on DNE, RFI and 3D-OPCR 113
3.2.5.2. The influence of feeding behaviour on DNE, RFI and 3D-OPCR 120
3.2.5.3. The influence of allometry 122
3.2.5.4. Principal Components Analysis..............................124

3.2.6. Discussion and Conclusions 125
3.2.6.1. Dental topographic analysis and feeding behaviour in living bears 125
3.2.6.2. Dietary inferences in cave bears based on dental topographic analysis 128
3.2.7. References 130
3.2.8. Supplementary material.. 137
3.3. Biomechanical simulations reveal a trade-off between adaptation to glacial climate and dietary niche versatility in European cave bears. 143
3.3.1. Abstract 145
3.3.2. Introduction 146
3.3.3. Materials and Methods 147
3.3.3.1. Materials 147
3.3.3.2. Three-dimensional processing 150
3.3.3.3. Finite Element Analysis of the skull with sinuses. . .151
3.3.3.4. Finite Element Analysis of the skull without sinuses. 154
3.3.3.5. Comparing the effects of paranasal sinuses in feeding biomechanics 155
3.3.4. Results 156
3.3.4.1. Finite Element Analysis with sinuses 156
3.3.4.2. Finite Element Analysis without sinuses 163
3.3.4.3. Comparing FE analyses with and without sinuses. 167
3.3.4.4. Structural analysis of the Von Mises stress of the skull due to sinus expansion in the speloid lineage.. 170
3.3.4.5. The role of paranasal sinuses in conforming the speloid morphotype.. 172
3.3.5. Discussion 176

3.3.5.1. Sinuses size and feeding biomechanics in living and extinct bears 176

3.3.5.2. The selective advantage of having large sinuses in bears: hibernation length 180

3.3.5.3. Sinuses, hibernation and feeding biomechanics in cave bears.. 182

3.3.6. References. 184

3.3.7. Supplementary material 189

3.4. Paranasal sinuses in European cave bears (*Ursus spelaeus* s.l.) allowed long hibernation periods by decreasing basal metabolic rates. 215

3.4.1. Abstract 217

3.4.2. Introduction 218

3.4.3. Material and methods..223

3.4.3.1. Material 223

3.4.3.2. Inferring BMRs and hibernation length in cave bears. 224

3.4.3.3.Testing the influence of sinus size on BMR and hibernation length 227

3.4.3.4. Histomorphometric analysis ofcancellous bone. .228

3.4.4. Results and discussion 231

3.4.4.1. Hibernation length in cave bears 231

3.4.4.2. Sinuses volume and basal metabolic rates 235

3.4.4.3. Trabecular density in cave bears. 241

3.4.5. Future research 245

3.4.6. References……………………………………………… 246

3.4.7. Supplementary material 252

3.5. Dental caries in the fossil record: a window to the evolution of dietary plasticity in an extinct bear 257

3.5.1. Abstract 259

3.5.2. Introduction 260

3.5.3. Material and Methods...261

3.5.3.1. Data acquisition...262

3.5.3.2. Three-dimensional (3D) models. 263

3.5.3.3. Microscopic analyses.. 263

3.5.3.4. CT scan. 264

3.5.4. Results.. 265

3.5.5. Discussion.. 268

3.5.6. References.. 272

3.5.7. Supplementary material.. 277

4. Conclusions... 335

4.1 Synthesis. 337

4.2 Conclusions 347

4.3 References 349

5. Resumen 357

5.1. Introducción 359

5.1.1. La paleobiología del oso de las cavernas (*Ursus spelaeus*) y el oso de cara corta norteamericano (*Arctodus simus*).. 361

5.2. Objetivos..365

5.3. Principales resultados 367

5.4. Síntesis y conclusiones 375

5.5. Referencias..381

6. Appendix 389

.Table 1 (**Table S1 Chapter 3.2**)..391

.Table 2 (**Table S2 Chapter 3.2**)..394

1

Introduction

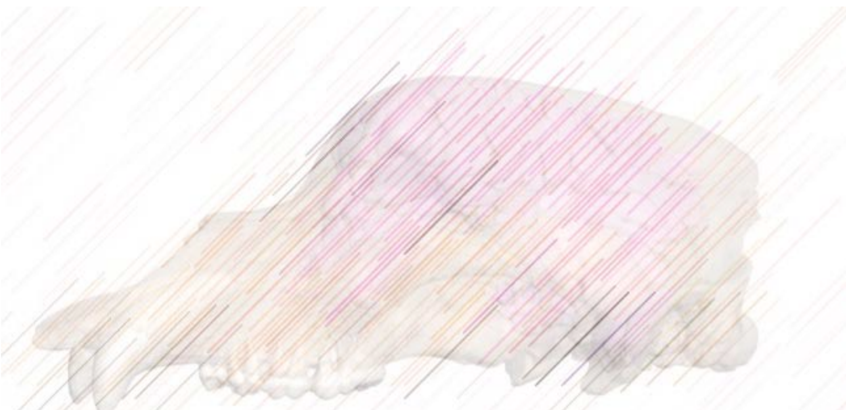

1.1. Introduction

1.1.1. General overview

During the last decade, the 'revolution' of digital technology has allowed the emergence of new digital tools of virtual analysis, such as high-resolution computed tomography, structured-light surface scanning or specific software for digital analysis of any kind. These new analytical tools have allowed to surpass the frontiers of knowledge in many fields, which have opened new horizons of research in many disciplines such are in Ecomorphology, Evolution, and specially in Palaeobiology. This digital 'revolution' has substantially changed the way of analyzing the scientific material, and more particularly fossils, generating new fields of research at different levels of analysis that were previously inaccessible. For example, this is the case of histological studies in fossils with non-invasive techniques (i.e., virtual palaeohistology; e.g., Sánchez et al. 2012), virtual reconstructions of distorted fossil specimens with lacking parts (i.e., retro-deformation techniques; e.g., Tallman et al. 2014), development of powerful biomechanical models (i.e., finite element analysis; e.g., Figueirido et al. 2018), or the study of internal structures, non-accessible without using invasive techniques such as brain endocasts (i.e., palaeoneurology; e.g., Cuff et al. 2016) or paranasal sinuses and turbinates (i.e., functional anatomy of internal structures; e.g., Curtis et al. 2014; Van Valkenburgh et al. 2014). All these techniques undoubtedly lead to new avenues for future research in ecomorphology and evolution of extinct vertebrates.

Moreover, this new 'virtual world' has significantly changed how scientists conceive the osteological collections of enduring data of three-dimensional virtual models, offering to the scientific community a new approach to access and investigate the material under study. As a matter of fact, virtual free-access collections to scientist, such as the recent Morphomuseum (https://morphomuseum.com/) or the pioneer Digimorph (http://digimorph.org/) are substantially increasing. In addition, such digital collections have been used to detect fossil fakes or to have a digital copy that can be preserved against possible loss of the original fossil.

All these virtual techniques of analysis are based on the three-dimensional acquisition of the object subject to analysis. This could be done by using laser, modulated-light, or structure-light surface scanning to digitalize the external surface or by using high-resolution Computed Tomography (CT) to digitalize both the external and internal structures. This process is usually based on different technologies, each with its own limitations, advantages and costs. Accordingly, for the generation of 3D virtual models, several acquisition parameters must be taken into account, such as the electrical voltage, the intensity, and distance between cuts, etc. (Zollikofer et al. 2005; Endo et al. 2009; Kak et al. 2002). Once the three-dimensional object has been digitized, the resulting image stacks should be enhanced eliminating the background noise and reconstructing possible artefacts. To do this, different algorithms and digital filters are already implemented in the specific software of virtual reconstruction and image processing such as Meshlab (Cignoni et al. 2008) or ImageJ (Rueden et al. 2017). Afterwards, the enhanced final images should be segmented by thresholding of the grey-values histogram (Pertusa 2010). This process is very sensitive and dependent on the property of the materials such as bone density and mineralization, among others. Subsequently, the virtual model of the object is generated and can be subject to ecomorphological or biomechanical analyses with the objective of investigating aspects of the palaeobiology and evolution of extinct species. In addition, such models can be printed out using rapid prototyping to have a physical replica of the object under study, and therefore, improving the anatomical understanding.

Therefore, these new three-dimensional analytical tools mark a before and an after in paleontological research.

In this PhD thesis, I use different three-dimensional techniques of analysis based on the acquisition of external and internal anatomy –using surface scanning and computed tomography, respectively– with a great potential to go far beyond the state of the art of ecomorphology and evolution across different groups of extinct vertebrates. In **chapter 2**, I summarize and explain in further detail the techniques used and I also give an intuitive perspective of its potential to open new avenues for future research. In the same chapter, I also describe more precisely all techniques used to restore the 3D models of fossil skulls in order to make appropriate cases to be analysed with the specific software.

To investigate the potential of such techniques, I focus on the palaeobiology of two iconic bears of the Late Pleistocene megafauna –the Eurasian cave bear, *Ursus spelaeus* s.l., and the American short-faced bear, *Arctodus simus*– as study cases. As detailed in the next section of this chapter, I chose these two extinct species of the Pleistocene megafauna for two main reasons. First, they inhabited during an epoch of severe climatic changes, and therefore, they are ideal candidates to explore how climate change could influence lineage evolution; and second, some aspects of their palaeobiology are still controversial in the literature, and therefore, the application of new analytical approaches is necessary to clarify their 'life and death' and how its palaeobiology was influenced by the severe climatic changes of the Late Pleistocene. The results obtained are exposed through sections **3.1-3.5** of **chapter 3**, and a concise synthesis of the main conclusions reached through the development of this PhD thesis is exposed in **chapter 4**.

Therefore, as each of the sections of **chapter 3** (results) has a detailed introduction of the specific problem addressed, here, I only make a general outline of some aspects necessary to understand the fundament of this PhD Thesis. Therefore, trough the next two sections, I will focus on: (i) the state-of-the-art of the palaeobiology of these two extinct ursids that are taken as model system to investigate the potential of these new three-dimensional techniques to expand new horizons of research on vertebrate palaeobiology and evolution (**section 1.1.2**); and on (ii) the paleoclimatological evidence of the Late Pleistocene, as severe climatic changes occurred during this epoch and the extinction of the cave bear has been proposed to be (in part) climatically-driven (**section 1.1.3**).

1.1.2. The palaeobiology of the cave bear (*Ursus spelaeus*) and the American short-faced bear (*Arctodus simus*)

The 'life and death' of the Pleistocene cave bear

The 'life and death' of the Eurasian Pleistocene cave bear (*Ursus spelaeus*) has been an exceptional topic in vertebrate paleobiology and has been an enjoyable challenge for scientists and the popular media alike. The cave bear inhabited the glacial ecosystems of Eurasia and served as the inspiration for a classic book written in 1976 by Björn Kurtén, entitled: *The cave bear story: life and death of a vanished animal*. Although 'The cave bear story' was a compendium of the knowledge acquired on cave bear biology at that time, four decades later, many aspects of its paleoecology, extinction and evolution are still controversial in the literature. For example, the cave bear feeding behaviour is a special case of disagreement among specialists, since different palaeobiological approaches, such as those based on dental wear, on isotopic biogeochemistry or on the morphometric analysis of the skull, give seemingly contradictory results. As a matter of fact, the cave bear has been traditionally envisioned as highly reliant on plant foods (Kurtén 1976; Bocherens et al.

1994), as a relatively herbivorous omnivore (Figueirido et al. 2009; Peigné et al. 2009a, 2009b; Jones and DeSantis 2016; Peigné and Merceron 2019), as a carnivore (Richards et al. 2008) or even as an occasional scavenger (Rabal-Garcés et al. 2012; Pinto-Llona 2013).

On the other hand, the feeding behaviour of the cave bear is not a trivial aspect of its palaeobiology, because feeding behaviour is intimately related to its initial demise and final extinction. Indeed, two main hypotheses have been proposed to explain the cave bear extinction: (i) a human-driven decline, either by competition for resources or by direct hunting (e.g., Münzel et al. 2004, 2011); and (ii) a substantial demise in population sizes as a result of the climatic cooling that occurred during the Late Pleistocene (Baca et al. 2016). Such cooling would lead to a lower primary productivity in the high-alpine ecosystems that inhabited the cave bear during the beginning of the Last Glacial. This Late Pleistocene cooling together with the proposed restricted diet to vegetal resources of the cave bear would facilitate their decline (Bocherens 2019; Terlatto et al. 2019, Allen et al. 2010). Accordingly, knowing the feeding behaviour of the cave bear could help to understand the potential causes of its extinction.

In this PhD thesis, I apply a set of relatively recent techniques that require three-dimensional models for its application, with the main objective to provide new evidence on whether cave bears were really strict herbivores, or in contrast, they have the ability to shifts their diets depending upon resource availability. To do this, in the first section of the results (**chapter 3.1**) I quantify the tooth-root areas across maxillary teeth, from the upper fourth premolar to the upper second molar, as previous studies have shown that they are indicative of both trophic specialization and bite force in mammals (e.g., Spencer 2003; Kupczik and Dean 2008) and especially in mammalian carnivores (e.g., Kupczik and Stynder 2012; Stynder and Kupczik 2013).

In addition, in the second section of the results (**chapter 3.2**), I perform a topographic analysis of the crowns of maxillary teeth using a three-dimensional surface scanner. The topographic analysis is the quantification of both the shape and characteristics of the dental crowns from 3D models (M'Kirera and Ungar 2003; Evans et al. 2007; Bunn et al. 2011; Winchester et al. 2014; Winchester 2016), and I applied this method because previous studies have shown a correlation of dental topographic variables with feeding behaviour across different mammalian groups, both living and extinct (M'Kirera and Ungar 2003; Ungar and M'Kirera 2003; Dennis et al. 2004; Ulhaas et al. 2004; King et al. 2005; Evans et al. 2007; Boyer 2008; Ungar and Bunn 2008; Bunn and Ungar 2009; Evans and Jernvall 2009; Bunn et al. 2011; Godfrey et al. 2012; Wilson et al. 2012 ; Pineda et al. 2017; Evans and Pineda 2018). However, to date, there are no studies that quantify the topography of the 3D dental crowns in living and extinct bears.

In the third section of the results (**chapter 3.3**), I build different biomechanical models in three-dimensions from CT scans to simulate different biting scenarios in living bears and in different specimens belonging to the cave bear group, in order to investigate whether the skull of cave bears was biomechanically restricted to feed exclusively on plant resources. Specifically, I use finite element analysis (FEA), which is an engineering and orthopedic technique that quantifies stress, tension and deformation in a given structure. However, during the last decade it has been extensively applied to both Palaeontology and Zoology to address questions about functional morphology in living and extinct organisms (Rayfield 2007). However, this method has never been applied to investigate if cave bears have a restricted diet to feed exclusively on plant resources.

Another aspect of the palaeobiology of the cave bear relatively unexplored is the physiology of hibernation and how they cope with the necessity of having longer hibernation periods to overcome the long and severe winters of the Late Pleistocene. The hibernation is largely controlled by several metabolic pathways, but three are the principal ones: (i) at the level of the thyroid and parathyroid glands (Lundber et al. 1976; Nelson et al. 1983; Watts and Jonkel 1988; Watts and Cuyler 1988; Hellgren 1998); (ii) at the level of the pituitary gland (Franzmann et al. 1981; Hissa et al. 1994); and (iii) by the level of concentration of different metabolites in blood such as leptins, insulin, glucagon, adiponectin, among others (Doherty et al. 2014). Also, the pineal gland also acts through the control of melanin, regulating the circadian rhythm and helping the entry in the lethargy that characterize hibernation (Ware et al. 2013). In all these routes, the paranasal sinuses segregate through their mucosa other metabolites such as hydrogen sulfide (H2S) and nitric oxide (NO) (Revsbech et al. 2014; Tøien et al. 2011). These metabolites are involved in decreasing the basal metabolic rate (Lundberg 2008; Petruson et al. 2005; Yan et al. 2017; Andersson et al. 2002). Accordingly, I hypothesize that the extremely developed paranasal sinuses of cave bears had a key role to overcome the long and cold winters of the Late Pleistocene.

Through **chapter 3.4**, I explore the length of hibernation in cave bears and their possible implications in the biomechanics of its feeding behaviour by disrupting the external profile of the frontal part of the skull, for the presence of the dome that characterizes the *speloid* lineage. To do this, I work with three-dimensional models of segmented sinuses in living bears and extinct cave bears. I also develop theoretical models to estimate basal metabolic rates in cave bears using the allometric equations of McNab (2008) for periods of activity and of Robbins et al. (2012) for periods of hibernation, based on the estimated body masses in the different species/subspecies belonging to the cave bear group. In this chapter, I also develop a new histo-morphometric method to quantify some properties of cancellous bone such as the connectivity among trabeculae (Odgaard et al. 1993; Toriwaki et al. 2002), thickness of trabeculae (Kim et al. 2018; Dougherty et al. 2007, 2014; Hildebrand et al. 1997), and the fractional volume of bone (Hildebrand et al. 1997, 1999; Ulrich et al. 1999). The main objective is to investigate whether the osteoclastic activity in cave bears was lower than in other bears with regular periods of hibernation because of a low metabolic activity (Burkhardt et al. 1987; Ding et al. 2018) but without experiencing bone resorption (Seger et al. 2011; Rubin et al. 2000, 2003). Among the factors that can cause an abnormality in bone density, can be a high control by the sinuses through the segregation of the metabolite NO by inhibiting part of the osteoclastic activity (Zheng et al. 2006; Doherty et al. 2014; Seger et al. 2011; Rubin et al. 2000, 2003) or even the scarcity of food resources causing starvation (Allen et al. 2010).

Arctodus simus, a proposed hypercarnivore that never was

The palaeobiology of the short-faced bear (*A. simus*) has also been a matter of debate. In fact, the feeding behaviour of *A. simus* is one of the most controversial topic in mammalian palaeobiology, as different researchers have proposed varying diets for *A. simus*, proposing the later as a hypercarnivore with a diet based on both flesh (Kurtén 1967; Kurtén and Anderson 1980; Yeakel et al. 2013) or carrion (Matheus 1995; Schubert and Wallace 2009; Christiansen 1999), omnivore (Sorkin 2006; Figueirido et al. 2009) or even the herbivore (Emslie and Czaplewski 1985). In this PhD thesis, I investigate the pre-mortem pathological lesions present in several dental remains of *A. simus* preserved in the exceptional site of Rancho La Brea in Los Angeles (California) with the main goal to ascertain its feeding behaviour. To do this, I use different three-dimensional techniques such as those based on 3D morphometrics of cavities counter-mold, on scanning electron microscopy (SEM), and on computed tomographic analysis to investigate the possible aetiology of the dental lesions that were present in the population of *A. simus*.

1.1.3. Brief introduction to Pleistocene palaeoclimatology

The Pleistocene epoch of the Quaternary period begins from 2.58 million years ago to 12.000 years, and it is characterized by severe climatic fluctuations, known as glacial and interglacial periods. Cold temperatures and glacier advances during periods of thousands of years characterize a glacial period. In contrast, the interglacials are periods of warm climates between glacials.

This PhD Thesis is focused on the last glacial cycle that is defined as the period between termination II and termination I that encompasses both the last interglacial period (i.e., Eemian stage) as well as the last cold stage (i.e., Weichselian stage). The Weichselian corresponds to the Würm glaciation in the Alpine region. This last period is the last cold glacial cycle, and it also is the longest of all glacials with duration of 118 ka. This Weichselian cold stage has two distinct cold and pronounced episodes during Marine Isotope Stage (MIS) 4 and 2 (Hughes et al. 2018). Based on the recorded data, it reached minimums of −10.2 ° C and −10.6 ° C, for MIS 4 and 2, respectively (Hughes et al. 2018). The MIS 4 and 2 states are separated by the warm interval of MIS 3, which is not considered a true interglacial period, but it is considered a complex interstate with oscillating climatic conditions from conditions of almost interglacial to glacial peaks on a time scale between 100 to 1000 years (van Andel 2002). Some $\delta^{18}O$ marine records suggest that the global ice volume was higher in MIS 6 (Saalian Stage) than in MIS 2 (Hughes et al. 2018). There are differences in the concentration of oxygen isotope ratios between MIS2 and MIS6, with $\delta^{18}O$ being slightly higher in MIS2 than in MIS 6. This may indicate a different global distribution of ice in the penultimate glacial maximum (PGM) in comparison with the last glacial maximum (LGM), with much larger ice masses over Eurasia in the PGM compared to the LGM, and smaller ice masses over North America in the PGM compared to the LGM (Rohling et al. 2017). Within the penultimate glaciation period (PGM), the coldest peak is in the MIS6a state (140Ka) (Hughes et al. 2018). The glacial maximum of MIS 6 was the most extensive glaciation of the last 400 ka over Eurasia, the largest since MIS 12 (Colleoni et al. 2016). In Europe, during the MIS 6 the largest ice advance of the Saalian Stage is recorded during the Drenthe Stadial (one hundred kilometers beyond the later limits of the Weichselian Stage (MIS 5d - 2) in the Netherlands and the northern Germany (Ehlers et al. 2011c) and more than 100 km further east of Germany and Poland (Ehlers et al. 2011c). Therefore, this stage had 56% greater volume of ice in extension than the Weichselian Stage ice sheet in Russia and the neighbouring states (Astakhov 2004). The maximum limits of the glaciers of the Saalian Stage (300Ka to 130 ka) in northern Europe were also more extensive than the previous glaciation of the Elsterian Stage (MIS 12) and, therefore, the Saalian Stage constitutes the glaciation more extensive recorded in much of northern continental Europe (Hughes et al. 2018). Compared to the LGM, the maximum extent of the MIS 6 glaciation in Eurasia was characterized by a generally considerably larger ice sheet.

This great extension of ice at the end of the PGP coincided with *Ursus deningeri*, the most basal species of the *speloid* lineage. In **Figure 1**, it is shown the evolution of the *speloid* lineage in the context of Pleistocene climate. It is appreciated that the appearance of the *speloid* lineage (Stiller et al. 2014) coincides between MIS 6e and MIS 6a. Towards the end of MIS 6, the global ice volume reached its maximum extent, which coincides with another divergence in MIS 6, and with the split of *Ursus ingressus*/*Ursus rossicus* from *Ursus spelaeus* sensu stricto (i.e., *Ursus spelaeus spelaeus*, *Ursus* *spelaeus ladinicus*, *Ursus spelaeus eremus*). In MIS 5e, there is an interglacial period of 123ka, and just after this period, in the following states MIS 5d (109ka) and 5b, there are two clear peaks of decreasing temperatures, that again, coincides with the branching event of *Ursus ingressus* and *Ursus rossicus*. Within the *speloid* group, at the same time, it coincides with another branching event, splitting *Ursus spelaeus* from the other two subspecies *Ursus spelaeus ladinicus* and *Ursus spelaeus eremus* (**Fig. 1**). Between MIS4 to MIS2, the extinction of the whole group occurs.

The first form that went extinct was *Ursus sp. eremus*, followed by *Ursus sp. ladinicus* and *U. rossicus*. Later, *Ursus sp. spelaeus* went extinct followed by *Ursus ingressus*. The hypothesis in this PhD Thesis is that both species are the last ones to go extinct because they were better adapted to overcome the long winters of the Pleistocene.

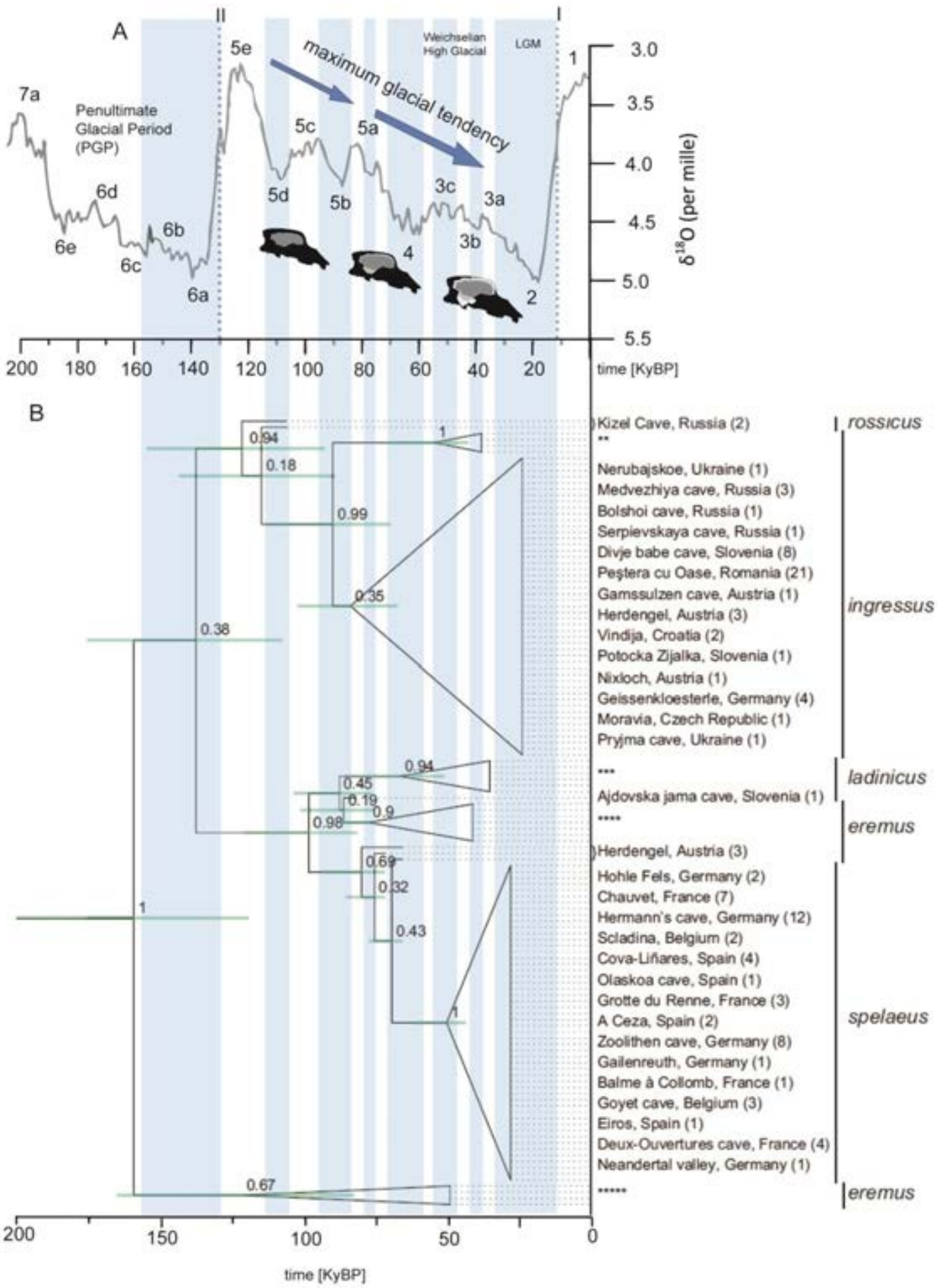

Figure 1. Cave bear evolution in the context of Pleistocene climate. (A) fluctuations in the δ18O/ δ16O as a proxy for temperature across time. Modified from Hughes et al. (2018). The blue shaded areas correspond to the coldest glacial periods. **(B)** comprehensive phylogeny of cave bears. Modified from Stiller et al. (2014).

In North America, Illinoian glaciation is equivalent to the MIS 6 state of the Eurasian region. In this continent, there was a large extension of the limits of the ice sheet to the south (more than 150 km) beyond Wisconsinan's later limits and in Illinois (MIS 5d - 2) with a glacial peak of 140 ka, corresponding to same MIS6a state of the Eurasian region (Colleoni et al. 2016; Hughes et al. 2018). In Wisconsin, the glacial boundaries of the Illinoian Stage reach a maximum of 30 km beyond the limits of Wisconsinan, and in some places the latter was even more extensive (Syverson and Colgan, 2011). As in the case of cave bears in Europe, the ecomorphological evolution of *A. simus* could have been also influenced by the profound climatic changes of the epoch.

Taking both extinct species of bears that inhabited in different continents but with similar climatic conditions could help to answer a fundamental palaecological question: *How climate cooling affected the evolution of the ice-age megafauna?* My findings suggest that both climate change and ecological competition among species are important mechanisms that motivate changes in the evolution of lineages at a global scale.

1.2. Aims

Although the ultimate goal of this PhD Thesis is to evaluate whether the relatively new three-dimensional techniques of analysis that have opened new avenues of future research in the fields of Ecomorphology and Evolution of vertebrates can help to resolve controversial paleobiological aspects of the cave bear and other Pleistocene ursids (i.e., *A. simus*), the specific objectives addressed are listed below:

- To evaluate whether the tooth-root analysis across maxillary teeth is a good proxy for the type of food consumed in living ursids. If this is the case, to investigate the possible diet of cave bears with this new type of ecomorphological analysis.

- To explore whether the topography of dental crowns is a good ecomorphological proxy in living bears and to investigate if they are related to diet. If there is such a relationship, to investigate the controversial feeding behaviour of cave bears.

- To explore whether computational biomechanics in 3D, using simulations of different biting scenarios by Finite Element Analysis, is an appropriate tool to address if cave bears had a restricted diet to feed exclusively on plant resources.

- To demonstrate how the analyses based on Computed Tomography are useful for the morphological characterization of internal structures, and therefore, how these techniques increase the knowledge on the palaeobiology of these species. To do this, I use the size and shape of the paranasal sinuses of cave bears as study case for internal structures.

- To test the hypothesis that cave bears could spend long periods of hibernation (more than six months) and how these long periods of inactivity could affect their basal metabolic rate and osteology.

- To show how the virtual methods based on 3D surface scanning and computed tomography provide significant evidences to clarify the controversial trophic ecology of the short-faced bear of the Pleistocene of North America (*A. simus*).

- To investigate and explore how climate change affected the evolution of cave bears and other extinct ursids of the Pleistocene megafauna that inhabited another continent, such as the North American *A. simus.*

1.3. References

- Allen JR, Hickler T, Singarayer JS, Sykes MT, Valdes PJ, Huntley, B. 2010. Last glacial vegetation of northern Eurasia. Quaternary Sci Rev. 29(19-20): 2604-2618.
- Andersson JA, Cervin, A., Lindberg, S., Uddman, R., & Cardell, L. O. 2002. The paranasal sinuses as reservoirs for nitric oxide. Acta otolaryngologica. 122(8): 861-865.
- Astakhov V. 2004. Pleistocene ice limits in the Russian northern lowlands. Quaternary Glaciations—Extent and Chronology. Part, 1: 309-319.
- Baca M, Popović D, Stefaniak K, Marciszak A, Urbanowski M, Nadachowski A, Mackiewicz P. 2016. Retreat and extinction of the Late Pleistocene cave bear (*Ursus spelaeus* sensu lato). Sci Nat. 103(11-12): 92.
- Bocherens H, Fizet M, Mariotti A. 1994. Diet, physiology and ecology of fossil mammals as inferred from stable carbon and nitrogen isotope biogeochemistry: implications for Pleistocene bears. Palaeogeography, Palaeoclimatology, Palaeoecology. 107(3-4): 213-225.
- Bocherens H. 2019. Isotopic insights on cave bear palaeodiet. Hist Biol. 31(4): 410-421.
- Boyer DM. 2008. Relief index of second mandibular molars is a correlate of diet among prosimian primates and other euarchontan mammals. J Hum Evol. 55(6): 1118-1137.
- Bunn JM, Ungar PS. 2009. Dental topography and diets of four old world monkey species. Am J Primatol: Official Journal of the American Society of Primatologists. 71(6):466-477.
- Bunn JM, Boyer DM, Lipman Y, St. Clair EM, Jernvall J, Daubechies I. 2011. Comparing Dirichlet normal surface energy of tooth crowns, a new technique of molar shape quantification for dietary inference, with previous methods in isolation and in combination. Am J Phys Anthropol. 145(2):247-261.
- Burkhardt R, Kettner G, Böhm W, Schmidmeier M, Schlag R, Frisch B, Gilg TH. 1987. Changes in trabecular bone, hematopoiesis and bone marrow vessels in aplastic anemia, primary osteoporosis, and old age: a comparative histomorphometric study. Bone. 8(3):157-164.

- Christiansen P. 1999. What size were *Arctodus simus* and *Ursus spelaeus* (Carnivora: Ursidae)?. Finnish Zoological and Botanical Publishing Board. In Annales Zoologici Fennici (pp. 93-102).
- Cignoni P, Callieri M, Corsini M, Dellepiane M, Ganovelli F, Ranzuglia G. 2008. Meshlab: an open-source mesh processing tool. In Eurographics Italian chapter conference (Vol. 2008, pp. 129-136).
- Colleoni F, Wekerle C, Näslund JO, Brandefelt J, Masina S. 2016. Constraint on the penultimate glacial maximum Northern Hemisphere ice topography (≈ 140 kyrs BP). Quaternary Sci Rev. (137):97-112.
- Cuff AR, Stockey C, Goswami A. 2016. Endocranial morphology of the extinct North American lion (*Panthera atrox*). Brain, behavior and evolution. 88(3-4):213-221.
- Curtis AA, Van Valkenburgh B. 2014. Beyond the sniffer: frontal sinuses in Carnivora. The Anatomical Record. 297(11):2047-2064.
- Dennis JC, Ungar PS, Teaford MF, Glander KE. 2004. Dental topography and molar wear in *Alouatta palliata* from Costa Rica. Am. J. phys. Anthropol. (125): 152-161.
- Ding M, Lin X, Liu W. 2018. Three-dimensional morphometric properties of rod- and plate-like trabeculae in adolescent cancellous bone. Journal of orthopaedic translation. (12): 26-35.
- Doherty AH, Florant GL, Donahue SW. 2014. Endocrine regulation of bone and energy metabolism in hibernating mammals. Integr Comp Biol. 54(3): 463-483.
- Dougherty R, Kunzelmann KH. 2007. Computing local thickness of 3D structures with ImageJ. Microsc Microanal. 13(S02): 1678-1679.
- Ehlers J, Grube A, Stephan HJ, Wansa S. 2011c. Pleistocene glaciations of North Germany—new results. In Developments in quaternary sciences. Elsevier. (Vol. 15, pp. 149-162).
- Endo H, Frey R. (Eds.). 2009. Anatomical imaging: towards a new morphology. Springer Science & Business Media.
- Emslie SD, Czaplewski NJ. 1985. A new record of giant short-faced bear, *Arctodus simus*, from western North America with a re-evaluation of its paleobiology. Natural History Museum of Los Angeles County.

- Evans AR, Jernvall J. 2009. Patterns and constraints in carnivoran and rodent dental complexity and tooth size. J Vertebr Paleontol. 29: 24A.
- Evans AR, Pineda-Munoz S. 2018. Inferring mammal dietary ecology from dental morphology. In Methods in Paleoecology. Springer, Cham. (pp. 37-51).
- Evans AR, Wilson GP, Fortelius M, Jernvall J. 2007. High-level similarity of dentitions in carnivorans and rodents. Nature. 445(7123): 78.
- Figueirido B, Palmqvist P, Pérez-Claros JA. 2009. Ecomorphological correlates of craniodental variation in bears and paleobiological implications for extinct taxa: an approach based on geometric morphometrics. J Zool. 277(1): 70-80.
- Figueirido B, Lautenschlager S, Pérez-Ramos A, Van Valkenburgh B. 2018. Distinct predatory behaviors in scimitar-and dirk-toothed sabertooth cats. Curr Biol. 28(20): 3260-3266.
- Figueirido B, Pérez-Ramos A, Schubert BW, Serrano F, Farrell AB, Pastor FJ, Romero A. 2017. Dental caries in the fossil record: a window to the evolution of dietary plasticity in an extinct bear. Sci Rep-Uk. 7(1): 17813.

- Figueirido B, Lautenschlager S, Pérez-Ramos A, Van Valkenburgh B. 2018. Distinct predatory behaviors in scimitar-and dirk-toothed sabertooth cats. Curr Biol. 28(20): 3260-3266.

- Franzmann AW, Flynn A, Schwartz CC, Calkins DG, Nichols JRL. 1981. Beta-endorphin levels in blood from selected Alaskan mammals. J Wildlife Dis. 17(4): 593-596.
- Godfrey LR, Winchester JM, King SJ, Boyer DM, Jernvall J. 2012. Dental topography indicates ecological contraction of lemur communities. Am J Phys Anthropol. 148(2): 215-227.
- Hellgren EC. 1998. Physiology of hibernation in bears. Ursus. 467-477.
- Hildebrand T, Rüegsegger P. 1997. A new method for the model-independent assessment of thickness in three-dimensional images. J Microsc-Oxford. 185(1): 67-75.

- Hildebrand T, Laib A, Müller R, Dequeker J, Rüegsegger P. 1999. Direct three-dimensional morphometric analysis of human cancellous bone: microstructural data from spine, femur, iliac crest, and calcaneus. J Bone Mineral Res. 14(7): 1167-1174.
- Hissa R, Siekkinen J, Hohtola E, Saarela S, Hakala A, Pudas J. 1994. Seasonal patterns in the physiology of the European brown bear (*Ursus arctos arctos*) in Finland. Comparative Biochemistry and Physiology Part A: Physiology. 109(3): 781-791.
- Hughes PD, Gibbard PL. 2018. Global glacier dynamics during 100 ka Pleistocene glacial cycles. Quaternary Res. 90(1): 222-243.
- Jones DB, & De Santis LR. 2016. Dietary ecology of the extinct cave bear: evidence of omnivory as inferred from dental microwear textures. Acta Palaeontol Pol. 61(4): 735-742.
- Kak AC, Slaney M, Wang G. 2002. Principles of computerized tomographic imaging. Med Phys. 29(1): 107-107.
- Kim JJ, Nam J, Jang IG. 2018. Computational study of estimating 3D trabecular bone microstructure for the volume of interest from CT scan data. Int J Numer Meth Bio. 34(4): e2950.
- King SJ, Arrigo-Nelson SJ, Pochron ST, Semprebon GM, Godfrey LR, Wright PC, Jernvall J. 2005. Dental senescence in a long-lived primate links infant survival to rainfall. P Natl A Sci. 102(46): 16579-16583.
- Kupczik K, Dean MC. 2008. Comparative observations on the tooth root morphology of *Gigantopithecus blacki*. J Hum Evol. 54(2): 196-204.
- Kupczik K, Stynder DD. 2012. Tooth root morphology as an indicator for dietary specialization in carnivores (Mammalia: Carnivora). Biol J Linn Soc. 105(2): 456-471.
- Kurtén B. 1976. The cave bear story Columbia University Press. New York.
- Kurtén B, Anderson E. 1980. Pleistocene mammals of North America. Columbia University Press.
- Lundberg DA, Nelson RA, Wahner HW, Jones JD. 1976. Protein metabolism in the black bear before and during hibernation. In Mayo Clinic Proceedings (Vol. 51, No. 11, pp. 716-722).

- Lundberg JO. 2008. Nitric oxide and the paranasal sinuses. The Anatomical Record: Advances in Integrative Anatomy and Evolutionary Biology: Anat Rec. 291(11): 1479-1484.
- M'kirera F, Ungar PS. 2003. Occlusal relief changes with molar wear in *Pan troglodytes troglodytes* and *Gorilla gorilla gorilla*. Am J Primatol: Official Journal of the American Society of Primatologists. 60(2): 31-41.
- Matheus PE. 1995. Diet and co-ecology of Pleistocene short-faced bears and brown bears in eastern Beringia. Quaternary Res. 44(3): 447-453.
- McNab BK. 2008. An analysis of the factors that influence the level and scaling of mammalian BMR. Comparative Biochemistry and Physiology Part A: Molecular & Integrative Physiology. 151(1): 5-28.
- Münzel SC, Conard NJ. 2004. Cave bear hunting in the Hohle Fels, a cave site in the Ach Valley, Swabian Jura. Revue de Paléobiologie. 23(2): 877-885.
- Münzel SC, Stiller M, Hofreiter M, Mittnik A, Conard NJ, Bocherens H. 2011. Pleistocene bears in the Swabian Jura (Germany): genetic replacement, ecological displacement, extinctions and survival. Quaternary Int. 245(2): 225-237.
- Nelson RA, Folk Jr GE, Pfeiffer EW, Craighead JJ, Jonkel CJ, Steiger DL. 1983. Behavior, biochemistry, and hibernation in black, grizzly, and polar bears. Bears: their biology and management, 284-290.
- Odgaard A, Gundersen HJG. 1993. Quantification of connectivity in cancellous bone, with special emphasis on 3-D reconstructions. Bone. 14(2): 173-182.
- Peigné S, Goillot C, Germonpré M, Blondel C, Bignon O, Merceron G. 2009a. Predormancy omnivory in European cave bears evidenced by a dental microwear analysis of *Ursus spelaeus* from Goyet, Belgium. P Natl A Sci. 106(36): 15390-15393.
- Peigné S, Goillot C, Germonpré M, Blondel C, Bignon O, Merceron G. 2009b. Reply to Bocherens: Dental microwear and stable isotopes on bone collagen are complementary to sort out cave bear diets. P Natl A Sci. 106(48): E134-E134.
- Peigné S, Merceron G. 2019. Palaeoecology of cave bears as evidenced by dental wear analysis: a review of methods and recent findings. Hist Biol. 31(4): 448-460.
- Pertusa JF. 2010.Técnicas de análisis de imagen (Universitat de València).

- Petruson K, Stalfors J, Jacobsson KE, Ny L, Petruson B. 2005. Nitric oxide production in the sphenoidal sinus by the inducible and constitutive isozymes of nitric oxide synthase. Rhinology. 43(1): 18-23.
- Pineda-Munoz S, Lazagabaster IA, Alroy J, Evans AR. 2017. Inferring diet from dental morphology in terrestrial mammals. Methods Ecol Evol. 8(4): 481-491.
- Pinto-Llona AC. 2013. Macrowear and occlusal microwear on teeth of cave bears *Ursus spelaeus* and brown bears *Ursus arctos*: Inferences concerning diet. Palaeogeography, Palaeoclimatology, Palaeoecology. 370: 41-50.
- Rabal-Garcés R, Cuenca-Bescós G, Ignacio CJ, De Torres T. 2012. Was the European cave bear an occasional scavenger?. Lethaia. 45(1): 96-108.
- Rayfield EJ. 2007. Finite element analysis and understanding the biomechanics and evolution of living and fossil organisms. Annu. Rev. Earth Planet. Sci. 35:541-576.
- Richards MP, Pacher M, Stiller M, Quilès J, Hofreiter M, Constantin S, Trinkaus E. 2008. Isotopic evidence for omnivory among European cave bears: Late Pleistocene *Ursus spelaeus* from the Peștera cu Oase, Romania. P Natl A Sci. 105(2): 600-604.
- Revsbech IG, Shen X, Chakravarti R, Jensen FB, Thiel B, Evans AL, Fago A. 2014. Hydrogen sulfide and nitric oxide metabolites in the blood of free-ranging brown bears and their potential roles in hibernation. Free Radical Bio Med. 73: 349-357.
- Robbins CT, Lopez-Alfaro C, Rode KD, Tøien Ø, Nelson OL. 2012. Hibernation and seasonal fasting in bears: the energetic costs and consequences for polar bears. J Mammal. 93(6): 1493-1503.
- Rohling EJ, Hibbert FD, Williams FH, Grant KM, Marino G, Foster GL, Webster JM. 2017. Differences between the last two glacial maxima and implications for ice-sheet, δ18O, and sea-level reconstructions. Quaternary Sci Rev. 176: 1-28.
- Rubin J, Murphy TC, Zhu L, Roy E, Nanes MS, Fan X. 2003. Mechanical strain differentially regulates endothelial nitric-oxide synthase and receptor activator of nuclear KB ligand expression via ERK1/2 MAPK. Journal of Biol Chem. 278(36): 34018-34025.
- Rubin J, Murphy T, Nanes MS, Fan X. 2000. Mechanical strain inhibits expression of osteoclast differentiation factor by murine stromal cells. American Journal of Physiology-Cell Physiology. 278(6): C1126-C1132.

- Rueden CT, Schindelin J, Hiner MC. et al. 2017, "ImageJ2: ImageJ for the next generation of scientific image data", BMC Bioinformatics 18:529, PMID 29187165, doi:10.1186/s12859-017-1934-z
- Sanchez S, Ahlberg PE, Trinajstic KM, Mirone A, Tafforeau P. 2012. Three-dimensional synchrotron virtual paleohistology: a new insight into the world of fossil bone microstructures. Micros Microanal. 18(5): 1095-1105.
- Schubert BW, Wallace SC. 2009. Late Pleistocene giant short-faced bears, mammoths, and large carcass scavenging in the Saltville Valley of Virginia, USA. Boreas. 38(3): 482-492.
- Seger RL, Cross RA, Rosen CJ, Causey RC, Gundberg CM, Carpenter TO, Keisler DH. 2011. Investigating the mechanism for maintaining eucalcemia despite immobility and anuria in the hibernating American black bear (*Ursus americanus*). Bone. 49(6): 1205-1212.
- Sorkin B. 2006. Ecomorphology of the giant short-faced bears *Agriotherium* and *Arctodus*. Hist Biol. 18(1): 1-20.
- Spencer MA. 2003. Tooth-root form and function in platyrrhine seed-eaters. American Journal of Physical Anthropology: The Official Publication of the American Association of Physical Anthropologists. 122(4): 325-335.
- Stiller M, Molak M, Prost S, Rabeder G, Baryshnikov G, Rosendahl W, Germonpré M. 2014. Mitochondrial DNA diversity and evolution of the Pleistocene cave bear complex. Quaternary Inter. 339, 224-231.
- Stynder DD, Kupczik K. 2013. Tooth root morphology in the early Pliocene African bear *Agriotherium africanum* (Mammalia, Carnivora, Ursidae) and its implications for feeding ecology. J Mammal Evol. 20(3): 227-237.
- Syverson KM, Colgan PM. 2011. The Quaternary of Wisconsin: an updated review of stratigraphy, glacial history and landforms. In Developments in Quaternary Sciences. Elsevier. (Vol. 15, pp. 537-552).
- Tallman M, Amenta N, Delson E, Frost SR, Ghosh D, Klukkert ZS, Sawyer GJ. 2014. Evaluation of a new method of fossil retrodeformation by algorithmic symmetrization: crania of papionins (Primates, Cercopithecidae) as a test case. PloS one. 9(7): e100833.

- Terlato G, Bocherens H, Romandini M, Nannini N, Hobson KA, Peresani M. 2019. Chronological and Isotopic data support a revision for the timing of cave bear extinction in Mediterranean Europe. Hist Biol. 31(4): 474-484.
- Tøien Ø, Blake J, Edgar DM, Grahn DA, Heller HC, Barnes BM. 2011. Hibernation in black bears: independence of metabolic suppression from body temperature. Science. 331(6019): 906-909.
- Toriwaki J, Yonekura T. 2002. Euler number and connectivity indexes of a three dimensional digital picture. FORMA-TOKYO-. 17(3): 183-209.
- Ulhaas L, Kullmer O, Schrenk F, Henke W. 2004. A new 3-d approach to determine functional morphology of cercopithecoid molars. Ann Anat. 186(5-6): 487-493
- Ulrich D, Van Rietbergen B, Laib A, Ruegsegger P. 1999. The ability of three-dimensional structural indices to reflect mechanical aspects of trabecular bone. Bone. 25(1): 55-60.
- Ungar PS, Bunn JM. 2008. 11 Primate dental topographic analysis and functional morphology. Technique and application in dental anthropology. 53: 253.
- Ungar PS, M'Kirera F. 2003. A solution to the worn tooth conundrum in primate functional anatomy. P Natl A Sci. 100(7): 3874-3877.
- Van Andel TH. 2002. The climate and landscape of the middle part of the Weichselian glaciation in Europe: the stage 3 project. Quaternary Res. 57(1): 2-8.
- Van Valkenburgh B, Pang B, Bird D, Curtis A, Yee K, Wysocki C, Craven BA. 2014. Respiratory and olfactory turbinals in feliform and caniform carnivorans: the influence of snout length. The Anatomical Record. 297(11): 2065-2079.
- Ware JV, Nelson OL, Robbins CT, Carter PA, Sarver BA, Jansen HT. 2013. Endocrine rhythms in the brown bear (*Ursus arctos*): evidence supporting selection for decreased pineal gland size. Physiological reports. 1(3).
- Watts PD, Cuyler C. 1988. Metabolism of the black bear under simulated denning conditions. Acta Physiol Scand. 134(1): 149-152.
- Watts PD, and Jonkel C. 1988. Energetic cost of winter dormancy in grizzly bear. J. Wildl. Manage. 52:654.

- Wilson GP, Evans AR, Corfe IJ, Smits PD, Fortelius M, Jernvall J. 2012. Adaptive radiation of multituberculate mammals before the extinction of dinosaurs. Nature. 483(7390): 457.
- Winchester JM. 2016. MorphoTester: an open source application for morphological topographic analysis. PloS one. 11(2): e0147649.
- Winchester JM, Boyer DM, St. Clair EM, Gosselin-Ildari AD, Cooke SB, Ledogar JA. 2014. Dental topography of platyrrhines and prosimians: convergence and contrasts. Am J Phys Anthropol. 153(1): 29-44.
- Yan CH, Hahn S, McMahon D, Bonislawski D, Kennedy DW, Adappa ND, Cohen NA. 2017. Nitric oxide production is stimulated by bitter taste receptors ubiquitously expressed in the sinonasal cavity. Am J Rhinol Allergy. 31(2): 85-92.
- Yeakel JD, Guimarães PR, Bocherens H, Koch PL. 2013. The impact of climate change on the structure of Pleistocene food webs across the mammoth steppe. Proceedings of the Royal Society B: Biological Sciences. 280(1762): 20130239.
- Zheng H, Yu X, Collin-Osdoby P, Osdoby P. 2006. RANKL Stimulates Inducible Nitric-oxide Synthase Expression and Nitric Oxide Production in Developing Osteoclasts An autocrine negative feedback mechanism triggered by rankl-induced interferon-β via nf-κb that restrains osteoclastogenesis and bone resorption. J Biol Chem. 281(23): 15809-15820.
- Zollikofer CP, De León MSP. 2005. Virtual reconstruction: a primer in computer-assisted paleontology and biomedicine. Wiley-Interscience.

2

Material and Methods

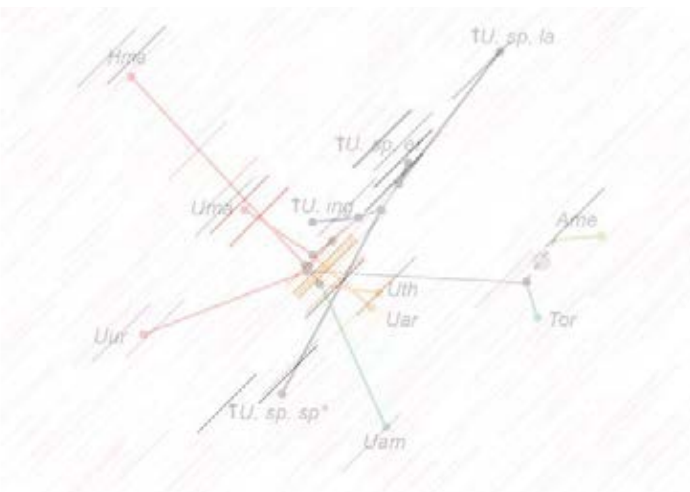

2.1. General overview

The results of this PhD Thesis are outlined through **chapters 3.1-3.5**, each of them with a detailed description of the material used and the specific methods applied. Accordingly, in **chapter 3.1**, I use 3D segmentation of roots and crowns across maxillary teeth from Computed Tomography (CT) scans. In **chapter 3.2**, I apply a topographic analysis of tooth crowns in the upper dental series from surface scanners. In **chapter 3.3**, I develop 3D biomechanical models of skulls, digitally acquired from CT scans. In **chapter 3.4**, I perform the virtual segmentation of paranasal sinuses and histo-morphometric analyses of cancellous bone from the use of CT scans. Finally, in **chapter 3.5**, I used surface scanners and high-resolution micro-CT scans of teeth. All these methodologies are described in detail through the respective **chapters 3.1-3.5**. However, the acquisition procedures and the pre-analytic processing of 3D meshes to virtually edit the models are described in this chapter.

Therefore, the main aim of this section is to provide the reader with a very general and intuitive idea on the techniques of external surface acquisition in 3D (i.e., surface scanning) and those that captures both external and internal structures such as the Computed Tomography Scanning (CT). I decided to explain this through this chapter because several acquisition parameters must be taken into account, such as electrical voltage, intensity, and distance between slices, among others (Zollikofer et al. 2005; Endo et al. 2009; Kak et al. 2002). Once the structures have been scanned, the resulting images have to be improved by deleting the background noise and different artefacts, using specific algorithms and a variety of digital filters that are also explained here. The segmentation of the structure (histogram thresholding) is also very sensitive and dependent on the property of the materials, such as bone density or mineralization, that should be commented in detail.

Therefore, through this section, I will give a general overview of the acquisition procedures, including the pre-analytical processing of meshes, as a first step to specifically analyze the 3D models with the appropriate methodology to address the main aims of this PhD Thesis.

2.2. Image acquisition of 3D models

2.2.1. Equipment

In this section, I present the technique of 3D acquisition of a real object that will be subject to analysis. Although there are several types of scanning machines, each of them with specific resolutions, the ones used in this PhD thesis is described below:

- *Medical CT scan*. The medical CT is the most common, due to its speed of acquisition (1-2 min), and the relatively economic cost. Its power and energy range between 60-140kV or 100-400 mA, but its resolution is low (1mm-0.2mm), which could be a problem for analysis that require more accurate models (**Fig. 1A**). This scanning procedure has been used to scan the skulls of some living and extinct bears analyzed in **chapters 3.1**, **3.3** and **3.4**. See **Tables 1**,**2.**
- *Micro CT scan*. The high-resolution micro CT is the best acquisition procedure available, because it has a high resolution (10-1 mµ) and a high energy range and power (0-225 kV / 0-100mA). However, the acquisition time is very long (1-10 hours) (**Fig. 1B**). This scanning procedure has been used to scan the skulls of some living and extinct bears analyzed in chapters 3.1, 3.3, 3.4, and 3.5. See **Tables 1,2.**
- *Surface scanner in 3D*. I use a Roland LPX-600, a high-quality scanning with an accuracy of 0.2mm of scanning-pitch. This scanner allows a large

working area, up to 254mm in diameter and 406.4mm in height (**Fig. 1C**). The software used is the LPX EZ studio. This scanning procedure has been used to scan the teeth of some living and extinct bears analyzed in **chapters 3.2** and **3.5**.

It is worth mentioning that it would be ideal to acquire the digital data in all skulls by means of a high-resolution micro-CT scanning. However, this ultimately depends on the availability of this kind of machines, the cost of the scanning, and the policies of the institutions and museums where the fossils are housed.

On the other hand, the teeth analysed in **chapters 3.2** and **3.5** were subject to surface scanning using the Roland LPX-600 machine. These specimens are housed in different museums: American Museum of Natural History (New York, USA), the Natural History Museum of London (NHM, UK), the Museum für Naturkunde (Berlin, Germany) and the Museum für Naturkunde (Vienna, Austria).

Table 1. CT-scans of the skulls belonging to living and extinct bears used in this PhD thesis.

Species	Museum Number	Collection/Museum	Geographical provenance	Geological age
Ailuropoda melanoleuca	VU 3156b	Valladolid, Spain	Zoological park, Spain	Living
Ursus arctos	USNM 82003	University of California, Los Angeles	Alaskan Peninsula	Living
Ursus americanus	VU 261	Valladolid, Spain	Zoological park, Spain	Living
Ursus americanus	USNM 227070	University of California, Los Angeles	British Columbia, Canada	Living
Ursus thibetanus	VU 2421	Valladolid, Spain	Zoological park, Spain	Living
Ursus maritimus	H. 001-05	University of California, Los Angeles	North Cornwall; North pole	Living
Tremarctos ornatus	VU 1661	Valladolid, Spain	Zoological park, Spain	Living
Helarctos malayanus	AMNH28254	American Museum of Natural History, New York, USA	Borneo, Indosenia	Living
Melursus ursinus	AMNH54464	American Museum of Natural History, New York, USA	Nepal	Living
Ursus spelaeus ladinicus	PIUW-CU 703 (paratype)	University of Vienna, Austria	Conturines cave, Italy.	Pleistocene 87±5 ka and 108+8/-7 ka
Ursus spelaeus eremus	PIUW-SW 483	University of Vienna, Austria	Schwabenreith cave, Austria.	Pleistocene 116±5 ka and 78+30/-23 ka
Ursus spelaeus spelaeus	E-ZYX-1000	University of Xeoloxia of the University of A Coruña, Spain	Eiros cave, Galicia, Spain.	Pleistocene (24ka- 32ka)
Ursus ingressus	PIUW3000/5/105	University of Vienna, Department of Paleontology.Vienna, Austria	Dragon cave of Mixnitz (Styria)	Pleistocene (65- 31ka)
Ursus spelaeus indet.	No number	University of Bonn, Germany	No specific locality (Germany)	Pleistocene

Table 2. CT-scan acquisition parameters of each skull belonging to living and extinct bears used in this PhD Thesis. Abbreviations: kv, kilovoltage; mA, milliamps. Note that the original conditions of acquisition have been modified to standardize the same conditions of analyses (processed).

Species	KV	mA	Image Matrix (original)	Voxel Size (X,Y,Z) mm (original)	Voxel Size Iso (X,Y,Z) mm (standardized)	Image Matrix (processed)	Voxel Size Post (processed)
Ailuropoda melanoleuca	120	250	512 x 512	0.520, 0.520, 0.3	0.520, 0.520, 0.520	1024 x 1024	0.260, 0.260, 0.260
Ursus arctos	450	300	1024 x 1024	0.241, 0.241, 1.00	0.241, 0.241, 0.241	1024 x 1024	0.241, 0.241, 0.241
Ursus americanus	120	250	512 x 512	0.468, 0.468, 0.3	0.468, 0.468, 0.468	1024 x 1024	0.234, 0.234, 0.234
Ursus thibetanus	120	250	512 x 512	0.468, 0.468, 0.3	0.468, 0.468, 0.468	1024 x 1024	0.234, 0.234, 0.234
Ursus maritimus	420	180	1024 x 1024	0.249, 0.249, 0.700	0.249, 0.249, 0.249	1024 x 1024	0.249, 0.249, 0.249
Tremarctos ornatus	120	250	512 x 512	0.381, 0.381, 0.5	0.381, 0.381, 0.381	1024 x 1024	0.191, 0.191, 0.191
Helarctos malayanus	170	250	1097 x 1126	0.142, 0.142, 0.142	0.142, 0.142, 0.142	1024 x 1024	0.142, 0.142, 0.142
Melursus ursinus	170	250	1536 x 1349	0.126, 0.126, 0.126	0.126, 0.126, 0.126	1024 x 1024	0.126, 0.126, 0.126
Ursus spelaeus ladinicus	130	330	1491 x 1139	0.15, 0.15, 0.15	0.15, 0.15, 0.15	512 x 512	0.333, 0.333, 0.333
Ursus spelaeus eremus	120	160	512 x 512	0.533, 0.533, 0.2	0.533, 0.533, 0.533	1024 x 1024	0.266, 0.266, 0.266
Ursus spelaeus spelaeus	120	160	512 x 512	0.75, 0.75, 0.365	0.75, 0.75, 0.75	1024 x 1024	0.375, 0.375, 0.375
Ursus ingressus	120	160	512 x 512	0.611, 0.611, 0.2	0.611, 0.611, 0.611	1024 x 1024	0.305, 0.305, 0.305

2.3. CT scans processing

2.3.1. Image stack calibration and CT segmentation

The values of the histogram of the raw images that are generated from CT scanning are usually expanded (Calzado et al. 2010; Gonzalez et al.

2002). These images are usually of 16 bits (there are 16 grey ranges or values, 0-4096). Therefore, the first step is to calibrate the range of the histogram by selecting the region of interest (ROI). This is computed in order to remove the background noise (Pertusa 2010, Bushberg 2011) (see **Fig. 2A,B**).

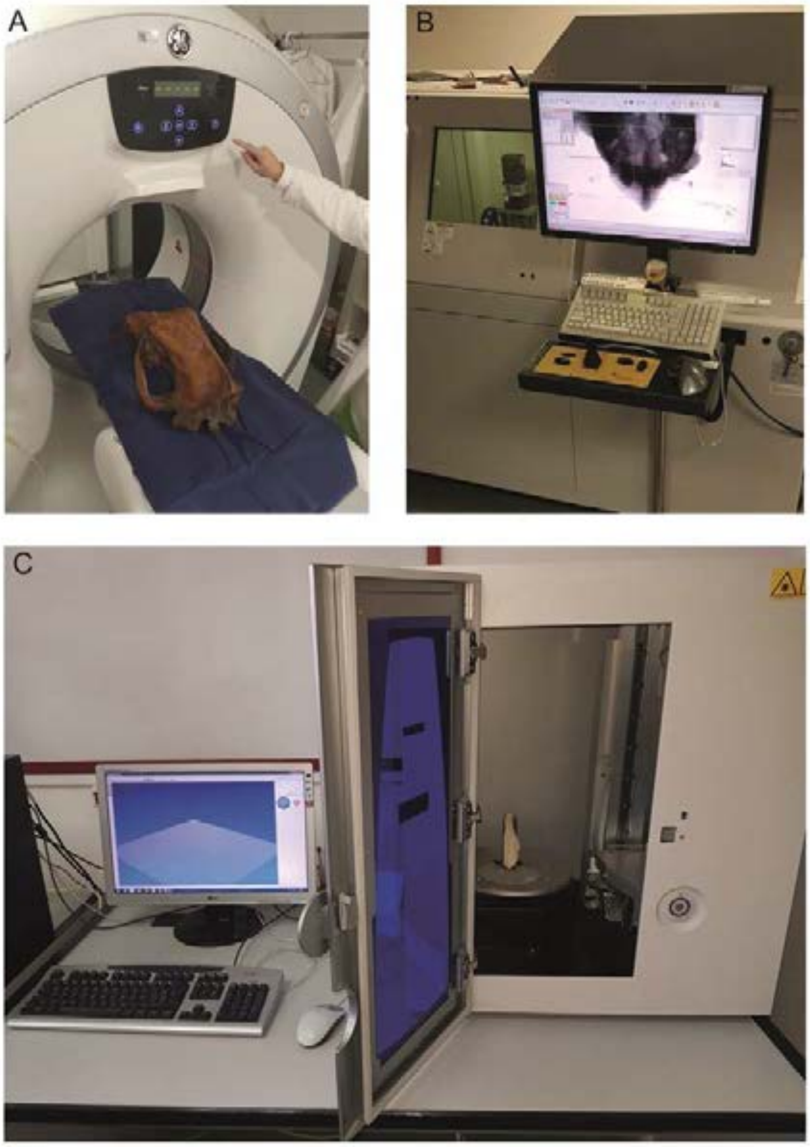

Figure 1. Acquisition machines used in this PhD thesis. (A) Medical CT machine used to scan some skulls of cave bears (Clínicas Rincón, Málaga); **(B)** High resolution micro-CT used to scan some specimens of living bears (American Museum of Natural History, New York); **(C)** Laser scanning used to recover the external surface of dental cast of chapters 3.2 and 3.5 (Servicio Central de Informática Universidad de Málaga).

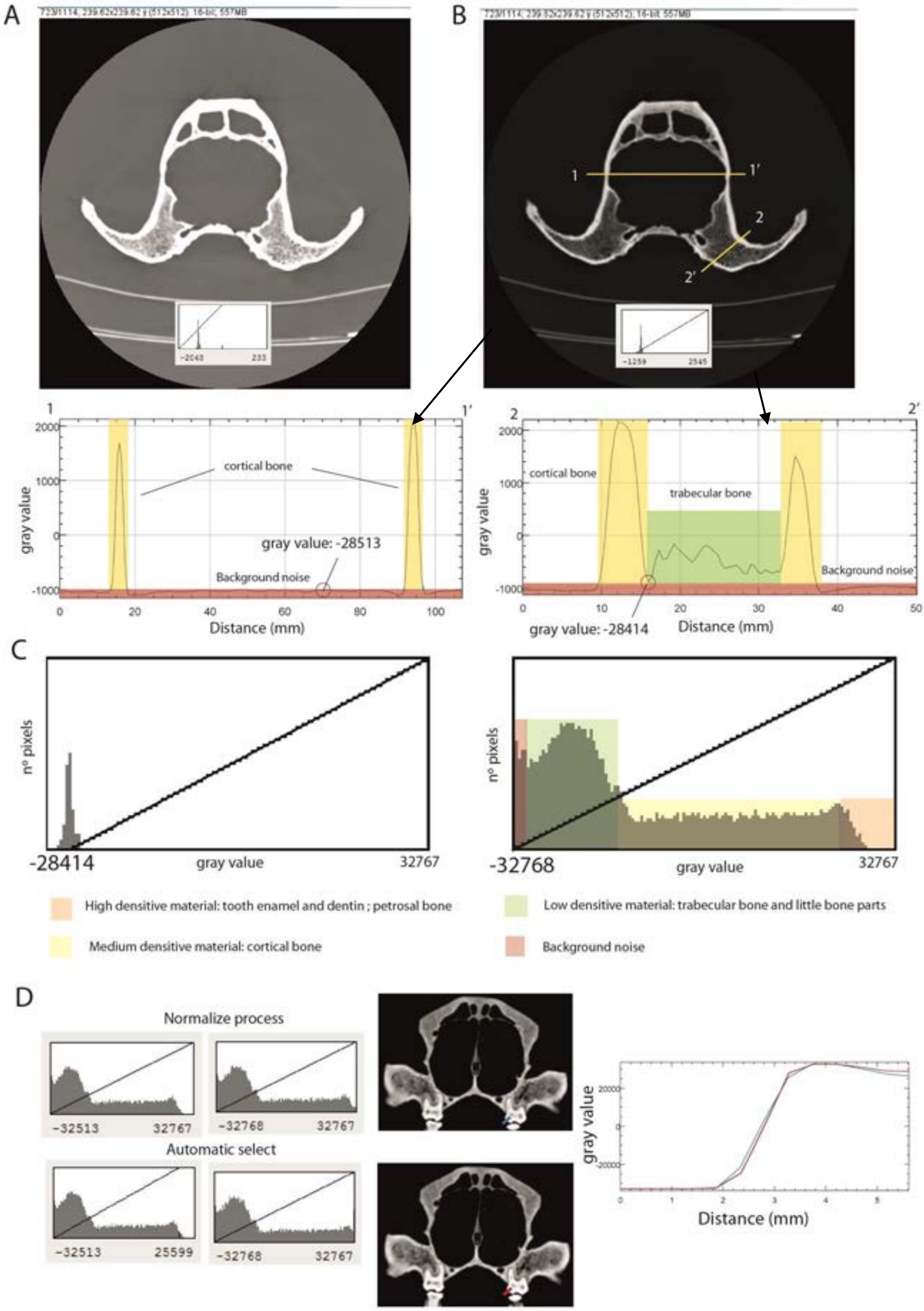
A
B
1
1'
2
2'
cortical bone
trabecular bone
gray value: -28513
gray value: -28414
Background noise
gray value
Distance (mm)
C
nº pixels
gray value
-28414
32767
-32768
32767
High densitive material: tooth enamel and dentin ; petrosal bone
Medium densitive material: cortical bone
Low densitive material: trabecular bone and little bone parts
Background noise
D
Normalize process
-32513
32767
-32768
32767
Automatic select
-32513
25599
-32768
32767
gray value
Distance (mm)

← **Figure 2. Image cleaning and calibration process using the skull of Ursus americanus as an example. (A)** Original image stack obtained from the CT scanning (upper) with a not calibrated histogram (lower) in coronal view; **(B)** First step for calibrating the histogram. Note that two different transects across the object are represented by a yellow line. The respective two plot profiles from these two transects are represented below, the cortical bone represented in yellow areas and the trabecular bone represented in green areas. Note that in the first transect there is not trabecular bone. The red colour in both plot profiles represents the background noise; **(C)** Results of histogram calibration and cleaning of the of the first step; The left graph is the original histogram of image stack and the right graph is the resulting histogram after cropping the grey values in the left diagram corresponding to the background noise; **(D)** After repeating the same process than in **(B)** and in **(C)**, the third step for the calibration of the histogram is using the process of normalization (upper graphs) and the automatic selection method (bottom graphs). On the right side, there is a plot comparing both methods, where the blue line corresponds to the grey values using the method of normalization across an object transect and the red line corresponds to the grey values using the automatic selection method across the same object transect.

The calibration of the histogram must be done across different steps. The first step is to obtain a plot profile for grey values of a transect in a convenient zone of the object but crossing the sample at two different locations. Accordingly, we can see the range of grey values associated with bone and other structures –i.e, background noise (**Fig. 2B**). Doing this, the range of values corresponding to the background noise is cropped in the histogram (**Fig. 2C**). The last step is to homogenize the histogram through a process named normalization (Pérez et al. 2013, Pertusa 2010; Burger et al. 2016) (**Fig. 2D**). One possibility is to use the automatic method of selection, but using this method there is an oversizing of the actual grey values of the histogram (red line; **Fig. 2E**) versus the method of histogram normalization used here (blue line; **Fig. 2E**). In the case that the objects do not present artefacts, the next step is to convert the images from 16 to 8 bits. In contrast, if the objects present artefacts (e.g., rings) different filters for image cleaning should be applied before converting the image from 16 bits to 8 bits. These filters are described below.

2.3.2. Image cleaning filters

Once the stack of images is cleaned from background noises, there are still artefacts in the image. Several image filters were applied to remove them. The artefacts can be rings (**Fig. 3**) due to a highly-dense anomalous material derived from taphonomic processes or human-made materials for reconstructing remains. To remove all these effects, I applied the 'mean' and 'sharp' filters available in ImageJ (Hsieh 2009; Pertusa 2010; Rueden et al. 2017). Afterwards, to separate gradients of gray values, I used mathematical operator processes, that is multiplying each pixel by certain values (1.25 to 1.5) to increase the contrast of image stack. This result was subtracted to a grey value (100 to 200). This process was iterated until having the separation between the whitest and the darkest range. After each iteration, the histogram was normalized to avoid calculation errors when applying the aforementioned filters (Maheswari et al. 2010; Maini et al. 2010).

In those images that have a low contrast between the object and the background, the use of contrast filters such as those of emphasis, help to delimit the object margins.

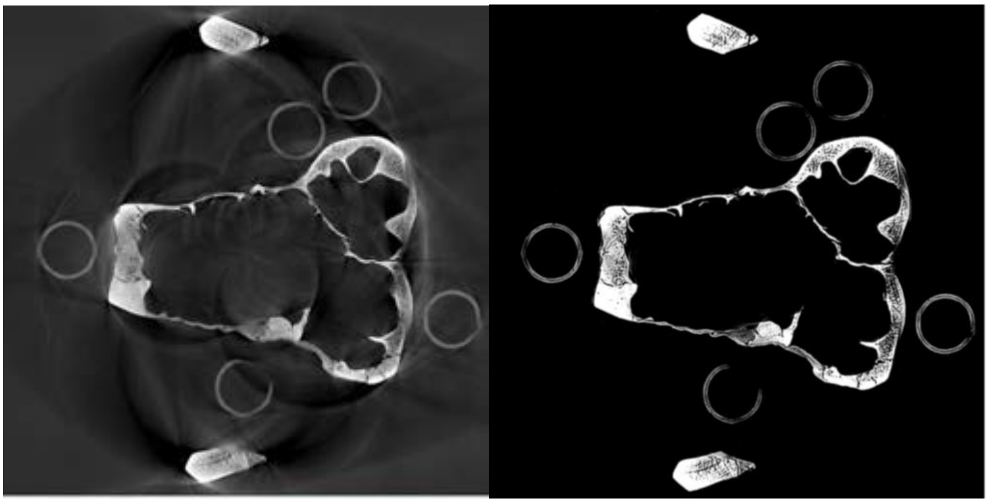

Figure 3. Artefact elimination in CTs, in this case a ring. Using the skull of cave bear as example. (A) Original image stack; **(B)** Image without ring-shaped artefacts after applying the 'mean' and 'sharp' filters.

A Sobel edge detector compares an approximation of the image gradient to a threshold, and automatically decide if a pixel is part of a given margin (Sujatha et al. 2015). A proper thresholding must be determined and computed so that the comparison produces useful results. An edge may be defined as the border between blocks of different colours or different grey levels (Qiu et al. 2012). Mathematically, the edges are represented by first- and second-order derivatives.

Among other edge detection operators (e.g., Banu et al. 2013), I used the Canny's edge detection algorithm (Canny et al 1986), which is an improved method of the Sobel operator and it is considered a powerful method for edge detection.

A second category of filters that detect edges are those that use a second-order derived expression of the image, usually the Laplacian or nonlinear deferential expression. This filter has been used in partial parts when edge detection was more complicated given the low gradient of neighbouring pixels (see **section 3.4**).

2.3.3. Unifying parts of image stacks

A general problem when working with CTs is the acquisition size limit of the machine used (Bushberg 2011). Usually, this acquisition size is smaller than the size of the object that a CT can scan, and therefore, a solution is to perform the scanning process by parts. The simplest case is when the object has the same position in all the acquisitions, and therefore, only change the acquisition window by the adjustment of the detector. In this case the process of unifying all the image stacks is automatic using an algorithm named Concatenate algorithm of ImageJ (Rueden et al. 2017). However, in those cases where the object should be moved to scan it again, the object (in our case the skull) is oriented differently in each acquisition, and this suppose a big problem to unify the image stacks. Different processes (described below) to fit all the images at the same orientation should be performed before using the Concatenate algorithm in order to obtain a high-quality matching of the image stacks. These methods are known under the rubric of re-slice.

The re-slice was applied specifically to a micro-CT scan of the skull of a cave bear (**Fig. 4**). This scan was performed at the Steinmann-institut (University of Bonn, Germany) and the micro-CT machine was a Phoenix x-ray 240kV. Specifically, the skull was scanned in five parts: the caudal part, the medial, the frontal part, and the two zygomatic arches (both laterals). All of them were joined considering the same pixel sizes on the X, Y, Z axes, obtaining 2087 slices. The conditions of the histogram must be the same as well as the voxel and pixel size, which in this case where 0.24637mm and 1024x1024, respectively.

The histogram and voxel size conditions must be the same. The characteristics of the CT data are 1024x1024 matrix and the voxel size x, y, z is 0.244637 mm. The conditions of acquisition in the CTscan for this specimen are 180 kV and 160 mA. The CT of the caudal part of the skull had 1024 slices, and from the slice 477 to the slice 1024 had relevant information of the object (i.e., bone represented). The CT of the medial part of the skull had 1024 slices and only the slices from 1 to 880 had relevant information of the object. From these subsets of slices, I used the stacking tool of ImageJ (Rueden et al. 2017) to merge the two blocks of image stacks of both CTs (medial and caudal) at their corresponding order. The rostral part is disoriented with respect to the fused part (caudal-medial). To make the alignment, the two parts were positioned in the same view (coronal) and in the same slice. This process was repeated to fit and merge the lateral parts of both the right and left zygomatic arch. Once the five CTs were merged, the final histogram was normalized and converted from 16 bits to 8 bits (**Fig. 2D**) and the concatenation the all image stacks was performed (**Fig. 4F-I**).

2.3.4. Interpolation process

In order to analyse the CTs of all the skulls, they should be comparable, that is that all of them should have the same resolution and orientation. Moreover, after doing this, in some cases the resolution of some small parts (e.g., connections among trabeculae) should be enhanced. To do this, I applied a method called Bicubic (Van Hecke et al. 2010; Parsania et al. 2016; Rajarapollu et al. 2017). This method of interpolation was applied through this PhD Thesis to: (i) convert non-isotropic to isotropic voxel in order to standardize the resolution; (ii) reorient the sample in the CT in order to have the same orientation; (iii) increase voxel resolution in order to have a higher resolution of the small structures at histological level.

(i) Converting non-isotropic to isotropic voxel

This method divides a non-isotropic voxel into two isotropic voxels (**Fig. 5A**, **B**). The process to perform such a conversion is to divide the value of voxel depth by the value of pixel width. The resulting value is used in the scale selection in ImageJ (Maret et al. 2012; Rueden et al. 2017) and in the Z axis of the scale, such value should be added. This process is performed as a preliminary method for the CT re-orientation and further histological analysis, methods for which the parameters used are based on voxels that should be isotropic (Parsania et al. 2016; Rajarapollu et al. 2017).

(ii) Reorienting the sample in the CT.

For comparative studies, the CT scans should be reoriented to the same position. In this case, I aligned the specimens putting the prostion/basion at the same plane (**Fig. 5C**). To do this, the re-slice method of ImageJ (Rueden et al. 2017) is used. This method only operates with image stacks with isotropic voxels. Therefore, the Bicubic method explained above is necessary to correctly execute this step. To reorient the skull, the zygomatic arches are oriented to the same plane in coronal view (**Fig. 5C**, left) and to know how many degrees the skull should be rotated. Afterwards, this angle is measured in sagittal, axial and coronal view **Fig. 5C**, intermediate) to re-orient the skull in order to have the prostion and basion in the same plane **Fig. 5C**, right).

(iii) Increasing voxel resolution

In some studies performed through this PhD Thesis, a resolution increase of the CT (increase in pixel size) was applied to improve the contrast of small structures such as the trabeculae of cancellous bone. To perform this process, pixel size was increased to images from medical CTs of 512 x 512 pixels to 1024 x 1024 pixels. This process was performed in image J (Rueden et al. 2017) using the Bicubic interpolation method (Maret et al. 2012; Parsania et al. 2016; Rajarapollu et al. 2017; Camardella et al 2017) (**Fig. 5D**).

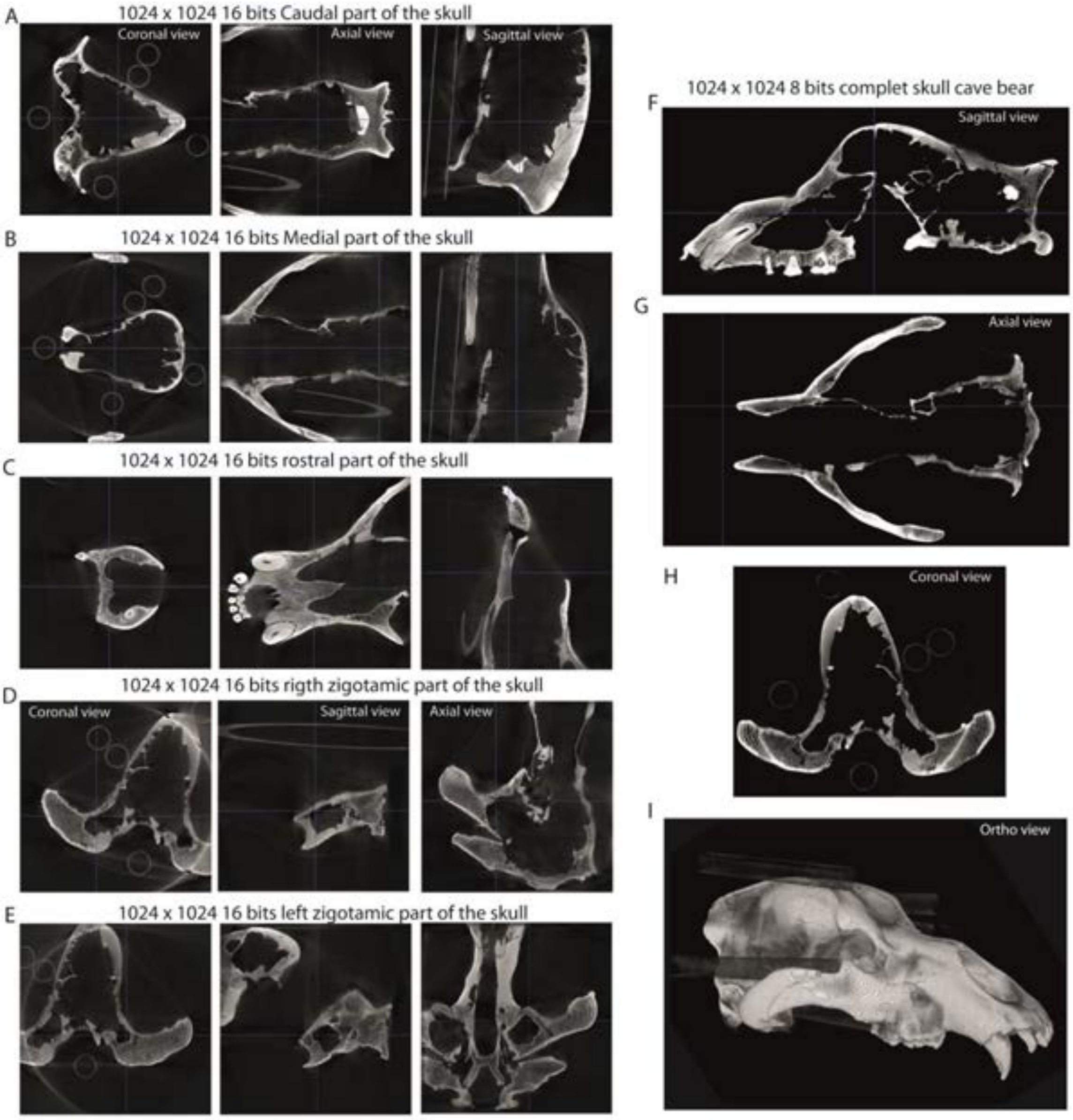

Figure 4. Schematic process of fitting different image stacks to the same orientation, using the re-slice method in imageJ (Rueden et al. 2017) in the cave bear skull (*U. spelaeus* ssp; **(A)** Image stack of the caudal part; **(B)** Image stack of the medial part; **(C)** Image stack of the frontal part; **(D)** Image stack of the right zygomatic arch; **(E)** Image stack of the left zygomatic arch; **(F)** skull resulted from the re-slice process by fitting all the image stacks at the same orientation in sagittal view; **(G)** the same than in (F) but in axial view; **(H)** the same than in (F) in coronal view; **(I)** orthoview of the fitted object.

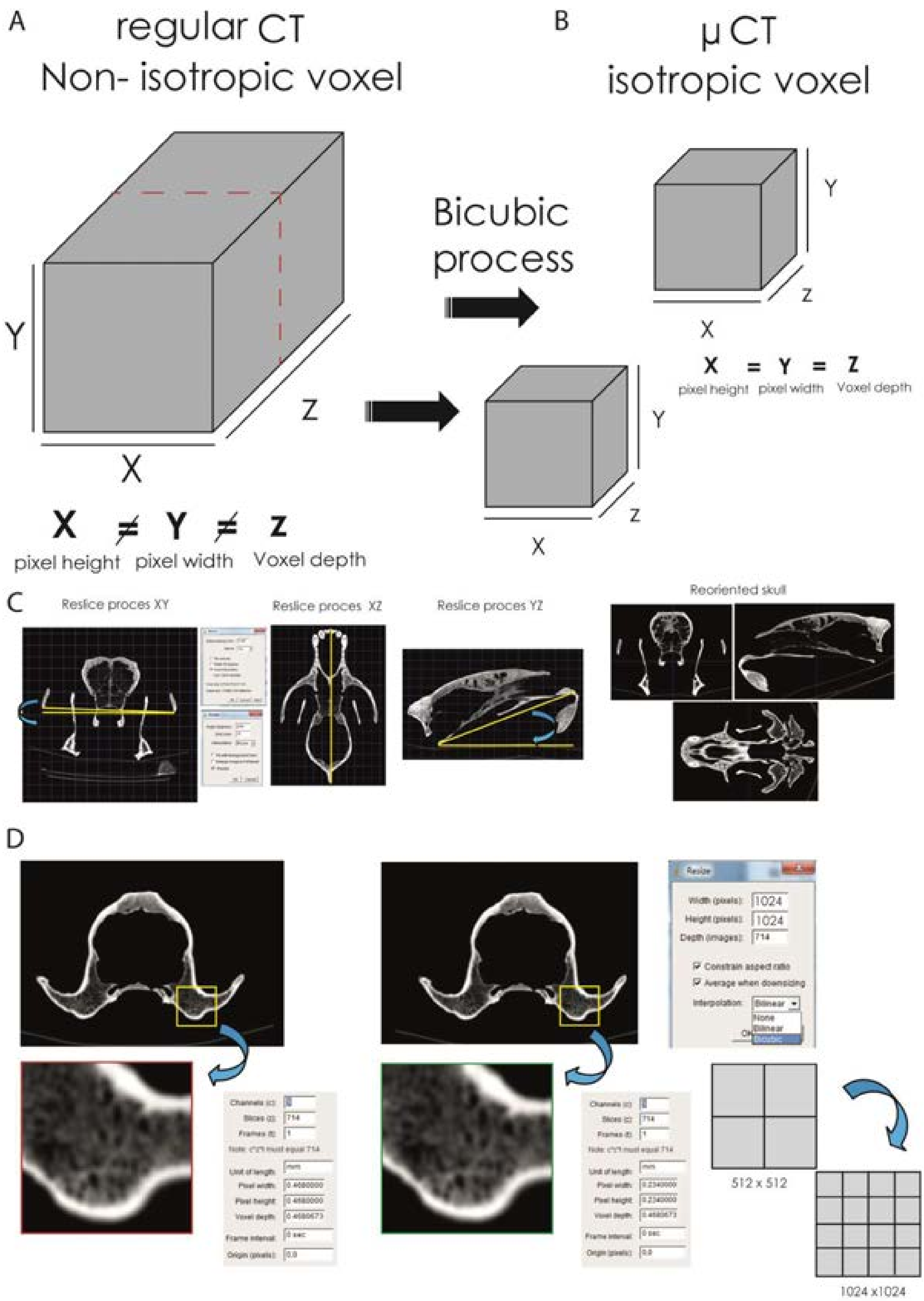

Figure 5. Bicubic interpolation method. Here it is shown the conversion from a non-isotropic voxel **(A)** to isotropic **(B)**; **(C)** reorienting the CT; **(D)** Increasing voxel resolution.

2.4. Virtual reconstruction of fossil skulls

This section describes the methods used for reconstructing in 3D the skulls of the specimens analysed through this PhD Thesis. For obvious reasons, the specimens that have required more reconstruction processes and virtual repairs are fossils (Pahl 1986; Novacek 1993; Zollikofer et al. 2005; Abel et al. 2012; Cunningham et al. 2014; Lautenschlager 2016).

2.4.1. *Ursus ingressus* skull (PIUW3000/5/105)

In the case of the skull of *Ursus ingressus* (**Fig. 6**), the optimal histogram range was chosen to create a *mask* (different layers) for both the skull bone and the teeth, as explained in the process of segmentation. The 3D surface model created from that mask for both skull and teeth is represented in **Figure 6** in green, and the parts of bone that are lacking due to preservational reasons are represented in red. I virtually selected the parts of actual bone that corresponds to those bone parts that are lacking in the mirror side of the skull (**Fig. 6**, in red) and I mirrored the actual part into the lacking part by duplicating the object selected (**Fig. 6**, in green).

Once the mirrored bone parts were obtained (i.e., front part of the maxilla, premaxilla, nasal, palatine, some frontal parts, and foramina of the sphenoid; **Fig. 6A-C**), they were fitted anatomically into the skull by means of polylines or contours. Using these contours in red, I generated a bone mask (**Fig. 6A-C**, in green) interpolating within the region bounded by the contours of the polylines. Finally, the lacking parts were reconstructed. This is the case for example of the mirrored canine, that was 'implanted' into the reconstructed alveolus (**Fig. 6D**). This same virtual reconstruction was also carried out in other fossil skulls.

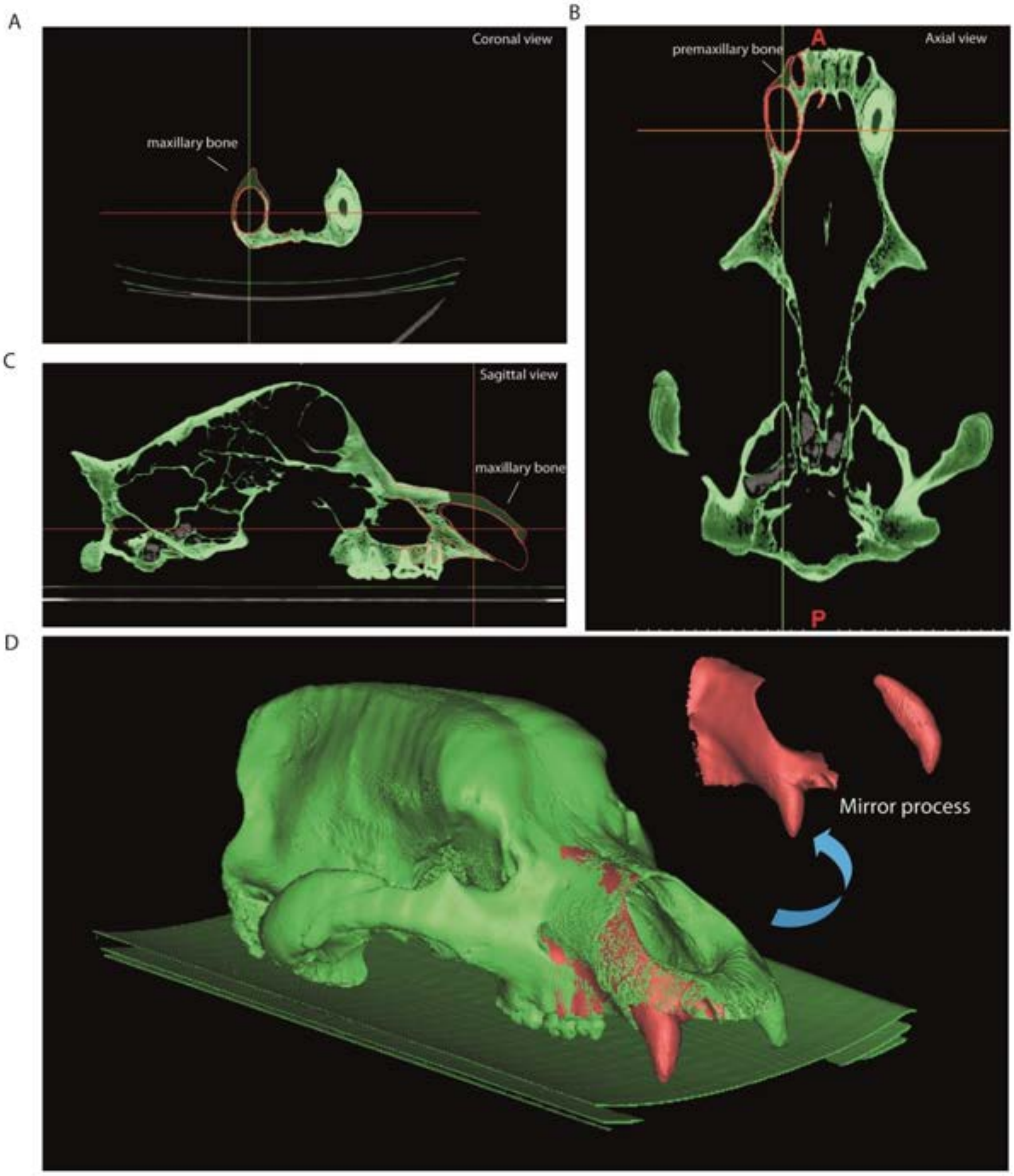

Figure 6. Schematic process of skull reconstruction from the CT of *Ursus ingressus*. (A) A red polyline of the reconstructed bone (in this case maxillary bone) In coronal view; **(B)** reconstructed parts of the premaxillar and maxillar, corresponding to the right canine dental alveolus; **(C)** sagittal view of the reconstructed bone parts (in this case maxillary bone); **(D)** final 3D model reconstructed showing the mirror partial bone skull and the canine (in red); in green is represented the original bone.

2.4.2. *Ursus spelaeus spelaeus* skull (E-ZYX-1000)

The virtual reconstruction of this skull is represented in **Fig. 7**. For the process of virtual reconstruction, we used a Gradient edge detection filter of grey intensity values between neighbouring voxels. The reason is that this skull was filled with several karstic particles, mainly carbonated material and clay sediments of different types of grain. Such material when occupying and filling internal spaces, such as paranasal structures, should be removed. To do this, I used virtual methods that allowed distinguishing the exogenous material from real bone (**Fig. 7 A-B**).

The algorithms used for the Gradient edge detection were based in the complex matrix operators of *Sobel* type (see **section 2.3.2** of this chapter). Therefore, we used a segmentation method by interpreting pixel values as altitudes, where a grey-level image can be seen as a topographic relief. The idea behind these algorithms is to compute lines form this topographic image. This process converts the original images into 3D topographic border gradients (**Fig. 7B**), which the program uses as a guide to generate segmentation layers based on the initial conditions of signalling and layer marking. In other words, in the original project, points in the three views along the CT will mark the different structures subject to separation in a rough way. The algorithm when interpolating the border gradient data (**Fig. 7B**) with the pre-marked signals generates the masks of the structures completely delimited from the others (**Fig. 7C**). In **Figure 7C**, the green layer is referred to bone, the yellow layer refers to the karstic material within the skull, the red layer is referred to the paranasal cavities, and the blue layer is referred to the teeth (only visible in frontal view). In the maxillo-dental reconstruction of this skull, the left dental series was very worn by taphonomic processes, and therefore, it was reconstructed (**Fig. 7D-E**) using the same procedure than for the skull of *U. ingressus*. For this process, the right dental series was chosen with perfect preservation, and a mirror process was performed to obtain the left dental series (**Fig. 7D**). The exact repositioning and positioning of the dental pieces were performed following the same process than the one used for the skull of *Ursus ingressus* (**section 2.4.1** of this chapter). The bone of the periodontal areas on the left side was partially reconstructed in the segmentation process (**Fig. 7E**), using the same procedure than in the skull of *Ursus ingressus* (**Fig. 6D**).

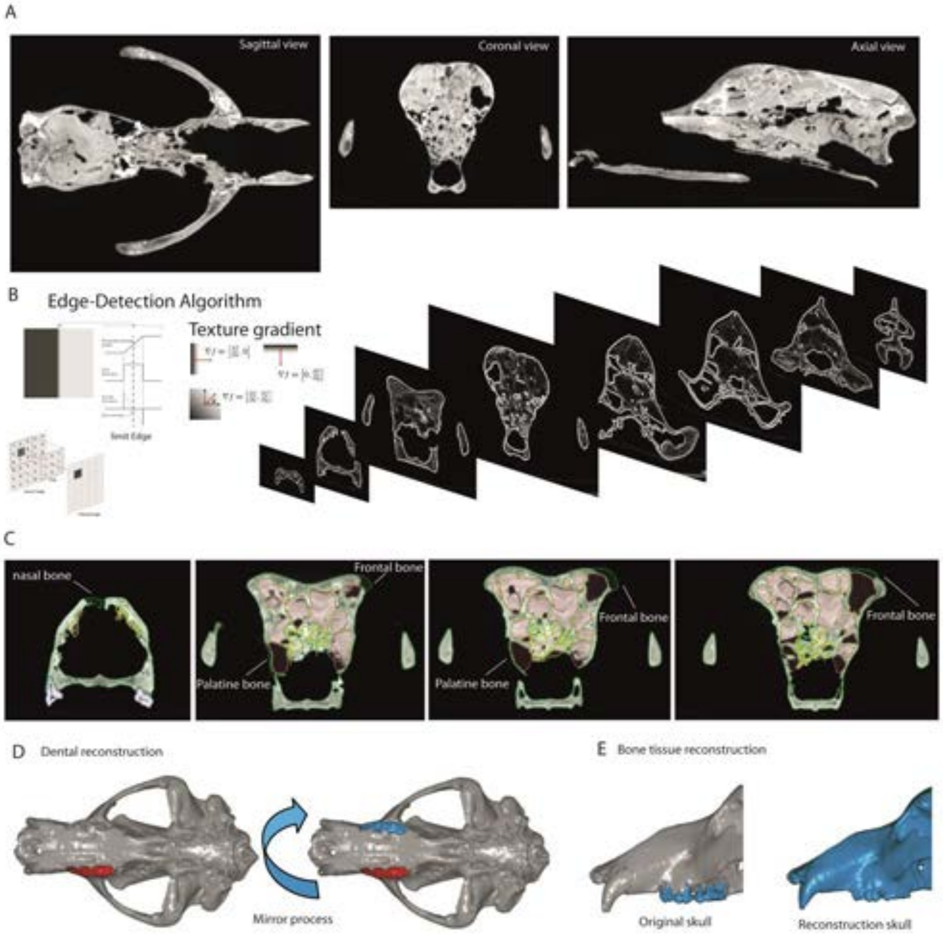

Figure 7. Virtual reconstruction of *Ursus spelaeus spelaeus* skull. (A) Sagittal, coronal and axial views of the skull infilled with exogenous material; **(B)** Edge-detection process applied to delimit the exogenous material from real bone; **(C)** Coronal views of different slices along the antero-posterior axis, showing the bone delimited through the gradient filtering and the reconstructed parts (nasal, frontal, and palatine bone); **(D)** Reconstruction of the upper left dental series. In red, the selected object, and in blue the object mirrored; **(E)** Comparison between the original skull (in grey) and the final skull (in blue) with the periodontal region of the maxillary bone reconstructed.

2.4.3. *Ursus spelaeus eremus* skull (PIUW-SW 483)

This skull is the one that needed a higher degree of virtual reconstruction in different areas of the skull (**Fig. 8**). I mirrored the preserved parts of the bone **Fig. 8E**, in red) and I use these parts to generate the reconstructed bone of the broken or lacking bone parts (**Fig. 8 A-D**).

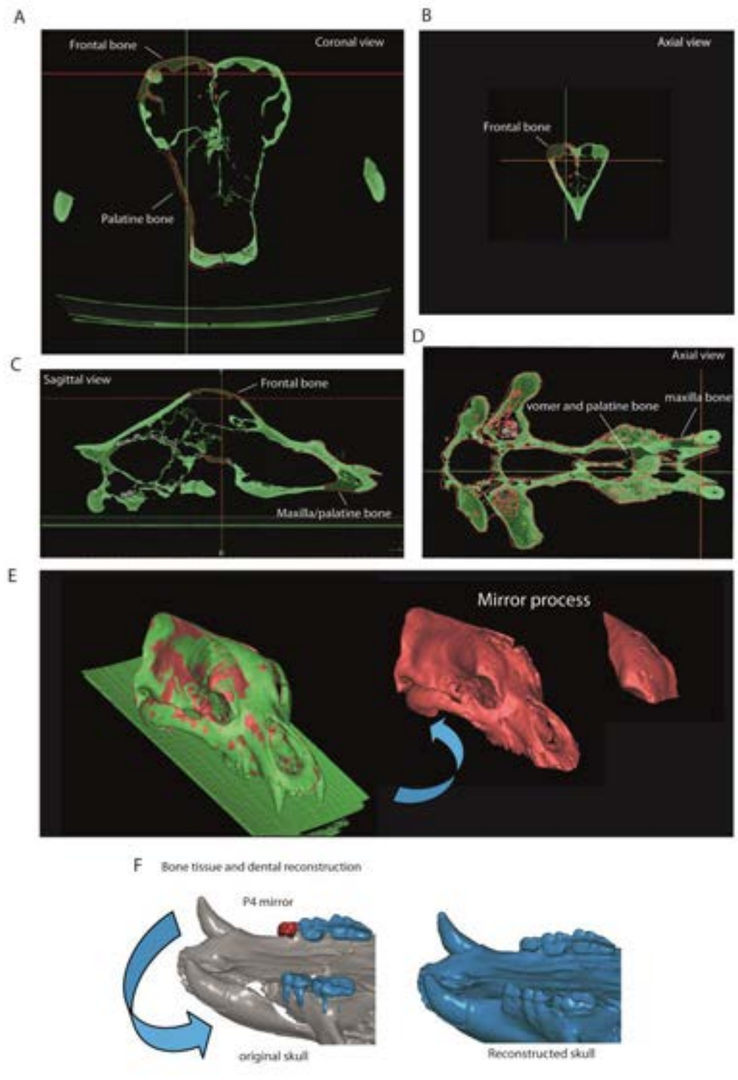

Figure 8. Virtual reconstruction of the skull of *Ursus spelaeus eremus*. (A) coronal view showing the red polyline to reconstruct the lacking parts of bone; **(B)** axial view showing the red polyline to reconstruct a left portion of the frontal bone; **(C)** sagittal view showing the reconstructed parts of the frontal, maxillar, and palatine bones; **(D)** axial view showing the reconstructed bone parts of the vomer, palatine bones, and maxillary bones; **(E)** Models showing in red the mirrored parts of the frontal dome and in green the original bone; **(F)** Dental reconstruction process. In red, the left fourth premolar for mirroring on the right dental series.

Once the skull was virtually reconstructed, it was post-processed, as explained in **section 2.5**. For the virtual reconstruction of the fourth right premolar, I mirrored the left fourth premolar and it was 'implanted' into its corresponding alveolus (**Fig. 8F**).

The fourth premolar was precisely reconstructed in the alveolar cavity, adapting the shape, size and orientation of such dental piece to the specific anatomical requirements.

2.4.4. *Ursus spelaeus ladinicus* skull (PIUW-CU 703)

The virtual reconstruction of *Ursus spelaeus ladinicus* is shown in **Figure 9**. In this case, only the right temporo-mandibular joint (TMJ) and the left canine were virtually reconstructed. For the reconstruction of the TMJ, a preliminary step was performed to preselect the left TMJ. With this anatomical selection, we proceeded to mirror the structure (**Fig. 9A-C**). As this structure is essentially formed by trabecular bone with a high complexity of the trabeculae, it is unfeasible to generate a new layer of bone as performed in other fossils. Therefore, the easiest way was to adapt the repositioned fragment and merge it later (**Fig. 9D**).

The meshes (a 3D topological surface whose basic units are triangles) of the skulls that have been virtually reconstructed were generated and exported into specific software for mesh post-processing.

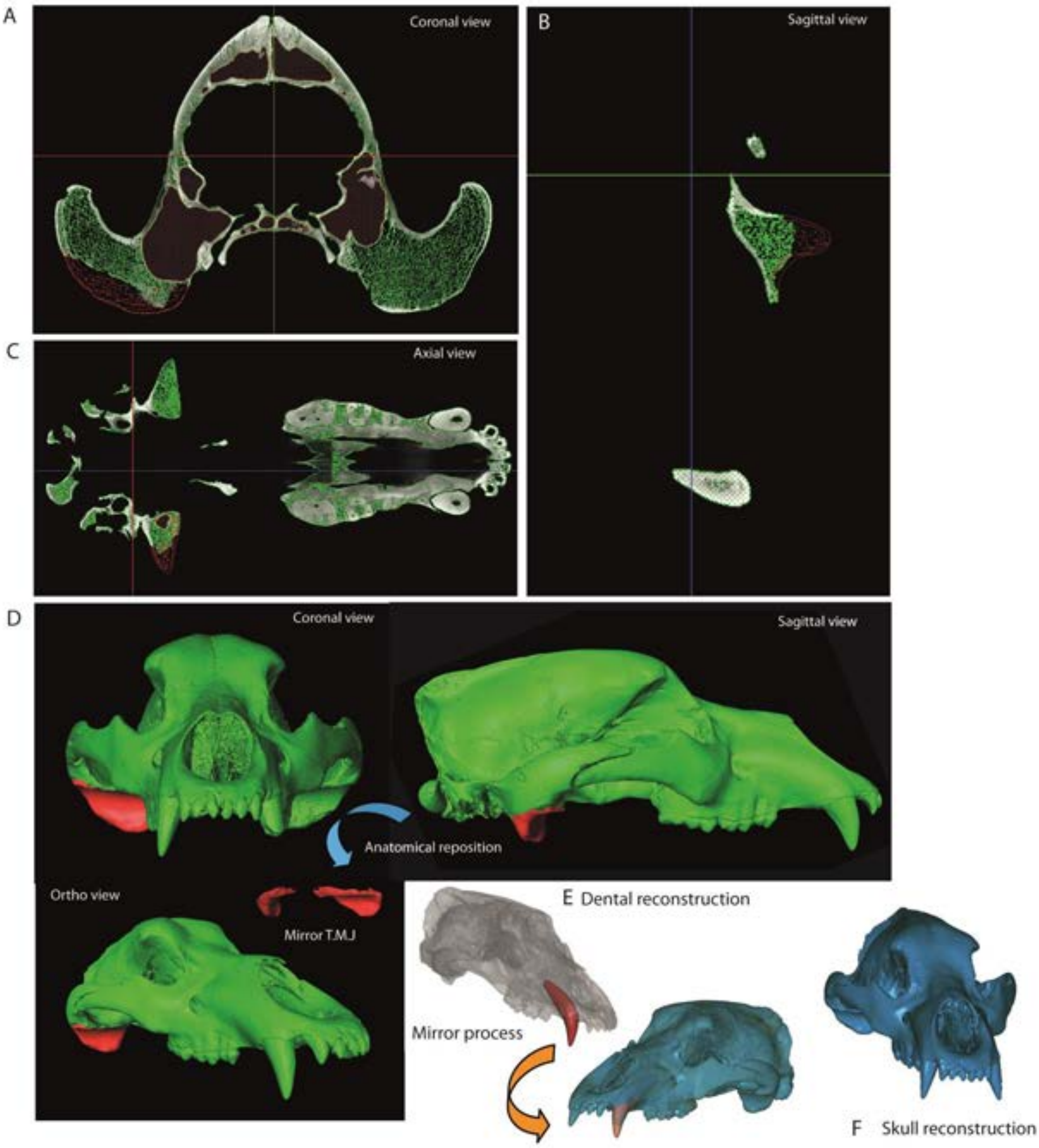

Figure 9. Virtual reconstruction of *Ursus spelaeus ladinicus*. The lacking right TMJ is shown in coronal **(A)**, sagittal **(B)**, and axial views **(C)**. In red is shown the polyline to mirror the left TMJ; **(D)** orthoview of the 3D models, showing in red the left TMJ, and in green the actual bone; **(E)** Dental reconstruction of the right canine. In red, the select object (left canine) to do the mirroring; **(F)** orthoview of the reconstructed skull.

2.5. Mesh post-processing and mesh topological deviation

The edition of meshes is known as tessellation (either to increase or decrease the number of triangles in a mesh). The mesh models generated were exported at maximum resolution to be conservative. This requires some work of mesh pre-processing, named decimation, which eliminates the density of topological triangles, without compromising its stability and integrity. This process is explained in **Figure 10**.

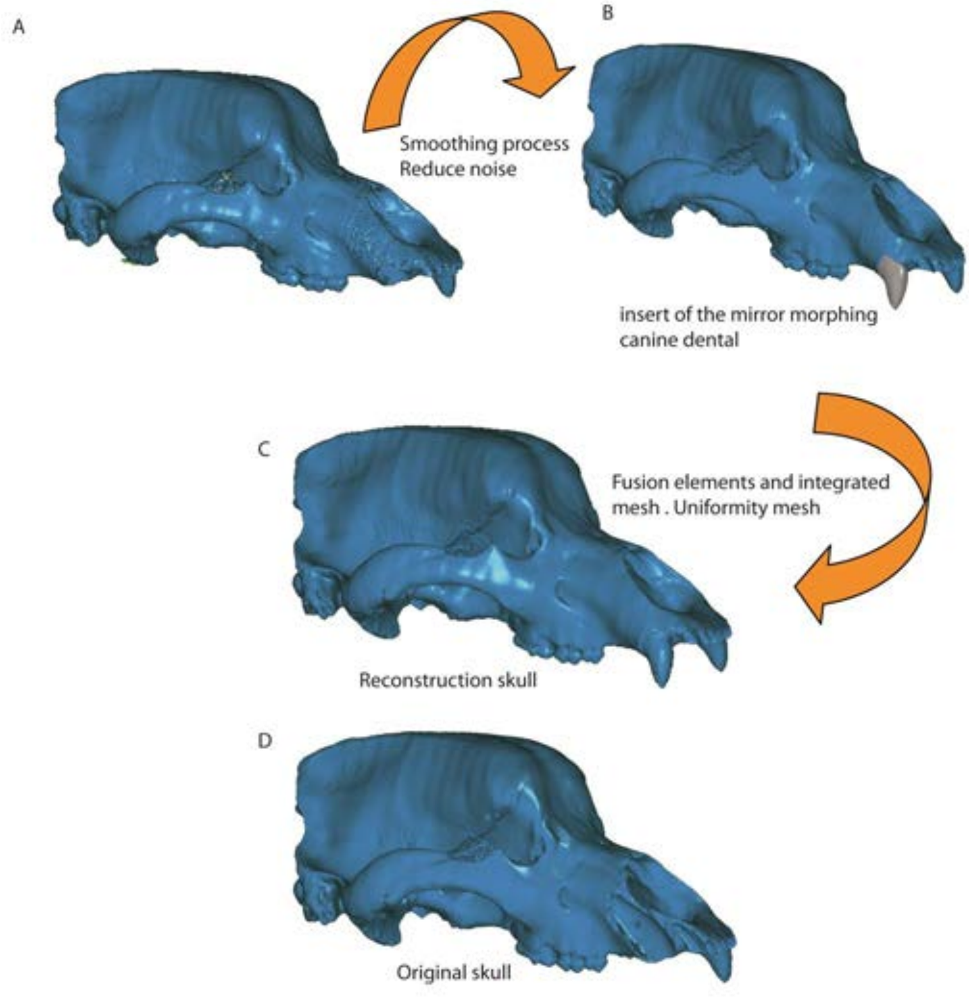

Figure 10. Schematic post-processing of *Ursus ingressus* skull as an example of mesh tesselation and decimation. **(A-B)** First step of mesh post-processing, based in the decimated of density of mesh triangulation and smoothing; **(B -C)** Second step of mesh post-processing, based in the fusion and integration of different elements, being in this case the lacking teeth; **(C)** Final step of mesh post-processing, based on noise deletion in the mesh; **(D)** Original skull before reconstruction.

In the case that some missing parts of the skulls were reconstructed, I verified if such reconstructions were anatomically correct. To do this, an analytical processing of topological deviations was applied. Such an analysis is based in a contour analysis by applying a curvature map to visualize if the model is correctly generated. In the case that the mesh was not correct, it may be due to (i) very folded triangles, or (ii) an error in the resulting curvature map. In this case, it will be necessary to see if the mesh is completely closed or the triangles of the mesh have the correct orientation (all the ventral and dorsal faces of all triangles have the same orientation). In the colour pattern of the curvature map, cold colours are assigned to the outside edges, green colours are assigned to the surfaces with little angle, and warm colours to the inside edges (**Fig. 11C**). If this first step of post-processing of the mesh is correct, then the second step of mesh post-processing (i.e., topological analysis) is carried out. This process is explained through **Figures 11-13** in the four skulls of cave bears analysed in this PhD Thesis. In the case of comparing the original skulls with the reconstructed ones, the information obtained is in the form of colour maps reflecting the topological arrangement of the added bone structures (**Fig. 11D**; **Fig.12C**; **Fig. 13C,F**)

Therefore, those structures artificially added will have a positive deviation with warm colours, and those that have been removed or are below the topological profile of the original skull will have cold colours (**Fig. 11E**,**12C**). For such comparison (**Fig. 12D**), the reconstructed skull is chosen as the topological pattern against the original skull. For example, comparing the original skull (original pattern topology) with the reconstructed skull, if the new topology is above the surface pattern topology, the result value is positive, and the colour is warm. In contrast, if the new topology is below of the surface pattern topology, the result value is negative, and the colour is cold. Therefore, the topological information obtained is different than in the first case (**Fig. 12C**). Accordingly, the parts that have been removed (i.e., the matrix) will appear in the topological model with warm colours. The parts added in the reconstruction of the skull will appear in the topological model with cold colours. This information is used to quantify the taphonomic level of the element (skull, jaw, etc.) and its conservation status.

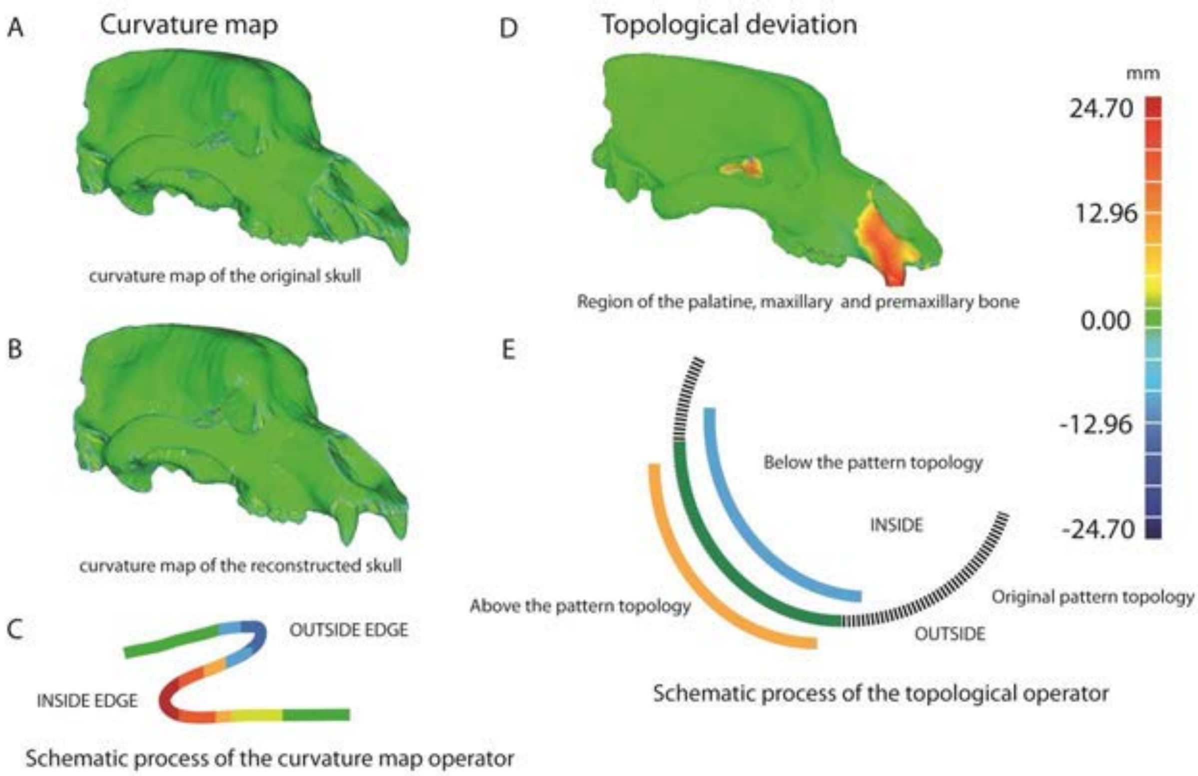

Figure 11. Schematic post-processing of *Ursus ingressus* skull as an example of topological deviations. (A-C) First post-processing mesh, based in the curvature map, original skull (A), and reconstructed skull (B); **(C)** Schematic process of the curvature map operator: outside edge, cold colours; inside edge, warm colours; **(D)** Second post-processing mesh, based in topological deviations. The regions of warm colours correspond with the reconstructed bone parts; **(E)** Schematic process of the operator of topological deviation.

Once all these processes have been performed on the CTs or on the regular surface scanners, the resulting 3D models are subject to analyses on ecomorphology and evolution. However, as these methodologies have been applied trough different chapters, they are explained in detail trough **chapters 3.1-3.5**.

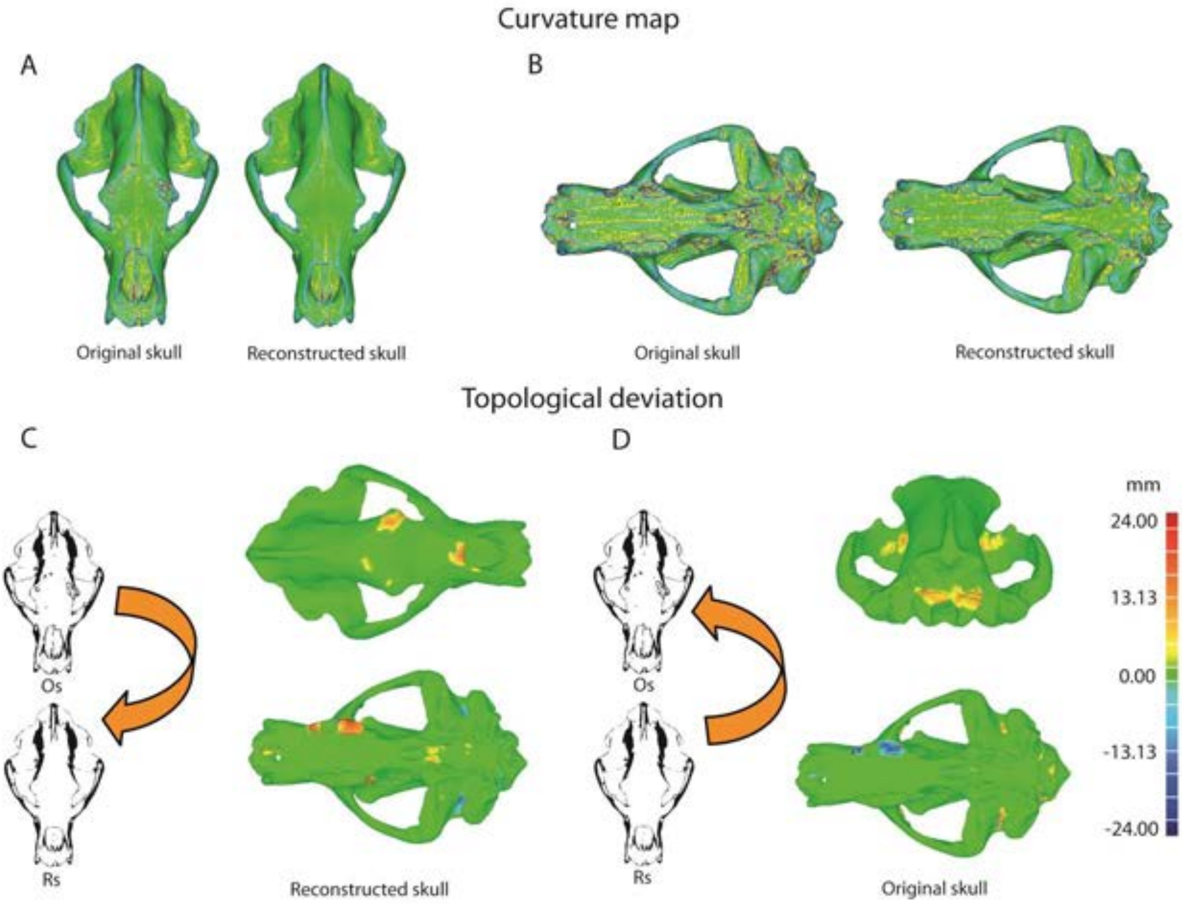

Figure 12. Schematic post-processing of *Ursus sp. spelaeus* skull as an example of topological deviations. (A-B) First post-processing mesh, based in curvature maps, in dorsal view (A) of the original skull (left side), and reconstructed skull (right side), and in ventral view (B) of the original skull (left side) and reconstructed skull (right side); **(C-D)** Second post-processing mesh, based in topological deviations; in (C) it is shown the comparison between the original skull with the reconstructed skull, and in (D) the comparison of the reconstructed skull with the original skull. **Abbreviations**: Os (original skull); Rs (Reconstructed skull).

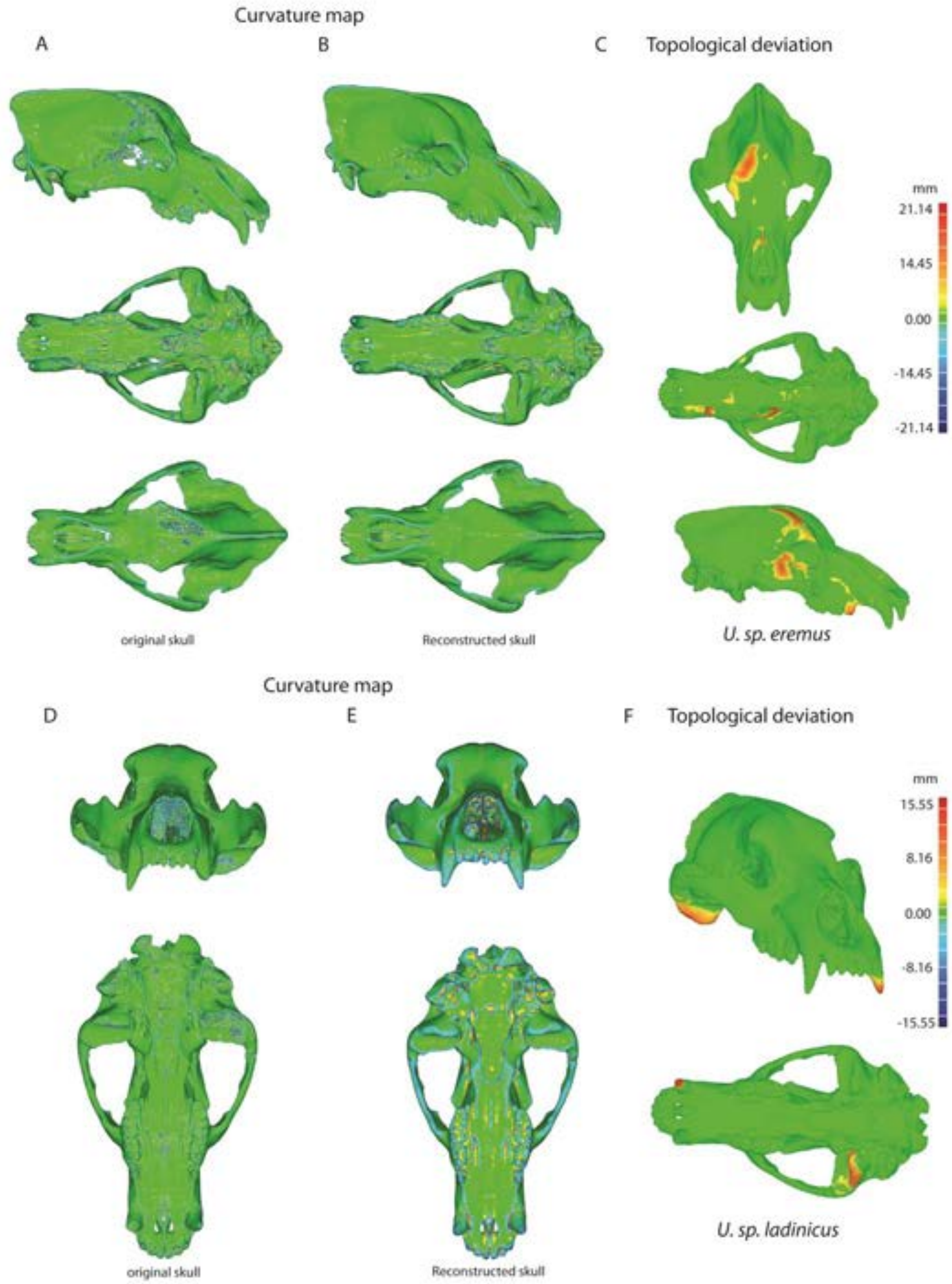

Figure 13. Analysis post-processing of *Ursus sp. eremus* skull and *Ursus sp. ladinicus.* In *U. sp. eremus*: **(A-B)** First step of mesh post-processing, based in curvature maps, showing in (A) the original skull in orthogonal, ventral, and dorsal view, and in (B) the reconstructed skull in orthogonal, ventral, and dorsal view; **(C)** Second step of mesh post-processing, based in topological deviations. In *U. sp. ladinicus*: **(D-E)** First post-processing mesh, based in the curvature map, showing in (D) the original skull in frontal and ventral view, and in (E) the reconstructed skull in frontal and ventral view; **(F)** Second step of mesh post-processing based in the topological deviations.

2.6. References

- Abel RL, Laurini CR, Richter M. 2012. A palaeobiologist's guide to virtual micro-CT preparation. Palaeontol Electron. 15(2): 1-17.
- Banu S, Giduturi A, Sattar SA. 2013. Interactive Image Segmentation and Edge Detection of Medical Images. ISSN (print). 2249-7277.
- Burger W, Burge MJ. 2016. Digital image processing: an algorithmic introduction using Java. Springer.
- Bushberg JT, Boone JM. 2011. The essential physics of medical imaging. Lippincott Williams & Wilkins.
- Calzado A, Geleijns J. 2010. Computed Tomography. Evolution, technical principles and applications. Revista de fisica medica. 11(3): 163-180.
- Camardella LT, Breuning H, Vilella ODV. 2017. Are there differences between comparison methods used to evaluate the accuracy and reliability of digital models?. Dental press journal of orthodontics. 22(1): 65-74.
- Canny J. 1986. A computational approach to edge detection. IEEE Transactions on pattern analysis and machine intelligence. (6): 679-698.
- Cunningham JA, Rahman IA, Lautenschlager S, Rayfield EJ, Donoghue PC. 2014. A virtual world of paleontology. Trends Ecol Evol. 29(6): 347-357.
- Endo H, Frey R. 2009. Anatomical imaging: towards a new morphology. Springer Science & Business Media.
- Gonzalez RC, Woods RE. 2002. Digital Image Processing, 2nd ed. Englewood Chiffs, NJ: Prentice-Hall
- Hsieh J. 2009. Computed tomography: principles, design, artefacts, and recent advances. Bellingham, WA: SPIE.
- Kak AC, Slaney M, Wang G. 2002. Principles of computerized tomographic imaging. Med Phys. 29(1): 107-107.
- Lautenschlager S. 2016. Reconstructing the past: methods and techniques for the digital restoration of fossils. Roy Soc Open Sci. 3(10): 160342.

- Maheswari D, Radha V. 2010. Noise removal in compound image using median filter. International journal on computer science and engineering. 2(04): 1359-1362.
- Maini R, Aggarwal H. 2010. A comprehensive review of image enhancement techniques. arXiv preprint arXiv:1003.4053.
- Maret D, Telmon N, Peters OA, Lepage B, Treil J, Inglèse JM, Sixou M. 2012. Effect of voxel size on the accuracy of 3D reconstructions with cone beam CT. Dentomaxillofac Rad. 41(8): 649-655.
- Novacek MJ. 1993. Patterns of diversity in the mammalian skull. In: Hanken J, Hall BK, eds. The skull, volume 2: patterns of structural and systematic diversity. Chicago: University of Chicago Press. 438–545.
- Pahl KP.1986. The Mammalian Skull. Biological Structure and Function.
- Parsania PS, Virparia PV. 2016. A comparative analysis of image interpolation algorithms. International Journal of Advanced Research in Computer and Communication Engineering. 5(1): 29-34.
- Pérez JMM, Pascau J. 2013. Image processing with ImageJ. Packt Publishing Ltd.
- Pertusa JF. 2010. Técnicas de análisis de imagen (Universitat de València).
- Qiu T, Yan Y. 2012. An autoadaptive edge detection algorithm for flame and fire image processing, IEEE Transactions on instrumentation and measurement. 61(5).
- Rajarapollu PR, Mankar VR. 2017. Bicubic interpolation algorithm implementation for image appearance enhancement. International Journal of Computer Science And Technology.
- Rueden CT, Schindelin J, Hiner MC, DeZonia BE, Walter AE, Arena ET, Eliceiri KW. 2017. ImageJ2: ImageJ for the next generation of scientific image data. BMC bioinformatics. 18(1): 529.
- Sujatha P, Sudha KK. 2015. Performance analysis of different edge detection techniques for image segmentation. Indian Journal of Science and Technology. 8(14):1.
- Van Hecke W, Leemans A, De Backer S, Jeurissen B, Parizel PM, Sijbers J. 2010. Comparing isotropic and anisotropic smoothing for voxel-based DTI analyses: A simulation study. Hum Brain Mapp. 31(1): 98-114.

- Zollikofer CP, de León, MSP. (2005). Virtual reconstruction: a primer in computer-assisted paleontology and biomedicine. Wiley-Interscience

3

Results & Discussion

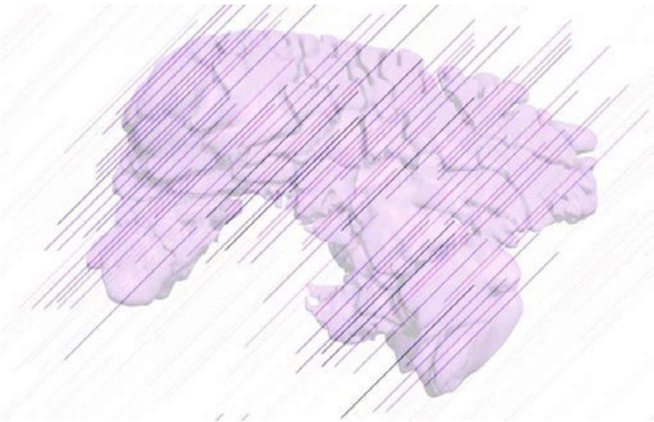

3

3.1. A three-dimensional analysis of tooth-root morphology in living bears and implications for feeding behaviour in the extinct cave bear

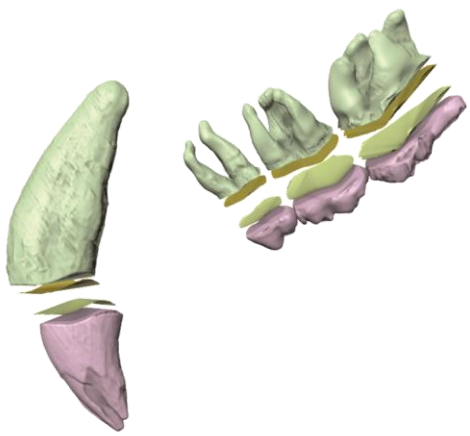

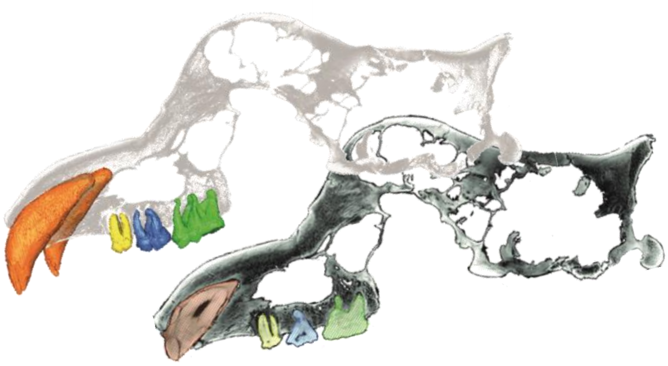

3.1. A three-dimensional analysis of tooth-root morphology in living bears and implications for feeding behaviour in the extinct cave bear

3.1.1. Abstract

The morphology of both crowns and tooth-roots reflects dietary specialisation in mammalian carnivores. In this article, we analyse the tooth-root morphology of maxillary teeth from CT scans of living bears (*Ursus arctos*, *Ursus americanus*, *Ursus maritimus*, *Ursus thibetanus*, *Melursus ursinus*, *Helarctos malayanus*, *Tremarctos ornatus* and *Ailuropoda melanoleuca*) in order to make inferences about the diet and feeding behaviour of the extinct cave bear (*Ursus spelaeus* sensu lato). Specifically, we investigate two major mitochondrial clades of extinct cave bears recognized by previous authors: *Ursus ingressus* and *Ursus spelaeus* (*U. spelaeus spelaeus*, *U. spelaeus ladinicus, U. spelaeus eremus*). Our results indicate a close association between tooth-root surface area and feeding behaviour in all living bear species. Tooth-root surface area values of cave bears suggest that they relied more on vegetative matter than living brown bears (*Ursus arctos*) but subtle differences between these species/subspecies could also indicate different feeding strategies among the members of cave bear complex.

3.1.2. Introduction

The extremely abundant fossil record of the cave bear (*Ursus spelaeus*) from the Pleistocene of Eurasia (Kurtén 1967; Peigné et al. 2009) has provided important information on its paleobiology. Accordingly, very recently, aspects of its metabolism (Grandal d'Anglade 2018), its phylogenetic relatedness (Knapp et al. 2018), its extinction timing (Terlato et al. 2018; Döppes et al. 2018), or even its longevity and life story (Veitschegger 2018) have been successfully addressed. Despite this, the feeding preferences of the cave bear are still controversial in the literature. In fact, the diet of the cave bear represents an interesting case in which different analytical methods –or even the same methods performed on different populations– apparently give disparate conclusions. Traditional studies based on functional morphology (Kurtén 1967; Mattson 1998) as well as more recent analyses based on 3D geometric morphometrics of the skull (van Heteren et al. 2009, 2014, 2016), on isotopic biochemistry ($\delta^{13}C$/ $\delta^{15}N$) of bones and teeth (Vila et al. 1999; Bocherens et al. 1997, 1999, 2006, 2011, 2018), and on feeding biomechanics (Grandal-d'Anglade 2010) indicate a highly herbivorous diet for the cave bear. However, 2D morphometric analyses (Figueirido et al. 2009), taphonomic evidence (Pinto 2005; Quilès 2006; Pacher and Stuart 2009), dental microwear (Peigné et al. 2009; Peigné and Merceron 2017) as well as biogeochemical analyses performed on specific populations (Richards et al. 2008; Robu et al. 2018) suggest a more omnivorous diet for the cave bear, similar to the one of the living brown bear (*Ursus arctos*).

Tooth-root surface area (hereafter RA) has been shown to be a proxy for dietary specialisation in extant and extinct mammals (e.g. for primates: Spencer 2003; Kupczik and Dean 2008; for carnivores: Kupczik and Stynder 2012; bats: Self 2015a; but see Self 2015b on cricetid rodents). Specifically, RA is correlated with bite force and differences in RA are related to variations in the material properties of the foods masticated (Kupczik and Stynder 2012). Accordingly, RA has been used to make dietary inferences in extinct primate and carnivoran taxa (Kupczik and Hublin 2010; Stynder and Kupczik 2013). Relative to the occlusal area of the teeth, RA avoids biases related to extreme wear in old specimens or to fractured crowns in fossil teeth due to preservational effects. Moreover, RA allows estimation of the bite force in species with incomplete preserved skulls as opposed to using the classic dry skull method of Thomason (1991), which requires complete skulls to estimate cross-sectional areas of the muscles involved in mastication.

In this article we investigate the relationship between tooth-root surface areas of maxillary teeth and feeding behaviour in all living species of the family Ursidae. Our main objective is to make dietary inferences in different species/subspecies of the Pleistocene cave bear complex, or *Ursus spelaeus* sensu lato (s.l.), that have been recognized based on morphology and ancient DNA (**Fig. 1**). Specifically, we analysed *Ursus ingressus* and the three subspecies recognized for *Ursus spelaeus* sensu stricto (s.s.): *U. spelaeus spelaeus*, *U. spelaeus ladinicus,* and *U. spelaeus eremus* (Rabeder and Hofreiter 2004; Rabeder et al. 2004a, 2004b, 2008). Our main purpose is to explore patterns of RA across maxillary teeth in the different species/subspecies of the cave bear complex and by extension their inferred feeding behaviours from this ecomorphological indicator.

3.1.3. Materials and Methods

3.1.3.1. Materials

Thirteen skulls of living and extinct bears (family Ursidae) were CT-scanned from different museum sources (see **Table 1**). Of these, eight represent all the living bear species (*U. arctos*, *U. maritimus*, *U. americanus*, *U. thibetanus*, *M. ursinus*, *H. malayanus*, *T. ornatus* and *A. melanoleuca*) and five belong to different extinct Pleistocene species/subspecies of the cave bear complex (*Ursus spelaeus* s.l.): *U. spelaeus* ssp. (unnumbered specimen, Sloup cave, in the northern part of

Moravian Karst, Czech Republic), Pleistocene and Holocene 115 Ka and 11.7 Ka; *U. spelaeus spelaeus* (E-ZYX-S-1000, Eiros cave, Triacastela, Galicia, Spain); *U. spelaeus ladinicus* (paratype PIUW-Cu 703, Conturines Cave, Italy); *U. spelaeus eremus* (PIUW- SW 483, Schwabenreith Cave, Lower Austria); and *U. ingressus* (PIUW3000/5/105, Dragon Cave of Mixnitz, Austria). The chronological position of all treated cave bear remains is Middle Wurmian (about 65 to 24ka) (Abel and Kyrle 1931; Ehrenberg 1929; Frischauf et al. 2014; Kadlec et al. 2001; Döppes et al. 2009; Döppes et al. 2011; Perez-Rama M et al. 2011; Diedrich 2012; Horacek et al. 2012; Döppes et al. 2016; Fortes et al. 2016; Kavcik-Graumann et al. 2016; Döppes et al. 2018; Nagel et al. 2018; Spötl et al. 2018). As sexual dimorphism among cave bears is well reported (e.g., Kurtén 1955; Grandal d'Anglade and López-González 2005), we sexed our specimens using a protocol detailed in the **Supplementary information**. Our results indicated that the cave bear specimens analysed in this paper are all males. The sampled skulls of living bears are shown in **Figure 2** and those of the extinct cave bears in **Figure 3**.

3.1.3.2. CT pre-processing

The stacks from the CTs were exported as 16bit images in TIFF or DICOM format. Subsequently, we calibrated these images to eliminate the background noises due to Photoelectric and Compton effects by selecting specific ranges of the histograms (Region of interest ROI) using the software ImageJ v. 1.50e (http://rsbweb.nih.gov/ij/). Once the background noise was removed, all images were converted to 8 bits and normalized to 0.5% of grey values to standardize the grey values of the histogram to 0 and 255, respectively.

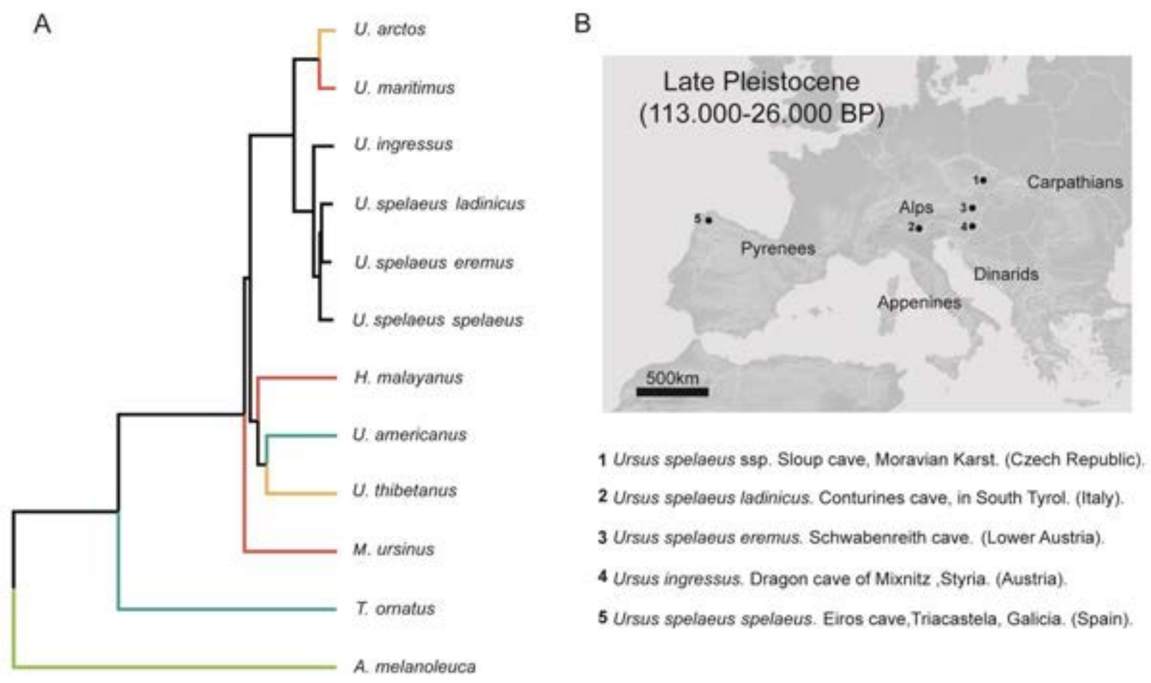

Figure 1. Phylogenetic tree of those ursids species analysed in this study and the geographic locations of fossils sites where the skulls of cave bears were found. (A) The relationships of living bears were taken from the study of Krause et al. (2008) based on ancient mitogenomes. The relationships of the cave bear complex were taken from Stiller et al. (2014). Branch colours represent the diets as established in this paper following the literature (see material and methods for detail). Black lines represent unknown diets; **(B)** geographic locations of the extinct cave bears sampled in this study. For more detail see **Table 1**

3.1.3.3. Tooth-root area calculation

To compute the RA of each maxillary tooth we followed the protocol of Kupczik and Stynder (2012) and compared our findings to those for extant bears by Kupczik and Stynder (2012). To this end, we calculated RA for the upper canine (C), fourth upper premolar (P4), first upper molar (M1), and second upper molar (M2). We chose either the left or right maxillary dentition of each of the specimens depending on the preservation of all tooth roots and the degree of wear.

Table 1. Species, museum numbers and location of the specimens.

Species	Abbreviations	Mus.numb	Location
A. melanoleuca	Ame	VU 3156b	Valladolid, Spain
U. arctos	Uar	USNM 82003	University of California, Los Angeles. Department of Organismic Biology.
U. americanus	Uam	VU 261	Valladolid, Spain
U. thibetanus	Uth	VU 2421	Valladolid, Spain
U. maritimus	Uma	H. 001-05	University of California, Los Angeles. Department of Organismic Biology
T. ornatus	Tor	VU 1661	Valladolid, Spain
H. malayanus	Hma	AMNH28254	Mammalogy collection to the AMNH, NY, USA.
M. ursinus	Uur	AMNH54464	Mammalogy collection to the AMNH, NY, USA.
U. sp. ssp.	U.sp sp**	unnumbered sp.	University of Bonn
U. sp.ladinicus	U.sp.la	PIUW-CU 703 (paratype)	University of Vienna, Department of Paleontology. Vienna, Austria
U. sp. eremus	U.sp.er	PIUW-SW 483	University of Vienna, Department of Paleontology. Vienna, Austria
U. ingressus	U.ing	PIUW3000/5/105	University of Vienna, Department of Paleontology.Vienna, Austria
U. sp. spelaeus	U.sp.sp*	E-ZYX-S-1000	University Institute of Xeoloxia of the University of A Coruña, Spain.

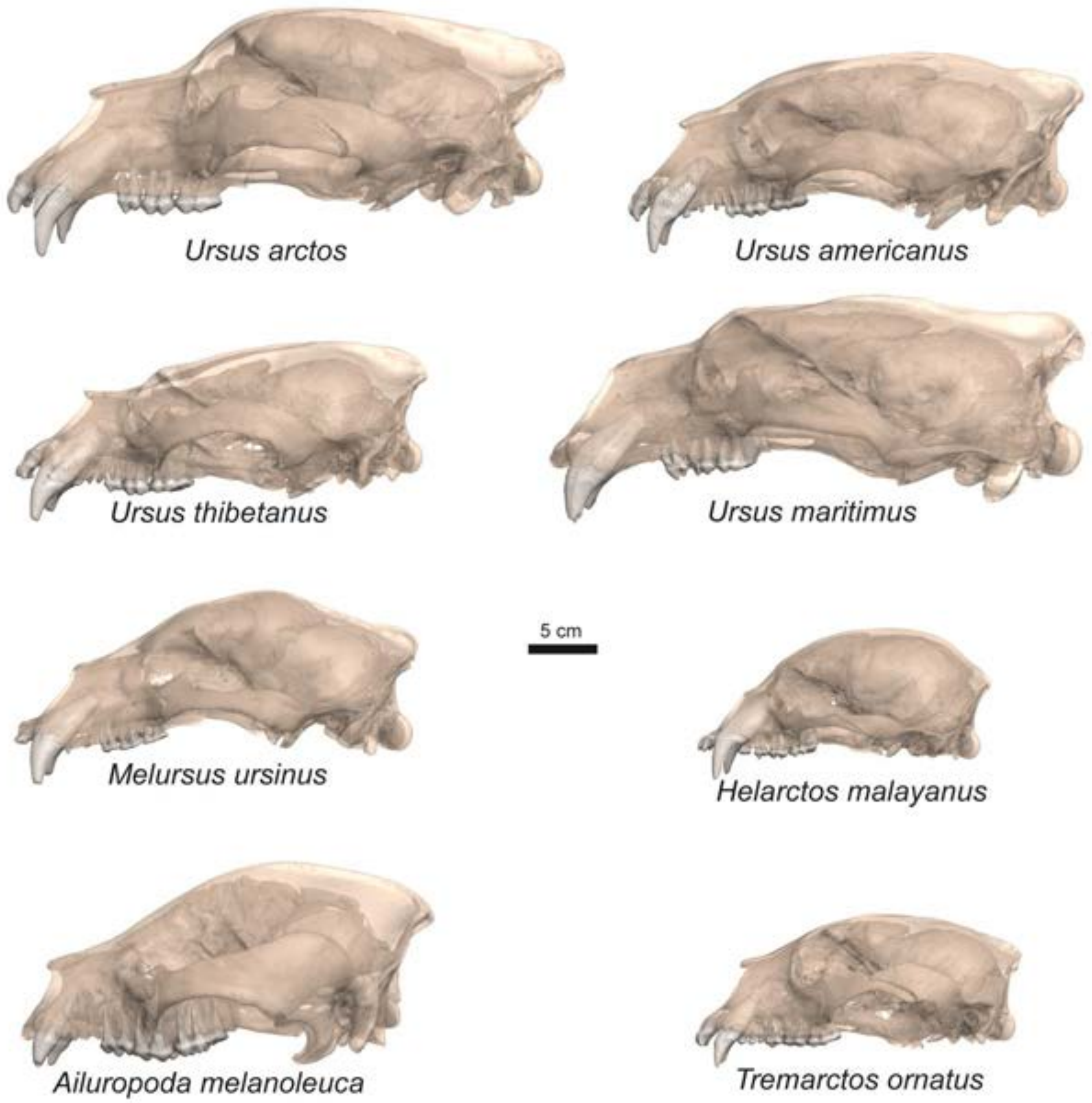

Figure 2. Three-dimensional models of the skulls of living bears analysed in this study.

We reconstructed the 3D models in 3D Slicer v 4.9.0 (Kikinis et al. 2014), and each tooth was segmented with a semi-automatic threshold-based approach with manual editing of the slices (**Fig. 4A**). We included the enamel, dentine, and pulp cavity as one material in the process of the segmentation. We then generated triangulated surface models for each tooth using the constrained smoothing algorithm (kernel size of 4).

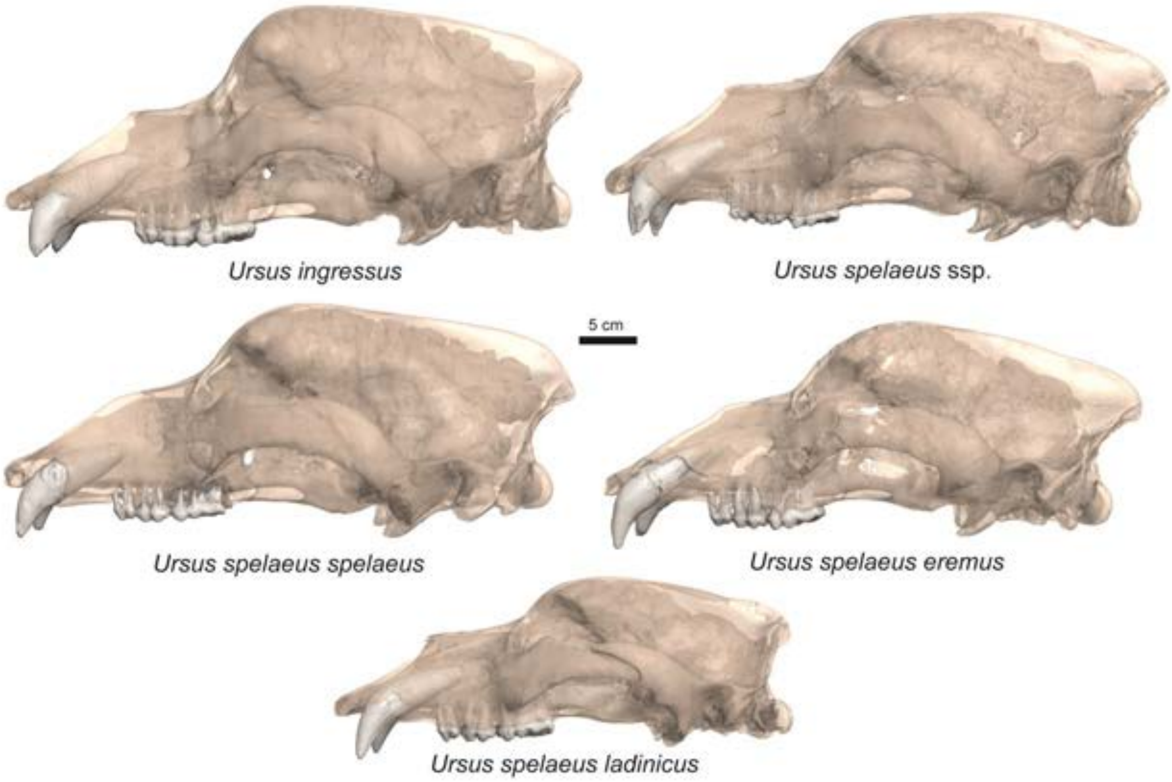

Figure 3. **Three-dimensional models of the skulls of cave bears analysed in this study**. For more detail see Supplementary information.

We used a topographic curve tool along the cemento-enamel junction (**Fig. 4B**) using MeshLab (Yuan et al. 2015) to virtually bisect each maxillary model tooth into its anatomical crown and root parts (**Fig. 4C**). From this virtual bisection, we obtained the cervical plane area, which represents the area of the plane between the crown and root for each tooth (**Fig. 4D**). Following this we calculated the RA and full crown areas of each tooth in mm^2 (**Fig. 4E**).

The RA of each tooth was scaled to the geometric mean (GMsK) of the skull as a proxy for cranial/masticatory apparatus size. To calculate the GMsK, we averaged the maximum skull length (MSL), bicanine breadth (CCB), maximum bizygomatic breadth (MZB) and occipital triangle height (OTH), following Kupczik and Stynder (2012). Moreover, we used the data published in Kupczik and Stynder (2012) to complement our data (**Table 3**).

3.1.3.4. Dietary classification of living taxa

The dietary groupings used to classify the living bear species were taken from previous published studies (Mattson 1998; van Heteren et al. 2014; van Heteren et al. 2016) but including 'Roots' as 'Hard mast' (fruits and seeds with a hard protective covering including both acorns and pine seeds; Mattson 1998). Roots are very fibrous, and feeding on them includes the ingestion of soil and grit, which can affect teeth durability (Schulz et al. 2013; Xia et al. 2015), although 'Hard mast' requires cracking adaptations and 'Roots' need grinding adaptations. Even though soil and grit might be ingested, this still does not require cracking adaptations, merely a resistance to wear from silica. In any case, 'Roots' and 'Hard mast' were included together because both are very different from 'Soft mast', which includes mostly fleshy fruits, as they have a substantial amount of lignin.

Therefore, the eight species were distributed among three broad dietary categories for facilitating the ecomorphological comparisons: omnivores (the brown bear, *U. arctos*, and the Asiatic black bear, *U. thibetanus*), folivores-frugivores (the American black bear, *U. americanus*, and the spectacled bear. *T. ornatus*), and faunivores (the sun bear, *H. malayanus*, the sloth bear, *M. ursinus*, and the polar bear, *U. maritimus*). Although Mattson (1998) considered bamboo as foliage, and hence, included the giant panda (*A. melanoleuca*) with other foliage-feeders bears such as the brown bear (*U. arctos*), we did not classify the giant panda in any of these categories because the material properties of bamboo are very different.

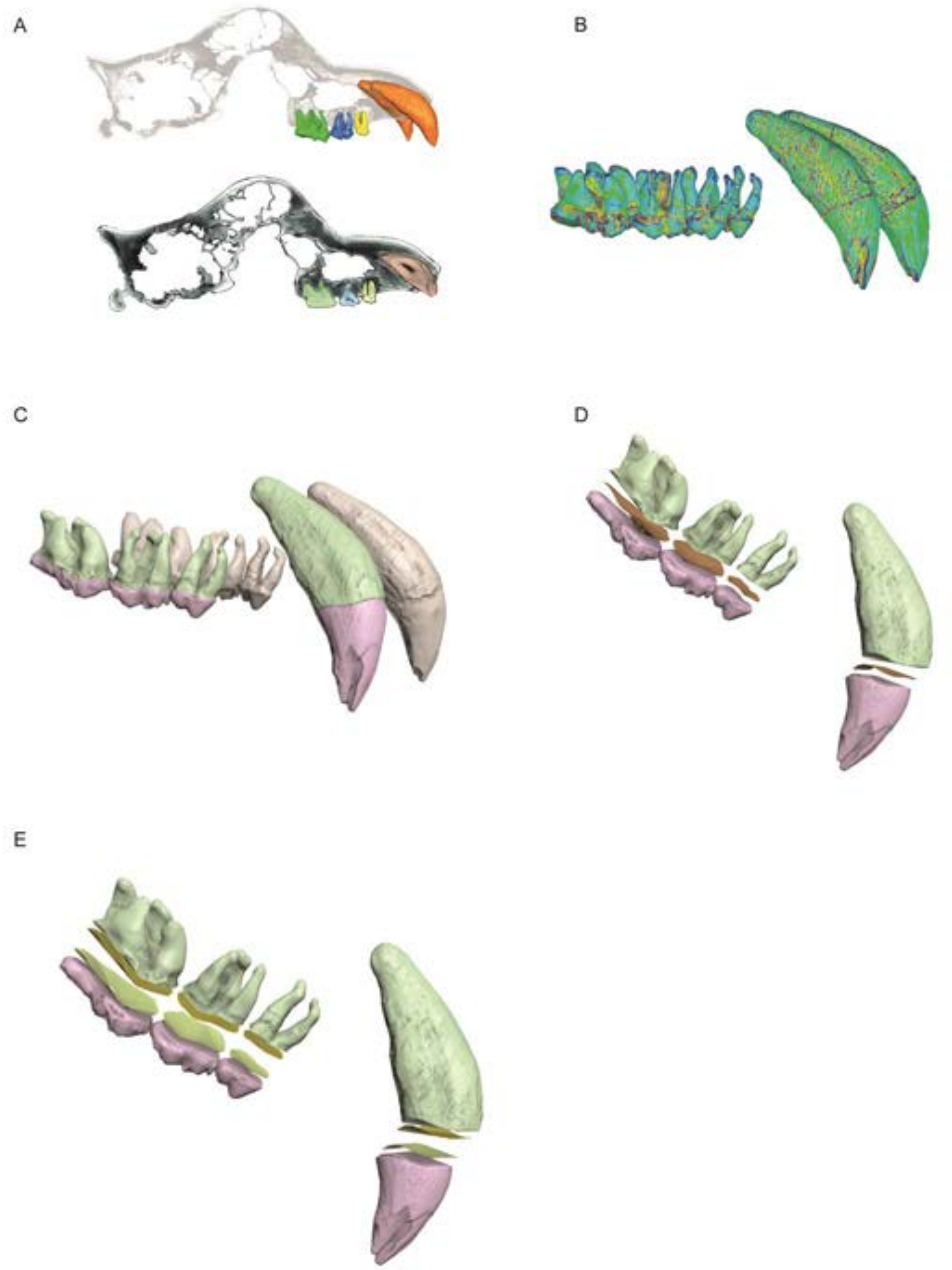

Figure 4. **Schematic protocol to calculate tooth-root surface areas (RA)**. **(A)** Three-dimensional model obtained from a CT-scan of a U. spelaeus skull with segmented teeth used as an example to illustrate the process of RA calculation; **(B)**, Visualization of surface topology of the teeth in order to find the cement-enamel junction; **(C)** Virtual dissection of the crown and root in each maxillary tooth by the cemento-enamel junction; (**D**) calculation of the area (mm2) of the plane obtained from the virtual dissection of crown and root (i.e., cervical plane area); **(E)** tooth-root and crown areas (mm2) calculated for each tooth.

Moreover bamboo-feeders (i.e., both the giant panda and the red panda, *Ailurus fulgens*) have adaptations to exert extremely high bite forces for chewing and biting on hard materials (Kupczik and Stynder 2012; Figueirido et al. 2013). Therefore, the panda was left apart in the dietary classifications. Moreover, as our brown bear skull is from the Peninsula of Alaska, we took the dietary data of brown bears inhabiting coniferous forest (**Table 2**) from Mattson (1998). In any case, it is worth mentioning that we did not use an approach that requires specifying distinct groups for the comparisons, such as in the discriminant analyses or canonical variates analysis. Instead, we use different methods, which are outlined below, for exploring the RA values of bears and only use the dietary categories for interpreting the results.

Table 2. **Dietary groupings used in this study**. The percentages ingested of each item for each species of living bears were taken from Mattson (1998). **Abbreviations**: B, Bamboo; F, Foliage; SM, Soft Mast; HM, Hard Mast; I, Invertebrate; V, Vertebrate; DG, Diet grouping.

Species	B	F	SM	HM	I	V	DG	Criterion
A. melanoleuca	99	0	0	0	0	0	Bamboo-feeder	> 50% of bamboo
T. ornatus	0	22	62	9	1	3	Folivore/Frugivore	feeding > 50% soft mast; < 15% hard mast
U. americanus	0	20	55	11	5	4	Folivore/Frugivore	feeding > 50% soft mast; < 15% hard mast
U. thibetanus	0	15	35	43	5	2	Omnivore	feeding < 50% soft mast; > 15% hard mast
U. arctos	0	31	40	17	3	8	Omnivore	feeding < 50% soft mast; > 15% hard mast
U. maritimus	0	1	1	0	0	98	Faunivore	feeding > 50% of animal protein. either vertebrates or invertebrates
H. malayanus	0	1	28	1	56	12	Faunivore	feeding > 50% of animal protein. either vertebrates or invertebrates
M. ursinus	0	1	34	3	61	0	Faunivore	feeding > 50% of animal protein. either vertebrates or invertebrates

3.1.3.5. Statistical analysis

Although sample variances were homoscedastic for the four dental variables (Levene´s test > 0.05), their values were not normally distributed (Shapiro-Wilk’s test < 0.05). Therefore, we tested the association between diet and root surface area scaled to skull size with a non-parametric Kruskal-Wallis test, using diet as a grouping variable with SPSS v.20. Post-Hoc Tukey’s range test was used to assess for differences between groups. We used the species of our sample and the sample of Kupczik and Stynder (2012).

It is worth to mention that the categories used to perform this analysis were broader than the categories used to interpret the results from other analysis because the low sample sizes within each dietary category compromise the significance of the results. Therefore, we used a new category of ‘omnivores in extenso’ that results from joining the folivores-frugivores (*T. ornatus* and *U. americanus*) plus the actual omnivores (*U. arctos* and *U. thibetanus*).

We also computed a multivariate cluster analysis (UPGMA) using the cosine as an index of similarity of the species averages for C, P4, M1 and M2 root areas scaled to the size of the skull using PAST version 2.07 (Hammer et al. 2001). Again, we averaged our specimens within those reported in Kupczik and Stynder (2012).

To explore the root area phenotypic space, we computed a Principal Components Analysis using a correlation matrix of the values of C, P4, M1 and M2 root areas scaled to the size of the skull using species averages of these variables from our sample and the sample of Kupczik and Stynder (2012) in PAST (Hammer et al., 2001). We used correlation matrix to standardized scale differences among large (i.e., M2) and small teeth (i.e., P4). To evaluate the effect of phylogenetic pattering in the phenotypic space we performed a phylomorphospace by plotting the phylogeny of Figure 1 on the first two Principal Components using MESQUITE v. 3.40 (Maddison and Maddison 2000).

To do this, the reconstructed ancestral shapes using squared-changed parsimony (Maddison 1991) were plotted into the shape spaces obtained in PCA connecting the branches of the tree (Polly 2008; Astúa 2009; Gidaszewski et al. 2009; Klingenberg and Gidaszewski 2010; Figueirido et al. 2010, 2013; Martín-Serra et al. 2014a, 2014b). This approach allows the possibility of exploring the history of the phylogenetic occupation of morphospaces.

3.1.4. Results

Figure 5 and **Figure 6** show surface renderings of the maxillary dentitions of living bears and of the species/subspecies of the cave bear complex, respectively. The values obtained for the RA of maxillary dentition are shown in **Table 3** and the values for the metric measurements taken from each skull to compute their geometric means are shown in **Table 4**.

3.1.4.1. Profiles of RA and the association with diet

The results of Kruskal-Wallis test were significant ($P<0.05$), which reveals overall differences in RA values among the established dietary groups (**Table 5**). The post-hoc Tukey's range test indicates that the giant panda significantly differed from omnivores and from faunivores in the RA values for all teeth. However, faunivores and omnivores are only significantly different in the RA values of the canine and the M2 (**Table 6**).

The obtained RA values adjusted to skull size profiles of maxillary teeth are shown in **Figure 7**. The highest RA values are found in the canines with the exception of the giant panda (**Fig. 7A**). In general, faunivores exhibit the highest values of RA for the canines (although this is mainly due to the extremely large canines of *H. malayanus*) followed by omnivores and folivores-frugivores.

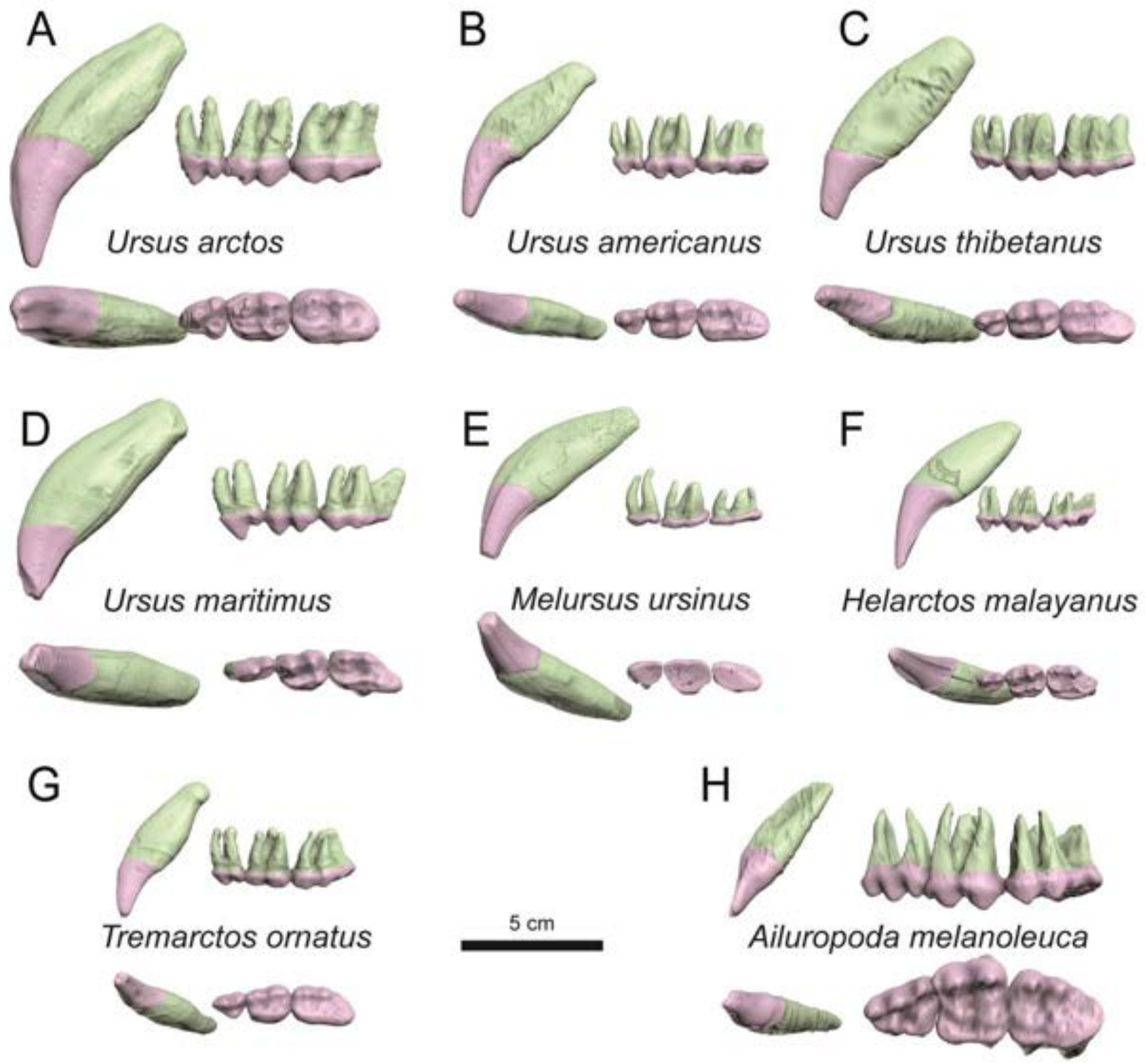

Figure 5. Segmented maxillary teeth of the living bear species analysed in this study.

All living bears follow a similar trend in RA across maxillary teeth with the exception of the giant panda **(Fig. 7A**); the highest RA values are found in the canines to followed by a decrease in RA values towards the P4. This is followed by a progressive increase from the P4 to M2. The most substantial increase occurs from P4 to M1. Between the M1 to M2 there is a very slightly increase, no increase, or even a decrease in RA values depending on the species.

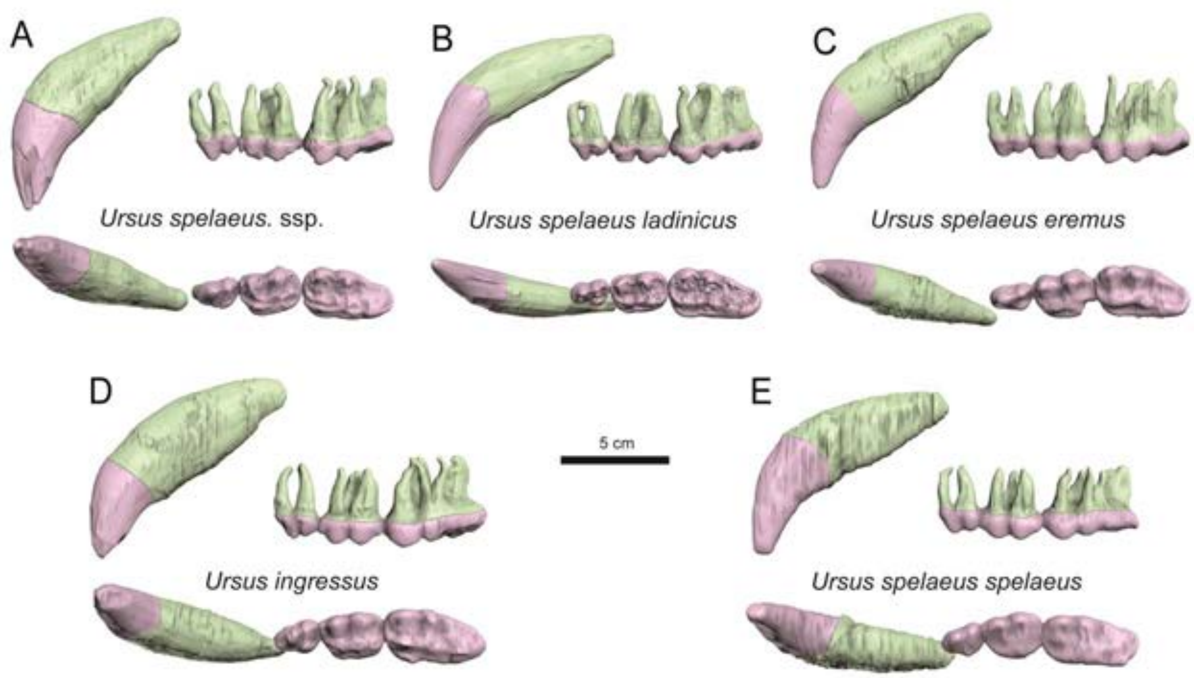

Figure 6. Segmented maxillary teeth of the cave bears analysed in this study.

Table 3. Maxillary root surface area (ra) in (mm2) and skull size-adjusted tooth roots area (ara). Abbreviations: C, canine; P4, fourth premolar; M1, first molar; M2, second molar. Asterisks denote specimens from Kupczik and Stynder (2012).

Species	Cra	P4ra	M1ra	M2ra	Cra	P4ara	M1ara	M2ara
A. melanoleuca	1502.28	1624.81	2604.49	2743.87	0.29	0.30	0.39	0.40
A. melanoleuca (*)	1218.00	1509.20	2563.20	2717.10	0.29	0.33	0.43	0.44
T. ornatus	1357.71	466.18	700.69	763.10	0.36	0.21	0.26	0.27
U. americanus	1972.33	411.91	724.38	892.65	0.33	0.15	0.20	0.22
U. americanus (*)	1510.20	316.90	672.80	826.90	0.37	0.17	0.25	0.27
U. thibetanus	3145.33	462.90	892.28	1231.44	0.42	0.16	0.22	0.26
U. thibetanus (*)	1202.30	295.60	612.20	701.90	0.34	0.17	0.24	0.26
U. arctos	4215.00	940.74	1405.04	1832.06	0.38	0.18	0.22	0.25
U. maritimus	4534.89	780.37	1055.41	1402.42	0.40	0.17	0.19	0.22
U. maritimus (*)	3826.20	692.70	923.90	942.40	0.43	0.18	0.21	0.22
H. malayanus	1964.60	234.69	382.15	399.07	0.46	0.16	0.20	0.21
M. ursinus	2588.13	426.43	485.99	402.42	0.41	0.17	0.18	0.16
***U. sp* ssp.**	5561.51	1466.21	1965.61	3087.14	0.35	0.18	0.21	0.26
U. sp. ladinicus	4530.87	894.01	1917.99	3079.83	0.41	0.18	0.27	0.34
U. sp. eremus	5445.14	999.65	1918.40	3095.39	0.40	0.17	0.24	0.30
U. ingressus	7406.38	1191.97	1868.31	3640.05	0.40	0.16	0.20	0.28
U. sp. spelaeus	5828.67	963.91	1519.95	2517.26	0.37	0.15	0.19	0.24

Subtle differences in postcanine RA values of living bears are appreciated among dietary categories. Accordingly, the lower postcanine RA values are found in faunivorous species, followed by omnivores and folivore-frugivores (**Fig. 7B**). The bamboo-feeding giant panda has, by far, the largest RA values from P4 to M2 (**Fig. 7B**). Faunivorous bears exhibit a very small increase in RA values from P4 to M1, with very few increase from M1 to M2 in *U. maritimus* and *H. malayanus*, or even a decrease in *M. ursinus* (**Fig. 7B**). Although omnivorous bears have the same RA values at P4 than faunivores (**Fig. 7B**), their values for RA at the M1 and M2 are particularly larger than the ones of faunivores (**Fig. 7B**). On the other hand, the folivores/frugivores have larger RA values at the P4 and M1 than faunivores (particularly *T. ornatus*) but only slight larger values of RA than omnivores (**Fig. 7B**).

Table 4. Skull dimensions and their the geometric mean (GMsK). Asterisks denote specimens taken from Kupczik and Stynder (2012). **Abbreviations**: maximum skull length (MSL), bicanine breadth (CCB), maximum bizygomatic breadth (MZB) and occipital triangle height (OTH).

Species	MSL	CCB	MZB	OTH	GMsk
U. americanus (*)	252.50	51.82	148.80	62.43	105.00
U. maritimus (*)	312.70	84.30	194.30	80.46	142.48
U. thibetanus (*)	236.90	57.41	152.83	51.63	101.78
A. melanoleuca (*)	265.21	43.52	186.20	93.00	118.90
A. melanoleuca	302.62	59.68	203.37	83.62	132.38
U. arctos	401.68	92.76	244.34	89.17	168.80
U. americanus	311.10	68.04	194.53	81.08	135.17
U. thibetanus	293.68	75.33	202.80	69.30	132.79
U. maritimus	392.83	89.97	239.43	92.16	167.11
T. ornatus	231.47	53.83	144.08	63.25	103.22
H. malayanus	201.10	56.93	146.36	52.94	97.05
M. ursinus	292.60	69.92	182.36	64.42	124.51
U. sp. ssp.	493.55	118.52	285.87	125.45	214.01
U. sp. ladinicus	397.23	90.91	213.76	89.69	162.21
U. sp. eremus	462.15	96.21	269.42	99.52	185.82
U. ingressus	501.15	113.95	290.53	130.82	215.84
U. sp. spelaeus	496.83	113.02	303.97	105.847	206.17

All cave bears follow a unique trend among the sample. In fact, contrary to the modern bears, the five cave bears show a relatively steep increase in RA values from P4 to M2 (**Fig. 7C**; see also **Figs. 5,6**), particularly in the case of *U. spelaeus ladinicus* and *U. spelaeus eremus*. On the other hand, all cave bears depart from the M2 RA values of faunivores (M1 RA values in *U. spelaeus ladinicus* and *U. spelaeus eremus* are also distincly larger) (**Fig. 7D**). Although *U. spelaeus* ssp. and *U. ingressus* have RA values that overlap with both folivores-frugivores (**Fig. 7E**) and omnivores (**Fig. 7F**) across all maxillary teeth, they have a higher slope in RA values from the M1 to M2. However, the *U. spelaeus spelaeus* have RA values that overlap only with the folivores-frugivores category.

Table 5. Results of the Kruskal-Wallis test preformed to assess for the association between maxillary RA and diet. Group 1.0, bamboo-feeders; group 2.0, omnivores; group 3.0, faunivores.

Dependet variable	Group comparisons		Average differences	Standard error	P-value	Confidence interval	
C	1,00	2,00	-0.07667	0.023	0.022	-0.141	-0.012
		3,00	-0.13500	0.025	0.001	-0.204	-0.066
	2,00	3,00	-0.05833	0.018	0.027	-0.109	-0.007
P4	1,00	2,00	0.14167	0.014	0.000	0.102	0.182
		3,00	0.14500	0.015	0.000	0.102	0.188
	2,00	3,00	0.003	0.011	0.954	-0.028	0.035
M1	1,00	2,00	0.17833	0.017	0.000	0.132	0.225
		3,00	0.21500	0.018	0.000	0.165	0.265
	2,00	3,00	0.037	0.013	0.052	0.000	0.074
M2	1,00	2,00	0.16500	0.019	0.000	0.111	0.219
		3,00	0.21750	0.020	0.000	0.160	0.275
	2,00	3,00	0.05250	0.015	0.018	0.010	0.095

Table 6. Results of the Post-Hoc Tukey's range test used to assess for differences among dietary groupings. Group 1.0, bamboo-feeders; group 2.0, omnivores; group 3.0, faunivores.

	C	P4	M1	M2
Chi-square	9.687	5.252	8.990	11.825
d.f.	3	3	3	3
P-value	.021	.154	.029	.008

3.1.4.1. Multivariate analyses

Figure 8A shows the dendrogram obtained from a cluster analysis performed on the species averages of the size-adjusted RA values for all maxillary teeth. From a visual inspection of this plot and in line with results presented a panda is the most distinct species of the sample as it displays the highest postcanine RA values for all teeth (see **Fig. 7A, C**). On the other hand, faunivorous bears (*H. malayanus*, *U. maritimus*, and *M. ursinus*) are grouped together and are separated from all other species of the genus *Ursus* and *Tremarctos* (**Fig. 8A**). They are all characterized by having high RA values for the canine; especially *U. maritimus* and *H. malayanus*, but low RA values from P4 to M2 (**Fig. 8B**). Strikingly, *U. ingressus* and *U. spelaeus* ssp. are placed in between *T. ornatus* –characterized by having high RA values for the P4 and M1 (Fig. 8B) and the remainder of the species belonging to *Ursus* (**Fig. 8A**), most probably because of their large RA values for the M2 (**Fig. 8B**). In contrast *U. spelaeus ladinicus* and *U. spelaeus eremus* are grouped together and are separate from *U. spelaeus spelaeus,* which is grouped with other living species of *Ursus* (**Fig. 8A**), according to its lower RA values for M1 and M2 than other cave bears (**Fig. 8B**).

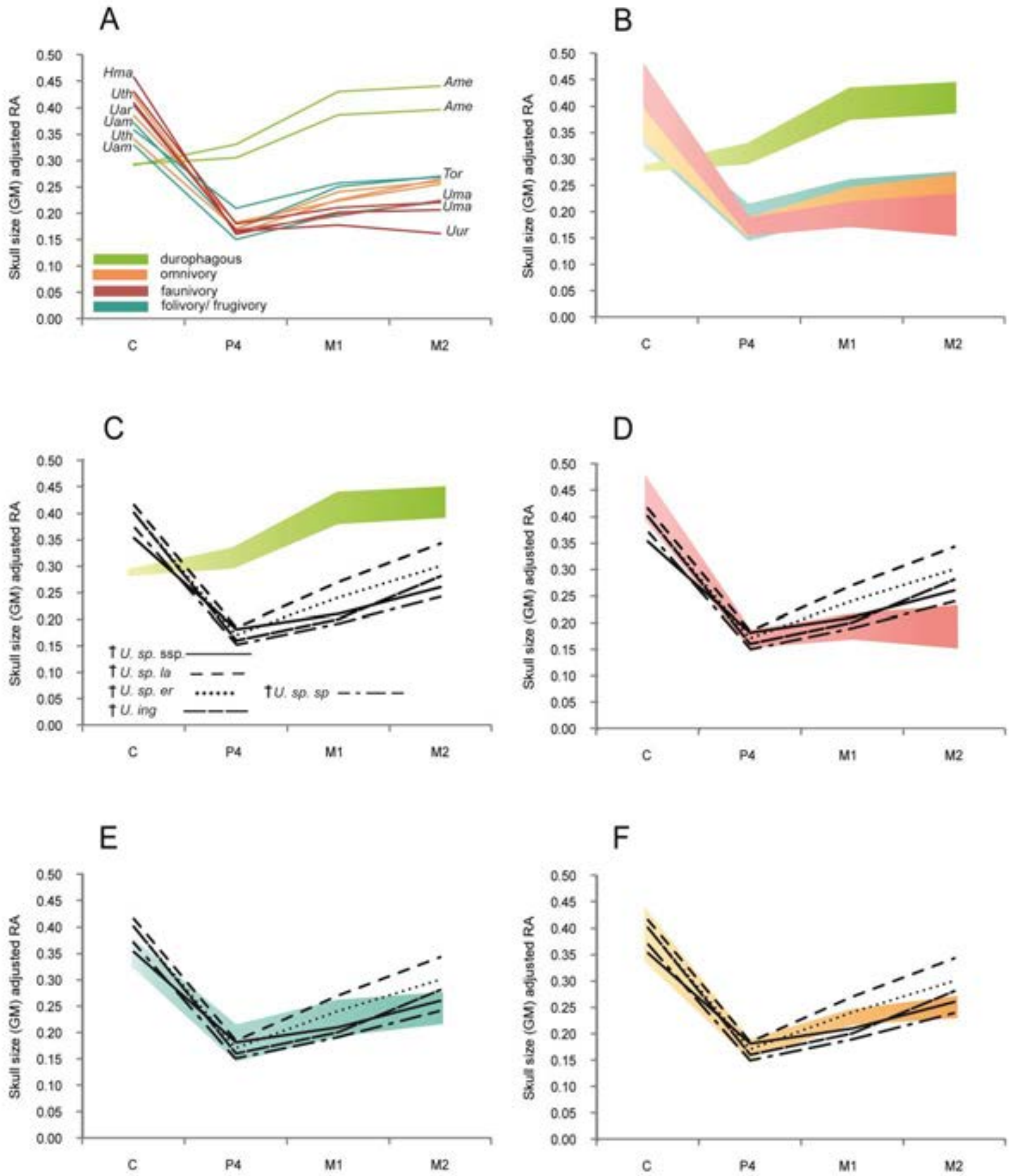

Figure 7. Tooth-root area values obtained for the living and extinct bears analysed in this article and in Kupczik and Stynder (2012). A, all living bear specimens; **B**, all living bear specimens grouped by diet. Green: the bamboo feeder *A. melanoleuca* (Ame); blue: the folivore-frugivores (*U. americanus* [Uam] and *T. ornatus*[Tor]), orange: the omnivores (*U. arctos* [Ua] and *U. thibetanus*[Uth]); red: the faunivores (H. malayanus [Hma], M. ursinus [Uur] and *U. maritimus* [Uma]); **C**, the bamboo feeder *A. melanoleuca* with the cave bears; **D**, the faunivores with the extinct cave bears; **E**, the folivore-frugivores with the extinct cave bears; **F**, the omnivores with the extinct cave bears. For abbreviation see **Table1.**

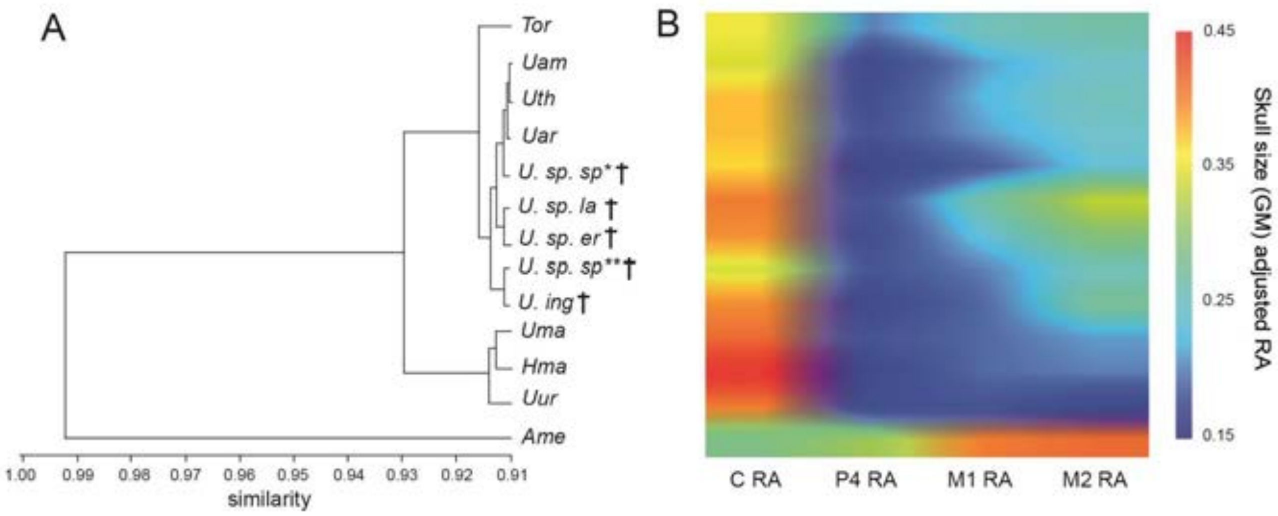

Figure 8. Cluster analysis; **(A)**, dendrogram obtained from hierarchical clustering performed for living and extinct bears using as variables the size-adjusted RA values for all maxillary teeth; **(B)**, density matrix plot for all living bear species computed from the size-adjusted RA values for all maxillary teeth. For abbreviation see **Table 1**.

The Principal components analysis of the correlation matrix for size-adjusted RA of all maxillary teeth yielded 4 eigenvectors (**Table 7**) but here we only show the results for the first two PCs accounting for 90% of the total variance. Figure 9A shows the scores for extant and extinct bears on the morphospace defined by the first two PCs. Along the first PC, *A. melanoleuca* and *T. ornatus* (positive scores) are separated from faunivores (negative scores; *H. malayanus*, *M. ursinus*, and *U. maritimus*). Factor loadings indicate that faunivorous bears are mainly characterized by having large canine RAs, while *A. melanoleuca* and *T. ornatus* are characterized by large postcanine RA values, in particular for the P4. The second PC separates *H. malayanus*, *U. spelaeus ladinicus*, *U. spelaeus eremus,* and *U. ingressus* (in a lesser degree) from *U. americanus* and *U. spelaeus* ssp. Accordingly, while *H. malayanus* have large RA values for the canine and the cave bears have large RA values for the canine, M1 and M2, *U. americanus* and both *U. spelaeus spelaeus* and *U. spelaeus* ssp. have lower RA values for the canine, M1 and M2. On the other hand, the living omnivorous bears score intermediate on both PCs.

Table 7. Eigenvalues (λ), percentages of variance and factor loadings of the size-adjusted RA values for each tooth obtained from the Principal Components Analysis.

	PC 1	PC 2	PC 3	PC 4
λ	3.280	0.444	0.255	0.019
% Variance	82.02	11.12	6.392	0.477
RA(Ca)	-0.446	0.871	0.202	0.043
RA(P4)	0.515	0.078	0.692	0.499
RA(M1)	0.538	0.283	0.133	-0.783
RA(M2)	0.497	0.394	-0.680	0.368

The phylomorphospace of **Figure 9** shows that folivore-frugivores (*T. ornatus* and *U. americanus*) depart from their hypothetical ancestors towards scoring more positively on PC1, and more negatively on PC2. In contrast, all faunivores (*H. malayanus*, *U. martitmus* and *M. ursinus*) depart from their hypothetical ancestors towards reaching more positive scores on PC1. However, while *H. malayanus* and *U. maritimus* have more positive scores than their ancestors on PC2, *M. ursinus* follows the opposite trend, i.e. it scores negatively on this axis. This is mainly due because *M. ursinus* reduce extremely RA values for post-canine teeth.

All fossil bears with the exception of *U. spelaeus spelaeus* (*U.sp.sp.**) exhibit a unique combination of RA values and hence occupy a region of the morphospace not covered by any living bear. Interestingly, *U. spelaeus spelaeus* departs from its hypothetical ancestral RA values towards an intermediate region within the morphospace close to *U. americanus*.

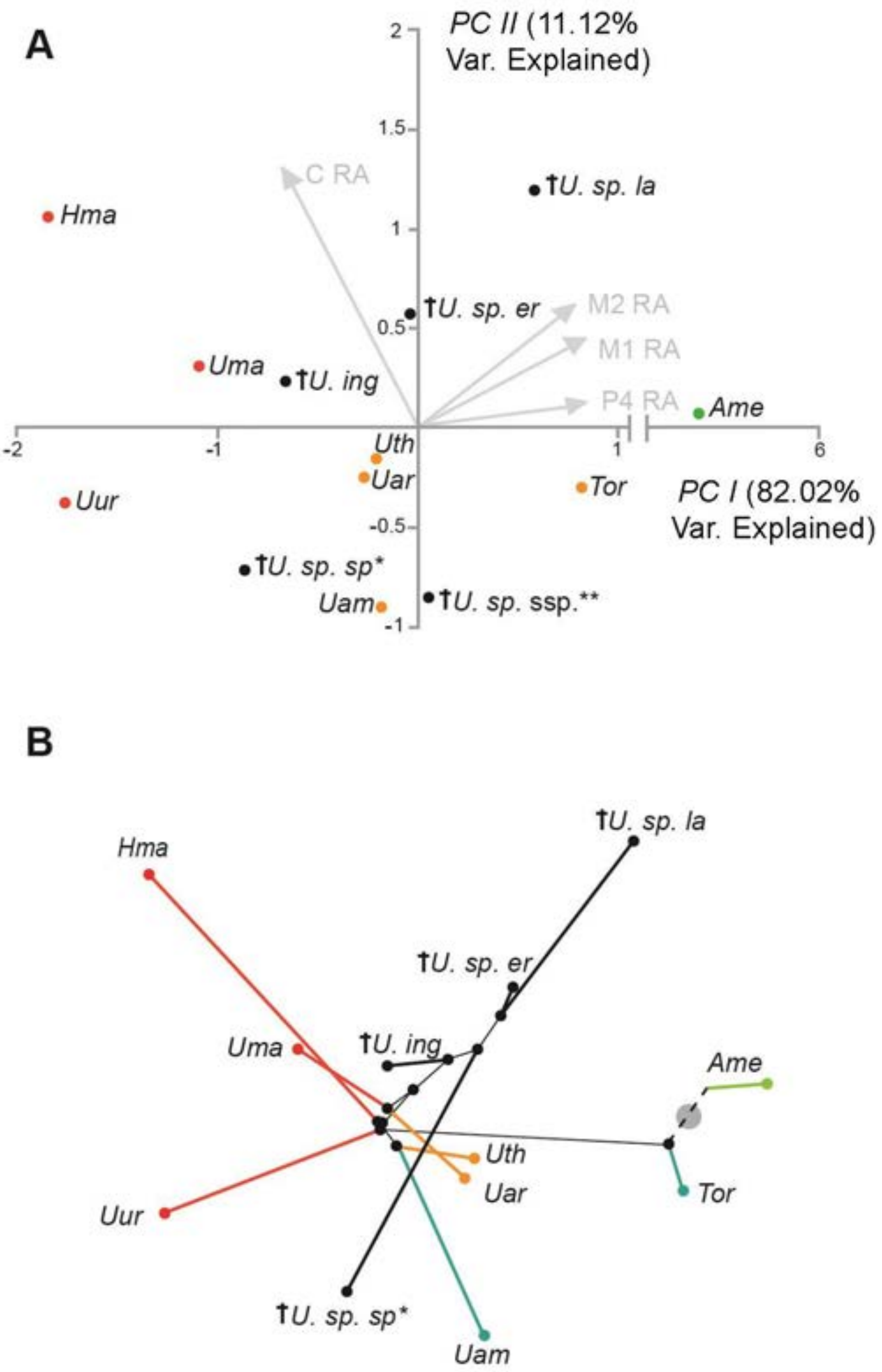

Figure 9. Principal component analysis (PCA); (A) morphospace depicted from the scores of the species in the first two PCs obtained in principal component analysis performed from the size-adjusted RA values for the maxillary teeth of living bears and extinct cave bears; **(B)** superimposed phylogeny on the morphospace showed in A using squared-changed parsimony. For abbreviation see **Table 1**.

3.1.5. Discussion

3.1.5.1. Patterns of RA profiles and feeding behaviour in living bears

Maxillary postcanine RA in living bears seems to be related with feeding behaviour (**Fig. 7B**): relative to skull size, faunivores exhibit the smallest RA followed by omnivores and folivore-frugivores, while the bamboo-feeding giant panda (*A. melanoleuca*) has the largest RA values (see also Kupczik and Stynder 2012; Stynder and Kupczik 2013). Canine RAs show an opposite trend, i.e. the blunt and cone-like canines of *A. melanoleuca* have the lowest RA among all bears examined (**Fig. 7C**). The association of RA and diet was further corroborated with a Kruskal Wallis test (**Tables 5,6**), particularly for the RA values of both the canine and M2, as the analysis found.

Faunivorous bears have the highest RA values for canine teeth among the sample (**Fig. 7D**), being the most extreme the highly insectivorous sun bear (*H. malayanus*), followed by the polar bear (*U. maritimus*) and the sloth bear (*M. ursinus*). Previous studies have demonstrated that the canines of the sun bear are mechanically more resistant to bending than are the canines of other living bears as an adaptation for frequent opening of hardwood trees in pursuit of insects such as beetle larvae or for breaking coconuts (Wong et al. 2002; Christiansen 2008). Similarly, although the canines of the sloth bear are not particularly more resistant to bending than the canines of other omnivorous bears (Christiansen 2008), its large RA values could be interpreted as an adaptation to breaking into hard structures in the search of insects such as termite mounds (Christiansen 2008). Moreover, the hypercarnivorous polar bear is a solitary predator of juvenile ringed seals (*Phoca hispida*) and bearded seals (*Erignathus barbatus*), and an occasional scavenger of beluga whales (*Delphinapterus leuca*) (DeMaster and

Stirling 1981) for which having large canine RA values are important (Sacco and Van Valkenburgh 2004; Figueirido et al. 2009).

Faunivorous bears are also characterized by having considerably reduced RA values for postcanine teeth, which could be related to their relatively low bite forces for their body masses (Christiansen 2008; Kupczik and Stynder 2012). This is due to the fact that, as in the case of the polar bear, the actual tissues of the prey (e.g., blubber of seal pups) are rather soft and do not require high bite force to be processed. Similarly, the low RA values of the sun bear and the sloth bear also reflect relatively low bite forces for their body mass (Christiansen 2008; Figueirido et al. 2009) as a result of their highly insectivorous diet, which is supplemented with fruits (Christiansen and Wroe 2007).

Both cluster analysis (**Fig. 8**) and principal components analysis (**Fig. 9**) reveal that faunivorous bears share the lowest RA values for postcanine teeth among the sample. Moreover, the phylomorphspace depicted in Figure 9B evidences that the three faunivore species follow a similar trend from the reconstructed RA values for their ancestors.

Folivorous-frugivorous bears are characterized by having relatively smaller canine roots than faunivores. However, they have larger postcanine RA values than the other bears (except for *A. melanoleuca*) particularly the RA values for the P4 and M1, and more especially the spectacled bear (*T. ornatus*). Although the spectacled bear does not exhibit especially higher bite forces at the carnassial or canine than omnivorous bears (Christiansen 2008), both the spectacled bear and the giant panda share convergent craniodental traits which are interpreted as adaptations to feeding on vegetable resources (Figueirido et al. 2009; Figueirido et al. 2010; Figueirido and Soibelzon 2010). These features are particularly extreme in the giant panda: a short jaw with large moment arms for the temporalis and masseter muscles; a horizontal ramus which is deep at the level of the third molar and shallow below the canines; well-developed upper and lower cheek teeth; relatively small canines; and well-developed zygomatic arches.

For the reasons exposed above, canine teeth are used for different roles depending on the species, either with dietary functions (e.g., opening of hardwood trees or breaking coconuts in the sun bear, breaking into hard structures in the search of insects in the sloth bear or to grapple with prey in the case of the polar bear) or even non-dietary tasks such as sexual display or as a weapons during competition for mates (e.g., Derocher et al. 2010). This fact opens the possibility that canine size would not be a good ecomorphological indicator (Christiansen 2008) of feeding preferences for the cave bear, as it accomplish different roles depending on the specific ecology of the species.

3.1.5.2. Feeding ecology of cave bears as inferred from RA profiles of maxillary teeth

All analyses show that cave bears follow a unique trend among bears: while living bears experience a substantial increase in RA values from P4 to M1 and a variable increase or decrease between M1 and M2 RA, cave bears exhibit a gradual increase from P4 to M2 (**Fig. 7C-F**). This is especially the case in *U. spelaeus ladinicus* and *U. spelaeus eremus* and less pronounced in *U. ingressus* and *U. spelaeus spelaeus*. All cave bears with the exception of *U. spelaeus spelaeus and U. spelaeus* ssp., the other cave bears occupy a portion of the morphospace not explored by any living bear (see **Fig. 8B, Fig. 9A**), suggesting that *U. spelaeus eremus*, *U. spelaeus ladinicus* and *U. ingressus* were exploiting a dietary niche that was distinct from any living bear. In contrast, given the similarity of *U. spelaeus spelaeus*, *U. spelaeus* ssp. with the American black bear, it is possible that both subspecies of *U. spelaeus* fed on similar food resources (**Table 2**). A previous study (van Heteren et al. 2012) has also shown that *U.*

spelaeus eremus, *U. spelaeus ladinicus* and *U. ingressus* have similar mandible morphology, but this study did not include *U. spelaeus spelaeus*. It is thus unclear whether the mandibular morphology would have been different in this subspecies.

This trend of RA distribution across maxillary teeth shared by all cave bears of our sample most probably reflects shared ancestry. The Middle Pleistocene *Ursus deningeri* is generally considered the ancestor of *U. spelaeus* s.l. (e.g., Andrews and Turner 1992; García et al. 1997; García et al. 2006) and the divergence between *Ursus deningeri* and *U. spelaeus* s.l. took place during the Middle Pleistocene boundary (Knapp et al. 2009). Van Heteren et al. (2018) demonstrated that the skull morphology of Middle Pleistocene cave bears (*U. deningeri*) was very similar to that of Late Pleistocene cave bears (*U. spelaeus* s.l.), suggesting that the herbivorous dietary component of the Late Pleistocene cave bear were already established in the Middle Pleistocene. We hypothesize that the unique trend in RA across maxillary teeth among cave bears revealed here is probably the result of the highly herbivorous diet inherited by the Middle Pleistocene cave bears *U. deningeri*.

Although our results are in accordance with previous biogeochemical studies suggesting that cave bears were more herbivorous than other species of *Ursus* (e.g., Bocherens et al. 1997; Bocherens et al. 1999; Bocherens et al. 2006; Bocherens et al. 2011), the differences obtained in RA values of maxillary teeth also point towards different dietary strategies among cave bears. This is evident for *U. spelaeus spelaeus* and the other three cave bears, because while the former inhabited areas of about 500m until 800m of altitude above sea level, *U. ingressus, U. spelaeus eremus* and *U. spelaeus ladinicus* foraged from high-alpine to alpine region, reaching altitudes up to 2.800m above sea level for the latter. The different ecosystems where they foraged may explain the differences reported here in RA values across maxillary teeth, and by extension, differences in their feeding behaviour. It is worth noting that a priori could seem a short period of time among the species/subspecies of cave bears to reflect dietary differences in the dentition. However, Rabeder et al. (2008) demonstrated by comparing morphological data from more than 30 bear populations belonging to the cave bear complex (*U. spelaeus eremus*, *U. spelaeus ladinicus*, and *U. ingressus*) living in the Alps between 40 and 50 Ka before present that the different species/subspecies developed very different tooth adaptations according to their habitats. Moreover, it has been demonstrated that these cave bear forms represented different gene pools without flow (Hofreiter et al. 2004, 2007). Therefore, if interbreeding was possible it did not prevent different adaptive responses of the cave bear forms to environmental changes (Rabeder et al. 2008).

We hypothesize that the largest RA values among the sample exhibited by *U. spelaeus eremus* and *U. spelaeus ladinicus* may represent an adaptation to feed on any resource present in the high-alpine biome relying more on hard or tough foods. Further research of dental microwear in *U. spelaeus eremus* and *U. spelaeus ladinicus* is necessary to confirm or refute this hypothesis (Frischauf et al. 2016). Moreover, although both subspecies present normal dimensions in caves of lower altitudes (i.e., Schwabenreith, Herdengel, Ajdovska), they are dwarfs in caves of higher altitudes (i.e., Conturines, Ramsch, Schreiberwand), and this has been proposed to be an adaption to high-alpine climatic conditions because it is easier for smaller animals to fulfil the needs of the metabolism during winter (Ehrenberg 1929). On the other hand, although the general pattern of RA values across the maxillary teeth of *U. ingressus* is very similar to both *U. spelaeus ladinicus* and *U. spelaeus eremus*, there are subtle differences that we interpret as a consequence of having an alternative strategy to forage in the alpine biome. Rabeder et al. (2008) have proposed that *U. ingressus* probably did not rely on hard or tough foods and its large body size probably forced this species to improve the performance of mastication to increase the daily food intake during the vegetation period, and thus at a sufficient fat storage before autumn.

An alternatively scenario was proposed by Bocherens et al. (2011), suggesting the possibility that *U. ingressus* was present in the area only during relatively colder periods and hibernating in lower altitude caves, and hence its large body size would be a consequence of Bergmann's rule. On the other hand, the smaller types were probably present in high alpine regions during relatively warmer periods and using the higher altitude cave as a winter den (Bocherens et al. 2011). However, compelling evidence for *U. ingressus* hibernating in low altitude caves, and for *U. spelaeus eremus* and *U. spelaeus ladinicus* in high altitude caves, is necessary to confirm or refute this hypothesis.

In any case, our results on RA suggest that although some cave bears were probably more herbivorous than any other living species of the genus *Ursus*, they had different foraging strategies. Further research combining refined biomechanical analysis of their skulls and tooth microwear analysis backed up by robust chronological data could give essential clues for niche partitioning among sympatric cave bears, populations dynamics, and selective extinction.

3.1.6. References

- Abel O, Kyrle G. 1931. Die Drachenhöhle bei Mixnitz. Speläolog. Monographien. 7–8. Wien.
- Andrews P, Turner A. 1992. Life and death of the Westbury bears. Ann Zool Fennici. 28(3–4): 139–149
- Astúa D. 2009. Evolution of scapula size and shape in didelphid marsupials (Didelphimorphia: Didelphidae). Evolution. 63(9): 2438-2456.
- Bocherens H, Mariotti A. 1997. Comments on: Diet, physiology and ecology of fossil mammals as inferred from stable carbon and nitrogen isotope

biochemistry: Implications for Pleistocene bears by Bocherenset al. -Repy. Palaeogeogr Palaeocl. 128: 362–364.

- Bocherens H, Billiou D, Patou-Mathis M, Otte M, Bonjean D, Toussaint M, Mariotti A. 1999. Palaeoenvironmental and Palaeodietary Implications of Isotopic Biogeochemistry of Late Interglacial Neandertal and Mammal Bones in Scladina Cave (Belgium). J Archaeol Sci. 26: 599–607.
- Bocherens H, et al. 2006. Bears and Humans in Chauvet Cave (Vallon-Pont-d'Arc. Ardèche. France): insights from stable isotopes and radiocarbon dating of bone collagen. J Hum Evol. 50:370-376.
- Bocherens H, et al. 2011. Niche partitioning between two sympatric genetically distinct cave bears (*Ursus spelaeus* and *Ursus ingressus*) and brown bear (*Ursus arctos*) from Austria: isotopic evidence from fossil bones. Quatern Int. 245(2): 238-248.
- Bocherens H. 2018. Isotopic insights on cave bear palaeodiet, Hist Bio, DOI: 10.1080/08912963.2018.1465419
- Christiansen P, Wroe S. 2007. Bite forces and evolutionary adaptations to feeding ecology in carnivores. Ecology. 88(2): 347-58.
- Christiansen P. 2008. Evolution of skull and mandible shape in cats (Carnivora: Felidae). PLoS One, 3(7): e2807.
- DeMaster DP, Stirling I. 1981. *Ursus maritimus*. Polar bear. Mamm Sp. 145: 1–7.
- Diedrich CG. 2012. An Ice Age spotted hyena *Crocuta crocuta spelaea* (Goldfuss 1823) population, their excrements and prey from the late Pleistocene hyena den of the Sloup Cave in the Moravian Karst, Czech Republic. Hist Biol. 24(2): 161-185.
- Derocher, A.E., Andersen, M., Wiig, Ø. et al. Behav Ecol Sociobiol (2010) 64: 939.

- Döppes D, Rosendahl W. 2009. Numerically dated palaeontological cave sites of Alpine region from Late Middle Pleistocene to Early Late Pleistocene. Preistoria Alpina. 44: 45-48.
- Döppes D, Rabeder G, Stiller M. 2011. Was the Middle Würmian in the High Alps warmer than today?. Quatern Int. 245(2): 193-200.
- Döppes D, Pacher M, Rabeder G, Lindauer S, Freidrich R, Kromer B, Rosendahl W. 2016. Unexpected! New AMS dating from Austrian cave bear sites. Cranium. 33: 26-30.
- Döppes D, Rabeder G, Frischauf C, Kavcik-Graumann N, Kromer B, Lindauer S, Friedrich R, Rosendahl W. 2018. Extinction pattern of Alpine cave bears - new data and climatological interpretation. Hist Biol. DOI: 10.1080/08912963.2018.1487422.
- Ehrenberg K. 1929. Die Ergebnisse der Ausgrabungen in der Schreiberwandhöhle am Dachstein. – Paläont. Z. 11 (3): 261–268.
- Fortes GG, Grandal-d'Anglade A, Kolbe B, Fernandes D, Meleg IN, García-Vázquez A, Frischauf C. 2016. Ancient DNA reveals differences in behaviour and sociality between brown bears and extinct cave bears. Mol Ecol. 25 (19): 4907-4918.
- Figueirido B, Palmqvist P, Pérez-Claros JA. 2009. Ecomorphological correlates of craniodental variation in bears and paleobiological implications for extinct taxa: An approach based on geometric morphometrics. J Zool 277: 70–80.
- Figueirido B, Serrano-Alarcón FJ, Slater GJ, Palmqvist P. 2010. Shape at the cross-roads: homoplasy and history in the evolution of the carnivoran skull towards herbivory. J Evolution Biol. 23(12): 2579-2594.
- Figueirido B, Soibelzon LH. 2010. Inferring palaeoecology in extinct tremarctine bears (Carnivora, Ursidae) using geometric morphometrics. Lethaia. 43(2): 209-222.

- Figueirido B, Tseng ZJ, Martín-Serra A. 2013. Skull shape evolution in durophagous carnivorans. Evolution. 67(7): 1975-1993.
- Frischauf C, Liedl P, Rabeder G. 2014. Revision der fossilen Fauna der Drachenhöhle (Mixnitz, Steiermark). Die Höhle. 66(1-4): 47-55.
- García N, Arsuaga JL, Torres T. 1997. The carnivore remains from the Sima de los Huesos Middle Pleistocene site (Sierra de Atapuerca, Spain). J Hum Evol. 33(2–3): 155–174.
- García N, Santos E, Arsuaga JL, Carretero JM. 2006. High-resolution X-ray computed tomography applied to the study of some endocranial traits in cave and brown bears. Scientific Annals, School of Geology Aristotle University of Thessaloniki. 98(141–146): 141
- Gidaszewski NA, Baylac M, Klingenberg CP. 2009. Evolution of sexual dimorphism of wing shape in the *Drosophila melanogaster* subgroup. BMC Evol Biol. 9 (1): 110.
- Grandal-d'Anglade A, Pérez-Rama M, García-Vázquez A, González-Fortes GM. 2018. The cave bear's hibernation: reconstructing the physiology and behaviour of an extinct animal. Hist Biol. DOI: 10.1080/08912963.2018.1468441.
- Hammer Ø, Harper DAT, Ryan PD. 2001. PAST: Paleontological statistics software package for education and data analysis. Palaeontol Electron 4: 9.
- Horacek M, Frischauf C, Pacher M, Rabeder G. 2013. Stable isotopic analyses of cave bear bones from the Conturines cave (2800 m, South Tyrol, Italy). Braunschweiger Naturkundliche Schriften. 11(1): 47-52.
- Hofreiter, M, Rabeder, G, Jaenicke, V, Withalm, G, Nagel, D, Paunovic, M, Jambrsi, G. Pääbo, S. 2004. Evidence for reproductive isolation between cave bear populations. Curr Biol. 14 (1): 40-43.
- Hofreiter, M, Münzel, S, Conard, N, Pollack, J, Weiss, G, Pääbo, S. 2007. Sudden replacement of cave bears mitochondrial DNA in the Late Pleistocene. Curr Biol. 17(4).

- Kadlec J, Hercman H, Beneš V, Šroubek P, Diehl J F, Granger D. 2001. Cenozoic history of the Moravian Karst (northern segment): cave sediments and karst morphology. Acta Mus. Moraviae, Sci. geol. 86: 111-160.
- Kavcik-Graumann N, Nagel D, Rabeder G, Ridush B, Withalm G. 2016. The bears of Illinka cave near Odessa (Ukraine). Cranium. 1-25.
- Kikinis R, Pieper SD, Vosburgh K. 2014. 3D Slicer: a platform for subject-specific image analysis. visualization. and clinical support. Intraoperative Imaging Image-Guided Therapy. Ferenc A. Jolesz. Editor 3(19): 277–289.
- Klingenberg CP, Gidaszewski NA. 2010. Testing and quantifying phylogenetic signals and homoplasy in morphometric data. Systematic Biol. 59(3): 245-261.
- Knapp M. 2018. From a molecules' perspective – contributions of ancient DNA research to understanding cave bear biology. Hist Bio. DOI: 10.1080/08912963.2018.1434168.
- Kupczik K, Dean MC. 2008. Comparative observations on the tooth root morphology of Gigantopithecus blacki. J Hum Evol. 54(2): 196-204.
- Kupczik K, Hublin, JJ. 2010. Mandibular molar root morphology in Neanderthals and Late Pleistocene and recent Homo sapiens. J Hum Evol. 59(5): 525-541.
- Kupczik K, Stynder DD. 2012. Tooth root morphology as an indicator for dietary specialisation in carnivores (Mammalia: Carnivora). Biol J Linn Soc. 105(2): 456–471.
- Kurtén B. 1967. Pleistocene bears of North America. II: Genus *Arctodus*. short-faced bears. Acta Zool. Fennica. 117: 1-60.
- Maddison WP. 1991. Squared-change parsimony reconstructions of ancestral states for continuous-valued characters on a phylogenetic tree. Systematic Biology. 40(3): 304-314.
- Maddison WP, Maddison DR. 2000. Mesquite: a modular programming system for Evolutionary analysis. Prototype v.0.9d17.

- Martín-Serra A, Figueirido B, Palmqvist P. 2014a. A three-dimensional analysis of morphological evolution and locomotor performance of the carnivoran forelimb. PLoS One. 9(1): e85574.
- Martín-Serra A, Figueirido B, Palmqvist P. 2014b. A three-dimensional analysis of the morphological evolution and locomotor behaviour of the carnivoran hind limb. BMC Evol Biol. 14(1): 129.
- Mattson DJ.1998. Diet and morphology of extant and recently extinct northern bears. Ursus. 10:479-496.
- Nagel D, Lindenbauer J, Kavcik-Graumann N, Rabeder G. 2018 (in press). Subtropical steppe inhabitants in the Late Pleistocene cave faunas of eastern Middle Europe. – Slovensk. Kras -Acta Carsologica Slovaka.
- Pacher M, Stuart AJ. 2009. Extinction chronology and palaeobiology of the cave bear (*Ursus spelaeus*) Boreas. 38: 189–206.
- Pérez-Rama M, Fernández-Mosquera D, Grandal-d'Anglade A. (2011). Effects of hibernation on the stable isotope signatures of adult and neonate cave bears. Quaternaire. 4: 79-88.
- Peigné S, et al. 2009. Predormancy omnivory in European Cave Bears evidenced by dental microwear analysis of *Ursus Spelaeus* from Goyet. Belgium. P Natl Acad Sci USA. 106:15390-15393.
- Peigné S, Merceron G. 2017. Palaeoecology of cave bears as evidenced by dental wear analysis: a review of methods and recent findings, Hist Biol. 1-13.
- Pinto Llona AC, Andrews PJ, Etxebarría F.2005. Taphonomy and Palaeoecology of Quaternary Bears from Cantabrian Spain (Grafinsa. Oviedo. Spain). Sci. Annals. Geol. School. AUTH. special vol. 103-108.
- Polly PD, MacLeod N. 2008. Locomotion in fossil Carnivora: an application of eigensurface analysis for morphometric comparison of 3D surfaces. Palaeontol Electron. 11(2):10-13.

- Quilès J, et al. 2006. Cave bears (*Ursus spelaeus*) from the Peçstera cu Oase (Banat. Romania): Paleobiology and taphonomy. C R Palevol 5:927–934.
- Rabeder G, Hofreiter M. 2004. Der neue Stammbaum der alpinen Höhlenbären. – Die Höhle. 55(1-4): 58–77.
- Rabeder G, Hofreiter M, Nagel D, Withalm G. 2004a. New taxa of alpine cave bears (Ursidae, Carnivora). Cahiers scientifiques. Hors série. 2: 49-67.
- Rabeder G, Hofreiter M, Withalm G. 2004b. The Systematic Position of the Cave Bear from Potočka zijalka (Slovenia). Mitt. Komm. Quartärforsch. Österr. Akad. Wiss.13:197–200.
- Rabeder G, Debeljak I, Hofreiter M, Withalm G. 2008. Morphological responses of cave bears (*Ursus spelaeus* group) to high-alpine habitats. Die Höhle. 59: 59-72.
- Richards MP, et al. 2008. Isotopic evidence for omnivory among European cave bears: Late Pleistocene *Ursus spelaeus* from the Peçstera cu Oase. Romania. Proc Natl Acad Sci USA. 105:600–604.
- Robu M, Wynn JG, Mirea IC, Petculescu A, Kenesz M, Puşcaş CM, Vlaicu M, Trinkaus E, Constantin S, O'Regan H. 2018. The diverse dietary profiles of MIS 3 cave bears from the Romanian Carpathians: insights from stable isotope (δ13C and δ15N) analysis. Palaeontology 61: 209-219.
- Sacco T, Van Valkenburgh B. 2004. Ecomorphological indicators of feeding behaviour in the bears (Carnivora: Ursidae). J Zoo. 263(1): 41-54.
- Self CJ. 2015a. Dental root size in bats with diets of different hardness. J Morphol. 276(9): 1065-1074.
- Self CJ. 2015b. Cricetid rodents: Is molar root morphology an indicator of diet?. Zoomorphology. 134(2): 309-316.
- Schulz E, Piotrowski V, Clauss M, Mau M, Merceron G, Kaiser TM. 2013. Dietary Abrasiveness Is Associated with Variability of Microwear and Dental Surface Texture in Rabbits. PLoS ONE. 8(2). e56167.

- Spencer MA. 2003. Tooth-root form and function in platyrrhine seed-eaters. Am J Phys Anthropol.122(4):325-335.
- Spötl C, Reimer, PJ, Rabeder G, Ramsey CB. 2018. Radiocarbon constraints on the age of the world's highest-elevation cave-bear population, Conturines Cave (Dolomites, Northern Italy). Radiocarbon. 60(1): 299-307.
- Stiner, M. 1999. Cave Bear Ecology and Interactions with Pleistocene Humans. Ursus.11: 41-58.
- Stynder DD, Kupczik K. 2013. Tooth root morphology in the early Pliocene African bear *Agriotherium africanum* (Mammalia. Carnivora. Ursidae) and its implications for feeding ecology. J Mammal Evol. 20(3): 227-237.
- Terlato G, Bocherens H, Romandini M, Nannini N, Hobson KA, Peresani M. 2018. Chronological and Isotopic data support a revision for the timing of cave bear extinction in Mediterranean Europe. Hist Bio. DOI: 10.1080/08912963.2018.1448395
- Thomason, JJ. 1991. Cranial strength in relation to estimated biting forces in some mammals. Can. J Zool. 69: 2326-2333.
- Van Heteren AH, MacLarnon A, Rae TC, Soligo C. 2009. Cave bears and their closest living relatives: a 3D geometric morphometrical approach to the functional morphology of the cave bear *Ursus spelaeus*. Slovenský Kras Acta Carsologica Slovaca 47(supplement 1):33-46.
- Van Heteren AH, MacLarnon AM, Soligo C, Rae TC. 2012. 3D geometric morphometrical analyses of intraspecific variation in the mandible of *Ursus spelaeus* from the Alpine region. Braunschweiger Naturkundliche Schriften. 11:111-128.
- Van Heteren AH, MacLarnon AM, Soligo C, Rae TC. 2014. Functional morphology of the cave bear (*Ursus spelaeus*) cranium: a three-dimensional geometric morphometric analysis. Quatern Int. 339–340. 209–216.

- Van Heteren AH, MacLarnon AM, Soligo C, Rae TC. 2016. Functional morphology of the cave bear (*Ursus spelaeus*) mandible: a 3D geometric morphometric analysis. Org Divers Evol. 16:299–314.
- Van Heteren AH, Arlegi M, Santos E, Arsuaga JL, Gómez-Olivencia A. 2018. Cranial and mandibular morphology of Middle Pleistocene cave bears (Ursus deningeri): implications for diet and evolution. Historical Biology, DOI: 10.1080/08912963.2018.1487965
- Veitschegger K, Kolb C, Amson E, Sánchez-Villagra M.R. 2018. Longevity and life history of cave bears – a review and novel data from tooth cementum and relative emergence of permanent dentition, Hist Bio, DOI: 10.1080/08912963.2018.1441293.
- Vila Taboada M, Fernández Mosquera D, López González F, Grandal D'Anglade A, Vidal Romaní JR. 1999. Paleoecological implications inferred from stable isotopic signatures (d13C. d15N) in bone collagen of *Ursu spelaeus* ROS.-HEIN. Cadernos do Laboratori Xeolxic deLax . 24: 73-87.
- Wong ST. 2002. Food habits of malayan sun bears in lowland tropical forest of Borneo. Ursus. 13:127-136.
- Xia J, Zheng J, Huang D, Tian ZR, Chen L, Zhou Z, et al. 2015. New model to explain tooth wear with implications for microwear formation and diet reconstruction. Proc Natl Acad Sci USA. 112(34). 10669-10672.
- Yuan B, Khechoyan D, Goldman R. 2015. A new objective automatic computational framework for evaluating and visualizing the results of infant cranial surgery. Paper presented at: ASE International Conference on Biomedical Computing., Dec. 14-16; Harvard University, Cambridge, USA.

This chapter has been published in Historical Biology:

Pérez-Ramos, A.*, Kupczik, K., Van Heteren, A. H., Rabeder, G., Grandal-D'Anglade, A., Pastor, F. J., ... & Figueirido, B*. (2019). A three-dimensional analysis of tooth-root morphology in living bears and implications for feeding behaviour in the extinct cave bear. Historical Biology. 31(4): 461-473.

*Borja Figueirido and Alejandro Pérez-Ramos contributed equally to this work.

Author contributions: A.P.-R. and B.F. designed research; A.P.-R., K.K. and B.F. performed research; B.F., and A.P.-R. analysed data; AHvH, GA, and F.J.P. contributed new reagents/analytic tools and assisted with writing; B.F., A.P.-R., and K.K wrote the paper.

3.1.7. Supplementary Material

Sex of the specimens

In order to assess the sex of the cave bear specimens analysed in this study, we measured the same metric variables of the skull reported in Grandal d'Anglade and López-Gonzalez (2005) in our sample of cave bears (Basilar length [BASL], Total length of the skull [TOTL], Occipital breath [OCCB], Bizigomatic breath [BIZB], Parietal minimum breadth [PARB], Frontal breadth [FORB], and Interorbital minimum breadth [INTB]). Afterwards, we performed a Principal components Analysis (PCA) of these variables using our cave bear sample (**Table S1**) plus the average of these variables for males and females across different populations of cave bears (Eiros [Spain], Liñares [Spain], Gailenreuther [Spain], Mixnitz, and Goffontaine [Spain]) taken from Grandal d'Anglade and López-Gonzalez (2005) in a comparative framework.

The results of the PCA are shown in **Fig. S1** and **Table S2**. The first PC explains 88.6% of the original variance (λ=6.2) and mainly separates males from females (**Fig. S1**). As all variables are positively loading on this eigenvector (**Table S3**), this indicates that the difference between males and females is due to size, being of course males bigger than females. The second PC (λ=0.46), however, only explains 6.5% of the original variance, and mainly separates the females from two Spanish populations (Eiros and Liñares) from the rest of the sample.

From a visual inspection of **Fig. S1**, it is deduced that all cave bear specimens included in our sample fall within the range of males with the sole exception of *Ursus spelaeus ladinicus*. However, it is worth considering that this specimen was found in Conturines cave (Italy) with an altitude of more than 2.800m above sea level, and it is well-known that these forms were dwarfs (e.g., Ehrenberg 1929, Rabeder et al. 2008, 2014). Therefore, and given that the first PC accounts for size differences between males and females, our results are uncertain concerning the sex attribution of *U. sp. ladinicus*. Therefore, it is doubtful to know if its small skull size is because it corresponds to a female, or in contrast, because it was a dwarf specimen as a result of its high-alpine adaptations (Ehrenberg 1929, Rabeder et al. 2008, 2014).

Ideally, one of the most widespread measures for sexual dimorphism in cave bears is the transverse diameter of the canine (Kurtén 1965, 1969). However, the lack of available data for the canine transverse diameter in the population of Conturines, as well as in other cave bear populations, precludes us to assess the sex of our *U. spelaeus ladinicus* specimen and the other cave bears included in our sample. However, following Kurtén (1955) the canine transverse diameter for males reach an average value of 21.87mm with a range between 21.62mm and 22.12mm, and for females 16.34 mm, ranging from 15.95mm to 16.73mm, at least for the regular-sized population of Mixnitz (Austria). The value of canine transverse diameter of our specimen of *U. spelaeus ladinicus* is 22.0mm, and therefore, within the range of the males of the Mixnitz population. As a result, as evidenced by its canine transverse diameter, the small skull of *U. spelaeus ladinicus* is not due because it belong to a female, but because it was a dwarf specimen as a consequence of the high-alpine region it inhabited, and for this reason, it plot with the females of other regular-sized populations of cave bears in **Fig. S1**. In summary, following our results we can conclude that the cave bears included in our sample are all male.

Supplementary References

- Grandal-d'Anglade A, López-González F. 2005. Sexual dimorphism and ontogenetic variation in the skull of the cave bear (*Ursus spelaeus* Rosenmüller) of the European Upper Pleistocene. Geobios. 38(3): 325-337.
- Kurtén B. 1955. Sex dimorphism and size trends in the cave bear. Acta Zool. Fennica. 90: 1-47.
- Kurtén B. 1969. Sexual dimorphism in fossil mammals. In: Westerman, G.E.G. (Ed.), Sexual Dimorphism in Fossil Metazoa and Taxonomic Implications. E. Schweizerbart'sche Verlagsbuchhandlung, Stuttgart. 226–233.

Table S1. Metric variables taken from the skull of the cave bear to assess the sex of the specimens. Units: mm. **Abbreviations**: Basilar length [BASL], Total length of the skull [TOTL], Occipital breath [OCCB], Bizigomatic breath [BIZB], Parietal minimum breadth [PARB], Frontal breadth [FORB], and Interorbital minimum breadth [INTB]).

Specimens	BASL	TOTL	OCCB	BIZB	PARB	FROB	INTB
U. spelaeus spelaeus	446.68	502.95	234.66	303.24	94.38	151.96	110.72
U. spelaeus ssp.	436.74	499.33	229.26	289.79	82.71	139.85	108.12
U. spelaeus ladinicus	358.85	394.19	161.74	212.65	75.89	101.52	72.91
U. spelaeus eremus	408.17	466.99	205.05	268.6	78.48	127.49	96.66
U.ingressus	446.65	501.34	213.42	290.69	88.17	139.55	104.05

Table S2. Factor loadings of the variables on the first two eigenvectors obtained from a PCA computed from the metric measurements of the skulls of different populations of cave bears with known sex and of the cave bears of our sample.

	Eigenvector	
	I	**II**
LogBASL	0.963	-0.197
LogTOTL	0.962	-0.218
LogOCCB	0.959	-0.142
LogBIZB	0.966	-0.132
LogPARB	0.823	0.548
LogFROB	0.967	0.181
LogiNTB	0.942	0.040

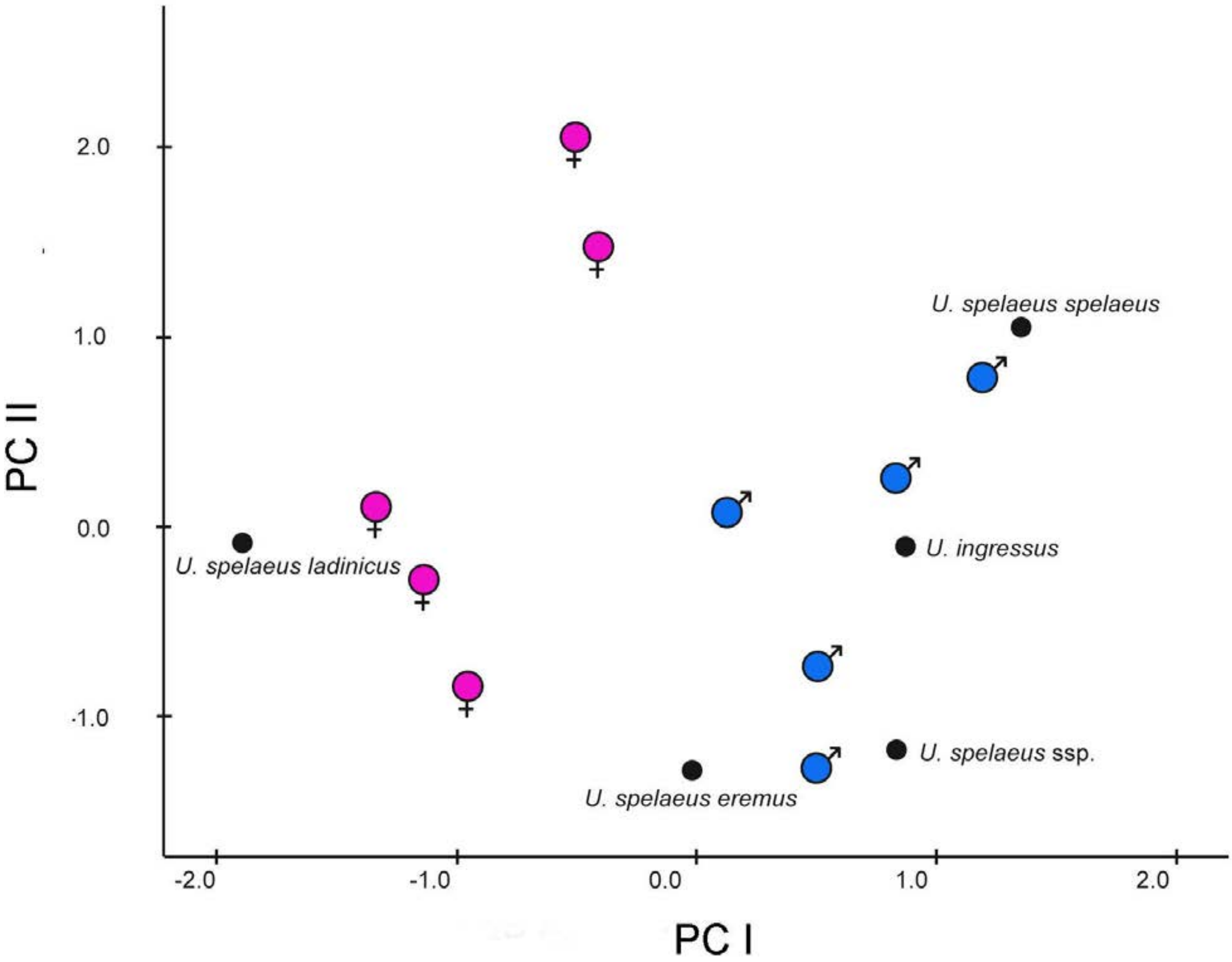

Figure S1. Bivariate plot of PCA results from metric measurements of our cave bear sample (black circles) plus the average of these variables for males and females across different populations of cave bears. The first PC explains 88.6% of original variance explained and the second PC explains 6.54%.

3

3.2. Evolution of dental topography in bears and feeding behaviour in extinct cave bears (*Ursus spelaeus* s.l.)

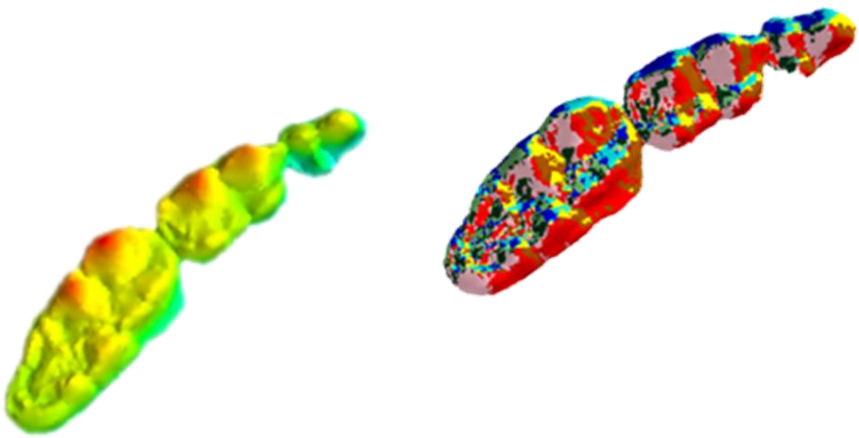

Chapter 3. Results II

3.2. Evolution of dental topography in bears and feeding behaviour in extinct cave bears (*Ursus spelaeus* s.l.)

3.2.1. Abstract

The diet of the cave bear represents a special case of disagreement, as different paleobiological approaches (e.g., dental wear, isotopic biochemistry, or geometric morphometrics from skull and teeth) result in different dietary inferences for the cave bear, ranging from carnivory to pure herbivory. Here, I apply a relatively recent homology-free technique to quantify the topography of the three-dimensional tooth crown surfaces in all living bear species to make dietary inferences in cave bears. The analysis of specimens belonging to ten species of living and extinct bears evidences that both DNE and OPCR are significantly associated with dietary adaptations in living taxa. A clear gradient in both DNE and OPCR was revealed, from bears adapted to feed on soft-matter (i.e., the animal-protein feeders and the soft-mast specialists) to the durophagous giant panda, with those bears than consume both soft and hard masts taking intermediate values of DNE and OPCR. I conclude that in bears both OPCR and DNE reflect the nature of the items consumed more than the type of food. Moreover, both DNE and OPCR are strongly influenced by tooth size, and therefore important allometric effects seem to be present in these dental topographic variables. Strikingly, cave bears take intermediate values of both DNE and OPCR to the ones of *A. melanoleuca* and those living bears specialist in feeding hard mast. According to our results, cave bears increase the outline areas of their most posterior dentition to almost reach the values exhibited by the giant panda, and this size increase entails a substantial increase in both OPCR and DNE, which improves chewing efficiency to feed on highly abrasive and lower-quality foods.

3.2.2. Introduction

The feeding ecology of the cave bear (*Ursus spelaeus*) from the Pleistocene of Eurasia has been a controversial topic in the literature (e.g., van Heteren and Figueirido 2019). While some authors have proposed that the cave bear was highly herbivore (e.g., Kurtén 1976; Bocherens et al. 1994), others authors have proposed that cave bears had a very similar diet to its living relative, the omnivorous brown bear (*Ursus arctos*) (Figueirido et al. 2009; Peigné et al. 2009a, 2009b; Jones and De Santis 2016; Peigné and Merceron 2017). However, other studies have hypothesized that the cave bear feed regularly on vertebrate flesh (Richards et al. 2008) or even on carrion (Rabal-Garcés et al. 2012; Pinto-Llona 2013).

Understanding the diet of the cave bear is key to identify the actual causes of its extinction. Some authors propose that cave bears were adapted to feed exclusively on vegetal resources from 100,000 to 20,000 years ago (Bocherens 2019) without evidence of a dietary shift towards omnivory at a time of lowered vegetation productivity as a consequence of the climate cooling occurred during the beginning of the Last Glacial Maximum (Terlatto et al. 2019). This lack of dietary flexibility intensified by human competition for cave space or direct hunting (Stiller et al. 2010), may have been a critical factor in the decline of the last populations of cave bears (Bocherens 2019) ~ 24,000 years ago.

Studies of isotopic biochemistry based on stable isotopes ($\delta\ ^{13}C/\ \delta\ ^{12}C$; $\delta\ ^{15}N/\ \delta\ ^{14}N$) preserved in teeth and bones (e.g., Bocherens et al. 1994,1997; Fernandez-Mosquera 1998; Nelson et al. 1998; VilaTaboada et al. 1999; Fernandez-Mosquera et al. 2001; Bocherens 2018; Robu et al. 2018) have predicted that the cave bear was a highly herbivorous bear. However, a biogeochemical analysis of a cave bear population preserved in the cave of Peştera cu Oase (Romania) has revealed that high levels of $\delta^{15}N$ extracted from bone collagen would indicate that these cave bears behaved as omnivores or even as carnivores (Richards et al. 2008; Quilès et al. 2006). However, other authors have claimed that this anomalous high $\delta^{15}N$ may also be a consequence of urea recycling during hibernation (Fernández Mosquera et al. 2001; Grandal-D'Anglade and Fernández Mosquera 2008).

Studies based on dental microwear in cave bears teeth and living bears have indicate that cave bears probably had an omnivorous diet because of the presence of more holes than pits compared to the living brown bear (Pinto-Llona 2006; Münzel et al. 2014; Jones and DeSantis 2016), at least during the predormancy period. However, the presence of more holes than pits could also be interpreted as evidence of ingesting plant material (Taylor and Hannam 1987). Similarly, another study based on dental microwear analysis of the cave bear population preserved in the Goyet cave (Belgium) showed that wear patterns and dental marks are typical of an omnivorous diet (Peigné et al. 2009). However, other authors (e.g., Bocherens et al. 2009) have proposed that the sample used in the aforementioned study was not adequate to conclude that the cave bear was an omnivore.

Several morphometric studies performed during the last decades (e.g., Altuna 1973; Torres 1978; Mattson 1998; van Heteren 2009) found that the cave bear had specific traits of its craniodental skeleton indicative of a highly-herbivorous diet. However, a multivariate morphometric analysis performed from the morphology of the jaw and skull in living bears and the cave shown that the morphology of its craniodental skeleton is not indicative of a specialized herbivorous diet (Figueirido et al. 2009). Accordingly, Figueirido et al. (2009) proposed that if the morphology of the craniodental skeleton of the cave bear indicates an omnivorous diet but it forages as an herbivore, the craniodental skeleton of the cave bear could represent a case of exaptation (Gould and Vrba 1972). In any case, a more recent and refined morphometric study performed from the mandibular morphology of living ursids and cave bears in three dimensions indicates that the mandible of the cave bear had specific traits indicative of a highly-herbivorous diet or, at least, more than their closest living relative, the brown bear (van Heteren and Figueirido 2019).

Tooth shape correlates with feeding behaviour because they play a key role in the mechanical breakdown of food and in the release of nutrients stored in them during chewing (Lucas 2004). However, despite this, few studies on tooth shape in bears related with feeding behaviour have been performed (but see Baryshnikov et al. 2003).

3.2.3. Dental Topography: a new tool for inferring feeding adaptation in mammal:

Advances in 3D scanning and image processing techniques during the last fifteen years have allowed the digital reconstruction of tooth-crown surface topography (Winchester 2016). Dental topographic analysis is the quantitative assessment of shape of three-dimensional models of tooth crowns and its features (M'Kirera and Ungar 2003; Evans et al. 2007; Bunn et al. 2011; Winchester et al. 2014). Molar topographic curvature (DNE), relief (RFI), and complexity (OPCR) correlate with feeding behaviour in many groups of living and extinct mammals (M'Kirera and Ungar 2003; Ungar and M'Kirera 2003; Dennis et al. 2004; Ulhaas et al. 2004; King et al. 2005; Evans et al. 2007; Boyer 2008; Ungar and Bunn 2008; Bunn and Ungar 2009; Evans and Jernvall 2009; Bunn et al. 2011; Godfrey et al. 2012; Wilson et al. 2012; Pineda et al. 2016; Evans and Pineda 2018). However, studies of tooth crowns and its features in 3D on the extinct cave bear are currently absent. Here, I quantify topographic curvature (DNE), relief (RFI), and complexity (OPCR) from three-dimensional tooth crown surfaces in living bears to explore their relationship with feeding behaviour. To do this, we quantify the influence of phylogeny, diet, and size on DNE, OPCR, and RFI. We also used these ecomorphological indicators to make dietary inferences in cave bears (*Ursus spelaeus* s.l.), an emblematic extinct group of bears belonging to the Pleistocene megafauna.

3.2.4. Materials and Methods

3.2.4.1. Materials

I have analysed the upper teeth from the upper fourth premolar (P4) to the upper second molar (M2) in all living bear species plus the two extinct species recognized for the cave bear: *Ursus ingressus* and *Ursus spelaeus*. Moreover, we have also included specimens belonging to each of the three subspecies recognized for *U. spelaeus*: *U. spelaeus spelaeus*, *U. spelaeus eremus*, *U. spelaeus ladinicus* (e.g., Hofreiter et al. 2004; Knapp et al. 2009).
In addition, we have included different subspecies of the brown bear teeth (*Ursus arctos alascensis*, *Ursus arctos gyas*, *Ursus arctos middendorffi*, *Ursus arctos horribilis*, *Ursus arctos sitkensis*, and *U. arctos pruinosus*) in order to have a better picture of both between-species and within-species variation in the topographic variables of the crown surface (**Table 1**).

3.2.4.2. Moulding dental casts

I obtained high-resolution dental replicas following procedures outlined (Figueirido et al. 2017). A dual-phase technique was used to produce polyvinylsiloxane-based molds (Virtual® Putty and Light Body compounds) from original tooth rows (P4-M2). High-resolution replicas were obtained from molds using non-reflective polyurethane (Feroca® Composites, Spain).

Table 1. Sample size of extinct and extant bears analysed in this study. All the specimens analysed in this study are housed in different museums: American Museum of Natural History (New York, USA), the Natural History Musum of London (NHM, UK), the Museum für Naturkunde (Berlin, Germany) and the Museum für Naturkunde (Vienna, Austria). See also **Table S1**.

Species	**N**
Ailuropoda melanoleuca	6
Helarctos malayanus	11
Melursus ursinus	8
Tremarctos ornatus	7
Ursus arctos	12
Ursus americanus	7
Ursus maritimus	11
Ursus thibetanus	10
Ursus ingressus	8
Ursus sp. spelaeus	5
Ursus sp. eremus	5
Ursus sp. ladinicus	4

3.2.4.3. Three-dimensional processing

Dental replicas were scanned at 0.2 mm resolution with a Roland LPX-600 located at the Central Research Services (University of Málaga, Spain). Meshes were merged and processed in MeshLab to obtain entire enamel caps (EEC) of each tooth row cropped at cervical margin (see Berthaume et al. 2019; Pampush et al. 2018), smoothed and down-sampled to 10,000 polygons faces (Whinchester 2016). The EEC method was used here to prevent planometric footprint area lost and produce metric values for whole tooth shape (Pampush et al. 2018). Meshes (*.ply file format) were then aligned orthogonal to the occlusal surfaces using MeshLab to mitigate impact of topographic metrics (Boyer 2008).

3.2.4.4. Quantifying complexity of tooth crown surfaces

I measured 3D-topographic shape metrics for each tooth row using MorphoTester following the parameters outlined by Winchester (2016). Data metrics included three topographic algorithms for describing tooth shape properties including *Dirichlet normal energy* (DNE) (Bunn et al. 2011), the *Surface relief index* (RFI) (Boyer 2008) and complexity using *Orientation patch count rotated* (OPCR) (Evans et al. 2007; Pineda-Munoz et al. 2017) and, a complementary size metric derived from the surface area (OA, in mm2).

The DNE is an integral measure that quantifies the amount of bending across a surface, reflecting the relative surface curvature and undulation, unaffected by structure sizes or orientation (Bunn et al. 2011; Whinchester 2016). Higher DNE values represent sharpened edges and troughs (Bunn et al. 2011). The DNE values were reported with 0.1% (the 99.9th percentile) energy*area outlier removal (Winchester 2016).

The RFI was calculated as a simple ratio of the 3D crown surface area (3da) divided by 2D occlusal plane (2da) (Whinchester 2016). Higher values of RFI indicate steeper dentitions (Pineda-Munoz et al. 2017), providing the relative tooth crown height when the EEC cropping methods is used (Berthaume et al. 2019).

Finally, OPCR was used to quantify tooth row complexity with a minimum patch size of 5 polygons (Winchester 2016). The OPCR parameter is calculated by dividing the occlusal surface into contiguous patches of equal orientation (45° sectors) based on slope and topographic elevation. The number of patches is counted and averaged following eight successive rotations of 5.625° where the amount of patches is associated with the row surface complexity (Whinchester 2016). The OPCR algorithm applied here is expected to store higher complexity variation in ursids than previously thought from raster-based dental maps (Evans et al. 2007; Whinchester 2016).

3.2.4.5. Statistical Analyses

To explore the influence of phylogeny on DNE, RFI and OPCR, we mapped their average values per species onto the assembled phylogeny of living bears and cave bears published by Pérez-Ramos et al. (2019). In this phylogeny, the relationships of living bears were taken from the study of Krause et al. (2008) and the relationships of cave bears were taken from Stiller et al. (2014).

To do this, we used the squared-changed parsimony method of Maddison (1991) using MESQUITE v. 3.40 (Maddison and Maddison 2000).

The association between DNE, RFI and OPCR with feeding ecology in living bears was explored using box-plots of the three variables according to the dietary groupings established by Pérez-Ramos et al. (2019). Therefore, the eight species were classified among three broad dietary categories for facilitating the ecomorphological comparisons: omnivores (the brown bear, *U. arctos*, and the Asiatic black bear, *U. thibetanus*), folivores-frugivores (the American black bear, *U. americanus*, and the spectacled bear, *T. ornatus*), and faunivores (the sun bear, *H. malayanus*, the sloth bear, *M. ursinus*, and the polar bear, *U. maritimus*). According to Pérez-Ramos et al. (2019) the giant panda was left apart in the dietary classifications.

Moreover, we performed a one-way ANOVA for testing the association between feeding behaviour and each of the dental variables quantified here (i.e., DNE, RFI and OPCR). The pairwise comparisons among dietary groupings based on the values of DNE, RFI and 3D-OPCR were tested with a parametric Post-Hoc Mann-Whitney pairwise comparison test, using PAST version 2.07 (Hammer et al. 2001). However, we also included the extinct taxa in a different category, named 'cave bears'. Our purpose here was to explore for differences and similarities between cave bears and the dietary groupings of living taxa.

Although all dental series were scaled to the same length, we regressed the variables DNE, RFI and OPCR against the outline area of the dental series for each specimen using Ordinary Least Squares (OLS). Similarly, the three variables had regressed each other in order to explore their association and the potential biological meaning. To explore the distribution of the specimens in a phenotypic space, we computed a Principal Components Analysis using correlation matrix.

3.2.5. Results

The average values of OPCR, DNE and RFI obtained from the merged three-dimensional models of the dental series (**Fig. 1**) for each species are shown in **Table 2** and the raw values for each specimen in **Table S2**.

3.2.5.1. The influence of phylogeny on DNE, RFI and 3D-OPCR

The values of DNE mapped on the phylogeny of Pérez-Ramos et al. (2019) using the squared-changed parsimony method of Maddison (1991) based on a Brownian Motion model of evolution are shown in **Figure 2**, and the results of DNE applied to molar tooth surfaces in **Figure 3**.

In general terms, it is observed that the bamboo-feeder giant panda (*A. melanoleuca*) exhibit the highest values of DNE (**Fig. 2**, left; **Table 2**), followed by the extinct species of cave bears: *U. sp. spelaeus*, *U. sp.*

ladinicus, *U. ingressus* and *U. sp. eremus*. The omnivorous bears (i.e., the brown bear, *U. arctos* and the Thibetan bear, *U. thibetanus*) exhibit intermediate values of DNE followed by the polar bear (*U. maritimus*), the American black bear (*Ursus americanus*) and the Malayan sun bear (*H. malayanus*). Finally, the sloth bear (*M. ursinus*), the American Black bear (*U. americanus*), and the Andean bear (*T. ornatus*) show the lowest values of DNE.

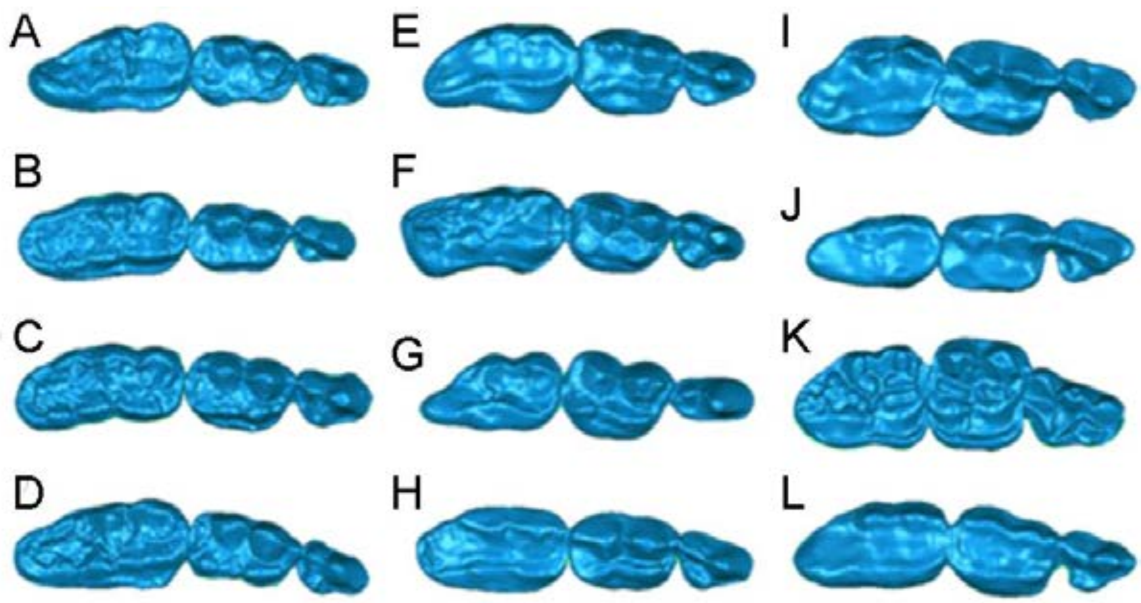

Figure 1. Merged three-dimensional models of living and extinct bears used to compute the variables DNE, RFI and OPCR with MorphoTester. (**A**) *U. ingressus*, (**B**) *U. sp. eremus*, (**C**) *U. sp. ladinicus*, (**D**) *U. sp. spelaeus*, (**E**) *U. americanus*, (**F**) U. *arctos*, (**G**) *U. maritimus*, (**H**) *U. thibetanus*, (**I**) *H. malayanus*, (**J**) *M. ursinus*, (**K**) *A. melanoleuca*, (**L**) *T. ornatus*. Only one specimen per especies is shown for clarity.

Table 2. Species averages for the OPCR, DNE, RFI, and OA (outline areas) obtained for the upper P4-M2 dental series in living and extinct bears. See also **Table S2.**

Species	OPCR	DNE	RFI	OA (mm2)
A. melanoleuca	354.15	1121.34	1.69	1601.62
H. malayanus	164.45	481.85	1.86	440.09
M. ursinus	172.13	409.34	1.72	454.77
T. ornatus	162.02	357.60	1.72	518.87
U. americanus	152.89	364.58	1.70	639.73
U. arctos	220.97	597.27	1.85	972.97
U. maritimus	186.28	520.37	1.88	629.53
U. thibetanus	192.25	494.58	1.67	647.28
U. sp. ladinicus	328.06	854.44	1.80	1537.39
U. sp. spelaeus	306.23	864.33	1.93	1397.15
Ursus sp.eremus	268.35	728.48	1.94	1500.00
Ursus ingressus	289.88	699.09	1.70	1597.43

The phylogenetic pattering of DNE is similar to the pattern obtained when mapping the values of OA onto the phylogeny of Pérez-Ramos et al. (2019) using squared-changed parsimony (**Fig. 2**, right). This indicates that most of the interspecific variation of DNE may be explained by changes in the outline area. However, it is striking that although the outline areas of cave bears are similar than the outline area of the giant panda, DNE values for cave bears are not as extreme as obtained for the giant panda. Similarly, the polar bear (*U. maritimus*) exhibit very low outline areas for the dental series, but values of DNE, although low, they are not as extremely low as in other species such as *U. thibetanus*, *H. malayanus*, *M. ursinus*, and *U. americanus*.

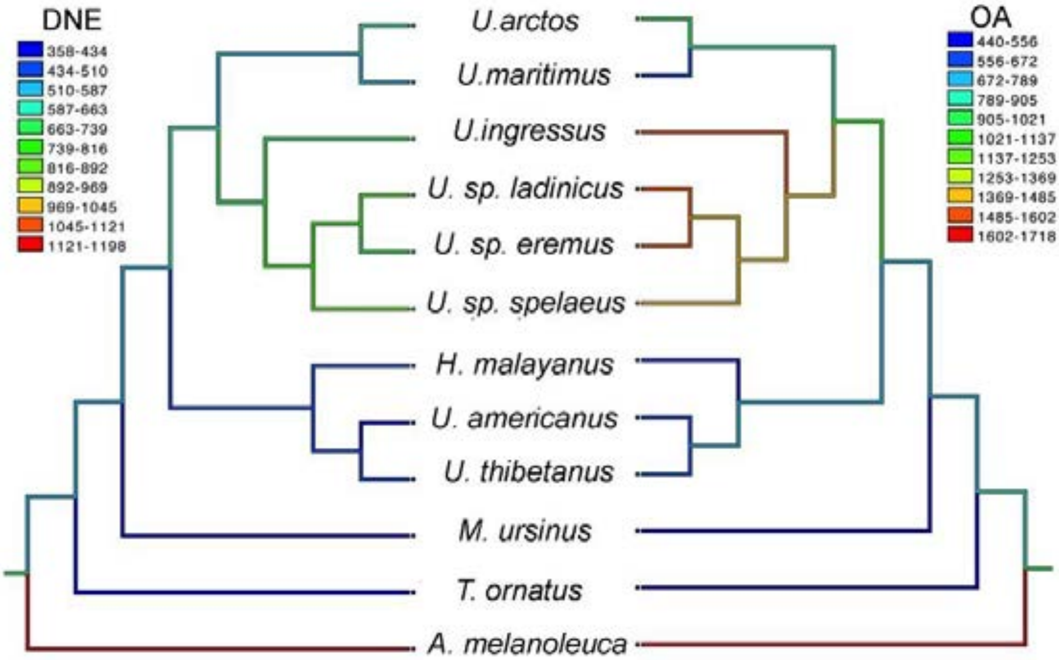

Figure 2. Species average of DNE and outline area (OA, as a proxy for size) values mapped on the phylogeny of Pérez-Ramos et al. (2019). Values at nodes and branches were reconstructed using squared-changed parsimony based on a Brownian motion model of evolution. Branch lengths were standardized to the same value for clarity.

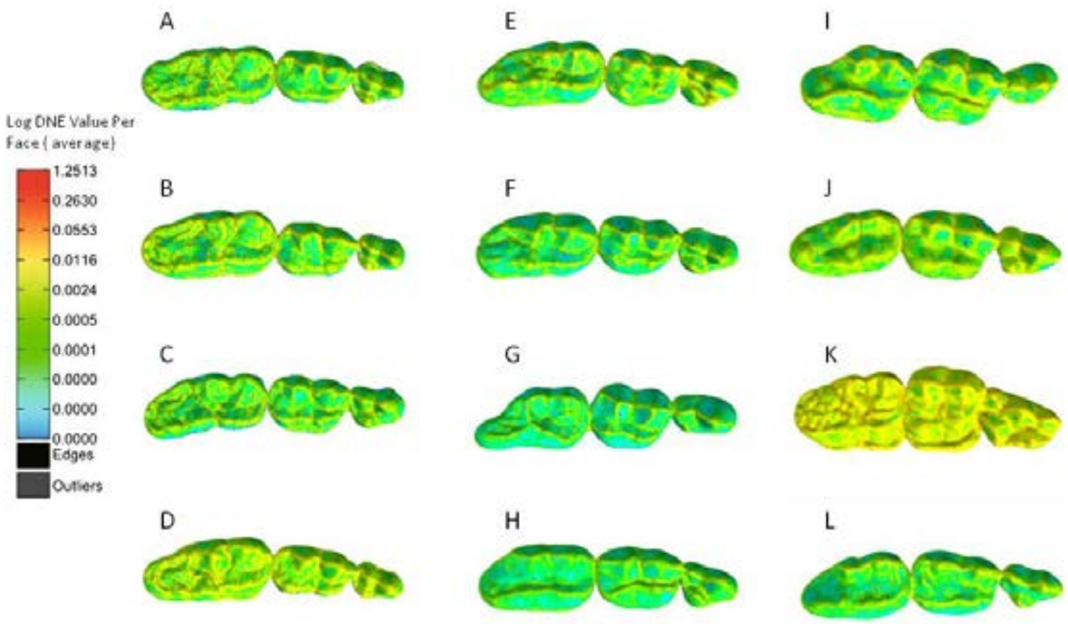

Figure 3. Results of DNE algorithm applied to molar tooth surfaces with MorphoTester. (A) *U. ingressus*; **(B)** *U. sp. eremus*; **(C)** *U. sp. ladinicus*; **(D)** *U. sp. spelaeus*; **(E)** *U. americanus*; **(F)** *U. arctos*; **(G)** *U. maritimus*; **(H)** *U. thibetanus*; **(I)** *H. malayanus;* **(J)** *M. ursinus*; **(K)** *A. melanoleuca*; **(L)** *T. ornatus*. Only one specimen per species is shown as an example.

The values of RFI mapped on the phylogeny of Pérez-Ramos et al. (2019) using the squared-changed parsimony method of Maddison (1991) based on a Brownian Motion model of evolution are shown in **Figure 4** and the results of DNE algorithms applied to molar tooth surfaces in **Figure 5**. Living and extinct bears exhibit a high variability for the values of RFI. Accordingly, the highest values of RFI are exhibited by *U. sp. spelaeus*, *U. sp. eremus*, and by *H. malayanus*, followed by *U. arctos*, *U. maritimus* and *U. sp. ladinicus* with intermediate values (**Fig. 5**, right; **Table 2**). Finally, the rest of living bears, including the giant panda, and *U. ingressus* have very low values of RFI. As expected, a visual comparison of the phylogenetic pattering of RFI with the mapped values of OA onto the phylogeny of Pérez-Ramos et al. (2019) evidence that RFI is not influenced by dental series size as DNE.

The values of 3D-OPCR mapped on the phylogeny of Pérez-Ramos et al. (2019) are shown in **Figure 6** and the results of DNE algorithms applied to molar tooth surfaces in **Figure 7**.

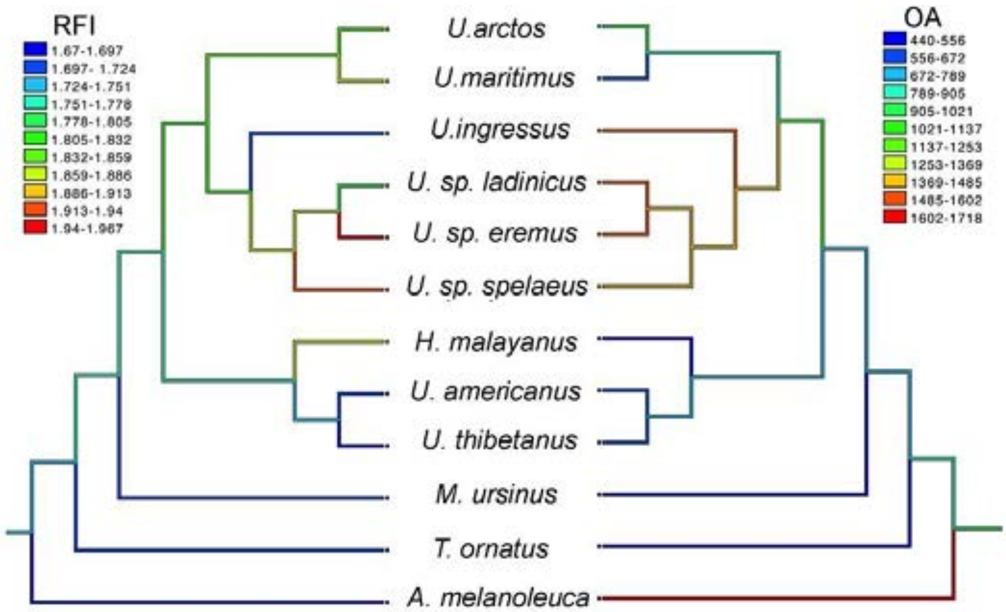

Figure 4. Species averages of RFI and outline area (OA) values mapped on the phylogeny of Pérez-Ramos et al. (2019). Values at nodes and branches were reconstructed using squared-changed parsimony based on a Brownian motion model of evolution. Branch lengths were standardized to the same value for clarity.

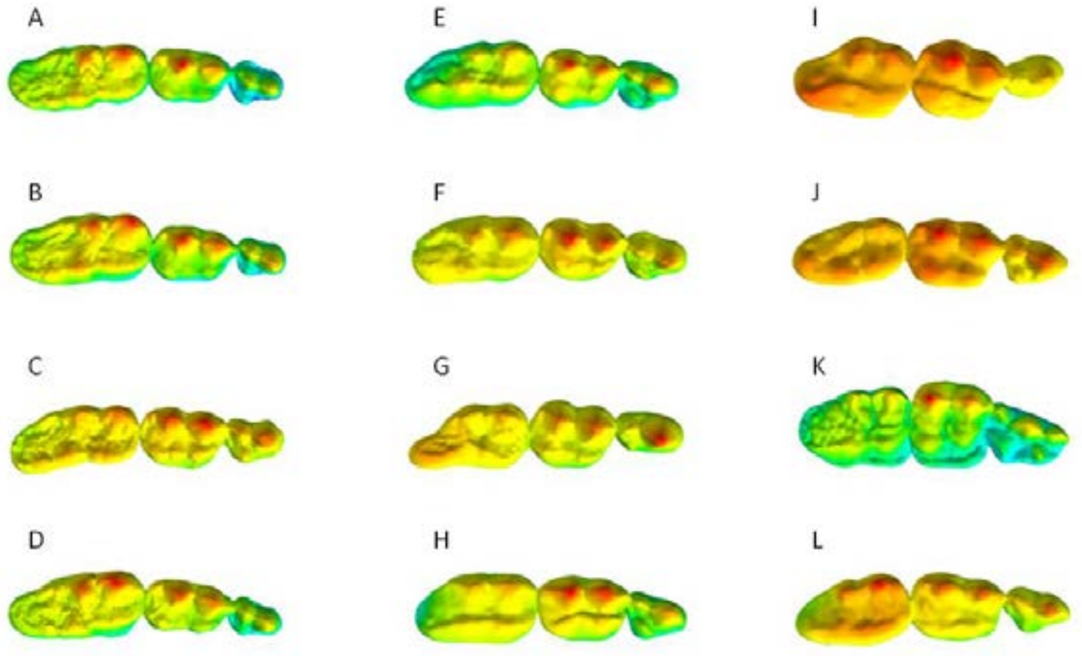

Figure 5. Results of RFI algorithm applied to molar tooth surfaces with MorphoTester. (**A**) *U. ingressus*; (**B**) *U. sp. eremus*; (**C**) *U. sp. ladinicus*; (**D**) *U. sp. spelaeus*; (**E**) *U. americanus*; (**F**) *U. arctos*; (**G**) *U. maritimus*; (**H**) *U. thibetanus*; (**I**) *H. malayanus*; (**J**) *M. ursinus*; (**K**) *A. melanoleuca*; (**L**) *T. ornatus*. Only one specimen per species is shown for clarity.

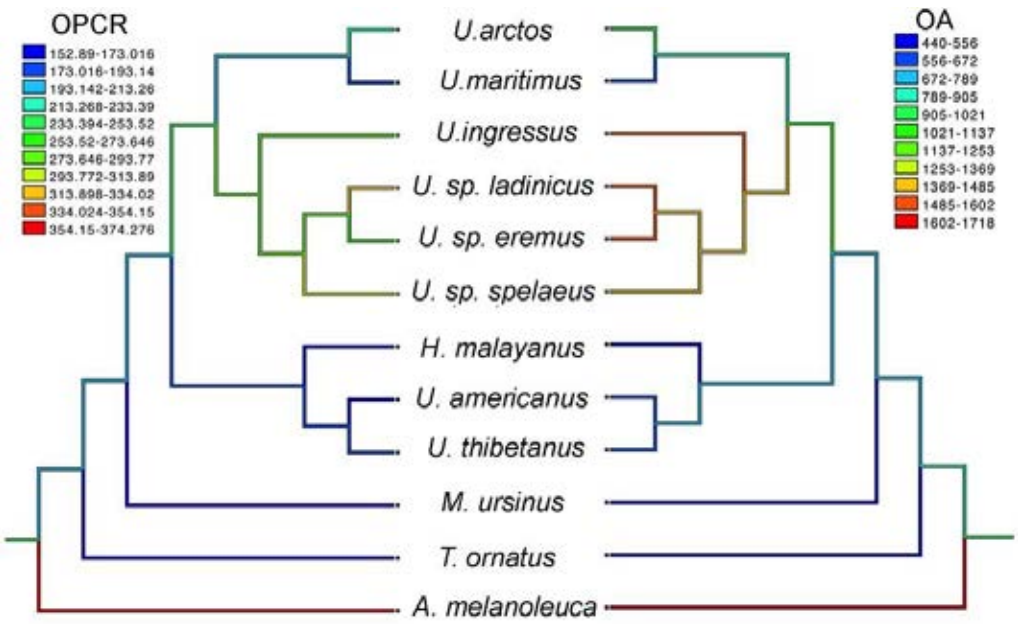

Figure 6. Species averages for OPCR and outline area (OA, as a proxy for size) for each species mapped on the phylogeny of Pérez-Ramos et al. (2019). Values at nodes and branches were reconstructed using squared-changed parsimony based on a Brownian motion model of evolution. Branch lengths were standardized to the same value for clarity.

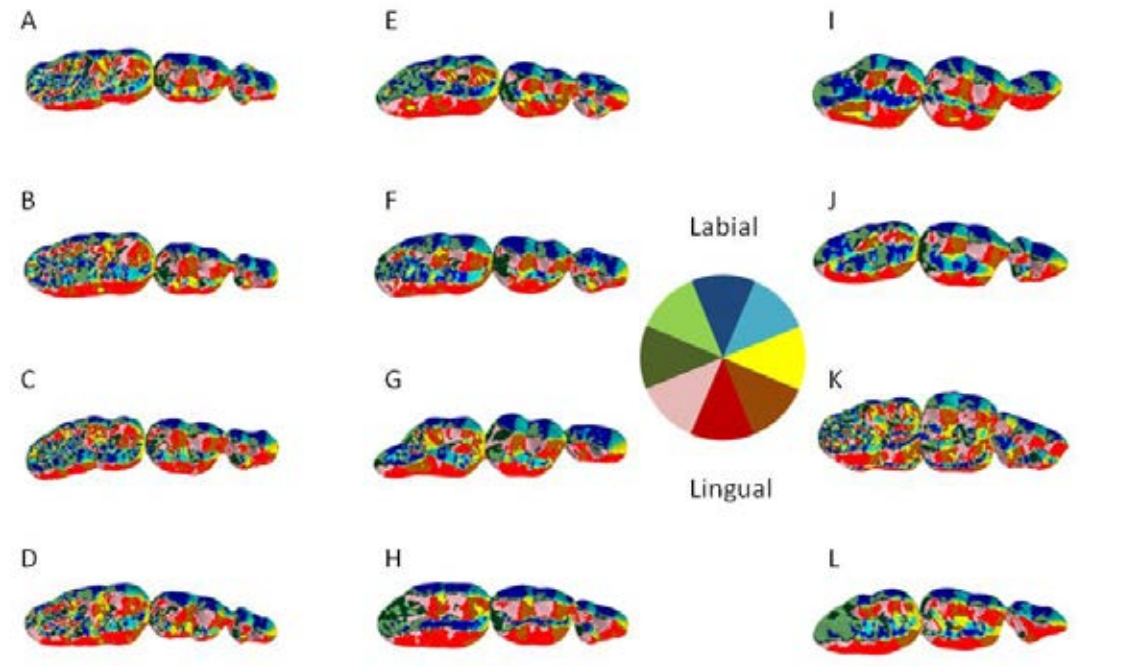

Figure 7. Results of RFI algorithm applied to molar tooth surfaces with MorphoTester. (**A**) *U. ingressus*; (**B**) *U. sp. eremus*; (**C**) *U. sp. ladinicus*; (**D**) *U. sp. spelaeus*; (**E**) *U. americanus*; (**F**) *U. arctos*; (**G**) *U. maritimus*; (**H**) *U. thibetanus*; (**I**) *H. malayanus*; (**J**) *M. ursinus*; (**K**) *A. melanoleuca*; (**L**) *T. ornatus*. Colour wheel indicates patch aspect direction for occlusal perspective.

The species with the highest values of OPCR is the giant panda (*A. melanoleuca*) followed by all cave bears, and specially, *U. sp. ladinicus*. The brown bear (*U. arctos*) and Thibetan bear (*U. thibetanus*) have intermediate values of OPCR, followed by *U. maritimus*, *H. malayanus*, and *M. ursinus*. Finally, the American black bear (*U. americanus*) and the Andean bear (*T. ornatus*) exhibit the lowest values of OPCR among the species sampled. A visual comparison of the phylogenetic pattering of RFI with the mapped values of OA onto the phylogeny of Pérez-Ramos et al. (2019) evidence that OPCR is also influenced by dental series size. However, despite cave bears exhibit high outline areas of dental series, their values of 3D-OPCR are not as higher as expected.

3.2.5.2. The influence of feeding behaviour on DNE, RFI and 3D-OPCR

The results of the three one-way ANOVA test performed to investigate the association between DNE, RFI, and OPCR with feeding preferences was significant in the three cases, which reveals overall differences in DNE, RFI, and OPCR values among the established dietary groupings (**Table 3**).

As shown by the Bonferroni corrected *p*-values obtained from the Post-Hoc Mann-Whitney pairwise comparison test, the dietary groups significantly differ in the values of DNE, with the sole exception of animal-protein feeders from omnivores (**Table 4**).

The giant panda (*A. melanoleuca*) shows the highest values of DNE, followed by cave bears (*U. ingressus* and the three subspecies *Ursus spelaeus*). The omnivorous bears exhibit intermediate values followed by the animal-protein feeders (*H. malayanus*, *M. ursinus*, and *U. maritimus*). Finally, the folivores-frugivores (*T. ornatus* and *U. americanus*) reach the lowest values of DNE among the sample (**Fig. 8**).

In the case of RFI, its significant association with feeding ecology obtained in the one-way ANOVA test is only due to the significant differences in RFI between the giant panda and the animal-protein feeders (**Table 4**). This is due to a high variability within dietary groups (**Fig. 8**).

Regarding OPCR, all pairwise comparisons among dietary groupings were significant, with the exception of folivores-frugivores from animal-protein feeders. As in the results obtained for DNE, the giant panda (*A. melanoleuca*) exhibit the highest values of OPCR, followed by cave bears. The omnivorous bears exhibit intermediate values followed by the animal-protein feeders (*H. malayanus*, *M. ursinus*, and *U. maritimus*).

Table 3. Results of the three one-way ANOVA tests performed between DNE, RFI and OPCR and using dietary groupings as factor.

	DNE				
	Sum of sqrs	***df***	***Mean square***	***F***	***p (same)***
Between groups	3.57E+06	4	892901	90.34	1.70E-30
Within groups	879674	89	9883.98		
Total	4.45E+06	93			
	RFI				
Between groups:	0.19748	4	0.0493699	3.266	0.01509
Within groups:	1.34524	89	0.0151151		
Total:	1.54272	93			
	OPCR				
Between groups:	353909	4	88477.1	137.7	3.01E-37
Within groups:	57203.8	89	642.739		
Total:	411112	93			

Table 4. Bonferroni corrected *p*-values obtained in the Post-Hoc Mann-Whitney pairwise comparison test used to assess for differences among dietary groupings. *Group 1*, giant panda; *group 2*, animal-protein feeders; *group 3*, folivores-frugivores; *group 4*, omnivores; *group 5*, cave bears. Light grey denotes significant differences.

	DNE			
	2	**3**	**4**	**5**
1	0.001452	0.006197	0.002451	0.004664
2		0.001098	0.1341	3.27E-08
3			3.22E-05	7.47E-06
4				1.59E-05
	RFI			
1	0.2881	1	1	1
2		0.02394	1	1
3			1	0.3352
4				1
	OPCR			
1	0.001452	0.006197	0.002442	0.003775
2		0.1174	0.0005391	1.04E-08
3			0.0001095	6.32E-06
4				4.82E-07

Finally, the folivores-frugivores (*T. ornatus* and *U. americanus*) reach the lowest values of OPCR (**Fig. 8**).

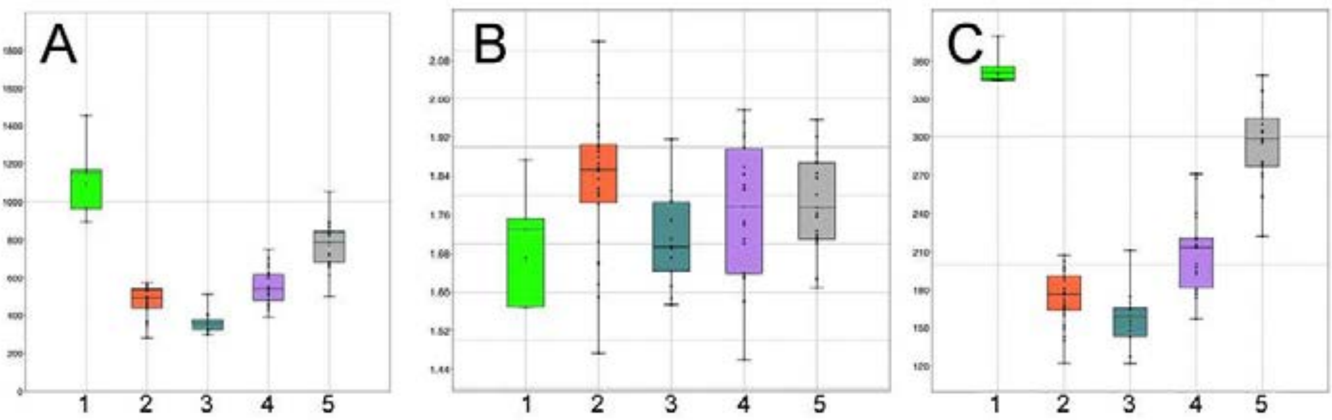

Figure 8. Box-plots showing the values of DNE (A), RFI (B) and OPCR (C) among dietary groupings of living bears and cave bears. The vertical line inside each box is the median. Box length is the interquartile range (IQR) and shows the difference between the 75th and 25th percentiles. Horizontal bars enclose values of 5–95%. Abbreviations: Group 1, giant panda; group 2, animal-protein feeders; group 3, folivores-frugivores; group 4, omnivores; group 5, cave bears. Light grey denotes significant differences.

3.2.5.3. The influence of allometry

The bivariate regression of DNE against the outline area of the dental series (**Fig. 9A**) was statistically significant ($p < 0.0001$) which indicates that DNE variation is influenced by tooth size (**Table 5**). However, the bivariate regression of RFI against the outline area of the dental series was not statistically significant ($p < 0.6401$) which indicates that DNE variation is not influenced by tooth size (**Table 5**). As in the case of DNE, the bivariate regression of OPCR against the outline area of the dental series (**Fig. 9B**) was statistically significant ($p < 0.0001$) which indicates that OPCR variation is influenced by tooth size (**Table 5**). This result was in part expected given the comparisons performed of the values of DNE, RFI and OPCR mapped on the phylogeny with the values of outline area (**Figs. 2,4,6**).

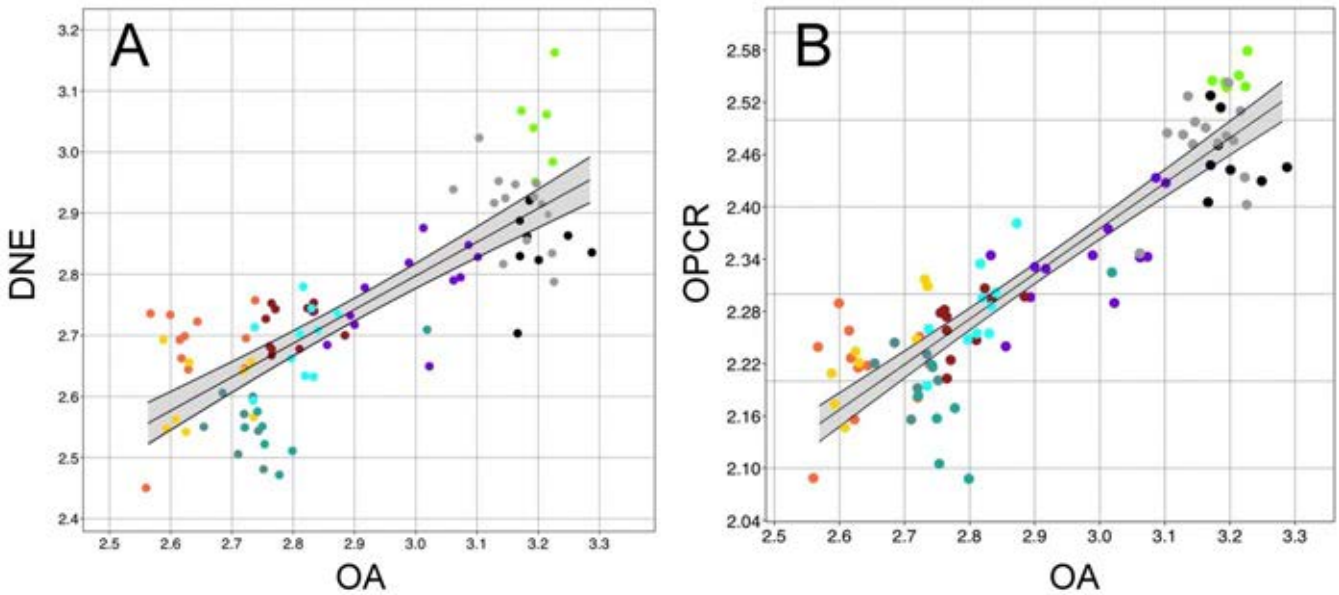

Figure 9. Bivariate graphs of DNE (A) and OPCR (B) against outline area (OA), using OLS (variables log-transformed). Grey shaded areas represent the 95% of confidence interval. The bivariate RFI against outline area was not represented, as the bivariate regression was not significant (see **Table 5**).

Table 5. **Results of the bivariate regressions performed of log-transformed DNE, RFI and OPCR against log-transformed OA.** The values for the slope and the intercept, Pearson's r correlation coefficient (*r*), the Pearson's coefficient squared (r^2) are given. The permutation test on correlation (r^2) uses 9,999 replicates.

	DNE-OA	RFI-OA	OPCR-OA
Slope	0.55114	-0.00714	0.51984
Intercept	1.1439	0.26922	0.81565
r:	0.80361	-0.049048	0.89988
r2:	0.64579	0.0024057	0.80978
t:	12.951	-0.47102	19.79
Perm. *p*:	0.0001	0.6401	0.0001

3.2.5.4. Principal Components Analysis

The PCA performed from the log-transformed variables yielded two significant eigenvectors, which jointly explained almost 99% of the original variance. The bivariate graph depicted from the first two principal components is shown in **Figure 10**. The first PC (93 % of the variance explained) mainly separates the giant panda (*A. melanoleuca*) and cave bears with positive scores from animal-protein feeders plus folivores-frugivores scoring negatively. The omnivorous bears score in between the giant panda plus cave bears and the animal-protein feeders plus folivores-frugivores (**Fig. 10**).

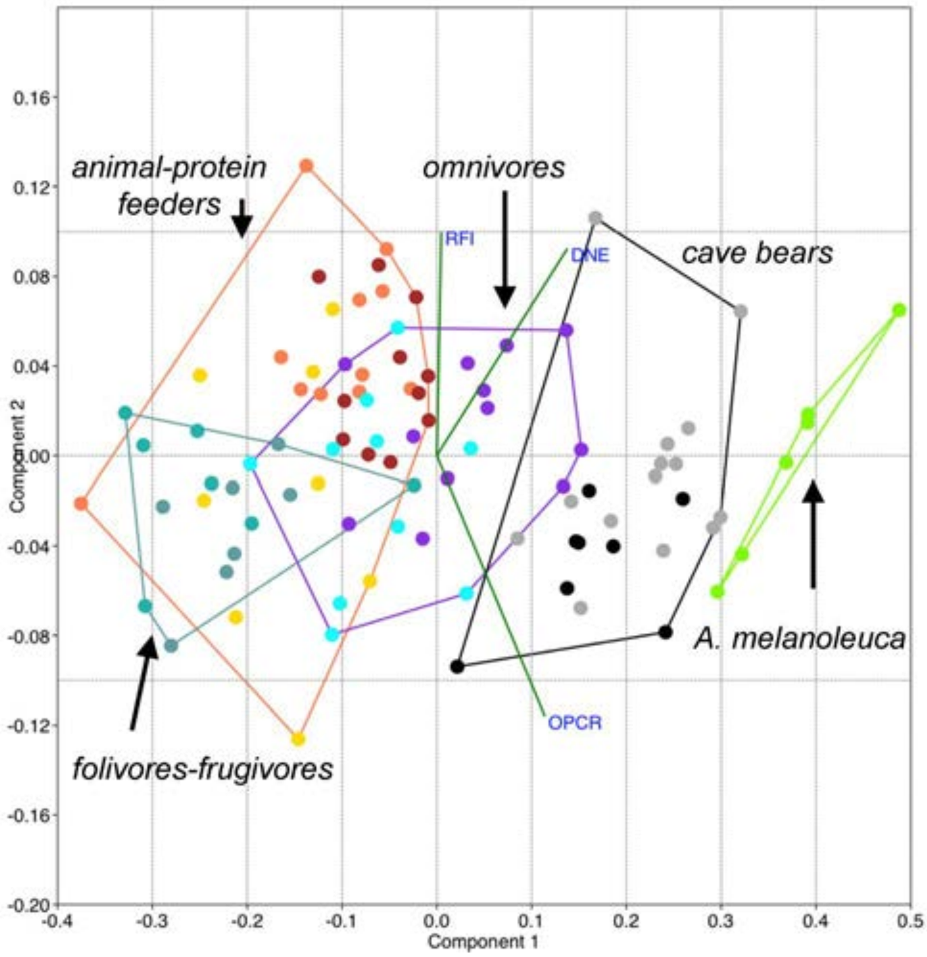

Figure 10. Bivariate graph depicted from the first two eigenvectors obtained from PCA of the log-transformed DNE, RFI and OPCR using the covariance matrix.

The factor loadings of the variables on each eigenvector indicates that while both the giant panda plus cave bears are characterized by having high values of DNE and OPCR, the animal-protein feeders plus folivores-frugivores are characterized by having low values of both variables. The omnivores are characterized by having intermediate ones. The second principal component, which explains 6% of the original variance, separates those specimens with high values of both DNE and RFI from those specimens with low values of both variables and high values of OPCR.

3.2.6. Discussion and Conclusions

3.2.6.1. Dental topographic analysis and feeding behaviour in living bears

The values of DNE, OPCR and RFI (**Figs. 3,5,7; Table 2**) mapped on the phylogeny of living and extinct ursids (**Figs. 2,4,6**) does not support a phylogenetic pattering on topographic curvature, relief and complexity. Moreover, despite the distribution of DNE, RFI and OPCR values across dietary groupings evidence a significant overlap of some feeding groups (**Fig. 8**), the ANOVA test demonstrates that the three variables are significantly associated with dietary adaptations (**Table 3**). Additionally, the post-Hoc Mann-Whitney pairwise comparison test reveals that DNE and OPCR significantly distinguishes most dietary groupings –with the exception of omnivores from animal protein feeders in the case of DNE, and of folivores-frugivores from animal-protein feeders in the case of OPCR (**Table 4**). Therefore, DNE and OPCR could be considered as dietary proxies in living ursids. However, RFI only distinguished the animal-protein feeders from folivores-frugivores, and therefore, relief index seems to be a poor indicator of dietary adaptations in living bears. Although in primates it has been shown that frugivore/gramnivores have significantly lower RFI values than omnivores, and insectivores/folivores having significantly higher RFI values than the other two, our results indicate a significant inaccuracy of RFI to distinguish among dietary groupings of living bears. This fact reflects that all living and extinct bears have the same sharpness, regardless of being insectivore such as the sloth bear (*M. ursinus*), hypercarnivore such as the polar bear (*U. maritimus*) or bamboo-feeder such as the giant panda (*A. melanoleuca*).

Moreover, both dental topographic curvature (DNE) and complexity (OPCR) are associated with size (**Fig. 9; Table 5**). As dental series were standardized to the same size, this evidence allometric effects in both variables. Therefore, those dental series with higher outline areas also exhibit higher values of DNE and OPCR. Of course, the relief index (RFI) was not associated with the outline area because it is computed as the ratio between 3D surface area of the crown divided by the 2D projected area in occlusal view.

In general, a larger tooth can process more food with each bite, either through a larger area of contact or because it forms a longer blade (Evans and Pineda 2016). Occlusal surface area seems to be correlated with the capacity to process food and with some aspects of physiology and metabolism (Vizcaíno et al. 2006). For example, among ungulates and kangaroos the cheek-teeth occlusal surface area is larger in grazers than in browsers (Janis 1990, 1995; Janis and Constable 1993; Mendoza et al. 2002). Moreover, Janis (1988, 1995) demonstrated that monogastric ungulates, such as perissodactyls, have longer molarized premolar rows than ruminant artiodactyls, and such differences should be due to different feeding strategies related to their physiology of digestion (Janis and Constable 1993;

Janis 1995). This suggests that in ungulates, chewing area is also related to the nutritional value of food: browsers consume succulent leaves while grazers ingest forage, which is a lower quality and highly abrasive food.

A PC analysis has been performed from the topographic curvature (DNE), relief (RFI) and complexity (OPCR) to find a possible combination of these variables that maximize the original variance within the sample and separation among dietary groups. The resulted morphospace depicted from the first two eigenvectors revealed a clear ordination according to feeding behaviour (**Fig. 10**). Indeed, it is observed a clear gradient from highly herbivorous bears to animal-protein feeders. Accordingly, with extreme positive values on PC1 (i.e., high OPCR and DNE) are scoring the giant pandas (*A. melanoleuca*) and cave bears (*U. spelaeus* and *U. ingressus*), with intermediate scores the omnivores (*U. arctos* and *U. thibetanus*) and with extreme negative scores, the animal protein-feeders (*M. ursinus* and *H. malayanus*). The exception to this pattern is the category of folivores-frugivores (*T. ornatus* and *U. americanus*) that exhibit negative values on PC1 and overlap with the animal-protein feeders. Apparently, this result seems counterintuitive, but the folivores-frugivores are soft-mast specialists –i.e., they feed more than 50% on soft mast and less than 15 on hard mast whereas the omnivores are characterized by feeding less than 50% on soft mast and more than 15% on hard mast. Soft-mast comprises mainly fleshy fruits or strobili (such as those of *Juniperus*) that are comparably soft (e.g., Mattson 1998). Therefore, following the results, both OPCR and RFI are more correlated with the mechanical properties of the material than with the nature of the food items.

3.2.6.2. Dietary inferences in cave bears based on dental topographic analysis

The results obtained here demonstrate that the giant panda (*A. melanoleuca*) show the highest values of OPCR and DNE among all the species included in the sample (**Fig. 8**) and its values are different from all other dietary groupings (**Tables 3,4**). This should be related to its peculiar diet feeding on bamboo. Similarly, the most complex teeth in living primates tend to be those of species that consume extremely fibrous vegetation, such as the bamboo-eating lemurs (Bunn et al. 2011). Bamboo is a hard and tough food because it has high values of yield strength (i.e., a large force is required to produce a material failure) and toughness (i.e., a high capacity to absorb a large amount of energy before breaking, [e.g., Wegst and Ashby 2004; Figueirido et al. 2013]). In fact, the physical and mechanical properties of bamboo are comparable to low-carbon steel and glass-reinforced plastics, which leads to its frequent use in industry for constructing scaffolds and as a reinforcement for cement, rubber, thermoplastic, and even aluminium (Low et al. 2006; Figueirido et al. 2013).

Strikingly, the second group of bears with the highest values of OPCR are all the species/subspecies of cave bears, which may indicate that these species were probably feeding on hard and tough materials such as tubercles or any other low-quality and highly fibrous vegetal resource. Therefore, in the case of both the bamboo-feeder giant panda and the cave bears, the concomitant increase in dental topographic complexity and curvature with the outline area of their dental series is probably related with an increase in efficiency for consuming highly abrasive and lower quality foods.

In **chapter 3.1**, I demonstrated that cave bears follow a unique trend of increasing tooth-root areas from canine to upper second molar; indeed, while living bears experience a substantial increase in tooth-root area values from the fourth upper premolar to upper first molar with a slight increase (or even a decrease) between upper first molar and upper second molar, cave bears uniquely exhibit a gradual and continuous increase from upper fourth premolar to upper second molar, reaching the values of the second upper molar of the giant panda (*A. melanoleuca*).

We hypothesize that cave bears increase the outline areas of their most posterior dentition to almost reach the values exhibited by the giant panda, and this increase entails a substantial increase in both OPCR and DNE, which improves efficiency to chew on highly abrasive and lower quality foods. In **chapter 3.1**, I also demonstrated that the largest values of tooth-root area among living and extinct bears were exhibited by cave bears, particularly by the subspecies *U. spelaeus eremus* and *U. spelaeus ladinicus*, and they proposed that it may represent an adaptation to feed on any hard or tough resource present in the high-alpine biome. Our new data on OPCR and DNE supports this hypothesis.

Moreover, our PCA analysis evidence that they combine values of OPCR and DNE in a unique manner among living bears (**Fig. 10**), as evidenced by their position in an empty space of the PC1 vs PC2 plot. Therefore, we hypothesize that most probably cave bears were feeding on a resource present in the high-alpine biome that they inhabited. Moreover, most probably, any living bear does not currently exploit this feeding resource with an intermediate mechanical property to bamboo and hard mast (i.e., fruits and seeds with a hard protective covering, including both acorns and pine seeds and roots and tubercles [Mattson 1998]). Inferring the specific vegetal resource that cave bears were specialized to feed on is, of course, tempting but the two brown bear specimens that plot within the cave bear space according to their values of DNE, OPCR, and RFI belong to *U. arctos pruinosus,* a subspecies that forage at 4,500m of altitude in the Tibetan plateau. However, unfortunately, the ecology of this subspecies of brown bear is certainly unknown.

3.2.7. References

- Altuna J. 1973. Hallazgos de oso pardo (*Ursus arctos*, Mammalia) en cuevas del País Vasco. MUNIBE. 2:121–170.
- Baryshnikov G, Germonpré M, Sablin M. 2003. Sexual dimorphism and morphometric variability of cheek teeth of the cave bear (*Ursus spelaeus*). Belgian J Zool. 133:111–119.
- Bocherens H, Fizet M, Mariotti A. 1994. Diet, physiology and ecology of fossil mammals as inferred from stable carbon and nitrogen isotope biogeochemistry: implications for Pleistocene bears. Palaeogeogr Palaeoclimatol Palaeoecol. 107:213–225.
- Bocherens H, Billiou D, Patou-Mathis M, Bonjean D, Otte M, Mariotti A. 1997. Paleobiological implications of the isotopic signatures (^{13}C,^{15}N) of fossil mammal collagen in Scladina cave (Sclayn, Belgium). Quat Res. 48:370–380.
- Bocherens H. 2019. Isotopic insights on cave bear palaeodiet. Hist Biol. 31:410-421.
- Boyer DM. 2008. Relief index of second mandibular molars is a correlate of diet among prosimian primates and other euarchontan mammals. J Human Evol. 55:1118–1137.
- Bunn JM, Ungar PS. 2009. Dental topography and diets of four old world monkey species. Am J Primatol: Official Journal of the American Society of Primatologists. 71:466-477.

- Bunn JM, Boyer DM, Lipman Y, Clair EM, Jernvall J, Daubechies I. 2011. Comparing Dirichlet normal surface energy of tooth crowns, a new technique of molar shape quantification for dietary inference, with previous methods in isolation and in combination. Am J Phys Anthropol. 145:247–261.
- Dennis JC, Ungar PS, Teaford MF, Glander KE. 2004. Dental topography and molar wear in *Alouatta palliata* from Costa Rica. Am J Phys Anthropol. 125:152-161.
- Evans AR, Jernvall J. 2009. Patterns and constraints in carnivoran and rodent dental complexity and tooth size. J Vertebr Paleontol. 29:24A.
- Evans AR, Pineda-Munoz S. 2018. Inferring Mammal Dietary Ecology from Dental Morphology. In: Croft D, Su D, Simpson S. (eds). Methods in Paleoecology. Vertebr Paleobiol Pa. Springer, Cham.
- Evans AR, Wilson GP, Fortelius M, Jernvall J. 2007. High-level similarity of dentitions in carnivorans and rodents. Nature. 445:78–81.
- Fernandez-Mosquera D, M. Vila-Taboada, A. Grandal-D'Anglade. 2001. Stable isotopes data (delta C-13, delta N-15) from the cave bear (*Ursus spelaeus*): a new approach to its palaeoenvironment and dormancy. Proc R Soc Lond Ser B Biol Sci. 268:1159–1164.
- Fernandez-Mosquera D. 1998. Biogeoquímica isotópica (d^{13}C, d^{15}N) de *Ursus spelaeus* del yacimiento de Cova Eiròs, Lugo. Cadernos do Laboratorio Xeolóxico de Laxe. 23:237–249.
- Figueirido B, Palmqvist P, Pérez-Claros JA. 2009. Ecomorphological correlates of craniodental variation in bears and paleobiological implications for extinct taxa: an approach based on geometric morphometrics. J Zool. 277:70–80.
- Figueirido B, Tseng ZJ, Martín-Serra A. 2013. Skull shape evolution in durophagous carnivorans. Evolution. 67:1975–1993.
- Figueirido B, Pérez-Ramos A, Schubert BW, Serrano F, Farrell AB, Pastor FJ, Romero A. 2017. Dental caries in the fossil record: a window to the evolution of dietary plasticity in an extinct bear. Scientific reports 7:17813.

- Godfrey LR, Winchester JM, King SJ, Boyer DM, Jernvall J. 2012. Dental topography indicates ecological contraction of lemur communities. Am J Phys Anthropol. 148:215–227.
- Gould SJ, Vrba ES. 1982. Exaptation—a missing term in the science of form. Paleobiology. 8:4-15.
- Grandal-D'Anglade A, Mosquera DF. 2008. Hibernation can also cause high δ15N values in cave bears: A response to Richards et al. P Natl Acad Sci USA. 105:E14-E14.
- Ø H, Harper DAT, Ryan PD. 2001. PAST: Paleontological statistics software package for education and data analysis. Palaeontol Electron. 4:9.
- Hofreiter M, Rabeder G, Jaenicke V, Withalm G, Nagel D, Paunovic M, Jambrsi G, Pääbo S. 2004. Evidence for reproductive isolation between cave bear populations. Curr Biol. 14:40–43.
- Janis CM. 1988. An estimation of tooth volume and hypsodonty indices in Ungulate mammals, and the correlation of these factors with dietary preference. In: Russell DE, Santoro JP, Sigogneau-Russell D. (eds.), Teeth revisited: Proceedings of the VII International Symposium on Dental Morphology. Mémoirs du Muséum national d'Histoire naturelle. (série C). 53:367-387.
- Janis CM. 1990. Correlation of cranial and dental variables with dietary preferences: a comparison of macropodoid and ungulate mammals. Memoirs of the Queensland Museum. 28:349-366.
- Janis CM. 1995. Correlations between craniodental morphology and feeding behavior in ungulates: reciprocal illumination between living and fossil taxa. In: J. Thomason (ed.), Functional Morphology in Vertebrate Palaeontology, Cambridge University Press. 76-98.
- Janis CM, Constable E. 1993. Can ungulate craniodental features determine digestive physiology?. J Vertebr Paleontol. 13:43A.
- Jones DB, DeSantis LR. 2016. Dietary ecology of the extinct cave bear: evidence of omnivory as inferred from dental microwear textures. Acta Palaeontol Pol. 61:735-742.

- King SJ, Arrigo-Nelson SJ, Pochron ST, Semprebon GM, Godfrey LR, Wright PC, Jernvall J. 2005. Dental senescence in a long-lived primate links infant survival to rainfall. Proc Natl Acad Sci USA. 102:16579–16583.
- Knapp M. 2019. From a molecules' perspective – contributions of ancient DNA research to understanding cave bear biology. Hist Biol. 31:442-447
- Krause J, Unger T, Noçon A, Malaspinas A-S, Kolokotronis S-O, Stiller M, Soibelzon L, Spriggs AW, Bray SCE, O'Brien S.J. et al. 2008. Mitochondrial genomes reveal an explosive radiation of extinct and extant bears near the Miocene-Pliocene boundary. BMC Evol Biol. 8:e220.
- Kurtén B. 1976. The cave bear story: life and death of a vanished animal. New York: Columbia University Press.
- Lazzari V, Tafforeau P, Aguilar JP, Michaux J. 2008. Topographic maps applied to comparative molar morphology: the case of murine and cricetine dental plans (Rodentia, Muroidea). Paleobiology. 34:46-64.
- Low IM, Che ZY, Latella BA, Sim KS. 2006. Mechanical and fracture properties of bamboo. In Key Engineering Materials. Trans Tech Publications. 312:15-20.
- Lucas, P. W. 2004. Dental functional morphology: how teeth work. Cambridge University Press.
- M'Kirera F, Ungar PS. 2003. Occlusal relief changes with molar wear in *Pan troglodytes troglodytes* and *Gorilla gorilla gorilla*. Am J Primatol. 60:31–41.
- Maddison WP. 1991. Squared-change parsimony reconstructions of ancestral states for continuous-valued characters on a phylogenetic tree. Syst Biol. 40:304-314.
- Maddison W, Maddison D. 2007. Mesquite 2. A modular system for evolutionary analysis.
- Mattson DJ. 1998. Diet and morphology of extant and recently extinct northern bears. Ursus. 10:479–496.
- Mendoza M, Janis CM, Palmqvist P. 2002. Characterizing complex craniodental patterns related to feeding behaviour in ungulates: a multivariate approach. J Zool. 258:223-246.

- Münzel MC, Rivals F, Pacher M, Döppes D, Rabeder G, Conard NJ, Drucker DG, Bocherens H. 2014. Behavioural ecology of Late Pleistocene cave bears (*Ursus spelaeus*, *U. ingressus*): insights from stable isotopes (C, N, O) and tooth microwear. Quat Int. 339–340:148–163.
- Nelson DE, Angerbjörn A, Lidén K, Turk I. 1998. Stable isotopes and the metabolism of the European cave bear. Oecologia. 116:177–181.
- Peigné S, Merceron G. 2017. Palaeoecology of cave bears as evidenced by dental wear analysis: a review of methods and recent findings. Hist Biol. 31:1–13.
- Peigné S, Goillot C, Germonpré M, Blondel C, Bignon O, Merceron G. 2009a. Predormancy omnivory in European cave bears evidenced by a dental microwear analysis of *Ursus spelaeus* from Goyet, Belgium. P Natl Acad Sci. 106:15390-15393.
- Peigné S, Goillot C, Germonpré M, Blondel C, Bignon O, Merceron G. 2009b. Reply to Bocherens: Dental microwear and stable isotopes on bone collagen are complementary to sort out cave bear diets. P Natl Acad Sci. 106:E134-E134.
- Pérez-Ramos A, Kornelius K, Van Heteren AH, Rabeder G, Grandal-D'Anglade A, Pastor FJ, Serrano FJ, Figueirido B. 2019. A three-dimensional analysis of tooth-root morphology in living bears and implications for feeding behaviour in the extinct cave bear. Hist Biol. 31:461-473
- Pineda-Munoz S, Lazagabaster IA, Alroy J, Evans AR. 2017. Inferring diet from dental morphology in terrestrial mammals. Methods Ecol Evol. 8:481-491.
- Pinto-Llona AC, Andrews PJ, Etxebarría F. 2005. Taphonomy and Palaeoecology of Quaternary Bears from Cantabrian Spain. Oviedo: Fundación Oso de Asturias.
- Quilès J, Petrea C, Moldovan O, Zilhão J, Rodrigo R, Rougier H, Trinkaus E. 2006. Cave bears (*Ursus spelaeus*) from the Peştera cu Oase (Banat, Romania): Paleobiology and taphonomy. C R Palevol. 5:927-934.
- Rabal-Garcés R, Cuenca-Beccós G, Ignacio Canudo J, De Torres T. 2012. Was the European cave bear an occasional scavenger? Lethaia. 45:96-108.
- Richards MP, Pacher M, Stiller M, Quilès J, Hofreiter M, Constantin S, Trinkaus E. 2008. Isotopic evidence for omnivory among European cave bears: Late

Pleistocene *Ursus spelaeus* from the Peştera cu Oase, Romania. Proc Natl Acad Sci. 105:600-604.

- Robu M, Wynn JG, Mirea IC, Petculescu A, Kenesz M, Puşcaş CM, Trinkaus E, Constantin S, O'Regan H. 2018. The diverse dietary profiles of MIS 3 cave bears from the Romanian Carpathians: insights from stable isotope ($\delta^{13}C$ and $\delta^{15}N$) analysis. Palaeontology. 61:209–219.
- Stiller M, Molak M, Prost S, Rabeder G, Baryshnikov G, Rosendahl W, Germonpré M. 2014. Mitochondrial DNA diversity and evolution of the Pleistocene cave bear complex. Quatern Int. 339:224-231.
- Stiller M, Baryshnikov G, Bocherens H, Grandal d'Anglade A, Hilpert B, Münzel SC, Hofreiter M. 2010. Withering away—25,000 years of genetic decline preceded cave bear extinction. Mol Biol Evol. 27:975-978.
- Taylor ME, Hannam AG. 1987. Tooth microwear and diet in the African Viverridae. Can J Zool. 65:1696-1702.
- Terlato G, Bocherens H, Romandini M, Nannini N, Hobson KA, Peresani M. 2018. Chronological and Isotopic data support a revision for the timing of cave bear extinction in Mediterranean Europe. Hist Biol. 31:474-484
- Torres JT, Amador IQ, Nogueroles EG, Mansilla Izquierdo H, Martinez Diaz C. 1978. Estudio comparativo de las mandíbulas de *Ursus spelaeus*, Rosemmuller-Heinrooth (sic)-*Ursus deningeri*, Von Reichenau y *Ursus arctos*, Linneo. Boletín Geológico y Minero. LXXXIX(III):203–222.
- Ulhaas L, Kullmer O, Schrenk F, Henke W. 2004. A new 3-d approach to determine functional morphology of cercopithecoid molars. Ann Anat. 186:487-493.
- Ungar PS, Bunn JM. 2008. Primate dental topographic analysis and functional morphology. Technique and application in dental anthropology. 53-253.
- Ungar P, Williamso M. 2000. Exploring the effects of tooth wear on functional morphology: a preliminary study using dental topographic analysis. Paleontol Electr. 3:1-18.
- Van Heteren AH, MacLarnon A, Rae TC, Soligo C. 2009. Cave bears and their closest living relatives: a 3D geometric morphometrical approach to the

functional morphology of the cave bear *Ursus spelaeus*. Slovenský Kras Acta Carsologica Slovaca. 47(supplement1):33–46.

- Van Heteren AH, Figueirido B. 2019. Diet reconstruction in cave bears from craniodental morphology: past evidences, new results and future directions. Hist Biol. 31:500-509.
- Vila Taboada M, Fernández Mosquera D, López González F, Grandal D'Anglade A, Vidal Romaní JR. 1999. Paleoecological implications inferred from stable isotopic signatures (d13C. d15N) in bone collagen of *Ursus spelaeus* ROS.-HEIN. Cadernos do Laboratori Xeolxic de Lax. 24:73–87
- Vizcaíno SF, Bargo MS, Cassini GH. 2006. Dental occlusal surface area in relation to body mass, food habits and other biological features in fossil xenarthrans. Ameghiniana. 43(1):11-26.
- Wegst UGK, Ashby MF. 2004. The mechanical efficiency of natural materials. Philos Mag. 84(21):2167-2186.
- Wilson GP, Evans AR, Corfe IJ, Smits PD, Fortelius M, Jernvall J. 2012. Adaptive radiation of multituberculates before the extinction of dinosaurs. Nature. 483:457–460.
- Winchester JM, Boyer DM, St Clair EM, Gosselin-Ildari AD, Cooke SB, Ledogar J.A. 2014. Dental topography of platyrrhines and prosimians: convergence and contrasts. Am J Physical Anthropol. 153:29–44.
- Winchester JM. 2016. MorphoTester: an open source application for morphological topographic analysis. PLoS ONE. 11:e0147649.
- Winchester JM, Boyer DM, St. Clair EM, Gosselin-Ildari AD, Cooke SB, Ledogar JA. 2014. Dental topography of platyrrhines and prosimians: convergence and contrasts. Am J Phys Anthropol. 153(1):29-44.

3.2.8. Supplementary material

Table S1. Specimens used in this study.

Mus. nº	*Species*
89029	*A. melanoleuca*
89030	*A. melanoleuca*
110451	*A. melanoleuca*
110452	*A. melanoleuca*
147745	*A. melanoleuca*
89028	*A. melanoleuca*
89854	*H. malayanus*
17531	*H. malayanus*
17532	*H. malayanus*
2439	*H. malayanus*
17245	*H. malayanus*
28472	*H. malayanus*
A5351	*H. malayanus*
60772	*H. malayanus*
28254	*H. malayanus*
103987	*H. malayanus*
19155	*H. malayanus*
46074	*M. ursinus*
56748	*M. ursinus*
90388	*M. ursinus*
44143	*M. ursinus*
35898	*M. ursinus*
99308	*M. ursinus*
16186	*M. ursinus*
217682	*M. ursinus*
6121	*T. ornatus*
1661	*T. ornatus*
99308	*T. ornatus*
217682	*T. ornatus*

149302	*T. ornatus*
174256	*T. ornatus*
16186	*T. ornatus*
2245	*U. americanus*
3561	*U. americanus*
6704	*U. americanus*
16705	*U. americanus*
16706	*U. americanus*
16707	*U. americanus*
41327	*U. americanus*
1280	*U. arctos arctos*
3034	*U. arctos arctos*
3632	*U. arctos arctos*
212872	*U. arctos arctos*
21809	*U. arctos gyas*
194567	*U. arctos horribilis*
1951107	*U. arctos horribilis*
19765	*U. arctos middendorffi*
113701	*U. arctos pruinosus*
165798	*U. arctos sitkensis*
165798	*U. arctos sitkensis*
163825	*U. arctos sitkensis*
19259	*U. maritimus*
15709	*U. maritimus*
14883	*U. maritimus*
15687	*U. maritimus*
1893341	*U. maritimus*
11051	*U. maritimus*
15686	*U. maritimus*
42080	*U. maritimus*
14888	*U. maritimus*
WGTDe	*U. maritimus*
1951101	*U. maritimus*
11089	*U. thibetanus*
3247	*U. thibetanus*
2446	*U. thibetanus*

114544	*U. thibetanus*
87411	*U. thibetanus*
57076	*U. thibetanus*
119476	*U. thibetanus*
45293	*U. thibetanus*
19511013	*U. thibetanus*
110457	*U. thibetanus*
45	*U. ingressus*
21	*U. ingressus*
Mix3	*U. ingressus*
Mix3	*U. ingressus*
22UVIP	*U. ingressus*
Gs524	*U. ingressus*
5022	*U. ingressus*
5022	*U. ingressus*
2029NNB	*U. sp. spelaeus*
2029NNB	*U. sp. spelaeus*
5017MNB	*U. sp. spelaeus*
5017MNB	*U. sp. spelaeus*
5019	*U. sp. spelaeus*
BC4(02)	*U. sp. ladinicus*
CV704	*U. sp. ladinicus*
CV703	*U. sp. ladinicus*
714	*U. sp. ladinicus*
SW483	*U. sp. eremus*
SW630C	*U. sp. eremus*
Sw512	*U. sp. eremus*
Sw512	*U. sp. eremus*
2724	*U. sp. eremus*

Table S2. Raw values for the OPCR, DNE, RFI, and OA (outline areas) obtained for the upper P4-M2 dental series in living and extinct bears analysed in **chapter 3.2.**

Species	DNE	RFI	OPCR	OA
A. melanoleuca	893.506	1.569	344.625	1567.923
A. melanoleuca	1168.242	1.729	350.75	1488.595
A. melanoleuca	1152.285	1.752	355.625	1635.781
A. melanoleuca	1095.186	1.671	349.25	1556.732
A. melanoleuca	1454.857	1.873	379.375	1686.206
A. melanoleuca	963.965	1.57	345.25	1674.489
H. malayanus	499.952	2.119	143.25	419.742
H. malayanus	440.948	1.849	164.25	425.337
H. malayanus	459.946	1.816	168.5	414.587
H. malayanus	282.055	1.617	122.625	362.908
H. malayanus	541.504	1.865	194.75	397.385
H. malayanus	495.998	1.814	178.125	528.36
H. malayanus	572.041	1.905	166	546.824
H. malayanus	442.847	1.783	151.75	524.851
H. malayanus	544.304	1.943	173.5	368.97
H. malayanus	527.912	1.857	165.125	440.106
H. malayanus	492.871	1.92	181.125	411.974
M. ursinus	452.962	1.891	166.375	426.614
M. ursinus	365.284	1.88	140.25	406.088
M. ursinus	493.198	1.9	161.875	387.238
M. ursinus	348.613	1.59	171.375	421.445
M. ursinus	353.074	1.657	149.125	391.297
M. ursinus	453.654	1.661	207.375	538.56
M. ursinus	369.05	1.473	203.625	543.636
M. ursinus	438.853	1.705	177	523.315
T. ornatus	349.797	1.643	164.5	553.379
T. ornatus	320.408	1.711	143.25	512.899
T. ornatus	398.128	1.916	170.25	542.132
T. ornatus	372.898	1.694	155.625	524.728
T. ornatus	355.237	1.694	166.125	450.782
T. ornatus	404.063	1.786	175.5	483.717
T. ornatus	302.692	1.575	158.875	564.48

U. americanus	296.279	1.587	147.625	598.882
U. americanus	332.701	1.612	127.375	566.663
U. americanus	324.374	1.672	122.375	629.059
U. americanus	376.413	1.69	165.5	551.806
U. americanus	355.856	1.788	143.625	561.889
U. americanus	354.388	1.748	152.5	525.977
U. americanus	512.056	1.809	211.25	1043.81
U. arctos arctos	599.809	1.976	213.25	826.048
U. arctos arctos	483.592	1.898	173.75	716.965
U. arctos arctos	446.221	1.744	194.875	1052.714
U. arctos arctos	704.158	1.92	271.125	1219.741
U. arctos gyas	750.856	1.928	237	1029.254
U. arctos horribilis	623.729	1.821	220.125	1183.294
U. arctos horribilis	540.103	1.745	197.875	782.314
U. arctos middendorffi	616.546	1.897	219.75	1152.751
U. arctos pruinosus	673.609	1.843	267.625	1263.021
U. arctos sitkensis	658.831	1.951	221	974.958
U. arctos sitkensis	521.841	1.639	214.25	794.663
U. arctos sitkensis	547.93	1.813	221	679.915
U. maritimus	553.399	1.929	167.625	589.962
U. maritimus	565.582	2.034	187.875	581.604
U. maritimus	501.484	1.785	198.125	766.406
U. maritimus	549.21	1.855	197.375	682.78
U. maritimus	555.318	1.799	202.5	665.831
U. maritimus	476.227	2.05	159.625	582.276
U. maritimus	464.717	1.801	181.25	581.869
U. maritimus	481.091	1.807	191.375	577.246
U. maritimus	533.546	1.946	189.875	569.221
U. maritimus	476.541	1.833	176.625	646.043
U. maritimus	566.951	1.853	196.875	681.614
U. thibetanus	459.865	1.738	177	626.558
U. thibetanus	392.14	1.701	156.625	542.919
U. thibetanus	555.185	1.858	179.75	676.013
U. thibetanus	510.966	1.58	200.25	692.293
U. thibetanus	517.199	1.632	181.875	546.001
U. thibetanus	428.946	1.46	193.125	681.39

U. thibetanus	504.491	1.777	179.75	646.769
U. thibetanus	602.024	1.71	216.125	655.377
U. thibetanus	544.523	1.629	240.5	745.283
U. thibetanus	430.443	1.582	197.5	660.215
U. ingressus	505.197	1.628	254.25	1466.478
U. ingressus	729.719	1.708	268.875	1773.018
U. ingressus	771.62	1.626	337.125	1479.376
U. ingressus	832.462	1.867	326.625	1533.575
U. ingressus	684.83	1.718	278.875	1939.158
U. ingressus	665.709	1.609	277	1587.788
U. ingressus	675.464	1.756	280.5	1479.771
U. ingressus	727.752	1.727	295.75	1520.264
U. sp. spelaeus	825.135	1.846	304	1343.03
U. sp. spelaeus	1054.708	2.189	305.375	1269.45
U. sp. spelaeus	840.101	1.887	314.5	1400.504
U. sp. spelaeus	884.659	1.887	309.75	1454.197
U. sp. spelaeus	717.024	1.847	297.5	1518.591
U. sp. ladinicus	896.005	1.713	336.625	1365.888
U. sp. ladinicus	887.952	1.836	348.875	1574.859
U. sp. ladinicus	790.12	1.763	323.625	1644.853
U. sp. ladinicus	843.686	1.868	303.125	1563.973
U. sp. eremus	822.369	1.776	299.125	1606.266
U. sp. eremus	655.692	1.702	296.375	1389.706
U. sp. eremus	613.15	1.71	252.625	1682.039
U. sp. eremus	682.87	1.801	271.5	1670.071
U. sp. eremus	868.305	2.727	222.125	1151.895

3

3.3. Biomechanical simulations reveal a trade-off between adaptation to glacial climate and dietary niche versatility in European cave bears

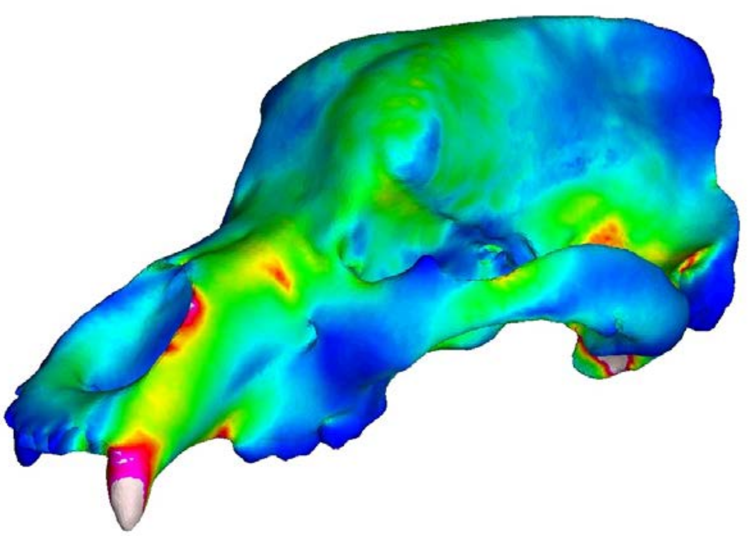

3.3. Biomechanical simulations reveal a trade-off between adaptation to glacial climate and dietary niche versatility in European cave bears

3.3.1. Abstract

The cave bear is one of the best known extinct large mammals that inhabited Europe during the 'Ice Age', becoming extinct ≈24,000 years ago along with other members of the Pleistocene megafauna. Long-standing hypotheses speculate that many cave bears died during their long hibernation periods, which were necessary to overcome the severe and prolonged winters of the Last Glacial. Here, we investigate how long hibernation periods in cave bears would have directly impacted their feeding biomechanics, using CT-based biomechanical simulations of skulls of cave and extant bears. Our results demonstrate that although large paranasal sinuses were necessary for, and consistent with, long hibernation periods, trade-offs in sinus-associated cranial biomechanical traits restricted cave bears to feed exclusively on low-energetic vegetal resources during the predormancy period. This biomechanical trade-off constitutes a new key factor to mechanistically explain the demise of this dominant Pleistocene megafaunal species as a direct consequence of climate cooling.

3.3.2. Introduction

The cave bear (*Ursus spelaeus* s.l.) is an extinct species of the Pleistocene megafauna that inhabited Europe during the Last Glacial Period, and it is one of the best known extinct species that lived alongside prehistoric humans. A long-standing hypothesis suggests that cave bears were more dependent on caves than their closest relative, the living brown bear (*Ursus arctos*) (e.g., Kurtén 1976). Indeed, a recent analysis of mitochondrial DNA revealed that cave bears had extreme fidelity to their birth sites and they formed stable maternal social groups for the purpose of hibernation, returning to the same cave every winter (Fortes et al. 2016). Furthermore, cave bears had longer hibernation periods than other living bears in order to overcome the long and cold winters of the Last Glacial (e.g., Pérez-Rama et al. 2011). Their high dependency on cave shelters explains why Late Pleistocene caves of Europe have yielded a huge number of fossil remains of bears that likely died during hibernation, the accumulation of these fossils occurring over periods of hundreds or even thousands of years (Kurtén1976; Pacher and Stuart 2009). Although mortality causes for the older individuals is usually attributed to either accidents, illness, or a lack of sufficient fat storage to endure winter hibernation (e.g., Grandal-D'Anglade et al. 2019), it has also been proposed that humans competed for cave environment with cave bear. Archaeological records show cut marks in cave bear remains from several sites attributed to human processing of bear bones (e.g., Münzel et al. 2011). Based on this evidence, competition for resources, or direct hunting by *Homo* in Europe are among the prevailing hypotheses to explain a human-driven cave bear decline (e.g., Münzel et al. 2004).

Climate cooling has also been considered as a major factor to explain the demise of the cave bear during the coldest phase of the Last Glacial (Baca et al. 2016). Biogeochemical studies of bone collagen suggest that cave bears were adapted to feed exclusively on vegetal resources from 100,000 to 20,000 years ago (Bocherens 2019), and there is no evidence of a dietary shift towards omnivory at a time of lowered vegetation productivity as a consequence of climate cooling during the beginning of the Last Glacial Maximum (Terlatto et al. 2019). This lack of dietary flexibility may have been a critical factor in the decline of the last populations of cave bears (Bocherens 2019), intensified by human competition for cave space (Stiller et al. 2010), with these factors compounding to cause the final extinction of the species at the beginning of the Last Glacial Maximum (~ 24,000 years ago).

Here we investigate if cave bears were biomechanically restricted to feed exclusively on vegetal resources using three-dimensional computer simulations of different feeding scenarios computed from CT-scanned skulls of the extinct cave bears. As the sinuses play a key role in the control of hibernation (Lundberg 2008; Petruson et al. 2005; Yan et al. 2017), we specifically address the impact of large sinuses in cave bear feeding biomechanics by comparing skull models with sinuses and with artificially-removed sinuses. Our results demonstrate that the characteristic large sinuses of cave bears restricted them biomechanically to feed exclusively on low-energetic vegetal resources. We hypothesize that, although the retention of large sinuses in cave bears was key to overcome the long and severe winters of the Last Glacial in hibernation, this biomechanical constraint must certainly have played a key role in the extinction of this enigmatic species of the Pleistocene megafauna.

3.3.3. Materials and Methods

3.3.3.1.Materials

Twelve skulls of living and extinct bears were CT-scanned from different museums (**Table 1**). Of them, eight skulls belong to living bears (*Ursus arctos*, *Ursus maritimus*, *Ursus americanus*, *Ursus thibetanus*, *Melursus ursinus*, *Helarctos malayanus*, *Tremarctos ornatus* and *Ailuropoda melanoleuca*) and four belong to different extinct Pleistocene species/subspecies of the cave bear complex (*Ursus spelaeus* sensu lato): *U. spelaeus spelaeus*, *U. spelaeus ladinicus*, *U. spelaeus eremus*, and *U. ingressus* (**Table 1**).

The specimens of *Ursus thibetanus*, *Ailuropoda melanoleuca* and *Tremarctos ornatus* are housed at the osteological collections of the University of Valladolid (Spain). The CT scanner used for these skulls is a CT medical scanner of model Aquilion 32 TOSHIBA with 32 multislicer at University Hospital of Valladolid. The conditions of acquisition in the CTscan were a 512x512 image matrix. 120 Kv and 250 mA. For each specimen the following CT data was obtained. For *U. thibetanus* the voxel size is 0.4680 (X.Y) and 0.3 mm of inter-slice (Z). For the first specimen were obtained 1114 slices and for of second 1127 slices. The voxel size for *T. ornatus* was 0.3819 (X.Y) and 0.5 mm of inter-slices (Z) and the voxel size for *Ailuropoda melanoleuca* were 0.5200 (X.Y) and 0.3 mm of inter-slices (Z).

Furthermore, the CTs of *Ursus arctos*, *Ursus maritimus* and *U. americanus* were obtained from the Digimorph website (http://www.digimorph.org). The scans were performed at the University of Texas High-Resolution X-ray CT Facility with either a 1024X1024 image matrix, resulting in inter-slice spacing in the range 0.70–1 mm.

The conditions of acquisition in the CT scanning for *Ursus arctos* were 450 kV, 3 mA, obtaining 425 slices. For *Ursus maritimus* was 420kV, 1.8 mA, obtaining 540 slices. The CT of *Ursus americanus* (USNM 227070) were performed with either a 1024X1024 image matrix, pixel slice is 0.325 mm thick and each pixel size (x) and (y) were 0,2930 mm with an interslice spacing of 0.325 mm in (z) with a field of reconstruction of 300 mm. The conditions of acquisition in the CT scanning were P250D, 450 kV and 1.3 mA; obtaining 475 slices.

The CT of *Ursus spelaeus ladinicus* (PIUW-CU 703) was scanned at the University of Vienne using a microCT machine Viscom X8060. The conditions of acquisition were 130kV and 330 microA, obtaining 2732 slices and voxel size

0.15mm in X, Y, Z axes. The CT of *Ursus spelaeus eremus* (PIUW-SW 483) and *Ursus ingressus* were CT scanned at the private medical center of the city of Málaga (Spain), using GE Medical Systems (Brivo CT385 Series) scanner machine. The conditions of acquisition were 512x512 image matrix, 120Kv and 160 mA, with an interslice of 0.2mm. For *Ursus spelaeus eremus*, we obtained 2573 slices with a voxel size of 0.5332 for (X, Y) and 0.2 (Z). For *Ursus ingressus*, we obtained 2601 slices with a voxel size of 0.6113 for (X. Y) and 0.2 (Z).

Table 1. Sample used in this study. The species, museum numbers, and abbreviations are also given.

Species	Abbreviations	Museum Number
Ursus arctos	Uar	USNM 82003
Ursus americanus	Uam	USNM 227070
Ursus maritimus	Uma	H. 001-05
Ailuropoda melanoleuca	Ame	VU 3156b
Ursus thibetanus	Uth	VU 2421
Tremarctos ornatus	Tor	VU 1661
Melursus ursinus	Mur	AMNH54464
Helarctos malayanus	Hml	AMNH28254
Ursus spelaeus ladinicus	Ulad	PIUW-CU 703
Ursus spelaeus eremus	Uere	PIUW-SW 483
Ursus spelaeus spelaeus	Uspe	E-ZYX-S-1000
Ursus ingressus	Uing	PIUW3000/5/105

The CT of *Ursus spelaeus spelaeus* (E-ZYX-1000) was CT scanned at a veterinarian Hostpital Rof Codina, Lugo. Spain. The conditions of acquisition were 512x512 image matrix, 120Kv and 160 mA, with an interslice of 0.365mm. For this specimen we obtained 1386 slices with a voxel size of 0.75 for (X, Y) and 0.3650 (Z).

3.3.3.2. Three-dimensional processing

The stacks from the CTs were exported as 16 bit images in TIFF or DICOM format. We calibrated these images to eliminate the background noises due to Photoelectric and Compton effects by selecting specific ranges of the histograms (Region of interest ROI) using the software ImageJ v.1.50e (http://rsbweb.nih.gov/ij/). Once the background noise was removed, all images were converted to 8 bits and normalized to 0.5% of grey values to standardize the grey values of the histogram to 0 and 255, respectively. The standardized images stacks in TIFF formats were imported into Avizo Lite 9.2.

The cortical bone was segmented with a range of the histogram in the thresholding of 70-255. The trabecular bone was segmented within a range of 40-70. For the teeth, the dental pulp was segmented together with the enamel and dentine. To generate the triangulated surface models, we used the constrained smoothing algorithm (kernel size of 4).

The 3D models of each specimen were imported into Geomagic Wrap (3D Systems, USA); where this 3D models were decimated to ~200,000 triangular elements in a sequence of successive steps, fix boundaries always active, with constrained maximum edge-length ratio of 10, and edge-edge ratio of 10 on all triangles (medium priority level of curvature and mesh). These conditions are for a correct topology and shape stability mesh. In this decimated process, we never used more than twice the "quick smooth" tool, only in the first step and when of the 3D models have about 1,000,000 triangular elements. Afterwards, we used the mesh doctor function to check the errors of the mesh (non-manifold edges, self-intersections, etc). The cavities representing broken areas or osteological regions not captured during the CT scanning were manually patched using the “fill holes” function or "defeature" function. Some lost parts –e.g., the teeth or little parts of the skull– were reconstructed with the "mirror" function. Any remaining trabecular regions were removed during subsequent decimation; so all models represent cortical bone models only and natural cavities and holes. In **Chapter 2.4** and **2.5**, this steps and processes described are detailed.

3.3.3.3.Finite Element Analysis of the skull with sinuses

The CT stacks were processed to obtain meshes of the 3D models that were imported into Strand7 Release 2.4.6 (Strand7 Pty Ltd, Sydney, Australia). We removed the duplicated nodes of the meshes, and we converted into coarse, medium, and fine resolution solid meshes following Tseng and Flynn (2018). The centroids of each muscular insertion and the subsequent vectors forces, essential for the biomechanical calculations, were calculated using BONELOAD (Grosse et al. 2007) from 3D mandibular models (**Fig. 1B,C**).

We calculated the insertion surface areas in the skull of masticatory muscles (temporalis, masseter, and medial pterygoid groups; **Fig. 1B,D**) using Strand7 Release 2.4.6 (Strand7 Pty Ltd, Sydney, Australia). These surface areas (**Fig. 1B,D**) were delimited using bony rugosities and comparative anatomical studies. To calculate the input muscle force we followed the dry skull method (Thomason 1991). The muscle forces were adjusted to reflect differential activation between the working (biting) and balancing side, with the balancing side muscle forces adjusted to 60% of maximum forces estimated for the working side. Finally, the centroids of the attachment areas of masticatory muscles in the mandible plus the muscle attachment sites for both the mandible and the skull in the left and right temporalis, masseter, and medial-pterygoid group (**Fig. 1**), were imported into the BONELOAD script of the MATLAB software to distribute the calculated muscle forces over the attachment areas using the tangential forces (Grosse et al. 2007).

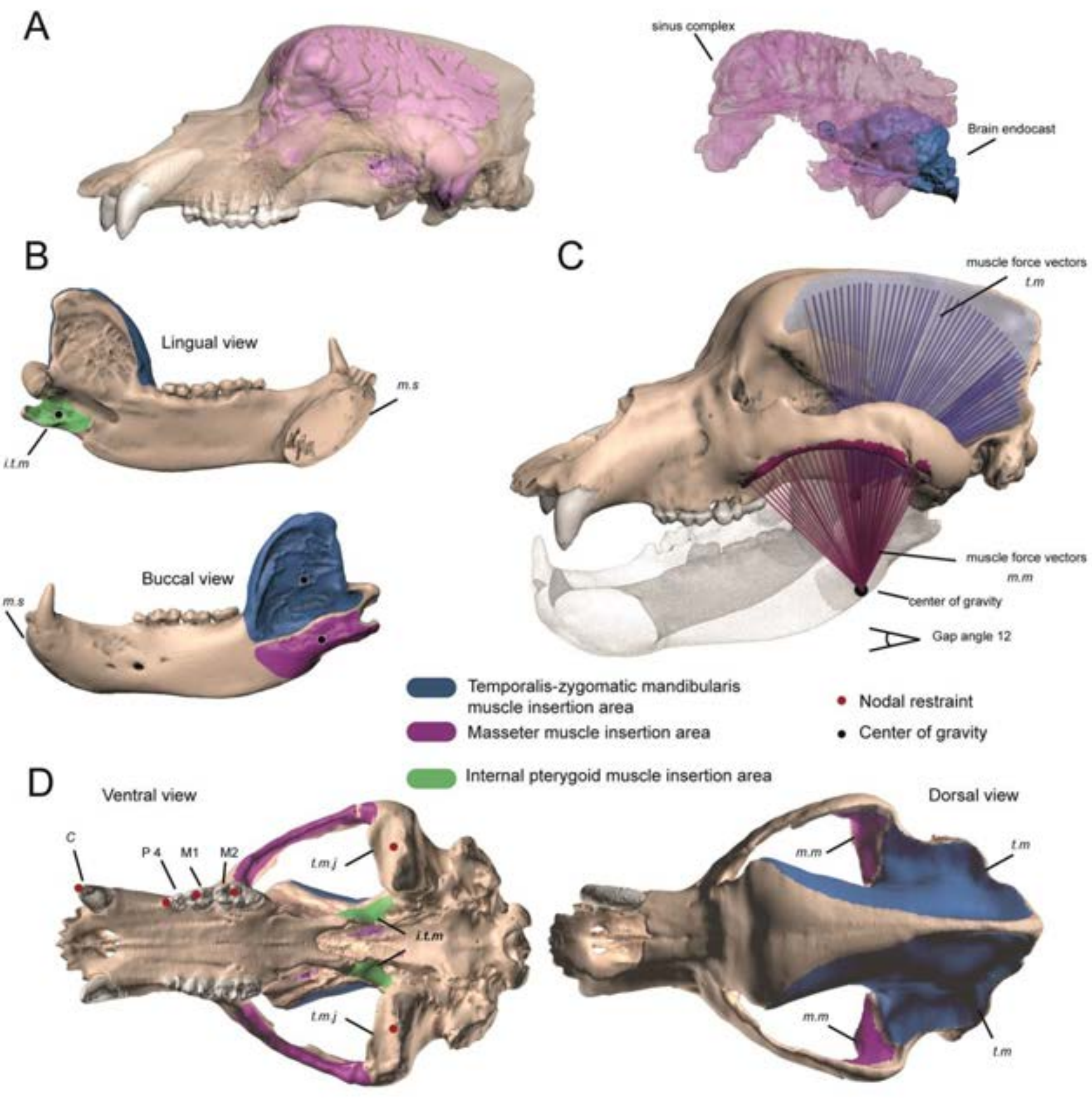

Figure 1. Biomechanical settings for FE analyses represented in *Ursus ingressus*. (A) Model of *U. ingressus* skull showing the disposition of the sinuses in the frontal dome (left) and its topographical relationship with the brain. **(B)** Centers of gravity (black circles) of mandible muscle insertion areas. Centers of gravity represented by black circles. **(C)** Simulation of loading muscle forces used in biomechanical simulations and obtained with the BONELOAD scrip in MATLAB. **(D)** Muscle attachments of the skull used in the biomechanical simulations and the nodals restraint (red points) used for each biting scenario. **Abbreviations**: C, canine; P, premolar; M, molar; i.t.m.: internal pterygoid muscle (green); m.m.: masseter muscle group (dark pink) ; t.m.: temporalis muscle group (dark blue); t.m.j.: temporomandibular joint, and m.s.: mandibular symphysis.

We used three nodal constrains on the three-dimensional models: left and right temporo-mandibular joints (TMJ [center of the condylar process]) plus the unilateral bite point, the latter depending on each simulated scenario: left and right upper canines (C), fourth upper premolar (P4), first upper molar (M1), and second upper molar (**Fig. 1**). The unilateral bite points were placed at the center of the occlusal surface of the tooth, except for the P4, where a single nodal constraint was placed on the top of the tallest cusp (**Fig. 1**). Accordingly, while the nodal constraint of the TMJ on the working side prevents translational movement in all three axes, the constraint of the TMJ on the balancing side allows translation along the axis of the joint. All the biting scenarios models were simulated at a chewing scenario of 12º of gape angle. Moreover, in all the models we used isotropic material properties with Young's Modulus of 18 GPa and a Poisson's Ratio of 0.3 (Dummont et al. 2005).

We measured nodal reaction forces at the nodal constraint of each tooth in the respective biting scenarios, and the values of strain energy (hereafter SE; is a measure of stiffness or structural stability) were calculated from all simulations. We also obtained the mechanical efficiency (hereafter ME; i.e., the nodal reaction force divided by the total input muscle force [average of all the forces of each muscle on both the right and left sides]). Following this, we averaged the values of ME and SE of both left and right sides in coarse, medium and high-resolution models for each skull. The total strain energy values for each biting simulation were adjusted to the cranial volume (VA) and total input force (FA) according to the equation of Ref (Dummont et al. 2005). We used the brown bear (*Ursus arctos*) as the adjusted reference because it is the closest living relative of the cave bear and it has a generalist omnivorous diet.

3.3.3.4. Finite Element Analysis of the skull without sinuses

To test if the extremely developed sinuses in the cave bear influences its biomechanical performance for feeding behavior, we eliminated virtually the paranasal sinuses by filling the cavities with artificial bone material using Geomagic (*sensu* Tanner et al. 2008). The sinuses have a potential dual effect on feeding biomechanics for: *(i)* having large empty spaces in the paranasal cavities, and *(ii)* for the appearance of a dome as a consequence of sinus inflation on the frontal area. Therefore, removing the sinuses from 3D models allows us to quantify the effects of: *(i)* having large empty spaces plus skull geometry together (the appearance of a frontal dome), and *(ii)* the frontal dome on skull geometry.

We considered as paranasal sinuses the nasomaxillary, ethmoid, frontal, and sphenoid sinuses. **Figure S5**. We excluded the maxillary sinuses because they are not included within the frontal dome. This terminology is related to the bone from which the cavity is generated (Moore 1981; Hanken and Hall 1993).

To segment the sinuses the following works are used for the current specimens, Yee et al. 2016; Negus et al. 1954; Joeckel 1998; Alsafy et al. 2013; Bahar et al. 2014; König et al. 2013; the book PALASIATICA 2011; Weeden et al. 2016; Treuting et al. 2017; and Farke 2008. For fossil specimens has been followed Rabeder et al. 2009, 2010.

We calculated in each specimen the volume of the sinuses in order to quantify the degree of the development of the paranasal sinuses in cave bears relative to living bears.

Each model without sinuses was imported into Strand7 and we computed the same process for Finite Element Analysis (FEA) as for the original models (i.e., with paranasal structures –i.e., not filled cavities). We also calculated the ME and SE for each model without sinuses and we compared the effects of having sinuses on feeding biomechanics for each bear species, including living and extinct forms.

In total, our analyses comprised in a total of 1248 simulations, one per each tooth (C, P4, M1, M2) on both sides (left, right) and on models with and without sinuses.

3.3.3.5. Comparing the effects of paranasal sinuses in feeding biomechanics

To compare the effect of the paranasal sinus on skull biomechanics, we divided the mΔSEa values obtained in the biomechanics simulations with sinuses for all feeding scenarios to the mΔSEa values obtained in the simulations without sinuses (hereafter named as index mΔSEa). Accordingly, when this ratio is > 1 means that the biomechanical simulations with sinuses have higher values of mΔSEa than in the biomechanical simulations without sinuses, which indicates that the sinuses have a disadvantageous effect given that the structural integrity of the skull (or stiffness) is lower when having sinuses. In contrast, when this ratio is < 1 this means that the biomechanical simulations with sinuses have lower values of mΔSEa than in the simulations without sinuses. This suggest that the sinuses have an advantageous effect on feeding biomechanics given that the structural integrity of the skull (or stiffness) is higher when having sinuses. Finally, when this ratio is close to 1 indicates that the sinuses have a neutral effect on feeding biomechanics.

To explore the influence of phylogeny on index mΔSEa, we also performed a traitgram with the phytools package of R (Revell 2012). We used the phylogeny published in Pérez-Ramos et al. (2019) which includes all living bear species and cave bears with branch lengths incorporated in million years before present taken from different sources.

We regressed the volume of the sinuses adjusted to the total cranial volume against the difference of SE obtained in both set of analyses (i.e., difference between the SE values obtained from the FE analyses computed on the models with and without sinuses for each skull). We used Ordinary Least Squares (OLS) regression analysis computed with the software PAST version 3.15 (Ø. Hammer).

3.3.4. Results

3.3.4.1. Finite Element Analysis with sinuses

The values of strain energy (SE), a measure of skull stiffness or structural stability, and of mechanical efficiency (ME) obtained using Finite Element Analysis (FEA) from 3D models of skulls of all the species/subspecies of the cave bear complex (*Ursus spelaeus* s.l.) and of all living bear species (**Table 1**), computed for all biting scenarios at a gape angle of 12º (**Fig. 1**) are shown in **Figure 2** and **Tables 2, 3**.

The difference between the values in mechanical efficiency obtained for the canine and second molar (mΔME), as well as the differences between the maximum and minimum values of adjusted strain energy across all teeth simulations (mΔSEa) for each species obtained from models with sinuses are shown in **Table 4**. This informs us on the functional differentiation of the dentition -i.e., higher maximum differences indicate a higher degree of functional differentiation across the tooth row, and therefore, more restrictive diets. In contrast, lower maximum differences indicate a lower degree of functional differentiation across the tooth row, and therefore, more flexible diets (Tseng and Flynn 2018). A bivariate plot of mΔSea against mΔME is shown in **Figure 3A**.

While *A. melanoleuca* has the greatest mΔME (0.27±0.02), indicating a large functional differentiation among teeth, the values for the rest of species range between 0.13 ± 0.02 (for *U. arctos*) and 0.19 ± 0.02 (for *H. malayanus*). The values of mΔSEa among living bears range from values of 0.14 ± 0.03 (for *U. americanus*) and from values of 0.40 ± 0.02 for *A. melanoleuca* (**Fig. 3A**) indicating higher differences in resisting stresses with different teeth.

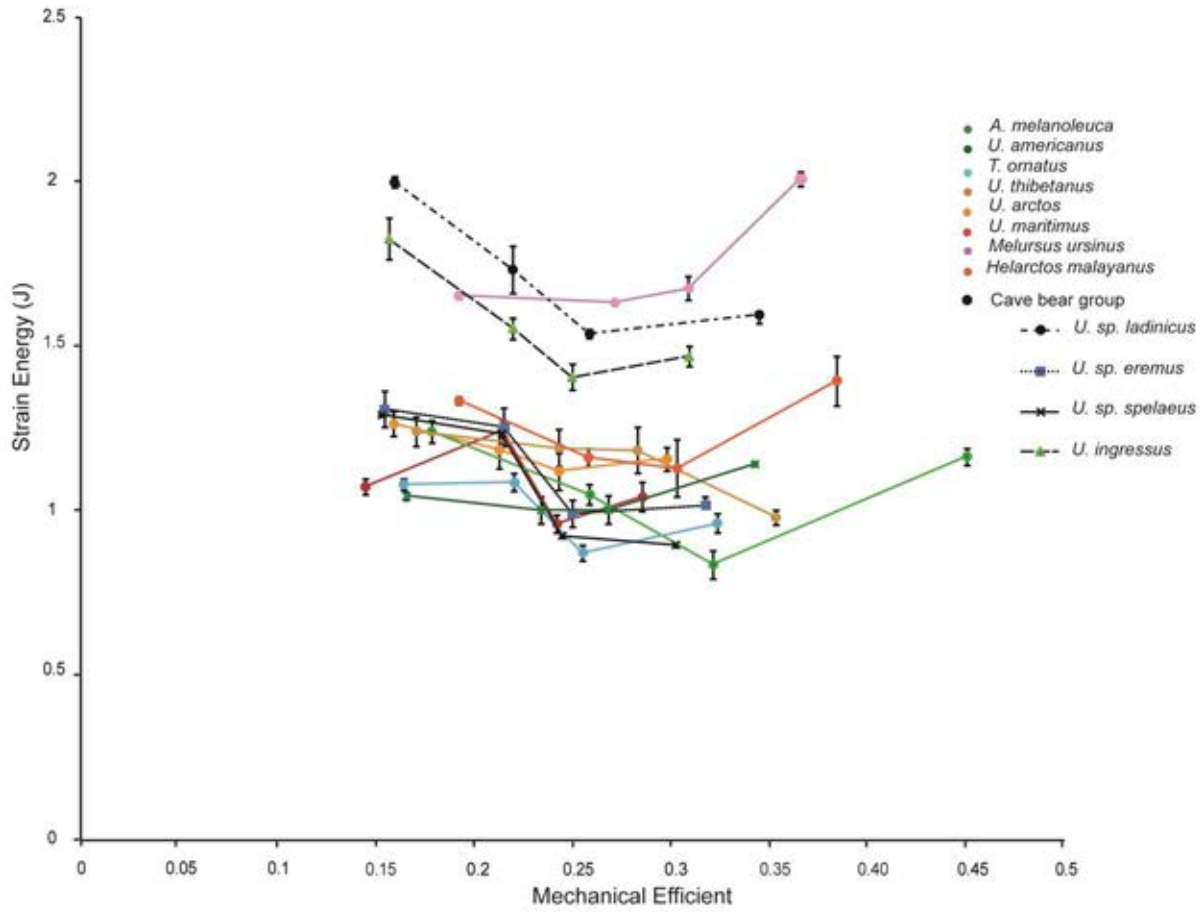

Figure 2. Bivariate plot of the adjusted strain energy (SE) against mechanical efficiency (ME). The SE is adjusted to the volume and forces of a standard model using *Ursus arctos*. The SE value adjusted for each chewing scenario, both for the right and left sides, is averaged. See also **Tables 2,3**.

Cave bears have a range in mΔME from 0.14 ± 0.01 (for *U. sp. spelaeus*) to 0.18 ± 0.01 (for *U. sp. ladinicus*). The values of mΔSEa in cave bears are among the highest of all bears, ranging from 0.46 ± 0.01 (for *U. sp. ladinicus*) to 0.31 ± 0.01 for *U. sp. eremus*, and only comparable to the living *A. melanoleuca* and *M. ursinus* (**Fig. 3A**). This indicates that cave bears have similar values of mechanical advantage to extant bears, but in general they have higher differences in resisting stresses with different teeth.

Table 2. Mean mechanical efficiency (ME) obtained from FEA in the simulations of low, medium, and high-resolution models with sinus analyzed for each species.

Specimens	C Me	P4 Me	M1 Me	M2 Me
U. arctos	0.1589	0.2126	0.2430	0.2981
U. americanus	0.1653	0.2339	0.2684	0.3428
U. maritimus	0.1445	0.2143	0.2420	0.2857
A. melanoleuca	0.1782	0.2588	0.3216	0.4508
U. thibetanus	0.1705	0.2431	0.2830	0.3534
T. ornatus	0.1639	0.2205	0.2552	0.3236
M. ursinus	0.1920	0.2715	0.3091	0.3662
H. malayanus	0.1922	0.2580	0.3032	0.3845
U. sp. ladinicus	0.1592	0.2194	0.2586	0.3450
U. sp. eremus	0.1542	0.2153	0.2499	0.3178
U. sp. spelaeus	0.1653	0.2339	0.2684	0.3428
U. ingressus	0.1529	0.2140	0.2447	0.3025

The von Mises stress distribution across the skulls in all of the living species indicates that the stress is distributed along the frontal region of the skull, from the anterior part of the rostrum to the anterior part of the neurocranium, as well as at the temporomandibular joint. The species with the highest stresses in all feeding scenarios are *M. ursinus* and *U. americanus*. In contrast, the species with the lowest stresses across all scenarios are *A. melanoleuca* and *U. thibetanus* followed by *T. ornatus* and *H. malayanus* (**Fig. 4A**).

Table 3. Mean strain energy (SE) obtained from FEA in the simulations of low, medium, and high-resolution models with sinus analyzed for each species. The 95% confidence intervals (CI) were calculated from the averaged simulation results of low, medium, and high-resolution models analyzed for each species.

Specimens with sinuses	Statistics	C SE	P4 SE	M1 SE	M2 SE
U. arctos	mean	1.2652	1.1856	1.1214	1.1586
	95% CI	0.0384	0.0565	0.0563	0.0366
U. americanus	mean	1.0457	1.0026	1.0040	1.1426
	95% CI	0.0132	0.0398	0.0434	0.0050
U. maritimus	mean	1.0737	1.2439	0.9613	1.0424
	95% CI	0.0242	0.0370	0.0282	0.0441
A. melanoleuca	mean	1.2425	1.0503	0.8378	1.1660
	95% CI	0.0349	0.0311	0.0430	0.0257
U. thibetanus	mean	1.2427	1.1921	1.1847	0.9808
	95% CI	0.0437	0.0566	0.0700	0.0223
T. ornatus	mean	1.0815	1.0868	0.8741	0.9634
	95% CI	0.0175	0.0273	0.0234	0.0295
M. ursinus	mean	1.6538	1.6329	1.6769	2.0084
	95% CI	0.0085	0.0010	0.0367	0.0216
H. malayanus	mean	1.3357	1.1631	1.1300	1.3964
	95% CI	0.0116	0.0282	0.0879	0.0752
Ursus sp. ladinicus	mean	1.9990	1.7335	1.5393	1.5964
	95% CI	0.0172	0.0722	0.0137	0.0277
U. sp. eremus	mean	1.3090	1.2560	0.9926	1.0179
	95% CI	0.0546	0.0574	0.0424	0.0249
U. sp. spelaeus	mean	1.2920	1.2350	0.9251	0.8975
	95% CI	0.0011	0.0188	0.0029	0.0058
U. ingressus	mean	1.8270	1.5551	1.4071	1.4698
	95% CI	0.0628	0.0326	0.0388	0.0315

Table 4. Maximum differences in mechanical efficiency (m∆ME) and adjusted strain energy (m∆SEa) corrected for the input force and volume differences across each tooth loci for each species with sinuses.

Specimens with sinuses	m∆ME	m∆SEa	95%CI SE
U. arctos	0.1392	0.1438	0.0180
U. americanus	0.1775	0.1400	0.0330
U. maritimus	0.1412	0.2827	0.0090
A. melanoleuca	0.2726	0.4048	0.0152
U. thibetanus	0.1829	0.2619	0.0217
T. ornatus	0.1597	0.2127	0.0282
M. ursinus	0.1741	0.3756	0.0226
H. malayanus	0.1924	0.2665	0.0225
U. sp. ladinicus	0.1857	0.4597	0.0143
U. sp. eremus	0.1636	0.3165	0.0128
U. sp. spelaeus	0.1496	0.3945	0.0049
U. ingressus	0.1528	0.4199	0.0272

The patterns of stress distribution in cave bears is similar to the living species – i.e., affecting the frontal region and the temporomandibular joint – but in these taxa, the stress is not distributed continuously from rostrum to neurocranium (**Fig. 4B**). The species with the highest stresses in all scenarios is *U. sp. eremus* and the species with the lowest stresses is *U. sp. spelaeus*.

Moreover, the stresses are significantly higher at the temporomandibular joint in all cave bears than in living bears, with the exception of *H. malayanus* and *U. americanus*. Among cave bears, the taxa with the highest stresses at the temporomandibular joint are *U. sp. ladinicus* and *U. ingressus* and the species with the lowest stresses is *U. sp. eremus*. Moreover, it is noteworthy that all cave bears exhibit less stress on all molar biting scenarios than with the canine and fourth premolar biting scenarios (**Fig. 4B**). This is agreeing with their high values in mΔSEa (**Fig. 3A**).

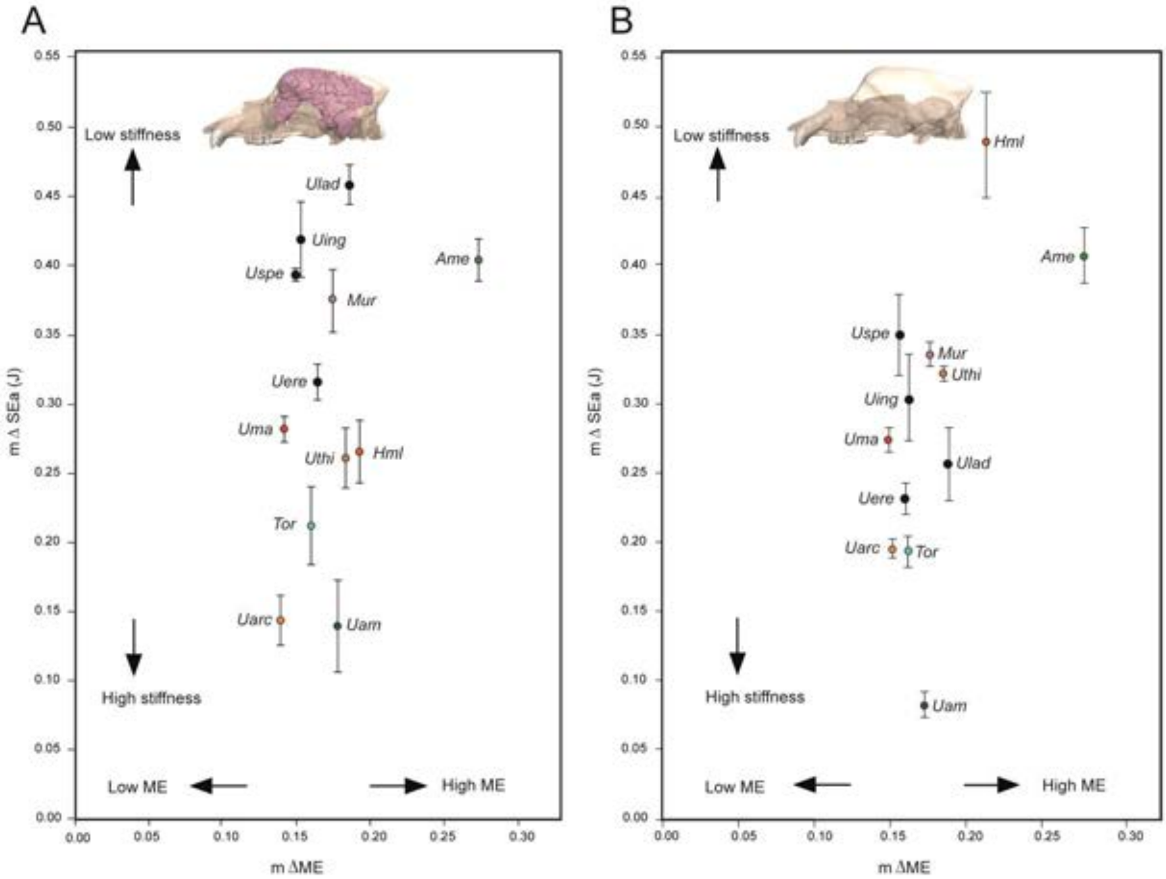

Figure 3. Results of FE analyses. (**A**) Bivariate plot of the maximum differences in mechanical efficiency (mΔME) and strain energy (mΔSEa) across each tooth loci simulations for each species obtained from models with sinuses. (**B**) Bivariate plot the maximum differences in mechanical efficiency (mΔME) and strain energy (mΔSEa) across each tooth loci simulations for each species obtained from models without sinuses. For abbreviations see **Table 1**.

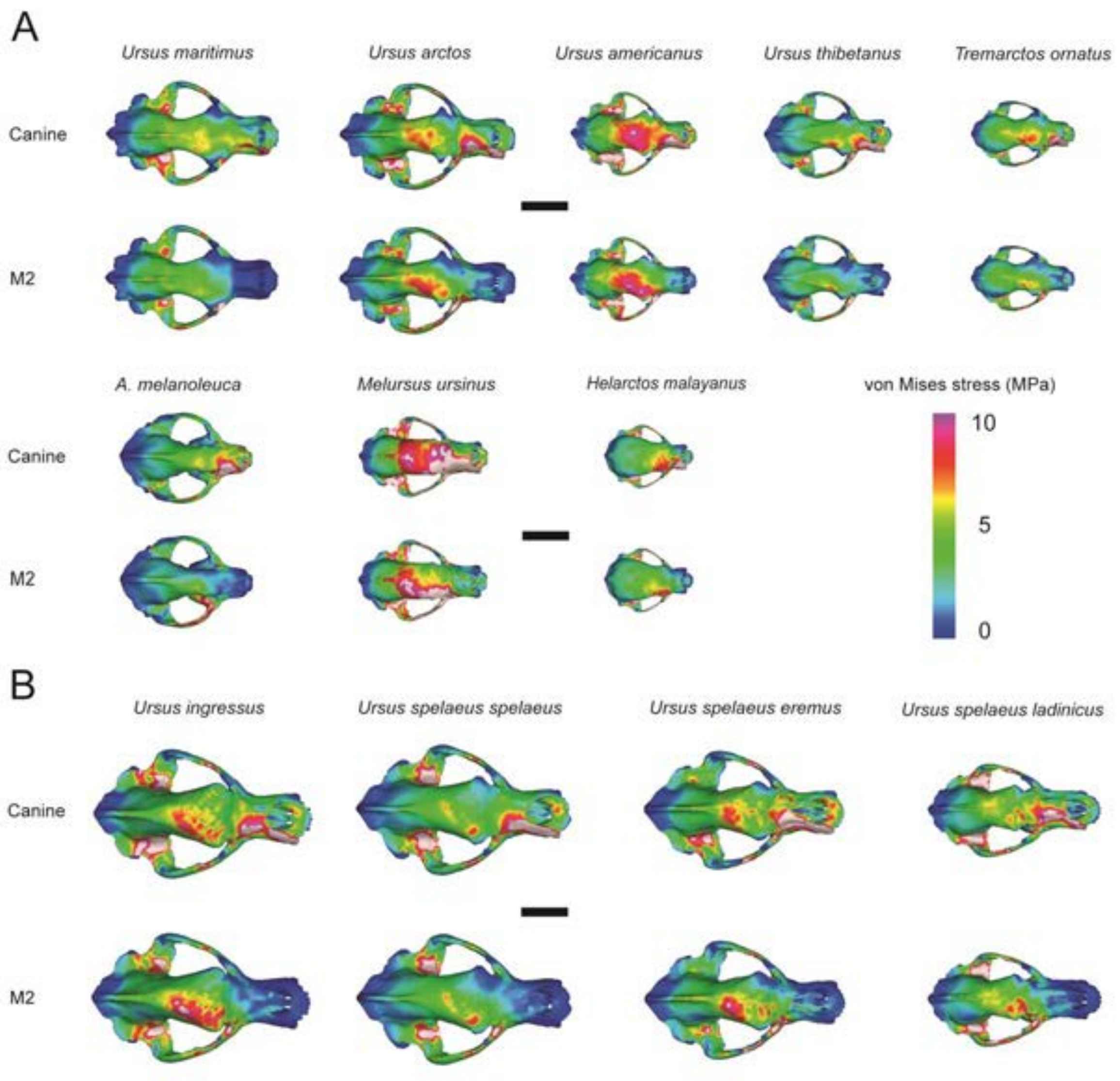

Figure 4. Contour plots of von Mises stress distribution obtained from FE analyses on each cranial model with sinuses. All models are obtained from each biting scenario for the right working side. **(A)** cranial models of living bears; **(B)** cranial models of cave bears. Only two chewing scenarios (canine and second upper molar) are shown for clarity. For the simulations in all the scenarios see **Figures S1-S3**. Scale bar 10cm.

3.3.4.2. Finite Element Analysis without sinuses

The values of strain energy (SE) and of mechanical efficiency (ME) obtained using FEA from 3D models of sinuses infilled computed for all biting scenarios at a gape angle of 12° (**Fig. 1**) are shown in **Table 5, 6**. Removing the sinuses from 3D models allows us to quantify how large sinus cavities (i.e., empty spaces) and the resulting modification of skull geometry (i.e., the appearance of an external frontal dome) influence feeding biomechanics.

Table 5. Mean mechanical efficiency (ME) obtained from FEA in the simulations of low, medium, and high-resolution models with sinus analyzed for each species. The 95% confidence intervals (CI) were calculated from the averaged simulation results of low, medium, and high-resolution models analyzed for each species.

Specimens without sinuses	Statistics	C Me	P4 Me	M1 Me	M2 Me
U. arctos	mean	0.1627	0.2170	0.2485	0.3066
U. americanus	mean	0.1543	0.2183	0.2515	0.3198
U. maritimus	mean	0.1445	0.2143	0.2420	0.2857
A. melanoleuca	mean	0.1782	0.2588	0.3216	0.4508
U. thibetanus	mean	0.1576	0.2261	0.2605	0.3363
T. ornatus	mean	0.1568	0.2146	0.2439	0.3110
M. ursinus	mean	0.1842	0.2614	0.2985	0.3530
H. malayanus	mean	0.1970	0.2658	0.3120	0.4048
U. sp. ladinicus	mean	0.1492	0.2099	0.2436	0.3303
U. sp. eremus	mean	0.1449	0.2027	0.2357	0.2991
U. sp. spelaeus	mean	0.1536	0.2151	0.2457	0.3036
U. ingressus	mean	0.1520	0.2155	0.2421	0.3074

Table 6. Mean strain energy (SE) obtained from FEA in the simulations of low, medium, and high-resolution models with sinus analyzed for each species. The 95% confidence intervals (CI) were calculated from the averaged simulation results of low, medium, and high-resolution models analyzed for each species.

Specimens without sinuses	Statistics	C SE	P4 SE	M1 SE	M2 SE
U. arctos	mean	1.1196	0.9784	0.9258	1.0232
	95% CI	0.0833	0.0808	0.0869	0.0848
U. americanus	mean	1.0015	0.9359	0.9973	1.0169
	95% CI	0.0105	0.0393	0.0576	0.0288
U. maritimus	mean	0.9951	1.1684	0.8951	0.9730
	95% CI	0.0235	0.0358	0.0273	0.0426
A. melanoleuca	mean	1.1923	0.9978	0.7856	1.0812
	95% CI	0.0511	0.0312	0.0396	0.0238
U. thibetanus	mean	1.1370	0.9809	0.8748	0.8165
	95% CI	0.0055	0.0054	0.0058	0.0001
T. ornatus	mean	0.9762	0.9253	0.7852	0.8978
	95% CI	0.0277	0.0233	0.0285	0.0280
M. ursinus	mean	1.4218	1.2702	1.4819	1.6047
	95% CI	0.0107	0.0050	0.0041	0.0140
H. malayanus	mean	1.1644	1.0538	0.9317	1.4205
	95% CI	0.0133	0.0137	0.0041	0.0371
U. sp. ladinicus	mean	1.1357	0.9375	0.8800	1.0359
	95% CI	0.0349	0.0152	0.0260	0.0349
U. sp. eremus	mean	1.0500	1.0492	0.8196	0.8415
	95% CI	0.0568	0.0258	0.0539	0.0631
U. sp. spelaeus	mean	0.9773	0.9693	0.6357	0.6278
	95% CI	0.0736	0.0882	0.0591	0.0502
U. ingressus	mean	1.3046	1.0563	1.0013	1.0812
	95% CI	0.0376	0.0529	0.0289	0.0584

The difference between the values in mechanical efficiency obtained for the canine and second molar (m∆ME), as well as the differences between the maximum and minimum values of adjusted strain energy across all teeth simulations (m∆SEa) for each species obtained from models without sinuses are shown in **Table 7**. The bivariate plot of m∆ME on m∆SEa derived from FEA for all living bears without sinuses are shown in **Figure 3B**. The values of m∆ME for both living and extinct bears do not significantly change from the models with sinuses (**Fig. 3; Tables 5, 7**). However, the values of m∆SEa among living bears range from 0.08± 0.01 for *U. americanus* to 0.48±0.04 for *A. melanoleuca* (**Fig. 3B**). Strikingly, the m∆SEa values for cave bears without sinuses decrease to the level of living bears, which indicates that when sinuses are removed the skull stiffness increases.

Table 7. Maximum differences in mechanical efficiency (m∆ME) and adjusted strain energy (m∆SEa) corrected for the input force and volume differences across the tooth loci of each species without sinuses. See also **Tables S4, S5**.

Specimens without sinuses	m∆ME	m∆SEa	95%CI SE
U. arctos	0.1440	0.1938	0.0068
U. americanus	0.1655	0.0810	0.0093
U. maritimus	0.1412	0.2733	0.0087
A. melanoleuca	0.2726	0.4067	0.0201
U. thibetanus	0.1787	0.3205	0.0056
T. ornatus	0.1542	0.1910	0.0112
M. ursinus	0.1688	0.3345	0.0090
H. malayanus	0.2079	0.4888	0.0406
U. sp. ladinicus	0.1811	0.2557	0.0262
U. sp. eremus	0.1521	0.2303	0.0112
U. sp. spelaeus	0.1500	0.3495	0.0297
U. ingressus	0.1555	0.3033	0.0313

The species that experiences the greatest decrease in mΔSEa values is *U. sp. ladinicus* with a value of 0.25±0.03 followed by *U. ingressus* with a value of 0.30±0.03. Therefore, as the values of mΔSEa are lower, this indicates few differences in SE when biting with different teeth.

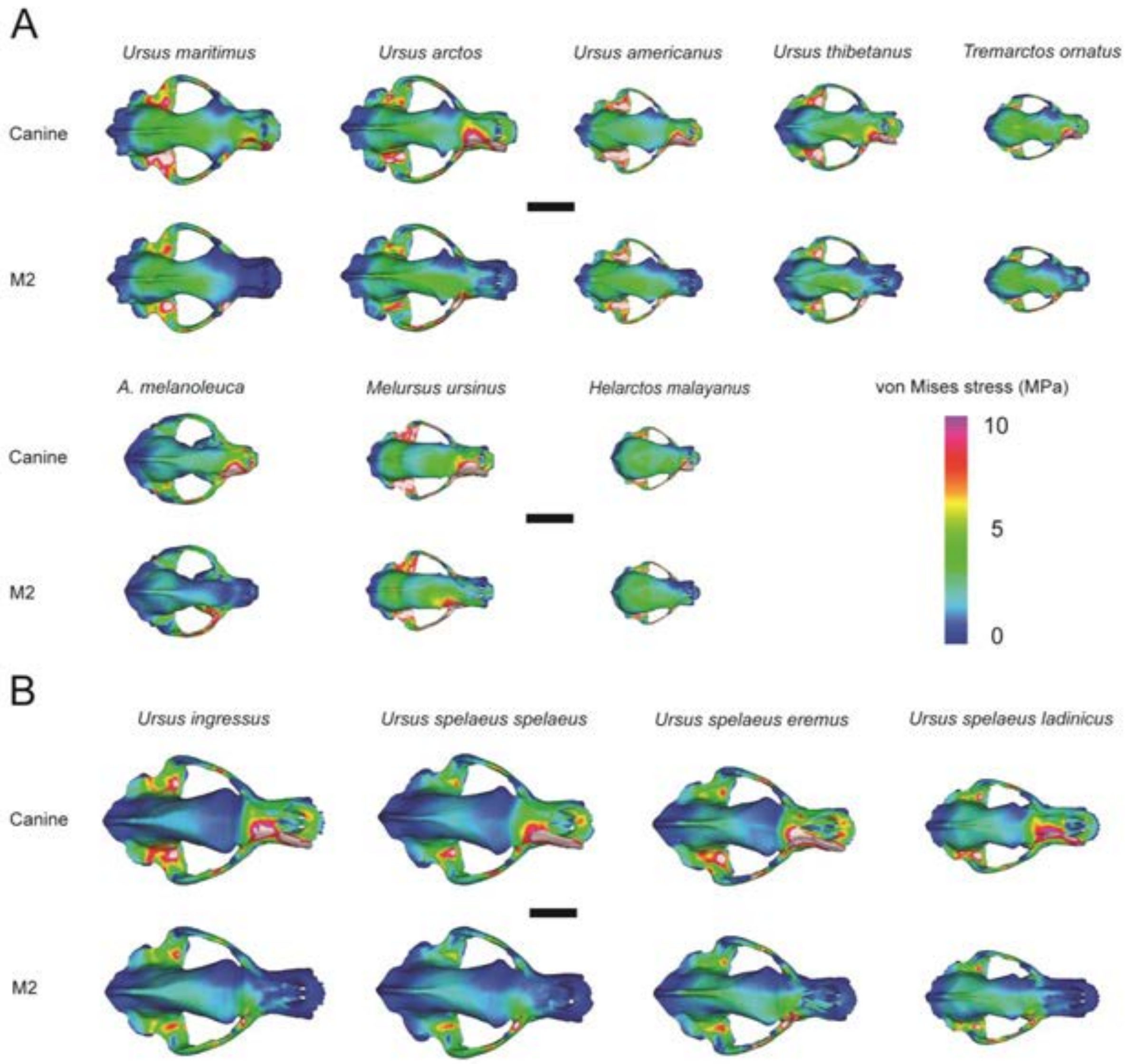

Figure 5. Contour plots of von Mises stress distribution obtained from FE analyses on each cranial model without sinuses. All models are obtained from FE analyses of each chewing scenario for the right working side. **(A)** cranial models of living bears; **(B)** cranial models of cave bears. Only two chewing scenarios (canine and second upper molar) are shown for clarity. For the simulations in all the scenarios see **Figures S1-S3**. Scale bar 10cm.

The von Mises stress distribution across the skulls without sinuses in all living species shown that the stress is not homogeneously distributed, as it is mainly concentrated at the temporo-mandibular joint and at the posterior part of the rostrum (**Fig. 5A**). Among cave bears, as expected for their large sinuses than living bears, the stress distribution is even more localized at the rostrum with a low concentration of stress in the neurocranium but they also experience a lower concentration of stress at the temporomandibular joint compared to living species (**Fig. 5B**). Therefore, the level of von Mises stress obtained when biting from different teeth are more similar than in the models with sinuses (**Fig. 4B**).

3.3.4.3. Comparing FE analyses with and without sinuses

Figure 6A shows the values of mΔSEa obtained by FEA in models with sinuses divided by the values of mΔSEa computed by FEA in models without sinuses (hereafter *i*mΔSEa) for the species sampled in a phylogenetic context. This index informs us on the gains/losses in mΔSEa (or skull stiffness) when sinuses are artificially removed (**Table 8**).

Comparing the values of *i*mΔSEa: (i) *H. malayanus*, *U. arctos* and *U. thibetanus* exhibit values of *i*mΔSEa <1, suggesting that their sinuses increase their skull structural stability; (ii) *T. ornatus*, *U. americanus*, *M. ursinus* and all the cave bears, reach values of *i*mΔSEa > 1, suggesting that their sinuses decrease structural stability of their skull; (iii) *A. melanoleuca*, *U. maritimus* exhibit values of *i*mΔSEa ≈1, demonstrating a neutral effect of their sinuses in maintaining structural stability of their skulls while chewing.

The bivariate regression of the values of *i*mΔSEa against sinuses volume relativized to total skull volume (**Fig. 6B; Table 9**) was significant (r^2= 0.6 *p*-value = 0.04), indicating that the *i*mΔSEa is associated with sinus volume. In those species in which the sinuses increase structural stability (i.e., *i*mΔSEa < 1) their sinus volume does not exceed 25% of total skull volume (**Fig**. **6B**). In contrast, in those species in which the sinuses decrease structural stability (i.e., *i*mΔSEa > 1) their sinus volume exceeds 25% of total skull volume (**Fig. 6B**).

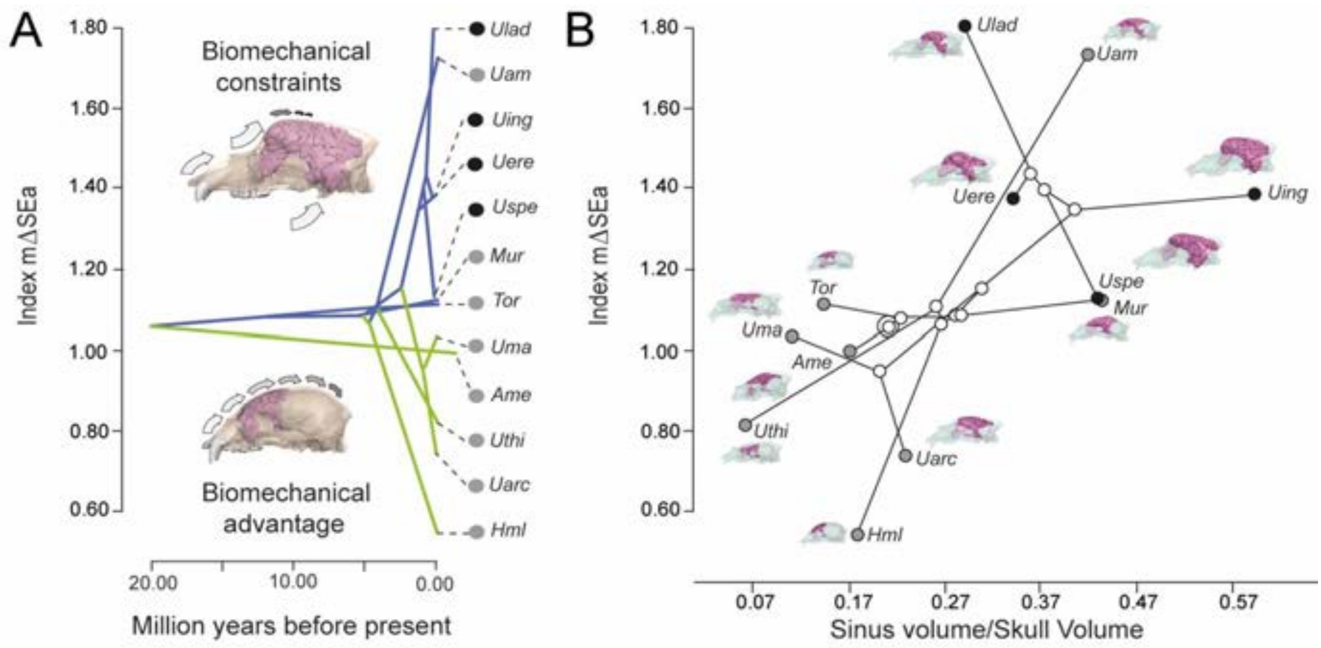

Figure 6. The biomechanical effects of the sinuses. (A) Traitgram of the *i*mΔSEa (see text for details). Green branches represent those species in which the sinuses are advantageous and those in blue those that the sinuses are disadvantageous; **(B)** phylomorphospace of the bivariate plot depicted from the *i*mΔSEa against the relativized sinuses volume to skull volume. In all cases, black circles represent extinct taxa and grey circles living taxa. The virtual models of the sinuses analyzed are indicated in dark pink.

Table 8. Maximum differences in adjusted strain energy (m∆SEa) within sinus and without sinus. Unites SE (Joules). The index of the maximum differences in adjusted strain energy (im∆SEa) results from the division of m∆SEa with sinus by m∆SEa without sinus.

Species	m∆SEa with sinus	m∆SEa without sinus	*i*m∆SEa
U. arctos	0.143783685	0.193827054	0.741814324
U. americanus	0.139959095	0.081019924	1.727465148
U. maritimus	0.282672792	0.273268286	1.034414919
A. melanoleuca	0.404770142	0.406743623	0.995148096
U. thibetanus	0.261923128	0.320493325	0.817249869
T. ornatus	0.212724799	0.191010783	1.11367953
M. ursinus	0.375555192	0.334479037	1.122806366
H. malayanus	0.266466524	0.48882383	0.545117704
U. sp. ladinicus	0.459691829	0.255711971	1.797693816
U. sp. eremus	0.316453519	0.230339684	1.373855835
U. sp. spelaeus	0.394512175	0.349452273	1.128944367
U. ingressus	0.419867578	0.303314443	1.384265035

A visual comparison of the results of the von Mises stress (VM) distribution across the skull in models with sinuses (**Fig. 4**) and without sinuses (**Fig. 5**) indicates that the distribution of the stress with sinuses is more homogeneous than in the models without sinuses in all species. This stress distribution difference is especially extreme in cave bears.

Table 9. Volumes (**mm³**) obtained from solid model in Strand7. The sinus volume (SV) is the result of the difference in cranial volume with sinuses (SKSS) and without sinuses (SKSwS). The percentage of sinuses volume is the result of sinus volume divided by cranial volume multiplied by 100.

Specimens	SKS	SKSwS	SV	V relat. %
U. arctos	1309671.96	1611496.35	301824.40	23.05
U. americanus	435122.62	617483.37	182360.76	41.91
U. maritimus	1469770.11	1635231.90	165461.79	11.26
A. melanoleuca	944352.30	1106359.03	162006.73	17.16
U. thibetanus	785899.85	835312.36	49412.50	6.29
T. ornatus	279704.80	320237.66	40532.87	14.49
M. ursinus	426104.99	611165.89	185060.89	43.43
H. malayanus	242533.61	286170.68	43637.06	17.99
U. sp. ladinicus	1120912.32	1446957.37	326045.04	29.09
U. sp. eremus	1952438.38	2620787.51	668349.14	34.23
U. sp. spelaeus	3050893.64	4360161.68	1309268.04	42.91
U. ingressus	2452029.21	3905046.77	1453017.57	59.26

3.3.4.4. Structural analysis of the Von Mises stress of the skull due to sinus expansion in the *speloid* lineage.

Figures 4 and **5** shows the contour plots of the von Mises stress distribution through the skull of living and extinct bears. This section explains the quantification of von Mises stress in MPa (Mega Pascal) through the skull. To obtain stress data, two ways have been followed. (i) Across the skull in twelve homologous anatomical points in all specimens. (**Fig. S4A**). (ii) Through three homologous points in the dorsal zone of the temporomandibular joint region (TMJ) (**Fig. S4B**). These data are shown in **Tables S1-S5**. In **Figure 7A,** it is shown the bite scenario with the canine, and when the sinus is involved, there is a more homogeneous transmission of the stress (**Figs. 4A** and **5B)**.

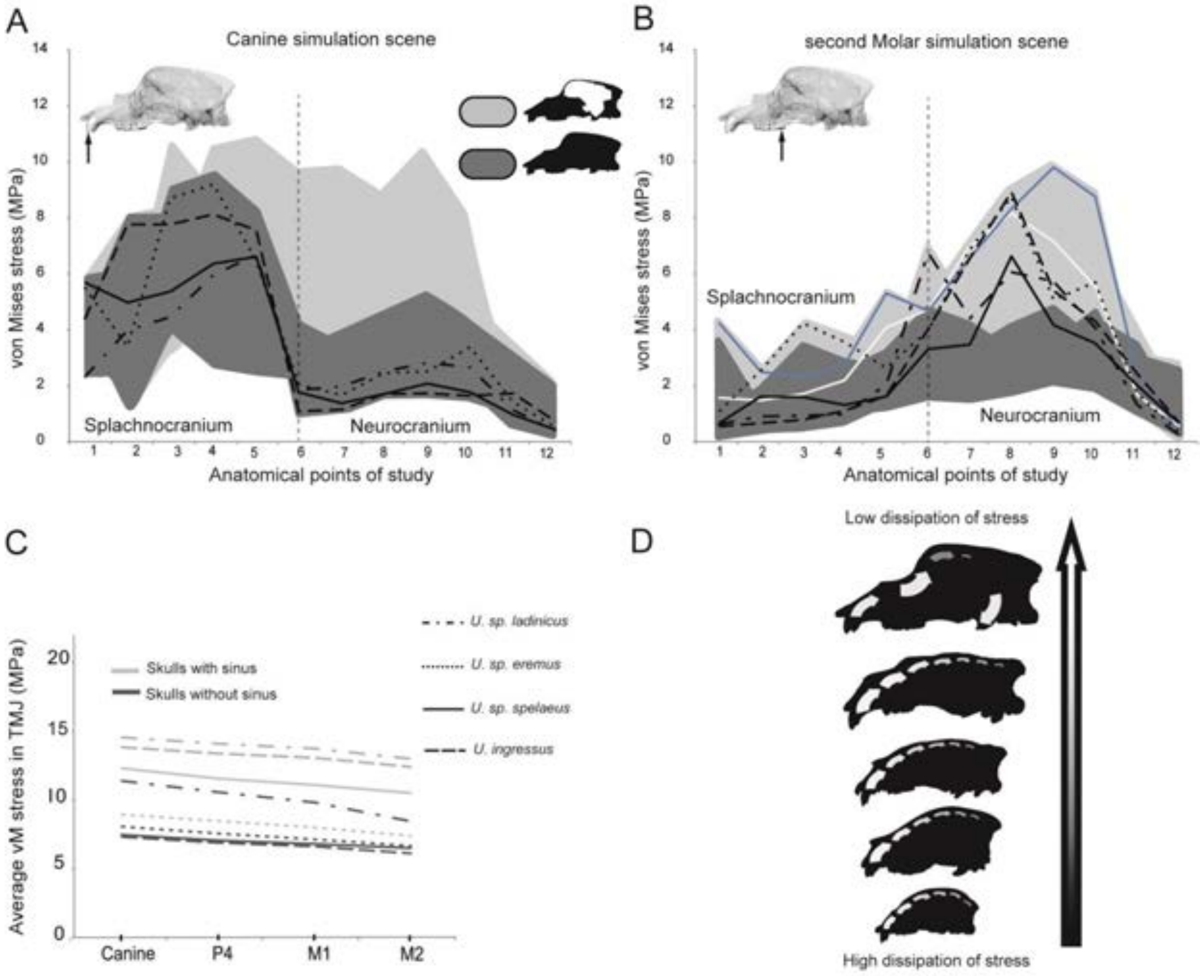

Figure 7. Behaviour of the von Mises stress scenario during biting. (A) Values of the von Mises stress obtained during a simulating scenario of biting with the canine along the 12 anatomical points of the skull sampled. The stress patterns of the cave bear are shown with black lines using different patterns (see legend); **(B)** Values of the von Mises stress obtained during a simulating scenario of biting with the second upper molar along the 12 anatomical points of the skull sampled . The light gray area corresponds to the case with sinuses and the dark gray areas corresponds to models without sinuses. The stress patterns of the cave bear are shown with black lines using different patterns (see legend); dotted line corresponds to upper second molar marking the limit between splachnocraium and neurocranium;**(C)** Average values of von Mises stress sampled across the dorsal region of the skull from the TMJ in each bite scenario (x-axis). Grey lines correspond to skulls models with sinuses and black lines correspond to skulls models without sinuses. Living taxa not shown; **(D)** Hypothesis of the relationship between skull shape and the optimization of stress distribution. Silhouettes are ordered from bottom (highest dissipation of stress) to top (lowest dissipation of stress) as follows: *H. malayanus*; *A. melanoleuca*; *U. americanus*; *U. maritimus*, and *U. ingressus.*

In contrast, when biting with the second molar (**Fig. 7B**), there are not differences of stress transmission from the splachnocranium to the neurocranium between the models with sinuses and without sinuses . I hypothesize that this is due to two different aspects: (i) that the point of action of the force is closer to the fulcrum (TMJ); and (ii) that the point of action is in a region located posteriorly to the frontal dome, and therefore, dome geometry produces a negative effect in stress dissipation in this scenario. In fact, when comparing several skull shapes with their ability to dissipate stress from the splachnocranium to the neurocranium, the skulls with a circular profile (*H. malayanus*) or with an almost null frontal dome (*A. melanoleuca*) are the ones that best dissipate the stress (**Fig. 7D**).

A characteristic of the speleoid lineage is the large expansion of the sphenoid sinus along with the sinus region of pars lateralis and the sacculus, joining these regions with the sphenoid sinus (Rabeder et al. 2009, 2010). This produces an invagination and expansion in the internal region of the TMJ. Among living bears, this anatomical characteristic is only observed in the American black bear (*U. americanus*) and partly in the sloth bear (*M. ursinus*), with a large development of the sacculus region but without expanding the TMJ region. In **Figure 7C**, it is observed that in the models without sinuses, the stress dissipation through the dorsal region of the TMJ for each bite scenario is much lower than in the models with sinuses.

3.3.4.5. The role of paranasal sinuses in conforming the *speloid* *morphotype*

Figure 8 shows my hypothesis on how the typical skull shape of the *speloid* lineage is generated, attending to an internal consequence of a large development of the paranasal sinuses. As shown in **Figs. 8A**,**B**, the large development of frontal sinuses and the sinuses of the parietal and sacculus region, together with the sphenoid sinus, expand in the axial axis in both frontal and caudal direction and in the ventral dorsal axis, invading the internal regions of the squamous bone that forms the region of the temporomandibular joint (TMJ).

This expansion causes a change in the external geometry of the skull (**Fig. 8C**). First, a higher and a wider dome is generated, and therefore, the slope of the dome increases. At the same time, the occipital and sagittal regions change their plane of inclination. The distance in height between inion and basion increase. The plane in this region (red dashed line) is positioned more vertically together with the plane of the frontal region (red dashed line). These two planes play an important role in cranial stability to dissipate frontal stresses in biomechanical models.

Based on the expansion of the paranasal sinuses, the plane of the dome may have a more vertical inclination (i.e., a higher dome). This changes in dome inclination negatively affect to the biomechanical requirements of each cave bear species. Therefore, a relatively degree of variability between the occlusal plane of the second upper molar and the inclination of the dome profile exist. The combination of both factors with having a TMJ filled with sinuses suppose a double biomechanical limitation. Accordingly, in **Figure 9** it is observed that there is a trade-off between the plane of inclination of the dome and the occlusal plane of the molar region, specifically at the second upper molar.

Regarding the maximum values of strain energy, m∆SEa, (difference between the values obtained when biting with the upper second molar and the canine), among the cave bears, *U. sp. eremus* has the highest stability (m∆SEa=0.32), and the one with the least stability is *U. sp. ladinicus* with a value of m∆SEa=0.46, followed by *U. ingressus* with a value of m∆SEa=0.42.

Therefore, in the case of *U. sp. eremus* to afford its less dental stability and a higher stress in the frontal region, most probably possess the occlusal plane of the second upper molar at about 15.95º, which is the highest value within the group of cave bears, even having a more marked basicranial angle with respect to other cave bears.

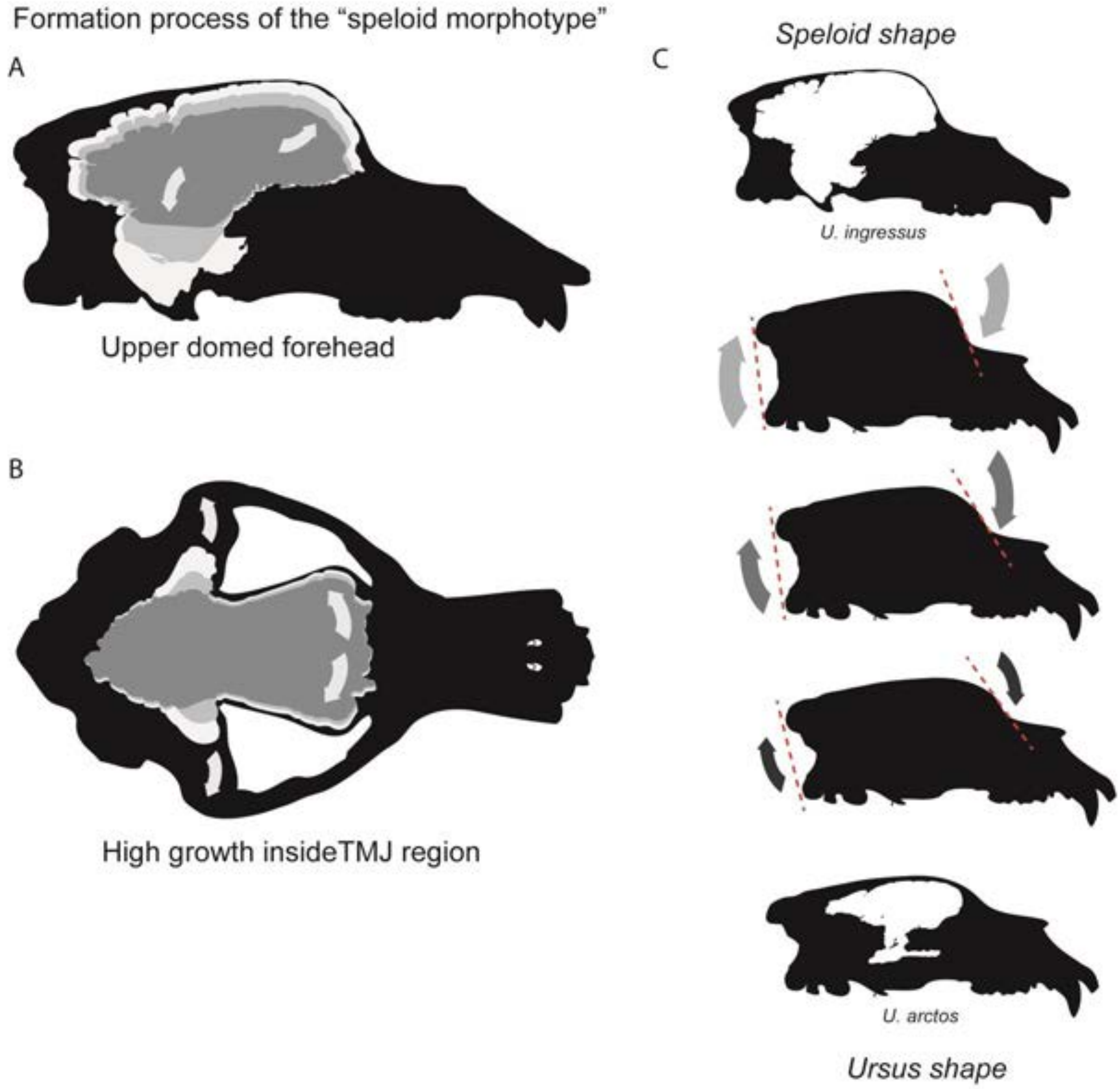

Figure 8. The role of sinuses in the formation of the *speloid morphotype*. (A) Sagittal view and **(B)** dorsal view of the skull of *U. ingressus*. In both views, the expansion in different phases (different colors of gray), one in the frontal direction and the other in the ventral direction towards the parietal region and the TMJ are shown. This expansion occurs both axially and laterally; **(C)** the role of sinuses in conforming the external skull shape of the speloid lineage.

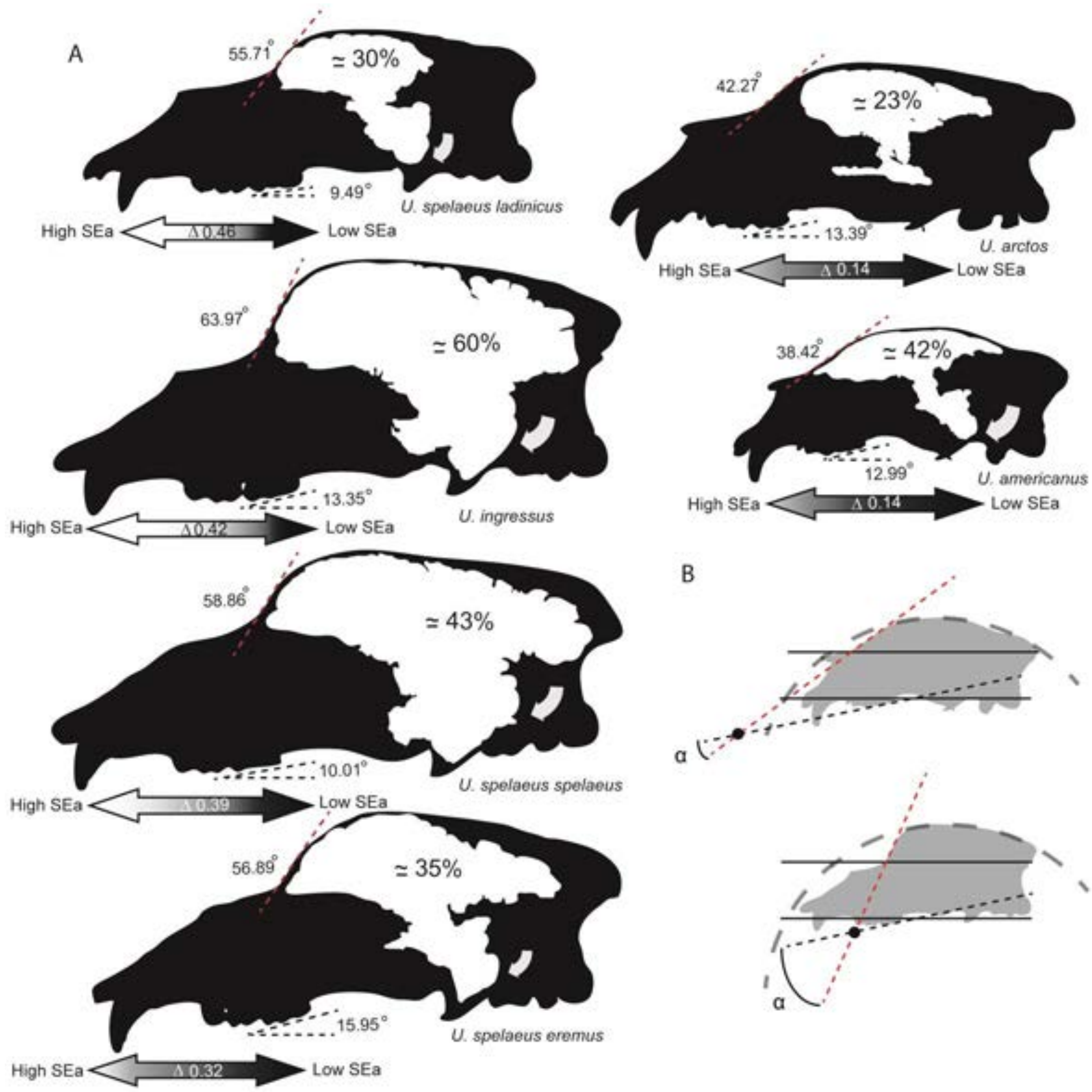

Figure 9. The role of the dome profile and occlusal plane in shaping the *speloid* shape. (A) skull profiles of cave bears and the brown bear (*U. arctos*) and the American black bear (*U. americanus*) showing the dome inclination, and the occlusal plane inclination at the second upper molar. The range of dental stability values (strain energy SE) obtained in FE analysis, as well as the mΔSEa are given for each skull. White shaded areas represent the areas filled with sinuses (numbers indicate the sinuses volume relativized to skull volume, in percentages); **(B)** scheme of the skull geometry related to both paranasal sinuses and occlusal plane inclination in *Ursus americanus* (top) and *Ursus ingressus* (bottom). The inclination of the frontal dome is represented by a dashed red line. The occlusal plane of the second molar is represented by a dashed black line. The intersection between these two axes is marked by a black dot, and the angle formed by this intersection is named as α. The projection of the outline of the skull is marked by a dashed gray curve.

Comparing the American black bear (relative sinus volume =42%) with *U. sp. spelaeus*, a cave bear species with a similar relative sinus volume (43%), the former has a greater inclination of the occlusal plane (12.9º) compared to the 10º exhibited by the later. The resulting angle of the intersection between the occlusal plane and the dome profile plane (α; see **Fig. 9**) is 25.43° for the American black bear and 48.85º for *U. sp spelaeus.* Accordingly, those species with lower angle projection (α) will have a better efficiency in the transmission of stress across the skull when biting. Therefore, the American black bear show a greater dental stability (mΔSEa=0.14) compared to *U. sp. spelaeus* (mΔSEa=0.39).

3.3.5. Discussion

3.3.5.1. Sinuses size and feeding biomechanics in living and extinct bears

The simulation of different chewing scenarios of skull models with sinuses (**Fig. 3A** and **Fig. 4**) and without sinuses (**Fig. 3B** and **Fig. 5**) using FEA allowed us to distinguish three groups of living bears depending upon the effect of the sinuses on feeding biomechanics:

- **(i)** Bears (*A. melanoleuca* and *U. maritimus*) in which the sinuses do not affect feeding biomechanics (those with *i*mΔSEa ≈ 1; **Fig. 6A,B**). *U. maritimus* has relatively small sinuses (≈ 17% sinus volume/skull volume) without expanded frontal areas of the skull, which is also reflected in its moderately flattened forehead. This entails that the cranial geometry of *U. maritimus* is not compromised by sinus size. On the other hand, given that *U. maritimus* usually feeds primarily on blubber of prey much smaller than itself (*Phoca hispida* and *Erignathus barbatus* (Figueirido et al. 2013), the actual biomechanical requirements of its skull are low. Therefore, the sinuses of *U.*

maritimus, together with its vascular counter-current system, are more involved in avoiding dehydration and freezing in the Arctic polar environment (Blix et al. 2016) than to provide structural stability and stress dissipation to the skull during feeding. Our results also support the hypothesis that the dietary specialization of *U. maritimus* decreases cranial functional performance (Slater et al. 2010).

The skull geometry of *A. melanoleuca* is optimized to confer structural stability (stiffness) by having a triangular section along the dorso-sagittal region of the skull as a consequence of a verticalized temporalis muscle resembling the skull of the durophagous hyaenas (Figueirido et al. 2013). This is also reflected in the similarity of sinus shape between *A. melanoleuca* and hyaenids (Curtis and Van Valkenburgh 2014). It is true that contrary to *A. melanoleuca*, the sinuses of hyaenids have an advantageous structure involved in dissipating the stresses generated during bone-cracking (Tanner et al. 2008), but while *A. melanoleuca* is adapted to feed with the post-carnassial dentition (Figueirido et al. 2013), hyaenids usually crack-bones with the pre-carnassial dentition (i.e., premolars). Therefore, the specific skull geometry of *A. melanoleuca* confers enough integrity for the biomechanical demands required for feeding on bamboo. This explains the absence of changes in mΔSEa in the models with and without sinuses (**Fig. 3**; **Fig. 6A**). Moreover, the relatively small sinuses of *A. melanoleuc*a (≈ 11% of sinuses volume/skull volume; **Fig. 6B**) distribute homogenously the stresses between the rostrum and neurocranium (**Figs. 4, 5**).

- **(ii)** The sinuses of some bears (*H. malayanus*, *U. arctos*, *U. thibetanus*) improve feeding biomechanics (those with *i*mΔSEa < 1), providing structural stability of the skull (high stiffness), as previously demonstrated for hyaenas (Tanner et al. 2008). Moreover, their sinuses allow a more homogeneous distribution of stress across the skull. The models without sinuses concentrate the stress mainly on the rostro-frontal region and on the TMJ (**Figs. 4A, 5A**). Our results confirm the predictions made by

Buckland-Wright (1978) who proposed that the forces generated during biting must pass through the face anterior to the orbit, and then run along the vaulted forehead to the sagittal crest (Tanner et al. 2008). Accordingly, the sinuses play a key role for the load-bearing integration of the neurocranium and rostrum in this group of bears. For *H. malayanus* stress dissipation is necessary for opening hardwood trees in the search of insects such as beetle larvae or for breaking coconuts (Wong et al. 2002). Moreover, although the canines of sun bears seem to be adapted to accomplish these tasks (Pérez-Ramos et al. 2019), the external morphology of the skull does not appear to be equipped to perform these biomechanically-demanding tasks. Both *U. arctos* and *U. thibetanus* are adapted to feed on high proportion of hard mast (< 50% soft mast > 15% hard mast) compared to other bear species such as *U. americanus* or *T. ornatus* that usually feed on a lower proportion of hard mast (feeding > 50% soft mast < 15% hard mast), and therefore, they should require a skull less equipped to resist the forces generated during chewing (Pérez-Ramos et al. 2019).

Our results also show that these taxa have a low-relativized sinus volume (i.e., less than 25% of sinuses volume/skull volume; **Fig. 6B**), which leads to a moderately-flattened forehead (see silhouettes in **Fig. 6A**), conferring structural stability when chewing and allowing effective stress dissipation. However, it should be noted that although *U. arctos* does not have sphenoidal sinuses developed in the frontal region or the temporo-mandibular joint; instead, it has expanded sinuses along the dorso-sagittal section of the skull.

- **(iii)** The sinuses in other living bears (*M. ursinus*, *U. americanus*) compromise feeding biomechanics (those with *i*mΔSEa > 1) by decreasing structural stability of the skull (high stiffness). This is also the case in *T. ornatus* but its values of *i*mΔSEa are only slightly higher than one. This is striking because the main function of the sinuses is thought to be involved in stress dissipation during feeding and to provide skull structural stability (Curtis and

Van Valkenburgh 2014; Tanner et al. 2008). However, the analyses of von Mises stress in *M. ursinus*, and *U. americanus* reveal higher stresses in models with sinuses than in models without sinuses (**Figs. 4A, 5A**), demonstrating that the sinuses have a minor role in the integration of the neurocranium and rostrum.

All cave bears, together with *U. americanus*, have the highest values of *i*mΔSEa index among the sample. This indicates that the sinuses compromise the feeding biomechanics of cave bears by decreasing structural stability of their skulls as observed in the biomechanical simulations outcomes of living *T. ornatus*, *M. ursinus* and *U. americanus*. Moreover, the analyses of von Mises stress reveal that the sinuses produce much higher stresses during biting in all simulated scenarios than in living bears, including *U. americanus,* which results in a higher concentration of stress in the rostro-frontal region and in the TMJ (**Figs. 4,5**). This disadvantageous effect of the sinuses on feeding biomechanics is related with the acquisition of a high-relativized sinus volume (i.e., exceeding 25% of sinus volume/skull volume; **Fig. 6B**), which leads to a pronounced step in the forehead, often called the 'frontal dome' that modifies the geometry of the skull (see silhouettes in **Fig. 6**). This is particularly extreme in cave bears, as they greatly expanded sinuses (between 30% in *U. sp. ladinicus* and 60% in *U. ingressus* of sinuses volume/skull volume; **Fig. 6B)**. Indeed, this frontal dome represents a diagnostic trait to distinguish brown bears from *speloid* bears. However, the frontal dome impedes stress dissipation during chewing with the anterior dentition (**Fig. 3; Figs. 4B; Fig. 5B**). Therefore, the sinuses in *T. ornatus*, *M. ursinus*, *U. americanus*, and more particularly in cave bears, lead to lower (and inefficient) stress dissipation between the rostrum and neurocranium as a consequence of the expansion in height of the frontal region of the skull. This also entails a decoupling between the rostrum and neurocranium on the role of stress dissipation. The relatively poor biomechanical capability for processing food using the anterior dentition would have impacted hunting and foraging behavior that require forceful use of incisors and canines, for example, in hunting active prey, as in *U. arctos* (Pérez-Ramos et al. 2019).

Our results demonstrate that the highly developed sinuses in cave bears constrain their dietary flexibility as in the living *U. americanus*, which is the most herbivorous living bear inhabiting high latitudes (Bojarska 2012). However, although *U. americanus* does not have a domed forehead to the same level than cave bears, its sinus volume is extremely large (**Fig. 6B**), which is enough to cause a disadvantageous effect on feeding biomechanics without having a modified skull geometry. Isotopic biochemistry studies (e.g., Bocherens 2019) indicate that cave bears were fully herbivorous without the flexibility to shift their diet towards omnivory during the Pleistocene climatic cooling at the beginning of the Last Glacial Maximum (Terlato et al. 2019). This was also supported by the analysis of tooth-root morphology in cave bears, as they tend to maximize tooth-root areas of their second upper molars towards an herbivorous diet (Pérez-Ramos et al. 2019). Therefore, if having large sinuses impose a biomechanical restriction to feed on different resources in cave bears and *U. americanus*, why are large sinuses selected in these taxa?.

3.3.5.2. The selective advantage of having large sinuses in bears: hibernation length

Living bears such as the brown bear (*Ursus arctos*) and the American black bear (*Ursus americanus*) overcome winters in hibernation (Hellgren 1998). In contrast other bears, either do not hibernate (*U. maritimus*) or instead exhibit a facultative hibernation (*U. thibetanus*) –i.e., a special type of lethargy (Sathyakumar 2013). *Ursus thibetanus* only reduce their physical activity if the environmental conditions require it rather than to decrease their basal metabolism and body temperature (Watts et al. 1987). Neither *T. ornatus* nor *A. melanoleuca* hibernate, as both bears inhabit low-latitude ecosystems without severe winters.

Hibernation is the ability to stay in an energy-conserving state of torpor during the coldest months of the year when food is scarce or unavailable (Grandal d'Anglade 2019). During this time period, which can reach up to six months for some living bear species, the bear's metabolism changes to a special state by decreasing the basal metabolic rate (e.g., Nelson et al. 1973). As a consequence, a substantial decrease in heart rate is accompanied by a decrease in body temperature (e.g., Tøien et al. 2011). Accordingly, during this time the bear does not drink, eat, urinate or defecate: it survives by mobilising its fat reserves acquired during the active period or predormancy (Hellgren 1998).

The length of hibernation in living bears depends on several factors such as latitude and climate, rainfall, food availability or sex (Hellgren 1998). In cave bears, it is widely accepted that they had longer hibernation periods than living bears due to the length of the winters at those latitudes during the end of the Pleistocene (Pérez-Rama et al. 2011; Pacher and Stuart 2009; Grandal d'Anglade et al. 2019; Stiller et al. 2010). The physiology in animals that hibernate is mainly regulated by the activation of enzymes via stress pathways. Among these enzymes, the nitric oxide synthase (NOs) is activated when the concentration of CO_2 in blood increases (hypercapnia) and the levels of O_2 decrease (hypoxia) at the beginning of hibernation (e.g., O'Hearn et al. 2007). The response to these stimuli is to decrease body temperature, heart rate and blood pressure (Kudej et al. 2007). Recent studies link NO and Hydrogen sulfide (H_2S) pathways with the control of the hibernation in bears, as these metabolites (NO and H_2S) are related to the induction of several responses to stimuli of biological stress (Revbesch et al. 2014).

Interestingly, the production of NO and H_2S is segregated by the epithelium of the sphenoidal sinuses (e.g., Lundberg 2008; Petruson et al. 2005; Yan et al. 2017) and all the paranasal sinuses function as a reservoir for NO (Andersson et al. 2002). With the exception of *M. ursinus*, the species that have large sinuses hibernate. *M. ursinus* and *U. americanus* have the lowest metabolic rates among living bears. While in *U. americanus* its low metabolic rate is related to hibernation, in *M. ursinus* is mostly related to its low-energy diet based on insects (McNab 1992). These observations are consistent with the key role of sinuses in lowering basal metabolic rates to afford either a low-energy diet (as in *M. ursinus*) or to hibernate (as in *U. americanus*). However, *U. arctos* hibernate and it has a higher metabolic rate than *U. americanus*, but the predormancy period of *U. arctos* is comparatively longer than in *U. americanus* (Brown 1993). The high metabolic rate of *U. arctos* compared to *U. americanus* also explains the fact that *U. arctos* is the only taxa among the sample that hibernate with sinus volume lower than 25% of skull volume. However, although neither sphenoidal sinuses across the temporo-mandibular joint or sinuses within the frontal dome are developed in brown bears, the frontal sinuses along the dorso-sagittal section are developed, and may be involved in NO and H_2S sequestration butt at a lower rate than in *U. americanus*. In fact, this disposition of the sinuses in *U. arctos* allows maintaining relatively long periods of hibernation without lacking the biomechanical flexibility to feed on different resources, including meat (Bojarska 2012).

3.3.5.3. Sinuses, hibernation and feeding biomechanics in cave bears

The 3D biomechanical simulations of different chewing scenarios demonstrate that cave bears lack the degree of biting efficiently with all teeth, leading to an absence of the dietary flexibility of the omnivorous *U. arctos* –i.e., their closest living relative. Moreover, this lack of dietary flexibility is a consequence of having expanded sinuses in the frontal region, which forms the domed forehead that characterizes the *speloid* lineage. This dome significantly reduces the dissipation of stress when biting with the anterior dentition, and hence, forced cave bears to have a skull biomechanically constrained for chewing vegetal matter with their posterior teeth, as in the living *U. americanus* (Pérez-Ramos et al. 2019). On the other hand, the selective advantage of having extremely large sinuses in cave bears is probably related to their necessity to overcome long winters in hibernation of the Last Glacial, with the hibernation process largely controlled by various enzymes segregated in the sphenoidal sinuses (Lundberg 2008; Petruson et al. 2005; Yan et al. 2017; Andersson et al. 2002). We hypothesize that this was the key selective agent to increase sinus size along the evolutionary history of the *speloid* lineage. At the same time, the large sinuses of cave bears caused a life history trade-off between feeding and hibernation.

Our study demonstrates that the anatomical specialization in cave bears for longer hibernation periods explain the lack of dietary flexibility in cave bears by having a restricted low-energetic, herbivorous diet constrained biomechanically by skulls less able to dissipate biting stresses. Whether this lack of dietary flexibility precluded cave bears to acquire sufficient fat storage to overcome the extreme winters of the Late Pleistocene cooling in hibernation remains a tantalizing question. However, the new findings of this study demonstrates that this biomechanical restriction imposed by the necessity of having large periods of hibernation is likely to be a more critical factor in the decline and ultimate extinction of the cave bear than previously suspected. Our new life history trade-off hypothesis also formulates a specific, mechanistic pathway by which climatic changes during the Last Glacial could have directly influenced the ability of some members of the Ice Age megafauna to obtain adequate nutrients and successfully survive during the extreme ecological conditions of the coldest months.

3.3.6. References

- Alsafy MAM, El-Gendy SAA, El-Sharaby AA. 2013. Anatomic reference for computed tomography of paranasal sinuses and their communication in the Egyptian buffalo (Bubalus bubalis). Anat Histol Embryol. 42(3):220-231.
- Andersson JA, Cervin A, Lindberg S, Uddman R, Cardell LO. 2002. The paranasal sinuses as reservoirs for nitric oxide. Acta Oto-Laryngol. 122: 861–865.
- Baca M, Popović D, Stefaniak K, Marciszak A, Urbanowski M, Nadachowski A, Mackiewicz P. 2016. Retreat and extinction of the Late Pleistocene cave bear (*Ursus spelaeus* sensu lato). Sci Nat. 103**:** 92.
- Bahar S, Bolat D, Dayan MO, Paksoy Y. 2014. Two-and three-dimensional anatomy of paranasal sinuses in Arabian foals. J Vet Med Sci. 76(1):37-44.
- Blix AS. 2016. Adaptations to polar life in mammals and birds. J Exp Biol 219: 1093-1105.
- Bocherens H. 2019. Isotopic insights on cave bear palaeodiet. Hist Biol. 31: 410-421.
- Bojarska K, Selva N.. 2012. Spatial patterns in brown bear *Ursus arctos* diet: the role of geographical and environmental factors. Mammal Rev. 42: 120-143.
- Buckland-Wright JC. 1978. Bone structure and the patterns of force transmission in the cat skull (*Felis catus*). J Morphol. 155: 35-61.
- Brown G. 1993. The great bear almanac. (Lyons and Burford, Publishers, New York, 325pp.
- Curtis AA, Van Valkenburgh B. 2014. Beyond the sniffer: frontal sinuses in Carnivora. Anat. Rec. 297: 2047-2064.
- Dumont ER, Piccirillo J, Grosse IR. 2005. Finite element analysis of biting behaviour and bone stress in the facial skeletons of bats. Anat Rec Part A. 283: 319-330.
- Farke AA. 2008. Frontal sinuses and head-butting in goats: a finite element analysis. J Exp Biol. 211(19):3085-3094.
- Figueirido B. Tseng ZJ, A. Martín-Serra. 2013. Skull shape evolution in durophagous carnivorans. Evolution. 67:1975-1993.
- Fortes GG, Grandal-D'Anglade A, Kolbe B, Fernandes D, Meleg IN, García-Vázquez A, Frischauf C. 2016. Ancient DNA reveals differences in behaviour and sociality between brown bears and extinct cave bears. Mol ecol. 25: 4907-4918.

- Grandal-D'Anglade A, Pérez-Rama M, García-Vázquez A, González-Fortes GM. 2019. The cave bear's hibernation: reconstructing the physiology and behaviour of an extinct animal. Hist Biol. 31: 429-441.
- Grosse IR, Dumont ER, Coletta C, Tolleson A. 2007. Techniques for modeling muscle-induced forces in finite element models of skeletal structures. Anat Rec 290: 1069-1088.
- Hammer Ø, Harper DA, Ryan PD, 2001. PAST: paleontological statistics software package for education and data analysis. Palaeontol Electron. 4: 9.
- Hanken J, Hall BK. (Eds.). 1993. The skull, volume 2: patterns of structural and systematic diversity . University of Chicago Press. 2(9):438-529.
- Hellgren EC. 1998. Physiology of hibernation in bears. Ursus 10: 467-477.
- Joeckel RM. 1998. Unique frontal sinuses in fossil and living Hyaenidae (Mammalia, Carnivora): description and interpretation. J Vertebr Paleontol. 18(3):627-639.
- König HE, Liebich HG. (Eds.). 2013. Veterinary anatomy of domestic mammals: textbook and colour atlas. Schattauer Verlag.
- Kudej RK, Depre C. 2007. NO with no NOS in ischemic heart.. Cardiovasc. Res.74:1-3.
- Kurtén B. 1976. The cave bear story: life and death of a vanished animal (Columbian University Press), 163pp.
- Lundberg JO. 2008. Nitric oxide and the paranasal sinuses. Anat Rec. 291: 1479-1484.
- McNab BK. 1992. Rate of metabolism in the termite-eating sloth bear (*Ursus ursinus*). J. Mammal. 73: 168-172.
- Moore WJ. 1981. The Mammalian Skull Cambridge Univ. Press, Cambridge. 264-279.
- Münzel SC, Stiller M, Hofreiter M, Mittnik A, Conard NJ, Bocherens H. 2011. Pleistocene bears in the Swabian Jura (Germany): genetic replacement, ecological displacement, extinctions and survival. Quatern Int. 245: 225-237.
- Münzel SC, Conard NJ. 2004. Cave bear hunting in the Hohle Fels, a cave site in the Ach Valley, Swabian Jura. Revue de Paléobiologie 23: 877-885.
- Negus VE, Street H. 1954. The function of the paranasal sinuses. Acta oto-laryngologica. 44(5-6):408-426.
- Nelson RA, Wahner HW, Jones JD, Ellefson RD, Zollman PE. 1973. Metabolism of bears before, during, and after winter sleep. American Journal of Physiology-Legacy Content. 224: 491-496.

- O'Hearn DJ, Giraud GD, Sippel JM, Edwards C, Chan B, Holden WE. 2007. Exhaled nasal nitric oxide output is reduced in humans at night during the sleep period. Resp Physiol Neurobi. 156: 94-101.
- Pacher MA, Stuart J. 2009. Extinction chronology and palaeobiology of the cave bear (*Ursus spelaeus*). Boreas 38: 189–206.
- PALASIATICA V. 2011. **大熊猫**颅内腔的演化. (EVOLUTION OF CRANIAL CAVITIES IN GIANT PANDAS (AILUROPODA, CARNIVORA, MAMMALIA).
- Pérez-Rama MD. Fernández-Mosquera A. Grandal-d'Anglade. 2011. Effects of hibernation on the stable isotope signatures of adult and neonate cave bears. Quaternaire 4: 79-88.
- Pérez-Ramos A, Kupczik K, Van Heteren AH, Rabeder G, Grandal-D'Anglade A, Pastor FJ, Figueirido B. 2019. A three-dimensional analysis of tooth-root morphology in living bears and implications for feeding behaviour in the extinct cave bear. Hist Biol. 31: 461-473.
- Petruson K, Stalfors J, Jacobsson KE, Ny L, Petruson B. 2005. Nitric oxide production in the sphenoidal sinus by the inducible and constitutive isozymes of nitric oxide synthase. Rhinology. 43: 18-23.
- Rabeder G, Pacher M, Withalm G. 2009. Die altpleistozänen Bären von Deutsch-Altenburg (Niederöster¬reich) – Early Pleistocene Bear Remains from Deutsch-Altenburg (Lower Austria Wien). — Mitt. Komm. Quartärforsch. Österr. Akad. Wiss. 17:1–135.
- Rabeder G, Pacher M, Withalm G. 2010. EARLY PLEISTOCENE BEAR REMAINS FROM DEUTSCH ALTENBURG LOWER AUSTRIA. Geol Carpath. 61(3):192.
- Revell L J. 2012. Phytools: an R package for phylogenetic comparative biology (and other things). Methods Ecol Evol. 3: 217-223.
- Revsbech IG, Shen X, Chakravarti R, Jensen FB, Thiel B, Evans AL, Fago A. 2014. Hydrogen sulfide and nitric oxide metabolites in the blood of free-ranging brown bears and their potential roles in hibernation. Free Radical Bio Med. 73: 349-357.
- Sathyakumar S, Sharma LK, and Charoo SA. 2013. Ecology of Asiatic Black Bear in Dachigam National Park, Kashmir, India. Final project report. Wildlife Institute of India, Dehradun, 169.

- Slater GJ, Figueirido B, Louis L, Yang P, Van Valkenburgh B. 2010. Biomechanical consequences of rapid evolution in the polar bear lineage. PLOS ONE. 5: 13871–13877.
- Stiller M, Baryshnikov G, Bocherens H, Grandal d'Anglade A, Hilpert B, Münzel SC, Hofreiter M. 2010. Withering away—25,000 years of genetic decline preceded cave bear extinction. Mol Biol Evol. 27:975-978.
- Tanner JB, Dumont ER, Sakai ST, Lundrigan BL, Holekamp KE. 2008. Of arcs and vaults: the biomechanics of bone-cracking in spotted hyenas (*Crocuta crocuta*). Biol J Linn Soc. 95:246-255.
- Terlato G, Bocherens H, Romandini M, Nannini N, Hobson KA, Peresani M. 2019. Chronological and Isotopic data support a revision for the timing of cave bear extinction in Mediterranean Europe. Hist Biol. 31:474-484.
- Tøien Ø, Blake J, Edgar DM, Grahn DA, Heller HC, Barnes BM. 2011. Hibernation in black bears: independence of metabolic suppression from body temperature. Science. 331:906-909.
- Thomason JJ. 1991. Cranial strength in relation to estimated biting forces in some mammals. Can J Zool. 69:2326-2333.
- Treuting PM, Dintzis SM, Montine KS. (Eds.). 2017. Comparative anatomy and histology: a mouse, rat, and human atlas. Academic Press.
- Tseng ZJ, Flynn JJ. 2018. Structure-function covariation with nonfeeding ecological variables influences evolution of feeding specialization in Carnivora. Sci Ad. 4: eaao5441.
- Watts PD, Øritsland NA, Hurst RJ. 1987. Standard metabolic rate of polar bears under simulated denning conditions. Physiol Zool. 60:687-691.
- Weeden AM, Degner DA. 2016. Surgical approaches to the nasal cavity and sinuses. Veterinary Clinics: Small Animal Practice. 46(4):719-733.
- Wong ST, Servheen C, Ambu L. 2002. Food habits of Malayan sun bears in lowland tropical forest of Borneo. Ursus. 13:127– 136.
- Yan CH, Hahn S, McMahon D, Bonislawski D, Kennedy DW, Adappa ND, Cohen NA. 2017. Nitric oxide production is stimulated by bitter taste receptors ubiquitously expressed in the sinonasal cavity. Am J Rhinol Allergy. 31:85-92.

- Yee KK, Craven BA, Wysocki CJ, Van Valkenburgh B. 2016. Comparative Morphology and Histology of the Nasal Fossa in Four Mammals: Gray Squirrel, Bobcat, Coyote, and White-Tailed Deer. The Anatomical Record. 299(7):840-852.

3.3.7. Supplementary material

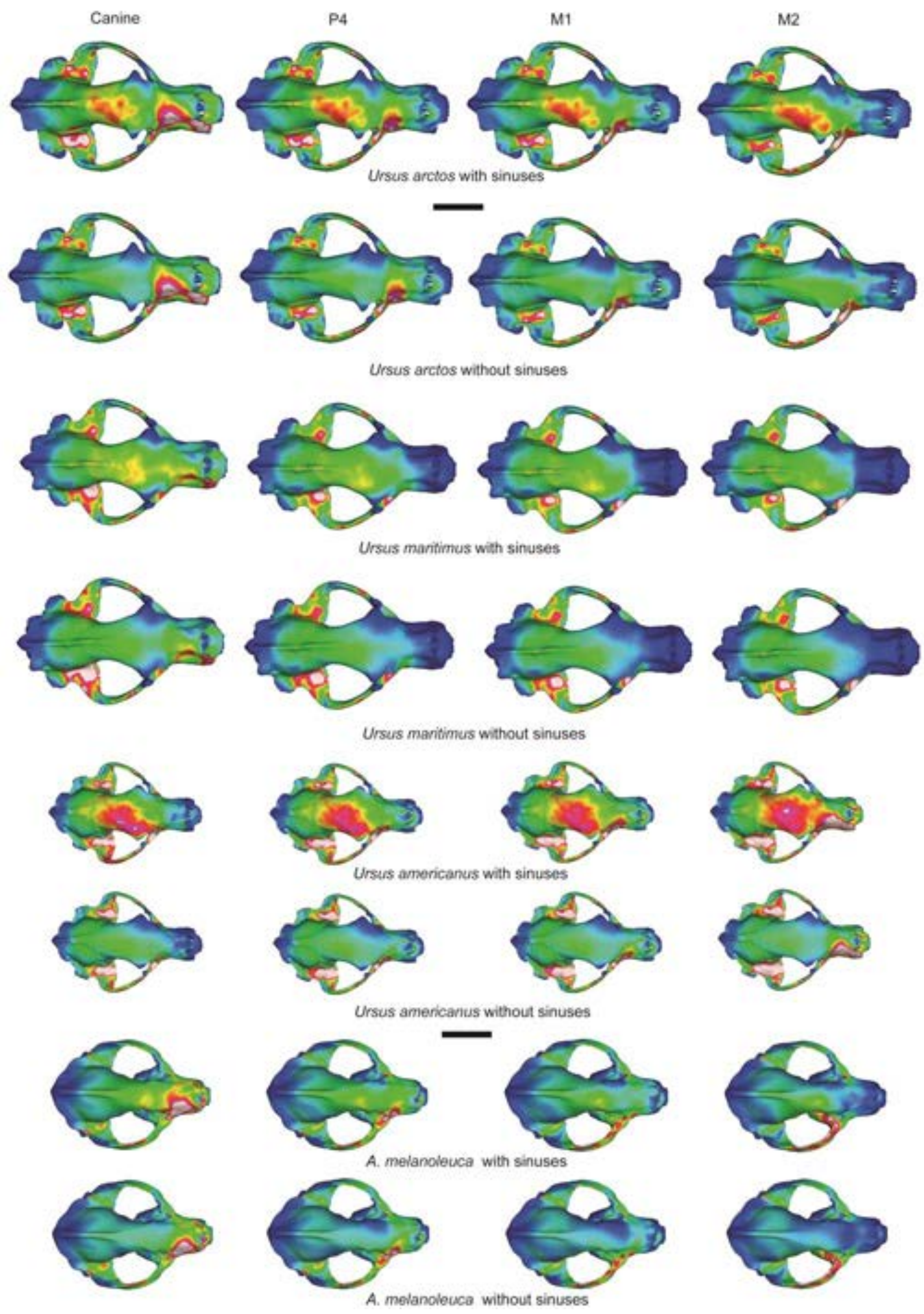

Figure S1. Contour plots of von Mises stress distribution obtained from FE analyses for all biting scenarios in living bears. Abbreviations: P4, fourth upper premolar; M1, first upper molar; M2, second upper molar. Scale Bar: 10cm

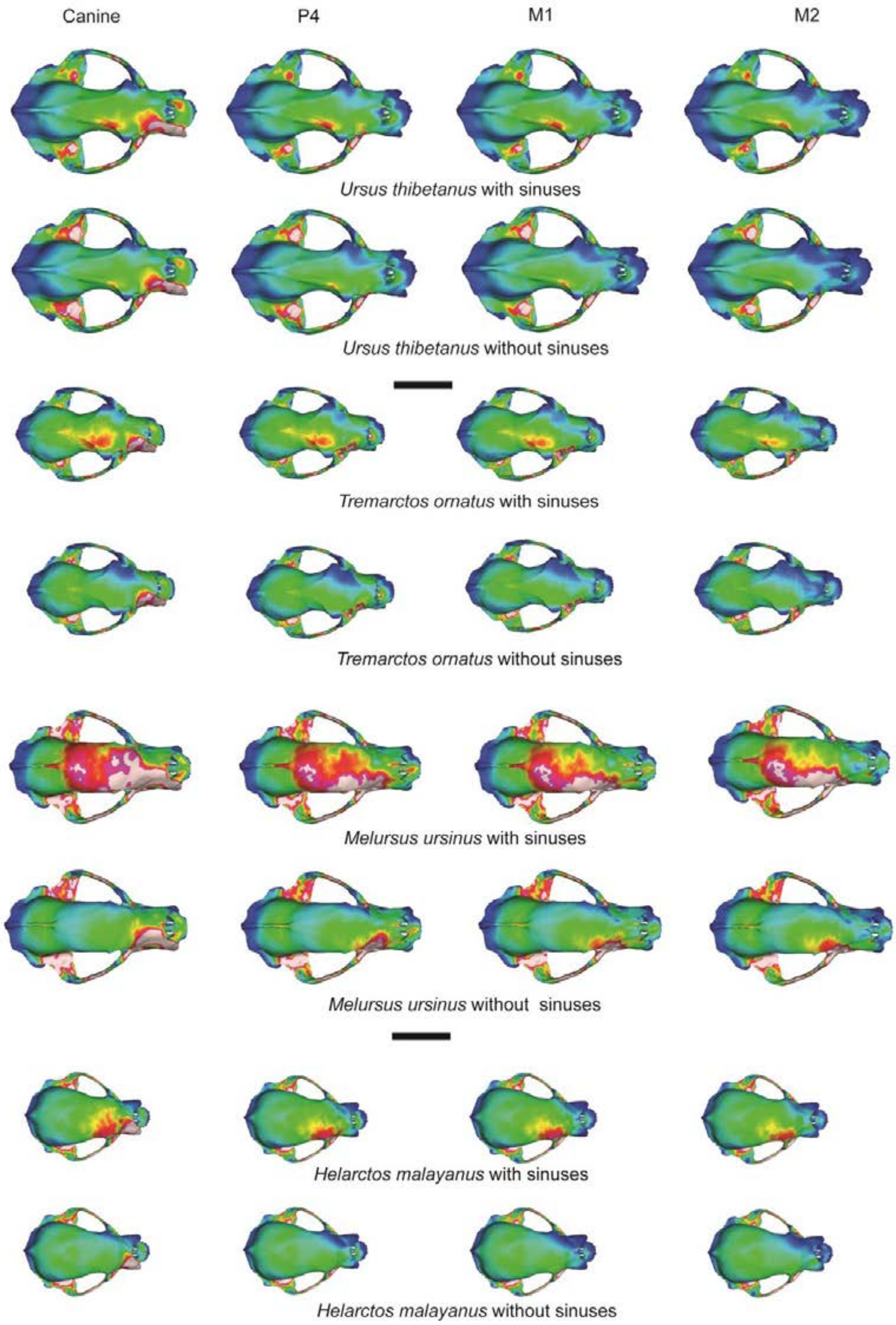

Figure S2. Contour plots of von Mises stress distribution obtained from FE analyses for all biting scenarios in living bears. Abbreviations: P4, fourth upper premolar; M1, first upper molar; M2, second upper molar. Scale Bar: 10cm

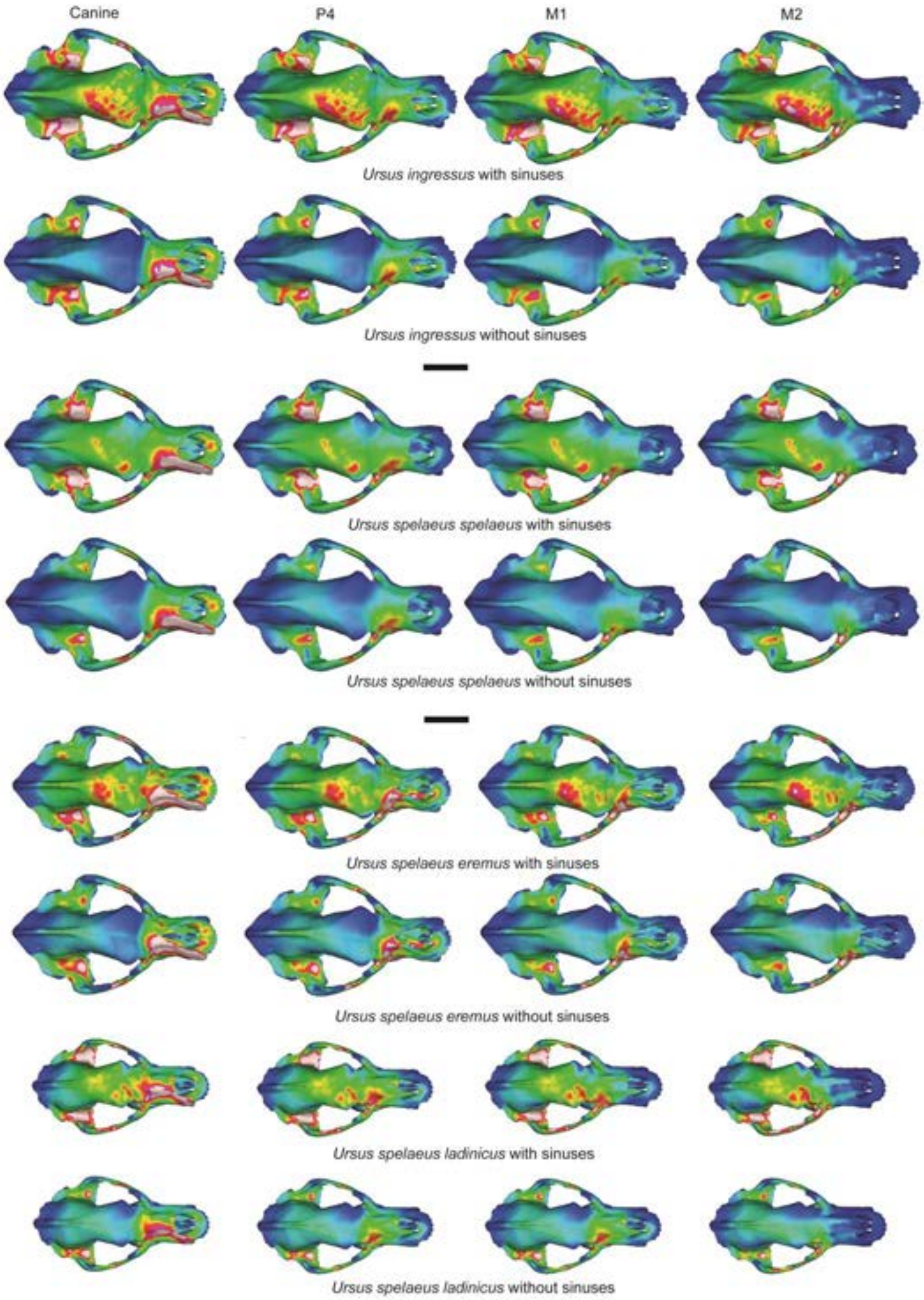

Figure S3. Contour plots of von Mises stress distribution obtained from FE analyses for all biting scenarios in cave bears. Abbreviations: P4, fourth upper premolar; M1, first upper molar; M2, second upper molar. Scale bar: 10cm

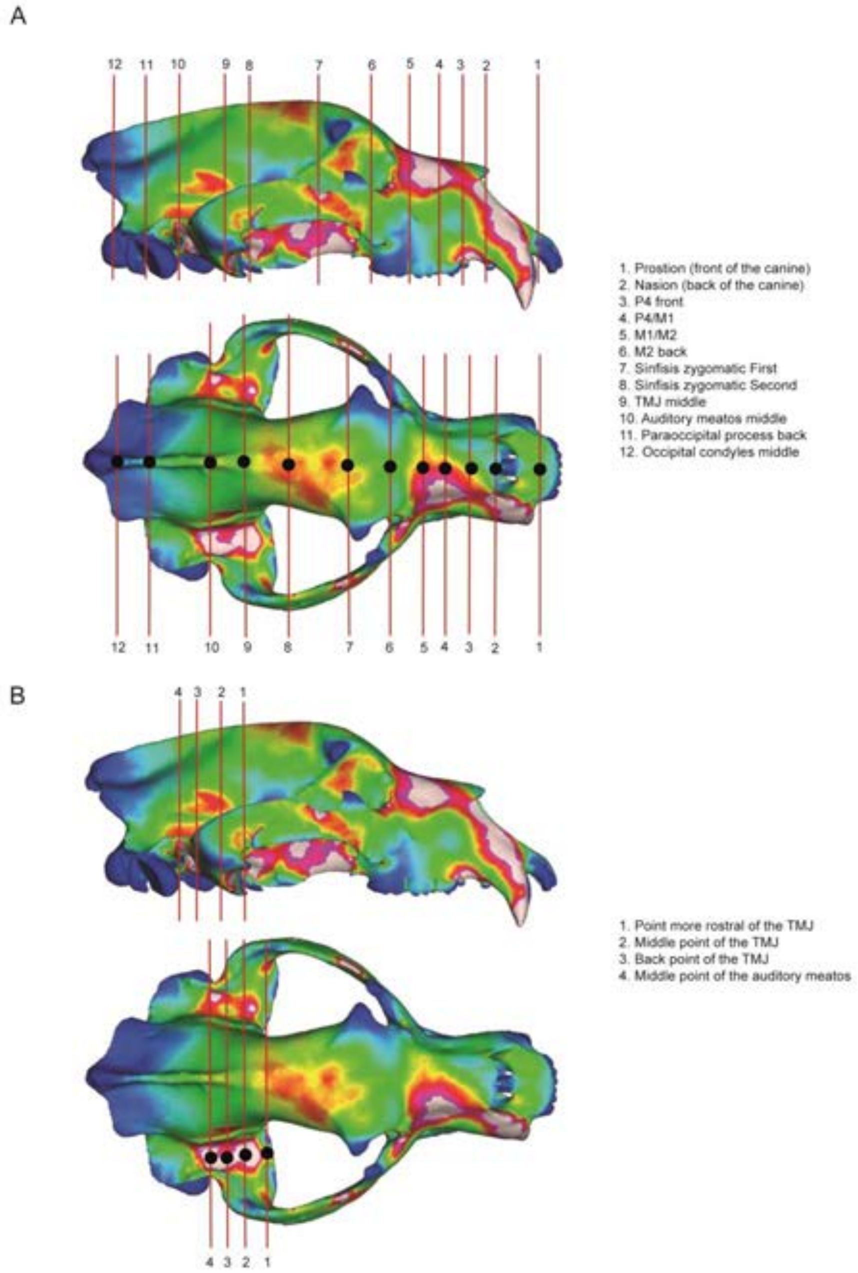

Figure S4. Sampling of Von Mises stress (MPa) values across the skull and TMJ. (**A**) Analysis of VM stress along the axial plane of the skull, using the same twelve anatomic points in all specimens. (**B**) Analysis of VM stress in the dorsal region of the TMJ, using the same four anatomic points in all specimens.

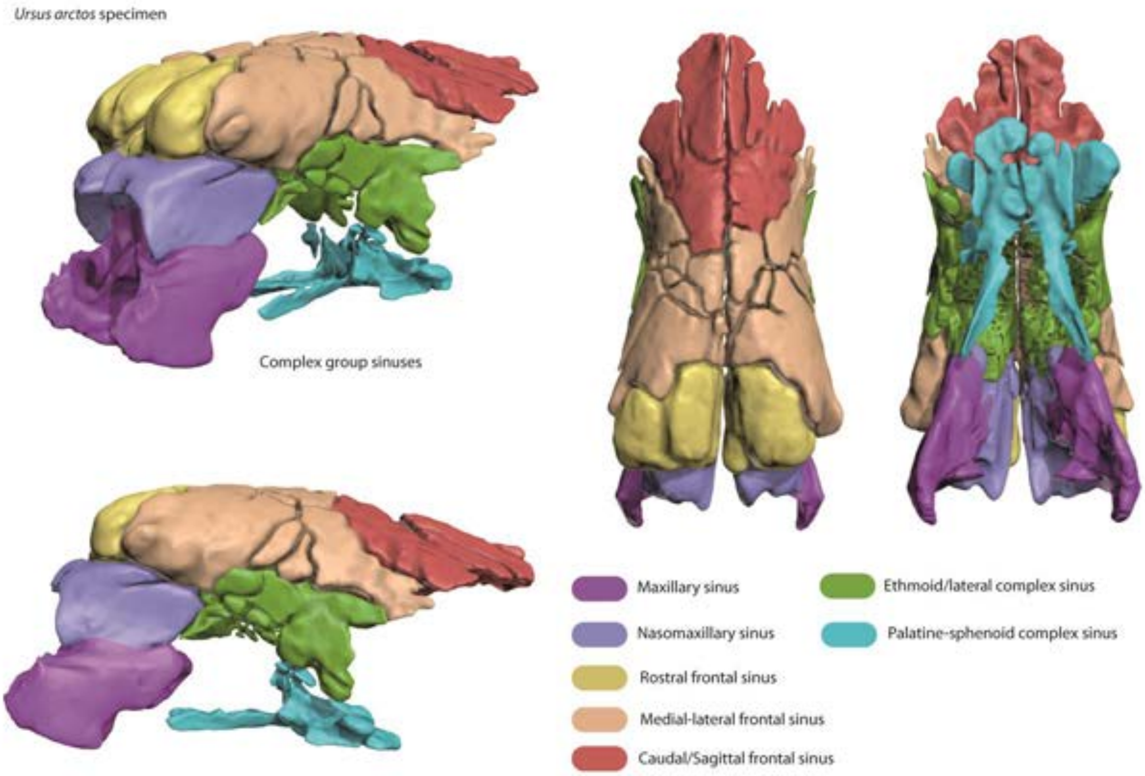

Figure S5. **The anatomical sinus from *Ursus arctos* (USNM 82003).** Anatomical systemic of the sinus. The different functional parts in different colors. Purple (Maxillary sinus); gray-blue (nasomaxillary); yellow (rostral frontal sinus); light-salmon (medial-lateral frontal sinus); red (caudal/sagittal frontal sinus); green (ethmoid/ lateral complex sinus); turquoise (Palatine-sphenoid complex sinus).

Table S1. Von Mises stress across the axial plane of the skull in twelve anatomic points. They are stress values obtained from skull models with sinuses, in a bite scenario in the right canine in all specimens.

Case canine right with sinuses				
Anatomic points	Von Mises stress (MPa)			
U. arctos	Y (Average)	Y (Min)	Y (Max)	Desvest
1	3.26E+00	2.74E+00	4.15E+00	0.70398714
2	1.90E+00	1.07E+00	2.67E+00	0.79876948
3	4.32E+00	3.47E+00	5.41E+00	0.97181614
4	5.93E+00	4.66E+00	7.27E+00	1.30541456
5	8.01E+00	5.96E+00	9.84E+00	1.94251081
6	4.42E+00	3.83E+00	4.89E+00	0.52871778
7	6.36E+00	5.58E+00	7.12E+00	0.76882937
8	6.60E+00	5.96E+00	7.03E+00	0.53521875
9	4.81E+00	4.22E+00	5.39E+00	0.58342878
10	5.74E+00	5.43E+00	6.17E+00	0.37131998
11	3.31E+00	3.21E+00	3.38E+00	0.08387108
12	1.09E+00	9.13E-01	1.28E+00	0.18475553
U. americanus	Y (Average)	Y (Min)	Y (Max)	Desvest
1	3.70E+00	2.40E+00	4.52E+00	1.06230664
2	2.60E+00	1.30E+00	3.97E+00	1.33332507
3	7.51E+00	5.27E+00	1.17E+01	3.23312832
4	6.47E+00	4.84E+00	9.55E+00	2.35506083
5	6.71E+00	5.52E+00	8.79E+00	1.63502329
6	7.32E+00	6.65E+00	8.11E+00	0.73359217
7	9.40E+00	8.46E+00	1.07E+01	1.14214302
8	7.92E+00	7.50E+00	8.85E+00	0.6741437
9	6.45E+00	5.80E+00	6.91E+00	0.55068091
10	4.92E+00	4.53E+00	5.30E+00	0.38675969
11	1.20E+00	8.97E-01	1.48E+00	0.29029625
12	4.39E-01	3.47E-01	5.84E-01	0.11847422
U. maritimus	Y (Average)	Y (Min)	Y (Max)	Desvest

1	2.38E+00	2.19E+00	2.68E+00	0.24475651
2	2.95E+00	1.79E+00	4.07E+00	1.14254831
3	3.27E+00	2.77E+00	3.98E+00	0.60522944
4	4.82E+00	4.03E+00	7.10E+00	1.53570621
5	4.96E+00	4.42E+00	5.41E+00	0.4956715
6	5.70E+00	5.19E+00	6.34E+00	0.5771592
7	6.11E+00	5.43E+00	7.00E+00	0.78747408
8	5.53E+00	5.34E+00	5.93E+00	0.29496161
9	5.88E+00	5.34E+00	6.51E+00	0.583503
10	6.03E+00	5.20E+00	7.07E+00	0.93609242
11	1.69E+00	1.44E+00	1.92E+00	0.23821683
12	2.60E-01	2.27E-01	3.08E-01	0.04067098
A. melanoleuca	Y (Average)	Y (Min)	Y (Max)	Desvest
1	4.97E+00	3.47E+00	6.15E+00	1.33986859
2	4.30E+00	2.67E+00	5.84E+00	1.58405765
3	7.31E+00	5.91E+00	9.34E+00	1.71581688
4	7.57E+00	6.44E+00	8.80E+00	1.18184133
5	4.95E+00	4.33E+00	5.72E+00	0.69747304
6	4.36E+00	3.78E+00	4.67E+00	0.44148722
7	4.65E+00	4.35E+00	5.00E+00	0.32285099
8	3.43E+00	3.21E+00	3.76E+00	0.27475866
9	3.59E+00	3.48E+00	3.74E+00	0.12807421
10	2.89E+00	2.73E+00	3.11E+00	0.19025872
11	7.87E-01	6.86E-01	8.77E-01	0.09540939
12	2.97E-01	2.41E-01	3.59E-01	0.0590556
U. thibetanus	Y (Average)	Y (Min)	Y (Max)	Desvest
1	4.77E+00	3.71E+00	5.55E+00	0.91943283
2	2.69E+00	1.89E+00	3.33E+00	0.71660483
3	5.25E+00	4.40E+00	6.55E+00	1.07655676
4	5.15E+00	3.83E+00	6.27E+00	1.2197566
5	4.35E+00	4.03E+00	5.11E+00	0.53894966
6	4.97E+00	4.00E+00	5.86E+00	0.93277376
7	4.53E+00	3.88E+00	5.30E+00	0.70997479

8	3.77E+00	3.47E+00	3.99E+00	0.25960484
9	3.32E+00	3.19E+00	3.44E+00	0.12612184
10	2.00E+00	1.81E+00	2.14E+00	0.16563922
11	1.81E+00	1.72E+00	2.01E+00	0.14739092
12	5.99E-01	5.64E-01	6.84E-01	0.06016133
T. ornatus	Y (Average)	Y (Min)	Y (Max)	Desvest
1	4.27E+00	3.61E+00	4.97E+00	0.68208494
2	2.11E+00	8.23E-01	4.15E+00	1.66233372
3	4.04E+00	2.70E+00	4.86E+00	1.0802525
4	4.80E+00	3.93E+00	5.76E+00	0.91724443
5	4.55E+00	3.40E+00	5.40E+00	0.99757311
6	6.07E+00	4.70E+00	9.23E+00	2.26190751
7	5.64E+00	3.96E+00	7.12E+00	1.58045845
8	5.51E+00	5.11E+00	5.95E+00	0.41802334
9	6.32E+00	6.08E+00	6.71E+00	0.31654197
10	3.46E+00	2.98E+00	4.10E+00	0.55878019
11	1.65E+00	1.52E+00	1.83E+00	0.15566692
12	4.38E-01	3.77E-01	5.06E-01	0.06423969
M. ursinus	Y (Average)	Y (Min)	Y (Max)	Desvest
1	3.18E+00	2.28E+00	4.38E+00	1.04756853
2	7.37E+00	6.42E+00	9.65E+00	1.61219367
3	6.97E+00	3.61E+00	1.20E+01	4.20745891
4	1.05E+01	7.95E+00	1.21E+01	2.09054434
5	1.08E+01	8.34E+00	1.33E+01	2.49972366
6	9.51E+00	8.12E+00	1.06E+01	1.24690018
7	9.76E+00	8.89E+00	1.06E+01	0.83858755
8	8.82E+00	7.98E+00	9.68E+00	0.84840371
9	1.04E+01	9.20E+00	1.16E+01	1.19119917
10	8.12E+00	7.92E+00	8.39E+00	0.23277291
11	1.90E+00	1.81E+00	2.00E+00	0.09354339
12	2.26E-01	2.05E-01	2.38E-01	0.01617
H. malayanus	Y (Average)	Y (Min)	Y (Max)	Desvest

1	2.65E+00	1.65E+00	3.92E+00	1.13698695
2	4.25E+00	3.08E+00	6.88E+00	1.89996998
3	5.99E+00	4.39E+00	7.80E+00	1.70918104
4	5.04E+00	4.23E+00	6.27E+00	1.02013388
5	5.32E+00	4.37E+00	6.35E+00	0.9900967
6	6.88E+00	6.04E+00	7.56E+00	0.76265134
7	6.32E+00	5.38E+00	7.89E+00	1.25693056
8	4.31E+00	3.81E+00	5.45E+00	0.8218048
9	3.42E+00	3.06E+00	3.86E+00	0.39907875
10	2.55E+00	2.24E+00	2.95E+00	0.35530519
11	2.79E+00	2.57E+00	2.95E+00	0.18559927
12	2.09E+00	1.84E+00	2.41E+00	0.28579319
U. sp. ladinicus	Y (Average)	Y (Min)	Y (Max)	Desvest
1	2.43E+00	1.84E+00	3.63E+00	0.89593112
2	5.27E+00	4.36E+00	7.61E+00	1.62700274
3	5.46E+00	3.97E+00	6.87E+00	1.44762252
4	6.73E+00	4.89E+00	7.97E+00	1.54034212
5	7.63E+00	6.07E+00	9.45E+00	1.69046353
6	6.87E+00	4.89E+00	8.99E+00	2.05334731
7	4.17E+00	3.41E+00	4.75E+00	0.67215329
8	6.04E+00	5.60E+00	6.76E+00	0.58089249
9	5.11E+00	4.62E+00	5.72E+00	0.55100656
10	3.60E+00	3.03E+00	3.98E+00	0.47661215
11	9.95E-01	9.16E-01	1.04E+00	0.06078032
12	1.56E-01	1.10E-01	2.38E-01	0.06405837
U. sp. eremus	Y (Average)	Y (Min)	Y (Max)	Desvest
1	6.07E+00	4.93E+00	7.24E+00	1.15847548
2	3.96E+00	2.70E+00	6.68E+00	1.98671672
3	1.06E+01	4.74E+00	2.03E+01	7.77336348
4	8.72E+00	6.69E+00	1.43E+01	3.82505927
5	7.83E+00	5.35E+00	1.03E+01	2.45553176
6	6.27E+00	4.83E+00	7.54E+00	1.35096269
7	7.97E+00	4.60E+00	1.52E+01	5.3189103

8	7.76E+00	6.34E+00	8.99E+00	1.32578692
9	4.56E+00	4.43E+00	4.67E+00	0.11887495
10	5.09E+00	4.84E+00	5.40E+00	0.28247986
11	1.36E+00	1.26E+00	1.44E+00	0.08946534
12	2.48E-01	1.56E-01	3.36E-01	0.08985595
U. sp. spelaeus	Y (Average)	Y (Min)	Y (Max)	Desvest
1	5.90E+00	4.21E+00	7.60E+00	1.697364
2	7.70E+00	6.40E+00	9.68E+00	1.6376516
3	5.84E+00	3.03E+00	8.03E+00	2.4993642
4	6.46E+00	4.13E+00	8.30E+00	2.08760144
5	5.43E+00	4.23E+00	6.42E+00	1.09509027
6	3.47E+00	2.37E+00	4.04E+00	0.83402753
7	3.13E+00	2.88E+00	3.46E+00	0.29206025
8	6.47E+00	4.98E+00	7.93E+00	1.47257216
9	4.11E+00	3.86E+00	4.57E+00	0.35445095
10	3.34E+00	3.12E+00	3.66E+00	0.27278016
11	1.58E+00	1.51E+00	1.64E+00	0.06691661
12	5.58E-01	5.01E-01	6.08E-01	0.05335239
U. ingressus	Y (Average)	Y (Min)	Y (Max)	Desvest
1	4.44E+00	3.76E+00	4.91E+00	0.57316555
2	8.01E+00	4.76E+00	1.17E+01	3.48411986
3	8.18E+00	6.54E+00	8.95E+00	1.2045619
4	7.79E+00	6.66E+00	9.01E+00	1.17644375
5	7.49E+00	6.79E+00	8.12E+00	0.66266498
6	3.26E+00	2.68E+00	3.80E+00	0.56122571
7	6.44E+00	3.41E+00	8.53E+00	2.55834125
8	8.00E+00	6.97E+00	9.40E+00	1.21333078
9	5.02E+00	4.71E+00	5.30E+00	0.29148282
10	3.75E+00	3.63E+00	3.93E+00	0.15392987
11	2.07E+00	1.95E+00	2.15E+00	0.10334888
12	5.61E-01	5.20E-01	6.72E-01	0.07596314

Table S2. Von Mises stress across the axial plane of the skull in twelve anatomic points. They are stress values obtained from skull models without sinuses, in a bite scenario in the right canine in all specimens.

Case canine right without sinuses				
Anatomic points	Von Mises stress (MPa)			
U. arctos	Y (Average)	Y (Min)	Y (Max)	Desvest
1	3.00E+00	2.50E+00	3.76E+00	0.63077091
2	2.15E+00	1.04E+00	3.06E+00	1.01008151
3	4.32E+00	3.48E+00	5.41E+00	0.96306201
4	7.29E+00	6.31E+00	8.65E+00	1.17030688
5	8.23E+00	6.39E+00	9.93E+00	1.76703433
6	2.70E+00	2.48E+00	2.94E+00	0.23047439
7	2.95E+00	2.76E+00	3.15E+00	0.19616795
8	3.34E+00	3.12E+00	3.55E+00	0.21520144
9	3.36E+00	3.18E+00	3.52E+00	0.17266316
10	3.80E+00	3.64E+00	3.90E+00	0.13050116
11	2.79E+00	2.64E+00	2.92E+00	0.13947823
12	9.35E-01	8.03E-01	1.08E+00	0.14033533
U. americanus	Y (Average)	Y (Min)	Y (Max)	Desvest
1	3.74E+00	2.69E+00	4.81E+00	1.05839145
2	1.24E+00	1.04E+00	1.62E+00	0.2895625
3	7.05E+00	5.69E+00	8.30E+00	1.30424071
4	4.28E+00	3.04E+00	6.66E+00	1.80656976
5	3.13E+00	2.47E+00	3.81E+00	0.67065198
6	2.28E+00	2.09E+00	2.47E+00	0.19184005
7	2.65E+00	2.43E+00	2.83E+00	0.19892507
8	3.07E+00	2.73E+00	3.44E+00	0.35201094
9	3.11E+00	3.00E+00	3.26E+00	0.13259981
10	3.02E+00	2.95E+00	3.08E+00	0.06292193
11	1.02E+00	8.86E-01	1.21E+00	0.16156156
12	4.23E-01	3.74E-01	5.04E-01	0.06524561
U. maritimus	Y (Average)	Y (Min)	Y (Max)	Desvest

1	2.41E+00	2.26E+00	2.57E+00	0.15601107
2	2.48E+00	1.67E+00	3.46E+00	0.8948758
3	4.91E+00	4.28E+00	5.54E+00	0.62960215
4	4.02E+00	3.50E+00	5.43E+00	0.96417546
5	3.26E+00	3.05E+00	3.52E+00	0.23383259
6	2.96E+00	2.65E+00	3.19E+00	0.26838121
7	3.82E+00	3.57E+00	4.11E+00	0.27289844
8	4.01E+00	3.82E+00	4.31E+00	0.24362253
9	4.68E+00	4.43E+00	4.96E+00	0.26699348
10	3.86E+00	3.49E+00	4.31E+00	0.41115811
11	1.40E+00	1.15E+00	1.65E+00	0.25004456
12	2.89E-01	2.41E-01	3.34E-01	0.04643641
A. melanoleuca	Y (Average)	Y (Min)	Y (Max)	Desvest
1	4.87E+00	3.78E+00	5.89E+00	1.05478472
2	3.28E+00	2.69E+00	3.68E+00	0.49492567
3	5.18E+00	3.90E+00	6.74E+00	1.42197859
4	3.01E+00	2.60E+00	3.52E+00	0.45976298
5	2.57E+00	2.42E+00	2.74E+00	0.16439354
6	2.45E+00	2.37E+00	2.57E+00	0.10148815
7	2.52E+00	2.36E+00	2.68E+00	0.16140561
8	2.59E+00	2.45E+00	2.80E+00	0.17681514
9	2.78E+00	2.70E+00	2.88E+00	0.09413272
10	2.38E+00	2.35E+00	2.42E+00	0.03266166
11	6.01E-01	5.19E-01	6.67E-01	0.07395274
12	2.49E-01	2.03E-01	3.02E-01	0.04941186
U. thibetanus	Y (Average)	Y (Min)	Y (Max)	Desvest
1	4.12E+00	2.91E+00	5.18E+00	1.13826126
2	2.43E+00	1.71E+00	3.00E+00	0.64556595
3	4.74E+00	3.96E+00	5.88E+00	0.95520279
4	5.22E+00	4.80E+00	5.73E+00	0.46326909
5	3.37E+00	2.80E+00	4.02E+00	0.6138
6	4.06E+00	3.42E+00	4.64E+00	0.61100125
7	3.64E+00	3.38E+00	3.94E+00	0.28209988

8	2.84E+00	2.70E+00	2.99E+00	0.14143055
9	2.79E+00	2.71E+00	2.90E+00	0.09956429
10	1.61E+00	1.44E+00	1.73E+00	0.14379315
11	1.56E+00	1.52E+00	1.60E+00	0.04081221
12	5.98E-01	5.64E-01	6.83E-01	0.05907814
T. ornatus	Y (Average)	Y (Min)	Y (Max)	Desvest
1	4.02E+00	3.43E+00	4.57E+00	0.5702061
2	2.48E+00	1.62E+00	3.59E+00	0.98440818
3	4.34E+00	3.18E+00	5.00E+00	0.9126207
4	3.34E+00	2.65E+00	4.44E+00	0.89334733
5	2.49E+00	2.15E+00	2.86E+00	0.35792448
6	2.62E+00	2.15E+00	3.01E+00	0.43449897
7	3.59E+00	3.09E+00	4.12E+00	0.51163191
8	4.42E+00	4.31E+00	4.61E+00	0.15070076
9	5.23E+00	5.10E+00	5.41E+00	0.15402402
10	3.35E+00	2.88E+00	4.00E+00	0.55918591
11	1.76E+00	1.53E+00	1.99E+00	0.23322713
12	4.11E-01	3.51E-01	4.75E-01	0.0617195
M. ursinus	Y (Average)	Y (Min)	Y (Max)	Desvest
1	3.20E+00	2.15E+00	4.06E+00	0.95342512
2	6.25E+00	3.81E+00	8.50E+00	2.34589577
3	6.09E+00	3.15E+00	9.78E+00	3.31864028
4	7.60E+00	6.33E+00	9.44E+00	1.55360686
5	6.49E+00	5.27E+00	7.80E+00	1.26309711
6	4.19E+00	3.89E+00	4.55E+00	0.32785758
7	3.40E+00	2.85E+00	3.70E+00	0.42565907
8	2.68E+00	2.44E+00	2.97E+00	0.26546334
9	2.27E+00	2.09E+00	2.44E+00	0.17342694
10	4.24E+00	3.92E+00	4.52E+00	0.2999872
11	1.99E+00	1.89E+00	2.08E+00	0.09665843
12	2.22E-01	1.95E-01	2.41E-01	0.02288439
H. malayanus	Y (Average)	Y (Min)	Y (Max)	Desvest

1	2.47E+00	1.51E+00	3.62E+00	1.05860499
2	3.12E+00	1.93E+00	5.21E+00	1.64401962
3	4.44E+00	3.07E+00	6.13E+00	1.53278103
4	2.74E+00	2.30E+00	3.07E+00	0.38085312
5	2.75E+00	2.46E+00	3.09E+00	0.3147576
6	3.33E+00	3.11E+00	3.63E+00	0.26462599
7	2.71E+00	2.28E+00	3.00E+00	0.36158746
8	2.93E+00	2.40E+00	3.20E+00	0.39733533
9	3.37E+00	2.91E+00	3.68E+00	0.38500607
10	2.67E+00	2.48E+00	3.06E+00	0.28905221
11	2.90E+00	2.67E+00	3.06E+00	0.19711718
12	2.01E+00	1.73E+00	2.43E+00	0.35458753
U. sp. ladinicus	Y (Average)	Y (Min)	Y (Max)	Desvest
1	2.27E+00	1.72E+00	3.36E+00	0.81620411
2	4.03E+00	2.29E+00	6.91E+00	2.3067023
3	4.53E+00	2.81E+00	7.61E+00	2.40091344
4	6.12E+00	4.47E+00	7.29E+00	1.41224289
5	6.87E+00	5.66E+00	8.29E+00	1.3168259
6	1.78E+00	1.54E+00	2.00E+00	0.22941581
7	1.93E+00	1.74E+00	2.08E+00	0.16745522
8	2.49E+00	2.38E+00	2.78E+00	0.19918118
9	2.82E+00	2.64E+00	3.01E+00	0.18659101
10	2.64E+00	2.56E+00	2.74E+00	0.09048179
11	1.02E+00	9.53E-01	1.06E+00	0.05384915
12	2.62E-01	2.04E-01	2.92E-01	0.04413991
U. sp. eremus	Y (Average)	Y (Min)	Y (Max)	Desvest
1	5.66E+00	4.60E+00	6.77E+00	1.08363804
2	3.43E+00	2.62E+00	4.51E+00	0.94432729
3	9.02E+00	5.69E+00	1.22E+01	3.25611688
4	9.54E+00	7.02E+00	1.69E+01	4.92042633
5	6.65E+00	4.78E+00	9.25E+00	2.23530236
6	2.00E+00	1.79E+00	2.26E+00	0.23703492
7	1.60E+00	1.46E+00	1.70E+00	0.12377975

8	2.43E+00	2.19E+00	2.72E+00	0.26596299
9	2.49E+00	2.41E+00	2.58E+00	0.08229308
10	3.40E+00	3.19E+00	3.62E+00	0.21372849
11	1.34E+00	1.24E+00	1.49E+00	0.1226055
12	3.67E-01	2.72E-01	4.42E-01	0.08510057
U. sp. spelaeus	Y (Average)	Y (Min)	Y (Max)	Desvest
1	5.84E+00	4.30E+00	7.60E+00	1.6458481
2	5.08E+00	3.60E+00	7.46E+00	1.9279566
3	5.50E+00	3.44E+00	7.17E+00	1.86335639
4	6.54E+00	5.53E+00	7.36E+00	0.91497646
5	6.82E+00	5.83E+00	8.51E+00	1.33950218
6	1.71E+00	1.56E+00	1.85E+00	0.14071078
7	1.29E+00	1.24E+00	1.35E+00	0.05111042
8	1.64E+00	1.47E+00	1.78E+00	0.15488983
9	2.04E+00	1.95E+00	2.12E+00	0.08554206
10	1.71E+00	1.61E+00	1.82E+00	0.10557425
11	8.51E-01	7.76E-01	8.81E-01	0.05263243
12	2.87E-01	2.22E-01	3.67E-01	0.07293012
U. ingressus	Y (Average)	Y (Min)	Y (Max)	Desvest
1	4.45E+00	4.26E+00	4.96E+00	0.3497864
2	8.03E+00	4.81E+00	1.18E+01	3.47809478
3	8.03E+00	6.30E+00	9.65E+00	1.67112579
4	8.39E+00	6.48E+00	9.70E+00	1.60999256
5	7.81E+00	6.60E+00	8.96E+00	1.18014604
6	9.94E-01	9.21E-01	1.03E+00	0.05286812
7	1.06E+00	1.03E+00	1.11E+00	0.04390846
8	1.64E+00	1.58E+00	1.69E+00	0.05813687
9	1.67E+00	1.62E+00	1.70E+00	0.03885254
10	1.57E+00	1.52E+00	1.60E+00	0.04492679
11	1.65E+00	1.58E+00	1.73E+00	0.07821196
12	5.93E-01	5.43E-01	7.00E-01	0.07843324

Table S3. Von Mises stress across the axial plane of the skull in twelve anatomic points. They are stress values obtained from skull models with sinuses, in a bite scenario in the right second molar (M2) in all specimens.

Case M2 right with sinuses				
Anatomic points	Von Mises stress (MPa)			
U. arctos	Y (Average)	Y (Min)	Y (Max)	Desvest
1	9.83E-01	5.79E-01	1.31E+00	0.36699545
2	8.94E-01	4.19E-01	1.16E+00	0.36912596
3	1.03E+00	6.42E-01	1.41E+00	0.38520935
4	1.12E+00	3.65E-01	2.24E+00	0.93707664
5	2.69E+00	1.71E+00	3.47E+00	0.87898371
6	3.78E+00	3.11E+00	4.28E+00	0.58560356
7	5.93E+00	5.20E+00	6.55E+00	0.67081461
8	6.71E+00	6.01E+00	7.14E+00	0.56440082
9	5.23E+00	4.64E+00	5.81E+00	0.58363605
10	6.47E+00	6.18E+00	6.93E+00	0.37582166
11	3.97E+00	3.84E+00	4.01E+00	0.08673012
12	1.18E+00	9.78E-01	1.39E+00	0.20714824
U. americanus	Y (Average)	Y (Min)	Y (Max)	Desvest
1	1.48E+00	9.42E-01	2.19E+00	0.62177834
2	1.39E+00	7.25E-01	2.47E+00	0.87288695
3	1.62E+00	8.14E-01	2.24E+00	0.71462542
4	2.10E+00	6.97E-01	3.14E+00	1.22134573
5	3.99E+00	2.68E+00	1.18E+01	4.54795408
6	4.65E+00	3.84E+00	5.52E+00	0.8409482
7	6.89E+00	5.06E+00	8.06E+00	1.49778584
8	8.09E+00	7.54E+00	8.93E+00	0.69290478
9	7.08E+00	6.39E+00	7.96E+00	0.7844215
10	5.46E+00	4.99E+00	5.91E+00	0.46031751
11	1.56E+00	1.21E+00	1.84E+00	0.31463805
12	4.74E-01	3.71E-01	6.36E-01	0.1328082
U. maritimus	Y (Average)	Y (Min)	Y (Max)	Desvest

1	1.48E-01	1.36E-01	1.64E-01	0.01442014
2	5.54E-01	3.86E-01	6.67E-01	0.14050626
3	4.09E-01	3.33E-01	4.90E-01	0.07870935
4	1.14E+00	7.25E-01	1.90E+00	0.58982036
5	2.34E+00	1.73E+00	2.89E+00	0.57608723
6	3.70E+00	3.17E+00	4.36E+00	0.59276181
7	4.26E+00	3.63E+00	4.99E+00	0.67862909
8	4.43E+00	4.22E+00	4.83E+00	0.30318631
9	5.29E+00	4.72E+00	5.83E+00	0.55527922
10	6.14E+00	5.32E+00	7.18E+00	0.92907569
11	2.09E+00	1.83E+00	2.36E+00	0.26482447
12	2.61E-01	2.29E-01	3.19E-01	0.04516036
A. melanoleuca	Y (Average)	Y (Min)	Y (Max)	Desvest
1	7.57E-01	4.60E-01	1.16E+00	0.34831648
2	8.17E-01	7.17E-01	9.56E-01	0.1193622
3	1.25E+00	8.45E-01	1.77E+00	0.46206492
4	1.34E+00	7.56E-01	2.27E+00	0.75670922
5	2.39E+00	1.53E+00	3.90E+00	1.18738468
6	3.45E+00	2.69E+00	4.19E+00	0.75227461
7	3.54E+00	2.93E+00	4.21E+00	0.64122963
8	2.89E+00	2.69E+00	3.29E+00	0.29875734
9	3.29E+00	3.14E+00	3.39E+00	0.12560331
10	3.02E+00	2.86E+00	3.20E+00	0.16601811
11	1.10E+00	1.01E+00	1.19E+00	0.08952057
12	3.85E-01	3.23E-01	4.48E-01	0.0623386
U. thibetanus	Y (Average)	Y (Min)	Y (Max)	Desvest
1	1.18E+00	7.01E-01	1.39E+00	0.3462766
2	3.95E-01	2.69E-01	7.15E-01	0.22319634
3	7.62E-01	4.65E-01	9.51E-01	0.24310231
4	2.19E+00	1.21E+00	3.08E+00	0.93542664
5	2.11E+00	1.73E+00	2.48E+00	0.37570729
6	2.98E+00	1.92E+00	4.07E+00	1.07633649
7	3.76E+00	2.73E+00	4.80E+00	1.03605831

8	4.20E+00	3.81E+00	4.43E+00	0.30969439
9	3.92E+00	3.78E+00	4.14E+00	0.18343885
10	2.52E+00	2.21E+00	2.72E+00	0.25491518
11	2.16E+00	2.05E+00	2.40E+00	0.17348555
12	6.48E-01	6.02E-01	7.44E-01	0.07123938
T. ornatus	Y (Average)	Y (Min)	Y (Max)	Desvest
1	2.25E+00	1.69E+00	2.94E+00	0.62543843
2	9.06E-01	3.71E-01	1.98E+00	0.80438159
3	9.50E-01	7.38E-01	1.19E+00	0.2268313
4	1.12E+00	7.60E-01	1.68E+00	0.46168773
5	3.16E+00	2.00E+00	3.98E+00	0.98810308
6	3.50E+00	2.12E+00	5.16E+00	1.52089812
7	4.02E+00	3.04E+00	5.21E+00	1.0829131
8	4.78E+00	4.49E+00	5.21E+00	0.36018819
9	5.33E+00	5.14E+00	5.70E+00	0.27907845
10	3.48E+00	3.06E+00	3.92E+00	0.42542455
11	1.88E+00	1.73E+00	2.08E+00	0.17939999
12	5.18E-01	4.55E-01	6.12E-01	0.07824135
M. ursinus	Y (Average)	Y (Min)	Y (Max)	Desvest
1	4.14E+00	2.75E+00	5.70E+00	1.47826589
2	2.42E+00	1.55E+00	4.10E+00	1.27494871
3	2.25E+00	9.79E-01	5.29E+00	2.15730904
4	2.67E+00	1.87E+00	3.24E+00	0.68293266
5	5.22E+00	3.46E+00	6.84E+00	1.69160026
6	4.59E+00	2.53E+00	7.01E+00	2.2422754
7	6.47E+00	5.44E+00	7.67E+00	1.11449804
8	8.24E+00	6.93E+00	9.70E+00	1.38404484
9	9.73E+00	8.07E+00	1.12E+01	1.53877881
10	8.69E+00	8.44E+00	9.00E+00	0.27792516
11	2.35E+00	2.27E+00	2.42E+00	0.07342034
12	2.35E-01	2.16E-01	2.54E-01	0.01898659
H. malayanus	Y (Average)	Y (Min)	Y (Max)	Desvest

1	2.00E+00	1.39E+00	2.66E+00	0.63875363
2	1.60E+00	1.15E+00	2.42E+00	0.63587809
3	2.01E+00	1.29E+00	2.60E+00	0.6570662
4	3.64E+00	2.80E+00	4.22E+00	0.70968111
5	2.80E+00	1.95E+00	3.62E+00	0.83509941
6	4.09E+00	3.28E+00	4.59E+00	0.65842669
7	4.85E+00	3.65E+00	5.78E+00	1.06550909
8	4.52E+00	4.01E+00	5.72E+00	0.85417237
9	3.71E+00	3.25E+00	4.26E+00	0.50201264
10	2.71E+00	2.30E+00	3.31E+00	0.5040662
11	2.95E+00	2.69E+00	3.13E+00	0.21920958
12	2.54E+00	2.29E+00	2.87E+00	0.29242482
U. sp. ladinicus	Y (Average)	Y (Min)	Y (Max)	Desvest
1	5.25E-01	3.85E-01	6.76E-01	0.14509567
2	8.21E-01	4.94E-01	1.26E+00	0.38469254
3	8.32E-01	3.66E-01	1.29E+00	0.46325684
4	8.88E-01	5.28E-01	1.94E+00	0.70544851
5	1.96E+00	1.12E+00	2.88E+00	0.88058338
6	6.68E+00	4.66E+00	8.92E+00	2.12692138
7	4.32E+00	3.50E+00	5.24E+00	0.86890956
8	5.97E+00	5.39E+00	6.91E+00	0.76203815
9	5.64E+00	5.04E+00	6.32E+00	0.64386096
10	3.97E+00	3.33E+00	4.40E+00	0.53244997
11	1.22E+00	1.14E+00	1.29E+00	0.07449119
12	1.58E-01	1.09E-01	2.44E-01	0.06719283
U. sp. eremus	Y (Average)	Y (Min)	Y (Max)	Desvest
1	9.86E-01	6.42E-01	1.31E+00	0.336267
2	2.46E+00	1.22E+00	4.69E+00	1.73310259
3	4.16E+00	2.36E+00	7.91E+00	2.77689735
4	3.47E+00	2.15E+00	5.41E+00	1.62626237
5	2.54E+00	1.22E+00	3.71E+00	1.24777001
6	3.89E+00	2.32E+00	5.43E+00	1.5507526
7	6.80E+00	4.17E+00	1.16E+01	3.71961043

8	8.67E+00	7.16E+00	1.04E+01	1.62321021
9	4.99E+00	4.91E+00	5.17E+00	0.12714993
10	5.60E+00	5.26E+00	5.98E+00	0.36215027
11	1.62E+00	1.50E+00	1.71E+00	0.10440754
12	2.75E-01	1.78E-01	3.72E-01	0.09738734
U. sp. spelaeus	Y (Average)	Y (Min)	Y (Max)	Desvest
1	5.65E-01	4.19E-01	8.49E-01	0.21491969
2	1.52E+00	1.27E+00	1.76E+00	0.2466737
3	1.50E+00	9.29E-01	2.49E+00	0.77932079
4	1.22E+00	9.76E-01	1.83E+00	0.42573804
5	1.51E+00	1.26E+00	1.96E+00	0.34614119
6	3.22E+00	2.32E+00	3.87E+00	0.77369574
7	3.38E+00	2.99E+00	3.67E+00	0.33902804
8	6.56E+00	4.38E+00	8.51E+00	2.06701049
9	4.09E+00	3.82E+00	4.60E+00	0.39037785
10	3.43E+00	3.19E+00	3.72E+00	0.26693458
11	1.93E+00	1.86E+00	1.98E+00	0.06290995
12	5.78E-01	5.31E-01	6.31E-01	0.05038181
U. ingressus	Y (Average)	Y (Min)	Y (Max)	Desvest
1	4.62E-01	3.76E-01	5.43E-01	0.08358703
2	5.79E-01	2.87E-01	1.26E+00	0.48521802
3	6.90E-01	2.89E-01	1.40E+00	0.55571048
4	1.01E+00	6.99E-01	1.31E+00	0.3041268
5	1.54E+00	1.21E+00	1.89E+00	0.3432402
6	3.95E+00	3.03E+00	4.79E+00	0.87972531
7	6.47E+00	3.83E+00	8.46E+00	2.31498361
8	8.84E+00	7.36E+00	1.02E+01	1.43343326
9	5.30E+00	4.81E+00	5.75E+00	0.46905544
10	4.23E+00	4.09E+00	4.43E+00	0.16869535
11	2.33E+00	2.15E+00	2.45E+00	0.1510738
12	5.85E-01	5.45E-01	6.77E-01	0.06624271

Table S4. Von Mises stress across the axial plane of the skull in twelve anatomic points. They are stress values obtained from skull models without sinuses, in a bite scenario in the right second molar (M2) in all specimens.

Case M2 right without sinuses				
Anatomic points	Von Mises stress (MPa)			
U. arctos	Y (Average)	Y (Min)	Y (Max)	Desvest
1	8.03E-01	5.33E-01	1.09E+00	0.27893293
2	9.86E-01	3.77E-01	1.65E+00	0.63761564
3	1.00E+00	4.45E-01	1.33E+00	0.44256038
4	1.27E+00	7.92E-01	1.48E+00	0.3455497
5	2.59E+00	1.40E+00	3.64E+00	1.12103287
6	3.21E+00	2.47E+00	3.82E+00	0.67493619
7	3.70E+00	3.35E+00	4.04E+00	0.3468604
8	3.74E+00	3.56E+00	4.04E+00	0.24042884
9	3.71E+00	3.57E+00	3.89E+00	0.15850155
10	4.42E+00	4.23E+00	4.53E+00	0.14891529
11	3.49E+00	3.28E+00	3.67E+00	0.19786107
12	1.02E+00	8.83E-01	1.18E+00	0.14846551
U. americanus	Y (Average)	Y (Min)	Y (Max)	Desvest
1	8.48E-01	5.87E-01	1.14E+00	0.27451149
2	4.20E-01	1.77E-01	6.52E-01	0.23769759
3	1.01E+00	3.75E-01	1.66E+00	0.64390515
4	1.49E+00	6.96E-01	2.53E+00	0.91787641
5	2.37E+00	1.03E+00	3.19E+00	1.08070746
6	2.75E+00	2.35E+00	3.13E+00	0.39366916
7	3.05E+00	2.66E+00	3.34E+00	0.34007504
8	3.44E+00	3.10E+00	3.98E+00	0.44032493
9	3.45E+00	3.34E+00	3.61E+00	0.13160128
10	3.46E+00	3.38E+00	3.55E+00	0.08339053
11	1.22E+00	1.07E+00	1.44E+00	0.18666199
12	4.35E-01	3.87E-01	5.23E-01	0.0679219
U. maritimus	Y (Average)	Y (Min)	Y (Max)	Desvest

1	1.39E-01	1.33E-01	1.49E-01	0.00811488
2	3.85E-01	2.76E-01	4.84E-01	0.10395136
3	4.04E-01	2.82E-01	5.51E-01	0.13435486
4	9.29E-01	6.32E-01	1.37E+00	0.36886547
5	1.94E+00	1.72E+00	2.19E+00	0.23602628
6	2.05E+00	1.66E+00	2.31E+00	0.32663404
7	3.11E+00	2.75E+00	3.43E+00	0.33893271
8	3.14E+00	2.93E+00	3.43E+00	0.2533393
9	3.94E+00	3.73E+00	4.22E+00	0.24356221
10	4.08E+00	3.66E+00	4.54E+00	0.44276978
11	1.85E+00	1.58E+00	2.15E+00	0.286885
12	2.86E-01	2.37E-01	3.32E-01	0.04758947
A. melanoleuca	Y (Average)	Y (Min)	Y (Max)	Desvest
1	7.44E-01	3.64E-01	1.19E+00	0.4105564
2	4.10E-01	3.20E-01	4.71E-01	0.07544851
3	4.21E-01	1.89E-01	6.31E-01	0.22085932
4	7.11E-01	3.15E-01	1.03E+00	0.35863894
5	1.46E+00	1.26E+00	1.74E+00	0.23809432
6	1.53E+00	1.40E+00	1.73E+00	0.16541868
7	1.59E+00	1.47E+00	1.79E+00	0.15638428
8	1.74E+00	1.61E+00	1.94E+00	0.16568621
9	2.09E+00	2.05E+00	2.16E+00	0.05302213
10	2.31E+00	2.25E+00	2.38E+00	0.06304692
11	1.03E+00	9.60E-01	1.11E+00	0.07525309
12	3.77E-01	3.18E-01	4.39E-01	0.06042463
U. thibetanus	Y (Average)	Y (Min)	Y (Max)	Desvest
1	9.64E-01	6.66E-01	1.25E+00	0.29393249
2	3.84E-01	2.21E-01	5.97E-01	0.18774292
3	7.07E-01	4.17E-01	9.16E-01	0.24959966
4	1.54E+00	1.30E+00	1.77E+00	0.23345653
5	2.00E+00	1.14E+00	3.16E+00	1.01040755
6	2.84E+00	2.19E+00	3.43E+00	0.6219219
7	3.56E+00	3.26E+00	3.99E+00	0.36702012

8	3.23E+00	3.01E+00	3.41E+00	0.19843128
9	3.52E+00	3.35E+00	3.74E+00	0.19336417
10	2.16E+00	1.99E+00	2.26E+00	0.13719851
11	1.90E+00	1.86E+00	1.96E+00	0.04660286
12	6.52E-01	6.06E-01	7.49E-01	0.07130454
T. ornatus	Y (Average)	Y (Min)	Y (Max)	Desvest
1	1.83E+00	1.38E+00	2.39E+00	0.50170421
2	7.37E-01	5.75E-01	1.00E+00	0.21268392
3	1.35E+00	1.01E+00	1.62E+00	0.30560321
4	1.32E+00	8.47E-01	1.68E+00	0.41489318
5	2.28E+00	2.03E+00	2.69E+00	0.33214057
6	2.38E+00	1.75E+00	2.84E+00	0.54626193
7	3.16E+00	2.55E+00	3.73E+00	0.59398732
8	4.09E+00	3.89E+00	4.42E+00	0.26397074
9	4.82E+00	4.75E+00	4.99E+00	0.11991832
10	3.47E+00	3.06E+00	3.88E+00	0.40908535
11	2.05E+00	1.78E+00	2.28E+00	0.25287445
12	5.17E-01	4.56E-01	6.13E-01	0.07878492
M. ursinus	Y (Average)	Y (Min)	Y (Max)	Desvest
1	3.58E+00	2.77E+00	4.44E+00	0.83561906
2	9.44E-01	5.88E-01	1.47E+00	0.44354811
3	1.80E+00	9.52E-01	3.45E+00	1.24985473
4	2.45E+00	1.16E+00	3.67E+00	1.25222547
5	3.12E+00	1.47E+00	4.97E+00	1.74906582
6	4.76E+00	4.09E+00	5.49E+00	0.70018195
7	4.21E+00	3.19E+00	4.84E+00	0.82567356
8	3.25E+00	2.85E+00	3.70E+00	0.42192024
9	2.67E+00	2.39E+00	3.02E+00	0.31750965
10	4.65E+00	4.24E+00	5.03E+00	0.39522121
11	2.32E+00	2.21E+00	2.43E+00	0.11128617
12	2.34E-01	2.07E-01	2.59E-01	0.02598272
H. malayanus	Y (Average)	Y (Min)	Y (Max)	Desvest

1	1.02E+00	6.69E-01	1.42E+00	0.37792525
2	9.86E-01	6.65E-01	1.46E+00	0.39706072
3	1.22E+00	9.81E-01	1.50E+00	0.25776332
4	2.27E+00	1.80E+00	2.66E+00	0.43016162
5	2.08E+00	1.68E+00	2.62E+00	0.47146788
6	2.69E+00	2.53E+00	2.93E+00	0.19831193
7	2.56E+00	2.08E+00	2.91E+00	0.41450677
8	3.09E+00	2.37E+00	3.49E+00	0.56176328
9	3.42E+00	2.80E+00	3.83E+00	0.51599462
10	2.81E+00	2.53E+00	3.27E+00	0.37086901
11	3.07E+00	2.79E+00	3.28E+00	0.24460126
12	2.49E+00	2.02E+00	2.94E+00	0.45821384
U. sp. ladinicus	Y (Average)	Y (Min)	Y (Max)	Desvest
1	3.45E-01	2.34E-01	4.48E-01	0.10692117
2	3.19E-01	1.56E-01	4.44E-01	0.14392671
3	5.44E-01	2.18E-01	9.00E-01	0.34114868
4	6.31E-01	3.84E-01	1.58E+00	0.59880505
5	1.83E+00	1.02E+00	2.80E+00	0.88815595
6	2.41E+00	1.76E+00	2.99E+00	0.6107874
7	2.56E+00	2.24E+00	2.87E+00	0.31472003
8	2.87E+00	2.63E+00	3.22E+00	0.29277049
9	3.11E+00	2.89E+00	3.38E+00	0.24480487
10	3.08E+00	2.92E+00	3.18E+00	0.12899455
11	1.19E+00	1.11E+00	1.24E+00	0.06547574
12	2.51E-01	1.87E-01	2.84E-01	0.0487164
U. sp. eremus	Y (Average)	Y (Min)	Y (Max)	Desvest
1	8.80E-01	5.69E-01	1.18E+00	0.30316733
2	1.77E+00	1.34E+00	2.29E+00	0.47670727
3	3.41E+00	1.93E+00	5.11E+00	1.59127456
4	2.79E+00	1.52E+00	5.21E+00	1.84364672
5	2.55E+00	1.12E+00	3.76E+00	1.32071121
6	2.93E+00	2.00E+00	3.64E+00	0.8215437
7	2.41E+00	2.19E+00	2.50E+00	0.15779051

8	2.91E+00	2.76E+00	3.07E+00	0.15755083
9	2.97E+00	2.83E+00	3.06E+00	0.11685512
10	4.09E+00	3.86E+00	4.34E+00	0.24204134
11	1.63E+00	1.50E+00	1.79E+00	0.14100434
12	3.90E-01	2.96E-01	4.65E-01	0.08452952
U. sp. spelaeus	Y (Average)	Y (Min)	Y (Max)	Desvest
1	4.84E-01	3.08E-01	7.47E-01	0.21943384
2	7.64E-01	4.54E-01	1.21E+00	0.37757021
3	1.18E+00	3.81E-01	1.54E+00	0.58003412
4	1.42E+00	1.30E+00	1.60E+00	0.14942057
5	1.66E+00	1.03E+00	2.20E+00	0.58335986
6	1.90E+00	1.70E+00	2.14E+00	0.21995927
7	1.50E+00	1.44E+00	1.55E+00	0.05540562
8	1.80E+00	1.60E+00	1.94E+00	0.16862141
9	2.20E+00	2.10E+00	2.30E+00	0.10314857
10	1.95E+00	1.83E+00	2.08E+00	0.12615995
11	1.08E+00	9.79E-01	1.12E+00	0.06986851
12	3.08E-01	2.38E-01	3.95E-01	0.07831362
U. ingressus	Y (Average)	Y (Min)	Y (Max)	Desvest
1	3.70E-01	3.30E-01	4.43E-01	0.0563614
2	6.01E-01	1.61E-01	1.32E+00	0.58196727
3	9.58E-01	3.03E-01	1.45E+00	0.57439703
4	1.00E+00	4.40E-01	1.72E+00	0.63790344
5	1.82E+00	1.32E+00	2.06E+00	0.3698022
6	1.56E+00	1.44E+00	1.65E+00	0.10275005
7	1.55E+00	1.50E+00	1.59E+00	0.0493721
8	2.18E+00	2.07E+00	2.29E+00	0.11096269
9	2.17E+00	2.11E+00	2.21E+00	0.0494413
10	1.96E+00	1.91E+00	2.01E+00	0.05206925
11	2.11E+00	2.01E+00	2.22E+00	0.10621696
12	6.53E-01	6.01E-01	7.47E-01	0.07275294

Table S5. Von Mises stress across the TMJ dorsal region of the skull in four anatomic points. They are stress values obtained from skull models with and without sinuses for each bite scenario (canine, four premolar, first molar, and second molar) in all specimens.

Model skulls with sinus				
Average VM stress TMJ	C	P4	M1	M2
Species	VM (MPa)	VM (MPa)	VM (MPa)	VM (MPa)
Ursus spelaeus ladinicus	1.4538E+01	1.4094E+01	1.3709E+01	1.2979E+01
Ursus spelaeus eremus	8.9460E+00	8.4734E+00	7.9901E+00	7.3512E+00
Ursus spelaeus spelaeus	1.2293E+01	1.1529E+01	1.1090E+01	1.0468E+01
Ursus ingressus	1.3839E+01	1.3358E+01	1.3040E+01	1.2396E+01
Model skulls without sinus				
Ursus spelaeus ladinicus	1.1382E+01	1.0560E+01	9.7916E+00	8.4263E+00
Ursus spelaeus eremus	8.0884E+00	7.5450E+00	7.1266E+00	6.6302E+00
Ursus spelaeus spelaeus	7.5288E+00	7.0964E+00	6.8463E+00	6.5283E+00
Ursus ingressus	7.3214E+00	6.8718E+00	6.6230E+00	6.0993E+00

3

3.4. Paranasal sinuses in European cave bears (*Ursus spelaeus* s.l.) allowed long hibernation periods by decreasing basal metabolic rates

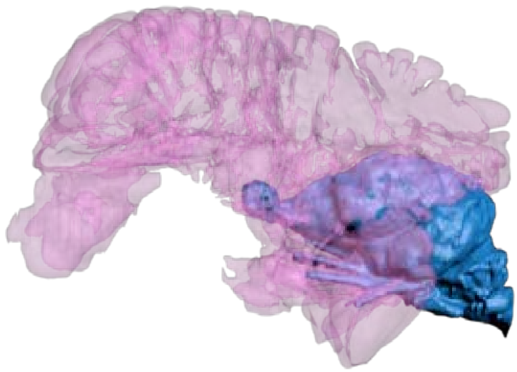

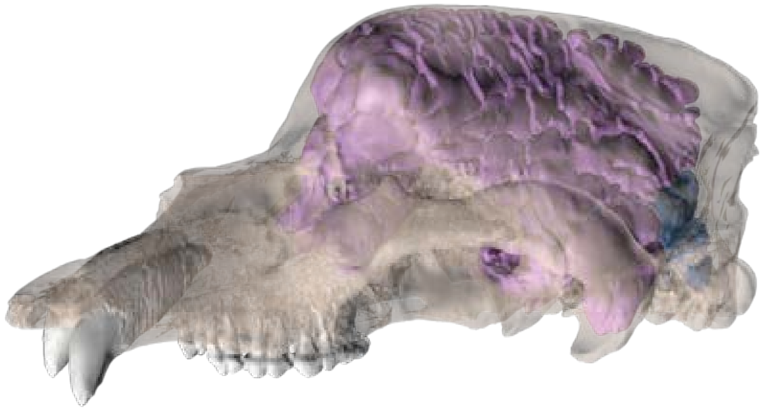

3.4. Paranasal sinuses in European cave bears (*Ursus spelaeus* s.l.) allowed long hibernation periods by decreasing basal metabolic rates

3.4.1. Abstract

The cave bear (*Ursus spelaeus s.l.*) was an emblematic species of the Pleistocene megafauna that presumably spent long periods in hibernation to overcome the long and cold winters of the late Pleistocene. Here, I use allometric equations to estimate body mass, basal metabolic rate (BMR), and the annual intake in cave bears to address if they could have spent long periods in hibernation feeding on highly-fibrous, low-energetic resources during the active period. Moreover, as paranasal sinuses seem to be involved in decreasing BMRs in hibernating mammals, we investigate whether the extremely large sinuses of cave bears could be involved in decreasing their BMRs, and hence, allowing longer periods of hibernation than extant hibernating bears. Following our results, I predict an energetically possible period of hibernation for cave bears up to eight months. The results indicate a significant negative association between paranasal sinuses size and BMR in living bears, demonstrating that those species with larger sinuses also posses low BMRs. Therefore, the extremely large sinuses of cave bears could have allowed the long periods of hibernation necessary to overcome the longer and more severe winters than today of the Late Pleistocene. Moreover, an histo-morphometric analysis of cancellous bone (i.e., the density of connections among trabeculae), indicates that cave bears possessed a trabecular bone of very low-density, which could evidence a metabolically economized ossification by the effect of high levels of NO in blood during hibernation.

3.4.2. Introduction

Closely related to the brown bear (*U. arctos*) and the polar bear (*U. maritimus*), the cave bear (*Ursus spelaeus* s.l.) was an emblematic bear species of the Pleistocene megafauna that went extinct *ca*. 24,000 years ago during the beginning of the Last Glacial Maximum. Previous hypothesis predict that cave bears were more dependent of caves than living bears and they spent long periods in hibernation to overcome the long and cold winters of the late Pleistocene. In fact, Late Pleistocene caves of Europe have yielded a huge number of cave bear remains that likely died during hibernation, generation after generation, over periods of hundreds or even thousands of years. The mortality profile in most of the sites corresponds to an accretionary, non-violent accumulation (Kurtén 1957; Kurtén 1976; Stiner 1998), where young individuals represent up to 70% of the total population (Weinstock 2000). While mortality causes for young individuals are proposed to be due to their lack of experience in obtaining food for themselves or to the difficulties of successfully overwintering, mortality causes for older individuals is usually attributed to either accidents, illness, or a lack of sufficient fat storage to endure winter hibernation (e.g., Grandal-d'Anglade et al. 2019)

Hibernation is the ability to stay in an energy-conserving state of torpor during the coldest months of the year when food is scarce or unavailable (Grandal-d'Anglade 2019). Therefore, hibernation is obviously a 'winter activity' to overcome the scarcity of food during this season in septentrional parts of the world (Nedergaard and Cannon 1990). Previous studies have demonstrated that the duration of the hibernation bouts are correlated with surrounding temperature (**Fig. 1A**), at least in small mammals with repeated arousals to normothermia that periodically interrupts torpor

(Lyman et al. 1982); hibernation bouts are indeed longer in those mammals exposed to lower environmental temperatures.

During winter, animals have to increase its metabolism several-fold to counteract heat loss to the surroundings, which implies an important energetic expenditure. In fact, oxygen consumption increases with decreasing environmental temperatures (**Fig. 1B**).

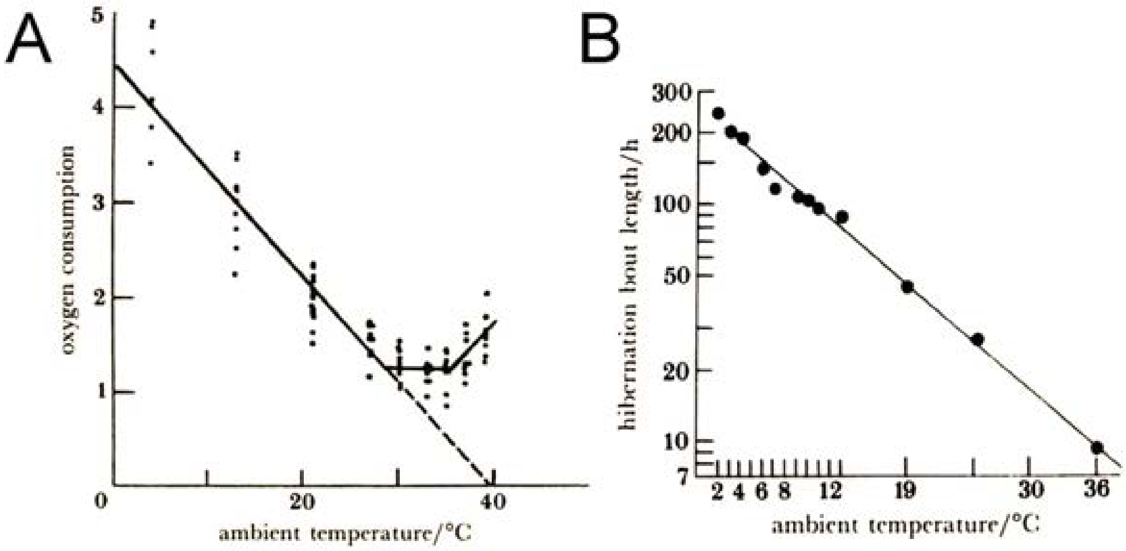

Figure 1. **Effect of environmental temperature on mammalian hibernation**. **A**, effect of environmental temperature on metabolic rate (oxygen consumption) in the Eastern chipmunk (*Tamias striatus*). **B**, Length of hibernation bout as a function of environmental temperature in ground squirrels. Modified from Nedergaard and Cannon (1990).

Hibernating mammals save this energetic expenditure by decreasing body temperature to that of the surroundings (Nedergaard and Cannon 1990). A reduction of body temperature from 37 °C to about 7 °C for the whole winter suppose a 10-30-fold reduction in energetic expenditure (Nedergaard and Cannon 1990).

Given the negative allometric relationship between basal metabolic rate and body mass (McNabb 2008), size increase entails that the amount of energy stored to overwintering in hibernation becomes smaller relative to body mass. Accordingly, in large mammals the energetic cost of a winter is affordable (Nedergaard and Cannon 1990). For this reason, during decades, it has been though that no mammals larger than 5 kg (including bears) do a 'true' hibernation in the strict sense. In fact, in contrast to hibernating small mammals, bears do not display repeated arousals, but instead showed multiday oscillations of body temperature between 30° C and 36°C (Tøien et al. 2011). However, it has been demonstrated that hibernating bears reduce their metabolic rate to 75% below basal metabolic rate (BMR) (Tøien et al. 2011). Due to the allometric relationship of BMR with body mass, this metabolic reduction is less important than in small mammals, which reduce their metabolic rate up to 98% below BMR (Tøien et al. 2011). Moreover, the observed minimum metabolic rate in hibernating bears is within the range of those observed in small hibernating mammals (Heldmaier 2011), which implies that bears use the entire mammalian scope of metabolic inhibition in torpor and are true hibernators (Tøien et al. 2011).

During hibernation, which can reach up to six months for some living bear species (e.g., the American black bear, *Ursus americanus*) the bear's metabolism changes to a special state by decreasing the metabolic rate to 75% below BMR (e.g., Nelson et al. 1973; Tøien et al. 2011) and the bear does not drink, eat, urinate or defecate (Hellgren 1998). As a consequence, a substantial decrease in heart rate is accompanied by a moderate decrease (≈ 7ºC) in body temperature (e.g., Tøien et al. 2011) and the bear survives by mobilizing its fat reserves acquired during predormancy.

This decrease in bear body temperature, heart rate and blood pressure are the response to the activation of the nitric oxide synthase (NOs), which is activated when the levels of CO_2 (hypercapnia) in blood are high and the levels of O_2 (hypoxia) are low at the beginning of hibernation (e.g., Carnio et al. 1999; Arnal et al. 1999; O'Hearn et al. 2007; Kudej et al. 2007).

The pathways of NO and Hydrogen sulfide (H_2S) are linked to the control of hibernation in bears, as both metabolites (NO and H_2S) are related to the induction of several responses to stimuli of biological stress (Revbesch et al. 2014).

The epithelium of the paranasal (sphenoidal) sinuses are involved in the production of NO and H_2S (Lundberg et al. 1995, 2008; Haight et al. 1999; Kim et al. 2001; Petruson et al. 2005; Arnal et al.1999; Keir et al. 2009; Yan et al. 2017) and they function as a reservoir for NO (Andersson et al. 2002). These metabolites are involved in decreasing metabolic rates to 75% of basal metabolic rates. Moreover, in **chapter 3.3**, I demonstrated that paranasal sinuses volume in hibernating bears are > 25% of the skull volume, and this should be related to the necessity of decreasing metabolic rates during hibernation. However, the 'termitophagous' sloth bear *M. ursinus* possesses the larger relative sinuses volume among living bears and it does not hibernate. A possible explanation is that *M. ursinus* have the lowest metabolic rate among living bears as a consequence to subsist on a low-energetic diet based on termites (McNab 1992). Therefore, while large sinuses are necessary to spend large periods of hibernation with a low metabolic activity in *U. americanus* or in *U. arctos*, the large sinuses of *M. ursinus* are involved in decreasing its basal metabolic rate to subsist on a low-energetic diet (McNab 1992). This explains the key role of large sinuses in lowering basal metabolic rates to afford either a low energetic diet or to hibernate.

In this chapter, I specifically explore if paranasal sinuses allowed the long hibernation periods proposed by other researchers for cave bears by decreasing their BMRs. To investigate this, I perform a bivariate regression approach of sinuses volume against BMRs in living bears (both variables independent of body mass). Sinuses volume were obtained from segmented sinuses using skull CT scans and I calculated the BMRs in living bears using the allometric equations of McNab (2008) for active periods and of Robbins et al. (2012) for periods of hibernation. The results confirm a negative association between sinuses size and basal metabolic rates, and those species with larger sinuses and lower metabolic rates are those species that regularly hibernate.

I also estimated the body masses of all species/subspecies within the cave bear group (*U. spelaeus* s.l.) using the equation of Figueirido et al. (2011) to estimate theoretical BMRs in cave bears using the aforementioned allometric equations.

To test the hypothesis that the low BMRs in cave bears could have allowed to extend their hibernation periods to overcome the longer and severe winters of the Late Pleistocene, I perform theoretical calculations of the mean annual intake of cave bears using the equation of Farlow (1976) to estimate their energetic requirements according to their inferred BMRs. The results reveal that a period of 8 months of hibernation is plausible according to their inferred energetic requirements. Moreover, a new histo-morphometric method based on the density of connections among trabeculae of cancellous bone is developed. The main objective is to investigate whether the osteoclastic activity in cave bears was lower than in other bears because of a low metabolic activity (Burkhardt et al. 1987; Ding et al. 2018) but without experiencing bone resorption (Seger et al. 2011; Rubin et al. 2000, 2003).

3.4.3. Material and methods

3.4.3.1. Material

We CT-scanned eight skulls belonging to all living bear species (*Ursus arctos* [USNM 82003], *Ursus maritimus* [H. 001-05], *Ursus americanus* [USNM 227070], *Ursus thibetanus* [VU 2421], *Melursus ursinus* [AMNH54464], *Helarctos malayanus* [AMNH28254], *Tremarctos ornatus* [VU 1661] and *Ailuropoda melanoleuca* [VU 3156b]) and four skulls belonging to the cave bear group (*Ursus spelaeus* s.l.): *Ursus ingressus* [PIUW3000/5/105] and *U. spelaeus s.s.* (*U. spelaeus spelaeus* [E-ZYX-S-1000]; *U. spelaeus ladinicus* [PIUW-CU 703]; *U. spelaeus eremus* [PIUW-SW 483]). For the conditions of CT-scan acquisition see Supplementary Material.

The CT scanner used for *Ailuropoda melanoleuca* and *Tremarctos ornatus* was a medical scanner Aquilion 32 TOSHIBA with 32 multislicer at University Hospital of Valladolid. The conditions of acquisition in the CTscan were a 512x512 image matrix. 120 Kv and 250 mA. For each specimen the following CT data was obtained: The voxel size for *T. ornatus* was 0.3819 (X.Y) and 0.5 mm of inter-slices (Z) and the voxel size for *Ailuropoda melanoleuca* were 0.5200 (X.Y) and 0.3 mm of inter-slices (Z).

The CTs of *Ursus arctos*, *Ursus maritimus* and *U. americanus* were obtained from the Digimorph website (http://www.digimorph.org). The scans were performed at the University of Texas High-Resolution X-ray CT Facility with either a 1024X1024 image matrix, resulting in inter-slice spacing in the range 0.70–1 mm.

The conditions of acquisition in the CT scanning for *Ursus arctos* were 450 kV, 3 mA, obtaining 425 slices. For *Ursus maritimus* was 420kV, 1.8 mA, obtaining 540 slices. The CT of *Ursus americanus* (USNM 227070) were performed with either a 1024X1024 image matrix, pixel slice is 0.325 mm thick and each pixel size (x) and (y) were 0,2930 mm with an interslice spacing of 0.325 mm in (z) with a field of reconstruction of 300 mm. The conditions of acquisition in the CT scanning were P250D, 450 kV and 1.3 mA; obtaining 475 slices.

The CT of *Ursus spelaeus ladinicus* (PIUW-CU 703) was scanned at the University of Vienne using a microCT machine Viscom X8060. The conditions of acquisition were 130kV and 330 microA, obtaining 2732 slices and voxel size 0.15mm in X, Y, Z axes. The CT of *Ursus spelaeus eremus* (PIUW-SW 483) and *Ursus ingressus* were CT scanned at the private medical center of the city of Málaga (Spain), using GE Medical Systems (Brivo CT385 Series) scanner machine. The conditions of acquisition were 512x512 image matrix, 120Kv and 160 mA, with an interslice of 0.2mm. For *Ursus spelaeus eremus*, we obtained 2573 slices with a voxel size of 0.5332 for (X, Y) and 0.2 (Z). For *Ursus ingressus,* we obtained 2601 slices with a voxel size of 0.6113 for (X. Y) and 0.2 (Z).

The CT of *Ursus spelaeus spelaeus* (E-ZYX-1000) was CT scanned at a veterinarian Hostpital Rof Codina, Lugo. Spain. The conditions of acquisition were 512x512 image matrix, 120Kv and 160 mA, with an interslice of 0.365mm. For this specimen we obtained 1386 slices with a voxel size of 0.75 for (X, Y) and 0.3650 (Z).

3.4.3.2. Inferring BMRs and hibernation length in cave bears

During hibernation, the bear's metabolism changes to a special state by decreasing the BMR (e.g., Nelson et al. 1973), heart rate and a decrease in body temperature (e.g., Tøien et al. 2011). Therefore, reliable estimates of BMR are key to investigate if cave bears could have longer hibernation periods that living bears. To estimate reliable BMRs in cave bears, we use two allometric equations that allow obtaining the daily basal metabolic rates, during active periods (BMR_a) and during hibernation (BMR_h). The BMR_a was computed from McNab (2008), which considered both physiological and ecological factors:

(1) BMR_a (kJ/day) = 0.064*(M * I * S * T * C * H * E * F) * BM (g)$^{0.694}$

where *M,* makes reference to mountain or lowlands factor; *I* island or continents; *S* is the substrate use; *T* is a torpor factor (torpor/hibernation or no torpor-no hibernation); *C* is a climatic factor; *F* is food habits; E is the infraclass) and BM is body mass in grams (see McNab 2008). As McNab (2008) considered mean BMRs for all mammalian species, in those species that hibernate, the BMRs for active periods and during hibernation collapse. Therefore, we only considered in the calculations of BMR_a, the highest values in active behaviour and we included the *T* factor without effect of hibernation or torpor.

The second equation was used to estimate the BMR_h using the allometric equation of Robbins et al. (2012) but modified to obtain kJ/day as unit, in order to make the values comparable with those obtained from McNab (2008) for the BMR_a:

(2) BMR_h (kJ/day) = (7.4* BM (kg)$^{1.06}$)* 4.184

The body masses for the living species were obtained from different sources: PanTHERIA database (Jones et al. 2009), Nie et al. (2015), and Shimozuru et al. (2012) (see Table S2 for details). The body masses of cave bears were estimated using a multiple regression function published by Figueirido et al. (2011) for living caniforms:

(3) Log10 (*BM*) = −6.641 (±.469) + 0.692 (±0.477) Log10 (*POP*) +6.7209 (±1.242) Log10 (*SKl*) − 3.790 (±0.868) Log10 (*BSCl*)

where *POP* is the postorbital process, *SKl*, skull length and *BSCl*, basicranial length. These variables were measured from the 3D models of the specimens of cave bears with MeshLab.

From these values of daily BMR_h and BMR_a, we can estimate the annual BMR ($_{an}$BMR) with varying periods of activity/hibernation using the equation:

(4) $_{an}BMR$ (MJ/year) = ((BMR_a * dia) + (BMR_h * dih)) / 1000

where *dia* are the number of days during the period of activity and *dih* are the number of days during the period of hibernation. We considered six different periods of activity/hibernation: 270, 240, 210, 180, 150 and 120 days, following the periods of activity/hibernation in living bears and the proposed periods for cave bears from previously published studies.

For inferring the annual energy intake (AI) necessary for cave bears, we applied an equation developed by Farlow (1976) to predict the energetic requirements of herbivorous mammals, using as references the values for brown bears:

(5) AI: log *intake* (kcal/day) = (0.72830±0.01976) * log *BM* (g) + 0.18124

We used this equation because both biogeochemical (e.g., Bocherens et al. 1994; Bocherens et al. 1999) and morphological studies (e.g., Pérez-Ramos et al. 2019; van Heteren and Figueirido 2019) predict that cave bears were highly herbivorous. Moreover, different studies have demonstrated that the living brown bear (*U. arctos*), American black bear (*U. americanus*) and the giant panda (*A. melanoleuca*) have a similar efficiency for digesting proteins; they are characterized by a lack of symbiotic microflora and fermentation compensated by a large retention time during digestion (Dierenfeld et al.1982, Pritchard and Robbins 1990). Pritchard and Robbins (1990) claimed that bears could increase the intake of a large amount of low quality food in order to reach the necessary energetic requirements to avoid starvation.

3.4.3.3. Testing the influence of sinus size on BMR and hibernation length

To test our hypothesis that sinuses volume has a role in decreasing metabolic rates in living ursids, we performed the following bivariate regressions: First, we regressed the sinuses volume (SiV) on skull volume (SkV), both variables log-transformed, in all living bear species, and we extracted the residuals of this regression –i.e., the amount of SiV that is not explained by the amount of SkV according to the adjusted regression model; Second, we regressed the basal metabolic rates (BMR) on average body mass for each living species, both variables log-transformed, and we extracted the residuals of this regression –i.e., the amount of BMR that is not explained by the amount of body mass according to the adjusted regression model. Both regressions were performed using Ordinary Least Squares (OLS). Afterwards, the residuals of the first regression (res [SiV-SkV] were regressed on the residuals of the second regression (res [BMR-BM]) using Reduced Major Axis (RMA) in order to explore the association of SiV on BMR independent of body mass.

We obtained the SiV and SkV from the segmented 3D models of sinuses and skulls for each species analysed with the software Strand7 (**Fig. 2**). To segment the sinuses the following works are used for the current specimens, Yee et al. 2016; Negus et al. 1954; Joeckel 1998; Alsafy et al. 2013; Bahar et al. 2014; König et al. 2013; the book PALASIATICA 2011; Weeden et al. 2016; Treuting et al. 2017; and Farke 2008. For fossil specimens has been followed Rabeder et al. 2009, 2010.

The values of BMR used were those of MacNabb (2008), which is an average BMR for activity and hibernation. All analyses of this section were performed with PAST version 2.07 (Hammer et al. 2001).

3.4.3.4. Histomorphometric analysis of cancellous bone

A cube of 1000 mm3 of cancellous bone was virtually dissected on the temporo-mandibular joint of each CT scan (see **Fig. 3; Supp. Info**). Different parameters of cancellous bone were computed such as the degree of connectivity among trabeculae, bone thickness, and bone volume fraction. The connectivity is the number of connected trabeculae in a network (Odgaard et al. 1993). Prior to calculate the connectivity, it is required to prepare the stack images by removing all isolated particles from the foreground and background. Bone thickness and Bone volume fraction (Bone Volume/Total Volume) indicate the degree of bone mineralization (Hildebrand et al. 1997). Therefore, while the first one is the volume of mineralized bone per unit volume of the sample (1000 mm^3 in our case), the second measures the total thickness of bone (see **Fig. 3**).

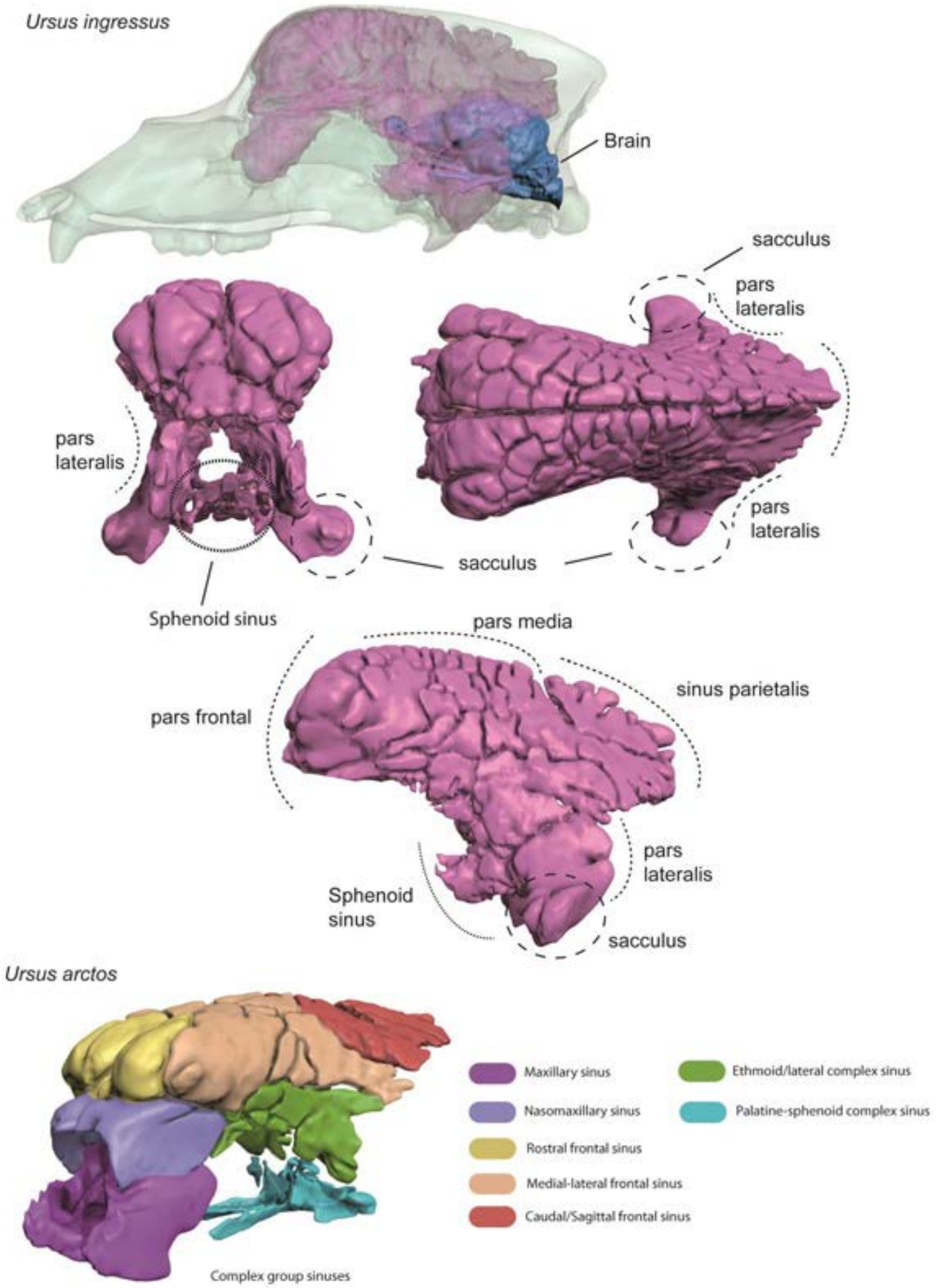

Figure 2. **Segmentation of paranasal sinuses necessary to calculate paranasal sinuses volume and skull volume**. The anatomical comparison of the sinus between the living species, *Ursus arctos* and the extinct species, *Ursus ingressus*. From left to right: lateral, dorsal and frontal views of the paranasal sinuses.

Afterwards, the relationships among these variables were explored using Ordinary Least Squares (OLS) Bivariate Regression Analysis with PAST version 2.07 (Hammer et al. 2001).

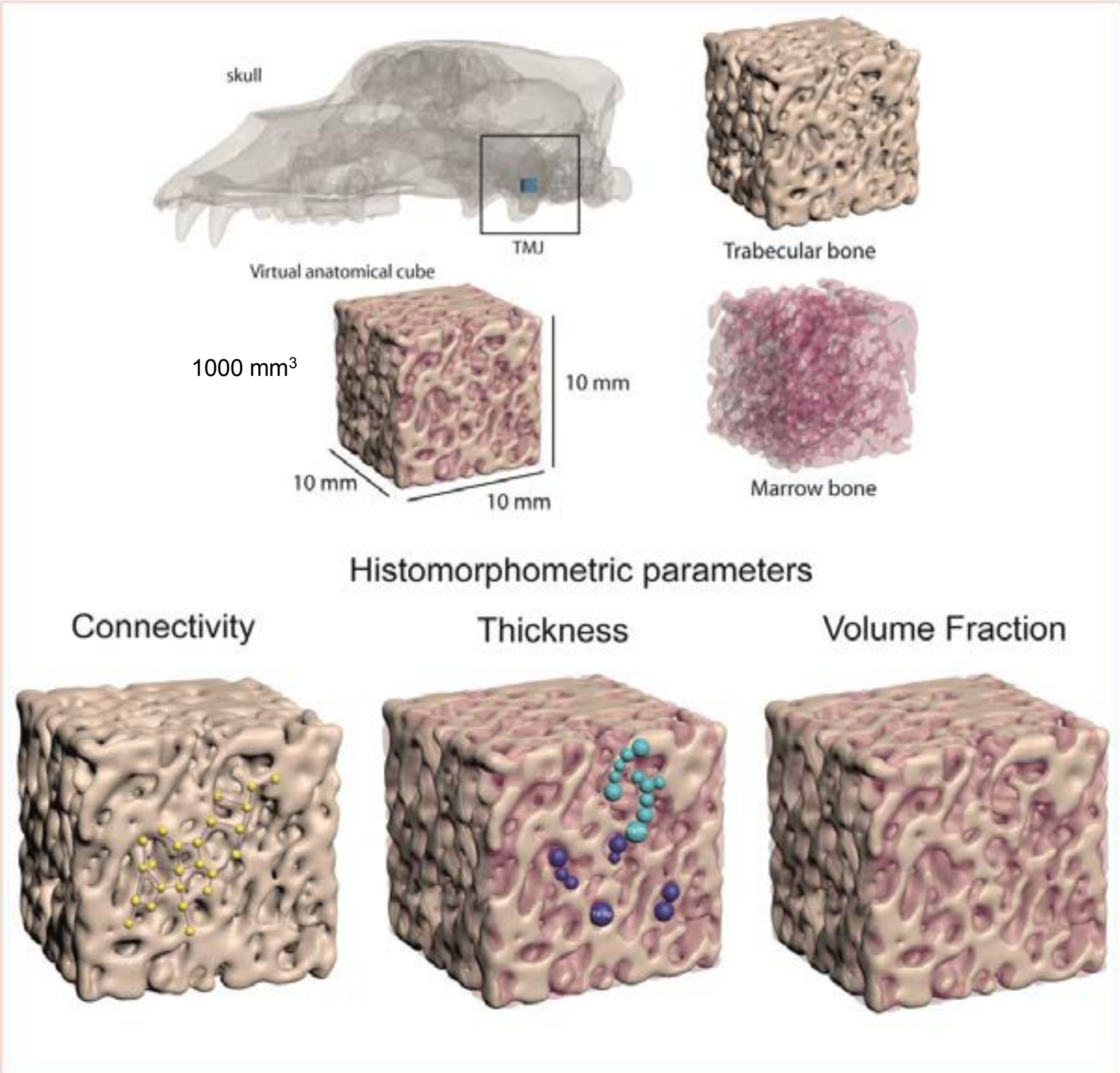

Figure 3. **Histomorphometric analysis of a 1000 mm^{3}cube obtained from the temporo-mandibular joint (TMJ)**. Light blue spheres represent the trabecular thickness (Tb.Th), and purple spheres represent the trabecular space (Tb.Sp).

3.4.4. Results and discussion

3.4.4.1. Hibernation length in cave bears

The inferred body masses for cave bears using the multivariate regression equation of Figueirido et al. (2011) range from 148.75 kg for *U. sp. ladinicus* to 745.41 Kg for *U. ingressus* which are within the range values estimated for cave bears using the mediolateral diameter of the femur midshaft (Veitschegger et al. 2018). The estimated body masses for *U. sp. spelaeus* is 657.48 Kg and for *U. sp. eremus* 443.50 (**Table 1**). The inferred BMR_a and BMR_h using the allometric equation of MacNabb (2008) for activity periods and the equation of Robbins (2012) during hibernation (**Table 1**) indicated that BMR_a decreases between 3.3 kJ/day in the brown bear (*U. arctos*) and 1.4 kJ/day in the sloth bear (*M. ursinus*). However, Robbins et al. (2012) only included living bears with a maximum average body mass of 300 kg, and therefore, the values of BMR_h for those species with average body masses exceeding 300 kg –i.e., *U. sp. spelaeus*, *U. sp. eremus*, and *U. ingressus*– are very close (or even higher) than the inferred values of BMR_a. Accordingly, we corrected the allometric equation of Robbins (2012) for *U. spelaeus eremus*, *U. spelaeus spelaeus*, and *U. ingressus*. To do this, we computed a ratio of BMR_h obtained from Robbins (2012) and BMR_a obtained from McNab (2008), and we took the highest value of this ratio for living species (i.e., 68.4 % for *U. arctos*; **Table 1**) as a correction factor for the three specimens with an average body mass greater than 300Kg. Accordingly, the BMR_h values for *U. spelaeus eremus*, *U. spelaeus spelaeus*, and *U. ingressus* were 15,835 kJ/day, 20,811 kJ/day, and 22,705 kJ/day, respectively.

The inferred $_{an}BMR$ for different periods of activity/hibernation –i.e., 270, 240, 210, 180, 150 and 120 days are shown in **Table 2**. In general terms, higher hibernation periods entail lower $_{an}BMR$. As expected for the greater body mass of cave bears, recent species had lower $_{an}BMR$ than extinct bears, excepting *U. spelaeus ladinicus* that had values of body mass and $_{an}BMR$ between the range of the values for the brown (*U. arctos*) and black bears (*U. americanus*). In the case of *U. ingressus*, given its huge body mass, its $_{an}BMR$ could be approximately three-fold higher than the $_{an}BMR$ of the brown bear.

Table 1. Body masses, basal metabolic rates in activity (BMR_a) and in hibernation (BMR_h) (and the relative percentage of BMR_h against BMR_a in hibernating bears, living and extinct.

Species	BM (kg)	BMR_a (kJ/day)	BMR_h (kJ/day)	BMR_h / BMR_a (%)
U. arctos	170.00	10,466	7,163	68.4
U. americanus	129.50	8,665	5,368	62.0
M. ursinus	66.96	4,078	2,668	65.4
U. sp. ladinicus	148.75	10,841	6,218	57.4
U. sp. eremus	443.50	23,138	15,835*	85.5
U. sp. spelaeus	657.48	30,409	20,811*	98.8
U. ingressus	745.41	33,176	22,705*	103.5

The inferred energetic requirements for cave bears using the equation of Farlow (1976) using as reference values those of their close relative, the brown bear (*U. arctos*) are shown in **Table 3**. The length of hibernation of the brown bear (*U. arctos*) is 150 days on average (range between 180 and 120 days. The $_{an}BMR$ for the brown bear with 150 days of hibernation is 3,325 MJ year (**Table 2**) and the *AI* is 13,342 MJ (**Table 3**).

Table 2. Annual Basal Metabolic Rate (${}_{an}BMR$) (in megajoules (MJ) per year) of living hibernating bears and cave bears for different hibernation periods (in days).

Species	**${}_{an}BMR$ (MJ/year) for different periods of hibernation (in days)**					
	270	**240**	**210**	**180**	**150**	**120**
U. arctos	2,928	3,027	3,127	3,226	3,325	3,424
U. americanus	2,273	2,372	2,470	2,569	2,668	2,767
M. ursinus	1,108	1,150	1,192	1,235	1,277	1,319
U. sp. ladinicus	2,709	2,847	2,986	3,125	3,263	3,402
U.sp. eremus	6,474	6,693	6,912	7,131	7,350	7,569
U. sp. spelaeus	8,508	8,796	9,084	9,372	9,660	9,947
U. ingressus	9,282	9,596	9,910	10,225	10,539	10,853

Therefore, the energetic requirements per year for the brown bear (*U. arctos*) is four times its ${}_{an}BMR$ with a period of 150 days of hibernation. However, it should be noted that the equation of Farlow (1976) is adjusted using herbivorous mammals and brown bears possess an omnivorous diet.

To estimate hibernation length in cave bears, we have used as reference the ratio between the *AI* and the ${}_{an}BMR$ for the brown bear with a period of 150 days of hibernation, i.e. approximately four times. A ratio close to 4 corresponds with a hibernation length between 150-120 days for *U. americanus*, 210 days for *U. spelaeus ladinicus*, between 240 and 210 days for *U. spelaeus eremus*, *U. spelaeus spelaeus*, and *U. ingressus*. The results demonstrate that cave bears had longer hibernation than recent bears.

Table 3. Estimations of the annual intake (in megajoules, MJ), or energetic requirements, for living and extinct bear species using Farlow's equation (1976) for herbivorous mammals.

Species	Annual consumption (MJ)
U. arctos	13,342
U. americanus	10,943
M. ursinus	6,769
U. sp. ladinicus	12,106
U.sp. eremus	26,823
U. sp. spelaeus	35,731
U. ingressus	39,151

To translate these results into daily intake, we used the values of nutrient composition of Pritchard and Robbins (1990) and Erlenbach et al. (2014). For a diet based on tubers (carrots-yams), a gram of dry matter provides 17.25 kJ, being the percentage of dry matter 16.8% (Pritchard and Robbins 1990). If the $_{an}BMR$ of *Ursus ingressus* was 9,596 MJ/year with a period of hibernation of 240 days per year, it would consume 556 kg/year of dry and 3311 kg/year of fresh matter to fulfil its basal requirements, i.e., 26 kg/day (125 days of active mode). Furthermore, if we considered energetic requirements inferred from Farlow (1976) (**Table 3**), *Ursus ingressus* would daily consume 108 kg of tubers. Thus, we obtained a range of maximum and minimum consumption between the $_{an}BMR$ and the *AI*. Considering a diet based on apples (11.72 kJ/g of dry matter, with a percentage of dry matter 15.0%) (Erlenbach et al. 2014), *U. ingressus* could daily consume between 178 and 44 kg of apples during 125 days in active mode.

Erlenbach et al. (2014) analyzed the consumption of digestible energy by brown bears (*U. arctos*) in captivity and observed that bears feed 9.6±2.1 times the BMR_a in fall and 8.7±0.7 times the BMR_a in spring. We can contrast our results of *AI* with this proportion of digestible energy and BMR_a. For doing that, we estimated the consumption of digestible energy with a period of 150 days of hibernation for the brown bear (*Ursus arctos*), multiplying the BMR_a per the number of days in active behaviour and per the average of the ratios obtained by Erlenbach et al. (2014) in fall and in spring (i.e., 9.15). This calculation results in an annual intake of 20,590 MJ, which is higher that the inferred annual intake using Farlow's (1976) equation (**Table 3**).

3.4.4.2. Sinuses volume and basal metabolic rates

The segmented sinuses of living bears and of cave bears are shown in **Figures 4**,**5**, respectively. Despite the low sample size, the bivariate regression of SiV on SkV was slightly significant, which indicates that sinus volume is influenced by skull volume (**Table 4**; **Fig. 6A**). As expected, the bivariate regression of BMR_a obtained from McNab (2008) against body mass was highly significant (**Table 4**; **Fig. 6B**). Similarly, the res [SiV-SkV] was negatively associated with the res [BMR-BM] (**Fig. 6C**; **Table 4**), which indicates that those species that possess a greater sinus volume than expected for their skull volume also possess lower values of BMR_a for their body masses and vice versa. Our results evidence that higher sinus volume is associated with lower BMR_a independent of body mass, which support the hypothesis that large sinuses should have a role in decreasing basal metabolic rates, and therefore, facilitates hibernation. In fact, while non-hibernating bears increase the relative sinus volume to skull volume (SiV/SkV) concomitant to the relative BMR_a to body mass (BMR_a/BM), non-hibernating bears decrease the first ratio against the second (**Fig. 6D)**.

The exception to this pattern is found in the sloth bear, *M. ursinus*, which is a non-hibernating bear with a basal hypometabolic rate, mostly related to its low-energy diet based on ants McNab (1992).

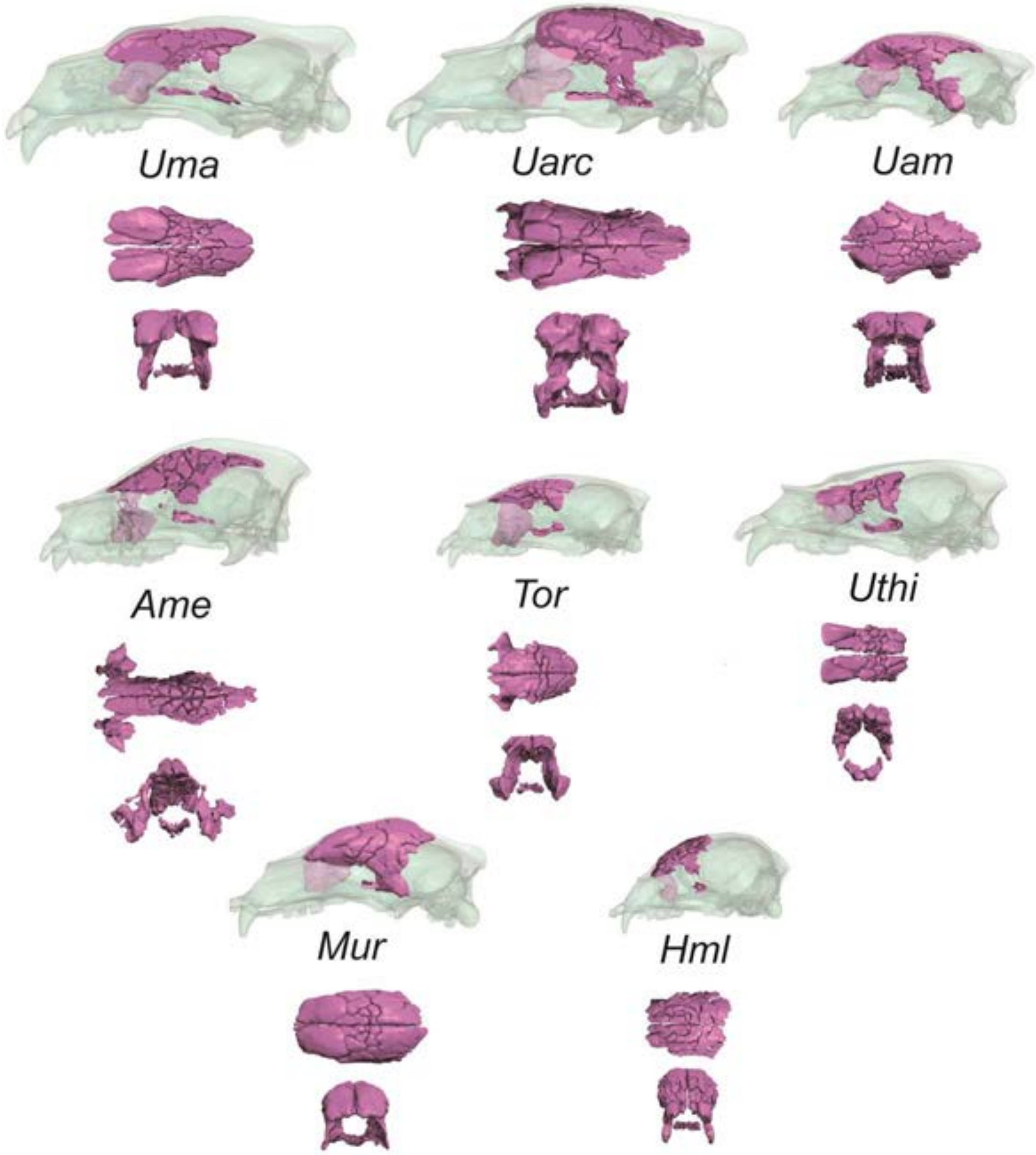

Figure 4. Segmented sinuses of living bears in lateral (inside the skull, in transparent), dorsal (medium) and frontal (bottom) views. Abbreviations: Uma, *U. maritimus*; Uarc, *U. arctos*; Uam, *U. americanus*; Ame, *A. melanoleuca*; Tor, *T. ornatus*; Uthi, *U. thibetanus*; Mur, *M. ursinus*; Hml, *H. malayanus*.

In any case, the fact that the sloth bear plots with truly hibernating bears such as the brown bear (*U. arctos*) and the American black bear (*U. americanus*) supports the key role of sinuses in decreasing basal metabolic rates to afford either a low-energetic diet or to hibernate.

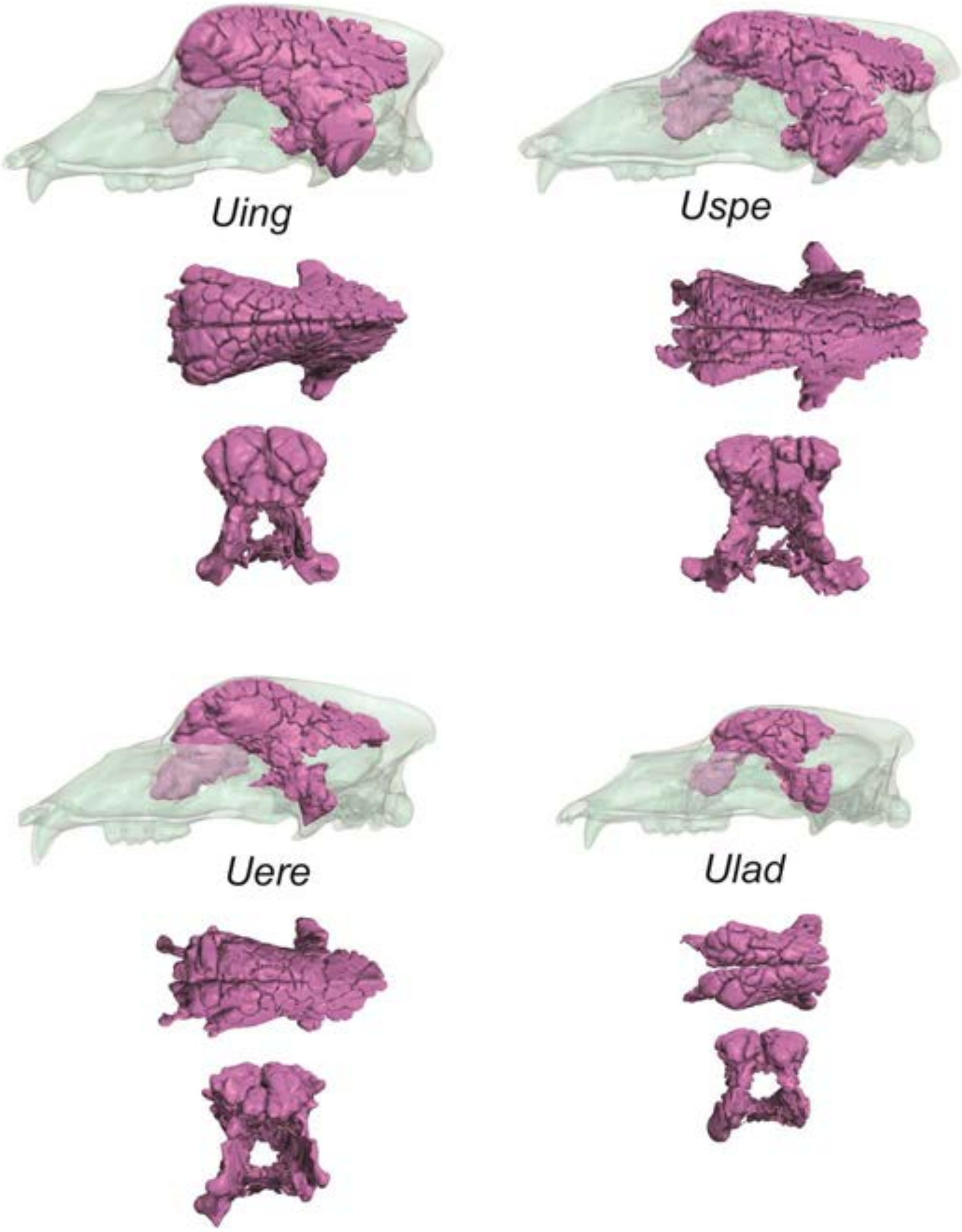

Figure 5. Segmented sinuses of cave bears in lateral (inside the skull, in transparent), dorsal (medium) and frontal (bottom) views. Abbreviations: Uing, *U. ingressus*; Usp, *U. sp. spelaeus*; Uere, *U. sp. eremus*; Ulad, *U. sp. ladinicus*.

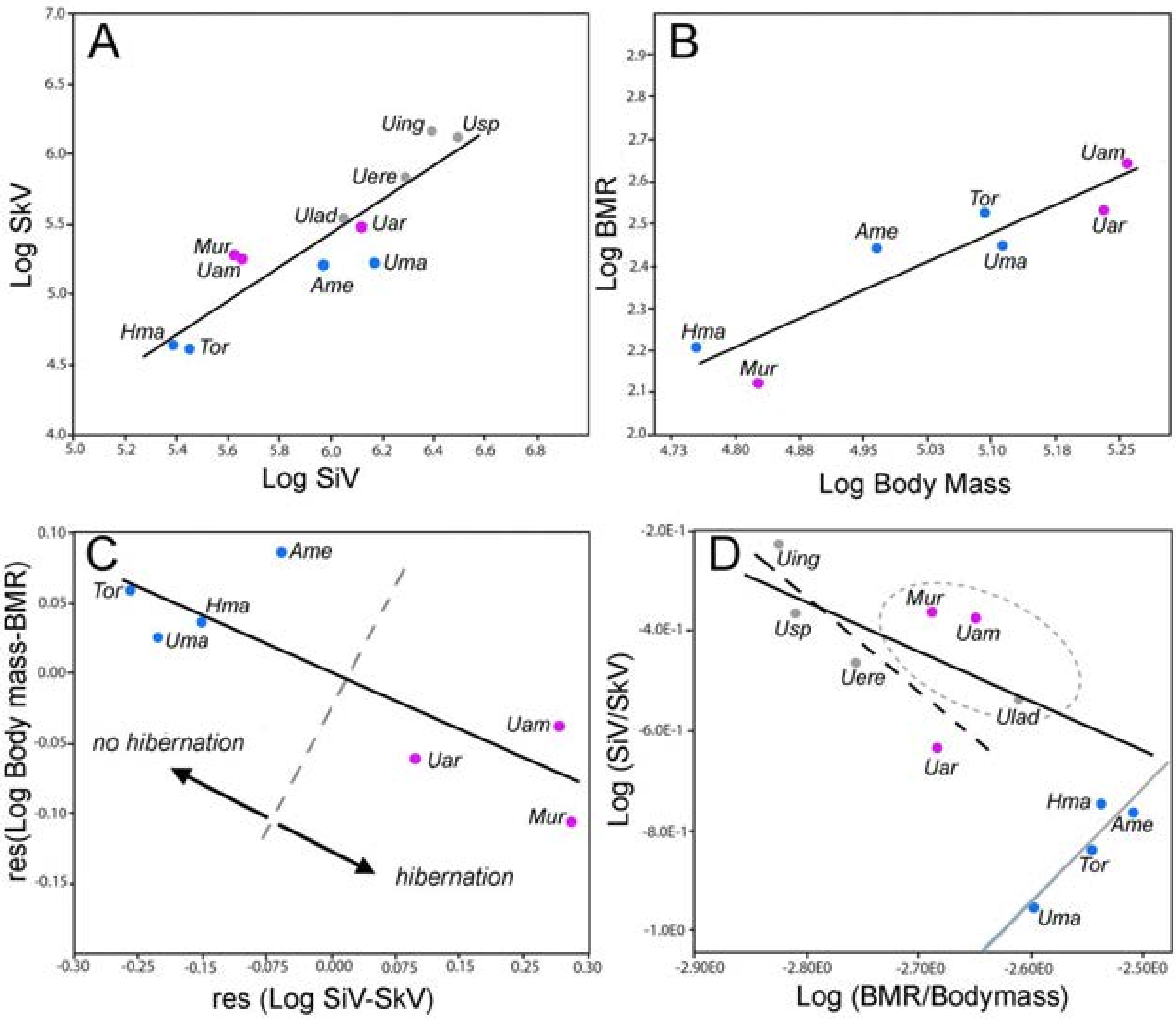

Figure 6. Association between sinuses size and BMRs. **(A)**, Bivariate regression of sinus volume (SiV) on skull (SkV), both variables log-transformed; **(B)** Bivariate regression of Body Mass (BM) in grams on Basal Metabolic rate (BMR) both variables log-transformed; **(C)** Bivariate regression of the residuals obtained in A (res [Log SiV-SkV]) against the residuals obtained in B (res [Log Body Mass-BMR]); **(D)** Bivariate regression between the ratio of SiV/SkV on the ratio BMR/Body Mass, both variables log-transformed; two regression lines are shown; one for purple taxa (hibernators) and the another for blue taxa (non-hibernators), the dotted regression line is only for cave bears (in grey). **Abbreviations**: Ame, *A. melanoleuca*; Hml, *Helarctos malayanus*; Mur, *Melursus ursinus*; Tor, *Tremarctos ornatus*; Uam, *Ursus americanus*; Uarc, *Ursus arctos*; Uere, *Ursus eremus*; Uing, *Ursus ingressus*; Ulad, *Ursus spelaeus ladinicus*; Uspe, *Ursus spelaeus spelaeus*.

Table 4. Results of the bivariate regressions performed from SiV on SkV (1), BMR on body mass (BM) (2), and the residuals of the regression (1) on regression (2). The three bivariate regressions are performed only with living taxa. SiV, SkV, BMR and BM are log-transformed. The values for the slope and the intercept, the Pearson's coefficient squared (r^2) and the permutation test on correlation (r^2) using permutation (9,999 replicates) are given.

Regression	Slope	intercept	r^2	*p*-value
LogSiv-LogSkV	0.81 (0.32,1.58)	-0.44 (-4.18, 3.22)	0.58	0.0481
LogBM-LogBMR	0.89 (0.58,1.28)	-2.11 (-4.05, -0.51)	0.86	0.0036
Res1-res2	-0.27 (-0.41,-0.11)	-0.07 (-0.04, 0.02)	0.69	0.0324

The epithelium of the paranasal (mainly the sphenoidal) sinuses are involved in the production of NO and HS, and they function as a reservoir for NO (Arnal et al.1999; Haight et al. 1999; Kim et al. 2001; Andersson et al. 2002; Petruson et al. 2005; Lundberg et al. 2008; Keir et al. 2009; Yan et al. 2017). These metabolites are related to the induction of several responses to stimuli of biological stress (Revbesch et al. 2014), and they seem to be linked to the control of hibernation in bears, as they decrease body temperature, heart rate and blood pressure as a response to blood hypercapnia and hypoxia at the beginig of the hibernation (e.g., Carnio et al. 1999; Arnal et al. 1999; O'Hearn et al. 2007; Kudej et al. 2007). Accordingly, following these results those bears that hibernate posses larger sinuses than those that do not regularly hibernate, because the formers have lower metabolic rates.

Moreover, one of the most studied hormonal pathways is thyroid hormones. During the seventies, both Nelson and Lundberg began to study the function of the Thyroid on the hibernation. Lundberg et al. (1976) reported increases in total thyroxine (T4) but decreases in total triiodothyronine (T3) in the three bears studied. These results on the role of the thyroid hormones were surprising because they tend to increase oxygen consumption and metabolic rate. Accordingly, with the reduced metabolism that characterizes hibernation (Watts et al. 1988), the thyroid function should also be reduced. Azizi et al. (1979) sampled a higher number of bear specimens and they also improved the control of the T3 and T4 levels during hibernation and during the active period. The results indicated lower levels of T3 and T4 in hibernation and much higher in non-hibernation. On the other hand, Hissa et al. (1994) reported a 50% decrease of T3 and T4 levels in blood during hibernation in brown bears.

Another hormonal control that must be taken into account is the Beta-endorphin (β-END), which is an opioid neuropeptide. At the level of the central nervous system, Franzmann et al. (1981) provided baseline serum levels of beta-endorphins, which are morphine-like peptides found in the brain and pituitary tissue of mammals, in hibernating and active bears. Hibernating black bears had higher levels of beta-endorphins than active black bears, active brown bears, and other non-hibernating mammals. Franzmann et al. (1981) cautiously suggested that because beta-endorphins can reduce blood pressure, respiration, body temperature, and metabolic rate, they might play a role in bear hibernation physiology. Recent data by Hissa et al. (1994), however, showed that beta-endorphin levels decreased during hibernation in brown bears. This fact supports the hypothesis of the relationship between the sphenoid sinus and high values of B-endorphin in blood, because the American black bears is the bear that has the larger sphenoid sinuses among the sample. In addition, its anatomical shape is very close to that found in cave bears, although further morphometric studies of paranasal sinuses in bears should be performed. This suggests that, most probably, cave bears would not only have the general hormonal control previously mentioned, they would have additionally this other hormonal way of the B-endorphin route, which potentiates the hypo-metabolic effect during the period of hibernation.

3.4.4.3. Trabecular density in cave bears

The bivariate regression between the log-transformed trabecular connectivity on bone volume fraction was highly significant (**Fig. 7A**) which indicates that connectivity among trabeculae decreases when the bone volume fraction increases (**Fig. 7A**). Moreover, while those specimens that are plotted above of the adjusted regression line are characterized by having a rod-type trabecular structure, those specimens plotted below of the line have a more plate-like structure. Accordingly, in plate-like structures, each plate-like trabecula contributes significantly to bone density. However, in rod-like structures, each trabecula does not significantly contribute to the total bone density.

The bivariate regression of Bone volume fraction on Body Mass (**Fig. 7B**) was not significant if cave bears were included (*p*-value=0.07). Strikingly, all cave bears (and the sloth bear) are well-below the adjusted regression line, which indicates that they had very low bone densities to their body masses. Another possibility to explain this pattern is that the body masses of cave bears were overestimated using the equation of Figueirido et al. (2011). However, the second possibility could be ruled out because: (i) the estimated body masses using the regression equation of Figueirido et al (2011) from craniodental dimensions gave values of body masses for cave bears within the range of other estimations from the postcranial skeleton (Veitschegger et al. 2018); and (ii) when we estimated the body masses for cave bears from their values of bone volume fraction using this regression function, the upper limit for cave bears –that is the body mass for *U. ingressus*– was only 150kg, which is an unrealistically low value. This could indicate that cave bears had bone densities characteristic of a bear of 150 kg.

Despite the high dispersion between the giant panda (*A. melanoleuca*) and the sloth bear (*M. ursinus*) in this graph (**Fig. 7B**), when the bivariate regression was repeated excluding cave bears, the association between bone volume fraction and body mass was highly significant (p-value<0.001) (**Fig. 7B**). The bivariate regression between the inferred BMRs (**Table 3**) and the bone volume fraction was highly significant (**Fig. 7C**). As expected, all cave bear specimens (excepting *U. sp. ladinicus*) are well-above the regression line, which indicates that cave bears have much higher BMRs than the ones expected according to their bone density values. In contrast, the giant panda *(A. melanoleuca*) is below of the regression line, indicating that this bear has a much lower BMR than the one expected according to its value of bone density. However, this could be interpreted that all cave bears have very low bone densities relative to their inferred BMRs, and that the giant panda has much higher bone density values to its BMR.

The high bone density in the giant panda is related to the mutation in the DUOX2 gene, which catalyses a key step in the synthesis of the thyroid hormones T4 (thyroxine hormone) and T3 (triiodothyronine) and generates very low levels of T3 and T4 in blood. This mutation leads to hypothyroidism and this is translated into a low metabolism (Nie et al. 2015; Fei et al. 2016) and a highly-dense skeleton (Wojcicka et al. 2013). Moreover, this mutation of the giant panda could be allowing to fed on bamboo because having a low metabolism allows them to survive with a hypocaloric intake.

On the other hand, a dense craniodental skeleton could contribute to have a high biomechanical advantage to fed on hard and tough foods (Figueirido et al. 2013; Figueirido et al. 2018).

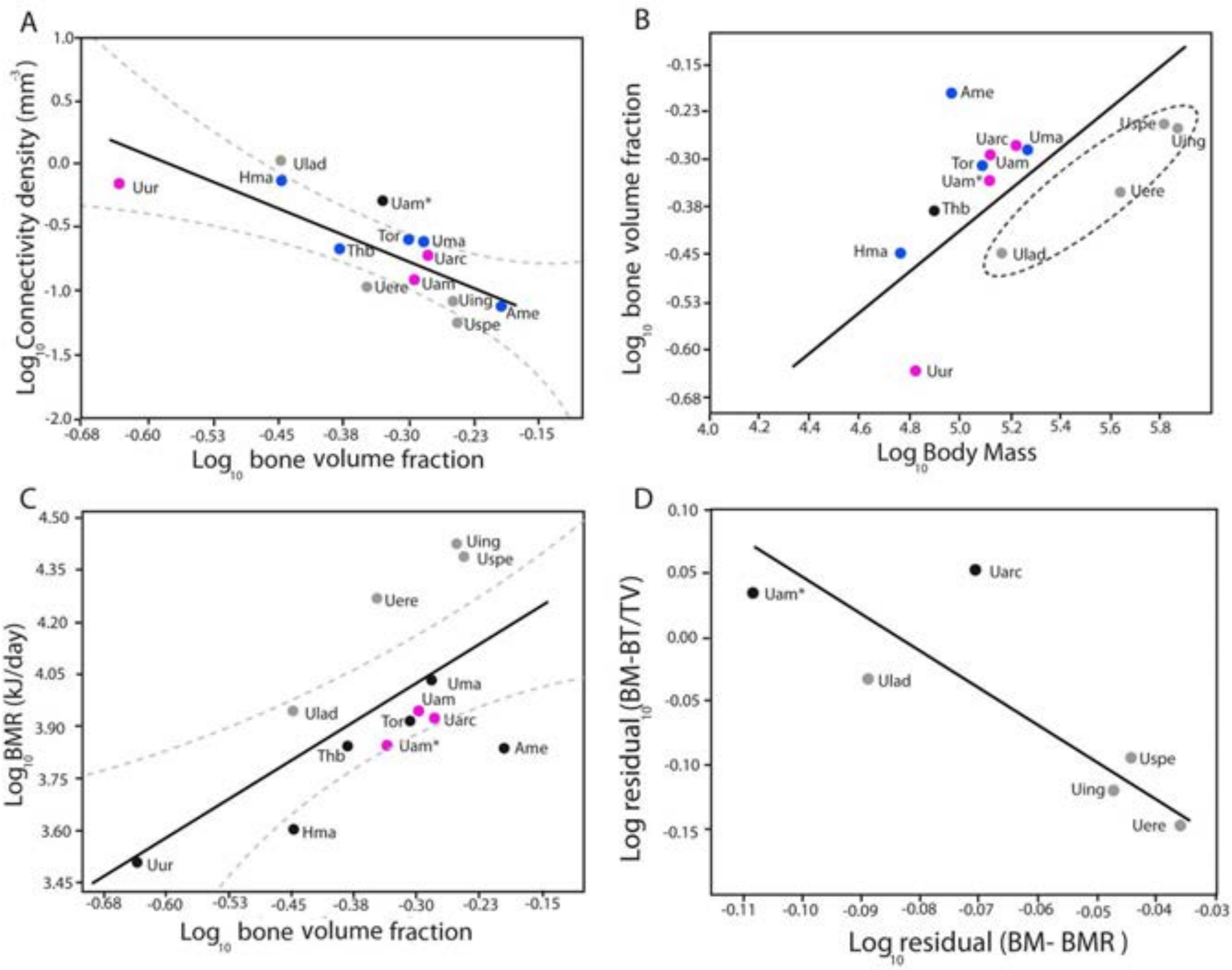

Figure 7. Histomorphometric analysis. (A) Bivariate regression of connectivity density on bone volume fraction bone (both variables log-transformed); **(B)** Bivariate regression of Bone volume fraction on Body mass (in grams), both variables log-transformed; **(C)** Bivariate regression of BMR on Bone volume fraction (both variables log-transformed); **(D)** Bivariate regression of the residuals between BM-BMR and BM- BV/TV). The gray circles are the extinct specimens and the black circles are living specimens. **Abbreviations**: Ame, *A. melanoleuca*; Hml, *Helarctos malayanus*; Uur, *Melursus ursinus*; Tor, *Tremarctos ornatus*; Uam, *Ursus Americanus* (; Uarc, *Ursus arctos*; Uere, *Ursus eremus*; Uing, *Ursus ingressus*; Ulad, *Ursus spelaeus ladinicus*; Uspe, *Ursus spelaeus spelaeus*. **See**: Uam* (from Canada).

Therefore, the histomorphometrics of the cancellous bone indicates that cave bears share the peculiarity of having a very thin trabecular bone, and the shape of their trabeculae is plate-like (Odgaard et al. 1993). A bone density lower than expected for their body mass, could indicate extremely low metabolic rates (Burkhardt et al. 1987; Ding et al. 2018). On possible factor that could explain this abnormality in bone may be the excessive control by the sinuses through NO, as this metabolite is an inhibitor of the osteoclastic activity (Doherty et al. 2014). Therefore, the great development of the sinuses not only can help to make a long period of hibernation lowering the basal metabolism, but also at the level of bone maintenance, avoiding problems associated with inactivity such as osteoporosis, as it happens in non-hibernating animals. This is because the continued production of NO by the sinuses inhibits the production of RANKL (i.e., the up-regulate osteoclastogenesis and bone resorption via receptor activator of nuclear factor-Kβ ligand) (Doherty et al. 2014). In this way, in non-hibernating mammals the bone tissue does not perceive the lack of biomechanical loads associated with hibernation (Seger et al. 2011). In the case of non-hibernating mammals, since they do not have developed sinuses, they do not generate continuously enough NO in blood, and therefore, the lack of biomechanical loading stimulates a greater production of osteblastic RANKL. This generates greater bone activity, leading to bone resorption or osteoporosis (Rubin et al. 2000 2003). This would be translated in greater energy savings for these bears, which together with periods of starvation due to lack of primary productivity (Allan et al 2010) could be an element subject to natural selection. Lower metabolic rates with a very optimal ossification metabolically economized by the effect of high levels of NO in blood. This will result in an exaggerated development of sinuses and bone with much lower densities for their expected body mass.

3.4.5. Future research

As the results of this paper are in progress, here, I outline the directions that I am going to follow in this line of research in the next future:

- To develop an accurate anatomical framework for the paranasal sinuses, with the main goal to investigate the evolutionary changes in sinuses shape using geometric morphometrics.
- To quantify the hormonal and metabolic requirements from histological data. This will allow (if possible) to find an osteological proxy for these biological aspects in fossil taxa.
- To expand the sample of cave bears together with other specimens of the ice age megafauna that show an expansion of the paranasal sinuses, and to explore these issues in the North American short-faced bear.
- To investigate the evolutionary pathways of sinuses development by studying more basal species of bears such as *Ursus deningeri*.

3.4.6. References

- Allen JR, Hickler T, Singarayer JS, Sykes MT, Valdes PJ, Huntley B. 2010. Last glacial vegetation of northern Eurasia. Quaternary Sci Rev. 29(19-20):2604-2618.
- Alsafy MAM, El-Gendy SAA, El-Sharaby AA. 2013. Anatomic reference for computed tomography of paranasal sinuses and their communication in the Egyptian buffalo (*Bubalus bubalis*). Anat Histol Embryol. 42(3):220-231.
- Andersson JA, Cervin A, Lindberg S, Uddman R, Cardell L.O. 2002. The paranasal sinuses as reservoirs for nitric oxide. Acta oto-laryngologica. 122(8):861-865.
- Arnal JF, Flores P, Ram J, Murris-Espin M, Bremont F, Aguilla IP, Didier A. 1999. Nasal nitric oxide concentration in paranasal sinus inflammatory diseases. Eur Respi J. 13(2):307-312.
- Azizi Fereidoun, Mannix JE, Howard Donald, Nelson RA. 1979. Effect of winter sleep on pituitary-thyroid axis in American black bear. Am J Physiol-Endoc M. 237(3):E227.
- Bahar S, Bolat D, Dayan MO, Paksoy Y. 2014. Two-and three-dimensional anatomy of paranasal sinuses in Arabian foals. J Vet Med Sci. 76(1):37-44.
- Bocherens H, Fizet M, Mariotti A. 1994. Diet, physiology and ecology of fossil mammals as inferred from stable carbon and nitrogen isotope biogeochemistry: implications for Pleistocene bears. Palaeogeography, Palaeoclimatology, Palaeoecology. 107(3-4): 213-225.
- Bocherens H, Billiou D, Mariott A, Patou-Mathis M, Otte M, Bonjean D, Toussaint M. 1999. Palaeoenvironmental and palaeodietary implications of isotopic biogeochemistry of last interglacial Neanderthal and mammal bones in Scladina Cave (Belgium). J Archaeol Sci. 26(6):599-607.
- Burkhardt R, Kettner G, Böhm W, Schmidmeier M, Schlag R, Frisch B, Gilg TH. 1987. Changes in trabecular bone, hematopoiesis and bone marrow vessels in aplastic anemia, primary osteoporosis, and old age: a comparative histomorphometric study. Bone. 8(3):157-164.
- Carnio EC, Almeida MC, Fabris G, Branco LG. 1999. Role of nitric oxide in 2-deoxy-D-glucose-induced hypothermia in rats. Neuroreport. 10(14):3101-3104.

- Dierenfeld ES, Hintz HF, Robertson JB, Van Soest PJ, Oftedal OT. 1982. Utilization of bamboo by the giant panda. The Journal of Nutrition. 112(4):636-641.
- Ding M, Lin X, Liu W. 2018. Three-dimensional morphometric properties of rod- and plate-like trabeculae in adolescent cancellous bone. Journal of orthopaedic translation. (12):26-35.
- Doherty AH, Florant GL, Donahue SW. 2014. Endocrine regulation of bone and energy metabolism in hibernating mammals. Integr Comp Biol. 54(3):463-483.
- Erlenbach JA, Rode KD, Raubenheimer D, Robbins CT. 2014. Macronutrient optimization and energy maximization determine diets of brown bears. J Mammal. 95(1):160-168.
- Farke AA. 2008. Frontal sinuses and head-butting in goats: a finite element analysis. J Exp Biol. 211(19):3085-3094.
- Farlow JO. 1976. A consideration of the trophic dynamics of a Late Cretaceous large-dinosaur community (Oldman Formation). Ecology. 57(5):841-857.
- Fei Y, Hou R, Spotila JR, Paladino FV, Qi D, Zhang Z. 2016. Metabolic rates of giant pandas inform conservation strategies. Sci Rep-Uk. 6:27248.
- Figueirido B, Pérez-Claros JA, Hunt RM, Palmqvist P. 2011. Body mass estimation in amphicyonid carnivoran mammals: A multiple regression approach from the skull and skeleton. Acta Palaeontol Pol. 56(2):225-247.
- Figueirido B, Tseng ZJ, Martín-Serra A. 2013. Skull shape evolution in durophagous carnivorans. Evolution. 67(7):1975-1993.
- Figueirido B, Lautenschlager S, Pérez-Ramos A, Van Valkenburgh B. 2018. Distinct predatory behaviors in scimitar-and dirk-toothed sabertooth cats. Curr Biol. 28(20):3260-3266.
- Franzmann AW, Flynn A, Schwartz CC, Calkins DG, Nichols JRL. 1981. Beta-endorphin levels in blood from selected Alaskan mammals. J Wildlife Dis. 17(4):593-596.
- Grandal-d'Anglade A, Pérez-Rama M, García-Vázquez A, González-Fortes GM. 2019. The cave bear's hibernation: reconstructing the physiology and behaviour of an extinct animal. Hist Biol. 31(4):429-441.

- Haight JS, Djupesland PG, Qjan W, Chatkin JM, Furlott H, Irish J, Zamel N. 1999. Does nasal nitric oxide come from the sinuses?. J Otolaryngol. 28(4):197-204.
- Hammer Ø, Harper DA, Ryan PD. 2001. PAST: paleontological statistics software package for education and data analysis. Palaeontol Electron. 4(1):9.
- Heldmaier G. 2011. Life on low flame in hibernation. Science. 331(6019):866-867.
- Hellgren EC. 1998. Physiology of hibernation in bears. Ursus. 467-477.
- Hildebrand T, Rüegsegger P. 1997. A new method for the model-independent assessment of thickness in three-dimensional images. J Microsc-Oxford. 185(1):67-75.
- Hissa R, Siekkinen J, Hohtola E, Saarela S, Hakala A, Pudas J. 1994. Seasonal patterns in the physiology of the European brown bear (*Ursus arctos arctos*) in Finland. Comparative Biochemistry and Physiology Part A: Physiology. 109(3):781-791.
- Joeckel RM. 1998. Unique frontal sinuses in fossil and living Hyaenidae (Mammalia, Carnivora): description and interpretation. J Vertebr Paleontol.18(3): 627-639.
- Jones DB, De Santis LR. 2016. Dietary ecology of the extinct cave bear: evidence of omnivory as inferred from dental microwear textures. Acta Palaeontol Pol. 61(4):735-742.
- Keir J. 2009. Why do we have paranasal sinuses?. The Journal of Laryngology & Otology. 123(1):4-8.
- Kim JW, Min YG, Rhee CS, Lee CH, Koh YY, Rhyoo C, Park SW. 2001. Regulation of mucociliary motility by nitric oxide and expression of nitric oxide synthase in the human sinus epithelial cells. The Laryngoscope, 111(2):246-250.
- König HE, Liebich HG. (Eds.). 2013. Veterinary anatomy of domestic mammals: textbook and colour atlas. Schattauer Verlag.
- Kudej RK, Depre C. 2007. NO with no NOS in ischemic heart. Cardiovasc Res. 74(1):1–3.
- Kurtén B. 1957. A case of Darwinian selection in bears. Evolution. 11(4):412-416.
- Kurtén B. 1976. The cave bear story: life and death of a van ished an i mal.

- Lundberg DA, Nelson RA, Wahner HW, Jones JD. 1976. Protein metabolism in the black bear before and during hibernation. In Mayo Clinic Proceedings. 51(11):716-722
- Lundberg JO, Farkas-Szallasi T, Weitzberg E, Rinder J, Lidholm J, Änggåar A, Alving K. 1995. High nitric oxide production in human paranasal sinuses. Nat Med. 1(4):370.
- Lundberg JO. 2008. Nitric oxide and the paranasal sinuses. The Anatomical Record: Advances in Integrative Anatomy and Evolutionary Biology: Anat Rec. 291(11):1479-1484.
- McNab BK. 1992. Rate of metabolism in the termite-eating sloth bear (*Ursus ursinus*). J Mammal. 73(1):168-172.
- McNab BK. 2008. An analysis of the factors that influence the level and scaling of mammalian BMR. Comparative Biochemistry and Physiology Part A: Molecular & Integrative Physiology. 151(1):5-28.
- Nedergaard J, Cannon B. 1990. Mammalian hibernation. Philosophical Transactions of the Royal Society of London. B, Biological Sciences. 326(1237):669-686.
- Negus VE, Street H. 1954. The function of the paranasal sinuses. Acta oto-laryngologica. 44(5-6):408-426.
- Nelson RA, Wahner HW, Jones JD, Ellefson RD, Zollman PE. 1973. Metabolism of bears before, during, and after winter sleep. Am J Physiology-Legacy Content. 224(2):491-496.
- Nie Y, Speakman JR, Wu Q, Zhang C, Hu Y, Xia M, Zhang J. 2015. Exceptionally low daily energy expenditure in the bamboo-eating giant panda. Science. 349(6244):171-174.
- O'Hearn DJ, Giraud GD, Sippel JM, Edwards C, Chan B, Holden WE. 2007. Exhaled nasal nitric oxide output is reduced in humans at night during the sleep period. Resp Physiol Neurobi. 156(1):94-101.
- Odgaard A, Gundersen HJG. 1993. Quantification of connectivity in cancellous bone, with special emphasis on 3-D reconstructions. Bone. 14(2):173-182.

- Jones KE, Bielby J, Cardillo M, Fritz SA, O'Dell J, Orme CD L, Connolly C. 2009. PanTHERIA: a species-level database of life history, ecology, and geography of extant and recently extinct mammals: Ecological Archives E090-184. Ecology. 90(9):2648-2648.
- PALASIATICA, V. 2011. 大熊猫颅内腔的演化. (EVOLUTION OF CRANIAL CAVITIES IN GIANT PANDAS (AILUROPODA, CARNIVORA, MAMMALIA).
- Pérez-Ramos A, Kupczik K, Van Heteren AH, Rabeder G, Grandal-D'Anglade A, Pastor FJ, Figueirido B. 2019. A three-dimensional analysis of tooth-root morphology in living bears and implications for feeding behaviour in the extinct cave bear. Hist Biol. 31(4):461-473.
- Petruson K, Stalfors J, Jacobsson KE, Ny L, Petruson B. 2005. Nitric oxide production in the sphenoidal sinus by the inducible and constitutive isozymes of nitric oxide synthase. Rhinology. 43(1):18-23.
- Pritchard GT, Robbins CT. 1990. Digestive and metabolic efficiencies of grizzly and black bears. Can J Zool. 68(8):1645-1651.
- Rabeder G, Pacher M, Withalm G. 2009. Die altpleistozänen Bären von Deutsch-Altenburg (Niederösterreich) – Early Pleistocene Bear Remains from Deutsch-Altenburg (Lower Austria Wien). — Mitt. Komm. Quartärforsch. Österr. Akad. Wiss. 17:1–135.
- Rabeder G, Pacher M, Withalm G. 2010. EARLY PLEISTOCENE BEAR REMAINS FROM DEUTSCH ALTENBURG LOWER AUSTRIA. Geol Carpath. 61(3):192.
- Revsbech IG, Shen X, Chakravarti R, Jensen FB, Thiel B, Evans AL, Fago A. 2014. Hydrogen sulfide and nitric oxide metabolites in the blood of free-ranging brown bears and their potential roles in hibernation. Free Radical Bio Med. 73:349-357.
- Robbins CT, Lopez-Alfaro C, Rode KD, Tøien Ø, Nelson OL. 2012. Hibernation and seasonal fasting in bears: the energetic costs and consequences for polar bears. J Mammal. 93(6):1493-1503.
- Ruediger J, Van der Zee EA, Strijkstra AM, Aschoff A, Daan S, Hut RA. 2007. Dynamics in the ultrastructure of asymmetric axospinous synapses in the frontal cortex of hibernating European ground squirrels (Spermophilus citellus). Synapse. 61(5):343-352.

- Seger RL, Cross RA, Rosen CJ, Causey RC, Gundberg CM, Carpenter TO, Keisler DH. 2011. Investigating the mechanism for maintaining eucalcemia despite immobility and anuria in the hibernating American black bear (*Ursus americanus*). Bone. 49(6):1205-1212.
- Shimozuru M, Kamine A, Tsubota T. 2012. Changes in expression of hepatic genes involved in energy metabolism during hibernation in captive, adult, female Japanese black bears (*Ursus thibetanus japonicus*). Comparative Biochemistry and Physiology Part B: Biochemistry and Molecular Biology. 163(2):254-261.
- Stieler JT, Bullmann T, Kohl F, Tøien Ø, Brückner MK, Härtig W, Arendt T. 2011. The physiological link between metabolic rate depression and tau phosphorylation in mammalian hibernation. PloS one. 6(1):e14530.
- Stiner MC, Achyuthan H, Arsebük G, Howell FC, Josephson SC, Juell KE, Quade J. 1998. Reconstructing cave bear paleoecology from skeletons: a cross-disciplinary study of middle Pleistocene bears from Yarimburgaz Cave, Turkey. Paleobiology. 24(1):74-98.
- Tøien Ø, Blake J, Edgar DM, Grahn DA, Heller HC, Barnes BM. 2011. Hibernation in black bears: independence of metabolic suppression from body temperature. Science. 331(6019):906-909.
- Treuting PM, Dintzis SM, Montine KS. (Eds.). 2017. Comparative anatomy and histology: a mouse, rat, and human atlas. Academic Press.
- Van Heteren AH, Figueirido B. 2019. Diet reconstruction in cave bears from craniodental morphology: past evidences, new results and future directions. Hist Biol. 31(4):500-509.
- Veitschegger K, Kolb C, Amson E, Scheyer TM, Sánchez-Villagra MR. 2018. Palaeohistology and life history evolution in cave bears, *Ursus spelaeus* sensu lato. PloS one. 13(11):e0206791.
- Watts PD, Cuyler C. 1988. Metabolism of the black bear under simulated denning conditions. Acta Physiol Scand. 134(1):149-152.
- Weeden AM, Degner DA. 2016. Surgical approaches to the nasal cavity and sinuses. Veterinary Clinics: Small Animal Practice. 46(4):719-733.

- Wojcicka A, Bassett JD, Williams GR. 2013. Mechanisms of action of thyroid hormones in the skeleton. Biochimica et Biophysica Acta (BBA)-General Subjects. 1830(7):3979-3986.
- Yan CH, Hahn S, McMahon D, Bonislawski D, Kennedy DW, Adappa ND, Cohen NA. 2017. Nitric oxide production is stimulated by bitter taste receptors ubiquitously expressed in the sinonasal cavity. Am J Rhinol Allergy. 31(2):85-92.
- Yee KK, Craven BA, Wysocki CJ, Van Valkenburgh B. 2016. Comparative Morphology and Histology of the Nasal Fossa in Four Mammals: Gray Squirrel, Bobcat, Coyote, and White-Tailed Deer. The Anatomical Record. 299(7):840-852.

3.4.7. Supplementary material

Histological image analysis

A cube of 1000 mm3 of cancellous bone was virtually dissected and I applied histogram correction filters to calibrate the grey values for the trabecular through a process of normalization (see **Fig. S1,S2**). Different contrast filters were applied to separate the grey values of cancellous bone from the background noise. After doing this, an average filter was applied to eliminate grey values that have been saturated by contrast. The process is iterative, until that the background noise is eliminated (see **Fig. S1,S3**). The analytical process of the image stacks was performed with BoneJ, a plugin tool for bone image analysis in ImageJ.

The main goal of dissecting virtually a cube of the same volume in all specimens is to standardize the histological values because of the differences in the acquisition parameters of the CTs (see **Table 2** from **Chapter 2** Material and Methods). To solve this problem, in those CTs with low resolution (512x512), the pixel size was increased to 1024x1024, using the Bicubic method to obtain isometric voxel size. I used the sharpe filters only in those CTs with a low to medial resolution (i.e., all of them with the exception of *Helarctos malayanus*, *Melursus ursinus* and *Ursus spelaeus ladinicus*). To avoid biases among the CTs of fossil skulls due to resolution differences, the resolution of *U. sp. ladinicus* (see **Fig. 3**; **Supp. Info**) was reduced. Afterwards the images were converted into binary using the thresholding optimization option (Zhang et al. 2008), in order to threshold the image stack optimizing the number of the connections between trabeculae.

The artefacts (small and free structures) inside the trabecular bone were removed. Finally, I analysed from each cube different parameters (connectivity, thickness, and volume fraction). The connectivity parameter, analysis the number of connected trabecular structures in a network (Odgaard et al. 1993). The method for determined this parameter is by calculating the Euler characteristic of this network. This parameter can be calculated by the volume of the sample, this ratio is connectivity density (Conn.D). For used this parameter, before we need to apply the Purify parameter. This step is required to use the connectivity parameter because removed all isolated particles from the foreground and background, as a filtering step to prepare the stack images for Connectivity. The other parameter used, is Thickness (Hildebrand et al. 1997). The third and last parameter used is Bone volume fraction (BV/TV) (**Figure 3**). This parameter indicates the degree of bone mineralization, that is the volume of mineralized bone per unit volume of the sample (around 1000 mm cubic). The method used in this parameter is the voxel-based, where the number of foreground (mineral bone) voxels divided by the total number of voxels in the image stack.

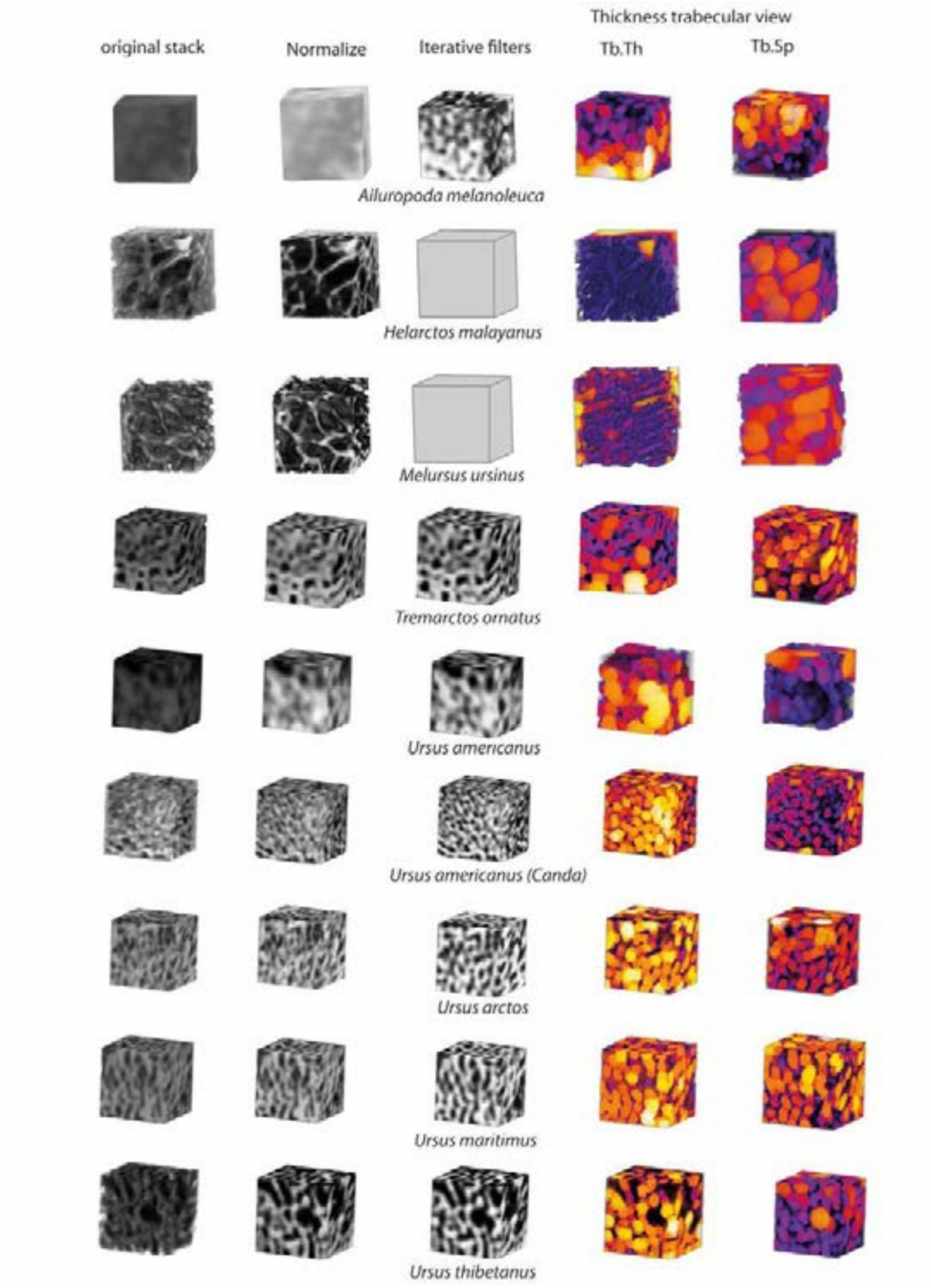

Figure S1. **Process for standardizing the resolution of the CTs necessary to collect the osteometric variables of cancellous bone in a cube of 1000m^3 for living species**. See Figure 3 for cave bears. Grey cubes indicate that the iterative process to eliminate background noise was not performed because the CTs were of high resolution. Tb.Th, trabecular thickness ; Tb.Sp, trabecular space.

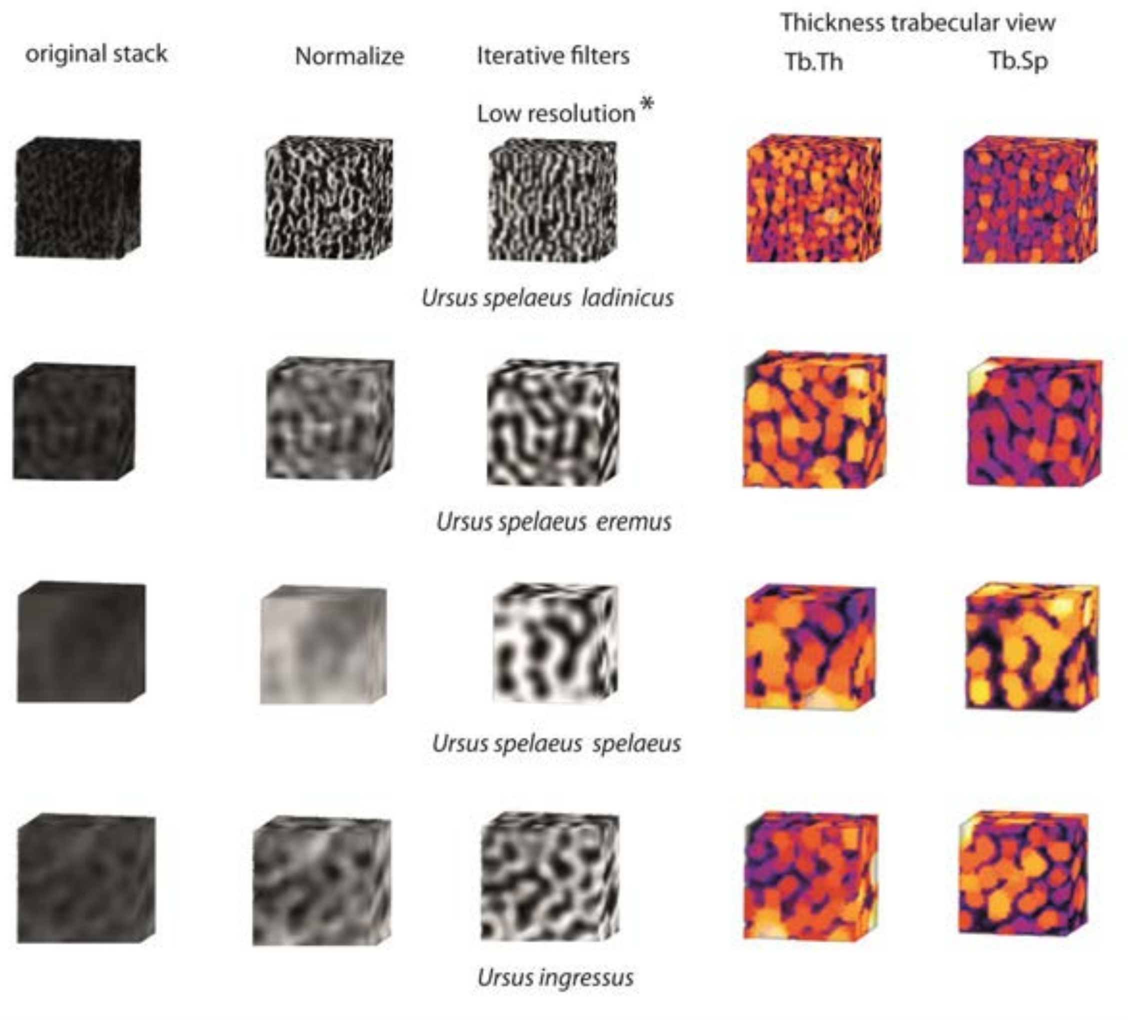

Figure S2. **Process for standardizing the resolution of the CTs necessary to collect the osteometric variables of cancellous bone in a cube of 1000m^3 for cave bears**. (*) Note that the resolution of *U. spelaeus ladinicus* was diminished to the rest of CTs. Tb.Th, trabecular thickness ; Tb.Sp, trabecular space.

3

3.5. Dental caries in the fossil record: a window to the evolution of dietary plasticity in an extinct bear

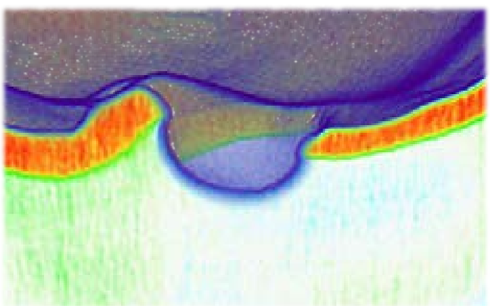

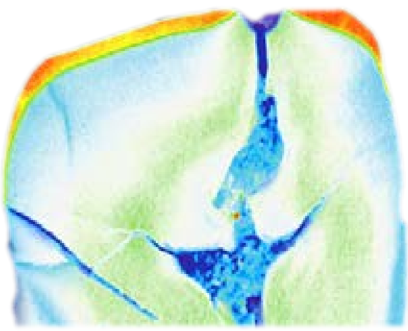

3.5. Dental caries in the fossil record: a window to the evolution of dietary plasticity in an extinct bear

3.5.1. Abstract

During the late Pleistocene of North America (≈36,000 to 10,000 years ago), saber-toothed cats, American lions, dire wolves, and coyotes competed for prey resources at Rancho La Brea (RLB). Despite the fact that the giant short-faced bear (*Arctodus simus*) was the largest land carnivoran present in the fauna, there is no evidence that it competed with these other carnivores for prey at the site. Here, for the first time, we report carious lesions preserved in specimens of *A. simus*, recovered from RLB. Our results suggest that the population of *A. simus* from RLB was more omnivorous than the highly carnivorous populations from the Northwest. This dietary variation may be a consequence of different competitive pressures.

3.5.2. Introduction

Unbalanced predator-prey densities during the Late Pleistocene of North America (≈36,000 to 10,000 years ago) resulted in more carcass encounters among large predatory mammals triggering kleptoparasitism and severe competition over kills (Van Valkenburgh et al. 1993; Van Valkenburgh 2009; Van Valkenburgh 2016). As a result, saber-toothed cats (e.g., *S. fatalis*), American lions (*Panthera atrox*), dire wolves (*Canis dirus*) and coyotes (*Canis latrans*) experienced dramatic feeding stresses (Van Valkenburgh et al. 1993; Van Valkenburgh 2009; Van Valkenburgh 2016), which led to a more fully and rapid consumption of carcasses (e.g., DeSantis and Haupt 2014; DeSantis et al. 2009; Donohue et al. 2013).

The extraordinary fossil deposits of Rancho La Brea (RLB) tar pits in Los Angeles, California, have provided significant elements to reconstruct North American ice-age ecosystems (Coltrain et al. 2004; Feranec et al. 2009). RLB represents a carnivore-trap where animals got stuck on the surface of the natural asphalt seeps and attracted meat-eaters in turn (Coltrain et al. 2004). Thus, the remains of large carnivores including thousands of dire wolves (*Canis dirus*), sabertoothed cats (*Smilodon fatalis*) and coyotes (*Canis latrans*) (Feranec et al. 2009; McHorse et al. 2012) were preserved. Other large carnivorans less represented, include the 'short-faced' bear (*Arctodus simus*), the American lion (*Panthera atrox*) and the 'scimitar-toothed' sabertooth (*Homotherium serum*) (Carbone et al. 2010). Despite *Arctodus* being the largest land carnivoran from these ecosystems, there is no evidence that it competed with these other carnivores for prey.

Here, we report the first pathological evidence in *A. simus* teeth preserved at RLB and we present a large dataset of living bear species from different North American populations affected with similar dental defects. We use macroscopic and microscopic approaches such as 3D-morphometrics of cavities from a counter mold, scanning electron microscopy (SEM), and CT analyses to ascertain the etiology of the lesions. The study confirms that unlike more northern specimens from Alaska and Yukon, dental caries were common in the population of *A. simus* from RLB, which demonstrate variable feeding preferences. Therefore, while the northern population (i.e., Alaska and Yukon) of *A. simus* was locally adapted to a highly carnivorous diet (Bocherens et al. 1995; Matheus et al. 1995), the population of *A. simus* from RLB was more omnivorous. We hypothesize that different competitive pressures may explain this dietary variation between both populations of this emblematic species of the North American megafauna. Moreover, this may represent evidence that the increase of the extension in the Laurentide and Cordilleran ice-sheets during the middle and late Wisconsinan isolated both populations of *Arctodus* that were adapted to feed on extremely different resources. Our findings suggest that both climatic change and local competition among ecologically interacting species are important mechanisms driving biodiversity changes at a global scale.

3.5.3. Material and Methods

We examined molar teeth for the two living bears that inhabit across North America today (the black bear, *U. americanus*, *n* = 1125; and the brown bear, *U. arctos*, *n* = 937), and the Pleistocene short-faced bear (*A. simus*) from Rancho La Brea (MNI = 33), and from the Northwest population of Alaska and the Yukon territory (MNI = 7), where dental remains are extremely scarce, and previous studies have demonstrated a highly carnivorous diet for these specimens (Bocherens et al. 1995; Matheus et al. 1995; Barnes et al. 2002). The specimens are housed in the collections of the American Museum of Natural History of New York (USA), the Natural History Museum of London (UK), the Museum für Naturkunde of Berlin (Germany), the National Museum of Natural History of Washington DC (USA), the Canadian Museum of Nature (Ottawa, Canada) and the Yukon-Beringia Interpretative Center. We detected >75 specimens of living and extinct bears affected with dental caries lesions. Dental caries etiology was defined based on clinical features (King et al. 1999) and morphological description in extant mammals, including carnivore taxa (Harvey et al. 1990; Hall 1945). See **Supplementary Table S1, S2, S3.**

3.5.3.1. Data acquisition

High-resolution hydrophobic polyvinylsiloxane silicone-based molds were obtained from original postcanine molar crowns of those individuals with evidence of pathological conditions. The tooth crown enamel surfaces were cleaned before applying the impression material using a cotton swab soaked in 70% ethanol to remove debris and air-dried. A dual-phase technique was used to produce molds. First, a high viscosity putty soft base and their catalyzer (Virtual® Putty) were mixed and applied pressed by hand against molar teeth. When the silicone was totally set and cured (~3 min), the mold was removed and a low viscosity compound (Virtual® Light Body) was applied on the primary impression and repositioned on the specimen to increase the tooth surface accuracy and fine details resolution.

Two different types of casts were produced from tooth molds following established protocols (Miles et al. 1990; Fiorenza et al. 2009). First, polyurethane Feropur PR-55 (Feroca® Composites, Spain) was used to obtain non-reflective highly accurate tooth replicas optimized for further digital 3D surface models and morphological analysis (Fiorenza et al. 2009). A second high-resolution epoxy replica (Araldite® 2020, Vantico Ltd.) was poured for scanning electron microscopy (SEM) analyses. Epoxy-base resins are highly reliable in replicating enamel surfaces at microscopic level (Fiorenza et al. 2009). Two-base component epoxy or polyurethane resins were mixed and put into the molds using a Pasteur pipette. Molds were then centrifuged at 3,000 rpm during ~1 min to prevent air bubbles formation and hardener.

3.5.3.2. Three-dimensional (3D) models

We scanned the surface of the polyurethane tooth replicas using a high-resolution NextEngine 3D laser scanner at the University of Málaga (Spain). As we already detected 72 specimens of living bears affected with dental caries, and the scanning process is highly time-consuming, we scanned a sample of 16 teeth of *U. arctos, U. americanus, U. malayanus, U tibethanus*. Later, we removed the redundant triangles, aligned different scanning views, and fusion them with Geomagic® studio. As we were interested in detecting different types of possible lesions, we compared the morphology of the cavities by constructing a diagram, commonly used in sedimentary petrology to characterize the sphericity-form for particle shapes (Folk 1980). In this diagram, the longest, shortest and intermediate diameters of each cavity countermold were calculated. Afterwards, we calculated the ratios (S/L) and (L-I/L-S) and the sphericity (Ψ = 3√ [S2/LI]) of each cavity (Folk 1980). Representing the three derived ratios, we can obtain a morphospace of countermold cavities with the compact, elongated and platy cavity shape variability. The Kolmogorov-Smirnov goodness-of-fit showed that the data comes from a normal distribution (Z = 0.794 to 1.113; $P > 0.05$). One-way analysis of variance (ANOVA) was computed to determine the source of significant variation among morphometric parameters. Descriptive and statistical analyses were conducted using IBM SPSS Statistics 19.0. The significant level was set at $P <$ 0.05.

3.5.3.3. Microscopic analyses

Molar teeth were examined using a scanning electron microscope (SEM) Hitachi S3000N (Servicios Técnicos Investigación, University of Alicante) for evidence of caries lesions (Teaford 1988). We mounted epoxy tooth replicas on aluminum stubs with fusible glue and coated with a ~15-nm layer of gold-palladium. We applied a colloidal silver solution to improve conductivity and prevent electrostatic charges. Occlusal enamel surfaces were placed in SEM chamber perpendicular to the electron beam with zero degrees of tilt. SEM micrographs (1280×960 pixels in BMP file format) were recorded between 25× and 100× magnifications at 15Kv in secondary electron (SE) mode, and working distance (WD) ranged between 10–20 mm, depending on the size of the tooth. Microscopic taphonomic features affecting tooth-enamel and dentine tissues, which are readily identifiable were considered according to experimental reports (Teaford 1988).

3.5.3.4. CT scan

To explore patterns of enamel and dentin demineralization consistent with a carious lesion, we explored using an industrial CT scanning two selected fossil tooth specimens (LACM-HC-619; LACM-RLP-R63179; but see **Fig. 1**) with occlusal holes differing in shape. We used a Nikon XTH 225 ST, with acquisition conditions of 160Kv with 123μa for the first specimen, and 160Kv with 94μa for the second. For the first one, we obtained 1800 projections with a voxel size (x,y,z) of 0.042515 mm, while for the second we obtained 1800 projections with a voxel size (x,y,z) of 0.024504 mm. This information was imported to ImageJ v.1.50e (https://imagej.nih.gov/ij/) and using image filters we removed the background noise, and we fitted the range of histogram to the levels of interest R.O.I using 'plot-profile' to see the grey values of dentine and enamel.

We used 'LUTs' (Look Up Table) command from the software ImageJ to explore enamel and dentine density as a proxy for mineralization. LUT converts brightness and darkness (8-bit gray scale system where black is set to zero, and white is 255, and all of the other gradations of intensity are given values between them) in an image into a color scale that indicates the mineralization degree where the zero value was assigned to violet and 255 to red (Pertusa 2010). In this way, those structures with more density that reach white values correspond to red values in LUT analysis.

3.5.4. Results

The 15.15% (5/33) of *A. simus* specimens preserved at the extraordinarily rich fossil deposits of RLB in Los Angeles (California) (*MNI* [Minimum number of individuals] =33; *NISPs* [number of identified specimens] =62) had pathological occlusal cavities (**Fig. 1A** and Supplementary **Fig. S1**). On the other hand, pathological occlusal cavities were not detected (0/7) in the specimens with preserved teeth from Alaska and Yukon (**Supplementary Fig. S2**). We also found several living bears from different North American localities affected by similar pathologies: e.g., 3.2% for brown bears (30/937) and 4.00% (45/1125) for black bears (**Supplementary Fig. S3**).

Furthermore, there is not any evidence of bias favoring the preservation of pathological specimens at RLB, because the 'carnivore trap' idea entails that carnivores were attracted by prey-dying herbivores, and the remains of *Arctodus* at RLB are substantially sparse compared to other hypercarnivores such as *Smilodon fatalis* or *Canis latrans*.

The pathologies found in *A. simus* teeth from RLB have similar locations and morphology to those observed in living bear species –i.e., in specific areas across teeth at regular intervals (**Fig. 1B** and **Supplementary Fig. S1**, **S3**), which differentiates *post-mortem* breakage from taphonomic processes. Based on 3D morphometric criteria (**Fig. 1C** and **Supplementary Table S1, S2, S3**), we identify two main groups of cavities in the teeth of extinct and extant bears. However, although both types of lesions show a continuous range, these two groups are fairly distinguishable in the Ternary diagram according to their shortest (S), longest (L), and intermediate (I) diameters of cavity countermolds, as well as their degree of sphericity (Ψ) in **Fig. 1C**. Accordingly, while platy-shaped lesions form the first group, the second group is formed by blade-shaped, and mainly located on fissures of the occlusal surface. The analyzed cavities of extinct and extant specimens are morphologically indistinguishable, and show no significant differences (ANOVA; $P < 0.05$) for the intermediate ($F = 0.578$; $P = 0.453$), short ($F = 3.148$; $P = 0.087$), large ($F = 2.817$; $P = 0.104$), elongated ($F = 0.133$; $P = 0.718$) or spherical ($F = 0.006$; $P = 0.938$) cavities.

The low degree of occlusal wear present in extant and fossil teeth allows the exclusion of chipping caused by repeated attrition as a possible etiological factor (Harvey 1990; Khan 2011). The observation of the cavities using scanning electron microscopy (SEM) dismisses attrition as a possible etiology, as internal dentine surfaces are smooth in texture with non-chipped areas. SEM analyses (**Fig. 1A**, **Fig. S4**, **S5**) also allow rejecting erosion as a cause of enamel cavity formation (Puech et al. 1995). Moreover, the cavities are located at specific points across the tooth row without any appreciable erosive action spread across the whole teeth (**Fig. 1A** and **Supplementary Fig. S3**). In addition, we did not find evidence of any extensive and uniform erosion damage of enamel and dentine consistent with acid exposure to low pH values (~0.5-2) (Puech et al. 1985; King et al. 1999). Instead, SEM analysis showed regular extensive enamel micro-flake defects in the pathological hollows, and enamel texture related to tissue demineralization (**Fig. 1A**), which is consistent with a caries infectious etiology (Dawes 2011). Indeed, this is the opposite to dental erosion, where acids originate from the diet and may thus affect the whole dentition, bacterial acids act on localized areas where biofilm is allowed to grow without disturbance and mature into an acid producing microenvironment causing carious lesions. Due to protective effects of salivary proteins, it progresses as a subsurface, rather than a surface lesion, extending their demineralization effect into dentine even before enamel breakdown (Dawes 2011). Both processes are generally independent and infrequently found in the same individual (Hardie 1997; Marsh 2003).

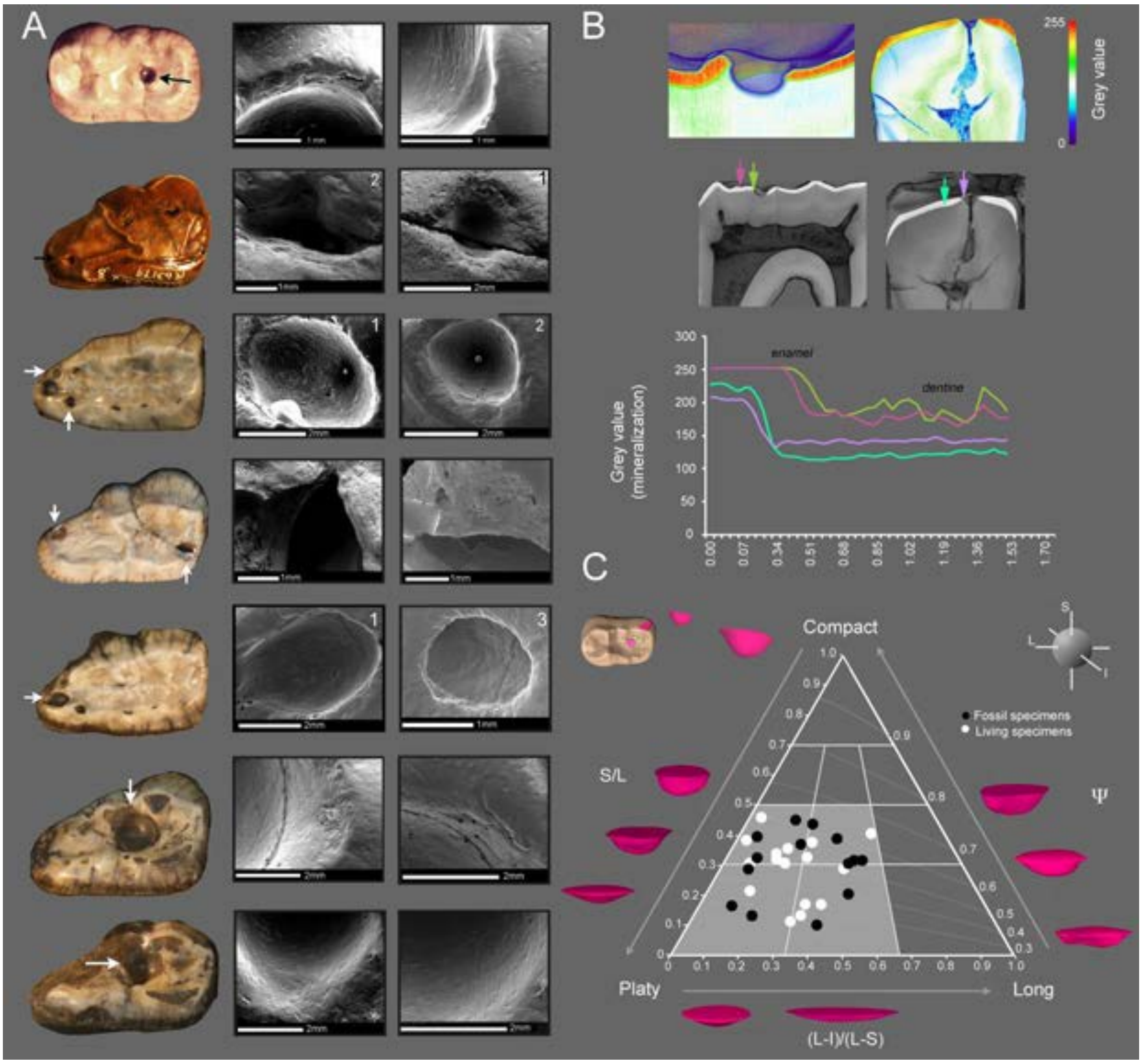

Figure 1. **Microscopic and macroscopic analyses performed on *A. simus* pathological teeth of RLB. (A)** Scanning Electron Microscopy (SEM) micrographs of *A. simus* teeth with carious lesions. For a complete description of fossil remains, see **Supplementary Fig. S1**. More details on SEM analyses are given in **Supplementary Fig. S4. (B)** Look Up Table analyses to evaluate the degree of density (mineralization) computed from CT data in LACMHC-619 (left) and LACMRLP-63179 (right). The bivariate graph shows a representation of mineralization degree across two transects sampled inside and outside the cavity (see arrows in the 3D models of above). **(C)** Ternary diagram showing size and shape of dental occlusal cavity countermolds of fossil and extant bears (see also **Supplementary Table S1,S2,S3**). For details on the three-dimensional cavity countermold extraction, see Methods section. **Abbreviations**: S, L, I represent shortest, longest and intermediate diameters of cavity countermolds, and Ψ represents the degree of sphericity.

Otherwise, the densitometry of teeth based on high-resolution CT images computed at grey scale (look-up-table analysis or LUTs) revealed demineralization in the cavity area compared to the unaffected area (**Fig. 1B**). This demineralization affects enamel and dentine of the specimen LACMHC-619 and LACMRLP-R63179, where a high degree of demineralization is observed in subjacent dentine, underneath the cavity (**Fig. 1B**). This could be attributed to the pathology progression of the occlusal carious cavity formation, where enamel fracture creates a new biofilm retentive site over the subjacent dentin, which in turn results in further progression of dentin demineralization by harboring metabolic active cariogenic bacteria.

3.5.5. Discussion

Our findings demonstrate that the population of *A. simus* from RLB regularly consumed carbohydrate-rich items, suggesting an omnivorous diet, or at least, a diet not relying solely on vertebrate flesh. Furthermore, we have found similar carious lesions across different species of living herbivorous and omnivorous bears. However, carious lesions are absent in the more flesh-eating polar bear (*U. maritimus*) (Supp. material). Although we have not found carious lesions in the bamboo-feeder giant panda (*A. melanoleuca*), they can exist in captive specimens (Jin et al. 2015). Despite this, the giant panda has a low incidence of dental caries that could reflect the low degree of sugars that contained in the bamboo stems (Chongtham et al. 2011) or the high-resistance of crenulated enamel (Stefen et al. 2001).

The diet of *A. simus* is a contentious topic in the literature, as different researchers have proposed differing diets, including hypercarnivory relying on flesh (Kurtén 1967; Kurtén & Anderson 1980; Yeakel et al. 2013; Fox-Dobbs et al. 2008; Richards et al. 1996) and carrion (Matheus 1995; Voorhies and Corner 1986; Guthrie 1988; Schubert and Wallace 2009; Christiansen 1999), omnivory (Sorkin

2006; Figueirido et al. 2009) or even herbivory (Emslie and Czaplewski 1985). Our results differ from the purely hypercarnivorous dietary interpretation of *A. simus* from RLB. On the other hand, although dental remains from the northern population are scarce, we have not detected specimens affected with similar pathologies (**Fig. S2**), which may indicate a non-carbohydrate (i.e., hypercarnivorous) based diet. Short-faced bears as primary predators or as scavengers are confirmed by the high proportions of $\delta^{15}N/\ \delta^{14}N$ found in bone collagen retrieved in specimens from Alaska and Yukon (Bocherens et al. 1995; Matheus 1995; Barnes et al. 2002). However, this population probably represents a local adaptation to feed on meat –or over the carcasses left by other carnivorans (e.g., 'scimitar-toothed' cat *Homotherium serum*, as proposed by others) (Matheus 1995; Voorhies and Corner 1986; Guthrie 1988; Schubert and Wallace 2009; Christiansen 1999), which may explain the absence of carious lesions. The lack of the saber-toothed cat *Smilodon fatalis* from this region may imply lower levels of stress for resources in this population (**Fig. 2**). Given that *H. serum* was adapted to behave in more open environments and its scarce fossil record (**Fig. 2**), there was a low proportion of competitors and probably a lower availability of carbohydrate-rich food supplies across the year in these latitudes. In this ecological scenario, *A. simus* may have been more specialized, eating a larger proportion of meat (e.g., Fox-Dobbs et al. 2008). Although *P. atrox* was also present at these latitudes in the Pleistocene, extensive radiocarbon dating suggests limited geographic and temporal overlap for *P. atrox* and *A. simus* in this region (12,990±70 to 20,970±180 ^{14}C yr BP for *P. atrox* vs. 20,524±180 to 39,565±1126 ^{14}C yr BP for *A. simus*) (e.g., Fox-Dobbs et al. 2008). This could explain a local adaptation towards hypercarnivory in the northwest population of *Arctodus* (**Fig. 2**).

The ecological scenario at RLB was dramatically different, as there was a higher predator density leading to extreme intra-guild competition among large predatory mammals (Van Valkenburgh et al. 1993; Van Valkenburgh 2009; Van

Valkenburgh 2016), and probably a greater availability of sugary-carbohydrates. We hypothesize that this ecological situation influenced *A. simus* to behave more as a carbohydrate-feeding omnivore than as a flesh-eating (or carrion-feeder) hypercarnivore, which explains the presence of dental caries in RLB population. Therefore, our results indicate that the diet of *Arctodus* at RLB during the Pleistocene was similar to the diet of the brown (*U. arctos*) and black (*U. americanus*) bears in North America today. *Juniperus* berries (Templeton 1964) or honey (Holden et al. 2014) could be possible food resources for this population of *Arctodus,* as fossil remains for both food supplies are preserved at the site. However, as stable isotopes are useful for determining feeding preferences in fossil mammals (Palmqvist et al. 2003), and more particularly in the case of *Arctodus* the $\delta^{15}N$/ $\delta^{14}N$ because each trophic level above herbivore is indicated by an increase in $\delta^{15}N_{collagen}$ between +1‰ and +6‰ (average −3.4‰) (Robinson 2001; Palmqvist et al. 2003), future studies on isotopic biogeochemistry (i.e., $\delta^{15}N$/ $\delta^{14}N$) could confirm (or refute) our hypothesis on the omnivorous diet for the population of *Arctodus* from RLB, based solely on caries data.

In either case, the dietary flexibility exhibited by *A. simus* in order to feed on different resources depending upon their availability compared with other large coeval carnivorans, may explain why the largest member of the carnivoran megafauna was one of the last to go extinct (10,000 yr BP) (Schubert 2010), but not why it was extinct while the brown bear (*U. arctos*) persisted across North America during the ice-age (Leonard et al. 2000).

It should also be noted that the Laurentide and Cordilleran ice-sheets separated northern and southern populations of *A. simus* during part of the late Wisconsinan glaciation (**Fig. 2**). The impact of this separation could have limited interaction between disparate populations of *A. simus*, which may have had differing dietary strategies. Thus, we further hypothesize that the evolution of the giant short-faced bear could be a case where both abiotic (climatic change) and biotic (local competition among ecologically interacting species) factors altered the direction of lineage and/or dietary evolution.

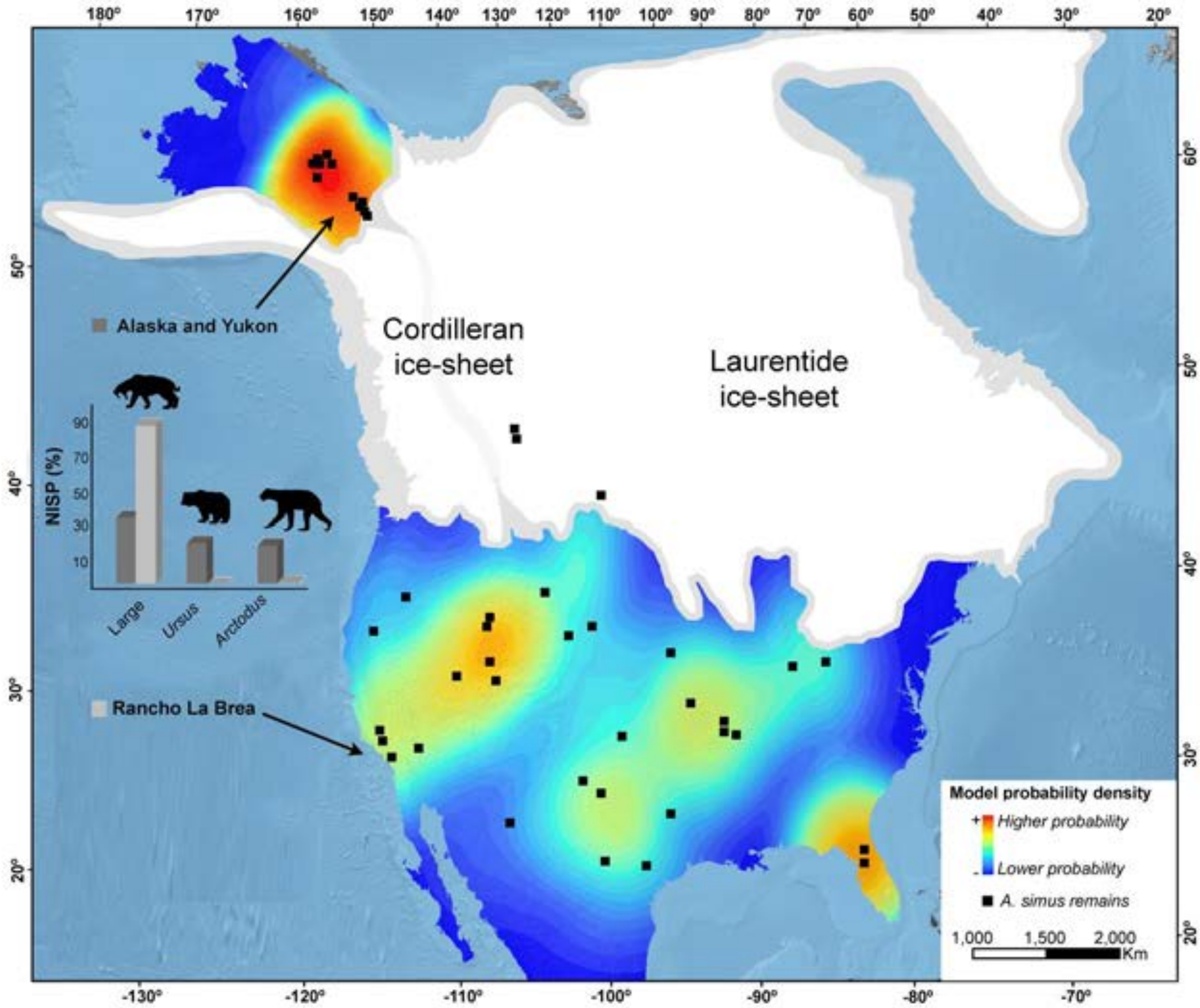

Figure 2. Distribution of *A. simus* in the context of intra-guild competition and climate. The North American map (i.e., excluding Mexico) is computed from a probability model based on the number of identified specimens (NISP) of *A. simus* obtained from Schubert et al. (2010). A Kernel filter for the Rancholabrean North American Land Mammal Age (NALMA) was used in ArcGis v.10.0. The extension of the Cordilleran and Laurentide ice-sheets during the early late Wisconsinan (>18,000 yr BP) were drawn from Dyke et al. (2002). Histograms represent NISP in percentage of large carnivores (*C. dirus, C. lupus, P. atrox, P. onca, H. serum, S fatalis*), *Ursus* (*U. americanus, U. arctos*) and *A. simus*. Data obtained from ref. 9, 52. While the coeval carnivores with *A. simus* in the north were *C. lupus* and *H. serum,* in the south were *C. dirus, C. lupus, P. atrox, P. onca, H. serum, and S. fatalis*. Note that both ice-sheets probably acted as a geographical barrier precluding a continuous genetic flow between the northwestern and southern populations.

3.5.6. References

- Barnes I, Matheus P, Shapiro B, Jensen D, Cooper A. 2002. Dynamics of Pleistocene population extinctions in Beringian brown bears. Science. 295:2267–2270.
- Bocherens H, Emslie S, Billiou D, Mariotti A. 1995. Stable isotopes (^{13}C, ^{15}N) and paleodiet of the giant short-faced bear (*Arctodus simus*). C R Acad Sci. 320:779–784.
- Carbone C. et al. 2009. Parallels between playbacks and Pleistocene tar seeps suggest sociality in an extinct sabretooth cat, Smilodon. Biol Lett. 5(1):81–85.
- Chongtham N, Bisht MS, Haorongbam S. 2011. Nutritional properties of bamboo shoots: potential and prospects for utilization as health food. Compr Rev Food Sci Food Saf. 10:153–168.
- Christiansen P. 1999. What size were *Arctodus simus* and *Ursus spelaeus* (Carnivora: Ursidae)? Annales Zoologici Fennici. 93-102.
- Dawes C. 2011. Salivary protection against toothwear and dental caries in Toothwear: The ABC of the Worn Dentition (eds. Khan, F. & Young, W. G.). 75–88.
- DeSantis LRG, Haupt RJ. 2014. Cougars' key to survival through the Late Pleistocene extinction: insights from dental microwear texture analysis. Biol Lett. 10:20140203.
- DeSantis LRG, Schubert BW, Scott JR, Ungar PS. 2012. Implications of diet for the extinction of saber-toothed cats and American lions. PLoS One. 7:e52453.
- Donohue SL, DeSantis LR, Schubert BW, Ungar PS. 2013. Was the giant short-faced bear a hyper-scavenger? A new approach to the dietary study of ursids using dental microwear textures. PLoS One. 8:e77531.
- Coltrain JB. et al. 2004. Rancho La Brea stable isotope biogeochemistry and its implications for the palaeoecology of late Pleistocene, coastal southern California. Palaeogeogr Palaeocl. 205:199-219.
- Dyke AS, Andrews JT, Clark PU, England JH, Miller GH, Shaw J, Veillette JJ. 2002. The Laurentide and Innuitian ice sheets during the Last Glacial Maximum. Quaternary Sci Rev. 21:9-31.
- Emslie SD, Czaplewski NJ. 1985. A new record of the giant short-faced bear, *Arctodus simus*, from western North America with reevaluation of its palaeobiology. Contrib Sci. 371:1–12.
- Environmental Systems Research Institute (ESRI), 1999–2010. ArcMap Version 10.0, GIS

- Feranec RS, Hadly EA, Paytan A. 2009. Stable isotopes reveal seasonal competition for resources between late Pleistocene bison (*Bison*) and horse (*Equus*) from Rancho La Brea, southern California. Palaeogeogr Palaeocl. 271:153-160.
- Figueirido B, Palmqvist P, Pérez-Claros JA. 2009. Ecomorphological correlates of craniodental variation in bears and paleobiological implications for extinct taxa: an approach based on geometric morphometrics. J Zool. 277:70–80.
- Fiorenza L, Benazzi S, Kullmer O. 2009. Morphology, wear and 3D digital surface models: materials and techniques to create high-resolution replicas of teeth. J Anthropol Sci. 87:211–218.
- Folk RL. 1980. Petrology of sedimentary rocks (Hemphill Publishing Company).
- Fox-Dobbs K, Leonard JA, Koch PL. 2008. Pleistocene megafauna from eastern Beringia: paleoecological and paleoenvironmental interpretations of stable carbon and nitrogen isotope and radiocarbon records. Palaeogeogr Palaeocl. 261:30–46.
- Graham RW. 1994. FAUNMAP: a database documenting late Quaternary distributions of mammal species in the United States. Illinois State Museum 25:1.
- Guthrie RD. 1988. Bone litter from an Alaskan Pleistocene carnivore den. Curr Res Pleistoc. 5:69–71.
- Hall ER. 1945. Dental caries in wild bears. Trans Kans Acad Sci. 48:79–85.
- Hardie JM. et al. 1977. A longitudinal epidemiological study on dental plaque and the development of dental caries – interim results after two years. J Dent Res. 56:90–98.
- Harvey CE, Orr HS. 1990. Manual of small animal dentistry (eds. Harvey, C.E. & Orr, H.S.).37–85.
- Holden AR, Koch JB, Griswold T, Erwin DM, Hall J. 2014. Leafcutter bee nests and pupae from the Rancho La Brea Tar Pits of southern California: Implications for understanding the paleoenvironment of the Late Pleistocene. PloS One I. (4):e94724.
- Jin Y. et al. 2015. Dental abnormalities of eight wild qinling giant pandas (*Ailuropoda melanoleuca qinlingensis*), Shaanxi province, China. J Wildl Dis. 51:849–859.
- Khan F, Young WG. 2011. The multifactorial nature of toothwear in Toothwear: The ABC of the Worn Dentition (eds. Khan, F. & Young, W. G.). 1–14.
- King T, Andrews P, Boz B. 1999. Effect of taphonomic processes on dental microwear. Am J Phys Anthropol. 108:359–373.

- Kurtén B, Anderson E. 1980. Pleistocene Mammals of North America (Columbia University Press).
- Kurtén B. 1967. Pleistocene bears of North America, II: Genus *Arctodus*, short-faced bears. Acta Zool Fennica. 117:1–60.
- Leonard JA, Wayne RK, Cooper A. 2000. Population genetics of Ice Age brown bears. P Natl Acad Sci USA. 97:1651-1654.
- Marsh PD. Are dental diseases examples of ecological catastrophes? Microbiology 149:279–294.
- Matheus PE. 1995. Diet and co-ecology of Pleistocene short-faced bears and brown bears in Eastern Beringia. Quarter Res. 44:447-453.
- McHorse BK, Orcutt JD, Davis EB. 2012. The carnivoran fauna of Rancho La Brea: Average or aberrant?. Palaeogeogr Palaeocl. 329:118–123.
- Miles AEW, Grigson C. 1990. Colyer's variations and diseases of the teeth of animals (Cambridge University Press).
- Palmqvist P, Gröcke DR, Arribas A, Fariña RA. 2003. Paleoecological reconstruction of a lower Pleistocene large mammal community using biogeochemical ($\delta^{13}C$, $\delta^{15}N$, $\delta^{18}O$, Sr: Zn) and ecomorphological approaches. Paleobiology. 29:205-229.
- Pearce EIF, Nelson DGA. 1989. Microstructural features of carious human enamel imaged with back-scattered electrons. J Dent Res. 68:113–118.
- Pertusa, J. F. 2010. Técnicas de análisis de imagen (Universitat de València).
- Puech PF, Prone A, Roth H, Cianfarani F. 1985. Reproduction experiementale de processus d’usure des surfaces dentaires des Hominides fossiles: consequences morphoscopiques et exoscopiques avec application a l’Hominide I de Garusi. C R Acad Sci. 30:59–64.
- Richards RL, Churcher CS, Turnbull WD. 1996. Distribution and size variation in North American short-faced bears, *Arctodus simus* in Palaeoecology and palaeoenvironments of late Cenozoic mammals: tributes to the career of C.S. (Rufus) Churcher (eds. Stewart, K. M. & Seymour, K. L.) (University of Toronto Press)p. 191–246.
- Robinson, D. 2001. δ 15N as an integrator of the nitrogen cycle. Trends Ecol Evol. 16: 153-162.

- Schubert BW, Wallace SC. 2009. Late Pleistocene giant short-faced bears, mammoths, and large carcass scavenging in the Saltville Valley of Virginia, USA. Boreas. 38:482–492.
- Schubert BW. 2010. Late Quaternary chronology and extinction of North American giant short-faced bears (*Arctodus simus*). Quatern Int. 217:188–194.
- Schubert BW, Hulbert RC, MacFadden BJ, Searle M, Searle S. 2010. Giant short-faced bears (*Arctodus simus*) in Pleistocene Florida USA, a substantial range extension. J. Paleo. 84:79–87.
- Sorkin B. 2006. Ecomorphology of the giant short-faced bears *Agriotherium* and *Arctodus*. Hist Biol. 18:1–20.
- Stefen C. 2001. Enamel structure of arctoid carnivora: Amphicyonidae, Ursidae, Procyonidae, and Mustelidae. J Mammal. 82:450–462.
- Teaford MF. 1988. Scanning electron microscope diagnosis of wear patterns versus artifacts on fossil teeth. Scanning Microsc. 2:1167–1175.
- Templeton BC. 1964. The fruits and seeds of the Rancho La Brea Pleistocene deposits. 224 pp. unpublished doctoral dissertation. Oregon State University, United States of America
- Van Valkenburgh B. 2009. Costs of carnivory: tooth fracture in Pleistocene and Recent carnivorans. Biol J Linn Soc. 96:68–81.
- Van Valkenburgh B, Hayward MW, Ripple WJ, Meloro C, Roth VL. 2016. The impact of large terrestrial carnivores on Pleistocene ecosystems. Proc Natl Acad Sci USA. 113:862-867.
- VanValkenburgh B, Hertel F. 1993. Tough times at La Brea: tooth breakage in large carnivores of the late Pleistocene. Science. 261:456–459.
- Voorhies MR, Corner RG. 1986. The giant bear *Arctodus* as a potential breaker and flaker of late Pleistocene megafaunal remains. Curr Res Pleistoc. 3:49–51.
- Yeakel JD, Guimarães PR, Bocherens H, Koch PL. 2013. The impact of climate change on the structure of Pleistocene food webs across the mammoth steppe. Proc R Soc B. 280:20130239.

This chapter has been published in Scientífic reports:

Figueirido, B.*, Pérez-Ramos, A.*, Schubert, B. W., Serrano, F., Farrell, A. B., Pastor, F. J. and Romero, A. 2017. Dental caries in the fossil record: a window to the evolution of dietary plasticity in an extinct bear. Scientific reports 7:17813.

*Borja Figueirido and Alejandro Pérez-Ramos contributed equally to this work.

Author contributions: B.F., A.R., and B.W.S., designed research; B.F., A.P.-R., A.R., B.W.S., and F.S. performed research; B.F., A.P.-R., A.R., and F.S. analyzed data; A.B.F., F.J.P. and A.A.N. contributed new reagents/analytic tools and assisted with writing; B.F., A.R., A.P.-R., B.W.S. wrote the paper.

3.5.7. Supplementary material

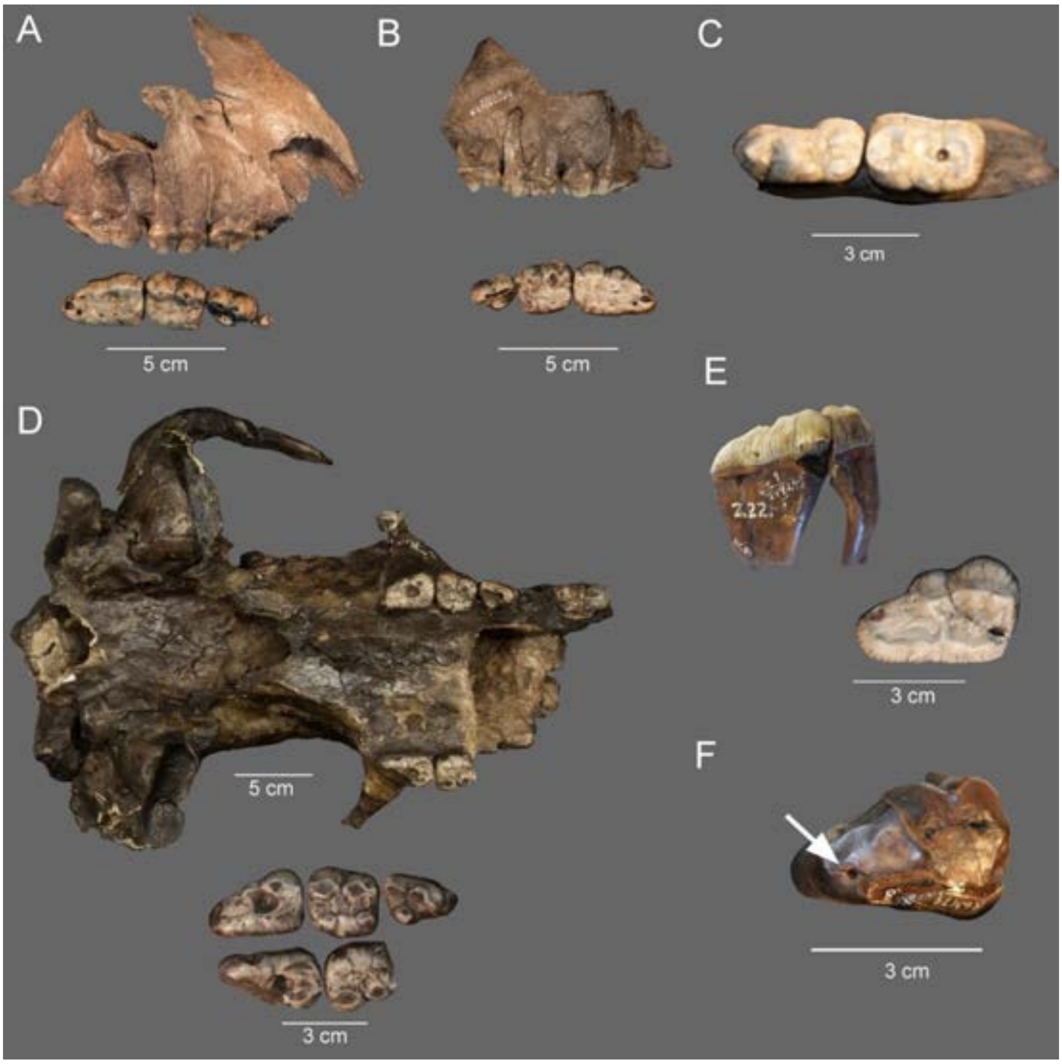

Figure S1. Fossil teeth of *A. simus* preserved at RLB affected with pathologies. **(A)** LACMRLP-R52237: right maxilla with preserved P3-M2; **(B)** LACMRLP-R52511: left maxilla with preserved P4-M2; **(C)** LACMHC-619: right dentary with m1-m2 preserved; **(D)** LACMHC-Z5: partial skull with right M1-M2 and left P4-M2 preserved; **(E)** LACMHC-83: right isolated M2; **(F)** LACMRLP-R63179: right isolated M2. Note that LACMRLP-R52511and LACMRLP-R52237are both found at Pit 91, possibly representing the same individual. Pictures in **A, B, D** taken by Carrie Howard.

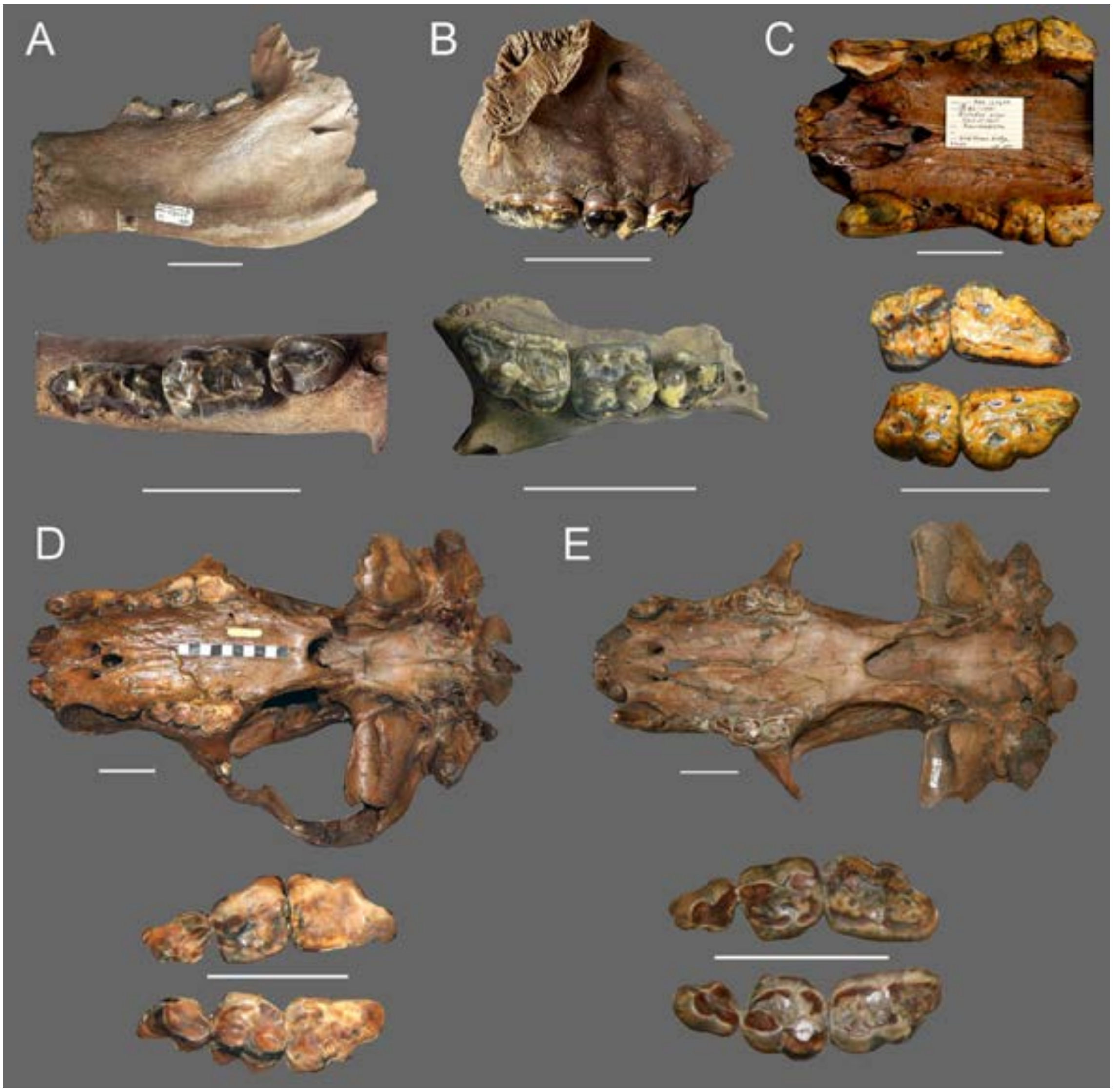

Figure S2. Fossil teeth of *A. simus* preserved at Alaska and Yukon. **(A)** NMC-43444: right mandible with preserved M1-M3. Old Crow (Yukon, Canada); **(B)** NMC-19006: right maxilla with preserved P4-M2. Old Crow (Yukon, Canada); **(C)** F:AM-127699: right dentary with m1-m2 preserved. Goldstream (Alaska); **(D)** AMNH-F:AM-30492: skull with left and right dentaries. Upper Cleary (Fairbanks, Alaska); **(E)** AMNH: FAM-99209: skull with left and right dentaries. Ester Creek (Fairbanks, Alaska). Pictures in **A, B** courtesy of Dr. Danielle Fraser.

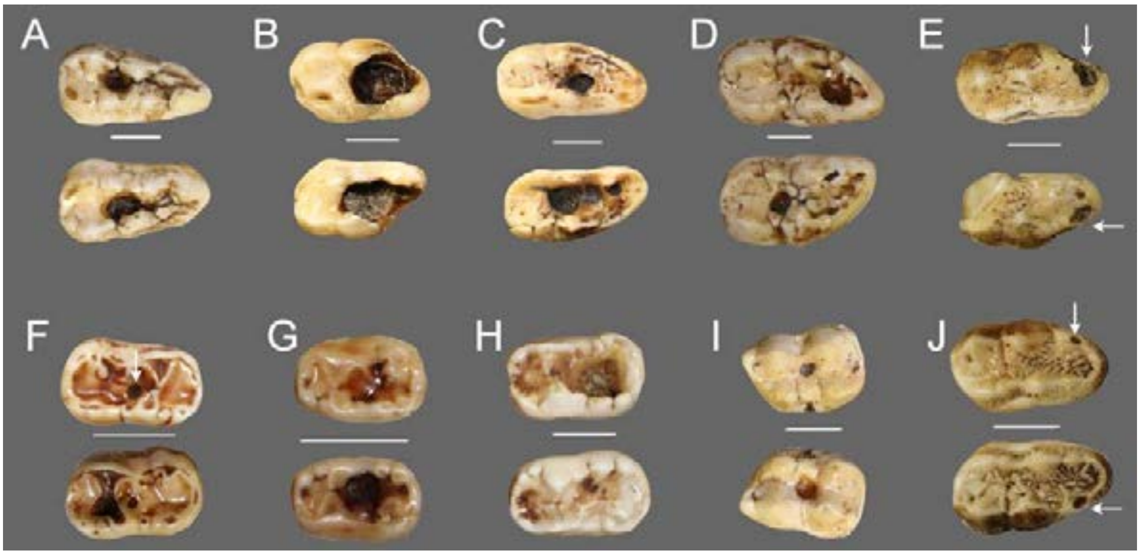

Figure S3. **Selected teeth of living bears affected with pathologies**. **(A)** *U. arctos* (USNM 205165; Yukon); **(B)** *U. americanus* (USNM 235458; Alaska); **(C)** *U. americanus* (USNM 267361; Alaska); **(D)** *U. arctos* (234457; Alaska); **(E)** *U. americanus* (USNM A21491; Nulato, Alaska); **(F)** *U. malayanus* (USNM 123139; Sumatra); **(G)** *U. malayanus* (USNM 123138; Sumatra); **(H)** *U. arctos* (A0441; Siberia); **(I)** *U. arctos* (206137; British Columbia); **(J)** *U. americanus* (USNM 136748; Alaska). Scale bar equals 10mm.

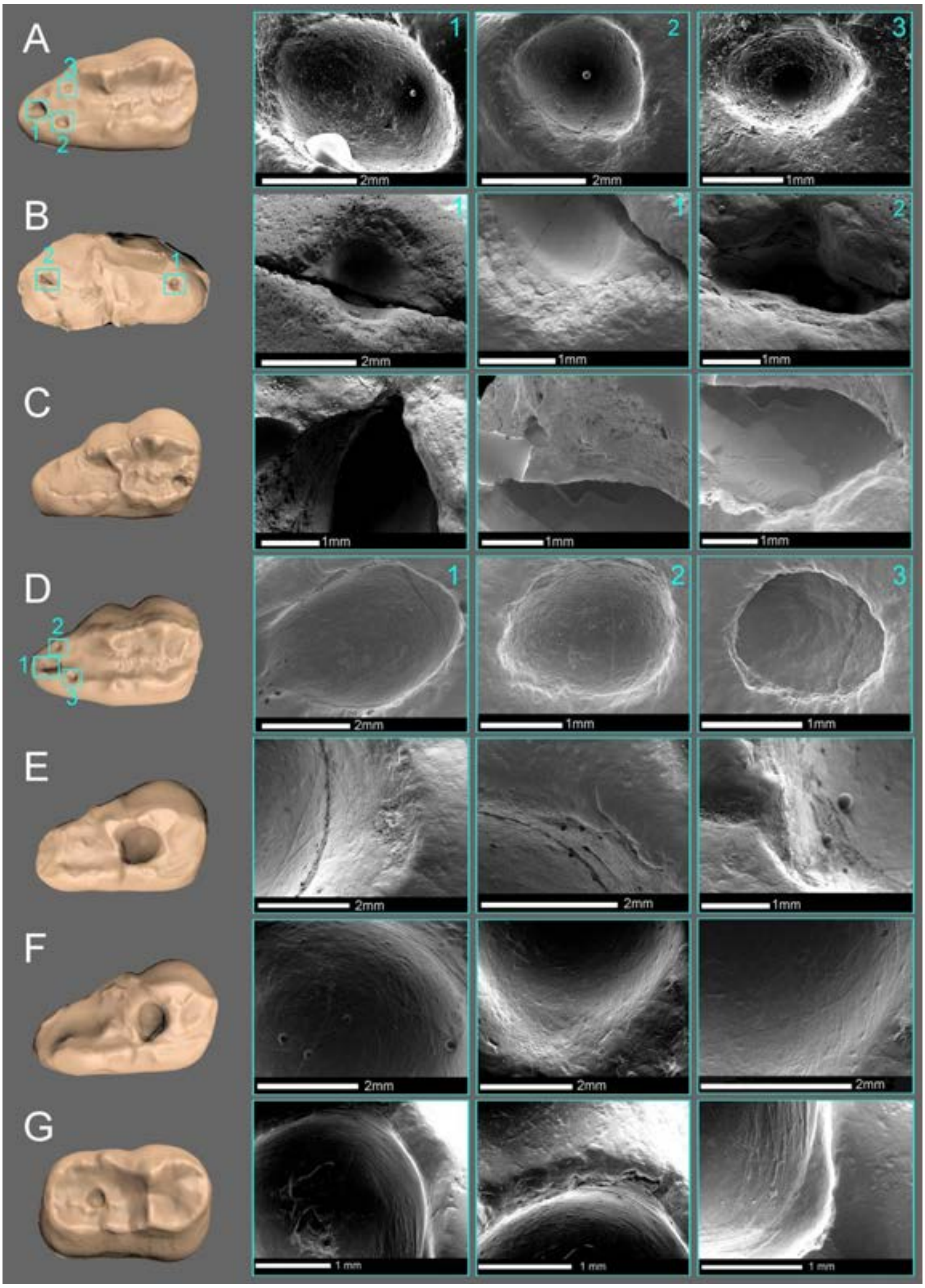

Figure S4. Scanning Electron Microscopy (SEM) micrographs of the complete sample of *A. simus* teeth preserved at RLB with carious lesions. **(A)** LACMRLP-R52511; **(B)** LACMRLP-R63179; **(C)** LACMHC-83; **(D)** LACMRLP-R52237; **(E)** LACMHC-Z5 (left); **(F)** LACMHC-Z5 (right); **(G)** LACMHC-619.

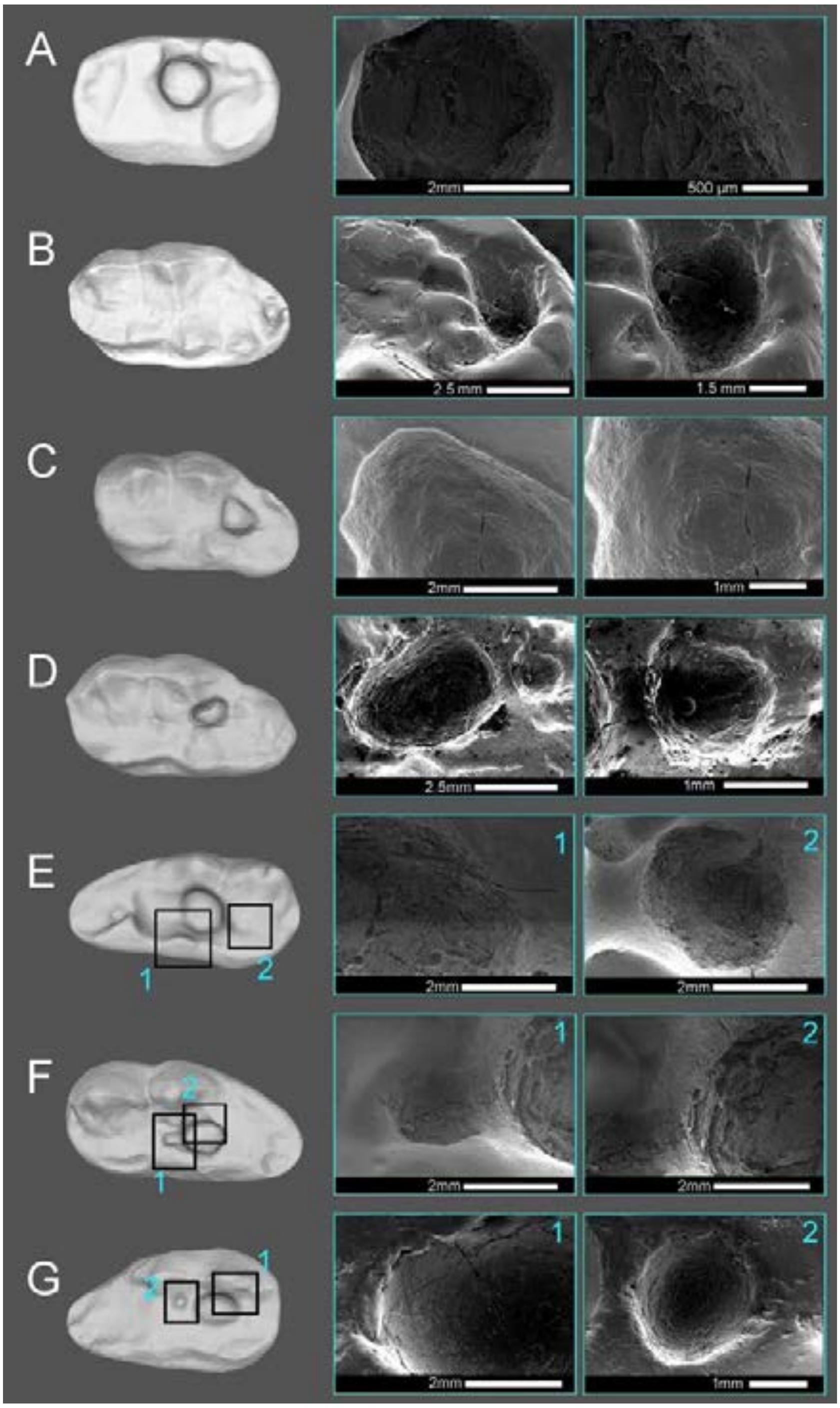

Figure S5. Scanning Electron Microscopy (SEM) micrographs of a sample of living bears with pathological teeth. (A) Lower first molar (USNM-123138) of *U. malayanus*; **(B)** upper second molar (USNM-074888) of *U. americanus*; **(C)** second upper left molar (USNM-206645) of *U. americanus*; **(D)** second upper left molar (USNM-231507) of *U. americanus*; **(E)** second upper right molar (USNM-267361) of *U. americanus*; **(F)** second upper left molar (USNM-267361) of *U. americanus*; **(G)** second upper right molar (USNM-218152) of *U. tibethanus*.

Table S1. Morphometric variables used to characterize the shape of cavities for extant and fossil bear species. **Abbreviations**: I, intermediate diameter of the cavity counter mould; S, shortest diameter of the cavity counter mould; L, largest diameter of the cavity counter mould; Cl, coefficient of lengthening; Ψ = coefficient of sphericity (see methods for details). Those specimens with more than one code refer to different cavities analyzed in the same specimen.

Specimen	Code	I mm	S mm	L mm	Cl	Ψ
U. americanus	USNM-206645_1	3.42	4.32	4.43	9.41	0.41
U. americanus	USNM-206645_2	0.87	1.63	2.50	1.87	0.41
U. americanus	USNM-231507	3.31	2.54	4.07	0.50	0.16
U. americanus	USNM-155560	1.78	3.67	5.27	2.18	0.48
U. americanus	USNM-235458_1	7.51	7.74	9.87	1.11	0.27
U. americanus	USNM-235458_2	5.84	7.84	9.54	2.18	0.37
U. americanus	USNM-74888	1.87	2.21	2.64	1.80	0.33
U. americanus	USNM-267361_1	4.23	5.01	6.53	1.51	0.30
U. americanus	USNM-267361_2	4.93	6.31	7.31	2.38	0.37
U. americanus	USNM-267361_3	1.13	2.27	2.57	4.83	0.59
U. thibetanus	USNM-218152_1	3.43	3.80	5.89	1.18	0.24
U. thibetanus	USNM-218152_2	1.26	1.66	1.92	2.55	0.38
U. thibetanus	USNM-218152_3	0.68	2.11	2.97	2.68	0.74
U. arctos	USNM-234457_1	3.15	4.75	5.09	5.71	0.47
U. arctos	USNM-234457_2	1.65	4.18	6.05	2.36	0.58
U. malayanus	USNM-123138	4.14	4.40	4.53	3.07	0.34
A. simus	LACMHC-Z5_1	7.64	7.30	8.44	0.70	0.28
A. simus	LACMHC-Z5_2	6.69	6.15	7.62	0.64	0.25
A. simus	LACMHC-83	2.84	2.58	3.63	0.75	0.22
A. simus	LACMHC-619	2.71	2.98	3.69	1.37	0.30
A. simus	LACMRLP-R52237_1	1.48	2.37	2.56	5.70	0.49
A. simus	LACMRLP-R52237 _2	0.42	1.21	1.92	2.13	0.61
A. simus	LACMRLP-R52237 _3	0.44	1.43	1.73	4.28	0.90
A. simus	LACMRLP-R52237 _4	2.75	2.84	4.45	1.06	0.22
A. simus	LACMRLP-R52511_1	1.33	1.86	2.02	4.14	0.43
A. simus	LACMRLP-R52511_2	2.74	2.64	4.37	0.94	0.19
A. simus	LACMRLP-R52511_3	2.76	2.78	4.41	1.02	0.21
A. simus	LACMRLP-R52511_4	0.62	1.63	1.79	7.34	0.80
A. simus	LACMRLP-R63179_1	1.31	1.86	3.14	1.43	0.28

Table S2. Specimens of living bears for the presence/absence of caries analyzed in **chapter 3.5.**

Mus	ID	SP	REGION	LOCALITY	C
USNM	234012	*Uar*	Alaska	Admiralty Island, White Water Bay	U
USNM	234013	*Uar*	Alaska	Admiralty Island, White Water Bay	U
USNM	234014	*Uar*	Alaska	Admiralty Island, White Water Bay	U
USNM	234015	*Uar*	Alaska	Admiralty Island, White Water Bay	U
USNM	234060	*Uar*	Alaska	Yakutat Bay, N Side	U
USNM	234061	*Uar*	Alaska	Yakutat Bay, N Side	U
USNM	234062	*Uar*	Alaska	Yakutat Bay, N Side	U
USNM	234063	*Uar*	Alaska	Yakutat Bay, N Side	U
USNM	234064	*Uar*	Alaska	Yakutat Bay, Near, Itaho River	U
USNM	234197	*Uar*	Alaska	Beaver MoUtains, Iditarod	U
USNM	234198	*Uar*	Alaska	Baranof Island, Silver Bay	U
USNM	234196	*Uar*	Alaska	Beaver MoUtains, Reindeer Camp, Iditarod	U
USNM	234199	*Uar*	Alaska	Baranof Island, Silver Bay	U
USNM	234200	*Uar*	Alaska	Admiralty Island, Gambier Bay	U
USNM	234201	*Uar*	Alaska	Admiralty Island, FUter Bay	U
USNM	234202	*Uar*	Alaska	Mckinley Park, Upper Kuskokwim River	U
USNM	234203	*Uar*	Alaska	Mckinley Park, Upper Kuskokwim River	U
USNM	234205	*Uar*	Alaska	Beaver MoUtains, Talstai Creek, Iditarod	U
USNM	234207	*Uar*	Alaska	Chicic Island, 10 Mi N, Snug Harbor On Cottonwood Creek	U
USNM	234208	*Uar*	Alaska	Chicic Island, 10 Mi N, Snug Harbor On Cottonwood Creek	U
USNM	234209	*Uar*	Alaska	Chicic Island, 10 Mi N, Snug Harbor On Cottonwood Creek	U
USNM	234210	*Uar*	Alaska	Chicic Island, 10 Mi N, Snug Harbor On Cottonwood Creek	A
USNM	234243	*Uar*	Alaska	Stikine River, 5 Mi SE Of First S Fork	U
USNM	234403	*Uar*	Alaska	Admiralty Island, FUter Bay	U
USNM	234404	*Uar*	Alaska	Chichagof Island, Tenakee Inlet	U
USNM	234459	*Uar*	Alaska	Basket Bay	A
USNM	234457	*Uar*	Alaska	Chesna River	A
USNM	234460	*Uar*	Alaska	Corner Bay	U
USNM	234465	*Uar*	Alaska	Admiralty Island, Hawk Inlet	U
USNM	234477	*Uar*	Alaska	Chisana	U
USNM	234478	*Uar*	Alaska	Chisana	U
USNM	234633	*Uar*	Alaska	Lituya Bay, NW Side	U
USNM	234634	*Uar*	Alaska	Lituya Bay, NW Side	U
USNM	234635	*Uar*	Alaska	Fairweather Glacier, 15 Mi NW Lituya Bay	U
USNM	234636	*Uar*	Alaska	Chichagof Island, Idaho Inlet	U
USNM	234637	*Uar*	Alaska	Admiralty Island, Head Of Hasselborg Lake, 15 Mi From Mole Harbor	U
USNM	234639	*Uar*	Alaska	Copper River, Iliamna Lake	U
USNM	234640	*Uar*	Alaska	Bering River	U
USNM	234641	*Uar*	Alaska	Bering River	U
USNM	234723	*Uar*	Alaska	Favorite Bay	U
USNM	234724	*Uar*	Alaska	Hood Bay, S Arm	U
USNM	234731	*Uar*	Alaska	Kokonok Lake	U
USNM	234732	*Uar*	Alaska	Kokonok Lake	U
USNM	234733	*Uar*	Alaska	Kokonok Lake	U

USNM	234734	*Uar*	Alaska	Eagle Bay	A
USNM	234735	*Uar*	Alaska	Kokonok Lake	U
USNM	234736	*Uar*	Alaska	Copper River	U
USNM	234737	*Uar*	Alaska	Copper River	U
USNM	234739	*Uar*	Alaska	Kukak Bay, Near MoUt Katmai	U
USNM	235043	*Uar*	Alaska	Kamishak Bay, U. Cove	U
USNM	235044	*Uar*	Alaska	Kamishak Bay, U. Cove	U
USNM	235045	*Uar*	Alaska	Kamishak Bay, U. Cove	U
USNM	235046	*Uar*	Alaska	Kamishak Bay, U. Cove	U
USNM	235060	*Uar*	Alaska	Copper River, Rabbit Creek	U
USNM	235146	*Uar*	Alaska	Kamishak Bay, W Shore, Bruin Bay	U
USNM	235147	*Uar*	Alaska	Kamishak Bay, W Shore, Bruin Bay	U
USNM	235148	*Uar*	Alaska	Kamishak Bay, Kamishak River	U
USNM	235149	*Uar*	Alaska	Kamishak Bay, SW Shore, Douglas River	U
USNM	235150	*Uar*	Alaska	Cook's Inlet, SW Shore Of Kamishak Bay	U
USNM	235276	*Uar*	Alaska	Beaver MoUtains	U
USNM	235282	*Uar*	Alaska	Big Bear Bay	U
USNM	235283	*Uar*	Alaska	Iniskin Bay	U
USNM	235296	*Uar*	Alaska	Admiralty Island, Gambier Bay	U
USNM	235297	*Uar*	Alaska	Baranof Island, Whale Bay	U
USNM	235298	*Uar*	Alaska	Baranof Island, Whale Bay	U
USNM	235299	*Uar*	Alaska	Admiralty Island, Pybus Bay	U
USNM	235300	*Uar*	Alaska	Admiralty Island, Pybus Bay	U
USNM	235554	*Uar*	Alaska	Copper River	U
USNM	235348	*Uar*	Alaska	Baranof Island, Near Old Sitka Village	U
USNM	235443	*Uar*	Alaska	Chichagof Island, Near SU Cove	U
USNM	235553	*Uar*	Alaska	Copper River	U
USNM	235347	*Uar*	Alaska	Baranof Island, Near Old Sitka Village	U
USNM	235555	*Uar*	Alaska	Tommy Point	U
USNM	235556	*Uar*	Alaska	Talerie Creek	U
USNM	235557	*Uar*	Alaska	Eagle Bay	A
USNM	235972	*Uar*	Alaska	Baranof Island	U
USNM	235974	*Uar*	Alaska	Admiralty Island, Gambier Bay	U
USNM	235981	*Uar*	Alaska	Admiralty Island, Seymour Canal	U
USNM	235976	*Uar*	Alaska	Admiralty Island, Killisnoo	U
USNM	235977	*Uar*	Alaska	Admiralty Island	U
USNM	235979	*Uar*	Alaska	Admiralty Island, Seymour Canal	U
USNM	235975	*Uar*	Alaska	Admiralty Island, Gambier Bay	U
USNM	235982	*Uar*	Alaska	Admiralty Island, Seymour Canal	U
USNM	235983	*Uar*	Alaska	Admiralty Island, Seymour Canal	U
USNM	235984	*Uar*	Alaska	Berner Bay	U
USNM	235988	*Uar*	Alaska	Pavlof Bay	U
USNM	235981	*Uar*	Alaska	Admiralty Island, Seymour Canal	U
USNM	235990	*Uar*	Alaska	Pavlof Bay	U
USNM	235989	*Uar*	Alaska	Pavlof Bay	U
USNM	235991	*Uar*	Alaska	Alaska Peninsula, 12 Mi NE Of Cold Bay	U
USNM	236080	*Uar*	Alaska	Egavik	U
USNM	236081	*Uar*	Alaska	Chichagof Island, Salisbury SoUd	U
USNM	236082	*Uar*	Alaska	Chichagof Island, Patterson Bay	U

USNM	236083	*Uar*	Alaska	Chichagof Island, Patterson Bay	U
USNM	236084	*Uar*	Alaska	Chichagof Island, Patterson Bay	U
USNM	236085	*Uar*	Alaska	Baranof Island, Rodman Bay	U
USNM	236086	*Uar*	Alaska	Baranof Lake, Warm Spring Bay	U
USNM	236087	*Uar*	Alaska	Kruzof Island, Shelikof Bay	U
USNM	236088	*Uar*	Alaska	Peterson, G. H.	U
USNM	236089	*Uar*	Alaska	Kruzof Island	U
USNM	236095	*Uar*	Alaska	Snug Harbor, 10 Mi N, Polly Creek	U
USNM	236096	*Uar*	Alaska	Cottonwood, 15 Mi N	U
USNM	236097	*Uar*	Alaska	Snug Harbor, 10 Mi N On Polly Creek	U
USNM	236579	*Uar*	Alaska	Toklat River, Clearwater Fork Near Little Moose Creek	U
USNM	241381	*Uar*	Alaska	Seward Peninsula	U
USNM	241608	*Uar*	Alaska	Cook's Inlet, W Side, Polly Creek	U
USNM	241609	*Uar*	Alaska	Cook's Inlet, W Side, Polly Creek	U
USNM	241624	*Uar*	Alaska	Cook's Inlet, Tuxedni Harbor	U
USNM	241649	*Uar*	Alaska	Robertson River, Near Head Of South Fork	U
USNM	241661	*Uar*	Alaska	Cook's Inlet, W Shore, Iniskin Bay	U
USNM	241662	*Uar*	Alaska	Cook's Inlet, W Shore, Kamishak Bay, Kamishak River	U
USNM	242192	*Uar*	Alaska	Iliamna Lake, A Tributary, Cheacock Creek	U
USNM	241959	*Uar*	Alaska	Kamishak Bay, Iliamna	U
USNM	242191	*Uar*	Alaska	Tulerie Creek	U
USNM	242193	*Uar*	Alaska	Iliamna Lake, A Tributary, Cheacock Creek	U
USNM	242231	*Uar*	Alaska	Cook's Inlet, W Shore, Iniskin Bay	U
USNM	242229	*Uar*	Alaska	Iliamna Bay	U
USNM	242230	*Uar*	Alaska	Exploration Creek, A Tributary Of Ualakleet River	U
USNM	242232	*Uar*	Alaska	Cook's Inlet, S Shore, Kamishak Bay, Douglas River	U
USNM	242233	*Uar*	Alaska	Cook's Inlet, Bruin Bay	U
USNM	242253	*Uar*	Alaska	Cook's Inlet, 14 Mi SW Of W Forland. On Big River, Close To Butte	U
USNM	242236	*Uar*	Alaska	Cook's Inlet, W Shore, SW Kamishak Bay	U
USNM	242235	*Uar*	Alaska	Cook's Inlet, W Side, Kamishak Bay	U
USNM	242194	*Uar*	Alaska	Nondalton MoUtain	U
USNM	242234	*Uar*	Alaska	Cook's Inlet, W Shore, Bruin Bay	U
USNM	242264	*Uar*	Alaska	Nondalton Village, Near, Lake Clark	A
USNM	242268	*Uar*	Alaska	Beaver MoUtains, Ophir	U
USNM	242504	*Uar*	Alaska	Robertson River	U
USNM	242505	*Uar*	Alaska	Alaska Peninsula, Cold Bay	U
USNM	242513	*Uar*	Alaska	Admiralty Island, Windfall Harbor	U
USNM	242514	*Uar*	Alaska	Admiralty Island, Windfall Harbor	U
USNM	242515	*Uar*	Alaska	Admiralty Island, Windfall Harbor	U
USNM	242533	*Uar*	Alaska	Yakutat Bay, N Side	U
USNM	242534	*Uar*	Alaska	Yakutat Bay, N Side	U
USNM	242535	*Uar*	Alaska	Yakutat, Dangerous River	U
USNM	242628	*Uar*	Alaska	Dry Bay	U
USNM	242653	*Uar*	Alaska	Kuskokwim River, Upper S Fork, Mcgrath P.O.	U
USNM	242654	*Uar*	Alaska	Kuskokwim River, Upper S Fork	U
USNM	242655	*Uar*	Alaska	Salmon River, 20 Mi S, Windy Fork Of Big River	U
USNM	242663	*Uar*	Alaska	Susitna	U
USNM	242664	*Uar*	Alaska	Kantishna, Mt. Chitsia	U
USNM	242699	*Uar*	Alaska	Norton SoUd, Head Of Egavik River	U

USNM	242787	*Uar*	Alaska	Delta River, Phelan Creek Tributary	U
USNM	242788	*Uar*	Alaska	Delta River, Phelan Creek Tributary	U
USNM	242789	*Uar*	Alaska	Good Paster River	U
USNM	242968	*Uar*	Alaska	Cook's Inlet, SW	U
USNM	242969	*Uar*	Alaska	Cook's Inlet, SW	U
USNM	242970	*Uar*	Alaska	Cook's Inlet, SW	U
USNM	243270	*Uar*	Alaska	Red MoUtain, Head Waters Kaktobitna River, Mulchatna	U
USNM	243291	*Uar*	Alaska	Mamitam Village	U
USNM	243292	*Uar*	Alaska	Distna River	U
USNM	243293	*Uar*	Alaska	Distna River	A
USNM	243350	*Uar*	Alaska	Kodiak Island, Uganik	U
USNM	243351	*Uar*	Alaska	Balboa Bay	U
USNM	243407	*Uar*	Alaska	Alaska Peninsula, Near Canoe Bay	U
USNM	243531	*Uar*	Alaska	Iliamna Lake, Upper Copper River	U
USNM	243584	*Uar*	Alaska	Pavlof Bay	U
USNM	243585	*Uar*	Alaska	Pavlof Bay	U
USNM	243586	*Uar*	Alaska	Pavlof Bay	U
USNM	243587	*Uar*	Alaska	Pavlof Bay	U
USNM	243588	*Uar*	Alaska	Pavlof Bay	U
USNM	243639	*Uar*	Alaska	Cook's Inlet, Iniskin Bay	U
USNM	243640	*Uar*	Alaska	Iliamna Lake, SE	U
USNM	243641	*Uar*	Alaska	Bristol Bay, Kagguing	U
USNM	243642	*Uar*	Alaska	Iliamna Lake, Checoc	U
USNM	262480	*Uar*	Alaska	Admiralty Island, Gambier Bay	U
USNM	262481	*Uar*	Alaska	Malina Bay, Aognak	U
USNM	262482	*Uar*	Alaska	Chinitna Bay	U
USNM	262483	*Uar*	Alaska	Tenakee Inlet	U
USNM	262484	*Uar*	Alaska	Admiralty Island, Eliza Harbor	U
USNM	262485	*Uar*	Alaska	Chinitna Bay	U
USNM	262486	*Uar*	Alaska	Chichagof Island, Corner Bay	U
USNM	262487	*Uar*	Alaska	Kenai Peninsula, Skilak Lake	U
USNM	262488	*Uar*	Alaska	Paxton	U
USNM	262489	*Uar*	Alaska	Paxton	A
USNM	262490	*Uar*	Alaska	Chichagof Island, Tenakee Inlet	U
USNM	262491	*Uar*	Alaska	Yakataga Beach	U
USNM	262492	*Uar*	Alaska	Telequana Lake Region	U
USNM	265076	*Uar*	Alaska	St. Lawrence Island	U
USNM	265080	*Uar*	Alaska	Kodiak Island, Kalsin Bay	U
USNM	265078	*Uar*	Alaska	Kodiak Island, Kalsin Bay	U
USNM	265079	*Uar*	Alaska	Kodiak Island, Kalsin Bay	U
USNM	265077	*Uar*	Alaska	Kodiak Island, Middle Bay	U
USNM	265083	*Uar*	Alaska	Kodiak Island, Kalsin Bay	U
USNM	265082	*Uar*	Alaska	Kodiak Island, Kalsin Bay	U
USNM	265081	*Uar*	Alaska	Kodiak Island, Kalsin Bay	U
USNM	265084	*Uar*	Alaska	Kodiak Island, Middle Bay	U
USNM	265085	*Uar*	Alaska	Buskin Valley	U
USNM	265934	*Uar*	Alaska	MoUt Hays, Little Delta River	U
USNM	265935	*Uar*	Alaska	MoUt Hays, Little Delta River	U
USNM	266118	*Uar*	Alaska	Little Delta River	U

USNM	266119	*Uar*	Alaska	Fielding Lake	U
USNM	266120	*Uar*	Alaska	Fielding Lake	U
USNM	267359	*Uar*	Alaska	Rainey Pass	U
USNM	267360	*Uar*	Alaska	Rainey Pass	U
USNM	271726	*Uar*	Alaska	Asognak	U
USNM	271734	*Uar*	Alaska	Fort Haines	U
USNM	275158	*Uar*	Alaska	Teller	U
USNM	286412	*Uar*	Alaska	Cook's Inlet, Chinitna Bay	U
USNM	286413	*Uar*	Alaska	Cook's Inlet, Chinitna Bay	U
USNM	286833	*Uar*	Alaska	Cook's Inlet, Tuxedni Bay, N Side	U
USNM	243643	*Uar*	Alaska	Iliamna Lake, Kozhonok	U
USNM	243644	*Uar*	Alaska	Iliamna Lake, Taleric Creek	U
USNM	243645	*Uar*	Alaska	Kamishak Bay, Little Bear Bay	U
USNM	243646	*Uar*	Alaska	Cook's Inlet, SW, Kamishak Bay	U
USNM	243647	*Uar*	Alaska	Cook's Inlet, SW, Kamishak Bay, Bruin Bay	A
USNM	243648	*Uar*	Alaska	Cook's Inlet, SW, Kamishak Bay, Bruin Bay	U
USNM	243649	*Uar*	Alaska	Cook's Inlet, SW	U
USNM	243650	*Uar*	Alaska	Cook's Inlet, SW	U
USNM	243651	*Uar*	Alaska	Cook's Inlet, SW	U
USNM	243652	*Uar*	Alaska	Cook's Inlet, SW	U
USNM	243781	*Uar*	Alaska	Snug Harbor	U
USNM	243794	*Uar*	Alaska	Cook's Inlet, SW, Kamishak Bay	U
USNM	243795	*Uar*	Alaska	Cook's Inlet, SW, Kamishak Bay	U
USNM	243796	*Uar*	Alaska	Cook's Inlet, SW, Kamishak Bay	U
USNM	243797	*Uar*	Alaska	Cook's Inlet, Iniskin Bay	U
USNM	243824	*Uar*	Alaska	Seward Peninsula, Sawtooth MoUtains	U
USNM	244199	*Uar*	Alaska	Ophir, Crater MoUtain	U
USNM	244496	*Uar*	Alaska	Cook's Inlet, Little Bear Bay	U
USNM	244499	*Uar*	Alaska	Nabesna River, Near Head, Tributary Of Tanana River	U
USNM	244500	*Uar*	Alaska	Alaska Peninsula, Cold Bay	U
USNM	244501	*Uar*	Alaska	Tanana River, Near Head Of Big Delta	U
USNM	245923	*Uar*	Alaska	Admiralty Island; on Sleepy Creek, near Windtall harbor.	U
USNM	244503	*Uar*	Alaska	Tanana River, Fork Of Head Delta	U
USNM	244504	*Uar*	Alaska	Tanana River, Fork Of Head Delta	U
USNM	244505	*Uar*	Alaska	Richardson Highway, Halfway Between Chitina And Fairbanks	U
USNM	245425	*Uar*	Alaska	Cook's Inlet, S, Douglas River	U
USNM	245426	*Uar*	Alaska	Cook's Inlet, Iniskin Bay	U
USNM	245655	*Uar*	Alaska	Chichagof Island, Near, Long Bay	U
USNM	245656	*Uar*	Alaska	Chichagof Island, Near, Long Bay	U
USNM	245733	*Uar*	Alaska	Icy Strait, Near Excursion Inlet	U
USNM	245922	*Uar*	Alaska	Admiralty Island; near Bota Mt. on Bear Mt. S. Slope	U
USNM	244502	*Uar*	Alaska	Tanana River, Fork Of Head Delta	U
USNM	245924	*Uar*	Alaska	Admiralty Island, Fools CreekSeymour Canal	U
USNM	246061	*Uar*	Alaska	Jarvis Creek	U
USNM	246310	*Uar*	Alaska	Carlson Creek, 16 Mi NE MoUt Mckinley	U
USNM	246002	*Uar*	Alaska	July Creek, Tributary Of Tokotna River	A
USNM	246062	*Uar*	Alaska	Jarvis Creek	U
USNM	246311	*Uar*	Alaska	Carlson Creek, 16 Mi NE MoUt Mckinley	U
USNM	246059	*Uar*	Alaska	Jarvis Creek	U

USNM	246063	*Uar*	Alaska	Healy River	U
USNM	246060	*Uar*	Alaska	Jarvis Creek, Near JUction Of Macomber Creek	U
USNM	246309	*Uar*	Alaska	Carlson Creek, 16 Mi NE MoUt Mckinley	U
USNM	246312	*Uar*	Alaska	Cooper MoUtain, E Of Muldrow Glacier, 32 Mi NE MoUt Mckinley	U
USNM	246313	*Uar*	Alaska	Birch Creek, NW Of MoUt Mckinley	U
USNM	246314	*Uar*	Alaska	Birch Creek, NW Of MoUt Mckinley	U
USNM	246315	*Uar*	Alaska	Kuskokwim River	U
USNM	246320	*Uar*	Alaska	Prince William SoUd, Montague Island	U
USNM	246372	*Uar*	Alaska	Pavlof MoUtain, 15 Mi W, N Slope	U
USNM	246373	*Uar*	Alaska	Pavlof MoUtain, 15 Mi W, N Slope	U
USNM	246556	*Uar*	Alaska	Prince William SoUd, Hinchinbrook Island	U
USNM	246747	*Uar*	Alaska	Flat, Moore Creek	U
USNM	247323	*Uar*	Alaska	Bartlett Bay	U
USNM	247324	*Uar*	Alaska	Chichagof Island, Head Of Port Frederick	U
USNM	247325	*Uar*	Alaska	Chichagof Island, Head Of Port Frederick	U
USNM	247356	*Uar*	Alaska	Bremner River, Tributary Of Copper River	U
USNM	248089	*Uar*	Alaska	Chichagof Island, Wachusetts Bay	U
USNM	248090	*Uar*	Alaska	Chichagof Island, Wachusetts Bay	U
USNM	248091	*Uar*	Alaska	Chichagof Island, Freshwater Bay	U
USNM	248092	*Uar*	Alaska	Chichagof Island, Freshwater Bay	U
USNM	248445	*Uar*	Alaska	Nabesna Glacier	U
USNM	248446	*Uar*	Alaska	White River Glacier, Near	U
USNM	248447	*Uar*	Alaska	White River Glacier, Near	U
USNM	248538	*Uar*	Alaska	Chichagof Island, Freshwater Bay	U
USNM	248539	*Uar*	Alaska	Chichagof Island, Freshwater Bay	U
USNM	248540	*Uar*	Alaska	Chichagof Island, Freshwater Bay	U
USNM	248585	*Uar*	Alaska	Kodiak Island, Karluk Lake	U
USNM	248692	*Uar*	Alaska	Talkeetna River, Mouth Of Aspen Creek	U
USNM	249320	*Uar*	Alaska	Chichagof Island, Crab Bay	U
USNM	249321	*Uar*	Alaska	Chichagof Island, Corner Bay	U
USNM	250522	*Uar*	Alaska	Chichagof Island, Corner Bay	U
USNM	250523	*Uar*	Alaska	Chichagof Island, Crab Bay	U
USNM	250524	*Uar*	Alaska	Chichagof Island, Finn Cove	U
USNM	250656	*Uar*	Alaska	Admiralty Island, W Side, Hawk Inlet	U
USNM	250657	*Uar*	Alaska	Rainey Pass, 3 Mi Creek, Tributary Of Happy River	U
USNM	256493	*Uar*	Alaska	Hinchinbrook Island	U
USNM	259307	*Uar*	Alaska	Admiralty Island, Windfall Harbor	U
USNM	259308	*Uar*	Alaska	Admiralty Island, Gambier Bay	U
USNM	261601	*Uar*	Alaska	Admiralty Island, S Side Mole Harbor	U
USNM	262478	*Uar*	Alaska	Chichagof Island, Tenakee Inlet	U
USNM	262479	*Uar*	Alaska	Hinchinbrook Island	U
USNM	286834	*Uar*	Alaska	Cook's Inlet, Tuxedni Bay, N Side	U
USNM	290385	*Uar*	Alaska	Anaktuvuk Pass	U
USNM	290386	*Uar*	Alaska	Anaktuvuk Pass	U
USNM	290387	*Uar*	Alaska	Tolugak Lake	U
USNM	290388	*Uar*	Alaska	Canning River Valley, 5 Mi W Of Schublick Spring	U
USNM	292035	*Uar*	Alaska	Brooks Range, Savioyuk Valley	U
USNM	292124	*Uar*	Alaska	Tolugak Lake	U
USNM	292125	*Uar*	Alaska	Tolugak Lake	U

USNM	293123	*Uar*	Alaska	Point Barrow, 115 Mi SE, Titalvk	U
USNM	293782	*Uar*	Alaska	Chandalar Valley, Arctic Village	U
USNM	294029	*Uar*	Alaska	Chandalar River, 4 Mi, Arctic Village	U
USNM	294405	*Uar*	Alaska	Kodiak Island, N Part	U
USNM	347457	*Uar*	Alaska	Yakataga Beach	U
USNM	347895	*Uar*	Alaska	Anchorage, Crocker Stores	U
USNM	514457	*Uar*	Alaska	Kodiak Island, Kaugnak Bay	U
USNM	143018	*Uar*	Arizona	Graham CoUty, Locality: Blue Post Office	U
USNM	157628	*Uar*	Arizona	Escudilla MoUtains	U
USNM	206451	*Uar*	Arizona	Greenlee CoUty, Locality: Blue, Near	U
USNM	210540	*Uar*	Arizona	Payson, 8 Mi N, Near Green Valley	U
USNM	242652	*Uar*	Arizona	William, 30 Mi S Bear Caon	U
USNM	A01219	*Uar*	California	Monterey	U
USNM	A01220	*Uar*	California	Monterey	U
USNM	A03537	*Uar*	California	Fort Tejon	U
USNM	A03538	*Uar*	California	Fort Tejon	U
USNM	A04161	*Uar*	California	indet	U
USNM	A06905	*Uar*	California	Monterey	U
USNM	A07401	*Uar*	California	Monterey	U
USNM	A15421	*Uar*	California	indet	U
USNM	A15682	*Uar*	California	San Fernando Mission	U
USNM	A16624	*Uar*	California	indet	U
USNM	A21668	*Uar*	California	indet	U
USNM	131902	*Uar*	California	indet	U
USNM	156594	*Uar*	California	Santa Ana MoUtains, Trabuco Caon	U
USNM	206624	*Uar*	California	Dobbins Creek Caon	U
USNM	223401	*Uar*	California	Humboldt CoUty, Locality: Blocksburg, 10 Mi From In Peat Caon	U
USNM	228225	*Uar*	California	Isabel Valley, Hubbard Ranch, MoUt Hamilton	U
USNM	228226	*Uar*	California	Isabel Valley, Hubbard Ranch, MoUt Hamilton	U
USNM	569133	*Uar*	California	San Francisco	U
USNM	75613	*Uar*	Alberta	Alberta, Locality: Henry House	U
USNM	75614	*Uar*	Alberta	Alberta, Locality: Henry House	U
USNM	180978	*Uar*	Alberta	N Saskatchewan River, Forks	U
USNM	180979	*Uar*	Alberta	N Saskatchewan River, Forks	U
USNM	210706	*Uar*	Alberta	Morley	U
USNM	222103	*Uar*	Alberta	Smoky River, District of	U
USNM	222107	*Uar*	Alberta	Smoky River, District of	U
USNM	222745	*Uar*	Alberta	Jasper	U
USNM	222759	*Uar*	Alberta	Brazeau River	U
USNM	225625	*Uar*	Alberta	Smoky River	U
USNM	228698	*Uar*	Alberta	Simpson Pass, E Slope Rockies	U
USNM	231529	*Uar*	Alberta	indet	U
USNM	231530	*Uar*	Alberta	indet	U
USNM	231531	*Uar*	Alberta	indet	U
USNM	231582	*Uar*	Alberta	Banff	U
USNM	233700	*Uar*	Alberta	Rocky MoUtain House	U
USNM	233701	*Uar*	Alberta	Smoky River	U
USNM	233702	*Uar*	Alberta	Smoky River	U
USNM	250217	*Uar*	Alberta	Sheep Creek, 18 Mi N, 25 Mi N Of Smoky River	U

USNM	71818	*Uar*	British Columbia	Shuswap	U
USNM	71819	*Uar*	British Columbia	Shuswap	U
USNM	71820	*Uar*	British Columbia	Shuswap	U
USNM	139188	*Uar*	British Columbia	Iskut River	U
USNM	156984	*Uar*	British Columbia	Iskut River	U
USNM	169223	*Uar*	British Columbia	Telegraph Creek	U
USNM	170662	*Uar*	British Columbia	Klappan MoUtains	U
USNM	171047	*Uar*	British Columbia	Stikine River, Klappan Creek	U
USNM	171048	*Uar*	British Columbia	Stikine River, Klappan Creek	U
USNM	171050	*Uar*	British Columbia	Stikine River, Klappan Creek	U
USNM	171510	*Uar*	British Columbia	Cassiar MoUtains, Head Of Salmon Creek, Tributary Of Stikine River	U
USNM	171511	*Uar*	British Columbia	Cassiar MoUtains, Head Of Salmon Creek, Tributary Of Stikine River	U
USNM	177648	*Uar*	British Columbia	Nahlin River	U
USNM	180878	*Uar*	British Columbia	Jack Pine River, 100 Mi N Of Grand TrUk Pacific Rr	U
USNM	180879	*Uar*	British Columbia	Jack Pine River, 100 Mi N Of Grand TrUk Pacific Rr	U
USNM	180881	*Uar*	British Columbia	Clearwater, Branch Of Stikine River	U
USNM	180882	*Uar*	British Columbia	Clearwater, Branch Of Stikine River	A
USNM	180883	*Uar*	British Columbia	Clearwater, Branch Of Stikine River	U
USNM	180884	*Uar*	British Columbia	Spence's Bridge Spring, 10 Mi N	U
USNM	180980	*Uar*	British Columbia	Stikine River, 20 Mi From Dease Lake	U
USNM	180981	*Uar*	British Columbia	Stikine River, 20 Mi From Dease Lake	A
USNM	180982	*Uar*	British Columbia	Stikine River, 20 Mi From Dease Lake	U
USNM	201364	*Uar*	British Columbia	Stikine River, 100 Mi From Telegraph Creek	U
USNM	201366	*Uar*	British Columbia	Stikine River, Headwaters, 130 Mi SE Telegraph Creek	U
USNM	202792	*Uar*	British Columbia	Tatletuey Lake, Head	U
USNM	202793	*Uar*	British Columbia	Tatletuey Lake, Head	U
USNM	202795	*Uar*	British Columbia	Upper Skeena	A
USNM	203479	*Uar*	British Columbia	Iskut River, 40 Mi Up Tributary Of Stikine River	U
USNM	203480	*Uar*	British Columbia	Iskut River, 40 Mi Up Tributary Of Stikine River	U
USNM	205166	*Uar*	British Columbia	Wapiti River	U
USNM	205171	*Uar*	British Columbia	Selkirk MoUtains, Upper Columbia River	U
USNM	206137	*Uar*	British Columbia	Shesley River, Strikine River	A
USNM	206626	*Uar*	British Columbia	Bella Bella	U
USNM	209378	*Uar*	British Columbia	N Fork Big Salmon River, Head	U
USNM	209898	*Uar*	British Columbia	Indian Point Creek, Barkerville	U
USNM	209899	*Uar*	British Columbia	Indian Point Creek, Barkerville	U
USNM	209900	*Uar*	British Columbia	Spillimacheen River, Head	U
USNM	209901	*Uar*	British Columbia	Columbia River	U
USNM	209902	*Uar*	British Columbia	Kootenay Lake, Cave Creek	U
USNM	209903	*Uar*	British Columbia	Cassiar MoUtains, Klappan River, 10 Mi S Of Klappan Crossing	U
USNM	209910	*Uar*	British Columbia	Selkirk MoUtains, Toby Creek	U
USNM	209913	*Uar*	British Columbia	Skeena River, Upper	U
USNM	209914	*Uar*	British Columbia	Skeena River, Upper	U
USNM	209915	*Uar*	British Columbia	Skeena River, Upper	U
USNM	210130	*Uar*	British Columbia	Salmon Creek, 30 Mi N Of Telegraph Creek	U
USNM	210131	*Uar*	British Columbia	Salmon Creek, 30 Mi N Of Telegraph Creek	U
USNM	210132	*Uar*	British Columbia	Salmon Creek, 30 Mi N Of Telegraph Creek	U
USNM	210133	*Uar*	British Columbia	Salmon Creek, 30 Mi N Of Telegraph Creek	U
USNM	210134	*Uar*	British Columbia	Shesley River, 45 Mi N Of Telegraph Creek	U

USNM	210135	*Uar*	British Columbia	Shesley River, 45 Mi N Of Telegraph Creek	U
USNM	210136	*Uar*	British Columbia	Shesley River, 45 Mi N Of Telegraph Creek	U
USNM	210137	*Uar*	British Columbia	Shesley River, 45 Mi N Of Telegraph Creek	U
USNM	210309	*Uar*	British Columbia	Indian Point Creek	U
USNM	210430	*Uar*	British Columbia	Athalmer, Findley Creek	U
USNM	210442	*Uar*	British Columbia	Poplar Creek	U
USNM	210444	*Uar*	British Columbia	Poplar Creek	U
USNM	210445	*Uar*	British Columbia	Poplar Creek	U
USNM	210443	*Uar*	British Columbia	Poplar Creek	U
USNM	210446	*Uar*	British Columbia	Nelson	U
USNM	210447	*Uar*	British Columbia	Nelson	U
USNM	210578	*Uar*	British Columbia	Atnarko River	U
USNM	210579	*Uar*	British Columbia	Atnarko River	U
USNM	242643	*Uar*	British Columbia	Bella Coola	U
USNM	242196	*Uar*	British Columbia	Bella Coola	U
USNM	242197	*Uar*	British Columbia	Bella Coola	U
USNM	242195	*Uar*	British Columbia	Bella Coola	U
USNM	243187	*Uar*	British Columbia	Atlin, Within 30 Mi	U
USNM	243188	*Uar*	British Columbia	Atlin, Within 30 Mi	U
USNM	244007	*Uar*	British Columbia	Barkerville, On Williams Creek	U
USNM	244497	*Uar*	British Columbia	Indian Point Creek	U
USNM	244498	*Uar*	British Columbia	Indian Point Creek	U
USNM	247076	*Uar*	British Columbia	Wapiti River, Headwaters	U
USNM	249873	*Uar*	British Columbia	Indian Point Creek	U
USNM	251406	*Uar*	British Columbia	Rapid River, Near Head	U
USNM	256520	*Uar*	British Columbia	Needham Creek, Head	U
USNM	256521	*Uar*	British Columbia	Redfern Lake	U
USNM	256522	*Uar*	British Columbia	Robb Lake	U
USNM	257442	*Uar*	British Columbia	SukUka River	U
USNM	266164	*Uar*	British Columbia	Barkerville, NE, Hogan Creek	U
USNM	261602	*Uar*	British Columbia	Columbia River, Selkirk MoUtains, Carnes Creek	U
USNM	268007	*Uar*	British Columbia	Henry River, Upper	U
USNM	271725	*Uar*	British Columbia	MoUt Robson	U
USNM	287669	*Uar*	British Columbia	Bull River	U
USNM	287670	*Uar*	British Columbia	Stikine - Klaplan Rivers	U
USNM	292955	*Uar*	British Columbia	Fort Nelson, 75 Mi W	U
USNM	349498	*Uar*	British Columbia	Pesika River, Headwaters	U
USNM	551611	*Uar*	British Columbia	Bull River, Sulphur Creek	U
USNM	A07146	*Uar*	NorthWest Territories	Franklin Bay	U
USNM	134237	*Uar*	Yukon	Pelly River, Near Hode's Canon	U
USNM	134486	*Uar*	Yukon	Macmillan River	U
USNM	135197	*Uar*	Yukon	Robinson, 8 Mi W, Midway Between White Horse And Lake Bennett	U
USNM	135204	*Uar*	Yukon	Coal Creek, Head	U
USNM	137521	*Uar*	Yukon	Klukwan and Dalton Post, Between	U
USNM	179892	*Uar*	Yukon	Macmillan River	U
USNM	180984	*Uar*	Yukon	Macmillan River, 150-175 Mi Up	U
USNM	202949	*Uar*	Yukon	White River, Head Of, Caldern Creek, 30 Mi E MoUt Natazat	U
USNM	203161	*Uar*	Yukon	White River, Head Of, Caldern Creek, 30 Mi E MoUt Natazat	U
USNM	204186	*Uar*	Yukon	Mcconell River	U

USNM	204187	*Uar*	Yukon	Mcconell River	U
USNM	205167	*Uar*	Yukon	Stewart River	U
USNM	205162	*Uar*	Yukon	St. Clair River	U
USNM	205163	*Uar*	Yukon	St. Clair River	U
USNM	205164	*Uar*	Yukon	St. Clair River	U
USNM	205165	*Uar*	Yukon	Kluane Lake	A
USNM	206530	*Uar*	Yukon	Kluane Lake	U
USNM	206531	*Uar*	Yukon	Kluane Lake	U
USNM	209894	*Uar*	Yukon	Jenerk River	U
USNM	209895	*Uar*	Yukon	Kluane Lake	U
USNM	209896	*Uar*	Yukon	White River	U
USNM	209897	*Uar*	Yukon	White River	U
USNM	210448	*Uar*	Yukon	Champagne Landing, Near	U
USNM	210449	*Uar*	Yukon	Champagne Landing, Near	U
USNM	214476	*Uar*	Yukon	Ross River	U
USNM	215708	*Uar*	Yukon	Pelly MoUtains	U
USNM	215709	*Uar*	Yukon	Pelly MoUtains	U
USNM	215710	*Uar*	Yukon	Pelly MoUtains	U
USNM	215711	*Uar*	Yukon	Pelly MoUtains	U
USNM	215713	*Uar*	Yukon	Ross MoUtains	U
USNM	221600	*Uar*	Yukon	Ross River	U
USNM	221620	*Uar*	Yukon	Kluane River	U
USNM	221621	*Uar*	Yukon	O'Conner River	U
USNM	221622	*Uar*	Yukon	Alsek River, Head	A
USNM	221623	*Uar*	Yukon	Donjek River	U
USNM	221624	*Uar*	Yukon	Kluane Lake	U
USNM	221629	*Uar*	Yukon	Alsek River	U
USNM	222758	*Uar*	Yukon	White Horse, E	U
USNM	223164	*Uar*	Yukon	Champagne Landing	U
USNM	223690	*Uar*	Yukon	Champagne	U
USNM	223751	*Uar*	Yukon	Hootalingua	A
USNM	223760	*Uar*	Yukon	Glenlyon Range	U
USNM	223761	*Uar*	Yukon	Little Salmon	U
USNM	223766	*Uar*	Yukon	Nesutlin River	U
USNM	223767	*Uar*	Yukon	Quiet Lake, Head Big Salmon River	U
USNM	223768	*Uar*	Yukon	Teslin Lake	U
USNM	223769	*Uar*	Yukon	Marsh Lake	U
USNM	225821	*Uar*	Yukon	Champagne	A
USNM	226412	*Uar*	Yukon	Kluane, Glodstone Creek	U
USNM	226413	*Uar*	Yukon	Kluane, Donjek River	U
USNM	226414	*Uar*	Yukon	Kluane, Donjek River	U
USNM	227064	*Uar*	Yukon	Mcmillan River	U
USNM	227838	*Uar*	Yukon	Enerk River	U
USNM	227973	*Uar*	Yukon	Dalton House	U
USNM	227975	*Uar*	Yukon	Dasadeash Lake	U
USNM	227977	*Uar*	Yukon		U
USNM	227993	*Uar*	Yukon	Dalton House	U
USNM	227996	*Uar*	Yukon	Kluane	U
USNM	227999	*Uar*	Yukon	Champagne	U

USNM	228213	*Uar*	Yukon	Little Arm Kluane	U
USNM	228214	*Uar*	Yukon	Donjek River	U
USNM	228215	*Uar*	Yukon	Little Arm Kluane	U
USNM	228216	*Uar*	Yukon	Donjek River	U
USNM	228217	*Uar*	Yukon	Donjek River	U
USNM	228228	*Uar*	Yukon	White Horse	U
USNM	228316	*Uar*	Yukon	Little Salmon River, Upper	U
USNM	228526	*Uar*	Yukon	Yukon	U
USNM	228711	*Uar*	Yukon	Nieling River, Head	U
USNM	228712	*Uar*	Yukon	Kluane Lake	U
USNM	228713	*Uar*	Yukon	Kluane, Duke River	U
USNM	228714	*Uar*	Yukon	Kluane, Duke River	U
USNM	228861	*Uar*	Yukon	Teslin Lake	U
USNM	228862	*Uar*	Yukon	Rose and Little Salmon Rivers, Between	U
USNM	228863	*Uar*	Yukon	Kluane River	U
USNM	228880	*Uar*	Yukon	Mcmillan River	U
USNM	228881	*Uar*	Yukon	Nieling River, Head	U
USNM	228882	*Uar*	Yukon	Lapp River	U
USNM	228883	*Uar*	Yukon	Pelly River	U
USNM	229232	*Uar*	Yukon	Dasadeash River	U
USNM	229233	*Uar*	Yukon	Ashikik River	U
USNM	229234	*Uar*	Yukon	Caon River	U
USNM	229235	*Uar*	Yukon	Atesk River	U
USNM	229236	*Uar*	Yukon	Klukshu River	U
USNM	229244	*Uar*	Yukon	Nordenskiold River	U
USNM	229245	*Uar*	Yukon	no data	U
USNM	229252	*Uar*	Yukon	Tahkeena	U
USNM	229254	*Uar*	Yukon	Lappie River, Upper Pelly	U
USNM	229255	*Uar*	Yukon	La Barge, Lower	U
USNM	229258	*Uar*	Yukon	Pelly Banks	U
USNM	230643	*Uar*	Yukon	Kluane, Donjek River	U
USNM	230644	*Uar*	Yukon	Kluane, Donjek River	U
USNM	230645	*Uar*	Yukon	Kluane, Duke River	U
USNM	230646	*Uar*	Yukon	Kluane Lake	U
USNM	230647	*Uar*	Yukon	Kluane, Donjek River	U
USNM	230730	*Uar*	Yukon	Glen Lyon Range, Pelly River	U
USNM	230731	*Uar*	Yukon	Big Salmon River	U
USNM	230732	*Uar*	Yukon	Kluane Lake, Long Arm	U
USNM	230733	*Uar*	Yukon	Kluane Lake	U
USNM	230734	*Uar*	Yukon	Kluane Lake	U
USNM	230735	*Uar*	Yukon	Kluane Lake	U
USNM	231298	*Uar*	Yukon	Chilkat River, Bear Creek	U
USNM	231301	*Uar*	Yukon	Nordenskiold River	U
USNM	231303	*Uar*	Yukon	Yukon	U
USNM	231577	*Uar*	Yukon	Whitehorse, 50 Mi W, Near Champagne Landing	U
USNM	231952	*Uar*	Yukon	Whitehorse, Near	U
USNM	232015	*Uar*	Yukon	Pelly River	U
USNM	232390	*Uar*	Yukon	Big Salmon River	U
USNM	232480	*Uar*	Yukon	Ogilvie Range, Klondike Headwaters	U

USNM	232481	*Uar*	Yukon	White Glacier and Tenana, Divide Between	U
USNM	232482	*Uar*	Yukon	Donjek River	U
USNM	232483	*Uar*	Yukon	Donjek River	U
USNM	232484	*Uar*	Yukon	Kluane Lake, Duke River	U
USNM	232485	*Uar*	Yukon	Kluane River	U
USNM	233023	*Uar*	Yukon	Teslin Lake, E Of, On B.C. BoUdary	U
USNM	233024	*Uar*	Yukon	Teslin Lake	U
USNM	233025	*Uar*	Yukon	Little Salmon River	U
USNM	233026	*Uar*	Yukon	Big Salmon River, Near Pelly Divide	U
USNM	233027	*Uar*	Yukon	Alsek River	U
USNM	233028	*Uar*	Yukon	White River, Head	U
USNM	233029	*Uar*	Yukon	Hootalingua River	U
USNM	233030	*Uar*	Yukon	Watron River, South Yukon Territory	U
USNM	233031	*Uar*	Yukon	Nieling River	U
USNM	233036	*Uar*	Yukon	Whitehorse, Ross River	U
USNM	233037	*Uar*	Yukon	Whitehorse, Ross River	U
USNM	233228	*Uar*	Yukon	Whitehorse, E Of	U
USNM	233231	*Uar*	Yukon	Whitehorse, E Of	U
USNM	233232	*Uar*	Yukon	Whitehorse, E Of	U
USNM	233233	*Uar*	Yukon	Whitehorse, E Of	U
USNM	233632	*Uar*	Yukon	Pelly River, Upper, Near Ross Lakes	U
USNM	233633	*Uar*	Yukon	Pelly River, Upper, Ross River	U
USNM	233634	*Uar*	Yukon	Pelly River, Upper, Ross River	U
USNM	233635	*Uar*	Yukon	Pelly River, Upper, Ketza River	U
USNM	233636	*Uar*	Yukon	Pelly River, Upper, Hoole Caon	U
USNM	233637	*Uar*	Yukon	Pelly MoUtains, Between Pelly And Nesultin Rivers	U
USNM	233638	*Uar*	Yukon	Macmillan River	U
USNM	233703	*Uar*	Yukon	Little Salmon River	U
USNM	233704	*Uar*	Yukon	Little Salmon River	U
USNM	234190	*Uar*	Yukon	Pelly River, Upper	U
USNM	234191	*Uar*	Yukon	Pelly River, Upper	U
USNM	234192	*Uar*	Yukon	Pelly River, Upper	U
USNM	234492	*Uar*	Yukon	Yukon River, 10 Mi Below Mouth Of Little Salmon River	U
USNM	235260	*Uar*	Yukon	Yukon	U
USNM	235261	*Uar*	Yukon	O'Connor River Kaskawulsh River	U
USNM	235262	*Uar*	Yukon	Kluane	U
USNM	235263	*Uar*	Yukon	Ashiak Lake	U
USNM	235264	*Uar*	Yukon	Dalton House	U
USNM	235301	*Uar*	Yukon	Champagne Landing	U
USNM	235302	*Uar*	Yukon	Big Salmon River, Near	U
USNM	235303	*Uar*	Yukon	Macmillan River, Head Of	U
USNM	235304	*Uar*	Yukon	Macmillan River, Head Of	U
USNM	235305	*Uar*	Yukon	Alsek River	U
USNM	235306	*Uar*	Yukon	Alsek River	U
USNM	235307	*Uar*	Yukon	Liard River, Head Of	U
USNM	235308	*Uar*	Yukon	Nahanni River, Near Northwest Territories BoUdary	U
USNM	235309	*Uar*	Yukon	Pelly River, Upper, On Head Of Orchay River	U
USNM	235310	*Uar*	Yukon	Pelly River, Upper, On Head Of Orchay River	U
USNM	235311	*Uar*	Yukon	Pelly River, Upper, Above Hoole Caon	U

USNM	235312	*Uar*	Yukon	Pelly River, Near Head	U
USNM	235313	*Uar*	Yukon	Pelly River, Upper	U
USNM	235324	*Uar*	Yukon	Kluane River	U
USNM	235325	*Uar*	Yukon	Kluane Lake	U
USNM	235326	*Uar*	Yukon	Kluane, Little Arm	U
USNM	235327	*Uar*	Yukon	Kluane, Big Arm	U
USNM	235328	*Uar*	Yukon	Kluane, Donjek River	U
USNM	235329	*Uar*	Yukon	Kluane, Donjek River	U
USNM	235520	*Uar*	Yukon	Whitehorse, Near	U
USNM	240403	*Uar*	Yukon	Big Horn Creek	U
USNM	242292	*Uar*	Yukon	Lake Arkel	U
USNM	242293	*Uar*	Yukon	Lake Arkel	U
USNM	242294	*Uar*	Yukon	Dalton House	U
USNM	242295	*Uar*	Yukon	Dalton House	U
USNM	242296	*Uar*	Yukon	Hooche	U
USNM	243189	*Uar*	Yukon	Crow's Nest Pass	U
USNM	243190	*Uar*	Yukon	Champagne	U
USNM	243191	*Uar*	Yukon	Champagne	U
USNM	243192	*Uar*	Yukon	Champagne	U
USNM	243684	*Uar*	Yukon	Carmacks	U
USNM	243685	*Uar*	Yukon	Carmacks	U
USNM	399315	*Uar*	Yukon	Lake Dezadeash	U
USNM	113410	*Uar*	Colorado	Marvine	U
USNM	113411	*Uar*	Colorado	Miller Creek	U
USNM	149016	*Uar*	Colorado	Pagosa Springs	U
USNM	150356	*Uar*	Colorado	Pagosa Springs	U
USNM	150358	*Uar*	Colorado	San Miguel MoUtains, Lone Cone	U
USNM	177551	*Uar*	Colorado	Cochetopa National Forest, California Gultch	U
USNM	177552	*Uar*	Colorado	Saquache, 12 Mi NE	U
USNM	203178	*Uar*	Colorado	Williams River, S Branch	U
USNM	203203	*Uar*	Colorado	Indian Creek	U
USNM	203204	*Uar*	Colorado	Indian Creek	U
USNM	206528	*Uar*	Colorado	Williams River, S Fork	U
USNM	211040	*Uar*	Colorado	Grand CoUty , Kremmling	U
USNM	213000	*Uar*	Colorado	Navaho Range, Near Cromo	U
USNM	213001	*Uar*	Colorado	Navaho Range, Near Cromo	U
USNM	213002	*Uar*	Colorado	Navaho Range, Near Cromo	U
USNM	248537	*Uar*	Colorado	Creede, S, On Middle Creek	U
USNM	274490	*Uar*	Colorado	Saguache CoUty, Saguache Creek, Upper	U
USNM	274179	*Uar*	Colorado	Mineral CoUty, Lake Fork, 20 Mi S Wagon Wheel Gap	U
USNM	A 12397	*Uar*	Idaho	Teton	U
USNM	A 31276	*Uar*	Idaho	Lemhi MoUtains, 10 Mi West Of JUction, Timber Cr. Valley	U
USNM	227058	*Uar*	Idaho	Salmon River, Five Mile Creek	U
USNM	228342	*Uar*	Idaho	Minidoka	U
USNM	233241	*Uar*	Idaho	Meadow Creek	U
USNM	242644	*Uar*	Idaho	Laidlaw Park, NW Corner	U
USNM	242698	*Uar*	Idaho	Minidoka, 25 Mi N, S End Of Valley Of The Moon	U
USNM	243603	*Uar*	Idaho	Bear Park, 33 Mi N Of Minidoka	U
USNM	243743	*Uar*	Idaho	Bear Park, 35 Mi NE Minidoka, Snake River Desert	U

USNM	243908	*Uar*	Idaho	Laidlaw Park, 30 Mi N Of Kimama	U
USNM	248335	*Uar*	Idaho	Wild Horse Butte, 20 Mi NE Kimama	U
USNM	274070	*Uar*	Idaho	Fremont CoUty, Targhee Creek, Near Henry's Lake	U
USNM	98320	*Uar*	Mexico	Chihuahua, Colonia Garcia, Near	U
USNM	98323	*Uar*	Mexico	Chihuahua, Colonia Garcia	U
USNM	98324	*Uar*	Mexico	Chihuahua, Colonia Garcia	A
USNM	98327	*Uar*	Mexico	Chihuahua, Colonia Juarez	A
USNM	99657	*Uar*	Mexico	Chihuahua, Colonia Garcia	U
USNM	99664	*Uar*	Mexico	Chihuahua, Colonia Garcia	A
USNM	170557	*Uar*	Mexico	Chihuahua, Galligo, Mts; 11 Mi W	U
USNM	203175	*Uar*	Mexico	Sonora, Casas Grandes, 60-70 Mi WSW, 12 Mi W Of Contiental Divide	U
USNM	A 13245	*Uar*	Montana	Big Horn Creek	U
USNM	74896	*Uar*	Montana	Flathead CoUty, Paola, Near, 1/2 Down W Slope From Summitt	U
USNM	74897	*Uar*	Montana	Paola, Near, Halfway Down W Slope From Summit Station	U
USNM	202739	*Uar*	Montana	Missouri Breaks, About 100 Mi N Of Fort Miles	U
USNM	203188	*Uar*	Montana	Blackfoot, Headwaters Of The N Fork	U
USNM	205168	*Uar*	Montana	Yellowstone Park Region	U
USNM	205184	*Uar*	Montana	Park CoUty, Tom Minor Basin	U
USNM	206594	*Uar*	Montana	Creves Creek, Just Outside Yellowstone Park N BoUdary	U
USNM	209905	*Uar*	Montana	Slough Creek	U
USNM	209907	*Uar*	Montana	Crevice Creek	U
USNM	211240	*Uar*	Montana	Sage Creek, Near NW Corner Yellowstone Park	A
USNM	212316	*Uar*	Montana	Gardiner, Near	U
USNM	212317	*Uar*	Montana	Gardiner, Near	U
USNM	212318	*Uar*	Montana	Gardiner, Near	U
USNM	212319	*Uar*	Montana	Gardiner, Near	U
USNM	216205	*Uar*	Montana	Park CoUty, Hell Roaring	U
USNM	216208	*Uar*	Montana	Park CoUty, Hell Roaring, Slough Creek	U
USNM	222097	*Uar*	Montana	Gardiner	U
USNM	222098	*Uar*	Montana	Gardiner	U
USNM	222100	*Uar*	Montana	Gardiner, Reece Creek	U
USNM	222753	*Uar*	Montana	Swan Range	U
USNM	222754	*Uar*	Montana	Swan Range	U
USNM	223271	*Uar*	Montana	Madison River, Near, Divide Between Teepee And Red Creeks	U
USNM	223699	*Uar*	Montana	Flathead, S Fork, Near Silver Tip Peak	U
USNM	223700	*Uar*	Montana	Flathead, S Fork	U
USNM	225609	*Uar*	Montana	Tom Minor Basin	U
USNM	225618	*Uar*	Montana	Tom Minor Basin	U
USNM	225621	*Uar*	Montana	Slough Creek	U
USNM	225622	*Uar*	Montana	Slough Creek	U
USNM	227091	*Uar*	Montana	Glacier National Park, Camas Creek, Just N Of Lake Mcdonald	U
USNM	227094	*Uar*	Montana	Swan Lake	U
USNM	227097	*Uar*	Montana	Gardiner, 35 Mi NE On Buffalo Fork Creek	U
USNM	227098	*Uar*	Montana	Swan Lake	U
USNM	227102	*Uar*	Montana	Swan Lake	U
USNM	227663	*Uar*	Montana	Crevice Creek	U
USNM	227847	*Uar*	Montana	Swan Lake	U
USNM	227848	*Uar*	Montana	Big Timber, Boulder Region	U
USNM	227970	*Uar*	Montana	Glacier National Park	U

USNM	227979	*Uar*	Montana	Rexford	U
USNM	227988	*Uar*	Montana	Flathead River, S Fork	U
USNM	228487	*Uar*	Montana	Madison CoUty, Norris	U
USNM	228610	*Uar*	Montana	Glacier National Park	U
USNM	228611	*Uar*	Montana	Flattop MoUtain, Glacier Park	U
USNM	228645	*Uar*	Montana	Glacier National Park, Adair Ranch	U
USNM	228728	*Uar*	Montana	Gardiner, 2 Mi From On L.H. Van Dyck Co. Ranch	U
USNM	228729	*Uar*	Montana	Gardiner, 2 Mi From, On L. H. Van Dyck Co. Ranch	U
USNM	228769	*Uar*	Montana	Flathead CoUty, Essex, Near, Mouth Of Park River	U
USNM	228793	*Uar*	Montana	Flathead CoUty, Essex	U
USNM	230650	*Uar*	Montana	St. Mary's Lake, Lower	U
USNM	230739	*Uar*	Montana	Flathead River	U
USNM	231426	*Uar*	Montana	Kalispel, West Of	U
USNM	231435	*Uar*	Montana	Grayling	U
USNM	231436	*Uar*	Montana	Madison CoUty	U
USNM	231552	*Uar*	Montana	Missoula CoUty, SU River, S Fork	U
USNM	231553	*Uar*	Montana	Carbella, Yellowstone River	U
USNM	231978	*Uar*	Montana	Tobacco Plains	U
USNM	234058	*Uar*	Montana	Contact	U
USNM	234059	*Uar*	Montana	Gardiner	U
USNM	234629	*Uar*	Montana	Hell Roaring	U
USNM	235494	*Uar*	Montana	Cliff Lake	U
USNM	236106	*Uar*	Montana	Slough Creek Ranch, On Yellowstone Park N BoUdary	U
USNM	236107	*Uar*	Montana	Slough Creek Ranch, On Yellowstone Park N BoUdary	U
USNM	236108	*Uar*	Montana	Slough Creek Ranch, 1 Mi Above, On N BoUdary Of Yellowstone Park	U
USNM	241625	*Uar*	Montana	Lewis and Clark National Forest, 35 Mi E Of Ovando	U
USNM	241627	*Uar*	Montana	Lewis and Clark National Forest, 35 Mi E Of Ovando	U
USNM	242261	*Uar*	Montana	Glacier National Park	U
USNM	242262	*Uar*	Montana	Tobacco Plains, Whitefish Range	U
USNM	242263	*Uar*	Montana	Tobacco Plains, N Fork Side	U
USNM	243283	*Uar*	Montana	Bitter Root MoUtains, Head Of Beaver River	U
USNM	267479	*Uar*	Montana	Lewistown, Badlands Near Missouri River	U
USNM	A00995	*Uar*	New mexico	Coppermines	U
USNM	67404	*Uar*	New mexico	Sliver City, MoUtain N Of City	U
USNM	67405	*Uar*	New mexico	Sliver City, MoUtain N Of City	U
USNM	140086	*Uar*	New mexico	Datil MoUtains, Kid Springs, 10 Mi NE Of Datil	U
USNM	147468	*Uar*	New mexico	Mimbres River	U
USNM	147469	*Uar*	New mexico	Mimbres River, Head, N Star Mesa	U
USNM	223393	*Uar*	New mexico	Central City, Gila National Forest, Diamond Creek	U
USNM	223394	*Uar*	New mexico	Sierra CoUty, Black Range, 25 Mi NW Of Chloride	U
USNM	223395	*Uar*	New mexico	Sierra CoUty, Black Range, 25 Mi NW Of Chloride	U
USNM	230651	*Uar*	New mexico	Sierra CoUty, Black Range, 25 Mi NW Of Chloride	U
USNM	231286	*Uar*	New mexico	Mogollon, 4 Mi E In Mogollon MoUtains	U
USNM	231287	*Uar*	New mexico	Taos, 20 Mi SE On Rio Chiquito	U
USNM	233671	*Uar*	New mexico	Taos, 20 Mi SE On Rio Chiquito	U
USNM	235098	*Uar*	New mexico	Fairview, 35 Mi NE	U
USNM	262373	*Uar*	New mexico	Hillsboro Peak, E Side Mimbres MoUtains	U
USNM	262374	*Uar*	New mexico	Magdalena Baldy	U
USNM	21783	*Uar*	North Dakota	Fort Buford	U

USNM	203524	*Uar*	North Dakota	Middle Butte, Now Called Bullion Butte, Little Missour River At Mouth Of Bear Creek	U
USNM	A02891	*Uar*	North Dakota	Williams CoUty, Fort Uion	U
USNM	283732	*Uar*	North Dakota	Mckenzie CoUty, Killdeer MoUtains, W Of	U
USNM	A 22393	*Uar*	Norway		U
USNM	252584	*Uar*	Norway	Sogn Og Fjordane, Laerdal MUicipality, Laerdal	U
USNM	160152	*Uar*	Oregon	Wallowa National Forest, Township 4 N Range 46 E, Near Billy Meadows	U
USNM	203162	*Uar*	Oregon	Wallowa MoUtain	U
USNM	250124	*Uar*	Oregon	Enterprise	U
USNM	264443	*Uar*	Oregon	Malheur Lake	U
USNM	A 21273	*Uar*	Russia	Kamchatka	U
USNM	A 21274	*Uar*	Russia	Kamchatka	U
USNM	A 21275	*Uar*	Russia	Kamchatka	U
USNM	A 21276	*Uar*	Russia	Kamchatka	U
USNM	A 21277	*Uar*	Russia	Kamchatka	U
USNM	A 21278	*Uar*	Russia	Kamchatka	U
USNM	A 21279	*Uar*	Russia	Kamchatka	U
USNM	A 21280	*Uar*	Russia	Kamchatka	A
USNM	A 21281	*Uar*	Russia	Kamchatka	U
USNM	A 21282	*Uar*	Russia	Kamchatka	U
USNM	A 21283	*Uar*	Russia	Kamchatka	U
USNM	A 21284	*Uar*	Russia	Kamchatka	U
USNM	A 21285	*Uar*	Russia	Kamchatka	U
USNM	A 21286	*Uar*	Russia	Kamchatka	U
USNM	A 21287	*Uar*	Russia	Kamchatka	U
USNM	A 21289	*Uar*	Russia	Kamchatka	U
USNM	A 21290	*Uar*	Russia	Kamchatka	U
USNM	A 21291	*Uar*	Russia	Kamchatka	U
USNM	A 21292	*Uar*	Russia	Kamchatka	U
USNM	A 21293	*Uar*	Russia	Kamchatka	A
USNM	A 21294	*Uar*	Russia	Kamchatka	A
USNM	A 21295	*Uar*	Russia	Kamchatka	U
USNM	A 21296	*Uar*	Russia	Kamchatka	U
USNM	A 21337	*Uar*	Russia	Kamchatka	U
USNM	A 22424	*Uar*	Russia	Kamchatka	U
USNM	83445	*Uar*	Russia	Kamchatka	U
USNM	83446	*Uar*	Russia	Kamchatka	U
USNM	105557	*Uar*	Russia	Kamchatka	U
USNM	A 4441	*Uar*	Russia	Siberia	A
USNM	A 7112	*Uar*	Russia	Chukotskiy, Plover Bay	U
USNM	175687	*Uar*	Russia	Siberia, Kooltook, 30 Mi S	U
USNM	175688	*Uar*	Russia	Siberia, Kooltook, 35 Mi S	U
USNM	200771	*Uar*	Russia	Siberia, Lesser Annui River	U
USNM	200772	*Uar*	Russia	Siberia, Greater Annui River	U
USNM	167390	*Uar*	Estados Uidos Utah	Pine Valley MoUtains	U
USNM	180207	*Uar*	Estados Uidos Utah	Mayfield, 2 Mi S Of The Nipple	U
USNM	209909	*Uar*	Estados Uidos Utah	Ashley National Forest	U
USNM	210431	*Uar*	Estados Uidos Utah	Phil Pico MoUtain, 1 Mi N Ashley National Forest	U
USNM	214088	*Uar*	Estados Uidos	Ashley National Forest	U

			Utah		
USNM	214089	*Uar*	Estados Uidos Utah	Ashley National Forest	U
USNM	223034	*Uar*	Estados Uidos Utah	Sevier National Forest	U
USNM	243439	*Uar*	Estados Uidos Utah	Fish Lake Forest, Brown's Hole CoUtry	U
USNM	245631	*Uar*	Estados Uidos Utah	Hyrum, Peterson's Ranch	U
USNM	245632	*Uar*	Estados Uidos Utah	Hyrum, Peterson's Ranch	U
USNM	246357	*Uar*	Estados Uidos Utah	Utah CoUty, Santaquin Caon	U
USNM	243786	*Uar*	Washington	Holman Pass, Head Of Holman Creek, Tributary Of W Fork Of Pasayton River	U
USNM	3698	*Uar*	Washington	Camp Cheloweyuck	U
USNM	A 2893	*Uar*	Wyoming	Yellowstone River	U
USNM	A 16360	*Uar*	Wyoming		U
USNM	1865	*Uar*	Wyoming	Fort Laramie	U
USNM	1866	*Uar*	Wyoming	Fort Laramie, MoUtains Near	U
USNM	1867	*Uar*	Wyoming	Medicine Bow MoUtains, Near Fort Laramie	U
USNM	3103	*Uar*	Wyoming	Medicine Bow MoUtains	U
USNM	55936	*Uar*	Wyoming	Del Norte Creek	U
USNM	145263	*Uar*	Wyoming	Yellowstone National Park	U
USNM	170459	*Uar*	Wyoming	Valley	U
USNM	177660	*Uar*	Wyoming	Yellowstone National Park, Lake Hotel	U
USNM	180985	*Uar*	Wyoming	Jackson Hole	U
USNM	181095	*Uar*	Wyoming	SUdance National Forest	U
USNM	181096	*Uar*	Wyoming	SUdance National Forest	U
USNM	181097	*Uar*	Wyoming	SUdance National Forest	U
USNM	187889	*Uar*	Wyoming	Uintah MoUtains	U
USNM	199699	*Uar*	Wyoming	Yellowstone National Park, Slough Creek	U
USNM	203186	*Uar*	Wyoming	Bighorn MoUtains	U
USNM	203761	*Uar*	Wyoming	Fort Fred Steele	U
USNM	210144	*Uar*	Wyoming	Wind River MoUtains, Near Wind River Peak, About 15 Mi N Of Elkhorn	U
USNM	210244	*Uar*	Wyoming	Yellowstone River, Upper	U
USNM	210584	*Uar*	Wyoming	Laramie MoUtains	U
USNM	211745	*Uar*	Wyoming	Shoshone River	U
USNM	211746	*Uar*	Wyoming	Shoshone River	U
USNM	211747	*Uar*	Wyoming	Shoshone River	U
USNM	212437	*Uar*	Wyoming	Absaroka MoUtains	U
USNM	215437	*Uar*	Wyoming	Laramie MoUtains	U
USNM	215438	*Uar*	Wyoming	Laramie MoUtains	U
USNM	216198	*Uar*	Wyoming	Lincoln CoUty, Aton, Deadman Creek	U
USNM	221718	*Uar*	Wyoming	Lincoln CoUty, Aton, Grass River	U
USNM	227924	*Uar*	Wyoming	Bridger Lake, Thoroughfare Creek	U
USNM	228107	*Uar*	Wyoming	Canfield Creek, E Of Yellowstone National Park	U
USNM	228108	*Uar*	Wyoming	Canfield Creek, E Of Yellowstone National Park	U
USNM	228109	*Uar*	Wyoming	Canfield Creek, E Of Yellowstone National Park	U
USNM	228791	*Uar*	Wyoming	Yellowstone National Park, Near Yellowstone Caon, Specimen Ridge	U
USNM	234699	*Uar*	Wyoming	Teton National Forest, Tp 45n R 114w 6th Pm, On Pacific Creek, 2 Mi N Of Maron Road	U
USNM	234709	*Uar*	Wyoming	Slide	U
USNM	235445	*Uar*	Wyoming	Dubois, 16 Mi NE, Twp 44n R 105w 6th Pm	U
USNM	243825	*Uar*	Wyoming	Squirrel Meadows	U

USNM	244175	*Uar*	Wyoming	Gros Ventre Valley, Upper, N Fish Creek	U
USNM	244176	*Uar*	Wyoming	Black Rock Creek, Branch Of Buffalo Creek, Upper Part Jackson Hole	U
USNM	246358	*Uar*	Wyoming	Fish Creek, Near JUction With Park Creek, Jackson Hole Area	U
USNM	283629	*Uar*	Wyoming	Yellowstone National Park, Near Old Faithful	U
USNM	287668	*Uar*	Wyoming	NW Part	U
USNM	301690	*Uar*	Wyoming	Yellowstone National Park	U
USNM	301691	*Uar*	Wyoming	Yellowstone National Park	U
USNM	79293	*Uar*	Alaska	Cook's Inlet	U
USNM	79294	*Uar*	Alaska	Karta Bay, Prince Of Wales Island	U
USNM	79296	*Uar*	Alaska	Wrangell	U
USNM	80708	*Uar*	Alaska	Cook's Inlet	U
USNM	80710	*Uar*	Alaska	Sitka	U
USNM	81096	*Uar*	Alaska	Chichagof Island	U
USNM	81097	*Uar*	Alaska	Chichagof Island	U
USNM	81098	*Uar*	Alaska	Sitka	U
USNM	81099	*Uar*	Alaska	Sitka	U
USNM	81100	*Uar*	Alaska	Sitka	A
USNM	81101	*Uar*	Alaska	Admiralty Island	U
USNM	81102	*Uar*	Alaska	Admiralty Island	A
USNM	82003	*Uar*	Alaska	Pavlof Bay	U
USNM	82004	*Uar*	Alaska	Pavlof Bay	U
USNM	82005	*Uar*	Alaska	Chicago Bay	U
USNM	82006	*Uar*	Alaska	Chicago Bay	U
USNM	82007	*Uar*	Alaska	Pavlof Bay	U
USNM	82008	*Uar*	Alaska	Pavlof Bay	U
USNM	82009	*Uar*	Alaska	Pavlof Bay	U
USNM	82010	*Uar*	Alaska	Pavlof Bay	U
USNM	82011	*Uar*	Alaska	Pavlof Bay	U
USNM	82012	*Uar*	Alaska	Chicago Bay	U
USNM	82013	*Uar*	Alaska	Pavlof Bay	U
USNM	82014	*Uar*	Alaska	Pavlof Bay	U
USNM	82015	*Uar*	Alaska	Pavlof Bay	U
USNM	82016	*Uar*	Alaska	Kuskokwim River	U
USNM	82020	*Uar*	Alaska	South Coast Range, Norton SoUd	U
USNM	82021	*Uar*	Alaska	Yukon River	U
USNM	82022	*Uar*	Alaska	Walaklik, Norton SoUd	U
USNM	82023	*Uar*	Alaska	Shaktolik Hills, Norton SoUd	U
USNM	82024	*Uar*	Alaska	Norton SoUd, Ualaklik River	U
USNM	82025	*Uar*	Alaska	Nelson Lagoon	U
USNM	83703	*Uar*	Alaska	Kodiak Island	U
USNM	89526	*Uar*	Alaska	Yakutat, Near MoUt St. Elias	U
USNM	89527	*Uar*	Alaska	Yakutat	U
USNM	89528	*Uar*	Alaska	MoUt St. Elias	U
USNM	89530	*Uar*	Alaska	Sitka, 12 Mi W, Kruzoff Island, MoUt Edgecumb	U
USNM	89531	*Uar*	Alaska	Chichagof Island, Near Hoonah	U
USNM	89532	*Uar*	Alaska	Sitka, 28 Mi SE, Whale Bay, Baranoff Island	U
USNM	89533	*Uar*	Alaska	Admiralty Island	U
USNM	91669	*Uar*	Alaska	Alaska Peninsula, Pavlof Bay	U
USNM	91670	*Uar*	Alaska	Pavlof Bay	U

USNM	91671	*Uar*	Alaska	Pavlof Bay	U
USNM	91672	*Uar*	Alaska	Pavlof Bay	U
USNM	91673	*Uar*	Alaska	Pavlof Bay	U
USNM	91674	*Uar*	Alaska	Pavlof Bay	U
USNM	91675	*Uar*	Alaska	Pavlof Bay	U
USNM	91676	*Uar*	Alaska	Pavlof Bay	U
USNM	91677	*Uar*	Alaska	Pavlof Bay	U
USNM	91678	*Uar*	Alaska	Pavlof Bay	U
USNM	91679	*Uar*	Alaska	Morzhovoi Bay	U
USNM	91680	*Uar*	Alaska	Morzhovoi Bay	U
USNM	91681	*Uar*	Alaska	Morzhovoi Bay	U
USNM	91682	*Uar*	Alaska	Moroski Bay	U
USNM	91683	*Uar*	Alaska	Moroski Bay	U
USNM	91684	*Uar*	Alaska	Bear Bay	U
USNM	91685	*Uar*	Alaska	Bear Bay	U
USNM	91686	*Uar*	Alaska	Bear Bay	U
USNM	91687	*Uar*	Alaska	Bear Bay	U
USNM	91688	*Uar*	Alaska	Bear Bay	U
USNM	91689	*Uar*	Alaska	Bear Bay	U
USNM	91690	*Uar*	Alaska	Bear Bay	U
USNM	91691	*Uar*	Alaska	Bear Bay	U
USNM	91692	*Uar*	Alaska	Tonki Point	U
USNM	91693	*Uar*	Alaska	Tonki Point	U
USNM	91694	*Uar*	Alaska	Cold Bay	U
USNM	91695	*Uar*	Alaska	Isenbek Bay	U
USNM	91696	*Uar*	Alaska	Isenbek Bay	U
USNM	91697	*Uar*	Alaska	Isenbek Bay	U
USNM	91698	*Uar*	Alaska	Belkofski Bay	U
USNM	91699	*Uar*	Alaska	Belkofski Bay	U
USNM	91700	*Uar*	Alaska	Belkofski Bay	U
USNM	91701	*Uar*	Alaska	Belkofski Bay	U
USNM	91702	*Uar*	Alaska	Belkofski Bay	U
USNM	91703	*Uar*	Alaska	Belkofski Bay	U
USNM	61716	*Uar*	Alaska	Sitka, Between Sitka And Yakutat	U
USNM	61717	*Uar*	Alaska	Sitka	U
USNM	61718	*Uar*	Alaska	Sitka	U
USNM	61719	*Uar*	Alaska	Sitka	U
USNM	63141	*Uar*	Alaska	Portage Bay	U
USNM	67401	*Uar*	Alaska	Kodiak Island	U
USNM	68797	*Uar*	Alaska	Ugashik Lake	U
USNM	69242	*Uar*	Alaska	Ualakli River, Head	U
USNM	69243	*Uar*	Alaska	Nushagak River	U
USNM	69244	*Uar*	Alaska	Ugashik River	U
USNM	69245	*Uar*	Alaska	Ugashik River	U
USNM	69246	*Uar*	Alaska	Ugashik River	U
USNM	69247	*Uar*	Alaska	Ugashik River	U
USNM	75047	*Uar*	Alaska	MoUt St. Elias, Near	U
USNM	75048	*Uar*	Alaska	Yakutat Bay, NW side	U
USNM	75049	*Uar*	Alaska	St. Elias, Near	U

USNM	76465	*Uar*	Alaska	Shaktolik River, Norton SoUd	U
USNM	76466	*Uar*	Alaska	Ualaklik River, Norton SoUd	U
USNM	76467	*Uar*	Alaska	Koyuk River, Head, Norton SoUd	U
USNM	76468	*Uar*	Alaska	Norton SoUd, Ualaklik River	U
USNM	76469	*Uar*	Alaska	Norton SoUd, Shaktalik Hills	U
USNM	76470	*Uar*	Alaska	Shaktolik River, Norton SoUd	U
USNM	76471	*Uar*	Alaska	Pavlof MoUtain	U
USNM	76472	*Uar*	Alaska	Belkofori Bay	U
USNM	76473	*Uar*	Alaska	Belkofori Bay	U
USNM	76474	*Uar*	Alaska	Belkofori Bay	U
USNM	76578	*Uar*	Alaska	Sitka, 10 Mi From, Edgecumbe Island	U
USNM	76579	*Uar*	Alaska	Sitka, 12 Mi SE, Redoubt Lake	A
USNM	79291	*Uar*	Alaska	Yukutat	U
USNM	79292	*Uar*	Alaska	Chichagof Island	U
USNM	178254	*Uam*	Alabama	Carlton	U
USNM	178373	*Uam*	Alabama	Carlton	U
USNM	210061	*Uam*	Alabama	Bayou La Batre	U
USNM	228292	*Uam*	Alabama	Mobile	U
USNM	A21491	*Uam*	Alaska	Nulato	A
USNM	75053	*Uam*	Alaska	Kachemak Bay, Cook Inlet	U
USNM	A9477	*Uam*	Alaska	Kenai	U
USNM	A 8161	*Uam*	Alaska	Nulato - Yukon River	U
USNM	A 8695	*Uam*	Alaska		U
USNM	69240	*Uam*	Alaska	Sheep Creek, Upper Yukon River	U
USNM	69784	*Uam*	Alaska	Porcupine River, 100 NW Rampart House	A
USNM	69785	*Uam*	Alaska	Porcupine River, 100 NW Rampart House	A
USNM	82017	*Uam*	Alaska	Kuskokwim River	U
USNM	82018	*Uam*	Alaska	Yukon River	U
USNM	82019	*Uam*	Alaska	Ualakeet, Norton SoUd	U
USNM	83986	*Uam*	Alaska	MoUt St. Elias	U
USNM	97955	*Uam*	Alaska	White Pass, Glacier	U
USNM	102587	*Uam*	Alaska	MoUt St. Elias	U
USNM	119946	*Uam*	Alaska	DUdas, Area On Mainland Opposite	U
USNM	120358	*Uam*	Alaska	Yakutat	U
USNM	128661	*Uam*	Alaska	Nation Creek, Mouth Of	A
USNM	128668	*Uam*	Alaska	Cape Elizabeth, Near	U
USNM	128669	*Uam*	Alaska	Cape Elizabeth, Near	U
USNM	128670	*Uam*	Alaska	Kenai Peninsula	U
USNM	128671	*Uam*	Alaska	Cape Elizabeth, Near	U
USNM	128673	*Uam*	Alaska	Cape Elizabeth, Near	U
USNM	128674	*Uam*	Alaska	Cape Elizabeth, Near	U
USNM	131544	*Uam*	Alaska	Prince of Wales Island	U
USNM	131545	*Uam*	Alaska	Prince of Wales Island	U
USNM	131546	*Uam*	Alaska	Prince of Wales Island	U
USNM	131547	*Uam*	Alaska	Prince of Wales Island	U
USNM	131548	*Uam*	Alaska	Prince of Wales Island	U
USNM	131549	*Uam*	Alaska	Prince of Wales Island	U
USNM	136098	*Uam*	Alaska	Revillagegido Island	U

USNM	136748	*Uam*	Alaska	Kenai Peninsula	A
USNM	136749	*Uam*	Alaska	Kenai Peninsula	U
USNM	136750	*Uam*	Alaska	Kenai Peninsula	U
USNM	138678	*Uam*	Alaska	Snettisham	U
USNM	138679	*Uam*	Alaska	Snettisham	U
USNM	138700	*Uam*	Alaska	Yankee Cove	U
USNM	138701	*Uam*	Alaska	Yankee Cove	U
USNM	152263	*Uam*	Alaska	Yakutat Fall	U
USNM	155560	*Uam*	Alaska	Ikogmute, On The Yukon River	A
USNM	156974	*Uam*	Alaska	Stikine River, Warburton Pike	U
USNM	156975	*Uam*	Alaska	Stikine River, Warburton Pike	U
USNM	156976	*Uam*	Alaska	Stikine River	U
USNM	156977	*Uam*	Alaska	Stikine River, Warburton Pike	U
USNM	156978	*Uam*	Alaska	Stikine River, Warburton Pike	U
USNM	156979	*Uam*	Alaska	Stikine River, Warburton Pike	U
USNM	156980	*Uam*	Alaska	Stikine River, Warburton Pike	U
USNM	156981	*Uam*	Alaska	Stikine River, Warburton Pike	U
USNM	156982	*Uam*	Alaska	Stikine River, Warburton Pike	U
USNM	156983	*Uam*	Alaska	Sitkine River, Warburton Pike	U
USNM	167929	*Uam*	Alaska	Eagle River	U
USNM	167930	*Uam*	Alaska	Eagle River	U
USNM	176594	*Uam*	Alaska	Berners Bay	U
USNM	176595	*Uam*	Alaska	Berners Bay	U
USNM	177412	*Uam*	Alaska	Endicott River	U
USNM	177413	*Uam*	Alaska	Berners Bay	U
USNM	177414	*Uam*	Alaska	Berners Bay	U
USNM	177415	*Uam*	Alaska	Montana Creek	U
USNM	177657	*Uam*	Alaska	Berners Bay	U
USNM	177658	*Uam*	Alaska	Berners Bay	U
USNM	177659	*Uam*	Alaska	Berners Bay	U
USNM	177962	*Uam*	Alaska	Cook's Inlet, W Of	U
USNM	180276	*Uam*	Alaska	Montana Creek	U
USNM	180277	*Uam*	Alaska	Berners Bay	U
USNM	180278	*Uam*	Alaska	Montana Creek	U
USNM	180279	*Uam*	Alaska	Big River	U
USNM	180990	*Uam*	Alaska	Yes Bay Hatchery	U
USNM	198391	*Uam*	Alaska	Fort Reliance	U
USNM	200149	*Uam*	Alaska		U
USNM	201363	*Uam*	Alaska	Tanana	U
USNM	201585	*Uam*	Alaska	Ketchumstock	U
USNM	202563	*Uam*	Alaska	Chicken, 40 Mi River	U
USNM	202740	*Uam*	Alaska	Chicken	U
USNM	203292	*Uam*	Alaska	Chichagof Island	U
USNM	203294	*Uam*	Alaska	JUeau Region	U
USNM	203295	*Uam*	Alaska	JUeau Region	U
USNM	203296	*Uam*	Alaska	JUeau Region	U
USNM	203528	*Uam*	Alaska	JUeau, Near	U
USNM	203899	*Uam*	Alaska	Chicken	A

USNM	205175	*Uam*	Alaska	Shackeford Creek	U
USNM	205177	*Uam*	Alaska	Cottonwood, Knik Arm	U
USNM	205179	*Uam*	Alaska	Knik River	U
USNM	205181	*Uam*	Alaska	Mallaniska River, Near Mouth	U
USNM	205943	*Uam*	Alaska	Taku	U
USNM	206132	*Uam*	Alaska	Kenai Peninsula	U
USNM	206133	*Uam*	Alaska	Kenai Peninsula	U
USNM	206361	*Uam*	Alaska	Wrangell, 30 Mi SE	U
USNM	206643	*Uam*	Alaska	Kenai Peninsula	A
USNM	206644	*Uam*	Alaska	Kenai Peninsula, Cooper Lake	U
USNM	206645	*Uam*	Alaska	Kenai Peninsula	A
USNM	209867	*Uam*	Alaska	Ptarmigan Lake	U
USNM	209868	*Uam*	Alaska	Ptarmigan Lake	U
USNM	209869	*Uam*	Alaska	Johnson Pass	U
USNM	209871	*Uam*	Alaska	Cooper Lake	U
USNM	209872	*Uam*	Alaska	Kenai Peninsula	U
USNM	209873	*Uam*	Alaska	Cooper Lake	U
USNM	209879	*Uam*	Alaska	Taku Inlet	U
USNM	209880	*Uam*	Alaska	Chulitna River, Near Alaska Range MoUtains	U
USNM	209882	*Uam*	Alaska	Nizina River, Near Mccarthy	U
USNM	209886	*Uam*	Alaska	Snettisham	U
USNM	209888	*Uam*	Alaska	Kake	U
USNM	209893	*Uam*	Alaska	Yakutat Bay, SE Of	U
USNM	210138	*Uam*	Alaska	Chilkat River Valley	U
USNM	210141	*Uam*	Alaska	Chilkat River Valley	U
USNM	210248	*Uam*	Alaska	Toklat River, Near Head Of	U
USNM	210249	*Uam*	Alaska	Toklat River, Near Head Of	U
USNM	210250	*Uam*	Alaska	Taklat River, Near Head Of	U
USNM	210295	*Uam*	Alaska	Yakutat	U
USNM	210296	*Uam*	Alaska	Yakutat	U
USNM	210297	*Uam*	Alaska	Yakutat	U
USNM	210298	*Uam*	Alaska	Yakutat	U
USNM	210299	*Uam*	Alaska	Yakutat	U
USNM	210300	*Uam*	Alaska	Yakutat	U
USNM	210301	*Uam*	Alaska	Yakutat	U
USNM	210302	*Uam*	Alaska	Yakutat	U
USNM	210303	*Uam*	Alaska	Yakutat	U
USNM	210304	*Uam*	Alaska	Yakutat	U
USNM	210305	*Uam*	Alaska	Yakutat	U
USNM	210306	*Uam*	Alaska	Kenai Peninsula	U
USNM	210310	*Uam*	Alaska	Uuk River, Burroughs Bay	U
USNM	210311	*Uam*	Alaska	Uuk River, Burroughs Bay	U
USNM	210312	*Uam*	Alaska	Uuk River, Burroughs Bay	U
USNM	210313	*Uam*	Alaska	Uuk River, Burroughs Bay	U
USNM	210314	*Uam*	Alaska	Uuk River, Burroughs Bay	U
USNM	210315	*Uam*	Alaska	Uuk River, Burroughs Bay	U
USNM	210316	*Uam*	Alaska	Uuk River, Burroughs Bay	U
USNM	210317	*Uam*	Alaska	Uuk River, Burroughs Bay	U
USNM	210318	*Uam*	Alaska	Loring	U

USNM	210319	*Uam*	Alaska	Burroughs Bay	U
USNM	210320	*Uam*	Alaska	Burroughs Bay	U
USNM	210710	*Uam*	Alaska	Yakutat Bay	U
USNM	212258	*Uam*	Alaska	Oganik	U
USNM	213413	*Uam*	Alaska	Kupraenof, Cape Bendal	U
USNM	213702	*Uam*	Alaska	Yakutat Bay, S Side	U
USNM	214448	*Uam*	Alaska	Kluckwan, On The Chilkoot River	U
USNM	214461	*Uam*	Alaska	Chichagof Island	U
USNM	214687	*Uam*	Alaska	Kuiu Island, Saginaw Bay	U
USNM	214688	*Uam*	Alaska	Kuiu Island, Saginaw Bay	U
USNM	214689	*Uam*	Alaska	Kuiu Island, Saginaw Bay	U
USNM	214690	*Uam*	Alaska	Kuiu Island, 3 Mi Arm	U
USNM	214691	*Uam*	Alaska	Kuiu Island, Saginaw Bay	U
USNM	214692	*Uam*	Alaska	Kuiu Island	U
USNM	214693	*Uam*	Alaska	Kupraenof Island	U
USNM	214694	*Uam*	Alaska	Kupraenof Island, Fort Mccartney	U
USNM	214695	*Uam*	Alaska	Kupraenof Island	U
USNM	215457	*Uam*	Alaska	Trout Lake	U
USNM	215458	*Uam*	Alaska	Trout Lake	U
USNM	215459	*Uam*	Alaska	Rat Creek	A
USNM	215460	*Uam*	Alaska	Rat Creek	U
USNM	215461	*Uam*	Alaska	Twote MoUtains	U
USNM	215462	*Uam*	Alaska	Dike Creek	U
USNM	215463	*Uam*	Alaska	Dike Creek	U
USNM	215464	*Uam*	Alaska	Dike Creek	U
USNM	215465	*Uam*	Alaska	Kenai River	U
USNM	215466	*Uam*	Alaska	Chilkloone Flats	U
USNM	218338	*Uam*	Alaska	Chicken	U
USNM	218339	*Uam*	Alaska	No data	U
USNM	218340	*Uam*	Alaska	No data	U
USNM	98321	*Uam*	Mexico Chihuahua	Colonia Garcia	U
USNM	98322	*Uam*	Mexico Chihuahua	Colonia Garcia	U
USNM	98325	*Uam*	Mexico Chihuahua	Colonia Garcia	U
USNM	98326	*Uam*	Mexico Chihuahua	Colonia Garcia	U
USNM	98329	*Uam*	Mexico Chihuahua	Colonia Garcia	U
USNM	99338	*Uam*	Mexico Chihuahua	Colonia Garcia	U
USNM	99665	*Uam*	Mexico Chihuahua	Colonia Garcia	U
USNM	117100	*Uam*	Mexico Chihuahua	Colonia Garcia	U
USNM	132195	*Uam*	Mexico Chihuahua	Colonia Garcia	U
USNM	177661	*Uam*	Mexico Chihuahua	San Luis MoUtains, 12 Mi S of U.S. line.	U
USNM	177662	*Uam*	Mexico Chihuahua	San Luis MoUtains, 55 Mi S Of Us BoUdary	U
USNM	177663	*Uam*	Mexico Chihuahua	San Luis MoUtains	U
USNM	177664	*Uam*	Mexico Chihuahua	San Luis MoUtains	U
USNM	79571	*Uam*	Mexico Coahuila	Sierra Encarnacion	U
USNM	116952	*Uam*	Mexico Coahuila	Sierra Guadalupe	U

USNM	157840	*Uam*	Mexico Coahuila	Muzquiz, 25 Mi NW, Near Hacienda De La Palma	U
USNM	158247	*Uam*	Mexico Coahuila	Muzquiz, 25 Mi NW	U
USNM	159254	*Uam*	Mexico Coahuila	Muzquiz	U
USNM	159258	*Uam*	Mexico Coahuila	Muzquiz, 36 Mi NW	U
USNM	159369	*Uam*	Mexico Coahuila	Muzquiz, 160 Mi NW, Santa Rosa MoUtains	U
USNM	262695	*Uam*	Mexico Coahuila	Carmen MoUtains	U
USNM	177665	*Uam*	Mexico sonora	San Luis MoUtains	U
USNM	203206	*Uam*	Mexico sonora		U
USNM	168824	*Uam*	Michigan	Calderwood	U
USNM	170568	*Uam*	Michigan	Hubbert	U
USNM	170569	*Uam*	Michigan	Sheldrake Lake	U
USNM	170570	*Uam*	Michigan	Sheldrake Lake	U
USNM	177960	*Uam*	Michigan	Marquette CoUty,Turin	U
USNM	177963	*Uam*	Michigan	Marquette CoUty,Turin	U
USNM	514297	*Uam*	Michigan	SchoolcrAt CoUty, Seney National Wildlife Refuge, T45N, R15W, Sec3	U
USNM	A 1162	*Uam*	Michigan	Lake Superior	U
USNM	187886	*Uam*	Minnesota	No data	U
USNM	592332	*Uam*	Minnesota	Saint Louis CoUty	U
USNM	592890	*Uam*	Minnesota	Wadena CoUty, NE ¼ of Sec 4 Aldrich Twp 134N 34W	U
USNM	592891	*Uam*	Minnesota	Wadena CoUty, NE ¼ of Sec 4 Aldrich Twp 134N 34W	U
USNM	225824	*Uam*	Montana	Reese Creek	U
USNM	74887	*Uam*	Montana	Columbia Falls, 35 Mi E, Paola	U
USNM	74888	*Uam*	Montana	Columbia Falls, 35 Mi E, Paola	A
USNM	74889	*Uam*	Montana	Columbia Falls, 35 Mi E, Paola	U
USNM	74890	*Uam*	Montana	Columbia Falls, 35 Mi E, Paola	U
USNM	74891	*Uam*	Montana	Columbia Falls, 35 Mi E, Paola	U
USNM	74892	*Uam*	Montana	Columbia Falls, 35 Mi E, Paola	U
USNM	74893	*Uam*	Montana	Columbia Falls, 35 Mi E, Paola	U
USNM	74894	*Uam*	Montana	Columbia Falls, 35 Mi E, Paola	U
USNM	74895	*Uam*	Montana	Columbia Falls, 35 Mi E, Paola	U
USNM	74898	*Uam*	Montana	Flathead CoUty, Paola, Near, 1/2 Way Down W Slope From Summit Station On Great N R & R	U
USNM	74899	*Uam*	Montana	Flathead CoUty, Paola, Near, 1/2 Way Down W Slope From Summit Station On Great N R & R	U
USNM	74900	*Uam*	Montana	Flathead CoUty, Paola, Near, 1/2 Way Down W Slope From Summit Station On Great N R & R	U
USNM	74901	*Uam*	Montana	Flathead CoUty, Paola, Near, 1/2 Way Down W Slope From Summit Station On Great N R & R	U
USNM	122616	*Uam*	Montana	Flathead CoUty, Columbia Falls, 2 Mi E	U
USNM	167687	*Uam*	Montana	Ravalli CoUty, Corvallis	U
USNM	168827	*Uam*	Montana	Ravalli CoUty, Darby	U
USNM	168828	*Uam*	Montana	Ravalli CoUty, Darby	U
USNM	168829	*Uam*	Montana	Ravalli CoUty, Darby	U
USNM	169222	*Uam*	Montana	Missoula CoUty, Woodman	U
USNM	203187	*Uam*	Montana	Park CoUty, Livingstone	U
USNM	203189	*Uam*	Montana	Flathead River, S Fork	U
USNM	203200	*Uam*	Montana	Flathead River, S Fork	U
USNM	203201	*Uam*	Montana	Flathead River, S Fork	U
USNM	203202	*Uam*	Montana	Flathead River, S Fork	U
USNM	205955	*Uam*	Montana	Park CoUty, Gardiner, Reese Creek	U
USNM	205956	*Uam*	Montana	Park CoUty, Gardiner, Reese Creek	U
USNM	209906	*Uam*	Montana	Reese Creek	U

USNM	212320	*Uam*	Montana	Park CoUty, Gardiner, Near	U
USNM	222099	*Uam*	Montana	Park CoUty, Gardiner	U
USNM	222101	*Uam*	Montana	Park CoUty, Gardiner	A
USNM	223442	*Uam*	Montana	Beaverhead CoUty, Monida	U
USNM	223443	*Uam*	Montana	Alder	U
USNM	63156	*Uam*	Kansas	Oswego, La Bette River	U
USNM	269187	*Uam*	Kansas	Doniphan Site, Doniphan	U
USNM	69983	*Uam*	Louisiana	Iberia Parish, Avery Island	U
USNM	80704	*Uam*	Louisiana	Iberia Parish, Avery Island	U
USNM	80705	*Uam*	Louisiana	Iberia Parish, Avery Island	U
USNM	80706	*Uam*	Louisiana	Iberia Parish, Avery Island	U
USNM	80707	*Uam*	Louisiana	Iberia Parish, Avery Island	U
USNM	132546	*Uam*	Louisiana	Madison Parish, Tallulah	U
USNM	132547	*Uam*	Louisiana	Madison Parish, Tallulah	U
USNM	132548	*Uam*	Louisiana	Madison Parish, Tallulah	U
USNM	132549	*Uam*	Louisiana	Madison Parish, Tallulah, 14 Mi W	U
USNM	133684	*Uam*	Louisiana	Madison Parish, Tallulah, 20 Mi W	U
USNM	135132	*Uam*	Louisiana	Madison Parish, Tallulah, 28 Mi W	U
USNM	135136	*Uam*	Louisiana	Madison Parish, Tallulah, 28 Mi W	U
USNM	135141	*Uam*	Louisiana	St. Joseph, 25 Mi NW	U
USNM	135198	*Uam*	Louisiana	Madison Parish, Indian Lake	U
USNM	136780	*Uam*	Louisiana	Madison Parish, Tallulah, 21 Mi SW	U
USNM	138680	*Uam*	Louisiana	Vermilion Parish, Abberville	U
USNM	138681	*Uam*	Louisiana	Vermilion Parish, Abberville	U
USNM	139150	*Uam*	Louisiana	Vermilion Parish, Abberville, 25 Mi SW	U
USNM	139171	*Uam*	Louisiana	Vermilion Parish, Abberville	U
USNM	146371	*Uam*	Louisiana	Saint Mary Parish, Franklin	U
USNM	150643	*Uam*	Louisiana	Tensas Bayou	U
USNM	150661	*Uam*	Louisiana	Tensas Bayou	U
USNM	150662	*Uam*	Louisiana	Tensas Bayou	U
USNM	150663	*Uam*	Louisiana	Tensas Bayou	U
USNM	156595	*Uam*	Louisiana	Tensas Parish, Newlight	U
USNM	156596	*Uam*	Louisiana	Tensas Parish, Newelton	U
USNM	156597	*Uam*	Louisiana	Tensas Parish, Newlight	U
USNM	159368	*Uam*	Louisiana	Tensas Parish, Newlight, 8 Mi N	U
USNM	234626	*Uam*	Louisiana	Iberia Parish, Avery Island	U
USNM	234627	*Uam*	Louisiana	Iberia Parish, Avery Island	U
USNM	234628	*Uam*	Louisiana	Iberia Parish, Avery Island	U
USNM	242732	*Uam*	Louisiana	Iberia Parish, Avery Island	U
USNM	242733	*Uam*	Louisiana	Iberia Parish, Avery Island	U
USNM	247319	*Uam*	Louisiana	Saint Mary Parish, Morgan City	U
USNM	A 987	*Uam*	Louisiana	Morehouse Parish, Prairie Mer Rouge	U
USNM	A 988	*Uam*	Louisiana	Prairie Mer Rouge	U
USNM	A 1154	*Uam*	Louisiana	Prairie Mer Rouge	U
USNM	A 1155	*Uam*	Louisiana	Prairie Mer Rouge	U
USNM	A 1156	*Uam*	Louisiana	Prairie Mer Rouge	U
USNM	206787	*Uam*	Maine	Moosehead Lake	U
USNM	206788	*Uam*	Maine	Franklin CoUty, Rangeley	U
USNM	206789	*Uam*	Maine	Franklin CoUty, Rangeley	U

USNM	252298	*Uam*	Maine	Somerset CoUty, Troutdale	U
USNM	A 3399	*Uam*	Maine	No data	U
USNM	221601	*Uam*	Alaska	Yakutat Bay, SE Of	U
USNM	221602	*Uam*	Alaska	Yakutat Bay, SE Of	U
USNM	221603	*Uam*	Alaska	Yakutat Bay, SE Of	U
USNM	221604	*Uam*	Alaska	Yakutat Bay, SE Of	U
USNM	221605	*Uam*	Alaska	Yakutat Bay, SE Of	U
USNM	221606	*Uam*	Alaska	Yakutat Bay, SE Of	U
USNM	221607	*Uam*	Alaska	Yakutat Bay, SE Of	U
USNM	221608	*Uam*	Alaska	Yakutat Bay, SE Of	U
USNM	221609	*Uam*	Alaska	Yakutat Bay, SE Of	U
USNM	221610	*Uam*	Alaska	Yakutat Bay, SE Of	U
USNM	221611	*Uam*	Alaska	Yakutat Bay, SE Of	U
USNM	221612	*Uam*	Alaska	Yakutat Bay, SE Of	U
USNM	221616	*Uam*	Alaska	Beaver MoUtains, Iditarod	U
USNM	221617	*Uam*	Alaska	Beaver MoUtains, Iditarod	U
USNM	221713	*Uam*	Alaska	Bradfield Canal; Mainland	U
USNM	221714	*Uam*	Alaska	Aaron Creek, On The SE Mainland	U
USNM	221715	*Uam*	Alaska	JUeau, Near Mainland	U
USNM	221716	*Uam*	Alaska	Bradfield Canal; Mainland	U
USNM	221717	*Uam*	Alaska	Yakutat	U
USNM	221724	*Uam*	Alaska	Marten Arm, Boca De Quadra	U
USNM	221725	*Uam*	Alaska	Marten Arm, Boca De Quadra	U
USNM	222724	*Uam*	Alaska	Kupraenof Island, Keku Straits	U
USNM	222725	*Uam*	Alaska	Kuiu Island, Pillar Bay	U
USNM	222726	*Uam*	Alaska	Kupraenof Island, Wrangell Narrows	U
USNM	222727	*Uam*	Alaska	Kuiu Island, Pillar Bay	U
USNM	222728	*Uam*	Alaska	Kuiu Island	U
USNM	222729	*Uam*	Alaska	Kupraenof Island, Keku Straits	U
USNM	223291	*Uam*	Alaska	Yakutat Bay	U
USNM	223302	*Uam*	Alaska	Knik River	U
USNM	223303	*Uam*	Alaska	Mantanuska River	U
USNM	223385	*Uam*	Alaska	Admiralty Island	U
USNM	223386	*Uam*	Alaska	Kupraenof Island	U
USNM	223759	*Uam*	Alaska	No data	U
USNM	223823	*Uam*	Alaska	Knik River	U
USNM	223938	*Uam*	Alaska	Knik - Mantanuska Rivers	U
USNM	223939	*Uam*	Alaska	Knik - Mantanuska Rivers	U
USNM	223940	*Uam*	Alaska	Knik - Mantanuska Rivers	U
USNM	223941	*Uam*	Alaska	Knik River	U
USNM	225373	*Uam*	Alaska	Port Houghton, SE Mainland	U
USNM	225374	*Uam*	Alaska	Port Houghton, SE Mainland	U
USNM	225402	*Uam*	Alaska	Admiralty Island	U
USNM	225403	*Uam*	Alaska	Admiralty Island	U
USNM	225405	*Uam*	Alaska	Berners Bay	U
USNM	225406	*Uam*	Alaska	Berners Bay	U
USNM	225407	*Uam*	Alaska	Berners Bay	U
USNM	225408	*Uam*	Alaska	Berners Bay	U
USNM	225462	*Uam*	Alaska	Cape Fanshaw	U

USNM	225463	*Uam*	Alaska	Port Houghton	U
USNM	225466	*Uam*	Alaska	Port Houghton, Head Of Bay	U
USNM	225467	*Uam*	Alaska	Port Houghton, S Arm	U
USNM	225468	*Uam*	Alaska	Port Houghton, Head Of Bay	U
USNM	225620	*Uam*	Alaska	Glacier Bay	U
USNM	225809	*Uam*	Alaska	Kuiu Island, Saginaw Bay	U
USNM	225810	*Uam*	Alaska	Kuiu Island, Tadenkof Bay	U
USNM	225811	*Uam*	Alaska	Kuiu Island, Port Camden	U
USNM	225812	*Uam*	Alaska	Kupraenof Island, Cape Bendal	U
USNM	225813	*Uam*	Alaska	Kuiu Island, Port Camden	U
USNM	225814	*Uam*	Alaska	Kuiu Island, Port Camden	U
USNM	225815	*Uam*	Alaska	Tadenkof Bay, Tadenkof Bay	U
USNM	226149	*Uam*	Alaska	Kenai Peninsula, Kellie River	U
USNM	226150	*Uam*	Alaska	Kenai Peninsula, Kellie River	U
USNM	227066	*Uam*	Alaska	Snettisham	U
USNM	227849	*Uam*	Alaska	Ahrnklin River	U
USNM	227850	*Uam*	Alaska	Ahrnklin River	U
USNM	227851	*Uam*	Alaska	Yakutat Bay, S Side	U
USNM	227917	*Uam*	Alaska	Dry Bay	U
USNM	227983	*Uam*	Alaska	Eagle River, E Lynn Canal	U
USNM	228105	*Uam*	Alaska	Admiralty Island	U
USNM	228222	*Uam*	Alaska	Beaver MoUtains, Iditarod	U
USNM	228223	*Uam*	Alaska	Ophir, On Innoko River	U
USNM	228224	*Uam*	Alaska	Beaver MoUtains, Iditarod	U
USNM	228236	*Uam*	Alaska	Cooper Creek	U
USNM	228237	*Uam*	Alaska	Cooper Creek	U
USNM	228289	*Uam*	Alaska	Kaltag	U
USNM	228290	*Uam*	Alaska	Kaltag	U
USNM	228291	*Uam*	Alaska	Kaltag	U
USNM	228327	*Uam*	Alaska	Kuiu Island, Pillar Bay	U
USNM	228329	*Uam*	Alaska	Admiralty Island	U
USNM	228330	*Uam*	Alaska	Kuiu Island, Pillar Bay	U
USNM	228331	*Uam*	Alaska	Kuiu Island, Port Camden	U
USNM	228332	*Uam*	Alaska	Kuiu Island, Port Camden	U
USNM	228333	*Uam*	Alaska	Kuiu Island, Port Camden	U
USNM	228334	*Uam*	Alaska	Kuiu Island, Port Camden	U
USNM	228715	*Uam*	Alaska	Chilkat River Valley	U
USNM	228716	*Uam*	Alaska	Chilkat River Valley	U
USNM	228718	*Uam*	Alaska	No data	U
USNM	228719	*Uam*	Alaska	No data	U
USNM	228720	*Uam*	Alaska	No data	U
USNM	228721	*Uam*	Alaska	No data	U
USNM	228722	*Uam*	Alaska	No data	U
USNM	228723	*Uam*	Alaska	No data	U
USNM	228724	*Uam*	Alaska	Chilkat River Valley	U
USNM	228781	*Uam*	Alaska	Eagle River	U
USNM	228782	*Uam*	Alaska	Eagle River	U
USNM	228783	*Uam*	Alaska	Eagle River	U
USNM	228784	*Uam*	Alaska	Eagle River	U

USNM	228785	*Uam*	Alaska	Eagle River	U
USNM	228786	*Uam*	Alaska	Eagle River	U
USNM	228787	*Uam*	Alaska	Eagle River	U
USNM	228788	*Uam*	Alaska		U
USNM	228797	*Uam*	Alaska	Mud Bay	U
USNM	228798	*Uam*	Alaska		U
USNM	228895	*Uam*	Alaska	Port Houghton	U
USNM	228896	*Uam*	Alaska	Kupraenof Island, Keku Straits	U
USNM	228897	*Uam*	Alaska	Kupraenof Island, Portage Bay	U
USNM	228898	*Uam*	Alaska	Kupraenof Island, Portage Bay	U
USNM	228899	*Uam*	Alaska	Hobart Bay	U
USNM	228900	*Uam*	Alaska	Kupraenof Islansd	U
USNM	228901	*Uam*	Alaska	Kupraenof Island, Point Barrie	U
USNM	228902	*Uam*	Alaska	Hobart Bay	U
USNM	228903	*Uam*	Alaska	Thomas Bay	U
USNM	228904	*Uam*	Alaska	Hobart Bay, Stephens Passage	U
USNM	228905	*Uam*	Alaska	Prince of Wales Island, Skakan	U
USNM	228906	*Uam*	Alaska	Shakan, Shakan	U
USNM	228907	*Uam*	Alaska	Hobart Bay, Stephens Passage	U
USNM	228908	*Uam*	Alaska	Kupraenof Island, Sumner Straits	U
USNM	228909	*Uam*	Alaska	Hobart Bay, Stephens Passage	U
USNM	228910	*Uam*	Alaska	Cape Fanshaw	U
USNM	228911	*Uam*	Alaska	Mitkof Island	U
USNM	228912	*Uam*	Alaska	Hobart Bay	U
USNM	228913	*Uam*	Alaska	Mitkof Island	U
USNM	228914	*Uam*	Alaska	Farragut Bay	U
USNM	229227	*Uam*	Alaska	Chichagof Island	U
USNM	229228	*Uam*	Alaska	Chichagof Island	U
USNM	230947	*Uam*	Alaska	No data	U
USNM	230972	*Uam*	Alaska	No data	U
USNM	231295	*Uam*	Alaska	Kupraenof Island, Keku Straits	U
USNM	231296	*Uam*	Alaska	Kuiu Island, Security Bay	U
USNM	231297	*Uam*	Alaska	Kuiu Island, Kadakes Bay	U
USNM	231413	*Uam*	Alaska	Admiralty Island	U
USNM	231414	*Uam*	Alaska	Sumdum	U
USNM	231415	*Uam*	Alaska	SE	U
USNM	231416	*Uam*	Alaska	SE	U
USNM	231417	*Uam*	Alaska	SE	U
USNM	231418	*Uam*	Alaska	SE	U
USNM	231419	*Uam*	Alaska	SE	U
USNM	231420	*Uam*	Alaska	SE	U
USNM	231421	*Uam*	Alaska	SE	U
USNM	231422	*Uam*	Alaska	SE	U
USNM	231423	*Uam*	Alaska	SE	U
USNM	231424	*Uam*	Alaska	SE	U
USNM	231425	*Uam*	Alaska	SE	U
USNM	231461	*Uam*	Alaska	SE, Distna River	U
USNM	231506	*Uam*	Alaska	Kantishna, Bear Creek	U
USNM	231507	*Uam*	Alaska	Kantishna, Bear Creek	A

USNM	231508	*Uam*	Alaska	Kantishna, Bear Creek	U
USNM	231509	*Uam*	Alaska	Kantishna, Bear Creek	U
USNM	231510	*Uam*	Alaska	Kantishna, Bear Creek	U
USNM	231956	*Uam*	Alaska	Snettisham	U
USNM	231958	*Uam*	Alaska	Snettisham	U
USNM	231959	*Uam*	Alaska	Snettisham	U
USNM	231960	*Uam*	Alaska	Snettisham	U
USNM	232379	*Uam*	Alaska	Glacier Bay	U
USNM	232381	*Uam*	Alaska	Glacier Bay	U
USNM	232382	*Uam*	Alaska	Glacier Bay	U
USNM	232383	*Uam*	Alaska	Glacier Bay	U
USNM	233235	*Uam*	Alaska	Admiralty Island, FUter Bay	U
USNM	233236	*Uam*	Alaska	Admiralty Island, FUter Bay	U
USNM	233504	*Uam*	Alaska	Baranof Island, Silver Bay	U
USNM	233510	*Uam*	Alaska	Chilkat River	U
USNM	233511	*Uam*	Alaska	Claena, Boulder Creek	U
USNM	233696	*Uam*	Alaska	Chichagof Island	U
USNM	233761	*Uam*	Alaska	Skilak Lake	U
USNM	233763	*Uam*	Alaska	Skilak Lake	U
USNM	233764	*Uam*	Alaska	Skilak Lake	U
USNM	233765	*Uam*	Alaska	Skilak Lake	U
USNM	233766	*Uam*	Alaska	Nieling River	U
USNM	233767	*Uam*	Alaska	Skilak Lake	U
USNM	233768	*Uam*	Alaska	Skilak Lake	U
USNM	234193	*Uam*	Alaska	Ophir	A
USNM	234194	*Uam*	Alaska	Bethel, 80 Mi N, Oganik, Lower Kushokwim River	U
USNM	234195	*Uam*	Alaska	Bethel, 80 Mi N, Oganik, Lower Kushokwim River	U
USNM	234244	*Uam*	Alaska	Beaver MoUtains	A
USNM	234405	*Uam*	Alaska	Chichagof Island, Fort Fredrick	U
USNM	234406	*Uam*	Alaska	Chichagof Island, Fort Fredrick	U
USNM	234458	*Uam*	Alaska	Talsona River	U
USNM	234464	*Uam*	Alaska	Indian River	U
USNM	234479	*Uam*	Alaska	Chisana	U
USNM	234630	*Uam*	Alaska	Lituya Bay, N End	U
USNM	234631	*Uam*	Alaska	Lituya Bay, N End	U
USNM	234632	*Uam*	Alaska	Lituya Bay, N End	U
USNM	235042	*Uam*	Alaska	Kamishak Bay	U
USNM	235275	*Uam*	Alaska	Beaver MoUtains	U
USNM	235456	*Uam*	Alaska	Beaver MoUtains	U
USNM	235457	*Uam*	Alaska	Beaver MoUtains	U
USNM	235458	*Uam*	Alaska	Beaver MoUtains	A
USNM	235459	*Uam*	Alaska	Beaver MoUtains	U
USNM	235973	*Uam*	Alaska	Farragut	U
USNM	235978	*Uam*	Alaska	Hood Bay	U
USNM	235985	*Uam*	Alaska	Berners Bay	U
USNM	235986	*Uam*	Alaska	Berners Bay	U
USNM	235987	*Uam*	Alaska	Berners Bay	U
USNM	241533	*Uam*	Alaska	Ruby, On The Yukon	U

USNM	241650	*Uam*	Alaska	Tanana Crossing	U
USNM	241651	*Uam*	Alaska	Robertson River	U
USNM	242198	*Uam*	Alaska	Mchenry Inlet	U
USNM	242239	*Uam*	Alaska	Iditerod	U
USNM	242590	*Uam*	Alaska	Killey River	U
USNM	242591	*Uam*	Alaska	Killey River	U
USNM	242592	*Uam*	Alaska	Killey River	U
USNM	242593	*Uam*	Alaska	Killey River	U
USNM	245732	*Uam*	Alaska	Distna River, Brush House	U
USNM	245916	*Uam*	Alaska	Holy Cross	U
USNM	245917	*Uam*	Alaska	Holy Cross	U
USNM	245918	*Uam*	Alaska	Holy Cross	U
USNM	245919	*Uam*	Alaska	Holy Cross	U
USNM	245920	*Uam*	Alaska	Holy Cross	U
USNM	245921	*Uam*	Alaska	Holy Cross	U
USNM	246003	*Uam*	Alaska	Moose Creek, 3 Mi From Brush House	U
USNM	246004	*Uam*	Alaska	Moose Creek, 3 Mi From Brush House	U
USNM	246493	*Uam*	Alaska	Alaska Range, NE Slope SW Of Tanana River Btw Big Gerstle And And Berry Creeks	U
USNM	246494	*Uam*	Alaska	Alaska Range, NE Slope SW Of Tanana River Btw Big Gerstle And And Berry Creeks	U
USNM	246495	*Uam*	Alaska	Alaska Range, NE Slope Between Big Gerstle And And Berry Creeks	U
USNM	246496	*Uam*	Alaska	Alaska Range, NE Slope Between Big Gerstle And And Berry Creeks	U
USNM	246497	*Uam*	Alaska	Alaska Range, NE Slope Between Big Gerstle And And Berry Creeks	U
USNM	246657	*Uam*	Alaska	Flat	U
USNM	247015	*Uam*	Alaska	Fort Hamlin, Yukon River	U
USNM	267361	*Uam*	Alaska	Rainey Pass	A
USNM	267362	*Uam*	Alaska	Rainey Pass	A
USNM	286411	*Uam*	Alaska	Iniskin Bay, North Side Of Cook Inlet	U
USNM	287664	*Uam*	Alaska	No data	U
USNM	289116	*Uam*	Alaska	Ham Cove, Dall Island	U
USNM	289117	*Uam*	Alaska	Ham Cove, Dall Island	U
USNM	292927	*Uam*	Alaska	Inukposukruk Creek, Near Head Of John R. Brooks Range	U
USNM	308857	*Uam*	Alaska	Anchorage	U
USNM	308858	*Uam*	Alaska	Glenallen, Mile 125, Glenn Highway	U
USNM	324857	*Uam*	Alaska	Little Susitna River, Talkeetna MoUtians	U
USNM	324858	*Uam*	Alaska	Anchorage	U
USNM	324859	*Uam*	Alaska	Kenai Peninsula	U
USNM	324860	*Uam*	Alaska	Valdez, Near, Richardson Highway-Mile 46	U
USNM	324861	*Uam*	Alaska	Chistochina Lodge	U
USNM	324862	*Uam*	Alaska	Chistochina Lodge, Chugach MoUtains	U
USNM	324863	*Uam*	Alaska	Talkeetna MoUtains	U
USNM	324864	*Uam*	Alaska	Glen Highway, Mile 40, Between Anchorage And Palmer	U
USNM	324865	*Uam*	Alaska	Lake Louise	U
USNM	324866	*Uam*	Alaska	Chugach MoUtains	U
USNM	324867	*Uam*	Alaska	Sutton, Alaska Railroad Station	U
USNM	324868	*Uam*	Alaska	Copper Center	U
USNM	324869	*Uam*	Alaska	Skilak Lake, Kenai Peninsula	U
USNM	324870	*Uam*	Alaska	Portage	U
USNM	324871	*Uam*	Alaska	Anchorage, Near, 6 Mi Up Eagle River	U

USNM	324872	*Uam*	Alaska	Anchorage	U
USNM	529883	*Uam*	Alaska	Burroughs Bay	U
USNM	529884	*Uam*	Alaska	Loring	U
USNM	529889	*Uam*	Alaska	Burroughs Bay	U
USNM	69458	*Uam*	Arizona	Navajo CoUty, Fort Apache, 40 Mi E	U
USNM	157629	*Uam*	Arizona	White MoUtains, Blue River	U
USNM	157630	*Uam*	Arizona	White MoUtains, Little Colorado River	U
USNM	179065	*Uam*	Arizona	White MoUtains, Head Of Black River	U
USNM	203481	*Uam*	Arizona	Apache CoUty, Springerville, Near	U
USNM	203482	*Uam*	Arizona	Apache CoUty, Springerville, Near	U
USNM	203901	*Uam*	Arizona	Graham MoUtains	U
USNM	206452	*Uam*	Arizona	Greenlee CoUty, Blue	U
USNM	206453	*Uam*	Arizona	Greenlee CoUty, Blue	U
USNM	206454	*Uam*	Arizona	Greenlee CoUty, Blue	U
USNM	206455	*Uam*	Arizona	Greenlee CoUty, Blue	U
USNM	206527	*Uam*	Arizona	Apache CoUty, Coreer, E. F. K. Little Colorado River	U
USNM	206790	*Uam*	Arizona	Greenlee CoUty, Blue	U
USNM	206791	*Uam*	Arizona	Greenlee CoUty, Blue	U
USNM	206792	*Uam*	Arizona	Greenlee CoUty, Blue	U
USNM	206793	*Uam*	Arizona	Greenlee CoUty, Blue	U
USNM	206794	*Uam*	Arizona	Greenlee CoUty, Blue	U
USNM	210539	*Uam*	Arizona	Magollon MoUtain, Head Of Tonto Creek	U
USNM	211212	*Uam*	Arizona	Greenlee CoUty,Blue, Near	U
USNM	211213	*Uam*	Arizona	Greenlee CoUty,Blue, Near	U
USNM	211214	*Uam*	Arizona	Greenlee CoUty,Blue, Near	U
USNM	211215	*Uam*	Arizona	Greenlee CoUty,Blue, Near	U
USNM	223547	*Uam*	Arizona	Greenlee CoUty, Clifton	U
USNM	224465	*Uam*	Arizona	Navajo CoUty, Fort Apache	U
USNM	224466	*Uam*	Arizona	Navajo CoUty, Fort Apache	U
USNM	224467	*Uam*	Arizona	Navajo CoUty, Fort Apache	U
USNM	224468	*Uam*	Arizona	Navajo CoUty, Fort Apache	U
USNM	224469	*Uam*	Arizona	Navajo CoUty, Fort Apache	U
USNM	228257	*Uam*	Arizona	Williams, 18 Mi SE	U
USNM	228258	*Uam*	Arizona	Springerville	U
USNM	231352	*Uam*	Arizona	Vernon, 12 Mi S	U
USNM	231354	*Uam*	Arizona	Vernon	U
USNM	235450	*Uam*	Arizona	Santa Rita MoUtains	U
USNM	242651	*Uam*	Arizona	Lukac Hukai, 10 Mi NE	U
USNM	289007	*Uam*	Arizona	Apache CoUty, Chuska MoUtains	U
USNM	289008	*Uam*	Arizona	Apache CoUty, Chuska MoUtains	U
USNM	563310	*Uam*	Arkansas	Desha CoUty, White River National Wildlife Refuge, Tichenor, Ca. 10 Km E	U
USNM	563311	*Uam*	Arkansas	Desha CoUty, White River National Wildlife Refuge, Tichenor, Ca. 10 Km E	U
USNM	563312	*Uam*	Arkansas	Desha CoUty, White River National Wildlife Refuge, Tichenor, Ca. 10 Km E	U
USNM	563313	*Uam*	Arkansas	Desha CoUty, White River National Wildlife Refuge, Tichenor, Ca. 10 Km E	U
USNM	563314	*Uam*	Arkansas	Desha CoUty, White River National Wildlife Refuge, Tichenor, Ca. 10 Km E	U
USNM	563315	*Uam*	Arkansas	Desha CoUty, White River National Wildlife Refuge, Tichenor, Ca. 10 Km E	U
USNM	14124	*Uam*	California	Baird	U

USNM	14125	*Uam*	California	Baird	U
USNM	32130	*Uam*	California	Kern River, E Fork	U
USNM	32131	*Uam*	California	Kern River, E Fork	U
USNM	32132	*Uam*	California	Kern River, E Fork	U
USNM	32133	*Uam*	California	Kern River, E Fork	U
USNM	81844	*Uam*	California	Shasta CoUty, Cassel, Hat Creek	U
USNM	100686	*Uam*	California	Stanislaus River, Middle Fork	U
USNM	139784	*Uam*	California	Smith River	U A
USNM	139785	*Uam*	California	Smith River	
USNM	139786	*Uam*	California	Smith River	U
USNM	139787	*Uam*	California	Smith River	U
USNM	139788	*Uam*	California	Smith River	U
USNM	139789	*Uam*	California	Smith River	U
USNM	140658	*Uam*	California	Siskiyou CoUty, Beswick	U
USNM	146261	*Uam*	California	Upper Mattole	U
USNM	147673	*Uam*	California	Snville, 4 Mi W	U
USNM	177626	*Uam*	California	Mccloud, 19 Mi NW, Cold Creek	U
USNM	178795	*Uam*	California	Yosemite	U
USNM	178796	*Uam*	California	Yosemite	U
USNM	178797	*Uam*	California	Yosemite	U
USNM	205949	*Uam*	California	Blocksburg	U
USNM	205950	*Uam*	California	Blocksburg	U
USNM	205951	*Uam*	California	Blocksburg	U
USNM	205952	*Uam*	California	Blocksburg	U
USNM	205953	*Uam*	California	Blocksburg	U
USNM	205954	*Uam*	California	Blocksburg	U
USNM	206138	*Uam*	California	Siskiyou CoUty, Caon Creek	U
USNM	209908	*Uam*	California	Mendocino CoUty, Hell Hole Caon, Eel River, Near Covelo	U
USNM	210789	*Uam*	California	Siskiyou CoUty, Beswick	U
USNM	222496	*Uam*	California	Glenn CoUty, St. John MoUtain, E Side	U
USNM	223299	*Uam*	California	Humboldt CoUty, Weitspek, Near Mouth Of Pine Creek	U
USNM	223300	*Uam*	California	Humboldt CoUty, Weitspek, Near Pine Creek	U
USNM	223301	*Uam*	California	Humboldt CoUty, Weitspek, Near Head Of Bully Creek	U
USNM	223824	*Uam*	California	Humboldt CoUty, Blocksburg	U
USNM	223825	*Uam*	California	Humboldt CoUty, Blocksburg	U
USNM	223826	*Uam*	California	Humboldt CoUty, Blocksburg, 5 Mi N, Vanduzen River	U
USNM	223827	*Uam*	California	Humboldt CoUty, Blocksburg, 5 Mi From Vanduzen River	U
USNM	223828	*Uam*	California	Humboldt CoUty, Blocksburg, 5 Mi From Vanduzen River	U
USNM	223829	*Uam*	California	Humboldt CoUty, Fort Seward	U
USNM	223830	*Uam*	California	Humboldt CoUty, Blocksburg	U
USNM	223831	*Uam*	California	Humboldt CoUty, Blocksburg, 10 Mi, Dobins Creek	U
USNM	223850	*Uam*	California	Humboldt CoUty, Fort Seward	U
USNM	227662	*Uam*	California	Trinity CoUty, Hayfork, 22 Mi SW	U
USNM	230699	*Uam*	California	Mendocino CoUty, Covelo, 30 Mi NE Of Barney Meadow	U
USNM	230700	*Uam*	California	Trinity CoUty, Hyampom	U
USNM	300001	*Uam*	California	Shasta CoUty, Baird	U
USNM	75304	*Uam*	Alberta	Jasper House	U A
USNM	75305	*Uam*	Alberta	Henry House	
USNM	75306	*Uam*	Alberta	Henry House	U

USNM	75631	*Uam*	Alberta	Jasper House	U
USNM	75632	*Uam*	Alberta	Jasper House	U
USNM	75633	*Uam*	Alberta	Jasper House	U
USNM	75634	*Uam*	Alberta	Henry House	U
USNM	77740	*Uam*	Alberta	Jasper House	U
USNM	81789	*Uam*	Alberta	Root Creek	U
USNM	89509	*Uam*	Alberta	Red Deer, 20 Mi W, Snake Lake	U
USNM	89510	*Uam*	Alberta	Red Deer, 20 Mi W, Snake Lake	U
USNM	93950	*Uam*	Alberta	Blind Man River	U
USNM	93951	*Uam*	Alberta	Blind Man River	U
USNM	93952	*Uam*	Alberta	Blind Man River	U
USNM	93953	*Uam*	Alberta	Blind Man River	U
USNM	180242	*Uam*	Alberta	Peace River Crossing	U
USNM	206459	*Uam*	Alberta	Siffleur Valley, Head, N End Rocky MoUtains Park	U
USNM	210450	*Uam*	Alberta	Saskatchewan River	U
USNM	219918	*Uam*	Alberta	Massive Switch Street	U
USNM	222766	*Uam*	Alberta	Hananaskie	U
USNM	222767	*Uam*	Alberta	Morley	U
USNM	222768	*Uam*	Alberta	Morley	U
USNM	222769	*Uam*	Alberta	Morley	U
USNM	223159	*Uam*	Alberta	Brazian River	U
USNM	223160	*Uam*	Alberta	Morley	U
USNM	225387	*Uam*	Alberta	MoUt Robson	U
USNM	225388	*Uam*	Alberta	Jasper, 20 Mi E	U
USNM	235995	*Uam*	Alberta	Peace River, Point Providence	U
USNM	A 47037	*Uam*	British Columbia	Stuart Lake	U
USNM	A 47038	*Uam*	British Columbia	Stuart Lake	U
USNM	A 47039	*Uam*	British Columbia	Stuart Lake	U
USNM	A 47040	*Uam*	British Columbia	Stuart Lake	U
USNM	A 47041	*Uam*	British Columbia	Stuart Lake	U
USNM	A 47042	*Uam*	British Columbia	Stuart Lake	U
USNM	A 47043	*Uam*	British Columbia	Stuart Lake	U
USNM	A 47044	*Uam*	British Columbia	Stuart Lake	U
USNM	A 47045	*Uam*	British Columbia	Stuart Lake	U
USNM	A 47046	*Uam*	British Columbia	Stuart Lake	U
USNM	A 47047	*Uam*	British Columbia	Stuart Lake	U
USNM	A 47048	*Uam*	British Columbia	Stuart Lake	U
USNM	A 47049	*Uam*	British Columbia	Stuart Lake	U
USNM	A 48017	*Uam*	British Columbia	Stuart Lake	U
USNM	A 48018	*Uam*	British Columbia	Stuart Lake	U
USNM	A 48019	*Uam*	British Columbia	Stuart Lake	U
USNM	A 48020	*Uam*	British Columbia	Stuart Lake	U
USNM	A 48021	*Uam*	British Columbia	Stuart Lake	U
USNM	A 48022	*Uam*	British Columbia	Stuart Lake	U
USNM	A 48023	*Uam*	British Columbia	Stuart Lake	U
USNM	A 48024	*Uam*	British Columbia	Stuart Lake	U
USNM	A 48025	*Uam*	British Columbia	Stuart Lake	U
USNM	A 48026	*Uam*	British Columbia	Stuart Lake	U
USNM	A 48027	*Uam*	British Columbia	Stuart Lake	U

USNM	A 48028	*Uam*	British Columbia	Stuart Lake	U
USNM	A 48029	*Uam*	British Columbia	Stuart Lake	A
USNM	A 48032	*Uam*	British Columbia	Stuart Lake	U
USNM	A 48033	*Uam*	British Columbia	Stuart Lake	U
USNM	A 48234	*Uam*	British Columbia	Stuart Lake	U
USNM	A 48235	*Uam*	British Columbia	Stuart Lake	U
USNM	A 48236	*Uam*	British Columbia	Stuart Lake	U
USNM	A 48237	*Uam*	British Columbia	Stuart Lake	U
USNM	A 48238	*Uam*	British Columbia	Stuart Lake	U
USNM	A 48239	*Uam*	British Columbia	Stuart Lake	U
USNM	A 48240	*Uam*	British Columbia	Stuart Lake	U
USNM	A 48241	*Uam*	British Columbia	Stuart Lake	U
USNM	A 48242	*Uam*	British Columbia	Stuart Lake	U
USNM	A 48243	*Uam*	British Columbia	Stuart Lake	U
USNM	A 48244	*Uam*	British Columbia	Stuart Lake	U
USNM	A 48245	*Uam*	British Columbia	Stuart Lake	U
USNM	A 48381	*Uam*	British Columbia	Stuart Lake	U
USNM	A 48382	*Uam*	British Columbia	Stuart Lake	U
USNM	53577	*Uam*	British Columbia	Stuart Lake	U
USNM	53578	*Uam*	British Columbia	Stuart Lake	U
USNM	53579	*Uam*	British Columbia	Stuart Lake	A
USNM	53580	*Uam*	British Columbia	Stuart Lake	U
USNM	53581	*Uam*	British Columbia	Stuart Lake	U
USNM	53582	*Uam*	British Columbia	Stuart Lake	U
USNM	53583	*Uam*	British Columbia	Stuart Lake	U
USNM	53584	*Uam*	British Columbia	Stuart Lake	U
USNM	53585	*Uam*	British Columbia	Stuart Lake	U
USNM	53586	*Uam*	British Columbia	Stuart Lake	U
USNM	63298	*Uam*	British Columbia	Alert Bay	U
USNM	68819	*Uam*	British Columbia	Field, 4 Mi W	U
USNM	71178	*Uam*	British Columbia	Stuart Lake	U
USNM	71179	*Uam*	British Columbia	Stuart Lake	U
USNM	71180	*Uam*	British Columbia	Stuart Lake	U
USNM	71181	*Uam*	British Columbia	Stuart Lake	U
USNM	71182	*Uam*	British Columbia	Stuart Lake	U
USNM	71183	*Uam*	British Columbia	Stuart Lake	U
USNM	71184	*Uam*	British Columbia	Stuart Lake	U
USNM	71185	*Uam*	British Columbia	Stuart Lake	U
USNM	71186	*Uam*	British Columbia	Stuart Lake	U
USNM	71187	*Uam*	British Columbia	Stuart Lake	U
USNM	71304	*Uam*	British Columbia	Stuart Lake	U
USNM	71305	*Uam*	British Columbia	Stuart Lake	U
USNM	71306	*Uam*	British Columbia	Stuart Lake	U
USNM	71307	*Uam*	British Columbia	Stuart Lake	U
USNM	71308	*Uam*	British Columbia	Stuart Lake	U
USNM	71309	*Uam*	British Columbia	Stuart Lake	U
USNM	71310	*Uam*	British Columbia	Stuart Lake	U
USNM	71311	*Uam*	British Columbia	Stuart Lake	U
USNM	71312	*Uam*	British Columbia	Stuart Lake	U

USNM	71313	*Uam*	British Columbia	Stuart Lake	U
USNM	71314	*Uam*	British Columbia	Stuart Lake	U
USNM	71817	*Uam*	British Columbia	Stuart Lake	U
USNM	71821	*Uam*	British Columbia	Shuswap	U
USNM	72332	*Uam*	British Columbia	Stuart Lake, Adams Lake	U
USNM	72333	*Uam*	British Columbia	Stuart Lake, Adams Lake	U
USNM	72334	*Uam*	British Columbia	Stuart Lake, Adams Lake	U
USNM	72335	*Uam*	British Columbia	Stuart Lake, Adams Lake	U
USNM	72337	*Uam*	British Columbia	Stuart Lake, Adams Lake	U
USNM	72338	*Uam*	British Columbia	Stuart Lake, Adams Lake	U
USNM	72339	*Uam*	British Columbia	Stuart Lake, Turtle Valley	U
USNM	72340	*Uam*	British Columbia	Stuart Lake, N Thompson River	U
USNM	72341	*Uam*	British Columbia	Stuart Lake, N Thompson River	U
USNM	72342	*Uam*	British Columbia	Stuart Lake, N Thompson River	U
USNM	72343	*Uam*	British Columbia	Stuart Lake, N Thompson River	U
USNM	72344	*Uam*	British Columbia	Stuart Lake, N Thompson River	U
USNM	72345	*Uam*	British Columbia	Shuswap, N Thompson River	U
USNM	72346	*Uam*	British Columbia	Shuswap, N Thompson River	U
USNM	72863	*Uam*	British Columbia	Shuswap, Adams Lake	U
USNM	75052	*Uam*	British Columbia	Charlotte Island, Massett	U
USNM	77166	*Uam*	British Columbia	Stuart Lake	U
USNM	77167	*Uam*	British Columbia	Stuart Lake, 9 Mi E	A
USNM	77168	*Uam*	British Columbia	Stuart Lake, 5 Mi E	U
USNM	77169	*Uam*	British Columbia	Stuart Lake	U
USNM	77170	*Uam*	British Columbia	Stuart Lake	U
USNM	77171	*Uam*	British Columbia	Stuart Lake, 25 Mi NE	U
USNM	77172	*Uam*	British Columbia	Stuart Lake, 25 Mi NE	U
USNM	77173	*Uam*	British Columbia	Stuart Lake	U
USNM	77174	*Uam*	British Columbia	Stuart Lake	U
USNM	77175	*Uam*	British Columbia	Stuart Lake	U
USNM	77176	*Uam*	British Columbia	Stuart Lake, 6 Mi NE	U
USNM	77177	*Uam*	British Columbia	Stuart Lake, 15 Mi NW	U
USNM	77178	*Uam*	British Columbia	Stuart Lake, 60 Mi NE	U
USNM	77179	*Uam*	British Columbia	Stuart Lake, 10 Mi N	U
USNM	77180	*Uam*	British Columbia	Stuart Lake, 20 Mi NW	U
USNM	77181	*Uam*	British Columbia	Stuart Lake, 15 Mi NW	U
USNM	77182	*Uam*	British Columbia	Stuart Lake, 10 Mi N	U
USNM	77183	*Uam*	British Columbia	Stuart Lake	U
USNM	77184	*Uam*	British Columbia	Stuart Lake, 3 Mi From	U
USNM	77185	*Uam*	British Columbia	Stuart Lake, 3 Mi From	U
USNM	77741	*Uam*	British Columbia	Port Moody	U
USNM	77742	*Uam*	British Columbia	Port Moody	U
USNM	77743	*Uam*	British Columbia	Port Moody	U
USNM	78065	*Uam*	British Columbia	Queen Charlotte Islands, Massett	U
USNM	79663	*Uam*	British Columbia	Port Moody	U
USNM	79664	*Uam*	British Columbia	Port Moody	U
USNM	87617	*Uam*	British Columbia	Queen Charlotte Islands, Massett	U
USNM	87618	*Uam*	British Columbia	Queen Charlotte Islands	U
USNM	87619	*Uam*	British Columbia	Queen Charlotte Islands, Massett	U

USNM	87620	*Uam*	British Columbia	Queen Charlotte Islands, Massett, Graham Island	U
USNM	87621	*Uam*	British Columbia	Queen Charlotte Islands, Massett	U
USNM	135453	*Uam*	British Columbia	Vancouver Island, Quatsino SoUd	U
USNM	135454	*Uam*	British Columbia	Iskut River, Quatsino SoUd	U
USNM	137809	*Uam*	British Columbia	Iskut River, Quatsino SoUd	U
USNM	137810	*Uam*	British Columbia	Vancouver Island, Quatsino	U
USNM	139189	*Uam*	British Columbia	Iskut River	U
USNM	148512	*Uam*	British Columbia	Queen Charlotte Islands, Graham Island	U
USNM	148513	*Uam*	British Columbia	Queen Charlotte Islands, Graham Island	U
USNM	148514	*Uam*	British Columbia	Queen Charlotte Islands, Graham Island	U
USNM	148515	*Uam*	British Columbia	Queen Charlotte Islands, Graham Island	U
USNM	148516	*Uam*	British Columbia	Queen Charlotte Islands, Graham Island	U A
USNM	175569	*Uam*	British Columbia	Resplendent Valley	
USNM	177633	*Uam*	British Columbia	Stikine River	U
USNM	177634	*Uam*	British Columbia	Kehtelah Creek, Near, Stikine River	U
USNM	177635	*Uam*	British Columbia	Stikine River, Lower	U
USNM	177636	*Uam*	British Columbia	Stikine River, Lower	U
USNM	177637	*Uam*	British Columbia	Iskut River, Foothills Between Iskut River And Kahtelah Creek	U
USNM	177638	*Uam*	British Columbia	Campbell River, Vancouver Island	U
USNM	177639	*Uam*	British Columbia	Shesley River	U
USNM	177640	*Uam*	British Columbia	Shesley River	U
USNM	177641	*Uam*	British Columbia	Shesley River	U
USNM	177642	*Uam*	British Columbia	Inklin River	U
USNM	177643	*Uam*	British Columbia	Inklin River	U
USNM	177644	*Uam*	British Columbia	Inklin River	U
USNM	177645	*Uam*	British Columbia	Inklin River	U
USNM	177646	*Uam*	British Columbia	Inklin or Nahlin River	U
USNM	177647	*Uam*	British Columbia	Nahlin River	U
USNM	177675	*Uam*	British Columbia	Inklin River	U
USNM	206126	*Uam*	British Columbia	Shesley River	U
USNM	209379	*Uam*	British Columbia	Big Salmon River, N Fork, Near Head	U
USNM	209388	*Uam*	British Columbia	Big Salmon River, Below Forks	U
USNM	209904	*Uam*	British Columbia	Sheep Creek	U
USNM	210307	*Uam*	British Columbia	Stikine River	U
USNM	210580	*Uam*	British Columbia	Atnarko River	U
USNM	211393	*Uam*	British Columbia	Vancouver Island, Quinsome River	U
USNM	211394	*Uam*	British Columbia	Vancouver Island, Campbell Lake	U
USNM	211395	*Uam*	British Columbia	Vancouver Island, Campbell Lake	U
USNM	211396	*Uam*	British Columbia	Vancouver Island, Mcivor Lake	U A
USNM	211397	*Uam*	British Columbia	Vancouver Island, Quinsome River	
USNM	211398	*Uam*	British Columbia	Vancouver Island, Quinsome River	U
USNM	211399	*Uam*	British Columbia	Vancouver Island, Quinsome River	U A
USNM	211458	*Uam*	British Columbia	Stikine River, Head Of Iskut Creek	
USNM	211486	*Uam*	British Columbia	Vancouver Island, Campbell River Valley	U
USNM	211487	*Uam*	British Columbia	Vancouver Island, Campbell River Valley, Elk River	U
USNM	211488	*Uam*	British Columbia	Vancouver Island, Mcivor Lake, Campbell River	U
USNM	211489	*Uam*	British Columbia	Vancouver Island, Gooseneck Lake	U
USNM	214098	*Uam*	British Columbia	Creston	U

USNM	214099	*Uam*	British Columbia	Creston	U
USNM	214100	*Uam*	British Columbia	Creston	U
USNM	214101	*Uam*	British Columbia	Creston	U
USNM	216199	*Uam*	British Columbia	Barkerville, Indian Point Creek	U
USNM	216200	*Uam*	British Columbia	Barkerville, Indian Point Creek	U
USNM	216201	*Uam*	British Columbia	Barkerville, Indian Point Creek	U
USNM	216202	*Uam*	British Columbia	Barkerville, Indian Point Creek	U
USNM	221707	*Uam*	British Columbia	No data	U
USNM	222106	*Uam*	British Columbia	Golden	A
USNM	222760	*Uam*	British Columbia	Hazelton	U
USNM	222761	*Uam*	British Columbia	Pacific Slope	U
USNM	223686	*Uam*	British Columbia	Nelson	U
USNM	223833	*Uam*	British Columbia	Fort Steele, Adraain Indian	U
USNM	223834	*Uam*	British Columbia	Fort Steele, Adraain Indian	U
USNM	223835	*Uam*	British Columbia	Fort Steele, Adraain Indian	U
USNM	223959	*Uam*	British Columbia	Arrowhead	U
USNM	224811	*Uam*	British Columbia	Graham Island	U
USNM	224812	*Uam*	British Columbia	Graham Island	A
USNM	224813	*Uam*	British Columbia	Graham Island	U
USNM	224814	*Uam*	British Columbia	Graham Island	U
USNM	224840	*Uam*	British Columbia	Stikine River	U
USNM	225386	*Uam*	British Columbia	Fortress Lake	U
USNM	225392	*Uam*	British Columbia	Graham Island	U
USNM	225612	*Uam*	British Columbia	Yellowhead Pass	U
USNM	225800	*Uam*	British Columbia	Stikine River, Caon Of	U
USNM	227070	*Uam*	British Columbia	Lillooet, Bridge River	U
USNM	227071	*Uam*	British Columbia	Lillooet, Cayoosh Creek	A
USNM	227075	*Uam*	British Columbia	Shuswap	U
USNM	227076	*Uam*	British Columbia	Shuswap	U
USNM	227969	*Uam*	British Columbia	Cassiar	U
USNM	228096	*Uam*	British Columbia	Graham Island	U
USNM	228717	*Uam*	British Columbia	Iskut River	U
USNM	228816	*Uam*	British Columbia	Cassiar	U
USNM	228915	*Uam*	British Columbia	Kinboshet Lake	U
USNM	228916	*Uam*	British Columbia	Kinboshet Lake	U
USNM	228917	*Uam*	British Columbia	Kinboshet Lake	U
USNM	228918	*Uam*	British Columbia	Kinboshet Lake	U
USNM	230652	*Uam*	British Columbia	Telegraph Creek, 30 Mi S, Stikine River	U
USNM	230701	*Uam*	British Columbia	Shuswap	U
USNM	230702	*Uam*	British Columbia	Shuswap	U
USNM	230703	*Uam*	British Columbia	Shuswap	U
USNM	231549	*Uam*	British Columbia	Stikine River, Clearwater River	U
USNM	234638	*Uam*	British Columbia	Hector	U
USNM	239706	*Uam*	British Columbia	Lake Windermere	U
USNM	243186	*Uam*	British Columbia	Atlin, Within 30 Mi	U
USNM	262134	*Uam*	British Columbia	Kootenay River Tributary, Timberline Between Yearling Creek And Cochrane Creek	U
USNM	287660	*Uam*	British Columbia	Cassiar	U
USNM	287661	*Uam*	British Columbia	Kingcome Inlet	U

USNM	287662	*Uam*	British Columbia	Atlin	U
USNM	287663	*Uam*	British Columbia	Atlin	U
USNM	287703	*Uam*	British Columbia	Cassiar, Near	U
USNM	287704	*Uam*	British Columbia	Cassiar, Near	U
USNM	287705	*Uam*	British Columbia	Cassiar, Near	U
USNM	287706	*Uam*	British Columbia	Cassiar, Near	U
USNM	551610	*Uam*	British Columbia	Cranbrook, Bull River	A
USNM	107503	*Uam*	Manitoba	No data	U
USNM	107505	*Uam*	Manitoba	Oxford House	U
USNM	107506	*Uam*	Manitoba	Oxford House	U
USNM	107507	*Uam*	Manitoba	Oxford House	U
USNM	107508	*Uam*	Manitoba	Oxford House	U
USNM	107509	*Uam*	Manitoba	Oxford House	U
USNM	187873	*Uam*	New BrUswick	No data	U
USNM	202684	*Uam*	New BrUswick	New Castle, 50 Mi NNW	U
USNM	207102	*Uam*	New BrUswick	Frederickton	U
USNM	223398	*Uam*	New BrUswick	New Castle	U
USNM	223399	*Uam*	New BrUswick	New Castle	U
USNM	223400	*Uam*	New BrUswick	New Castle	U
USNM	223546	*Uam*	New BrUswick	New Castle	U
USNM	228212	*Uam*	New BrUswick	New Castle, Near	U
USNM	283131	*Uam*	New BrUswick	No data	U
USNM	283132	*Uam*	New BrUswick	St. Johns, 35-40 Mi NW, Wirral Station	A
USNM	168750	*Uam*	NewfoUdland	Topsail, 9 Mi N, N Central NewfoUdland	U
USNM	168751	*Uam*	NewfoUdland	Topsail, 9 Mi N, N Central NewfoUdland	U
USNM	203276	*Uam*	NewfoUdland	Labrador, Wain, Near	U
USNM	210005	*Uam*	NewfoUdland	Labrador, Paradise	U
USNM	294020	*Uam*	NewfoUdland	Labrador, Wain	U
USNM	A35388	*Uam*	NewfoUdland	Labrador, Grand Lake	A
USNM	134132	*Uam*	Northwest Territories	Mackenzie District, Mackenzie River, San Sault Rapid	U
USNM	134169	*Uam*	Northwest Territories	Mackenzie District, Fort Good Hope	U
USNM	134170	*Uam*	Northwest Territories	Mackenzie District, Fort Providence	U
USNM	134769	*Uam*	Northwest Territories	Mackenzie District, Fort Smith	U
USNM	134770	*Uam*	Northwest Territories	Mackenzie District, Fort Smith	A
USNM	296493	*Uam*	Northwest Territories	Nueltin Lake, NW Extremity	U
USNM	296494	*Uam*	Northwest Territories	Keewatin District, Nueltin Lake, NW Extremity	U
USNM	222744	*Uam*	Nova Scotia	No data	U
USNM	234237	*Uam*	Nova Scotia	Maitland	U
USNM	238721	*Uam*	Nova Scotia	Clyde River, Upper	U
USNM	238722	*Uam*	Nova Scotia	Clyde River, Upper	U
USNM	243995	*Uam*	Nova Scotia	Kedgemakooge Region	A
USNM	243996	*Uam*	Nova Scotia	Kedgemakooge Region	U
USNM	243997	*Uam*	Nova Scotia	Kedgemakooge Region	U
USNM	243998	*Uam*	Nova Scotia	Kedgemakooge Region	U
USNM	243999	*Uam*	Nova Scotia	Kedgemakooge Region	U
USNM	244000	*Uam*	Nova Scotia	Kedgemakooge Region	U

USNM	246555	*Uam*	Nova Scotia	Kedgemakooge Region	U
USNM	567173	*Uam*	Ontario	Chelmsford, 30 mi N	U
USNM	259797	*Uam*	Ontario	Hannah Bay	U
USNM	259798	*Uam*	Ontario	Hannah Bay	A
USNM	259799	*Uam*	Ontario	No data	U
USNM	A 6583	*Uam*	Ontario	No data	U
USNM	74902	*Uam*	Quebec	Godbout	U
USNM	74903	*Uam*	Quebec	Godbout	U
USNM	74904	*Uam*	Quebec	Godbout	U
USNM	74905	*Uam*	Quebec	Godbout	U
USNM	75051	*Uam*	Quebec	Godbout	U
USNM	75641	*Uam*	Quebec	Godbout	U
USNM	81198	*Uam*	Quebec	Point Des Monts	U
USNM	81199	*Uam*	Quebec	Point Des Monts	U
USNM	81200	*Uam*	Quebec	Point Des Monts	U
USNM	99427	*Uam*	Quebec	Godbout	U
USNM	102564	*Uam*	Quebec	Lake St. Johns	U
USNM	102565	*Uam*	Quebec	Lake St. Johns	U
USNM	140621	*Uam*	Quebec	Mattawa, 40 Mi NE	A
USNM	187867	*Uam*	Quebec	Godbout	U
USNM	187868	*Uam*	Quebec	Godbout	U
USNM	187869	*Uam*	Quebec	Godbout	U
USNM	187870	*Uam*	Quebec	Godbout	A
USNM	187871	*Uam*	Quebec	Godbout	U
USNM	187872	*Uam*	Quebec	Godbout	U
USNM	187874	*Uam*	Quebec	Point Des Monts	U
USNM	187875	*Uam*	Quebec	Point Des Monts	U
USNM	298691	*Uam*	Quebec	Knob Lake Airport	U
USNM	A 30202	*Uam*	Quebec	Montreal, N	U
USNM	69236	*Uam*	Yukon	Forty Mile Creek, Upper Yukon River	U
USNM	69237	*Uam*	Yukon	Fort Reliance, Upper Yukon River	U
USNM	69238	*Uam*	Yukon	Fort Reliance, Upper Yukon River	U
USNM	69239	*Uam*	Yukon	Fort Reliance, Upper Yukon River	U
USNM	69786	*Uam*	Yukon	Rampart House	U
USNM	69787	*Uam*	Yukon	Rampart House, 5 Mi E	U
USNM	134236	*Uam*	Yukon	Pelly River	U
USNM	134238	*Uam*	Yukon	Pelly River, MoUt Ross River	U
USNM	134239	*Uam*	Yukon	Pelly River, MoUt Ross River	U
USNM	134240	*Uam*	Yukon	Pelly River, MoUt Ross River	A
USNM	146370	*Uam*	Yukon	Pelly River, Tay River	U
USNM	146374	*Uam*	Yukon	Pelly River, 50 Mi Below Ross River	U
USNM	180983	*Uam*	Yukon	Macmillan River, 150-175 Mi Up	U
USNM	180991	*Uam*	Yukon	Old Crow River	A
USNM	210456	*Uam*	Yukon	Whitehorse	U
USNM	210457	*Uam*	Yukon	Whitehorse	A
USNM	210709	*Uam*	Yukon	Champagne Landing	U
USNM	214696	*Uam*	Yukon	Glenlyon Range	U

USNM	214697	*Uam*	Yukon	Glenlyon Range	U
USNM	214698	*Uam*	Yukon	Glenlyon Range	U
USNM	214699	*Uam*	Yukon	Glenlyon Range	U
USNM	214700	*Uam*	Yukon	Glenlyon Range	U
USNM	214701	*Uam*	Yukon	Glenlyon Range	U
USNM	214702	*Uam*	Yukon	Glenlyon Range	U
USNM	214703	*Uam*	Yukon	Glenlyon Range	U
USNM	214704	*Uam*	Yukon	Glenlyon Range	U
USNM	214705	*Uam*	Yukon	Glenlyon Range	U
USNM	214706	*Uam*	Yukon	Glenlyon Range	U
USNM	214707	*Uam*	Yukon	Glenlyon Range	U
USNM	215712	*Uam*	Yukon	Ross MoUtains	U
USNM	221708	*Uam*	Yukon	Ross MoUtains	A
USNM	222762	*Uam*	Yukon	Whitehorse	A
USNM	222763	*Uam*	Yukon	Whitehorse	U
USNM	222764	*Uam*	Yukon	Whitehorse	U
USNM	222765	*Uam*	Yukon	Whitehorse	U
USNM	223770	*Uam*	Yukon	Whitehorse	U
USNM	223771	*Uam*	Yukon	Little Salmon River	U
USNM	225419	*Uam*	Yukon	Tahkeena River, Upper	U
USNM	225420	*Uam*	Yukon	Tahkeena River, Upper	U
USNM	227065	*Uam*	Yukon	Ross River	U
USNM	227968	*Uam*	Yukon	Champagne	U
USNM	228218	*Uam*	Yukon	Little Arm Kluane	U
USNM	228219	*Uam*	Yukon	Little Arm Kluane	U
USNM	228220	*Uam*	Yukon	Little Arm Kluane	U
USNM	228513	*Uam*	Yukon	No data	U
USNM	228864	*Uam*	Yukon	Duke River, Head, Duke Glacier	U
USNM	228865	*Uam*	Yukon	Kluane River	U
USNM	228866	*Uam*	Yukon	Hooche Lake	U
USNM	228867	*Uam*	Yukon	Champagne	U
USNM	228884	*Uam*	Yukon	Rose MoUtains, Upper Pelly River	U
USNM	228885	*Uam*	Yukon	Rose MoUtains, Upper Pelly River	U
USNM	228886	*Uam*	Yukon	Rose MoUtains, Upper Pelly River	U
USNM	228887	*Uam*	Yukon	Lopp River	U
USNM	228888	*Uam*	Yukon	Lopp River	U
USNM	228889	*Uam*	Yukon	Lopp River	U
USNM	228890	*Uam*	Yukon	Lopp River	U
USNM	228891	*Uam*	Yukon	Nieling River, Head	U
USNM	229256	*Uam*	Yukon	White River	U
USNM	229257	*Uam*	Yukon	Five Fingers	U
USNM	229259	*Uam*	Yukon	Selkirk	U
USNM	229260	*Uam*	Yukon	Selkirk	U
USNM	229261	*Uam*	Yukon	Ross River, Upper	U
USNM	229262	*Uam*	Yukon	Ross River	U
USNM	229263	*Uam*	Yukon	Pelly River, Lower	U
USNM	229264	*Uam*	Yukon	Pelly River, Lower	U
USNM	229265	*Uam*	Yukon	Yukon River, Upper, Near Lake La Barge	U
USNM	229266	*Uam*	Yukon	Little Salmon River, Near	U

USNM	229267	*Uam*	Yukon	Big Salmon River, Near	U
USNM	229268	*Uam*	Yukon	Little Salmon River	U
USNM	229269	*Uam*	Yukon	Little Salmon River	U
USNM	231578	*Uam*	Yukon	Whitehorse, 50 Mi W, Near Champagne Landing	U
USNM	231951	*Uam*	Yukon	Whitehorse, Near	U
USNM	232391	*Uam*	Yukon	Big Salmon River	U
USNM	233005	*Uam*	Yukon	Ogilvie Range, 60 Mi Range Extension	U
USNM	233032	*Uam*	Yukon	Nordenskiold River	U
USNM	233033	*Uam*	Yukon	Yukon River, Upper	U
USNM	233035	*Uam*	Yukon	Lake Kluame	U
USNM	233226	*Uam*	Yukon	Whitehorse	U
USNM	233227	*Uam*	Yukon	Whitehorse, E Of	U
USNM	233229	*Uam*	Yukon	Whitehorse	U
USNM	233230	*Uam*	Yukon	Whitehorse	U
USNM	233631	*Uam*	Yukon	Whitehorse	U
USNM	233705	*Uam*	Yukon	Little Salmon River	U
USNM	235345	*Uam*	Yukon	Goldstone Creek	A
USNM	235346	*Uam*	Yukon	Kluane Lake	U
USNM	235521	*Uam*	Yukon	White Horse, Near	U
USNM	235522	*Uam*	Yukon	White Horse	U
USNM	235523	*Uam*	Yukon	White Horse	U
USNM	239304	*Uam*	Yukon	No data	U
USNM	242649	*Uam*	Yukon	Whitehorse	U
USNM	247016	*Uam*	Yukon	Old Crow River	U
USNM	A 3484	*Uam*	Florida	Miami-Dade CoUty, Key Biscayne	U
USNM	15458	*Uam*	Florida	Indian River	U
USNM	60369	*Uam*	Florida	Brevard CoUty,Micco	U
USNM	65369	*Uam*	Florida	Miami-Dade CoUty, Coconut Grove	U
USNM	67406	*Uam*	Florida	Cape Canaveral, Near	U
USNM	145265	*Uam*	Florida	New Smyrna	U
USNM	223943	*Uam*	Florida	Allenhurst, Merritts Island	U
USNM	231501	*Uam*	Florida	Chokoloskee	U
USNM	231502	*Uam*	Florida	Everglades	U
USNM	234242	*Uam*	Florida	Chossahowitzka	U
USNM	238011	*Uam*	Florida	Brevard CoUty, Merritt Island	U
USNM	247238	*Uam*	Florida	Franklin CoUty, Apalachicola	U
USNM	249311	*Uam*	Florida	Istokpoga Lake, NW Side	U
USNM	261311	*Uam*	Florida	Miami-Dade CoUty, Miami Beach	U
USNM	265147	*Uam*	Florida	Marion CoUty, Ocala National Forest, Mud Lake	U
USNM	200393	*Uam*	Georgia	White CoUty, Nacoochee MoUd	U
USNM	200394	*Uam*	Georgia	White CoUty, Nacoochee MoUd	U
USNM	209154	*Uam*	Georgia	Clinch CoUty, Fargo, In Okeefinokee Swamp	U
USNM	211454	*Uam*	Georgia	Clinch CoUty,Fargo	U
USNM	211455	*Uam*	Georgia	Clinch CoUty,Fargo	U
USNM	211456	*Uam*	Georgia	Clinch CoUty,Fargo	U
USNM	211457	*Uam*	Georgia	Clinch CoUty,Fargo	U
USNM	213695	*Uam*	Georgia	Clinch CoUty,Fargo	U
USNM	213697	*Uam*	Georgia	Clinch CoUty,Fargo	A
USNM	222676	*Uam*	Georgia	Okefenoke Swamp	U

USNM	286407	*Uam*	Georgia	Okefenoke National Wildlife Refuge	U
USNM	286408	*Uam*	Georgia	Okefenoke National Wildlife Refuge	U
USNM	A 3894	*Uam*	Georgia	No data	U
USNM	A 12398	*Uam*	Idaho	Clearwater CoUty, Orofino, Ceder Creek	U
USNM	A 20759	*Uam*	Idaho	Fremont CoUty, Snake River, N Fork, Ripley Ranch	U
USNM	A 30728	*Uam*	Idaho	Alturas Lake	U
USNM	A 31277	*Uam*	Idaho	Priest River	U
USNM	224538	*Uam*	Idaho	Bonner CoUty, Coolin	U
USNM	235992	*Uam*	Idaho	Bonner CoUty, Coolin	U
USNM	75050	*Uam*	Idaho	Bonner CoUty, Coolin	U
USNM	105993	*Uam*	Idaho	Bonner CoUty, Coolin	U
USNM	169105	*Uam*	Idaho	Bonner CoUty, Coolin	U
USNM	169106	*Uam*	Idaho	Lolo Hot Springs, S, Packer Meadow, Near State Line	U
USNM	169107	*Uam*	Idaho	Clearwater River	U
USNM	169108	*Uam*	Idaho	Selway National Forest	U
USNM	169109	*Uam*	Idaho	Idaho CoUty, Lowell	U
USNM	169145	*Uam*	Idaho	Idaho CoUty, Lowell, 3 miles from	U
USNM	170655	*Uam*	Idaho	Clearwater CoUty, Orofino, 12 mi from Cougar Basin	U
USNM	211039	*Uam*	Idaho	Clearwater CoUty, Orofino, 12 mi from Cougar Basin	U
USNM	211749	*Uam*	Idaho	Caribou CoUty, Soda Springs	U
USNM	215134	*Uam*	Idaho	Leesburg, Phelan Creek, 7 Mi S	U
USNM	215135	*Uam*	Idaho	Leesburg, Phelan Creek, 7 Mi S	U
USNM	215136	*Uam*	Idaho	Leesburg, Phelan Creek, 7 Mi S	U
USNM	215202	*Uam*	Idaho	Teton CoUty, Victor	U
USNM	215203	*Uam*	Idaho	Blaine CoUty, 15 mi W of Ketchum, Warm Spring Creek	U
USNM	215204	*Uam*	Idaho	Leesburg, 7 mi S Phelan Creek	U
USNM	215205	*Uam*	Idaho	Leesburg, 7 mi S Phelan Creek	U
USNM	216420	*Uam*	Idaho	Lemhi CoUty, 16 Mi E of Leadore at head waters of Road Caon	U
USNM	223812	*Uam*	Idaho	Bannock CoUty, Tygee Basin, Timber Creek	U
USNM	224534	*Uam*	Idaho	Clearwater CoUty, Orofino, Ceder Creek	U
USNM	224535	*Uam*	Idaho	Clearwater CoUty, Orofino, Ceder Creek	U
USNM	224536	*Uam*	Idaho	Clearwater CoUty, Orofino, 20 mi from Cow Creek	U
USNM	224537	*Uam*	Idaho	Clearwater CoUty, Orofino, 20 mi from Cow Creek	U
USNM	224539	*Uam*	Idaho	Idaho CoUty, Elk City, Cow Creek	U
USNM	224540	*Uam*	Idaho	Idaho CoUty, Elk City, Cow Creek	U
USNM	224541	*Uam*	Idaho	Lower Salmon River	U
USNM	224542	*Uam*	Idaho	Lower Salmon River	U
USNM	226060	*Uam*	Idaho	Lemhi CoUty, Leadore	U
USNM	226061	*Uam*	Idaho	Idaho CoUty, Elk City, 65 Mi E	U
USNM	226462	*Uam*	Idaho	Idaho CoUty, Elk City, 65 Mi E	U
USNM	226463	*Uam*	Idaho	Lemhi CoUty, Leadore	U
USNM	227093	*Uam*	Idaho	Blaine CoUty, Ketchum, 10 Mi N, Santooth National Forest	U
USNM	227658	*Uam*	Idaho	Blaine CoUty, Muldoon	U
USNM	227660	*Uam*	Idaho	Blaine CoUty, Muldoon	U
USNM	228796	*Uam*	Idaho	Custer CoUty, Challis	U
USNM	242728	*Uam*	Idaho	Custer CoUty, Challis	U
USNM	245509	*Uam*	Idaho	Caribou CoUty, Stump Creek	U
USNM	245512	*Uam*	Idaho	Boise National Forest, Sheep Creek	U
USNM	247077	*Uam*	Idaho	Boise National Forest, Crooked River	U

USNM	247078	*Uam*	Idaho	Boise National Forest, Swanholm Peak	U
USNM	251488	*Uam*	Idaho	Elmore CoUty, Boise National Forest	U
USNM	265280	*Uam*	Idaho	Boise National Forest, Swanholm Peak	U
USNM	271752	*Uam*	Idaho	Caribou CoUty, Henry Lake	U
USNM	271901	*Uam*	Idaho	Snake River	U
USNM	271902	*Uam*	Idaho	Lost River MoUtains	U
USNM	271903	*Uam*	Idaho	Salmon River MoUtains	U
USNM	113406	*Uam*	Colorado	No data	U
USNM	113407	*Uam*	Colorado	Rifle	U
USNM	113408	*Uam*	Colorado	No data	U
USNM	113409	*Uam*	Colorado	No data	U
USNM	147458	*Uam*	Colorado	Newcastle, 20 Mi S, Divide Creek	U
USNM	147459	*Uam*	Colorado	Newcastle, 20 Mi S, Divide Creek	U
USNM	147460	*Uam*	Colorado	Newcastle, 20 Mi S, Divide Creek	U
USNM	147461	*Uam*	Colorado	Newcastle, 20 Mi S, Divide Creek	U
USNM	147462	*Uam*	Colorado	Newcastle, 20 Mi S, Divide Creek	U
USNM	147463	*Uam*	Colorado	Newcastle, 20 Mi S, Divide Creek	U
USNM	147464	*Uam*	Colorado	Newcastle, 20 Mi S, Divide Creek	U
USNM	147465	*Uam*	Colorado	Newcastle, 20 Mi S, Divide Creek	U
USNM	147466	*Uam*	Colorado	Newcastle, 20 Mi S, Divide Creek	U
USNM	147467	*Uam*	Colorado	Newcastle, 20 Mi S, Divide Creek	U
USNM	150355	*Uam*	Colorado	Pagosa Springs	U
USNM	150357	*Uam*	Colorado	Pagosa Springs	U
USNM	216293	*Uam*	Colorado	Grand CoUty, Kremmling	U
USNM	222747	*Uam*	Colorado	Pagosa Springs, 25 Mi NW	U
USNM	224068	*Uam*	Colorado	Grand CoUty, Kremmling, Silver Creek	U
USNM	224509	*Uam*	Colorado	Grand CoUty, Kremmling	U
USNM	236227	*Uam*	Colorado	Hot Sulphur Springs	U
USNM	287665	*Uam*	Colorado	Montrose CoUty, San Miguel, Dry Creek Basin	U
USNM	287666	*Uam*	Colorado	Park CoUty, Black MoUtain	U
USNM	395845	*Hma*	-	Zoo	U
USNM	399301	*Hma*	-	Zoo	A
USNM	19206	*Hma*	Indonesia	Sapagaya River	U
USNM	115695	*Hma*	-	Zoo	U
USNM	123138	*Hma*	Indonesia	Kateman River	A
USNM	123139	*Hma*	Indonesia	Kateman River	A
USNM	142344	*Hma*	Indonesia	Landak River, Ngabong	A
USNM	145580	*Hma*	Indonesia	Sempang River	U
USNM	151866	*Hma*	Indonesia	Pamukang Bay	U
USNM	153835	*Hma*	Indonesia	Kendawangan River	U
USNM	153836	*Hma*	Indonesia	Kendawangan River	U
USNM	153837	*Hma*	Indonesia	Kendawangan River	A
USNM	153838	*Hma*	Indonesia	Kendawangan River	U
USNM	153839	*Hma*	Indonesia	Kendawangan River	U
USNM	197254	*Hma*	Indonesia	Tandjong Seglu	U
USNM	197255	*Hma*	Indonesia	Tandjong Seglu	U
USNM	198713	*Hma*	Indonesia	SUgai Mahakam	U
USNM	198714	*Hma*	Indonesia	SUgai Djambajan	U
USNM	198715	*Hma*	Indonesia	SUgai Djambajan	U
USNM	239451	*Hma*	-	Zoo	U

USNM	260227	*Hma*	-	Zoo	U
USNM	267586	*Hma*	-	Zoo	U
USNM	291756	*Hma*	Malaysia	Kuala Lumpur, Near	U
USNM	358645	*Hma*	Taiwan	Central MoUtains	U
USNM	538095	*Hma*	-	Zoo	U
USNM	A 49710	*Hma*	-	Zoo	U
NHM	15.12.1.9	*Hma*	-		U
NHM	47.451	*Hma*	-		U
NHM	67.12.4.202	*Hma*	-		U
NHM	79.9.11.128	*Hma*	-		U
NHM	1821.11.26.2	*Hma*	-		U
NHM	1938.11.30.69	*Hma*	-		U
NHM	1938.11.30.70	*Hma*	-		U
NHM	1955.11.24.1	*Hma*	-		U
NHM	47452	*Hma*	-		U
AMNH	16580	*Hma*	-		U
AMNH	35364	*Hma*	-		U
AMNH	60772	*Hma*	-		U
MFN	8626	*Hma*	-		U
MFN	14377	*Hma*	-		U
MFN	17245	*Hma*	-		U
MFN	17532	*Hma*	-		U
MFN	17533	*Hma*	-		U
MFN	28472	*Hma*	-		U
MFN	34002	*Hma*	-		U
MFN	85771	*Hma*	-		U
MFN	85772	*Hma*	-		U
MFN	85773	*Hma*	-		U
MFN	A5351	*Hma*			U
USNM	221064	*Uti*	Locality Uknown	Zoo	U
USNM	258593	*Uti*	Locality Uknown	Zoo	U
USNM	358644	*Uti*	Taiwan	Chia-I, Puli, Area Of MoUt Morrison	U
USNM	13821	*Uti*	Japan	Tate Yama	U
USNM	83453	*Uti*	Japan	No data	U
USNM	122607	*Uti*	Locality Uknown	Zoo	U
USNM	187866	*Uti*	Japan	No data	U
USNM	A 22998	*Uti*	Japan	Tate Yama	U
USNM	20119	*Uti*	India	Jammu And Kashmir, Lalab	U
USNM	21844	*Uti*	India	Jammu And Kashmir, Lalab	U
USNM	21845	*Uti*	India	Jammu And Kashmir, Lalab	U
USNM	84092	*Uti*	India	Per Panjal Range	U
USNM	84093	*Uti*	India	Jammu And Kashmir, Per Panjal Range	U
USNM	240615	*Uti*	China	Sichuan, Suifu	U
USNM	258349	*Uti*	China	Sichuan, West China MoUtains, Chengtu	U
USNM	258430	*Uti*	China	Sichuan, Kuan Shien	U
USNM	258645	*Uti*	China	Sichuan, Wen Chuan	U
USNM	258646	*Uti*	China	Sichuan, Wei Chow	U

USNM	258647	*Uti*	China	Sichuan, Wen Chuan	U
USNM	259011	*Uti*	China	Sichuan, Wen Chuan	U
USNM	259099	*Uti*	Thailand	Lan Ton Lane	U
USNM	168004	*Uti*	India	Assam, Lakhimpur District, N Lakhempur, Upper Assam, Dejoo =Diju	U
USNM	199684	*Uti*	China	Heilongjiang, I-Mien-Po	U
USNM	218152	*Uti*	China	Heilongjiang, I-Mien-Po	A
USNM	240668	*Uti*	China	Hebei,Eastern Tombs area, 150 mi E of Peking [= Beijing]	U
USNM	240669	*Uti*	China	Hebei, Eastern Tombs	U
USNM	240670	*Uti*	China	Hebei, Eastern Tombs	U
USNM	240671	*Uti*	China	Hebei, Eastern Tombs	U
USNM	271090	*Uti*	Locality Uknown	Zoo	U
NHM	18.4.61	*Uar*		Montana	A
NHM	21.8.2	*Uti*	India	No data	A
NHM	26.10.8.40	*Uti*	India	No data	A
NHM	26.10.8.41	*Uti*	Jaumazar	India	U
NHM	27.2.7.4	*Uti*	China		U
NHM	28.10.12.5	*Uti*	China		U
NHM	30.5.21.2	*Uti*	China		A
NHM	31.6.1.5	*Uti*	China		U
NHM	31.9.21.4	*Uti*	China		U
NHM	32.5.77	*Uti*	China		U
NHM	33.2.43	*Uti*	China		U
AMNH	23086	*Uti*	China		U
AMNH	35016	*Uti*	China		U
AMNH	35496	*Uti*	China		A
AMNH	57076	*Uti*	China		U
AMNH	70320	*Uti*	China		U
AMNH	80248	*Uti*	China		U
AMNH	84389	*Uti*	China		U
MFN	17530	*Uti*	China		U
MFN	56747	*Uti*	China		A
MFN	69379	*Uti*	China		U
MFN	69383	*Uti*	China		U
MFN	91075	*Uti*	China		U
MFN	91077	*Uti*	China		U
USNM	258425	*Ame*	China		U
USNM	259028	*Ame*	China		U
USNM	259402	*Ame*	China		U
USNM	259401	*Ame*	China		U
USNM	258423	*Ame*	China		U
USNM	258984	*Ame*	China		U
USNM	258836	*Ame*	China		U
USNM	259074	*Ame*	China		U
USNM	259029	*Ame*	China		U
USNM	259400	*Ame*	China		U
USNM	259075	*Ame*	China		U
USNM	258834	*Ame*	China		U
USNM	258335	*Ame*	China		U
USNM	399447	*Ame*	China		U

USNM	259076	*Ame*	China	U
USNM	259027	*Ame*	China	U
USNM	579891	*Ame*	China	U
USNM	258644	*Ame*	China	U
USNM	259403	*Ame*	China	U
USNM	582622	*Ame*	China	U
NHM	9.7.21.3	*Ame*	China	U
NHM	39.3908	*Ame*	China	U
NHM	1950.523	*Ame*	China	U
NHM	55587	*Ame*	China	U
NHM	55591	*Ame*	China	U
NHM	55592	*Ame*	China	U
NHM	968201	*Ame*	China	U
AMNH	89028	*Ame*	China	U
AMNH	89029	*Ame*	China	U
AMNH	89030	*Ame*	China	U
AMNH	110451	*Ame*	China	U
AMNH	110454	*Ame*	China	U
AMNH	147745	*Ame*	China	U
AMNH	147746	*Ame*	China	U
AMNH	17246	*Ame*	China	U
AMNH	17542	*Ame*	China	U
AMNH	37026	*Ame*	China	U
AMNH	85761	*Ame*	China	U
NHM	20.10.11.1	*Uma*		U
NHM	46.12.21	*Uma*		U
NHM	90.8.4.1	*Uma*		U
NHM	1937.5.6.3	*Uma*		U
NHM	1937.5.6.4	*Uma*		U
NHM	1937.5.6.7	*Uma*		U
NHM	1938.11.17.14	*Uma*		U
NHM	1952.2.25.1.	*Uma*		U
AMNH	10039	*Uma*		U
AMNH	156286	*Uma*		U
AMNH	213948	*Uma*		U
AMNH	215283	*Uma*		U
MFN	14382	*Uma*		U
MFN	14385	*Uma*		U
MFN	18695	*Uma*		U
MFN	18696	*Uma*		U
MFN	18700	*Uma*		U
MFN	43702	*Uma*		U
MFN	43703	*Uma*		U
MFN	43711	*Uma*		U
MFN	43713	*Uma*		U
MFN	43718	*Uma*		U
MFN	43719	*Uma*		U

MFN	43720	*Uma*			U
MFN	69373	*Uma*			U
MFN	69374	*Uma*			U
USNM	170656	*Tor*	Venezuela	Merida	A
NHM	9.7.6.1	*Tor*			U
NHM	27.1.11.70	*Tor*			U
NHM	27.11.1.71	*Tor*			U
NHM	39.4.2.40	*Tor*			U
NHM	55.12.24.309	*Tor*			U
NHM	73.6.27.5	*Tor*			D
NHM	73.6.27.11	*Tor*			U
NHM	78.8.31.12	*Tor*			U
NHM	1839-3617	*Tor*			U
AMNH	AMNH-67732	*Tor*			U
MFN	MFN-6121	*Tor*			U
MFN	MFN-7036	*Tor*			A
MFN	MFN-16186	*Tor*			U
MFN	MFN-44143	*Tor*			A
MFN	MFN-83338	*Tor*			U
MFN	MFN-85759	*Tor*			U
NHM	18.3.13.44	*Mur*			U
NHM	20.10.27.1	*Mur*			U
NHM	20.10.27.5	*Mur*			U
NHM	29.6.1.8	*Mur*			U
NHM	32.5.79	*Mur*			U
NHM	34.8.12.8	*Mur*			U
NHM	34.10.18.7	*Mur*			U
NHM	36.1.22.1	*Mur*			A
NHM	36.1.22.2	*Mur*			U
NHM	36.1.22.4	*Mur*			A
NHM	36.1.22.6	*Mur*			A
NHM UK	36.3.13.44	*Mur*			U
NHM	41.1.12.13	*Mur*			U
NHM	62.1963	*Mur*			U
NHM	62.1964	*Mur*			U
NHM	69.1962	*Mur*			U
NHM	88.3.20.1	*Mur*			U
AMNH	35989	*Mur*			U
AMNH	54464	*Mur*			A
AMNH	54465	*Mur*			U
AMNH	54466	*Mur*			U
AMNH	54467	*Mur*			U
AMNH	13384	*Mur*			U
AMNH	15579	*Mur*			U
AMNH	45074	*Mur*			U
AMNH	56748	*Mur*			U
AMNH	70510	*Mur*			U

Table S3. Specimens of *A. simus* analyzed in **chapter 3.5**.

Museum	Cat. #	Other cat. #	Locality: (Specimen Details)	Locality Remarks:	Group:	Element:	Side:	Remarks: (Element Information)	dental carries	same individual?
GP	5	HC 762	Hancock Collection : Deposit 9 : Grid H-13 : D1 11.5		cranial	skull			Y	
GP	22	HC 83	Hancock Collection : Deposit 9 : Grid I-14 : D1 24.5		tooth	M2/	rt		Y	
GP	63179		Pit 91 Collection : Deposit 91 : Field No. RLP 1948 : Grid I-8		tooth	M2/	rt	old indiv;	Y	
GP	619		Hancock Collection : Deposit 9 : Grid L-15 : D1 19		cranial	dentary	rt	w /m1-2; from Sparky Johnson;	Y	
GP	52237		Pit 91 Collection : Deposit 91 : Field No. RLP 1648 : Grid I-8		cranial	maxilla	rt	w P3-M2/; pits in M2/; fragment;	Y	possible-1
GP	52511		Pit 91 Collection : Deposit 91 : Field No. RLP 1748 : Grid I-8		cranial	maxilla	lt	fragment; w P4-M2/; (1+1 cap); waterworn	Y	possible-1
GP	52234		Pit 91 Collection : Deposit 91 : Field No. RLP 1748 : Grid I-8		cranial	dentary	rt	w /i2-c, /p4-m3, root of /i1; pathology resorbed premolar alveolus; (1+1 bot);		possible-1
GP	21	HC 1292	Hancock Collection : Deposit 9 : Grid J-13 : D1 17	grids J+K 13+14 and pit 17 caved	cranial	dentary	lt	dentary with /m1-2; also catalog #'s Z21b & HC 1129;		possible-2
GP	23	HC 1296	Hancock Collection : Deposit 17	caved	tooth	/m3	lt			possible-2
GP	129		Hancock Collection : Deposit 17	caved	cranial	maxilla	rt	fragment; with M1-2/; also catalog # 1293		possible-3
GP	128		Hancock Collection : Deposit 17	caved	cranial	maxilla	lt	fragment; with P4/, M1/; also catalog # HC 1294		possible-3
GP	26		Hancock Collection :	caved	toot	M2/	rt	also catalog #		possibl

			Deposit 17		h			HC 1291		e-4
GP	136		Hancock Collection : Deposit 17	caved	toot h	M1/	lt	also catalog # HC 628		possibl e-4
GP	126		Hancock Collection : Deposit 17	caved	toot h	M2/	rt	also catalog # HC 1290		possibl e-4
GP	127		Hancock Collection : Deposit 17	caved	toot h	M1/	lt	also catalog # HC 1289		possibl e-4
GP	72		Hancock Collection : Deposit 77	caved	toot h	/m2	lt	also catalog # HC 506		possibl e-5
GP	62	HC 511	Hancock Collection : Deposit 77 : Grid G-11 : D1 9		toot h	/m2	lt			possibl e-5
GP	14		Hancock Collection : Deposit no data		toot h	M1/	rt			possibl e-6
GP	13		Hancock Collection : Deposit no data		toot h	M1/	lt			possibl e-6
GP	974 8									possibl e-7
GP	624									possibl e-7
GP	2	HC 92	Hancock Collection : Deposit 3 : Grid D-3 : D1 9		cran ial	skull		reconstructed skull;		
GP	18	HC 90	Hancock Collection : Deposit 9 : D1 13	which grid	cran ial	dent ary	lt	with /c, /m1-3;		
GP	4		Hancock Collection : Deposit 9 : Grid D-13 : D1 25.5		cran ial	skull		with maxilla, premaxilla without I/ or C/; also catalog # HC 93		
GP	10	HC 626	Hancock Collection : Deposit 9 : Grid F-12 : D1 19.5		cran ial	dent ary	lt	fragment; with /c, /m1-3, root /p4;		
GP	575 38		Hancock Collection : Deposit 9 : Grid F-12 : D1 21		toot h	/m3	lt	box #10-94		
GP	574 90		Hancock Collection : Deposit 9 : Grid F-12 : D1 21		cran ial	maxi lla	lt	fragment; w M1/; root of M2/; box #10-94		
GP	16	HC 86	Hancock Collection : Deposit 9 : Grid G-3 : D1 15		cran ial	dent ary	rt	with /m1-3;		
GP	17	HC 89	Hancock Collection : Deposit 9 : Grid H-13 : D1 12		cran ial	dent ary	rt	with /m2-3;		
GP	3	HC 93	Hancock Collection : Deposit 9 : Grid H-13 : D1 15		cran ial	skull		reconstructed skull; w/ Rt P3-4/, M1-2/, and		

								Lt M1-2/;		
GP	25	HC 1128	Hancock Collection : Deposit 9 : Grid J-13 : D1 17	grids J+K 13+14	tooth	M1/	lt			
GP	132		Hancock Collection : Deposit 9 : Grid J-15 : D1 18.5	grids J+K-15	tooth	M2/	lt	also catalog # HC 1288		
GP	54	HC 618	Hancock Collection : Deposit 9 : Grid K-14 : D1 18.5	Questionable Information 2-60?; grids K-14+15	cranial	dentary	rt	with /m1-2;		
GP	575 14		Hancock Collection : Deposit 17	caved	cranial	dentary	rt	w /m1-2		
GP	1	HC 134	Hancock Collection : Deposit 60 : Grid H-10 : D1 9		cranial	skull				
GP	125	HC 1134	Hancock Collection : Deposit 77	caved	cranial	maxilla	rt	glued to Z 131,		
GP	71	HC 507	Hancock Collection : Deposit 77 : D1 9		tooth	/m3	lt			
GP	68	HC 509	Hancock Collection : Deposit 77 : Grid F-11 : D1 10	grid F(G)-11	tooth	/m3	rt			
GP	63	HC 510	Hancock Collection : Deposit 77 : Grid G-11 : D1 9.5		tooth	/m3	rt			
GP	6	HC 401	Hancock Collection : Deposit 77 : Grid H-11 : D1 9.5		cranial	dentary	rt			
GP	9		Hancock Collection : Deposit no data		cranial	dentary	lt	fragment; with /m1-2 path /c		
GP	138 725		Hancock Collection : Deposit no data		tooth	/m2	rt	worn;		
GP	574 91		Hancock Collection : Deposit no data		cranial	maxilla	lt	fragment; w M2/		
GP	575 10		Hancock Collection : Deposit no data		tooth	M1-2/	lt	associated		
GP	575 11		Hancock Collection : Deposit no data		tooth	M2/	lt			
GP	575 16		Hancock Collection : Deposit no data		cranial	dentary	lt	fragment; w /m3; roots of		

								/m2		
GP	575 19		Hancock Collection : Deposit no data		cran ial	dent ary	lt	fragment; w /m2		
GP	575 20		Hancock Collection : Deposit no data		cran ial	dent ary	rt	fragment; w /m1-3, in 5 pieces; box #11-94		
GP	575 21		Hancock Collection : Deposit no data		cran ial	dent ary	rt	fragment; w /m1-2		
GP	575 23		Hancock Collection : Deposit no data		cran ial	dent ary	rt	fragment; w /m2; posterior root of /m1		
GP	575 37		Hancock Collection : Deposit no data		toot h	/m2	rt	w broken anterior root		
GP	604 51		Hancock Collection : Deposit no data		toot h	M2/	rt			
GP	15		Hancock Collection : Deposit no data		toot h	M1/	rt			
GP	19		Hancock Collection : Deposit no data		cran ial	dent ary	lt	with /p4, /m1-2		
GP	7		Hancock Collection : Deposit no data		cran ial	dent ary	rt	with /c, /p4, /m1-2; glued to Z29; also catalog # HC 622		
GP	8		Hancock Collection : Deposit no data		cran ial	skull		fragment; lt mandible fragment with /p4-m3, and rt /c; rt maxilla fragment with M1-2/; glued to Z 29		
GP	20		Hancock Collection : Deposit no data		cran ial	maxi lla		lt and rt maxillae fragment with P4/s, M1-2/s, 3Cs		
GP	274 42		Pit 91 Collection : Deposit 91 : Field No. RLP 924 : Grid F-11		toot h	/m2	rt	1 + 1 capsule;		
GP	217 61		Pit 91 Collection : Deposit 91 : Field No. RLP 1156 : Grid H-11		toot h	M1/	lt	(1+1 cap)		
GP	547 54		Pit 91 Collection : Deposit 91 : Field No. RLP 1740 : Grid I-10		cran ial	maxi lla	lt	w erupting C/, P4-M2/; (1+1 bot);		
GP	525 18		Pit 91 Collection : Deposit 91 : Field No. RLP 1848 :		toot h	/m3	rt			

			Grid I-8							
GP	631 78		Pit 91 Collection : Deposit 91 : Field No. RLP 2068 : Grid K-8		toot h	/m1	rt	w lateral fragment of dentary; (1+1 cap);		
CM N	434 44		Old Crow Formation (Yukon Canada)		ma ndi ble	m1- m3	rt			
CM N	190 06		Old Crow Formation (Yukon Canada)		cran ial	P4- M2	rt			
AM NH	127 699		Goldstream (Alaska)		cran ial	c, m1- m2	rt			
AM NH	304 92		Upper Cleary, Fairbanks (Alaska)		skul l	c, p4- m2	rt,lt			
AM NH	992 09		Ester Creek (Alaska)		skul l	CO MPL ETE				

4

Conclusions

Through this section, I explain the main findings obtained in my PhD Thesis to provide a broader picture on how these studies contribute to the *state of the art* of the paleobiology of two iconic bears from the European and the North American ice-age (Late Pleistocene) megafauna, the cave bear (*Ursus spaleaus*) and the short-faced bear (*Arctodus simus*) as inferred by new ecomorphological approaches.

4.1 Synthesis

Regarding the cave bear, these approaches were applied to answer a fundamental question of its paleobiology that still unclear in the literature: why the cave bear went extinct? Core hypotheses predict: (i) a human-driven cave bear decline due to competition for resources or to direct hunting (e.g., Münzel et al. 2004, 2011); and (ii) a climate-driven demise of cave bears (Baca et al. 2016) due to a restrictive herbivorous feeding behaviour even at a time of lowered vegetation productivity during the beginning of the Last Glacial (Bocherens 2019; Terlatto et al. 2019). However, some studies based on geometric morphometrics, on dental microwear analysis and on isotopic biochemistry (Pinto et al. 2005; Quilès 2006; Richards et al. 2008; Figueirido et al. 2009; Pacher and Stuart 2009; Peigné et al. 2009; Peigné and Merceron 2017; Robu et al. 2018) suggest an omnivorous diet for cave bears.

These contradictory evidences pose another crucial question to understand the potential causes of the extinction of cave bears: *Were cave bears more herbivores than their closest living relative –i.e., the omnivorous brown bear (Ursus arctos)?* The answer of this demands new analytical techniques with potential to ascertain the feeding behaviour of the cave bear. Accordingly, in chapters 3.1 and 3.2 I use new ecomorphological techniques in 3D that have never been applied to investigate the diet of the cave bear.

In Chapter 3.1, I explore the size and morphology of the tooth-root of maxillary teeth from CT scans of living bears to make inferences about the feeding behaviour of extinct cave bears. This approach quantifies the relative tooth-root areas because previous studies have demonstrated that it reflects dietary specialisation and bite force in mammals (e.g., Spencer 2003; Kupczik and Dean 2008) and specially in mammalian carnivores (e.g., Kupczik and Stynder 2012; Stynder and Kupczik 2013). Not surprisingly, the results indicate a close association between tooth-root surface areas and feeding behaviour in living bears. All analyses show that cave bears follow a unique gradual increase in tooth-root areas from the fourth upper premolar to the second upper molar, approaching in the later teeth, the tooth-root areas of the bamboo-feeder giant panda. This is especially the case in *U. spelaeus ladinicus* and *U. spelaeus eremus* and less pronounced in *U. ingressus* and *U. spelaeus spelaeus*. Although this pattern of distribution of tooth-root areas across maxillary teeth was probably inherited from the middle Pleistocene *Ursus deningeri* (Van Heteren et al. 2018), it suggests that cave bears were more herbivores than its closest living relative, the living brown bear *U. arctos*. However, the tooth-root areas of cave bears also allowed me to hypothesize on their different feeding strategies.

All cave bears with the exception of *U. spelaeus spelaeus*, occupy a portion of the morphospace not explored by any living bear, suggesting that *U. spelaeus eremus*, *U. spelaeus ladinicus* and *U. ingressus* were exploiting a dietary niche that was distinct from any living bear. In contrast, given the similarity of *U. spelaeus spelaeus*, with the American black bear, it is possible that this subspecies fed on similar food resources, although this interpretation should be taken with caution. I interpret the differences between the patterns of toot-root areas across maxillary teeth, because while *U. spelaeus spelaeus* inhabited areas of about 500m until 800m of altitude above sea level, *U. ingressus, U. spelaeus eremus* and *U. spelaeus ladinicus* foraged from high-alpine to alpine region, reaching altitudes up to 2.800m above sea level for the latter. The different ecosystems where they foraged may explain the differences reported here in the tooth-root area values across maxillary teeth, and by extension, differences in their feeding behaviour. I proposed that while *U. spelaeus eremus* and *U. spelaeus ladinicus* may be adapted to feed on any resource present in the high-alpine biome relying more on hard or tough foods (as indicated by their large tooth-root areas), *U. ingressus* probably did not rely on this kind of resources. Therefore, the large body size of *U. ingressus* probably forced this species to improve the performance of mastication to increase the daily food intake during the vegetation period to acquire a sufficient fat storage before autumn. These results have been published as part of a special issue on cave bear paleobiology in the journal *Historical Biology* (Pérez-Ramos et al. 2019).

In **Chapter 3.2**, I explore how this unique increasing pattern of tooth-root area across maxillary teeth is reflected in the topography of their crowns. Dental topographic analysis is the quantitative assessment of shape of three-dimensional models of tooth crowns and its features (M'Kirera and Ungar 2003; Evans et al. 2007; Bunn et al. 2011; Winchester et al. 2014), and during the last years, significant advances in 3D scanning and image processing techniques have allowed the digital reconstruction of tooth-crown surface topography (Winchester 2016). Several authors have established a correlation of dental topographic variables with feeding behaviour in many groups of living and extinct mammals (M'Kirera and Ungar 2003; Ungar and M'Kirera 2003; Dennis et al. 2004; Ulhaas et al. 2004; King et al. 2005; Evans et al. 2007; Boyer 2008; Ungar and Bunn 2008; Bunn and Ungar 2009; Evans and Jernvall 2009; Bunn et al. 2011; Godfrey et al. 2012; Wilson et al. 2012; Pineda et al. 2016; Evans and Pineda 2018). However, studies of tooth crown topography and its features in 3D on living and extinct bears are currently absent. In this chapter, I obtained three variables from dental topographic analysis: the molar topographic curvature (DNE), relief (RFI), and complexity (OPCR) from three-dimensional tooth crown surfaces in living bears. To explore the relationship of these variables with feeding behaviour in living bears, I investigated the influence of phylogeny, diet, and size on DNE, OPCR, and RFI. As expected, the results indicated that the three variables are relatively independent of phylogeny but only some reflected diet. Accordingly, I used these ecomorphological indicators to make dietary inferences in cave bears (*Ursus spelaeus* s.l.).

The results indicated that while DNE and OPCR are good dietary proxies of living bears, RFI did not reflect dietary adaptations in living bears. A clear gradient in both DNE and OPCR was revealed, from soft-matter consumption (i.e., the animal-protein feeders [the insectivorous *M. ursinus* and the hypercarnivores polar bear *U. maritimus*] and the soft-mast specialists [the folivores-frugivores American black bear *U. americanus* and the Andean bear *T. ornatus*]) to the durophagous giant panda, *A. melanoleuca*, being the omnivores (*U. arctos* and *U. thibetanus*) in between. Therefore, both OPCR and DNE reflect the nature of the items consumed more than the type of food, at least in bears. Moreover, both DNE and OPCR are strongly influenced by size, and therefore profound allometric effects seem to be present in these dental topographic variables. Strikingly, cave bears take intermediate values of DNE and OPCR to the ones of *A. melanoleuca* and the rest of living bears.

Following this evidence, I propose the hypothesis that cave bears increase the outline areas of their most posterior dentition to almost reach the values exhibited by the giant panda (as demonstrated in the previous chapter), and this increase entails a substantial increase in both OPCR and DNE, which improves efficiency to chew on highly abrasive and lower-quality foods that were present in the high-alpine biome. Consequently, these new data on OPCR and DNE supports the hypothesis proposed in **chapter 3.1** in which I revealed that the subspecies of *U. spelaeus eremus* and *U. spelaeus ladinicus*, and to a lesser extent *U. ingressus,* represent an adaptation to feed on any hard or tough resource. Moreover, as obtained in **chapter 3.1**, they combine values of OPCR and DNE in a unique manner among living bears, as evidenced by their position in an empty space of the morphospace derived from a principal components analysis of these dental topographic variables. Accordingly, cave bears most probably were feeding on resources present in the high-alpine biome that is not currently exploited by any living bear. This food resources could have had intermediate mechanical properties to bamboo and hard mast. A clear argument that supports our hypothesis is that the two brown bear specimens that plot with cave bears in the aforementioned morphospace belong to the subspecies known as *U. arctos pruinosus,* a subspecies that forage at 4,500m of altitude in the Tibetan plateau.

The results obtained in these two chapters demonstrates that cave bears were more herbivorous than the living brown bear, and I hypothesize that they probably fed on a low-energetic, highly fibrous resource that was present in the high-alpine biomes where they foraged. However, the climate-driven hypothesis explains the decline of cave bears not only for being herbivores, but also because they relied exclusively on vegetal resources from 100,000 to 20,000 years ago (Bocherens 2019; Terlatto et al. 2019), and therefore, without evidence of a dietary shift towards omnivory –i.e., lack of dietary flexibility.

Accordingly, in **Chapter 3.3**, I investigate whether cave bears were biomechanically restricted to feed exclusively on vegetal resources using three-dimensional computer simulations of different feeding scenarios computed from CT-scanned skulls of the extinct cave bears. I specifically used an approach based on Finite Element Analysis (FEA). Finite Element Analysis is a technique borrowed from engineering and orthopedic sciences that quantifies stress, strain, and deformation in a given structure. During the last decade FEA has been used in the paleontological and zoological sciences to address questions of functional morphology and evolution of different organisms (Rayfield 2007). Although this approach has been recently developed to ascertain cranial mechanics in living bears with the main goal to make inferences on the diet of the extinct African ursid *Agriotherium africanum*, it has never been applied to cave bears.

Therefore, in this chapter I performed 3D biomechanical simulations of different chewing scenarios on the cave bear skull and on the skull of living bears, and I demonstrated that cave bears lack the degree of biting efficiently with all teeth, leading to a lack of the dietary flexibility that characterize the omnivorous brown bear. Therefore, my results supports the hypothesis that cave bears were fully herbivorous without the flexibility to shift their diet towards omnivory during the Pleistocene climatic cooling at the beginning of the Last Glacial Maximum (Bocherens 2019; Terlato et al. 2019). I also propose that this lack of dietary flexibility is a consequence of having expanded sinuses in the frontal region, which forms the domed forehead that characterizes the *speloid* lineage. This dome significantly reduces the dissipation of stress when biting with the anterior dentition, and hence, forcing cave bears to have a skull biomechanically constrained for chewing vegetal matter with their posterior teeth. On the other hand, I propose that the selective advantage of having extremely large sinuses in cave bears is probably related to their necessity to overcome long winters in hibernation of the Last Glacial, with the hibernation process largely controlled by various enzymes segregated in the sphenoidal sinuses to essentially decrease basal metabolic rates (Lundberg 2008; Petruson et al. 2005; Yan et al. 2017; Andersson et al. 2002). I hypothesize that the necessity of having large hibernation periods was the key selective agent to increase sinus size along the evolutionary history of the *speloid* lineage. At the same time, the 'selected' large sinuses caused a trade-off between feeding and hibernation.

The study performed in **chapter 3.3** is based on two assumptions well established in the literature: the first is that sinuses size is related to basal metabolic rates; and the second is that cave bears had longer hibernation periods than living bears. To mitigate this, in **Chapter 3.4**, I explore if paranasal sinuses allowed the long hibernation periods in cave bears by decreasing their basal metabolic rates.

The physiology in animals that hibernate is mainly regulated by the activation of enzymes via stress pathways. Among these enzymes, the nitric oxide synthase (NOs) is activated when the concentration of CO_2 in blood increases (hypercapnia) and the levels of O_2 decrease (hypoxia) at the beginning of hibernation (e.g., O'Hearn et al. 2007). The response to these stimuli is to decrease body temperature, heart rate and blood pressure (Kudej et al. 2007). Recent studies link NO and Hydrogen sulfide (HS) pathways with the control of the hibernation in bears, as these metabolites (NO and HS) are related to the induction of several responses to stimuli of biological stress (Revbesch et al. 2014). Interestingly, the production of NO and HS is segregated by the epithelium of the sphenoideal sinuses (e.g., Lundberg 2008; Petruson et al. 2005; Yan et al. 2017) and all the paranasal sinuses function as a reservoir for NO (Andersson et al. 2002). Accordingly, my prediction is that those species with larger paranasal sinuses do hibernate by decreasing basal metabolic rates. To investigate this, I perform a bivariate regression approach of sinuses volume against basal metabolic rates in living bears (both variables independent of body mass). The results confirm a negative association between sinuses size and basal metabolic rates, and those species with larger sinuses and lower metabolic rates are those bears that hibernate.

The findings mentioned above pose another crucial question to understand the paleobiology of cave bears: *Did the low metabolic rates of cave bears extend their hibernation periods to overcome the longer and severe winters of the Late Pleistocene?* To answer this question, I calculated basal metabolic rates of living bears using the allometric equations of McNab (2008) for active periods and of Robbins et al. (2012) for periods of hibernation. Moreover, we estimated the body masses of all species/subspecies within the cave bear group using the equation of Figueirido et al. (2011) to estimate theoretical basal metabolic rates of cave bears using the aforementioned allometric equations. Moreover, I calculated the mean annual intake of cave bears –using the inferred annual basal metabolic rates, and the energetic requirements of cave bears using the equation of Farlow (1976). The results reveal that a period of 8 months of hibernation is plausible according to their inferred energetic requirements. Additionally, a new histo-morphometric analysis of cancellous bone (i.e., the density of connections among trabeculae) indicates that cave bears possessed a trabecular bone with a very low-density, which could evidence a metabolically economized ossification by the effect of high levels of NO in blood during hibernation.

Therefore, the main conclusions of **chapters 3.1**-**3.4**, is that cave bears relied on a low-energetic, highly fibrous resource that was present in the high-alpine biome they inhabited without the flexibility to shift their diet towards omnivory during the Pleistocene climatic cooling (Bocherens 2019; Terlato et al. 2019). This lack of flexibility is a consequence (at least in part) of having large paranasal sinuses, necessary to decrease its basal metabolic rates for hibernating up to eight months. Moreover, I have obtained a significant negative association between paranasal sinuses size and basal metabolic rates in living bears, demonstrating that those species with larger sinuses also have low basal metabolic rates. Moreover, I use allometric equations to estimate body mass, basal metabolic rate (BMR), and the annual intake in cave bears to address if they could have spent long periods in hibernation feeding on highly-fibrous, low-energetic resources during the active period. I predict an energetically possible period of hibernation for cave bears up to eight months. Therefore, the extremely large sinuses of cave bears could have allowed the long periods of hibernation necessary to overcome the longer and more severe winters than today of the Late Pleistocene.

These new findings demonstrates that the biomechanical restriction imposed by the necessity of having large periods of hibernation is likely to be a more critical factor in the decline and ultimate extinction of the cave bear than previously suspected. Our new life history trade-off hypothesis also formulates a specific, mechanistic pathway by which climatic changes during the Last Glacial could have directly influenced the ability of some members of the Ice Age megafauna to obtain adequate nutrients and successfully survive during the extreme ecological conditions of the coldest months.

These findings pose another crucial palaecological question on the evolution of the ice-age megafauna: *How climate cooling affected to other species?* To answer this question, in **Chapter 3.5,** I report the first pathological evidence in *A. simus* teeth preserved at Rancho La Brea (California, USA) and it is compared with a large dataset of living bear species from different populations affected with similar dental defects. To ascertain the aetiology of the lesions, I developed new macroscopic and microscopic approaches such as 3D-morphometrics of cavities from a countermold, scanning electron microscopy (SEM), and CT analyses. The short-faced bear is an iconic bear species from the North American continent whose diet has been a controversial topic in the literature. In fact, the diet of *A. simus* is a contentious topic in the literature, as different researchers have proposed differing diets, including hypercarnivory relying on flesh (Kurtén 1967; Kurtén & Anderson 1980; Yeakel et al. 2013; Fox-Dobbs et al. 2008; Richards et al. 1996) and carrion (Matheus 1995; Voorhies and Corner 1986; Guthrie 1988; Schubert and Wallace 2009; Christiansen 1999), omnivory (Sorkin 2006; Figueirido et al. 2009) or even herbivory (Emslie and Czaplewski 1985). The results obtained confirm that unlike more northern specimens from Alaska and Yukon, dental caries were common in the population of *A. simus* from Rancho La Brea, demonstrating variable feeding preferences between both populations. In fact, while the northern population was locally adapted to a highly carnivorous diet (Bocherens et al. 1995; Matheus et al. 1995), the population of *A. simus* from RLB was more omnivorous. Following these results, I hypothesize that different competitive pressures between both populations may explain this dietary variation of this emblematic species of the North American megafauna. Moreover, this may represent evidence that the increase of the extension in the Laurentide and Cordilleran ice-sheets as a consequence of climate cooling during the middle and late Wisconsinan isolated both populations of *Arctodus* that were adapted to feed on extremely different resources. The findings suggest that both climatic change and local competition among ecologically interacting species are important mechanisms driving biodiversity changes at a global scale. This study is currently published in *Scientific reports* (Figueirido & Pérez-Ramos et al. 2017).

4.2 Conclusions

The most important conclusions reached in this PhD thesis are:

- The tooth-root areas of maxillary teeth relate to feeding behaviour in living bears and cave bears follow a unique gradual increase in tooth-root areas from the fourth upper premolar to second upper molar, approaching the tooth-root areas of the second upper molar to the values observed in the bamboo-feeder giant panda, *A. melanoleuca*. Although this pattern was probably inherited from *Ursus deningeri*, it suggests that cave bears relied more on plant materials than its closest living relative, the brown bear *U. arctos.*
- Differences in the pattern of tooth-root areas across maxillary teeth among cave bears are reported. This could relate to different feeding strategies, which in turn, could be explained by the different ecosystems they foraged but further studies are necessary to confirm this hypothesis.
- A clear gradient in DNE and OPCR obtained from dental topographic analysis of tooth crowns is revealed in living bears: from those bears that specialize in soft-matter consumption to the durophagous giant panda, being those species that consume both soft and hard masts in between. Therefore, both DNE and OPCR are good ecomorphological proxies in bears to address the nature of the items consumed. Cave bears take values of DNE and OPCR that are intermediate to the values taken by the giant panda and by those species that specialize in feeding hard-mast.
- Profound allometric effects are present in both DNE and OPCR and cave bears increase the areas of their most posterior dentition to almost reach the values exhibited by the giant panda. This size-increase entails a substantial growth of tooth crown complexity and

cusp surface and orientation, which leads to an improving efficiency to chew on highly abrasive and lower-quality foods. Cave bears combine values of OPCR and DNE in a unique manner among living bears, which most probably indicate that they were feeding on a resource present in the high-alpine biome that they inhabited.

- The 3D biomechanical simulations of different biting scenarios (with canines, fourth upper premolar, as well as with the first and second upper molars) demonstrate to be a good proxy to ascertain dietary adaptations in bears. Cave bears lack the dietary flexibility present in the more omnivorous brown bear, and therefore, they did not have the flexibility to shift their diet towards omnivory during periods of severe climatic cooling.
- The lack of dietary flexibility is a consequence of having expanded paranasal sinuses, which forms the domed forehead that characterizes the *speloid* lineage. On the other hand, paranasal sinuses allowed cave bears to spent periods of hibernation up to 8-9 months by the control of various enzymes segregated (mainly) in the sphenoidal sinuses that significantly decrease basal metabolic rates. Therefore, the selective advantage of having extremely large sinuses in cave bears was probably related to their necessity to overcome long winters in hibernation of the Last Glacial.
- There is a significant (negative) association between paranasal sinuses size and basal metabolic rates in living bears, demonstrating that those species with larger sinuses also posses low basal metabolic rates and they do hibernate.
- Using previously allometric equations of basal metabolic rates and body mass, I predict an energetically possible period of hibernation for cave bears up to eight months.

- A trade-off between hibernation vs dietary flexibility evidence that climate change during the Last Glacial could have directly influenced the ability of some members of the Ice Age megafauna to successfully survive during extreme ecological conditions.
- In fact, other members of the large carnivore guild of the Late Pleistocene, such as the North American short-faced bear (*A. simus*), also document how both climatic change and local competition among ecologically interacting species are important mechanisms driving biodiversity changes at a global scale.

4.3 References

- Andersson JA, Cervin A, Lindberg S, Uddman R, Cardell LO. 2002. The paranasal sinuses as reservoirs for nitric oxide. Acta Oto-Laryngol. 122:861–865.
- Baca M, Popović D, Stefaniak K, Marciszak A, Urbanowski M, Nadachowski A, Mackiewicz P. 2016. Retreat and extinction of the Late Pleistocene cave bear (*Ursus spelaeus* sensu lato). Sci Nat. 103:92.
- Bocherens H. 2019. Isotopic insights on cave bear palaeodiet. Hist Biol. 31:410-421.
- Bocherens H, Emslie S, Billiou D, Mariotti A. 1995. Stable isotopes (^{13}C, ^{15}N) and paleodiet of the giant short-faced bear (*Arctodus simus*). C R Acad Sci. 320: 779–784.
- Boyer DM. 2008. Relief index of second mandibular molars is a correlate of diet among prosimian primates and other euarchontan mammals. J Human Evol. 55: 1118–1137.
- Bunn JM, Ungar PS. 2009. Dental topography and diets of four old world monkey species. Am J Primatol: Official Journal of the American Society of Primatologists . 71:466-477.

- Bunn JM, Boyer DM, Lipman Y, Clair EM, Jernvall J, Daubechies I. 2011. Comparing Dirichlet normal surface energy of tooth crowns, a new technique of molar shape quantification for dietary inference, with previous methods in isolation and in combination. Am J Phys Anthropol. 145:247–261.
- Christiansen P. 1999. What size were *Arctodus simus* and *Ursus spelaeus* (Carnivora: Ursidae)? Ann Zool Fenn. 93-102.
- Dennis JC, Ungar PS, Teaford MF, Glander KE. 2004. Dental topography and molar wear in *Alouatta palliata* from Costa Rica. Am J Phys Anthropol. 125:152–161.
- Emslie SD, Czaplewski NJ. 1985. A new record of the giant short-faced bear, *Arctodus simus*, from western North America with reevaluation of its palaeobiology. Contrib Sci. 371:1–12.
- Evans AR, Jernvall J. 2009. Patterns and constraints in carnivoran and rodent dental complexity and tooth size. J Vertebr Paleontol. 29:24A.
- Evans AR, Pineda-Munoz S. 2018. Inferring Mammal Dietary Ecology from Dental Morphology. In: Croft D, Su D, Simpson S (eds). Methods in Paleoecology. Vertebr Paleobiol Pa. Springer, Cham.
- Evans AR, Wilson GP, Fortelius M, Jernvall J. 2007. High-level similarity of dentitions in carnivorans and rodents. Nature. 445:78–81.
- Farlow JO. 1976. A consideration of the trophic dynamics of a Late Cretaceous large ‐ dinosaur community (Oldman Formation). Ecology. 57:841-857.
- Figueirido B, Palmqvist P, Pérez-Claros JA. 2009. Ecomorphological correlates of craniodental variation in bears and paleobiological implications for extinct taxa: An approach based on geometric morphometrics. J Zool. 277:70–80.
- Figueirido B, Pérez-Claros JA, Hunt RM, Palmqvist P. 2011. Body mass estimation in amphicyonid carnivoran mammals: A multiple regression approach from the skull and skeleton. Acta Palaeontol Pol. 56:225-247.
- Figueirido B, Pérez-Ramos A, Schubert BW, Serrano F, Farrell AB, Pastor FJ, Romero A. 2017. Dental caries in the fossil record: a window to the evolution of dietary plasticity in an extinct bear. Sci Rep-Uk. 7:17813.

- Fox-Dobbs K, Leonard JA, Koch PL. 2008. Pleistocene megafauna from eastern Beringia: paleoecological and paleoenvironmental interpretations of stable carbon and nitrogen isotope and radiocarbon records. Palaeogeogr. Palaeocl. 261:30–46.
- Godfrey LR, Winchester JM, King SJ, Boyer DM, Jernvall J. 2012. Dental topography indicates ecological contraction of lemur communities. Am J Phys Anthropol. 148:215–227.
- Grandal-d'Anglade A, Pérez-Rama M, García-Vázquez A, González-Fortes GM. 2019. The cave bear's hibernation: reconstructing the physiology and behaviour of an extinct animal. Hist Biol. 31:429-441.
- Guthrie RD. 1988. Bone litter from an Alaskan Pleistocene carnivore den. Curr Res Pleistoc. 5:69–71.
- King SJ, Arrigo-Nelson SJ, Pochron ST, Semprebon GM, Godfrey LR, Wright PC, Jernvall J. 2005. Dental senescence in a long-lived primate links infant survival to rainfall. Proc Natl Acad Sci USA. 102:16579–16583.
- Kudej RK, Depre C. 2007. NO with no NOS in ischemic heart. Cardiovasc Res.74:1-3.
- Kupczik K, Dean MC. 2008. Comparative observations on the tooth root morphology of *Gigantopithecus blacki*. J Hum Evol. 54:196-204.
- Kupczik K, Stynder DD. 2012. Tooth root morphology as an indicator for dietary specialisation in carnivores (Mammalia: Carnivora). Biol J Linn Soc. 105:456–471.
- Kurtén B, Anderson E. 1980. Pleistocene Mammals of North America (Columbia University Press).
- Kurtén B. 1967. Pleistocene bears of North America. II: Genus Arctodus. short-faced bears. Acta Zool Fenn. 117:1-60.
- Lundberg JO. 2008. Nitric oxide and the paranasal sinuses. Anat Rec. 291:1479-1484.
- M'Kirera F, Ungar PS. 2003. Occlusal relief changes with molar wear in *Pan troglodytes troglodytes* and *Gorilla gorilla gorilla*. Am J Primatol. 60:31–41.
- Matheus PE. 1995. Diet and co-ecology of Pleistocene short-faced bears and brown bears in Eastern Beringia. Quarter Res. 44:447–453.

- McNab BK. 2008. An analysis of the factors that influence the level and scaling of mammalian BMR. Comp Biochem Physiol. 151:5–28.
- Münzel SC, Stiller M, Hofreiter M, Mittnik A, Conard NJ, Bocherens H. 2011. Pleistocene bears in the Swabian Jura (Germany): genetic replacement, ecological displacement, extinctions and survival. Quatern Int. 245:225-237.
- Münzel SC, Conard NJ. 2004. Cave bear hunting in the Hohle Fels, a cave site in the Ach Valley, Swabian Jura. Revue de Paléobiologie. 23:877-885.
- O'Hearn DJ, Giraud GD, Sippel JM, Edwards C, Chan B, Holden WE. 2007. Exhaled nasal nitric oxide output is reduced in humans at night during the sleep period. Resp Physiol Neurobi. 156:94-101.
- Pacher MA, Stuart J. 2009. Extinction chronology and palaeobiology of the cave bear (*Ursus spelaeus*). Boreas. 38:189–206.
- Peigné S, Merceron G. 2017. Palaeoecology of cave bears as evidenced by dental wear analysis: a review of methods and recent findings. Hist Biol. 31: 448-460.
- Peigné S, et al. 2009. Predormancy omnivory in European Cave Bears evidenced by dental microwear analysis of Ursus Spelaeus from Goyet. Belgium. P Natl Acad Sci USA. 106:15390-15393.
- Pérez-Ramos A, Kupczik K, Van Heteren AH, Rabeder G, Grandal-D'Anglade A, Pastor FJ, Figueirido B. 2019. A three-dimensional analysis of tooth-root morphology in living bears and implications for feeding behaviour in the extinct cave bear. Hist Biol. 31:461-473.
- Petruson K, Stalfors J, Jacobsson KE, Ny L, Petruson B. 2005. Nitric oxide production in the sphenoidal sinus by the inducible and constitutive isozymes of nitric oxide synthase. Rhinology. 43:18-23.
- Pineda-Munoz S, Lazagabaster IA, Alroy J, Evans AR. 2017. Inferring diet from dental morphology in terrestrial mammals. Methods Ecol Evol. 8:481-491.
- Pinto Llona AC, Andrews PJ, Etxebarría F. 2005. Taphonomy and Palaeoecology of Quaternary Bears from Cantabrian Spain (Grafinsa. Oviedo. Spain). Sci Annals Geol School AUTH. special vol. 103-108.

- Quilès J, Petrea C, Moldovan O, Zilhão J, Rodrigo R, Rougier H, Trinkaus E. 2006. Cave bears (*Ursus spelaeus*) from the Peştera cu Oase (Banat, Romania): Paleobiology and taphonomy. C R Palevol. 5:927-934.
- Rayfield EJ. 2007. Finite element analysis and understanding the biomechanics and evolution of living and fossil organisms. Annu Rev Earth Planet Sci. 35:541-576.
- Revsbech IG, Shen X, Chakravarti R, Jensen FB, Thiel B, Evans AL, Fago A. 2014. Hydrogen sulfide and nitric oxide metabolites in the blood of free-ranging brown bears and their potential roles in hibernation. Free Radical Bio Med. 73:349-357.
- Richards RL, Churcher CS, Turnbull WD. 1996. Distribution and size variation in North American short-faced bears, *Arctodus simus* in Palaeoecology and palaeoenvironments of late Cenozoic mammals: tributes to the career of C.S. (Rufus) Churcher (eds. Stewart, K. M. & Seymour, K. L.) (University of Toronto Press). pp 191–246
- Richards MP, Pacher M, Stiller M, Quilès J, Hofreiter M, Constantin S, Zilhão J, Trinkaus E. 2008. Isotopic evidence for omnivory among European cave bears: Late Pleistocene *Ursus spelaeus* from the Peçstera cu Oase. Romania. Proc Natl Acad Sci USA. 105:600–604.
- Robbins C, Lopez-Alfaro C, Rode KD, Tøien Ø, Nelson OL. 2012. Hibernation and seasonal fasting in bears: the energetic costs and consequences for polar bears. J Mammal. 93:1493-1503.
- Robu M, Wynn JG, Mirea IC, Petculescu A, Kenesz M, Puşcaş CM, Trinkaus E, Constantin S, O'Regan H. 2018. The diverse dietary profiles of MIS 3 cave bears from the Romanian Carpathians: insights from stable isotope (δ13C and δ15N) analysis. Palaeontology. 61:209–219.
- Schubert BW, Hulbert RC, MacFadden BJ, Searle M, Searle S. 2010. Giant short-faced bears (*Arctodus simus*) in Pleistocene Florida USA, a substantial range extension. J Paleo. 84:79–87.
- Sorkin B. 2006. Ecomorphology of the giant short-faced bears Agriotherium and Arctodus. Hist Biol. 18:1–20.

- Spencer MA. 2003. Tooth-root form and function in platyrrhine seed-eaters. Am J Phys Anthropol. 122:325-335.
- Stynder DD, Kupczik K. 2013. Tooth root morphology in the early Pliocene African bear *Agriotherium africanum* (Mammalia. Carnivora. Ursidae) and its implications for feeding ecology. J Mammal Evol. 20:227-237.
- Terlato G, Bocherens H, Romandini M, Nannini N, Hobson KA, Peresani M. 2018. Chronological and Isotopic data support a revision for the timing of cave bear extinction in Mediterranean Europe. Hist Biol. 31:474-484
- Ulhaas L, Kullmer O, Schrenk F, Henke W. 2004. A new 3-d approach to determine functional morphology of cercopithecoid molars. Ann Anat. 186:487-493.
- Ungar PS, Bunn JM. 2008. Primate dental topographic analysis and functional morphology. Technique and application in dental anthropology. 53-253.
- M'kirera F, Ungar PS. 2003. Occlusal relief changes with molar wear in *Pan troglodytes troglodytes* and *Gorilla gorilla gorilla*. Am J Primatol. 60:31-41.
- Van Heteren AH, Arlegi M, Santos E, Arsuaga JL, Gómez-Olivencia A. 2018. Cranial and mandibular morphology of Middle Pleistocene cave bears (*Ursus deningeri*): implications for diet and evolution. Hist Biol. 31:485-499.
- Voorhies MR, Corner RG. 1986. The giant bear Arctodus as a potential breaker and flaker of late Pleistocene megafaunal remains. Curr Res Pleistoc. 3:49–51.
- Wilson GP, Evans AR, Corfe IJ, Smits PD, Fortelius M, Jernvall J. 2012. Adaptive radiation of multituberculates before the extinction of dinosaurs. Nature. 483:457–460.
- Winchester JM, Boyer DM, St Clair EM, Gosselin-Ildari AD, Cooke SB, Ledogar JA. 2014. Dental topography of platyrrhines and prosimians: convergence and contrasts. Am J Phys Anthropol. 153:29–44.
- Winchester JM. 2016. MorphoTester: an open source application for morphological topographic analysis. PLoS ONE .11:e0147649.
- Yan CH, Hahn S, McMahon D, Bonislawski D, Kennedy DW, Adappa ND, Cohen NA. 2017. Nitric oxide production is stimulated by bitter taste receptors ubiquitously expressed in the sinonasal cavity. Am J Rhinol Allergy. 31:85-92.

- Yeakel JD, Guimarães PR, Bocherens H, Koch PL. 2013. The impact of climate change on the structure of Pleistocene food webs across the mammoth steppe. Proc R Soc B. 280:20130239.

5

Resumen

5. Resumen

5.1. Introducción

Durante los últimos años, las herramientas de análisis en tres dimensiones han abierto nuevos campos en diferentes disciplinas, especialmente en lo que se refiere a la ecomorfología y la evolución de vertebrados, lo cual ha conllevado importantes contribuciones en Paleobiología y en otras disciplinas. Estos nuevos avances han permitido desarrollar y abrir nuevas campos de investigación, ya sean a nivel histológico, macroestructural y anatómico o incluso biomecánico. Tales avances han propiciado una nueva concepción de las bases de datos, como son los repositorios digitales de modelos virtuales. Tales repositorios han favorecido el desarrollo de nuevas formas de conservación del material científico nunca antes vistas y han permitido la visualización de modelos craneales o elementos de la anatomía interna sin hacer uso de técnicas destructivas. En la actualidad, ya existen repositorios digitales que alojan modelos virtuales de libre acceso (p. ej., *Morphomuseum* o *Digimorph*), ofreciendo por tanto a la comunidad científica una nueva forma de investigar dicho material mediante técnicas no invasivas.

Para la recuperación digital de modelos virtuales se parte de técnicas que tienen que ver tanto con la captación tridimensional de las superficies objeto de análisis como con la digitalización de estructuras externas e internas mediante del uso de Tomografías Axiales Computarizadas (TACs). Para la generación de las imágenes de las estructuras internas y de los modelos virtuales hay que tener en cuenta diversos parámetros de adquisición, como la tensión eléctrica, la intensidad o la distancia entre cortes, entre otros (Zollikofer et al. 2005; Endo et al. 2009; Kak et al. 2002). Tras la adquisición, las imágenes se deben mejorar eliminando el ruido de fondo y los posibles artefactos generados durante el proceso de reconstrucción, todo ello mediante el uso algoritmos y filtros digitales. Con las imágenes finales se debe proceder a la segmentación o "umbralización" del histograma de la muestra (Pertusa 2010), siendo un proceso muy dependiente de las propiedades de los materiales como por ejemplo la densidad ósea o la mineralización. Posteriormente, se generan los modelos virtuales del objeto, los cuales pueden ser posteriormente estudiados mediante análisis de índole ecomorfológico o biomecánico. Además, tales móldelos posibilitan su reproducción física mediante el uso de las técnicas de impresión tridimensional, proceso conocido en la jerga especializada como "Rapid Prototyping", mejorando la comprensión anatómica y estructural al disponer de la réplica física de la pieza objeto de estudio. Por tanto, sin lugar a dudas, las nuevas herramientas de análisis en tres dimensiones marcan un antes y un después en el *modus operandi* de investigar y plantear nuevas hipótesis que someter a prueba.

En esta tesis doctoral se usan diferentes métodos de análisis tridimensional con un potencial único para descifrar aspectos ecomorfológicos y evolutivos en diferentes grupos de vertebrados. Tales métodos están basados en la captación tridimensional tanto de las superficies externas del objeto como de las estructuras externas e internas mediante del uso de Tomografías Axiales Computarizadas (TACs).

Específicamente, se investiga cómo tales técnicas permiten ir más allá del estado de la cuestión en la paleobiología de dos especies de úrsidos (Mammalia, Carnivora, Ursidae) emblemáticos de finales del Pleistoceno: el oso de las cavernas del continente europeo (*Ursus spelaeus* sensu lato) y el oso de cara corta del continente norteamericano (*Arctodus simus*). Tal y como se detalla en el siguiente apartado, la paleobiología de tales úrsidos es ciertamente controvertida en la literatura, siendo necesario, por tanto, la aplicación de nuevas técnicas analíticas que ofrezcan nuevas perspectivas para clarificar su paleobiología.

5.1.1. La paleobiología del oso de las cavernas (*Ursus spelaeus*) y el oso de cara corta norteamericano (*Arctodus simus*)

La paleobiología del oso de las cavernas ha sido un tema recurrente en la literatura. De hecho, ciertos aspectos de su paleobiología como por ejemplo de qué se alimentaba o el porqué de su extinción siguen siendo un reto para los especialistas. El oso de las cavernas habitaba los ecosistemas glaciales de Eurasia y sirvió como inspiración de un libro clásico escrito en 1976 por Björn Kurtén, titulado: "The cave bear story: the life and death of a vanished animal". Pese a que "The cave bear story" fue un compendio del conocimiento adquirido sobre la biología de los osos de las cavernas en aquel momento, cuatro décadas después, muchos aspectos de su paleoecología, extinción y evolución aún son temas controvertidos en la literatura. Por ejemplo, la dieta del oso de las cavernas representa un caso de especial desacuerdo, pues los diferentes estudios basados en el patrón de desgaste dental, en la biogeoquímica isotópica o en la morfometría del aparato craneodental dan resultados contradictorios sobre su dieta, abarcando hipótesis desde un régimen carnívoro o carroñero hasta exclusivamente herbívoro (p.ej., Pinto et al. 2005; Quilès 2006; Richards et al. 2008; Figueirido et al. 2009; Pacher y Stuart 2009; Peigné et al. 2009; Peigné y Merceron 2017; Robu et al. 2018).

Conocer el comportamiento trófico del oso de las cavernas no es baladí, pues dependiendo de su dieta se puede explicar de una manera u otra las causas potenciales de su extinción. Así, se han propuesto dos hipótesis principales para explicar la extinción de este plantígrado: (i) un declive impulsado por el ser humano, bien por la competencia por los recursos o por la caza directa (p. ej., Münzel et al. 2004, 2011); y (ii) una disminución cada vez mayor de los tamaños poblaciones como consecuencia del enfriamiento climático acontecido durante finales del Pleistoceno (Baca et al. 2016). Dicha disminución poblacional se explica porque el enfriamiento durante el comienzo del Último Máximo Glacial conllevaría una baja productividad primaria, lo cual, junto con una dieta restringida al consumo vegetal (Bocherens 2019; Terlatto et al. 2019) podría haber facilitado el declive del úrsido.

En esta tesis doctoral se aplican una serie de técnicas ecomorfológicas y biomecánicas, las cuales requieren modelos tridimensionales para su aplicación, con el objetivo de ofrecer nuevas evidencias sobre cual de las dos hipótesis planteadas en el párrafo anterior explican mejor la extinción de los osos de las cavernas. Para ello, en un primer lugar se investiga si oso de las cavernas fue realmente un herbívoro especializado haciendo uso de estas nuevas técnicas analíticas. Específicamente, se cuantifican las áreas relativas de las raíces de los dientes maxilares, desde el cuarto premolar superior hasta el segundo molar superior, pues estudios previos han demostrado que las mismas son indicadoras tanto la especialización trófica como la fuerza de mordida en mamíferos (v.g., Spencer 2003; Kupczik y Dean 2008) y especialmente en carnívoros (v.g., Kupczik y Stynder 2012; Stynder y Kupczik 2013). Además, para investigar la dieta del oso de las cavernas, también se lleva a cabo un análisis topográfico de las coronas de los dientes maxilares, de nuevo, desde el cuarto premolar superior hasta el segundo molar superior. El análisis topográfico de las coronas dentales cuantifica su forma y sus características topográficas a partir de modelos tridimensionales (M'Kirera y Ungar 2003; Evans et al. 2007; Bunn et al. 2011; Winchester et al. 2014; Winchester 2016), pues estudios previos han demostrado una correlación de ciertas variables topográficas dentales con el comportamiento trófico en muchos grupos de mamíferos, actuales y extintos (M'Kirera y

Ungar 2003; Dennis et al. 2004; Ulhaas et al. 2004; King et al. 2005; Evans et al. 2007; Boyer 2008; Ungar y Bunn 2008; Bunn y Ungar 2009; Evans y Jernvall 2009; Bunn et al. 2011; Godfrey et al. 2012; Wilson et al. 2012; Pineda et al. 2016; Evans y Pineda 2018). Sin embargo, hasta la fecha, no existen estudios en los que se cuantifique la topografía tridimensional de la corona dental en los osos de las cavernas en relación a su dieta.

Ambas técnicas anteriores –i.e., la cuantificación de las áreas de las raíces dentales y el análisis topográfico de las coronas dentales– se aplican con el objetivo de contestar si el oso de las cavernas podría haberse alimentado en su mayoría de recursos vegetales. Sin embargo, tales análisis no contestan a si, efectivamente, el oso de las cavernas podría haber tenido una dieta estrictamente herbívora y, por tanto, sin la capacidad de alimentarse de otro tipo de recursos en función de su disponibilidad. Para investigar la posible flexibilidad de dieta del oso de las cavernas, se realizan simulaciones biomecánicas en tres dimensiones de diferentes escenarios de mordida a partir de tomografías axiales computerizadas de diferentes cráneos de esta especie. El objetivo aquí es el de investigar si el cráneo de los osos de las cavernas estaba biomecánicamente restringido para alimentarse exclusivamente de recursos vegetales. Específicamente, se ha usado un enfoque basado en el análisis de elementos finitos. Dicho análisis es una técnica propia de ingeniería y ortopedia que cuantifica el estrés, la tensión y la deformación en una determinada estructura bajo distintos escenarios de cargas simuladas. Puesto que las estructuras de los organismos también obedecen a los principios físicos, durante la última década, el análisis de elementos finitos se viene utilizando tanto en Paleontología como en Zoología para abordar cuestiones sobre la morfología, la función y la evolución de los organismos, tanto actuales como extintos (Rayfield 2007). Sin embargo, dicho análisis no ha sido nunca aplicado para descifrar la posibles adaptaciones tróficas de los osos de las cavernas, aunque sí en otros úrsidos (Oldfield et al. 2012).

Otro aspecto de la paleobiología de los osos de las cavernas relativamente poco explorado es la fisiología de la hibernación y cómo la necesidad de sobrellevar inviernos más largos hibernando pudo influir en su paleobiología. Puesto que la hibernación está en gran medida controlada por varias enzimas segregadas por el epitelio de los senos paranasales que intervienen en la disminución de la tasa metabólica basal (Lundberg 2008; Petruson et al. 2005; Yan et al. 2017; Andersson et al. 2002), se investiga a partir de modelos tridimensionales de senos segmentados en úrsidos actuales y en osos de las cavernas, la posible función de los senos en la hibernación y sus posibles implicaciones en el comportamiento trófico de los mismos. En esta línea, también se desarrollan modelos teóricos para la estimación de las tasa metabólica basal en los osos de las cavernas usando ecuaciones alométricas publicadas por McNab (2008) para períodos de actividad y por Robbins et al. (2012) para períodos de hibernación, usando masas corporales estimadas en las distintas especies/subespecies de los osos de las cavernas (Figueirido et al. 2011)

Asimismo, en la tesis doctoral se presenta un nuevo método histomorfométrico de cuantificación de parámetros osteológicos del hueso esponjoso como la densidad de las conexiones entre las trabéculas, su forma (placa o varilla), grosor y espacio intra-trabecular, todo ello nos indica que los osos de las cavernas comparten la peculiaridad de tener un hueso trabecular muy poco denso. Aunque se necesita un estudio más pormenorizado sobre la posible etiología de esta anomalía ósea, esto podría indicar tasas metabólicas extremadamente bajas o, simplemente, deficiencias nutricionales durante momentos prolongados de inanición.

Por otra parte, la paleobiología del oso de cara corta también es controvertida. De hecho, la dieta de *A. simus* es un tema polémico, ya que diferentes investigadores han propuesto diferentes dietas, incluyendo la hipercarnívora basado en carne (Kurtén 1976; Kurtén y Anderson 1980; Yeakel et al. 2013; Fox-Dobbs et al. 2008; Richards et al. 1996) o en carroña (Matheus 1995; Voorhies y Corner 1986; Guthrie 1988; Schubert y Wallace 2009; Christiansen 1999), la omnívora (Sorkin 2006; Figueirido et al. 2009) o incluso la herbívora (Emslie y Czaplewski 1985). En este tesis doctoral se aplican métodos basados en morfometría, microscopía electrónica de barrido (SEM) y análisis de Tomografía Axial Computerizada para investigar la posible etiología de una serie de lesiones dentales *ante mortem* que presentaba la población de *A. simus* cuyos restos se han preservado en el yacimiento de Rancho La Brea (California, EE. UU.).

5.2. Objetivos

Aunque el objetivo último de la tesis doctoral es evaluar si las nuevas herramientas de análisis en tres dimensiones pueden ayudar a resolver aspectos controvertidos de la paleobiología de los dos úrsidos extintos anteriormente mencionados, a continuación se enumeran los objetivos específicos abordados durante el desarrollo de la tesis:

- Evaluar si el análisis de las raíces dentales de la dentición maxilar es un buen indicador del tipo de recursos consumidos en úrsidos actuales y, si es así, investigar la posible dieta de los osos de las cavernas con este nuevo tipo de análisis ecomorfológico.
- Explorar si la topografía de las coronas dentales se relaciona con la dieta en úrsidos, pues este grupo se caracteriza por poseer una alta variabilidad trófica pero una baja disparidad morfológica. Si es así, examinar el comportamiento trófico de los osos de las cavernas en

base a estos nuevos indicadores ecomorfológicos sobre el tipo de dieta.

- Investigar si las herramientas de simulación biomecánica en tres dimensiones, como es el método de Análisis de Elementos Finitos es una buena herramienta para ahondar sobre la versatilidad trófica en especies de úrsidos actuales y extintos. Mediante la consecución de este objetivo, también se somete a prueba la hipótesis de que los osos de las cavernas tuvieran una biomecánica craneal propia de organismos con una alimentación restringida a consumir alimentos exclusivamente de naturaleza vegetal.
- Demostrar cómo los análisis basados en Tomografía Computerizada son útiles para la caracterización morfológica de estructuras internas y, por ende, cómo las mismas pueden dar pistas, hasta ahora no reveladas, sobre la paleobiología de las especies actuales y extintas. Para ello, se procede a la cuantificación del tamaño y la forma de los senos paranasales de los osos de las cavernas e investiga su significado paleobiológico.
- Someter a prueba la hipótesis de que los osos de las cavernas podrían pasar largos periodos de hibernación (de más de seis meses) en relación a los largos inviernos de finales del Pleistoceno y cómo estos largos periodos de inactividad podría afectarles a su tasa metabólica basal y a su paleobiología.
- Investigar cómo los métodos basados en captación de la estructura superficial en tres dimensiones y de Tomografía Computerizada aportan evidencias significativas para clarificar la controvertida ecología trófica del oso de cara corta del Pleistoceno de Norteamérica.

- Indagar cómo el cambio climático afectó a la evolución de los osos de las cavernas y a otros úrsidos de la megafauna de finales del Pleistoceno pero de otro continente como es *A. simus*.

5.3. Principales resultados

En el **capítulo 3.1**, se explora el tamaño de las raíces de los dientes maxilares (cuarto premolar superior-segundo molar superior) a partir de tomografías computarizadas de osos actuales con el objetivo de hacer inferencias sobre la ecología trófica en el grupo de los osos de las cavernas (*Ursus spelaeus s.l.*). Tal grupo comprende las especies *Ursus ingressus* y *Ursus spelaeus*, y a la vez esta última, a las subespecies *U. spelaeus ladinicus*, *U. spelaeus eremus* y *U. spelaeus spelaeus*. Los resultados muestran que existe una relación entre las áreas de la superficie de la raíces de los dientes con el comportamiento trófico en las distintas especies de úrsidos actuales. Los distintos análisis realizados muestran que los osos de las cavernas experimentan de forma única entre las especies de úrsidos analizadas un aumento gradual en las áreas de los dientes maxilares, desde el cuarto premolar superior hasta el segundo molar superior, acercándose las áreas de las raíces de los molares posteriores del panda gigante (*Ailuropoda melanoleuca*) que se alimenta básicamente de bambú. Este es especialmente el caso de *U. spelaeus ladinicus* y de *U. spelaeus eremus*, siendo menos pronunciado en el caso de *U. ingressus* y *U. spelaeus spelaeus*. Aunque dicho patrón único de los osos de las cavernas fue probablemente heredado del úrsido *Ursus deningeri* del Pleistoceno medio (Van Heteren et al. 2019), tal evidencia podría indicar que los osos de las cavernas eran más herbívoros que el oso pardo actual (*U. arctos*). Sin embargo, existen diferencias en los patrones de distribución de las áreas de las raíces dentales entre las distintas especies/subespecies analizadas del complejo "espeloide", lo cual brinda la oportunidad de formular una hipótesis consistente sobre sus diferentes estrategias de alimentación.

Todos los osos de las cavernas con la excepción de *U. spelaeus spelaeus* ocupan una región del morfoespacio no explorada por ningún úrsido actual, lo que podría interpretarse como que *U. spelaeus eremus*, *U. spelaeus ladinicus* y *U. ingressus* estaban consumiendo algún tipo de recurso distinto al de cualquier otro úrsido actual. Por el contrario, dada la similitud entre *U. spelaeus spelaeus* y el oso negro americano (*Ursus americanus*), cabe la posibilidad que esta subespecie se alimentara de recursos tróficos similares, aunque esta última interpretación debe ser considerada con precaución. Asimismo, tales diferencias en los patrones de distribución de las áreas de las raíces dentales pueden ser interpretadas en función de sus hábitats de preferencia, pues mientras *U. spelaeus spelaeus* habitaba en áreas de entre 500-800m sobre el nivel del mar, *U. ingressus*, *U. spelaeus eremus* y *U. spelaeus ladinicus* habitaban zonas de la región alpina, llegando a alcanzar altitudes de hasta 2.800m sobre el nivel del mar en el caso de *U. spelaeus ladinicus*. Las diferencias entre los ecosistemas que habitaban los osos de las cavernas podría explicar las diferencias observadas en los patrones de distribución de las áreas de las raíces dentales y, por extensión, las diferencias en su comportamiento trófico. Así, se concluye que *U. spelaeus eremus*, *U. spelaeus ladinicus* y *U. ingressus* podrían estar adaptados a consumir algún tipo de recurso vegetal de altura de naturaleza dura y/o fibrosa, aunque el último probablemente no dependiera de alimentos tan duros y/o fibrosos, debido a su gran tamaño corporal. Estos resultados se han publicado como parte de un volumen especial sobre paleobiología de los osos de las cavernas en la revista *Historical Biology* (Pérez-Ramos et al. 2019).

En el **capítulo 3.2**, se explora cómo este patrón creciente del área de las raíces dentales, puesto de manifiesto en el capítulo anterior, se refleja en la topografía de sus coronas dentales. En este capítulo se obtienen tres variables de análisis topográfico dental: la curvatura topográfica (DNE), el relieve (RFI) y la complejidad (OPCR) de las superficies tridimensionales de la corona dental. Para explorar la relación de estas variables con el comportamiento trófico en úrsidos actuales, se investiga la señal filogenética, la asociación con la dieta y el efecto del tamaño en las tres variables estudiadas (DNE, OPCR y RFI).

Tal y como se esperaba, los resultados indican que las tres variables son relativamente independientes de la filogenia. Además, los resultados indicaron que si bien tanto la curvatura (DNE) como la complejidad (OPCR) de las coronas dentales son buenos indicadores de dieta en úrsidos actuales, el relieve (RFI) no presenta relación con la misma. En consecuencia, se utilizan tanto el DNE como el OPCR para hacer inferencias tróficas en los osos de las cavernas (*Ursus spelaeus s.l.*). Los resultados indican un gradiente tanto en DNE como en OPCR, desde especies que consumen recursos de naturaleza blanda [i.e., los consumidores de carne (*U. maritimus*) y/o insectos (*M. ursinus*) más los especialistas en alimentarse de recursos de tipo "soft-mast" (i.e., los folívoros-frugívoros (*U. americanus*, *T. ornatus*)] hasta el panda gigante, *A. melanoleuca* con una dieta durófaga basada en bambú. Aquellos úrsidos que se alimentan tanto de "soft-mast" como de "hard-mast" (*U. arctos* y *U. thibetanus*) toman valores de DNE y OPCR intermedios a los dos grupos anteriores. Por lo tanto, en úrsidos tanto el OPCR como el DNE reflejan la naturaleza de los recursos consumidos más que el tipo de alimento. Además, tanto el DNE como el OPCR están fuertemente influenciados por el tamaño y, por lo tanto, existen efectos alométricos importantes que parecen estar presentes en tales variables topográficas dentales. Curiosamente, los osos de las cavernas toman valores intermedios de DNE y OPCR a los de *A. melanoleuca* y el resto de úrsidos actuales.

Se propone, por tanto, que los osos de las cavernas han aumentado las áreas oclusales de la dentición posterior hasta prácticamente alcanzar los valores del panda gigante (como se demuestra a partir de las raíces en el capítulo anterior) y este aumento implica un aumento importante tanto del OPCR como del DNE, lo cual mejora la eficiencia para masticar alimentos altamente abrasivos y de baja calidad. Tal evidencia respalda la hipótesis propuesta en el capítulo anterior en la que se mostró que las subespecies *U. spelaeus eremus*, *U. spelaeus ladinicus* y *U. ingressus* representan una adaptación para alimentarse de algún tipo de recurso de naturaleza dura o resistente que estuvo presente en la región alpina. Además, los osos de las cavernas combinan valores de OPCR y DNE de una manera única en la muestra, lo cual viene a confirmar que probablemente este tipo de recurso del cual se alimentaban poseía unas propiedades mecánicas intermedias al bambú y al "hard-mast". Aunque ninguna especie de úrsido actual parece estar consumiendo este tipo de recurso, un argumento claro que respalda nuestra hipótesis es que los dos únicos especímenes de oso pardo que toman combinaciones de valores de DNE y OPCR similares a los osos de las cavernas pertenecen a la subespecie *U. arctos pruinosus*, tratándose de una subespecie que se alimenta a 4.500 m de altitud en la actual meseta del Tibet.

En el **capítulo 3.3**, se realizan simulaciones biomecánicas en 3D de diferentes escenarios de mordida a partir de tomografías axiales computerizadas de los cráneos de úrsidos actuales y de los osos de las cavernas. El objetivo será investigar si el cráneo de estos últimos estaba biomecánicamente restringido para alimentarse exclusivamente de recursos vegetales. Específicamente se ha usado un enfoque basado en el análisis de elementos finitos (FEA).

Las simulaciones biomecánicas en tres dimensiones de diferentes escenarios de masticación demuestran que los osos de las cavernas tenían un menor grado de eficiencia biomecánica que el oso pardo a la hora de masticar con las piezas más anteriores de la dentición. Esta restricción biomecánica se traduce en una menor flexibilidad trófica que la de los úrsidos omnívoros actuales. Por lo tanto, los resultados vienen a confirmar la hipótesis de que los osos de las cavernas eran exclusivamente herbívoros y carecían de la capacidad para alimentarse de cualquier tipo de recurso en aquellos periodos de enfriamiento climático severo que caracterizaron al último máximo glacial (Bocherens 2019; Terlato et al. 2019). Sorprendentemente, esta falta de flexibilidad trófica podría ser, al menos en parte, una consecuencia de tener unos senos paranasales expandidos en la región frontal que conforman el típico domo abovedado que caracteriza el linaje "espeloide". Este domo reduce significativamente la disipación del estrés al morder con la dentición anterior, restando estabilidad estructural al cráneo en todo momento y "obligando" a los osos de las cavernas a tener un cráneo biomecánicamente limitado a procesar alimentos con la dentición más posterior.

Por otra parte, se propone que la ventaja selectiva de tener unos senos extremadamente grandes en los osos de las cavernas probablemente estuviera relacionada con su necesidad de sobrellevar los largos inviernos que caracterizaron el Pleistoceno superior. Por tanto, la necesidad de tener grandes períodos de hibernación fue clave para aumentar el tamaño de los senos paranasales a lo largo de la historia evolutiva del linaje "espeloide". Sin embargo, al mismo tiempo, el desarrollo de estos senos comprometió la versatilidad trófica de los osos de las cavernas.

En el **capítulo 3.4**, se somete a prueba la nueva hipótesis formulada en el capítulo anterior, es decir, la de si los senos paranasales permitieron los largos períodos de hibernación propuestos para los osos de las cavernas. Para ello, se han calculado los volúmenes de los senos previamente segmentados en tres dimensiones y se han estimado las tasas metabólicas basales en los úrsidos actuales usando las ecuaciones alométricas de McNab (2008) para períodos de actividad y de Robbins et al. (2012) para períodos de hibernación. Además, a partir de las masas corporales obtenidas para todas las especies/subespecies del grupo de los osos de las cavernas se han estimado las tasas metabólicas basales para los mismos utilizando las ecuaciones alométricas anteriormente mencionadas.

La fisiología en los animales que hibernan está regulada principalmente por la activación de enzimas a través de vías de estrés. Entre estas enzimas, la óxido nítrico sintasa (NO) se activa cuando aumenta la concentración de CO2 en la sangre (hipercapnia) y los niveles de O2 disminuyen (hipoxia) al comienzo de la hibernación (p.ej., O'Hearn et al. 2007). La respuesta a estos estímulos es disminuir la temperatura corporal, la frecuencia cardíaca y la presión arterial (Kudej et al. 2007). Estudios recientes vinculan las vías de NO y sulfuro de hidrógeno (HS) con el control de la hibernación en los osos ya que estos metabolitos (NO y HS) están relacionados con la inducción de varias respuestas a estímulos de estrés biológico (Revbesch et al. 2014). Curiosamente, la producción de NO y HS está segregada por el epitelio de los senos esfenoideos (p.ej., Lundberg 2008; Petruson et al. 2005; Yan et al. 2017) y todos los senos paranasales funcionan como reservorio de NO (Andersson et al. 2002). En consecuencia, se propone que aquellas especies con senos paranasales más desarrollados son especies hibernantes debido a su papel en la disminución de la tasa metabólica basal, disminución que por otro lado es necesaria para sobrellevar los periodos de hibernación. Para investigar esta hipótesis, se realiza un análisis de regresión bivariante del volumen de los senos en función de las tasas metabólicas basales en úrsidos actuales. Los resultados confirman una relación negativa entre el tamaño de los senos y la tasa metabólica basal, una vez se eliminan los efectos alométricos de ambas variables. Además, aquellas especies con senos paranasales más grandes y tasas metabólicas más bajas son las especies que realizan una verdadera hibernación.

Tales hallazgos plantean otra pregunta crucial para comprender la paleobiología de los osos de las cavernas: ¿*Permitieron estas bajas tasas metabólicas de los osos de las cavernas extender sus períodos de hibernación lo suficiente como para superar los inviernos más largos y fríos del Pleistoceno tardío*? Para responder a esta pregunta, se calculó la ingesta media anual de los osos de las cavernas, utilizando las tasas metabólicas basales anuales estimadas. Paralelamente, se calcularon los requisitos energéticos de los osos de las cavernas utilizando la ecuación de Farlow (1976) y utilizando al oso pardo como modelo. Los resultados revelan que un período de 8 meses de hibernación es energéticamente posible de acuerdo con los requisitos energéticos inferidos.

Además, también se desarrolla un nuevo método histomorfométrico a partir de parámetros osteológicos del hueso esponjoso (es decir, la densidad de las conexiones entre las trabéculas) y se deduce que los osos de las cavernas comparten le peculiaridad de tener un hueso trabecular muy poco denso. Aunque se necesita un estudio más pormenorizado sobre la posible etiología de esta anomalía ósea, esto podría relacionarse con tener tasas metabólicas mucho más bajas, en relación a su masa corporal, que las de los úrsidos actuales, lo cual podría estar relacionado, al menos en parte, por la presencia de unos senos paranasales altamente desarrollados. Sin embargo, no se puede descartar la posibilidad de que tal anomalía ósea presente en los osos de las cavernas esté relacionada con momentos prolongados de inanición.

En el **capítulo 3.5**, se presenta la primera evidencia patológica en dientes (i.e., cavidades *ante mortem*) de *A. simus* preservados en Rancho La Brea (California, EE. UU.) y se compara con un base de datos amplia de especies actuales de diferentes poblaciones afectadas con patologías dentales similares. Para determinar la etiología de las lesiones, se han desarrollado nuevos enfoques macroscópicos y microscópicos, como la morfometría en tres dimensiones de las cavidades a partir de un contra-molde virtual, microscopía electrónica de barrido (SEM) y análisis de Tomografía Axial Computerizada.

El oso de cara corta es una especie icónica del continente norteamericano cuya dieta ha sido un tema controvertido en la literatura. De hecho diferentes investigadores han propuesto diferentes dietas, incluyendo la hipercarnívora basada en carne (Kurtén 1967; Kurtén y Anderson 1980; Yeakel et al. 2013; Fox-Dobbs et al. 2008; Richards et al. 1996) o en carroña (Matheus 1995; Voorhies y Corner 1986; Guthrie 1988; Schubert y Wallace 2009; Christiansen 1999), la omnívora (Sorkin 2006; Figueirido et al. 2009) o incluso la herbívora (Emslie y Czaplewski 1985). Los resultados obtenidos confirman que, a diferencia de otros especímenes del norte de Alaska y Yukón, las caries dentales eran comunes en la población de *A. simus* de Rancho La Brea, lo cual demuestra diferencias de alimentación entre ambas poblaciones. De hecho, mientras que la población del norte se adaptó localmente a una dieta altamente carnívora (Bocherens et al. 1995; Matheus et al. 1995), la población de *A. simus* de RLB era más omnívora. Según estos resultados, se plantea la hipótesis de que ambas poblaciones tendrían distintos competidores, lo que podría explicar la variabilidad trófica encontrada en esta especie icónica de la megafauna norteamericana.

Asimismo, se propone que el aumento de la extensión de los casquetes polares Laurentino y Cordillerano en relación al enfriamiento climático acontecido durante el Wisconsiniense, podría haber supuesto una barrera geográfica que aislara ambas poblaciones de *Arctodus.* Además, dicho aislamiento podría en última instancia haber facilitado que ambas poblaciones se adaptaran a una alimentación totalmente diferente. Los hallazgos sugieren que tanto el cambio climático como la competencia entre especies son mecanismos importantes que motivan los cambios en la evolución de los linajes a una escala global. Los resultados de este estudio se han publicado en la revista *Scientific reports* (Figueirido and Pérez-Ramos et al. 2017).

5.4. Síntesis y conclusiones

A través de esta sección, se explican los principales hallazgos obtenidos en la tesis doctoral con el objetivo de ofrecer una visión más amplia de cómo los estudios aquí recogidos contribuyen al estado de la cuestión de la paleobiología de los dos úrsidos icónicos de finales del Pleistoceno europeo y norteamericano analizados, el oso de las cavernas europeo y el oso de cara corta norteamericano. Tales estudios han sido realizados mediante la aplicación de metodologías de última generación que nunca habían sido aplicados a la problemática en cuestión.

Con respecto al oso de las cavernas, tales metodologías se aplicaron para responder una pregunta fundamental de su paleobiología que continua siendo objeto de discusión: *¿Por qué se extinguió el oso de las cavernas?*

Tal y como se ha comentado en la introducción, la respuesta a esta pregunta exige técnicas analíticas innovadoras que ofrezcan nuevas perspectivas para descifrar el comportamiento de alimentación de los osos de las cavernas y por ende de su extinción. Así, en los **capítulos 4.1** y **4.2** se utilizan nuevas técnicas ecomorfológicas en tres dimensiones para investigar el comportamiento de alimentación del oso de las cavernas. Los resultados de ambos capítulos demuestran que los osos de las cavernas eran más herbívoros que el oso pardo actual (*Ursus arctos*) y se propone que probablemente se alimentaran de algún tipo de recurso altamente fibroso y de baja energía que estuviera presente en las regiones alpinas en las que habitaron. Quizá una notable excepción podría ser la subespecie *U. sp. spelaeus*, pues no habitaba biomas Alpinos.

Ahora bien, la hipótesis 'climática' explica el declive de los osos de las cavernas no únicamente por ser herbívoros, sino también por su falta de capacidad de alimentarse de cualquier tipo de recurso en función de su disponibilidad, sobre todo en los momentos más infortunados de enfriamiento climático con una baja productividad primaria. De hecho, distintos estudios biogeoquímicos demuestran que los osos de las cavernas no cambiaron su dieta durante gran parte de su existencia, desde ≈100,000 a ≈20,000 años (Bocherens 2019; Terlatto et al. 2019). En consecuencia, los resultados obtenidos en el **Capítulo 4.3** sugieren que los osos de las cavernas tenían una alimentación restringida al consumo de material vegetal. Además, se obtiene que esta falta de flexibilidad en la dieta sea una consecuencia del desarrollo exagerado de los senos paranasales. Puesto que en mamíferos actuales los senos están involucrados en la disminución de la tasa metabólica basal, se plantea la hipótesis de que este desarrollo de lo senos en los osos de las cavernas pudiera deberse a sus largos períodos de hibernación necesarios para sobrellevar los inviernos más largos y más fríos de finales del Pleistoceno. Se concluye que dicho enfriamiento climático fue, probablemente, el agente selectivo para aumentar el tamaño de los senos a lo largo de la historia evolutiva del linaje. Por tanto, el estudio realizado en el **capítulo 4.3** propone que dichos senos paranasales tan desarrollados en los osos de las cavernas y que conforman el típico domo frontal que caracteriza al linaje "espeloide" fueron necesarios para sobrellevar los largos períodos de hibernación por su función a la hora de disminuir la tasa metabólica basal. Sin embargo, dichos senos a su vez conllevaron una restricción biomecánica craneal que impidió a los osos de las cavernas alimentarse de cualquier tipo de recurso en función de su disponibilidad, siendo por tanto estos úrsidos, unos herbívoros obligados por la necesidad de poseer largos periodos de hibernación.

El estudio realizado en el **capítulo 4.3** se basa en dos supuestos bien establecidos en la literatura: (i) que el tamaño de los senos se relaciona con la tasa metabólica basal en úrsidos; y (ii) que los osos cavernarios tuvieron períodos de hibernación más largos que los úrsidos actuales. Por tanto, en el **Capítulo 4.4**, se explora si los senos paranasales permitieron largos períodos de hibernación a los osos de las cavernas mediante la disminución de la tasa metabólica basal en úrsidos actuales y extintos. Los resultados obtenidos indican que el tamaño de los senos se relaciona con la tasa metabólica basal en úrsidos y, por lo tanto, se confirma la hipótesis propuesta en el capítulo 4.3: las especies de úrsidos con los senos más grandes son los úrsidos con tasas metabólicas basales más bajas, y además, son los úrsidos que hibernan. Por lo tanto, se concluye que los senos más grandes de los osos de las cavernas deberían estar relacionados con la disminución de su metabolismo y, probablemente, por tener largos períodos de hibernación. Además, se realizó un análisis histomorfométrico del tejido óseo esponjoso, cuantificando tanto la conectividad entre las trabéculas como su densidad y se observa que los osos de las cavernas presentaban una anomalía en su tejido óseo, pues éste es significativamente menos denso que el de los úrsidos actuales. Aunque se necesitan nuevos análisis, este resultado podría apuntar a que los osos de las cavernas tenían tasas metabólicas bastante más bajas, en relación a su masa corporal, que las estimadas a partir de ecuaciones alométricas. Sin embargo, por el momento tampoco se pueden descartar otro tipo de causas que expliquen esta baja densidad ósea como son los largos periodos de inanición.

Del mismo modo, la literatura asevera que los osos de las cavernas tendrían períodos de hibernación más largos que los úrsidos actuales (v.g., Kurtén 1976; Grandal-d'Anglade 2019). Sin embargo, hasta la fecha, no existen estudios que demuestren si, efectivamente, los osos de las cavernas podrían soportar períodos de hibernación más largos que los úrsidos actuales. Para ello, se aplican una serie de ecuaciones alométricas previamente publicadas y los resultados demuestran que los osos de las cavernas podrían estar hasta ocho meses hibernando.

Por lo tanto, las conclusiones principales de los **capítulos 4.1**-**4.4**, es que los osos de las cavernas se alimentaron de un recurso altamente fibroso y de baja energía que estaba presente en el bioma de altura típico de la región alpina en el que habitaban, y además, carecían de la flexibilidad necesaria para cambiar su dieta hacia una más omnívora durante periodos de enfriamiento con baja productividad primaria. Esta falta de flexibilidad se debe (al menos en parte) a tener senos paranasales muy desarrollados, necesarios para disminuir sus tasas metabólicas basales con el objetivo de tener periodos de hibernación de hasta ocho meses. Este periodo de tiempo sería necesario para sobrellevar los inviernos más largos y fríos que caracterizaban al Pleistoceno tardío. Sin embargo, tal restricción biomecánica impuesta por la necesidad de tener largos períodos de hibernación fue probable un factor crítico en la disminución y extinción última del oso de las cavernas. En consecuencia, los cambios climáticos de finales del Pleistoceno podrían haber influido directamente en la capacidad de algunos miembros de la megafauna a la hora de obtener los nutrientes adecuados y sobrevivir con éxito durante las condiciones ecológicas extremas de los meses más fríos. Tales hallazgos plantean otra pregunta paleobiológica crucial sobre la evolución de la megafauna del Pleistoceno: *¿Cómo afectó el enfriamiento* *climático a otras especies de la megafauna?* Para responder a esta pregunta, en el capítulo 4.5, se investiga la dieta de una especie de oso icónico del continente norteamericano: el oso de cara corta (*A. simus*). Este capítulo se centra en investigar si una serie de patologías de la dentición presentes en los dientes conservados en el yacimiento clásico de Rancho La Brea (California, EE. UU.) de finales del Pleistoceno obedecen a un proceso de caries. Los resultados confirman preferencias de alimentación variables entre diferentes poblaciones de *A. simus* de América del Norte como consecuencia del enfriamiento climático y la competencia de especies.

A continuación se detallan las conclusiones más importantes alcanzadas en esta tesis doctoral son:

- Las áreas de las raíces de los dientes maxilares se relacionan con el comportamiento de alimentación en los úrsidos actuales. Los osos de las cavernas siguen un aumento gradual único en las áreas de las raíces dentales desde el cuarto premolar superior hasta el segundo molar superior, acercándose a las áreas de las raíces dentales de los molares más posteriores del panda gigante, *A. melanoleuca*. Este resultado sugiere que los osos de las cavernas eran más herbívoros que el oso pardo actual *U. arctos*. Además, se revelan diferencias en el patrón de las áreas de las raíces dentales maxilares entre los osos de las cavernas. Esto podría relacionarse con diferentes estrategias de alimentación, que a su vez, podrían explicarse por los diferentes ecosistemas que habitaron y los recursos en ellos disponibles.
- Existe un gradiente claro en las variables DNE y OPCR obtenidas del análisis topográfico de las coronas dentales en úrsidos actuales, desde los úrsidos que consumen materiales de naturaleza blanda hasta el panda gigante que se alimenta de un material extremadamente duro

como es el bambú. Los úrsidos que consumen tanto "soft-mast" como "hard-mast" poseen valores intermedios de DNE y OPCR a los de los grupos anteriores. Por lo tanto, las variables DNE y OPCR parecen ser buenos indicadores ecomorfológicos en úrsidos de la naturaleza de los alimentos consumidos. Los osos de las cavernas toman valores intermedios de DNE y OPCR a los de *A. melanoleuca* y el resto de los osos actuales.

- Existen efectos alométricos importantes tanto en el DNE como en el OPCR. Los osos de las cavernas aumentan las áreas oclusales de su dentición más posterior (en comparación a las del oso pardo) hasta casi alcanzar los valores del panda gigante. Este aumento implica un aumento sustancial en los valores de OPCR y DNE, lo que conlleva una mejora en la eficiencia para masticar alimentos altamente abrasivos y de baja calidad. Los osos de las cavernas combinan los valores de OPCR y DNE de una manera única entre los úrsidos analizados, lo que probablemente se relaciona con la alimentación de un recurso presente en el bioma de altura que caracteriza a las regiones alpinas que habitaron.
- Las simulaciones biomecánicas en 3D de diferentes escenarios de masticación demuestran que el análisis de elementos finitos es un buen indicador biomecánico para determinar las adaptaciones tróficas en úrsidos. Los osos de las cavernas carecen de la flexibilidad trófica presente en los *U. arctos* más omnívoros y, por lo tanto, eran completamente herbívoros sin la flexibilidad de alimentarse de cualquier tipo de recurso en función de su disponibilidad durante los períodos de enfriamiento climático severo.
- Dicha falta de flexibilidad en la dieta es una consecuencia de tener senos paranasales expandidos, los cuales conforman el típico domo frontal abovedado que caracteriza el linaje "espeloide".

- Los senos paranasales permitieron a los osos de las cavernas pasar períodos de hibernación de hasta ocho meses mediante el control de varias enzimas segregadas en los senos esfenoideos para disminuir esencialmente su tasa metabólica basal, las cuales eran potencialmente más bajas que las de los úrsidos actuales.
- La ventaja selectiva de tener senos extremadamente desarrollados en los osos de las cavernas probablemente se relacionó con su necesidad de superar los largos inviernos en hibernación del último glacial.
- Un compromiso entre hibernación y flexibilidad trófica muestra que el cambio climático podría haber influido directamente en la capacidad de algunos miembros de la megafauna del Pleistoceno para sobrevivir con éxito durante condiciones ecológicas extremas.
- La evolución de otros miembros pertenecientes al nicho de los grandes carnívoros de la megafauna del Pleistoceno, como es el oso de cara corta de América del Norte (*A. simus*), también se vio afectada por el cambio climático y la competencia con otras especies contemporáneas, demostrando que ambos factores son importantes para determinar la evolución de los linajes a escala global.

5.4. Referencias

- Andersson JA, Cervin A, Lindberg S, Uddman R, Cardell LO. 2002. The paranasal sinuses as reservoirs for nitric oxide. Acta oto-laryngologica. 122(8): 861-865.
- Baca M, Popović D, Stefaniak K, Marciszak A, Urbanowski M, Nadachowski A, Mackiewicz P. 2016. Retreat and extinction of the Late Pleistocene cave bear (*Ursus spelaeus* sensu lato). Sci Nat. 103:92.
- Bocherens H. 2019. Isotopic insights on cave bear palaeodiet. Hist Biol. 31:410-421.

- Boyer DM. 2008. Relief index of second mandibular molars is a correlate of diet among prosimian primates and other euarchontan mammals. J Human Evol. 55: 1118–1137.
- Bunn JM, Ungar PS. 2009. Dental topography and diets of four old world monkey species. Ame J Primatol: Official Journal of the American Society of Primatologists 71:466-477.
- Bunn JM, Boyer DM, Lipman Y, Clair EM, Jernvall J, Daubechies I. 2011. Comparing Dirichlet normal surface energy of tooth crowns, a new technique of molar shape quantification for dietary inference, with previous methods in isolation and in combination. Am J Phys Anthropol. 145:247–261.
- Christiansen P. 1999. What size were *Arctodus simus* and *Ursus spelaeus* (Carnivora: Ursidae)?. In Annales Zoologici Fennici (pp. 93-102). Finnish Zoological and Botanical Publishing Board.
- Dennis JC, Ungar PS, Teaford MF, Glander KE. 2004. Dental topography and molar wear in *Alouatta palliata* from Costa Rica. Am J Phys Anthropol. 125: 152–161.
- Emslie SD, Czaplewski NJ. 1985. A new record of the giant short-faced bear, *Arctodus simus*, from western North America with reevaluation of its palaeobiology. Contributions in Science. 371:1–12.
- Endo H, Frey R. 2009. Anatomical imaging: towards a new morphology. Springer Science & Business Media.
- Evans AR, Wilson GP, Fortelius M, Jernvall J. 2007. High-level similarity of dentitions in carnivorans and rodents. Nature. 445: 78–81.
- Evans AR, Jernvall J. 2009. Patterns and constraints in carnivoran and rodent dental complexity and tooth size. J Vertebr Paleontol. 29:24A.
- Evans AR, Pineda-Munoz S. 2018. Inferring Mammal Dietary Ecology from Dental Morphology. In: Croft D., D. Su, S. Simpson (eds). Methods in Paleoecology. Vertebrate Paleobiology and Paleoanthropology. Springer, Cham.
- Figueirido B, Palmqvist P, Pérez-Claros JA. 2009. Ecomorphological correlates of craniodental variation in bears and paleobiological implications for extinct taxa: An approach based on geometric morphometrics. J Zool. 277:70–80.

- Fox-Dobbs K, Leonard JA, Koch PL. 2008. Pleistocene megafauna from eastern Beringia: Paleoecological and paleoenvironmental interpretations of stable carbon and nitrogen isotope and radiocarbon records. Palaeogeography, Palaeoclimatology, Palaeoecology. 261(1-2): 30-46.
- Godfrey LR, Winchester JM, King SJ, Boyer DM, Jernvall J. 2012. Dental topography indicates ecological contraction of lemur communities. Am J Phys Anthropol. 148:215–227.
- Grandal-d'Anglade A, Pérez-Rama M, García-Vázquez A, González-Fortes GM. 2019. The cave bear's hibernation: reconstructing the physiology and behaviour of an extinct animal. Hist Biol. 31(4): 429-441.
- Guthrie RD. 1988. Bone litter from an Alaskan Pleistocene carnivore den. Current Research in the Pleistocene. 5:69-71.
- Kak AC, Slaney M, Wang G. 2002. Principles of computerized tomographic imaging. Med Phys. 29(1): 107-107.
- King SJ, Arrigo-Nelson SJ, Pochron ST, Semprebon GM, Godfrey LR, Wright PC, Jernvall J. 2005. Dental senescence in a long-lived primate links infant survival to rainfall. Proc Natl Acad Sci USA. 102:16579–16583.
- Kudej RK, and Depre C. 2007. NO with no NOS in ischemic heart, Cardiovascular Research, Volume 74, Issue 1, April, Pages 1–3.
- Kupczik K, Dean MC. 2008. Comparative observations on the tooth root morphology of *Gigantopithecus blacki*. J Hum Evol. 54(2): 196-204.
- Kupczik K, Stynder DD. 2012. Tooth root morphology as an indicator for dietary specialisation in carnivores (Mammalia: Carnivora). Biol J Linn Soc. 105(2): 456–471.
- Kurtén B, Anderson E. 1980. Pleistocene mammals of North America. Columbia University Press.
- Lundberg JO, Farkas-Szallasi T, Weitzberg E, Rinder J, Lidholm J, Änggåar A, Alving K. 1995. High nitric oxide production in human paranasal sinuses. Nat Med. 1(4): 370.

- Lundberg JO. 2008. Nitric oxide and the paranasal sinuses. The Anatomical Record: Advances in Integrative Anatomy and Evolutionary Biology: Anat Rec. 291(11): 1479-1484.
- Matheus PE. 1995. Diet and co-ecology of Pleistocene short-faced bears and brown bears in eastern Beringia. Quaternary Res. 44(3): 447-453.
- McNab BK. 2008. An analysis of the factors that influence the level and scaling of mammalian BMR. Comparative Biochemistry and Physiology Part A: Molecular & Integrative Physiology. 151(1): 5-28.
- M'Kirera F, Ungar PS. 2003. Occlusal relief changes with molar wear in *Pan troglodytes troglodytes* and *Gorilla gorilla gorilla*. Am J Primatol. 60(2): 31–41.
- Münzel SC, Conard NJ. 2004. Cave bear hunting in the Hohle Fels, a cave site in the Ach Valley, Swabian Jura. Revue de Paléobiologie 23: 877-885.
- Münzel SC, Stiller M, Hofreiter M, Mittnik A, Conard NJ, Bocherens H. 2011. Pleistocene bears in the Swabian Jura (Germany): genetic replacement, ecological displacement, extinctions and survival. Quatern Int. 245: 225-237.
- O'Hearn DJ, Giraud GD, Sippel JM, Edwards C, Chan B, Holden WE. 2007. Exhaled nasal nitric oxide output is reduced in humans at night during the sleep period. Resp Physiol Neurobi. 156(1): 94-101.
- Oldfield CC, McHenry CR, Clausen PD, Chamoli U, Parr WCH, Stynder DD, Wroe S. 2012. Finite element analysis of ursid cranial mechanics and the prediction of feeding behaviour in the extinct giant *Agriotherium africanum.* J Zool. 286(2): 171-171.
- Pacher M, Stuart AJ. 2009. Extinction chronology and palaeobiology of the cave bear (*Ursus spelaeus*) Boreas. 38: 189–206.
- Peigné S, et al. 2009. Predormancy omnivory in European Cave Bears evidenced by dental microwear analysis of *Ursus Spelaeus* from Goyet. Belgium. P Natl Acad Sci USA. 106:15390-15393.
- Peigné S, Merceron G. 2017. Palaeoecology of cave bears as evidenced by dental wear analysis: a review of methods and recent findings, Hist Biol. 1-13.
- Pertusa JF. 2010. Técnicas de análisis de imagen (Universitat de València).

- Petruson K, Stalfors J, Jacobsson KE, Ny L, Petruson B. 2005. Nitric oxide production in the sphenoidal sinus by the inducible and constitutive isozymes of nitric oxide synthase. Rhinology. 43(1): 18-23.
- Pineda-Munoz S, Lazagabaster IA, Alroy J, Evans AR. 2017. Inferring diet from dental morphology in terrestrial mammals. Methods Ecol Evol. 8(4):481-491.
- Pinto Llona AC, Andrews PJ, Etxebarría F.2005. Taphonomy and Palaeoecology of Quaternary Bears from Cantabrian Spain (Grafinsa. Oviedo. Spain). Sci. Annals. Geol. School. AUTH. special vol. 103-108.
- Quilès J, et al. 2006. Cave bears (*Ursus spelaeus*) from the Peçstera cu Oase (Banat. Romania): Paleobiology and taphonomy. C R Palevol 5:927–934.
- Rayfield EJ. 2007. Finite element analysis and understanding the biomechanics and evolution of living and fossil organisms. Annu Rev Earth Planet Sci. 35:541-576.
- Revsbech IG, Shen X, Chakravarti R, Jensen FB, Thiel B, Evans AL, Fago A. 2014. Hydrogen sulfide and nitric oxide metabolites in the blood of free-ranging brown bears and their potential roles in hibernation. Free Radical Bio Med. 73: 349-357.
- Richards MP, et al. 2008. Isotopic evidence for omnivory among European cave bears: Late Pleistocene Ursus spelaeus from the Peçstera cu Oase. Romania. Proc Natl Acad Sci USA. 105:600–604.
- Robbins CT, Lopez-Alfaro C, Rode KD, Tøien Ø, & Nelson OL. 2012. Hibernation and seasonal fasting in bears: the energetic costs and consequences for polar bears. J Mammal. 93(6): 1493-1503.
- Robu M, Wynn JG, Mirea IC, Petculescu A, Kenesz M, Puşcaş CM, Vlaicu M, Trinkaus E, Constantin S, O'Regan H. 2018. The diverse dietary profiles of MIS 3 cave bears from the Romanian Carpathians: insights from stable isotope (δ13C and δ15N) analysis. Palaeontology.61: 209-219.
- Schubert BW, Wallace SC. 2009. Late Pleistocene giant short-faced bears, mammoths, and large carcass scavenging in the Saltville Valley of Virginia, USA. Boreas. 38(3):482-492.
- Sorkin B. 2006. Ecomorphology of the giant short-faced bears Agriotherium and Arctodus. Hist Biol. 18(1):1-20.

- Spencer MA. 2003. Tooth-root form and function in platyrrhine seed-eaters. Am J Phys Anthropol.122(4): 325-335.
- Stynder DD, Kupczik K. 2013. Tooth root morphology in the early Pliocene African bear *Agriotherium africanum* (Mammalia. Carnivora. Ursidae) and its implications for feeding ecology. J Mammal Evol. 20(3):227-237.
- Terlato G, Bocherens H, Romandini M, Nannini N, Hobson KA, Peresani M. 2019. Chronological and Isotopic data support a revision for the timing of cave bear extinction in Mediterranean Europe. Hist Biol. 31:474-484.
- Ulhaas L, Kullmer O, Schrenk F, Henke W. 2004. A new 3-d approach to determine functional morphology of cercopithecoid molars. Ann Anat. 186:487-493.
- Ungar PS, Bunn JM. 2008. Primate dental topographic analysis and functional morphology. Technique and application in dental anthropology. 53-253.
- van Heteren AH, Arlegi M, Santos E, Arsuaga JL,Gómez-Olivencia A. 2019. Cranial and mandibular morphology of Middle Pleistocene cave bears (*Ursus deningeri*): implications for diet and evolution. Histo Biol. 31(4):485-499.
- Voorhies MR, Corner RG. 1986. The giant bear Arctodus as a potential breaker and flaker of late Pleistocene megafaunal remains. Current Research in the Pleistocene. 3:49-51.
- Wilson GP, Evans AR, Corfe IJ, Smits PD, Fortelius M, Jernvall J. 2012. Adaptive radiation of multituberculates before the extinction of dinosaurs. Nature. 483: 457–460.
- Winchester JM, Boyer DM, St Clair EM, Gosselin-Ildari AD, Cooke SB, Ledogar JA. 2014. Dental topography of platyrrhines and prosimians: convergence and contrasts. Am J Phys Anthropol. 153:29–44.
- Winchester JM. 2016. MorphoTester: an open source application for morphological topographic analysis. PLoS ONE. 11:e0147649.
- Zollikofer CP, and de León, MSP. (2005). Virtual reconstruction: a primer in computer-assisted paleontology and biomedicine. Wiley-Interscience.

- Yan CH, Hahn S, McMahon D, Bonislawski D, Kennedy DW, Adappa ND, Cohen NA. 2017. Nitric oxide production is stimulated by bitter taste receptors ubiquitously expressed in the sinonasal cavity. Am J Rhinol Allergy. 31(2):85-92.
- Yeakel JD, Guimarães Jr PR, Bocherens H, Koch PL. 2013. The impact of climate change on the structure of Pleistocene food webs across the mammoth steppe. Proceedings of the Royal Society B: Biological Sciences. 280(1762): 20130239.

6

Appendix

Table 1. Specimens used in **chapter 3.2**.

Mus. nº	*Species*
89029	*A. melanoleuca*
89030	*A. melanoleuca*
110451	*A. melanoleuca*
110452	*A. melanoleuca*
147745	*A. melanoleuca*
89028	*A. melanoleuca*
89854	*H. malayanus*
17531	*H. malayanus*
17532	*H. malayanus*
2439	*H. malayanus*
17245	*H. malayanus*
28472	*H. malayanus*
A5351	*H. malayanus*
60772	*H. malayanus*
28254	*H. malayanus*
103987	*H. malayanus*
19155	*H. malayanus*
46074	*M. ursinus*
56748	*M. ursinus*
90388	*M. ursinus*
44143	*M. ursinus*
35898	*M. ursinus*
99308	*M. ursinus*
16186	*M. ursinus*
217682	*M. ursinus*
6121	*T. ornatus*
1661	*T. ornatus*
99308	*T. ornatus*
217682	*T. ornatus*
149302	*T. ornatus*

174256	*T. ornatus*
16186	*T. ornatus*
2245	*U. americanus*
3561	*U. americanus*
6704	*U. americanus*
16705	*U. americanus*
16706	*U. americanus*
16707	*U. americanus*
41327	*U. americanus*
1280	*U. arctos arctos*
3034	*U. arctos arctos*
3632	*U. arctos arctos*
212872	*U. arctos arctos*
21809	*U. arctos gyas*
194567	*U. arctos horribilis*
1951107	*U. arctos horribilis*
19765	*U. arctos middendorffi*
113701	*U. arctos pruinosus*
165798	*U. arctos sitkensis*
165798	*U. arctos sitkensis*
163825	*U. arctos sitkensis*
19259	*U. maritimus*
15709	*U. maritimus*
14883	*U. maritimus*
15687	*U. maritimus*
1893341	*U. maritimus*
11051	*U. maritimus*
15686	*U. maritimus*
42080	*U. maritimus*
14888	*U. maritimus*
WGTDe	*U. maritimus*
1951101	*U. maritimus*
11089	*U. thibetanus*

3247	*U. thibetanus*
2446	*U. thibetanus*
114544	*U. thibetanus*
87411	*U. thibetanus*
57076	*U. thibetanus*
119476	*U. thibetanus*
45293	*U. thibetanus*
19511013	*U. thibetanus*
110457	*U. thibetanus*
45	*U. ingressus*
21	*U. ingressus*
Mix3	*U. ingressus*
Mix3	*U. ingressus*
22UVIP	*U. ingressus*
Gs524	*U. ingressus*
5022	*U. ingressus*
5022	*U. ingressus*
2029NNB	*U. sp. spelaeus*
2029NNB	*U. sp. spelaeus*
5017MNB	*U. sp. spelaeus*
5017MNB	*U. sp. spelaeus*
5019	*U. sp. spelaeus*
BC4(02)	*U. sp. ladinicus*
CV704	*U. sp. ladinicus*
CV703	*U. sp. ladinicus*
714	*U. sp. ladinicus*
SW483	*U. sp. eremus*
SW630C	*U. sp. eremus*
Sw512	*U. sp. eremus*
Sw512	*U. sp. eremus*
2724	*U. sp. eremus*

Table 2. Raw values for the OPCR, DNE, RFI, and OA (outline areas) obtained for the upper P4-M2 dental series in living and extinct bears analysed in **chapter 3.2.**

Species	DNE	RFI	OPCR	OA
A. melanoleuca	893.506	1.569	344.625	1567.923
A. melanoleuca	1168.242	1.729	350.75	1488.595
A. melanoleuca	1152.285	1.752	355.625	1635.781
A. melanoleuca	1095.186	1.671	349.25	1556.732
A. melanoleuca	1454.857	1.873	379.375	1686.206
A. melanoleuca	963.965	1.57	345.25	1674.489
H. malayanus	499.952	2.119	143.25	419.742
H. malayanus	440.948	1.849	164.25	425.337
H. malayanus	459.946	1.816	168.5	414.587
H. malayanus	282.055	1.617	122.625	362.908
H. malayanus	541.504	1.865	194.75	397.385
H. malayanus	495.998	1.814	178.125	528.36
H. malayanus	572.041	1.905	166	546.824
H. malayanus	442.847	1.783	151.75	524.851
H. malayanus	544.304	1.943	173.5	368.97
H. malayanus	527.912	1.857	165.125	440.106
H. malayanus	492.871	1.92	181.125	411.974
M. ursinus	452.962	1.891	166.375	426.614
M. ursinus	365.284	1.88	140.25	406.088
M. ursinus	493.198	1.9	161.875	387.238
M. ursinus	348.613	1.59	171.375	421.445
M. ursinus	353.074	1.657	149.125	391.297
M. ursinus	453.654	1.661	207.375	538.56
M. ursinus	369.05	1.473	203.625	543.636
M. ursinus	438.853	1.705	177	523.315
T. ornatus	349.797	1.643	164.5	553.379
T. ornatus	320.408	1.711	143.25	512.899
T. ornatus	398.128	1.916	170.25	542.132
T. ornatus	372.898	1.694	155.625	524.728

T. ornatus	355.237	1.694	166.125	450.782
T. ornatus	404.063	1.786	175.5	483.717
T. ornatus	302.692	1.575	158.875	564.48
U. americanus	296.279	1.587	147.625	598.882
U. americanus	332.701	1.612	127.375	566.663
U. americanus	324.374	1.672	122.375	629.059
U. americanus	376.413	1.69	165.5	551.806
U. americanus	355.856	1.788	143.625	561.889
U. americanus	354.388	1.748	152.5	525.977
U. americanus	512.056	1.809	211.25	1043.81
U. arctos arctos	599.809	1.976	213.25	826.048
U. arctos arctos	483.592	1.898	173.75	716.965
U. arctos arctos	446.221	1.744	194.875	1052.714
U. arctos arctos	704.158	1.92	271.125	1219.741
U. arctos gyas	750.856	1.928	237	1029.254
U. arctos horribilis	623.729	1.821	220.125	1183.294
U. arctos horribilis	540.103	1.745	197.875	782.314
U. arctos middendorffi	616.546	1.897	219.75	1152.751
U. arctos pruinosus	673.609	1.843	267.625	1263.021
U. arctos sitkensis	658.831	1.951	221	974.958
U. arctos sitkensis	521.841	1.639	214.25	794.663
U. arctos sitkensis	547.93	1.813	221	679.915
U. maritimus	553.399	1.929	167.625	589.962
U. maritimus	565.582	2.034	187.875	581.604
U. maritimus	501.484	1.785	198.125	766.406
U. maritimus	549.21	1.855	197.375	682.78
U. maritimus	555.318	1.799	202.5	665.831
U. maritimus	476.227	2.05	159.625	582.276
U. maritimus	464.717	1.801	181.25	581.869
U. maritimus	481.091	1.807	191.375	577.246
U. maritimus	533.546	1.946	189.875	569.221
U. maritimus	476.541	1.833	176.625	646.043
U. maritimus	566.951	1.853	196.875	681.614

U. thibetanus	459.865	1.738	177	626.558
U. thibetanus	392.14	1.701	156.625	542.919
U. thibetanus	555.185	1.858	179.75	676.013
U. thibetanus	510.966	1.58	200.25	692.293
U. thibetanus	517.199	1.632	181.875	546.001
U. thibetanus	428.946	1.46	193.125	681.39
U. thibetanus	504.491	1.777	179.75	646.769
U. thibetanus	602.024	1.71	216.125	655.377
U. thibetanus	544.523	1.629	240.5	745.283
U. thibetanus	430.443	1.582	197.5	660.215
U. ingressus	505.197	1.628	254.25	1466.478
U. ingressus	729.719	1.708	268.875	1773.018
U. ingressus	771.62	1.626	337.125	1479.376
U. ingressus	832.462	1.867	326.625	1533.575
U. ingressus	684.83	1.718	278.875	1939.158
U. ingressus	665.709	1.609	277	1587.788
U. ingressus	675.464	1.756	280.5	1479.771
U. ingressus	727.752	1.727	295.75	1520.264
U. sp. spelaeus	825.135	1.846	304	1343.03
U. sp. spelaeus	1054.708	2.189	305.375	1269.45
U. sp. spelaeus	840.101	1.887	314.5	1400.504
U. sp. spelaeus	884.659	1.887	309.75	1454.197
U. sp. spelaeus	717.024	1.847	297.5	1518.591
U. sp. ladinicus	896.005	1.713	336.625	1365.888
U. sp. ladinicus	887.952	1.836	348.875	1574.859
U. sp. ladinicus	790.12	1.763	323.625	1644.853
U. sp. ladinicus	843.686	1.868	303.125	1563.973
U. sp. eremus	822.369	1.776	299.125	1606.266
U. sp. eremus	655.692	1.702	296.375	1389.706
U. sp. eremus	613.15	1.71	252.625	1682.039
U. sp. eremus	682.87	1.801	271.5	1670.071
U. sp. eremus	868.305	2.727	222.125	1151.895